



**HAL**  
open science

/  
Qaiser Sultan

► **To cite this version:**

Qaiser Sultan. /. Other. ISAE-ENSMA Ecole Nationale Supérieure de Mécanique et d'Aérotechnique - Poitiers, 2011. English. NNT: . tel-00640968

**HAL Id: tel-00640968**

**<https://theses.hal.science/tel-00640968>**

Submitted on 14 Nov 2011

**HAL** is a multi-disciplinary open access archive for the deposit and dissemination of scientific research documents, whether they are published or not. The documents may come from teaching and research institutions in France or abroad, or from public or private research centers.

L'archive ouverte pluridisciplinaire **HAL**, est destinée au dépôt et à la diffusion de documents scientifiques de niveau recherche, publiés ou non, émanant des établissements d'enseignement et de recherche français ou étrangers, des laboratoires publics ou privés.

---

# THÈSE

Pour l'obtention du grade de

## DOCTEUR DE L'ÉCOLE NATIONALE SUPÉRIEURE DE MÉCANIQUE ET D'AÉROTECHNIQUE DE POITIERS

(Diplôme National - Arrêté du 7 août 2006)

Ecole doctorale: Sciences pour l'Ingénieur et Aéronautique

Secteur de recherche : Mécanique des milieux fluides et Energie, Thermique, Combustion

Présenté par

**Qaiser SULTAN**

---

### CARACTÉRISATION EXPÉRIMENTALE AÉROTHERMIQUE D'UN JET PULSÉ DÉBOUCHANT DANS UN ÉCOULEMENT TRANSVERSAL: INFLUENCE DU NOMBRE DE STROUHAL D'EXCITATION SUR LE REFROIDISSEMENT DE PAROI PAR FILM.

---

Directeur de thèse : **Éva DORIGNAC**

Co-Directeur : **Gildas LALIZEL**

Soutenue le 15 Septembre 2011

Devant la Commission d'Examen

### JURY

Mme. PATTE-ROULAND	Professeur à l'Université de Rouen, CORIA, Rouen	Rapporteur
M. ARTS	Professeur à l'institut Von Karman, Bruxelles	Rapporteur
M. OULD EL MOCTAR	Maître de conférences à Polytech, Nantes	Examineur
M. LAROCHE	Ingénieur de recherche à l'ONERA, Toulouse	Examineur
M. BOREE	Professeur à l'ENSMA, Institut P <sup>2</sup> , Poitiers	Examineur
M. LEMONNIER	Directeur de recherche CNRS, Institut P <sup>2</sup> , Poitiers	Examineur
Mme. DORIGNAC	Professeur à l'Université de Poitiers, institut P <sup>2</sup> , Poitiers	Examineur
M. LALIZEL	Maître de conférences à l'ENSMA, institut P <sup>2</sup> , Poitiers	Examineur

---



## **Acknowledgement**

I want to express my deepest gratitude to my supervisor Mrs. Eva DORIGNAC and my co-supervisor Mr. Gildas LALIZEL, who were a constant source of knowledge, guidance and encouragement during my PhD.

I am also most grateful to Mr. Jean Louis TUHAULT and his group members for providing the technical assistance required to actualize the experimental facility as well as the calibration of various measurement systems.

I wish to thank my present and former colleagues and other staff in the department for their continuous support and encouragement throughout the duration of my thesis.

Qaiser SULTAN



---

# Synthèse

## 1. Introduction

Les moteurs aéronautiques sont assujettis à des contraintes thermiques de plus en plus importantes pour satisfaire les normes de pollutions ( $\text{CO}_2$ ,  $\text{NO}_x$ , sonores...) actuelles et futures. Deux types de refroidissement aérothermiques sont particulièrement utilisés actuellement: l'impact de jet et le refroidissement par film froid ou "film cooling". L'impact de jet consiste en une interaction entre un fluide froid et une structure dont la face opposée est soumise à des très hautes températures. Cette technique peut être utilisée lorsque les épaisseurs de matières permettent des résistances thermiques suffisamment faibles pour que les échanges convectifs face arrière permettent un refroidissement efficace en face avant. Cette technique est principalement utilisée pour le refroidissement des aubes de turbines des moteurs. Dans le cas où le refroidissement en face arrière n'est pas suffisant, on privilégiera le "film cooling". Cette technique consiste à générer un film d'air frais sur la surface à refroidir. Pour cela, la paroi est percée d'une ou de multiples rangées de trous par lesquels s'écoulent le fluide frais.

De nombreuses études se sont intéressées à étudier l'influence de la géométrie sur l'efficacité de refroidissement (design des trous d'injection, Sargison et al. (2002), positionnement des rangées de trous, Sinha et al. (1991), Ligrani et al. (1992), Ligrani et al. (1997), le taux de soufflage optimal (Eckert (1970), Yuen and Martinez-Botas (2003), Goldstein and Eckert (1974)).

Quelques études aérodynamiques ont porté sur les interactions entre l'écoulement principal et l'écoulement de soufflage, Walters et Leylek (2000), Mendez et Nicoud (2006). Le comportement instationnaire rencontré à l'intérieur des turbines et leurs impacts sur le refroidissement ont été étudiées par Ligrani et al. (1996), Ligrani et al. (1997) and Seo et al. (1998) en imposant un mouvement périodique à l'ensemble de l'écoulement en aval de veine.

Le concept d'écoulement de refroidissement pulsé a été abordé très récemment par Muldoon and Acharya (2009), Coulthard et al. (2007) et Kartuzova et al. (2009). Ces études, principalement thermiques, ont montré qu'à certaines fréquences d'excitation de l'écoulement soufflé, les échanges thermiques à la paroi pouvaient être diminués en maintenant un débit moyen constant. Toutefois, ces études ne permettent pas de comprendre ni de relier les phénomènes aérodynamiques instationnaires aux échanges de chaleur à la paroi. Ces résultats ont ainsi motivé cette étude expérimentale, consistant à la fois à la caractérisation des phénomènes instationnaires aérodynamiques et le mesure des transferts de chaleur à la paroi entre un jet chaud pulsé à nombre de Strouhal variable et un écoulement transverse.

## 2. Description du dispositif expérimental et des diagnostics de mesures aérodynamiques et thermiques

Tous les essais ont été réalisés dans une soufflerie thermo-régulée de section carré de 300 mm de coté. L'écoulement est maintenu à une température de 20 °C et à une vitesse

constante de 7.7 m/s ou 10 m/s. L'étude des couches limites à permis de positionner le trou d'injection à une distance permettant d'avoir un rapport  $\delta/d=1$ , où  $\delta$  représente l'épaisseur de la couche limite et  $d$  est le diamètre du tube générant l'écoulement secondaire ( $d=13$  mm). La valeur de ce rapport  $\delta/d$  permettra de comparer nos résultats à ceux des publications précédentes. L'angle d'inclinaison entre le jet secondaire et la paroi d'essai est de 30°.

Dans la réalité, l'écoulement secondaire est l'écoulement froid. Dans notre cas, nous avons appliqué l'inverse: l'écoulement secondaire est chauffé (40 et 60 °C) à l'aide d'une résistance chauffante et l'écoulement principal est froid. Ceci n'a pas d'influence sur l'aérodynamique des écoulements puisque nous sommes en régime de convection forcée (nombre de Richardson  $\ll 1$ , donc l'énergie de flottabilité est très faible devant l'énergie cinétique des écoulements). La vitesse de l'écoulement secondaire est calculée de telle sorte que les taux de soufflage ( $\overline{M} = \rho_i \overline{U}_i / \rho_\infty \overline{U}_\infty$ ) soient égaux à 0.65, 1 et 1.25.

L'écoulement secondaire est pulsé à l'aide d'un haut parleur situé au fond d'une buse d'injection. Les tensions d'alimentation du HP ont été calibrées de telle sorte que quelles que soit les fréquences d'excitation, l'amplitude de fluctuation de la vitesse en sortie de buse soit constante (avec une variation maximale de 14%) quel que soit le taux de soufflage  $\overline{M}$ . Les fréquences d'excitations sont choisies pour étudier des nombres de Strouhal (St) égaux 0, 0.2, 0.3 et 0.5.

$\overline{U}_\infty$ (m/s)	$Re_i = \overline{U}_\infty \cdot \delta / \nu$	$Re_i = \overline{U}_i \cdot d / \nu$	$\rho_i / \rho_\infty$	$\overline{M} = \rho_i \overline{U}_i / \rho_\infty \overline{U}_\infty$	St
10	8609	5596 / 8437	0.93 / 1	0.65 / 1	0, 0.2, 0.3, 0.5
7.7	6165	8220	0.93 / 1	1.25	0, 0.2, 0.3, 0.5

Table-1 : Description de conditionnement du travail.

Les mesures de vitesses sont réalisées à l'aide d'un système de Vélocimétrie par Image de Particules Résolue en Temps (TR-PIV) pour toutes les fréquences d'excitation et pour tous les taux de soufflage. Ensuite, une moyenne de phase est appliquée, ce pour représenter sur une période d'excitation les variations moyennes de l'écoulement. Environ une dizaine de temps sont utilisés pour représenter une période. Pour chaque point de la période, au moins 300 champs de vitesses sont utilisés. La taille de la fenêtre de calcul PIV est de 12\*12 pixels<sup>2</sup>, avec un recouvrement de 50 %. Ainsi, 3 champs de vitesse sont utilisés pour spatialement caractériser l'écoulement compris entre  $x/d=-1$  à 6.5 et  $y/d=0$  à 2.6. Ce champ de mesure permet de caractériser les différentes zones caractéristiques de l'écoulement: la couche de mélange externe entre le jet principal et le jet secondaire, la couche de mélange interne et la zone de sillage générée en aval de l'écoulement secondaire.

Les températures dans le fluide sont spatialement et temporellement étudiées à partir de thermométrie fil froid. La fréquence d'acquisition des températures est de 2 kHz et le nombre d'échantillons de température par point de mesures est de 32000 points. Cette fréquence est possible parce que le diamètre de la sonde fil froid est de 2.5  $\mu\text{m}$ .

Les coefficients d'échanges et la température adiabatique sont déterminés à partir d'une mesure infrarouge de la paroi. Cette méthode, appelée méthode des quatre flux, a été

---

développés par Fénot et al. (2005), et permet de déterminer très précisément les coefficients d'échanges (erreur inférieure à 6%). Les cartographies de température de la surface comprises entre  $x/d=-4.5$  à  $32.4$  et  $z/d=-3$  à  $3$ .

### 3. Caractérisations expérimentales des conditions limites aérodynamiques et thermiques de la soufflerie et la buse d'injection

Les profils de vitesses et d'écart-types ont été mesurés à la fois par LDV-1D (mesurer très proche paroi) pour déterminer la nature et l'épaisseur de la couche limite pariétale et par fil chaud pour entreprendre une étude spectrale, sans la présence de l'écoulement principal. Les profils de la vitesse longitudinale moyenne sont en très bon accord avec les résultats de DNS de Kim et al. (1987) et montrent que la couche limite est turbulente. Hors de la couche limite, l'écoulement est parfaitement homogène et constitue une faible intensité turbulente (<1.2%). Les évolutions des différentes échelles de turbulence (échelle intégrale, échelle de Taylor et échelle de Kolmogorov) ont également été déterminées à l'intérieur de la couche limite. Les densités spectrales de puissance de la fluctuation de vitesse ont montré que, hors de la couche limite, apparaît un pic dont la fréquence semble proportionnelle à la vitesse de rotation des pâles du moteur de la soufflerie. Ces fréquences sont de l'ordre du kHz.

### 4. Résultats aérodynamiques

Les résultats aérodynamiques sont issus des mesures de TR-PIV. Les résultats sont toujours présentés de la façon suivante : grandeur moyennée en temps puis grandeur moyennée par phase. Les résultats ont été mesurés pour des taux de soufflage  $\overline{M}=0.65, 1$  et  $1.25$  et pour un rapport de température égal à un.

Dans un premier temps, les variations des vitesses longitudinales et transversales, des fonctions densités de probabilités des vitesses, des termes du tenseur de Reynolds (écart types de  $u$  et  $v$ , ainsi que de la corrélation  $\overline{uv}$ ), le tenseur des gradient de vitesse pour caractériser les taux de déformations (cisaillement et étirement) et la vorticit  ont  t  calcul s. Enfin, les termes accessibles des  quations de la quantit  de mouvement et de l' nergie ont  t  d termin s.

Ces r sultats permettent de caract riser les diff rentes zones d'instabilit s se d veloppant dans l' coulement : les zones de m lange externe et interne, la zone de sillage ainsi que les instabilit s de paroi.

Les r sultats ont montr  que la pulsation n'a pas d'influence pour  $\overline{M}=0.65$ . Pour  $\overline{M}=1$ , on observe pour une grande valeur de pulsation ( $St=0.3$ ) une am lioration moyenne du recouvrement   la paroi, le jet d bouchant recolle   la paroi. Pour  $\overline{M}=1.25$ , on observe  galement ce ph nom ne pour  $St=0.2$  et  $0.3$ . Dans ces cas, la pulsation r duit les gradients moyens de vitesses dans la couche de m lange. La diminution du gradient de vitesse amenuise l'impact des paires de tourbillons contrarotatifs (CVP). Ainsi, l'entrainement de l' coulement principal et le ph nom ne de m lange avec le jet diminue par rapport au cas non puls . La variation p riodique de la trajectoire du jet permet un recouvrement plus

---

important de la paroi lorsque le taux de soufflage instantané est inférieur au taux de soufflage moyen.

## 5. Résultats thermiques

### Transfert de chaleur à la paroi

Les champs de température moyenne de la paroi ont été mesurés à partir de thermographie infrarouge en chauffant la paroi d'essai selon 4 flux de puissance injectés par effet Joule à la paroi. Cette technique a été utilisée pour déterminer les distributions spatiales des coefficients d'échanges convectifs à la paroi  $h$  ainsi que les champs d'efficacité thermique  $\eta$ , pour des taux de soufflage  $\overline{M} = 0.65, 1$  et  $1.25$  et des nombres de Strouhal d'excitation  $St = 0, 0.2, 0.3$  et  $0.5$ . De plus, la température de l'écoulement secondaire a été réglée à  $T_i = 20$  et  $40$  °C.

Afin de tester le dispositif expérimental, nous avons dans un premier temps comparé les distributions de  $h$  et de  $\eta$  avec des résultats de la littérature dans le cas où l'excitation acoustique est nulle,  $St = 0$ . Ces comparaisons, confrontées aux différences des paramètres aérothermiques des différentes expériences de la littérature valident le montage expérimental et la technique de mesure utilisée pour cette configuration.

Dans un second temps, une analyse des effets de la pulsation de l'écoulement injecté sur les échanges thermiques est proposée pour les taux de soufflage  $\overline{M} = 0.65, 1$  et  $1.25$  et les nombres de Strouhal  $St = 0, 0.2, 0.3$  et  $0.5$ . Trois paramètres sont présentés pour cette étude thermique :

- L'efficacité de film :  $\eta = (T_{ad} - T_{\infty}) / (T_i - T_{\infty})$
- Le rapport des coefficients d'échange  $h/h_0$ , où le coefficient  $h_0$  correspond au cas sans injection.
- La réduction net de flux de chaleur (NHFR):  $NHFR = 1 - h/h_0(1 - \eta\theta)$ , où  $\theta = (T_i - T_{\infty}) / (T_w - T_{\infty})$ .

Ce troisième paramètre est une combinaison des deux premiers et permet une présentation globale du problème de refroidissement. Les variations de ces paramètres sont données soit sous forme de cartes suivant le plan  $(x/d, z/d)$  ; soit sous forme de courbes suivant la direction  $x/d$  pour la ligne centrale  $y/d = 0$  ou pour zone latérale moyennée de  $z/d = 0$  à  $1.5$ .

Il est constaté que globalement l'efficacité ainsi que le rapport des coefficients d'échange diminuent le long de la paroi lorsque le nombre de Strouhal augmente quel que soit le taux de soufflage. Toutefois, il est à noter que pour le cas  $\overline{M} = 1$  et  $\overline{M} = 1.25$  l'optimum obtenu tant pour l'efficacité que pour le rapport des coefficients d'échange a lieu lorsque  $St = 0.3$ . Le paramètre NHFR confirme ces remarques.

### Mesures de température dans le fluide

Pour étudier l'interaction entre l'écoulement principal et l'écoulement pulsé injecté, une campagne de mesure de température dans le fluide a été effectuée à l'aide d'un fil froid par apport deux plans transversales ( $z/d = 0$  et  $z/d = 1.5$ ). Les conditions expérimentales relatives

---

aux taux de soufflage et aux nombres de Strouhal sont les mêmes que pour les cas des mesures précédents. La température de l'écoulement secondaire a été réglée à  $T_i=40$  °C. De ces mesures, il a été possible d'extraire les températures moyennes, les fluctuations de température et les moments d'ordre 3 (facteur de symétrie) et 4 (coefficient d'aplatissement).

Les résultats de ces mesures conduisent aux mêmes remarques que celles faites à l'aide des mesures pariétales, les cas permettant un meilleur refroidissement de paroi sont les cas de pulsation  $St = 0.2$  et  $St = 0.3$  pour les taux de soufflage  $\overline{M} = 1$  et  $\overline{M} = 1,25$ . En particulier, sur l'axe  $z/d = 0$ , on peut noter une meilleure performance du film de refroidissement, pour le taux de soufflage  $\overline{M} = 1$  et pour le cas de pulsation  $St = 0,2$  du fait de la présence de l'écoulement injecté en proche paroi. Par contre, sur l'axe  $z/d = 1,5$ , il semble que ce soit les cas  $St = 0.2$  et  $0.3$  qui provoquent un meilleur refroidissement. En effet, à cette pulsation, l'élargissement de l'écoulement injecté est plus important. Enfin, pour le taux de soufflage  $\overline{M} = 0,65$ , l'effet de pulsation amène une dégradation de l'efficacité du refroidissement.



---

# Table of Contents

---

## ***Chapter 1: INTRODUCTION***

<a href="#">1.1</a>	<a href="#">Scientific and industrial context</a> .....	2
<a href="#">1.2</a>	<a href="#">Techniques for material protection</a> .....	3
<a href="#">1.2.1</a>	<a href="#">Materials</a> .....	4
<a href="#">1.2.2</a>	<a href="#">Thermal barrier coating</a> .....	5
<a href="#">1.2.3</a>	<a href="#">Cooling with air injection</a> .....	5
<a href="#">1.2.3.1</a>	<a href="#">Internal cooling</a> .....	6
<a href="#">1.2.3.2</a>	<a href="#">External cooling</a> .....	7
<a href="#">1.3</a>	<a href="#">Flow field unsteadiness of gas turbine engine</a> .....	8
<a href="#">1.4</a>	<a href="#">Organization of the manuscript</a> .....	8
<a href="#">1.5</a>	<a href="#">References:</a> .....	11

## ***Chapter 2: BIBLIOGRAPHICAL REVIEW***

<a href="#">2.1.</a>	<a href="#">Definition of Jet-in-crossflow</a> .....	16
<a href="#">2.2.</a>	<a href="#">Description of the aerodynamics of a jet in crossflow</a> .....	16
<a href="#">2.2.1</a>	<a href="#">Flow field at low Reynolds number flow</a> .....	17
<a href="#">2.2.2</a>	<a href="#">Flow field at high Reynolds number flow</a> .....	18
<a href="#">2.2.3</a>	<a href="#">Development of the flow field in the wake region</a> .....	20
<a href="#">2.2.4</a>	<a href="#">Shedding frequency of wake structures</a> .....	21
<a href="#">2.2.5</a>	<a href="#">Influence of a slightly heated jet on the JICF</a> .....	22
<a href="#">2.3.</a>	<a href="#">Description of aerodynamic and heat transfer of an inclined Jet in crossflow applied to film cooling</a> .....	23
<a href="#">2.3.1</a>	<a href="#">Aerodynamic description</a> .....	23
<a href="#">2.3.2</a>	<a href="#">Thermal description</a> .....	26
<a href="#">2.3.2.1</a>	<a href="#">Fundamental parameters of film cooling analysis</a> .....	26
<a href="#">2.3.2.2</a>	<a href="#">Geometrical parameters</a> .....	27
<a href="#">2.3.2.3</a>	<a href="#">Influence of aerodynamic parameters on wall heat transfer</a> .....	31
<a href="#">2.4.</a>	<a href="#">Application of periodic velocity boundary limit on flow structure and wall heat transfer</a> .....	36
<a href="#">2.4.1</a>	<a href="#">Flow from a submerged pulsating jet</a> .....	36
<a href="#">2.4.2</a>	<a href="#">Effect of turbine flow unsteadiness on film cooling</a> .....	37
<a href="#">2.4.2.1</a>	<a href="#">Characterization of turbine unsteadiness through bulk flow pulsation</a> .....	38
<a href="#">2.4.2.2</a>	<a href="#">Characterization of turbine unsteadiness through injectant flow pulsation</a> .....	39
<a href="#">2.4.2.3</a>	<a href="#">Influence of jet Strouhal number pulsation on film cooling effectiveness</a> .....	40
<a href="#">2.5.</a>	<a href="#">Conclusion</a> .....	45
<a href="#">2.6.</a>	<a href="#">References</a> .....	47

## ***Chapter 3: EXPERIMENTAL SETUP AND MEASURING TECHNIQUES***

<a href="#">3.1</a>	<a href="#">Frame work of experimental measurement</a> .....	55
<a href="#">3.2</a>	<a href="#">Principle hardware components</a> .....	57
<a href="#">3.2.1</a>	<a href="#">Wind tunnel</a> .....	57
<a href="#">3.2.1.1</a>	<a href="#">Test section</a> .....	57
<a href="#">3.2.1.2</a>	<a href="#">Injection plate</a> .....	58
<a href="#">3.2.2</a>	<a href="#">Injection Flow System</a> .....	59
<a href="#">3.2.2.1</a>	<a href="#">Measurement of injection mass flow rate</a> .....	60
<a href="#">3.2.2.2</a>	<a href="#">Heating system for injectant flow</a> .....	61

3.2.2.3	<a href="#">Injectant temperature regulation system</a>	61
3.2.2.4	<a href="#">Pulse generation system</a>	62
3.3	<a href="#">Velocity measurement systems</a>	66
3.3.1	<a href="#">Laser Doppler Anemometry</a>	67
3.3.1.1	<a href="#">Descriptions of the measurement scenario</a>	67
3.3.1.2	<a href="#">Experimental conditions for LDV measurements</a>	67
3.3.1.3	<a href="#">Working principle</a>	68
3.3.2	<a href="#">Hot wire Anemometer</a>	69
3.3.2.1	<a href="#">Descriptions of the measurement scenario</a>	69
3.3.2.2	<a href="#">Experimental conditions for hot wire measurements</a>	70
3.3.2.3	<a href="#">Working principle</a>	71
3.3.3	<a href="#">Statistical errors in LDV and hot wire measurements</a>	72
3.3.4	<a href="#">Time Resolved Particle Image Velocimetry</a>	73
3.3.4.1	<a href="#">Descriptions of the measurement scenario</a>	73
3.3.4.2	<a href="#">Experimental conditions for TR-PIV measurements</a>	75
3.3.4.3	<a href="#">Fundamentals of PIV system</a>	77
3.3.4.4	<a href="#">Spatial resolution of PIV system</a>	77
3.3.4.5	<a href="#">Statistical errors in TR-PIV measurements</a>	78
3.4	<a href="#">Thermal measurements of film cooling configuration</a>	79
3.4.1	<a href="#">Infra-red thermography</a>	79
3.4.1.1	<a href="#">Descriptions of the measurement scenario</a>	79
3.4.1.2	<a href="#">Experimental conditions for TR-PIV measurements</a>	83
3.4.1.3	<a href="#">Injection wall heat dissipation system</a>	83
3.4.1.4	<a href="#">Infra-red camera</a>	84
3.4.1.5	<a href="#">Surface temperature map (without flow)</a>	85
3.4.2	<a href="#">Cold wire measurement</a>	86
3.4.2.1	<a href="#">Descriptions of the measurement scenario</a>	86
3.4.2.2	<a href="#">Experimental conditions for cold wire measurements</a>	87
3.4.2.3	<a href="#">Working principle</a>	87
3.5	<a href="#">Data treatments</a>	88
3.5.1	<a href="#">Phase average description of the flow</a>	88
3.5.2	<a href="#">Turbulence description of the flow</a>	90
3.5.3	<a href="#">Convective heat transfer coefficient and adiabatic wall temperature</a>	94
3.5.3.1	<a href="#">Heat transfer Models</a>	94
3.5.3.2	<a href="#">Steady state heat transfer model</a>	97
3.5.3.3	<a href="#">Convective heat flux</a>	98
3.5.4	<a href="#">Phase averaged description of the temperature field</a>	99
3.5.5	<a href="#">Thermal uncertainties</a>	100
3.6	<a href="#">Reference</a>	103

#### **Chapter 4: CHARACTERIZATION OF UPSTREAM FLOWS**

4.1	<a href="#">Velocity characterization of wind tunnel flow</a>	109
4.1.1	<a href="#">Evolution of mean and rms velocities</a>	109
4.1.2	<a href="#">Viscous scales</a>	111
4.1.3	<a href="#">Comparison of velocity profiles</a>	113
4.1.4	<a href="#">Turbulence intensity</a>	113
4.2	<a href="#">Description of turbulence scales and energy spectra</a>	114
4.2.1	<a href="#">Energy spectrum</a>	114
4.2.2	<a href="#">Turbulence length scale</a>	117

4.3	<a href="#">Temperature description of the wind tunnel flow</a>	119
4.4	<a href="#">Characterization of injectant flow</a>	121
4.4.1	<a href="#">Velocity profiles at the hole exit</a>	121
4.4.2	<a href="#">Characterization of pulsation amplitude</a>	123
4.5	<a href="#">Energy spectra</a>	125
4.6	<a href="#">Comparisons of baseline results</a>	126
4.7	<a href="#">Conclusion</a>	127
4.8	<a href="#">Reference</a>	131

**Chapter 5: STUDY OF THE FILM-COOLED BOUNDARY LAYER FLOW AERODYNAMICS**

5.1	<a href="#">Structure involved in the flow dynamics</a>	133
5.2	<a href="#">Velocity field</a>	137
5.2.1	<a href="#">Time-averaged velocity</a>	137
5.2.2	<a href="#">Phase-averaged velocity results</a>	141
5.3	<a href="#">Velocity probability density function (PDF)</a>	144
5.4	<a href="#">Turbulent description, tensor of Reynolds stresses</a>	147
5.4.1	<a href="#">Time-averaged normal stresses</a>	147
5.4.2	<a href="#">Time-averaged shear stresses</a>	151
5.4.3	<a href="#">Phase-averaged shear stresses</a>	153
5.4.4	<a href="#">Ratio of phase-averaged rms-velocity components</a>	155
5.4.5	<a href="#">Phase-averaged turbulent intensity</a>	157
5.5	<a href="#">Tensor of velocity gradient</a>	158
5.5.1	<a href="#">Time-averaged vorticity</a>	158
5.5.2	<a href="#">Phase-averaged vorticity</a>	161
5.5.3	<a href="#">Time-averaged rate of deformation</a>	162
5.6	<a href="#">Vortex identification</a>	164
5.7	<a href="#">Mass, momentum and energy conservation</a>	170
5.7.1	<a href="#">Balance of mass (Continuity equation)</a>	170
5.7.2	<a href="#">Balance of momentum</a>	171
5.7.2.1	<a href="#">Terms of momentum equation, time-averaged results</a>	172
5.7.2.2	<a href="#">Convection subterm, phase-averaged results</a>	175
5.7.3	<a href="#">Balance of energy</a>	176
5.7.3.1	<a href="#">Terms of Energy equation, time-averaged results</a>	177
5.7.3.2	<a href="#">Time-averaged turbulent kinetic energy</a>	181
5.7.3.3	<a href="#">Phase-averaged production of kinetic energy</a>	183
5.7.3.4	<a href="#">Phase-averaged energy dissipation rate</a>	184
5.7.3.5	<a href="#">Ratio of time-averaged Production and dissipation (<math>P_k/\epsilon_k</math>)</a>	185
5.8	<a href="#">Conclusion</a>	186
5.9	<a href="#">References</a>	189

**Chapter 6: STUDY OF WALL HEAT TRANSFER IN FILM-COOLED BOUNDARY LAYER FLOW**

6.1	<a href="#">Steady blowing (No pulsation)</a>	196
6.2	<a href="#">Unsteady blowing (with pulsation)</a>	199
6.2.1	<a href="#">Case-A</a>	199
6.2.2	<a href="#">Case-B</a>	201
6.2.3	<a href="#">Case-C</a>	202
6.2.4	<a href="#">Case-D</a>	204

6.2.5	<u>Case-E</u> .....	205
6.2.6	<u>Case-F</u> .....	205
6.3	<u>Centerline and laterally-averaged effectiveness</u> .....	206
6.4	<u>Centerline and laterally-averaged heat transfer coefficient</u> .....	207
6.5	<u>Comparison of results</u> .....	210
6.6	<u>Spatially-averaged effectiveness and heat transfer coefficient</u> .....	212
6.7	<u>Net heat flux reduction (NHFR)</u> .....	213
6.8	<u>Conclusion</u> .....	216
6.9	<u>References</u> .....	217

**Chapter 7: STUDY OF THE FILM-COOLED BOUNDARY LAYER FLOW**

**TEMPERATURE**

7.1	<u>Validation of cold wire thermometry to measure fluctuating temperature distribution</u> .....	221
7.2	<u>Temperature distribution in the central plane (<math>z/d=0</math>)</u> .....	226
7.2.1	<u>Comparison of the cases of different blowing ratio (steady blowing)</u> .....	226
7.2.2	<u>Comparison of the cases of different Strouhal numbers</u> .....	227
7.3	<u>Temperature distribution at off-centre plane (<math>z/d=1.5</math>)</u> .....	234
7.3.1	<u>Comparison of the cases of different blowing ratio (steady blowing)</u> .....	235
7.3.2	<u>Comparison of the cases of different Strouhal numbers</u> .....	236
7.4	<u>Skewness and flatness factor</u> .....	242
7.5	<u>Conclusion</u> .....	245
7.6	<u>References</u> .....	247

**Chapter 8: CONCLUSION**

8.1	<u>Conclusion</u> .....	249
8.2	<u>Perspective</u> .....	251

<u>ANNEXURE-A</u> .....	253
<u>ANNEXURE-B</u> .....	259
<u>ANNEXURE-C</u> .....	265
<u>ANNEXURE-D</u> .....	267
<u>ANNEXURE-E</u> .....	279





# Table of Contents

---

- 1.1 Scientific and industrial context ..... 2
- 1.2 Techniques for material protection..... 3
  - 1.2.1 Materials ..... 4
  - 1.2.2 Thermal barrier coating ..... 5
  - 1.2.3 Cooling with air injection..... 6
    - 1.2.3.1 Internal cooling ..... 6
    - 1.2.3.2 External cooling ..... 7
- 1.3 Flow field unsteadiness of gas turbine engine..... 8
- 1.4 Organization of the manuscript ..... 8
- 1.5 References: ..... 11

## ***INTRODUCTION***

The gas turbines have been a principal propulsion source for military and civil aircraft for the past 50 years (Penner et al., 1996). Modern gas turbine systems are the great example of highly complex, efficient and compact propulsion machines, figure (1.1). The ultimate goal of the turbine manufacturers is to minimize the total fuel burned per unit of payload, noise, NO<sub>x</sub> and to optimize the reliability. Generally, the basic computation involves engine weight, aerodynamic drag, and their effect on the total fuel required to complete a flight mission. A reduction of one unit of total engine weight translates to a reduction of between 1.5 and 4 units of aircraft empty weight, (Penner et al., 1996). An efficient propulsion system with state of the art cooling mechanism could provide large output from a relatively light and compact engine.

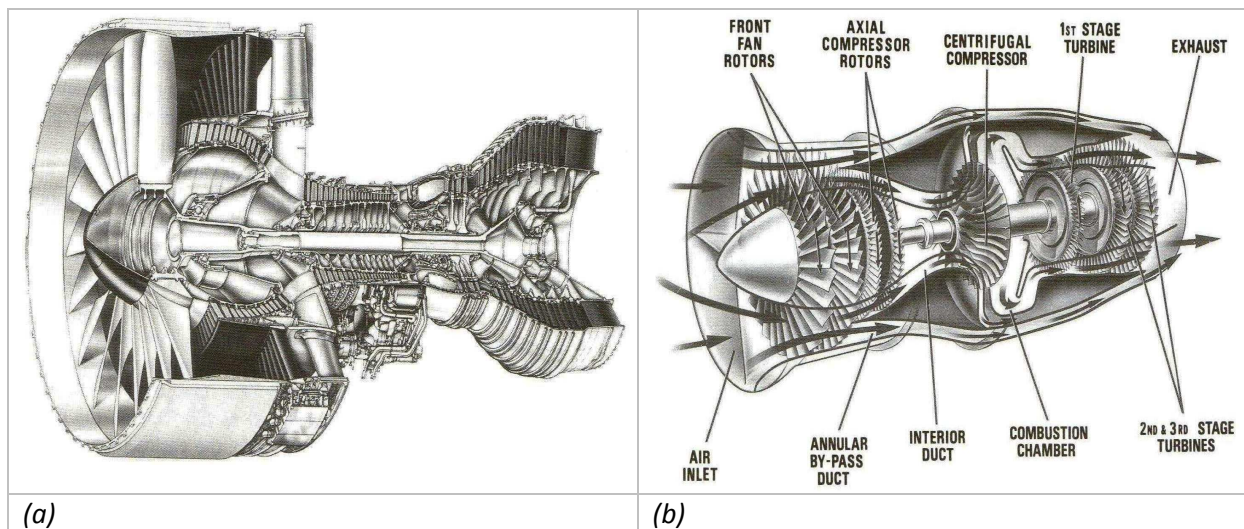


Figure (1. 1): (a) Pratt & Whitney PW 4084 turbo fan engine (Boeing 777), (b) World's smallest turbo fan engine (Williams F107); (Lakshminarayana, 1996).

### **1.1 Scientific and industrial context**

It is known from the of gas turbine cycle that higher cycle temperature produces a larger amount of work per unit mass flow and improves the (power/weight) ratio of the gas turbine. Lakshminarayana (1996) showed that the specific horsepower can be doubled from the levels of 200 hp/lb/s at 1950 °K to 450 hp/lb/s at 2500 °K, compared to the ideal specific horsepower of 540 that does not include any losses, see figure (1.2a). This improvement is one of the major goals of aerospace engine designers. A major problem associated in achieving this increased performance is the availability of material that can withstand such high temperature combined with material stresses (due to temperature, rotation, and aerodynamic loading).

Two important performance parameters of a turbojet are the thrust/unit mass flow rate ( $F/\dot{m}_a$ ) of air and thrust specific fuel consumption TSFC (fuel consumption per unit thrust), as indicated from the figure (1.2b). Optimization of these performance parameters with respect to both turbine inlet temperature (TIT) and the compressor pressure ratio (CPR) results in higher thrust-to-weight ratio, and thus resulting in a compact, efficient, and high performance engine.

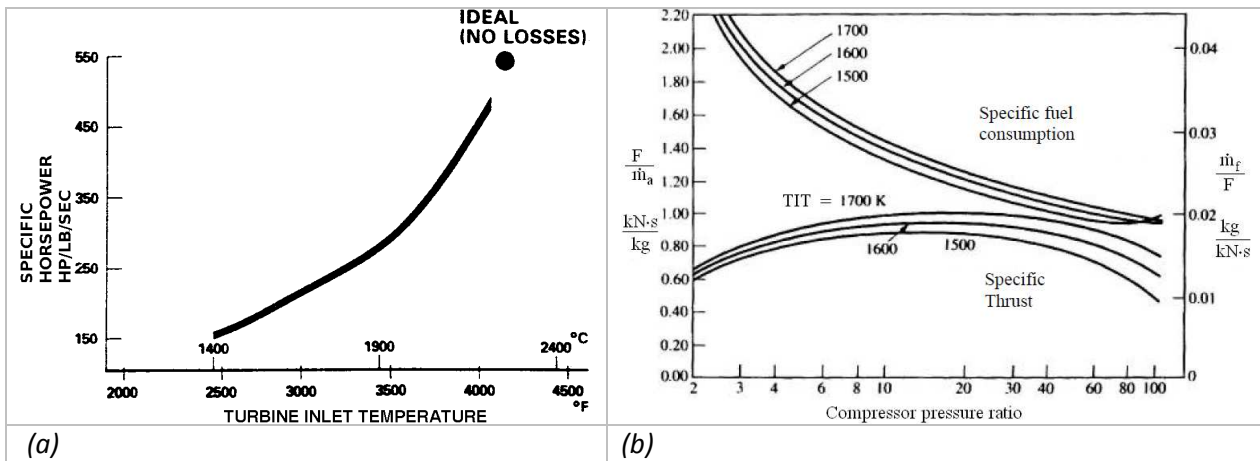


Figure (1. 2): (a) Advances in Core specific power possible with TIT, (b) Variation of thrust specific fuel consumption and specific thrust with compressor pressure ratio for typical turbojet engine; (Lakshminarayana, 1996).

## 1.2 Techniques for material protection

The rising tendency of higher thrust to weight ratio have added up some significant magnitude of turbine inlet temperature along with compressor pressure ratio in the last few decades as shown in figure (1.3a) and (1.3b), whilst newer opportunities for further improvement in the gas turbine efficiency is always the subject of interest for the manufacturers. These requirements deeply implicate to the techniques of surface protection against enormously hot combustion gases. Formal techniques for material surface protection include;

- Surface thermal treatment
- Advanced materials
- Surface coating
- cooling techniques

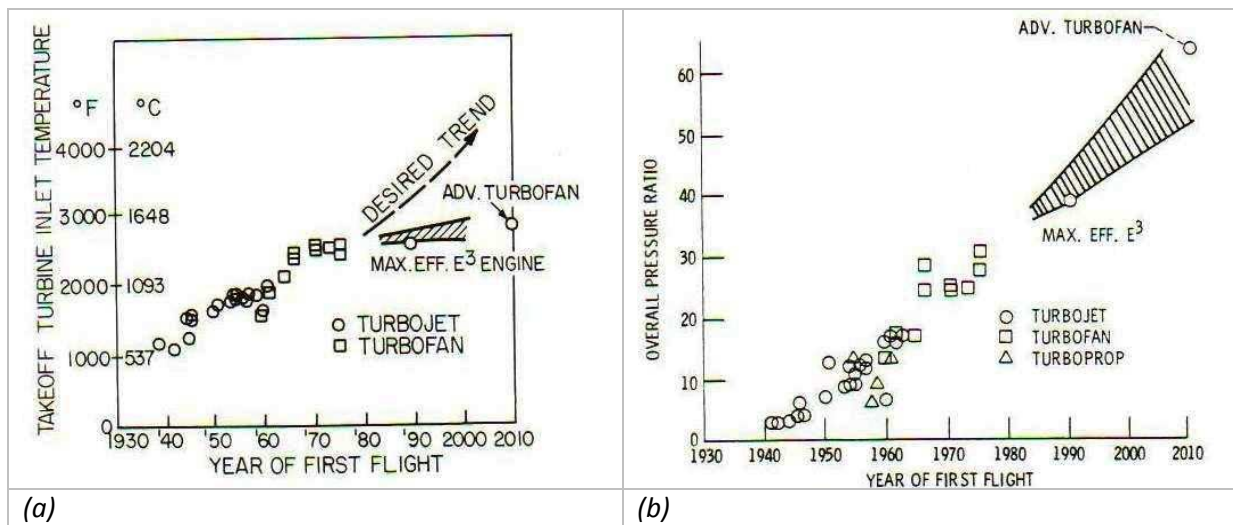


Figure (1. 3): (a) Progress of turbine inlet temperature, (b) Progress in pressure ratio; (Lakshminarayana, 1996)

### 1.2.1 Materials

Materials for gas turbine engines must exhibit high specific strength (strength/density) under high temperatures operating conditions extending thousand of hours (Penner et al., 1996). Materials under these conditions suffered from various kinds of loads, which include elevated thermal stresses caused by rapid temperature change and large temperature gradients, chemical reactions (causing oxidation/corrosion) and high mechanical stresses including impact and contact stresses, low and high frequency vibrational loading, and time and stress dependent effects such as creep, stress rupture, and cyclic fatigue (Lakshminarayana, 1996). Most common engine materials and the trend of utilization are shown in figure (1.4). An impressive progress in thrust-to-weight ratio has been achieved by the development of advanced materials. This includes materials such as titanium and nickel alloys, which have replaced steel. Ceramics can be operated to 1600 K without cooling but have problems of brittleness for rotating components. Moreover, the composites of different kinds have also emerged as a potential alternative for metal components of various regions of the gas turbine system. In a typical composite, metal, ceramic, glass aramid or carbon fibers are joined by a binder, usually a high temperature-resistant resin [8]. The high strength-to-weight ratios of these materials allow major improvements in both aerodynamics and heat transfer. Nowadays, the silicon carbide fiber reinforced titanium, commonly known as TMC, is being viewed as a potential candidate for both static and rotating components for mid-range temperature environments [3]. This material is attributed of elevated temperature strength and stiffness.

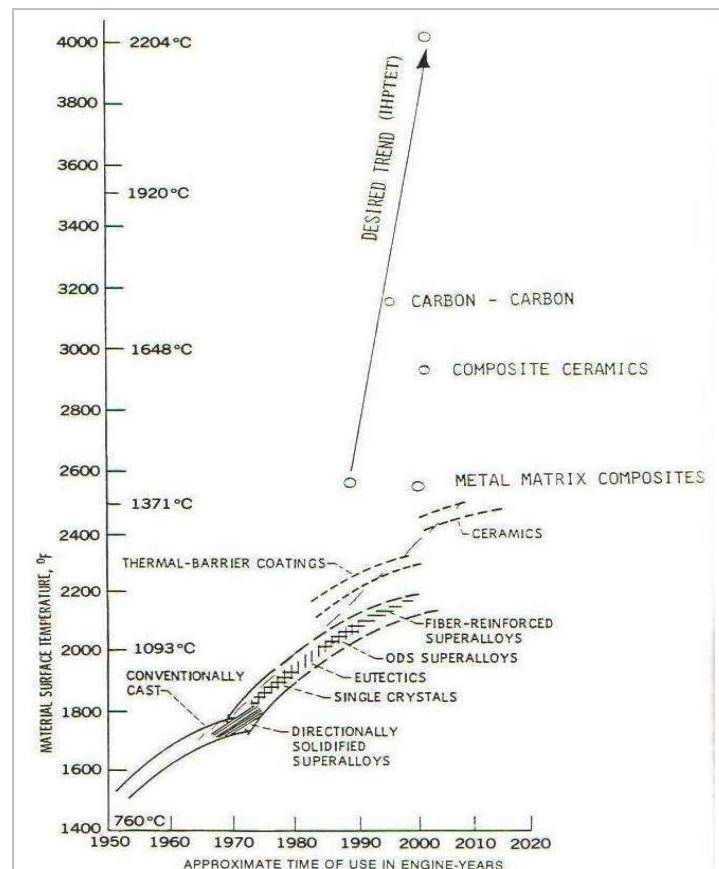


Figure (1. 4): Temperature capabilities of turbine blade materials (Lakshminarayana, 1996)

## 1.2.2 Thermal barrier coating

The parts inside aircraft engine go through surface degradation and wear due to high temperature and stresses inside the power plant. An attractive opportunity available to minimize these effects is recognized as applying some coating to the exposed surface. There are many kinds of coating materials that are being used in aircraft propulsion industry. Coatings are developed to counter the surface degradation due to erosion and rubbing between the contacting elements. Hard coatings reduce impact damage, and softer materials are used to minimize fretting and galling wear in parts that can rub against one another. It is common to use thermal spray coating on fan and compressor surfaces with carbides, titanium nitride, aluminum oxide, chrome oxide or solid film lubricants like epoxy resins [8]. In addition to that advanced coating technique makes use of a physical-vapour-deposited system applied by sputtering; cathodic arc deposition or other similar process for more elegant solution.

### 1.2.3 Cooling with air injection

In the process of turbine blades cooling, cooling air is flowed through several enhanced serpentine passages inside the airfoil, and exits through a myriad of holes in the airfoil surface to give an efficient exploitation of the injectant flow cooling capacity by a combination of convective, conductive, impingement and film cooling mechanisms. Cooling effects are enhanced by features like turbulators, rough projections constructed on the walls of the internal passages, as shown in figure (1.5a). The upper limit of the temperature that an engine can handle is a function of both material properties at the elevated temperatures and the effectiveness of the cooling techniques. The hot turbine components are cooled by both internal and external side thermal exchange and can be classified as follows (Lakshminarayana 1996).

- Internal cooling (for external stream temperatures of 1300-1600 K): convection cooling, impingement cooling and internally air-cooled thermal barrier
- External cooling (for external stream temperatures more than 1600 K): local film cooling, full-coverage film cooling and transpiration cooling

The engine cooling system must be designed to minimize the use of compressor bleed air for cooling purposes. Figure (1.5b) shows the trend of different cooling methods employed with respect to the turbine entry temperature.

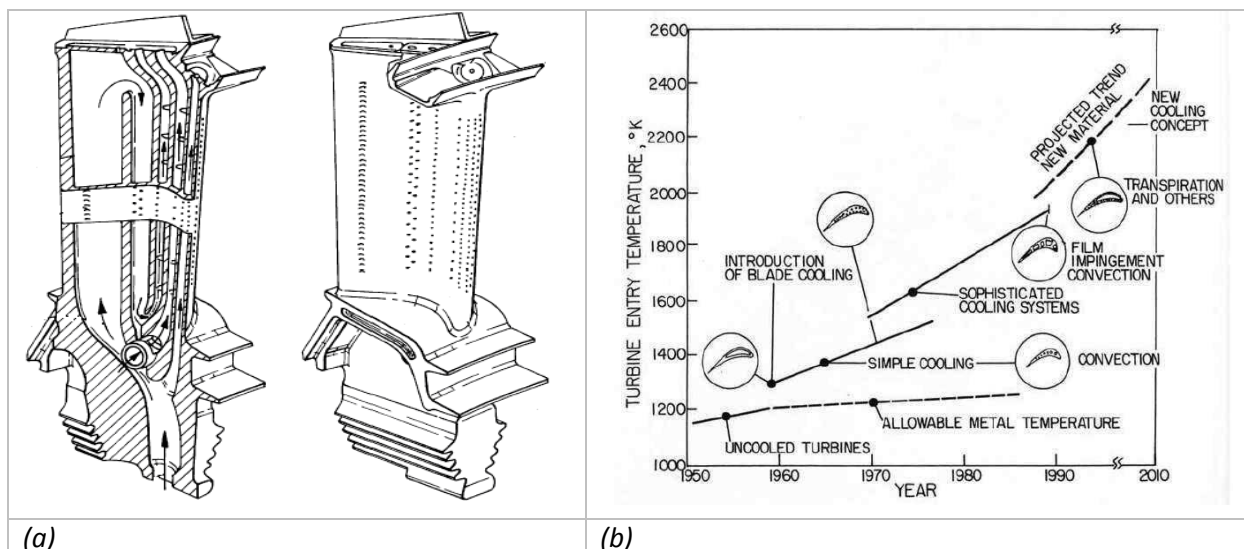


Figure (1. 5): (a) Airfoil complex internal air cooling circuit [4], (b) Use of different cooling methods for turbine blade cooling (Lakshminarayana, 1996).

#### 1.2.3.1 Internal cooling

Convection cooling is the simplest and one of the earliest techniques used. The coolant is passed through the multi-pass circuit from hub to tip and ejected at the trailing edge or at the blade tip. In impingement cooling, the cold air from one row or many rows of small holes ejected from an insert within a blade impacts the blade wall and reduces its temperature.

*“Experimental aerothermal characterization of a pulsating jet issuing in a crossflow: Influence of Strouhal number excitation on film cooling”*

The mean blade temperature will be at a lower temperature than the gas, thus enabling a higher turbine temperature to be used. Another method of keeping the blade cool is through a thermal barrier, which is a low-conductivity ceramic coating. Internal cooling is not as effective as external cooling, as it is used in the limited gas temperature range of 1300-1600K (Lakshminarayana 1996).

### 1.2.3.2 External cooling

In external cooling, film cooling is a technique in which a thin layer of cool air insulates the blade from the hot gas stream, especially near the leading-edge regions where high temperatures are encountered. A more efficient technique is the full-coverage film cooling, which utilizes a large number of closely spaced holes as shown in the figure (1.6). The gas temperature range where this technique is employed is 1560-1800K (Lakshminarayana, 1996).

A most efficient cooling technique, which is only in the conceptual stage, is transpiration cooling, where a layer of cool air is injected on the surface after passing through porous or woven materials. It is useful when inlet temperature is in excess of 1800K. Transpiration cooling combines two heat exchange effects: the convective one at the cooler surface and through the wall, and the “film” one at the warmer surface where hot and cold gases mix (Cerri et al (1987)). Transpiration cooling is obtained, for instance, through sintered stainless steel walls, which usually have a pore diameter ranging between 10 and 50  $\mu\text{m}$  and a wall thickness of about 1 mm (Lakshminarayana, 1996). Although, they have been extensively used to demonstrate the suitability of porous materials and evaluate their thermodynamic efficiencies, problems occurring when the component has to cope with both thermal and mechanical stress, which have limited the application of this technology to the turbomachinery field.

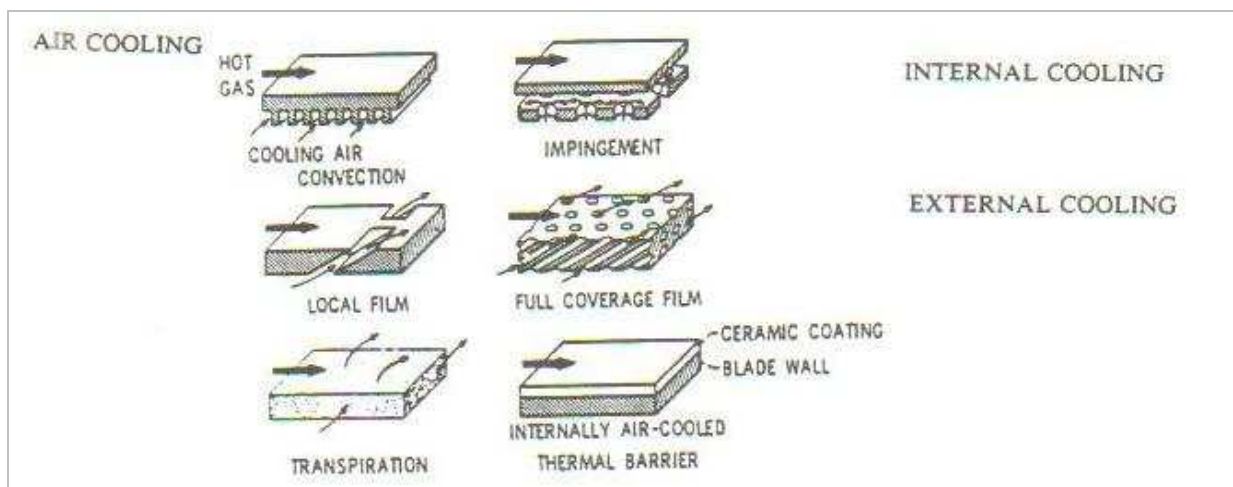


Figure (1. 6): Blade and Vane cooling techniques, (Lakshminarayana, 1996).

### 1.3 Flow field unsteadiness of gas turbine engine

In the actual gas turbine system unsteadiness of the mainstream flow influences the heat transfer and surface pressure distribution on the blade. The unsteadiness on the turbine airfoil develops from four different sources (Ligrani et al (1996a, 1996b))

- Potential flow interactions.
- Shock wave passage.
- Wake passage.
- Random free-stream turbulence from the combustion chamber.

The flow, coming from the upstream nozzle guide vanes located pretty close to the rotating blades, is subjected to a periodic variation of the potential flow during turbine operation. The flow approaching to the rotor blade with significant periodic variations of pressure field, as well as the wake resulting from the blunt trailing edge of the vane significantly influence the film cooling performance. Moreover, in case of a transonic turbine, additional unsteadiness generated by the release of shock waves from the vane row further influences the injectant distribution at the wall (Bons et al. (1995)). Out of different sources of flow unsteadiness, Ligrani et al. (1996a, 1996b) have recognized the potential flow interactions and passing of shock wave for imparting the significant effects on film cooling. Both of these unsteadiness results in important variations of the static pressure near the turbine airfoil surfaces as blade rows move relatively to each other. Film concentrations and film trajectories of the injectant flow move to and form the wall with such periodic unsteadiness in the bulk flow, because of instantaneous change in both film flow rate and momentum at the cooling hole exit.

In order to simulate these conditions, the film cooling study with externally imposed pulsation is performed with the purpose of characterizing both the effects of turbine unsteadiness on film cooling (with the frequency ranges typical to actual turbine), and also to figure out the range of Strouhal number pulsation under various blowing conditions, which could possibly deliver a performance improvement in film cooling. The fundamental objectives of the present study correspond to the second category of the pulsating film flow examination, where the injectant flow is pulsated to alter the attributes of the main flow structures and their distribution near the wall.

### 1.4 Organization of the manuscript

In the previous passages, we had a brief review of the developing technological aspects of the gas turbine system along with the major techniques of wall protection. Among those, there was the film cooling technique, which has a critical role in protecting various components of the gas turbine engine running in harsh thermal environment. In the forthcoming section, we will exclusively discuss the technique of film cooling and the impact of jet pulsation on the distribution of thin injectant film on the wall. The remaining part of

the thesis is divided into chapters 2 to 8, which comprise the chapter of bibliography, experimental setup and measuring techniques, characterization of upstream flows, study of the film-cooled boundary layer flow aerodynamics, study of the wall heat transfer in film-cooled boundary layer (infrared thermography), study of the film-cooled boundary layer flow temperature (cold wire measurements) and conclusion.

The chapter of the bibliographical review (*chapter-2*) attempts to encompass the global characteristics of the flow field known through the open literature for both an oblique and a perpendicular jet issuing in a mainstream flow. Then, the influences of some fundamental film cooling parameters are reviewed, usually presented with the help of film cooling performance parameters (adiabatic effectiveness and heat transfer coefficient). Finally, the recent developments on the issue of the jet pulsation influencing film cooling effectiveness are summarized.

The chapter of experimental setup and measuring techniques (*chapter-3*) describes the experimental arrangements realized to conduct the preliminary experiments for characterizing the mainstream flows by using the system of Laser Doppler Velocimetry 'LDV' and hot wire 'HW'. The arrangements of the injection system containing a loudspeaker to induce injectant pulsation are explained. The required hardware setup and working conditions of the aerodynamic experiments using time-resolved PIV, thermal experiments using infrared thermography and the flow thermometry using cold wire are presented. The procedures for determining the time- and phase-averaged quantities are described.

The chapter of characterization of upstream flows (*chapter-4*) presents the results of preliminary LDV and HW measurements, which were conducted to characterize the wind tunnel and jet flows. The study is undertaken to figure out associated mean and turbulence characteristics, along with the turbulent scales and energy spectra of the wind tunnel flow. The nominal velocity of the jet and the form of jet velocity profiles at the hole exit are determined under different flow configurations. The nature of the pulsating jet forced by a loudspeaker is also studied.

The chapter on the film-cooled boundary layer flow aerodynamic (*chapter-5*) presents the aerodynamic results without and with pulsation of the jet. The study of the flow aerodynamics is performed to figure out the relative behavior of the flow field established by the interaction of a crossflow and a pulsating jet. Flow field measurements performed by the system of Time-resolved Particle Image Velocimetry allow investigating the flow field attributes with higher temporal and spatial resolution. Time- and phase-averaged results are presented for various turbulent quantities.

The chapter on the wall heat transfer due to film-cooled boundary layer flow (*chapter-6*) presents the convective heat transfer coefficient and adiabatic wall temperature results, obtained from the infra-red thermography of the test wall. Film cooling performance is presented by non-dimensionalizing the adiabatic wall temperature by using freestream

and injection temperatures and the heat transfer coefficient by a two temperature heat transfer case (without injection).

The chapter on the film-cooled boundary layer flow temperature (*chapter-7*) presents a survey of the temperature distribution of the flow field resulting from the interaction of a mainstream boundary layer flow and a slightly heated injectant flow. Cold wire measurements allow us to determine the level to which injectant flow diffuses in the mainstream flow in different cases of blowing ratio with Strouhal number pulsations. Time- and phase-averaged results with rms fluctuations are presented.

The chapter of conclusion (*chapter-8*) outlines the concluding remarks about the present investigation and the future perspective.

## 1.5 References:

1. Bons JP, Rivir JB, Mac Arthur CD, Pestian DJ, “*The effect of unsteadiness on film cooling effectiveness*”, Wright Laboratory, WL-TR-96-2096, Jan-1995.
2. Cerri G, Giovannelli A, Battisti L, Fedrizzi R, “*Advances in effusive cooling techniques of gas turbines*”, Applied Thermal Engineering; 27 (2007) 692–698.
3. Gas turbine engine components, <http://www.specmaterials.com/gasturbineenginecomponents.htm>.
4. Harvy NW; “*Cooling of Gas turbine engine aerofoils*”, United States Patent, Patent No.: US 6,609,884 B2, Aug 2003.
5. Lakshminarayana B, “*Fluid Dynamic and heat transfer of turbomachinery*”, John Wiley & Sons, Inc. 1996.
6. Ligrani PM, Gong R, Cuthrell JM, “*Bulk flow pulsations and film cooling-I: Injectant behavior*”, Int. J Heat Mass Transfer, 39 (1996a) 2271-2282.
7. Ligrani PM, Gong R, Cuthrell JM, “*Bulk flow pulsations and film cooling-II: Flow structure and film effectiveness*”, Int. J. Heat Mass Transfer, 39 (1996b) 2283-2292.
8. Paul TC, “*Applied technology in gas turbine aircraft engine development*”, Def Sci J, 38 (1988) 333-340.
9. Penner JE, Lister DH, Griggs DJ, Dokken DJ, McFarland M, “*Aviation and the Global Atmosphere*”, Report of Intergovernmental Panel on Climate Change ‘IPCC’, Sep-1996, [www.grida.no/Climate/ipcc/aviation](http://www.grida.no/Climate/ipcc/aviation).



## Table of Contents

---

2.1.	Definition of Jet-in-crossflow .....	16
2.2.	Description of the aerodynamics of a jet in crossflow .....	16
2.2.1	Flow field at low Reynolds number flow .....	17
2.2.2	Flow field at high Reynolds number flow .....	18
2.2.3	Development of the flow field in the wake region .....	20
2.2.4	Shedding frequency of wake structures .....	21
2.2.5	Influence of a slightly heated jet on the JICF .....	22
2.3.	Description of aerodynamic and heat transfer of an inclined Jet in crossflow applied to film cooling .....	23
2.3.1	Aerodynamic description .....	23
2.3.2	Thermal description .....	26
2.3.2.1	Fundamental parameters of film cooling analysis .....	26
2.3.2.2	Geometrical parameters .....	27
2.3.2.3	Influence of aerodynamic parameters on wall heat transfer .....	31
2.4.	Application of periodic velocity boundary limit on flow structure and wall heat transfer ..	36
2.4.1	Flow from a submerged pulsating jet .....	36
2.4.2	Effect of turbine flow unsteadiness on film cooling .....	37
2.4.2.1	Characterization of turbine unsteadiness through bulk flow pulsation .....	38
2.4.2.2	Characterization of turbine unsteadiness through injectant flow pulsation .....	39
2.4.2.3	Influence of jet Strouhal number pulsation on film cooling effectiveness .....	40
2.5.	Conclusion .....	45
2.6.	References .....	47

## Nomenclatures

<u>Abbreviations</u>		<u>Subscripts/superscripts</u>	
$\rho$	Fluid density (kg/m <sup>3</sup> )	$i$	Injectant
$T$	Temperature (K)	$\infty$	Free-stream
$P$	Pressure (Pa)	$rms$	Root mean square
$d$	Hole diameter (mm)	$\bar{\quad}$	Time-averaged
$L$	Hole length (mm)	$\equiv$	Spatially-averaged
$U$	Streamwise velocity (m/s)	$\sim$	Periodic component
$V$	Normal velocity (m/s)	$a$	Amplitude
$W$	Lateral velocity (m/s)	$j$	Index number
$\overline{M}$	Blowing ratio ( $= \rho_i \overline{U_i} / \rho_\infty \overline{U_\infty}$ )	$acq$	Acquisition
$R$	Velocity ratio ( $= \overline{U_i} / \overline{U_\infty}$ )	$s$	Excitation
$DR$	Density ratio ( $= \rho_i / \rho_\infty$ )		
$I$	Momentum ratio ( $= \rho_i \overline{U_i^2} / \rho_\infty \overline{U_\infty^2}$ )		
$u$	Streamwise velocity fluctuation (m/s)		
$v$	Normal velocity fluctuation (m/s)		
$w$	Lateral velocity fluctuation (m/s)		
$\delta$	Boundary layer thickness (mm)		
$\delta_1$	Displacement thickness (mm)		
$u_\tau$	Friction velocity (m/s)		
$U^+$	U normalized by friction velocity ( $= U / u_\tau$ )		
$IT$	Turbulent intensity (%)		
$\sqrt{u^2}$	x-component of RMS velocity (m/s)		
$\sqrt{v^2}$	y-component of RMS velocity (m/s)		
$\overline{uv}$	Reynolds shear stress (m/s) <sup>2</sup>		
$\phi$	Heat flux (W/m <sup>2</sup> )		
$\lambda$	Thermal conductivity (W/m.k)		
$h$	Heat transfer coefficient (W/m <sup>2</sup> .K)		
$Nu$	Nusselt number		
$NHFR$	Net heat flux reduction ( $= 1 - \phi / \phi_o$ )		
$\theta$	Non-dimensionalized temperature ( $= (T - T_\infty) / (T_i - T_\infty)$ )		
$\eta$	Effectiveness ( $= (T_{ad} - T_\infty) / (T_i - T_\infty)$ )		
$t$	Time (s)		
$\tau$	Fraction of time period		
$f$	Frequency (Cycles/s)		
$x, y$	Streamwise and normal coordinates (mm)		

## ***BIBLIOGRAPHICAL REVIEW***

---

The Film cooling is a commonly used technique in modern gas turbine engines. It involves the injection of compressor bleed air onto the surface of the blade through several tiny holes, which forms a coolant protective layer on the blade surface to ensure its survival in extreme thermal conditions. The cooling efficiency has a direct impact on the overall performance of the engine, as it allows the designer to move to higher temperature and pressure conditions for the purpose of extracting larger thrust. Film cooling has great contribution in the overall cooling achieved through the combination of various other techniques in modern gas turbines system.

Over the years, a great amount of effort has been aimed towards the understanding of the critical dependence of the film cooling efficiency on various design parameters; such as the new innovation in injection hole design (Sargison et al. 2002a,b), arrangement of rows (Sinha et al. 1991b; Ligrani et al. 1992; Ligrani et al. 1997), optimal blowing and momentum ratio of injectant and free-stream flows (Eckert 1970; Yuen and Martinez-Botas 2003a; Goldstein and Eckert 1974), effect of injection hole position in free-stream boundary layer (Goldstein and Eckert 1974; Eriksen and Goldstein 1974), characteristics of both free-stream (Burd et al. 1996; Marek and Tacina 1975) and injectant flows at the hole exit (Burd et al. 1996; Brundage et al. 1999). Flow field unsteadiness encountered in the actual gas turbine system and its impact on film cooling were studied by imposing the bulk flow pulsation in the far downstream region of the interacting flows, (Ligrani et al. 1996a; Ligrani et al. 1997; Seo et al. 1998) and by periodically forcing the injectant flow (Bons et al. 1996; Rutledge et al. 2009). Besides these investigations, the concept of imposing the pulsation to the injectant flow were also investigated fairly recently by (Muldoon and Acharya 2009; Coulthard et al. 2007a; Coulthard et al. 2007b; Kartuzova et al. 2009) to figure out the range of Strouhal number pulsation and the blowing conditions which could possibly deliver a performance improvement in film cooling.

In the forthcoming sections, we will initially take a review of the global characteristics of the flow field both with an oblique and a perpendicular jet issuing in a mainstream flow. Then, we will summarize the influences of some fundamental film cooling parameters with the help of usual performance parameters of film cooling (adiabatic effectiveness and heat transfer coefficient). Finally we will look into the recent developments on the issue of film cooling effectiveness influenced by the introduction of jet pulsation.

## 2.1. Definition of Jet-in-crossflow

The problem of jet-in-crossflow (JICF) has a vast significance in the domain of fluid dynamics, because of its practical importance for various industrial applications. Some of those include the take-off and the landing of the VTOL (vertical take-off and landing) aircraft, film cooling of gas turbine systems, mixing of the pollutant with the cross winds, mixing of two different flow streams in a combustion chamber. The fundamental flow configuration involves the interaction of a uniform boundary layer flow passing over a flat wall with an axisymmetric jet. The resulting flow field for these configurations is usually quite complicated and the flow field characteristics depend significantly on the velocity ratio ( $R = U_i/U_\infty$ ), density ratio ( $D.R = \rho_i/\rho_\infty$ ) and the Reynolds number of both mainstream ( $Re_\infty = \overline{U}_\infty \cdot d/\nu$ ) and injection ( $Re_i = \overline{U}_i \cdot d/\nu$ ) flows (where;  $d$ =hole diameter).

## 2.2. Description of the aerodynamics of a jet in crossflow

Figure (2.1) shows pattern of the flow field proposed by Kelso et al. (1996). It indicates the existence of various kinds of vortex systems. For a vertical jet issuing in a cross flow, Andreopoulos (1984) investigated the physical understanding of the turbulence processes for the jet in crossflow with turbulence subjected to extra rates of strain, resulting from streamwise curvature, lateral divergence and longitudinal accelerations.

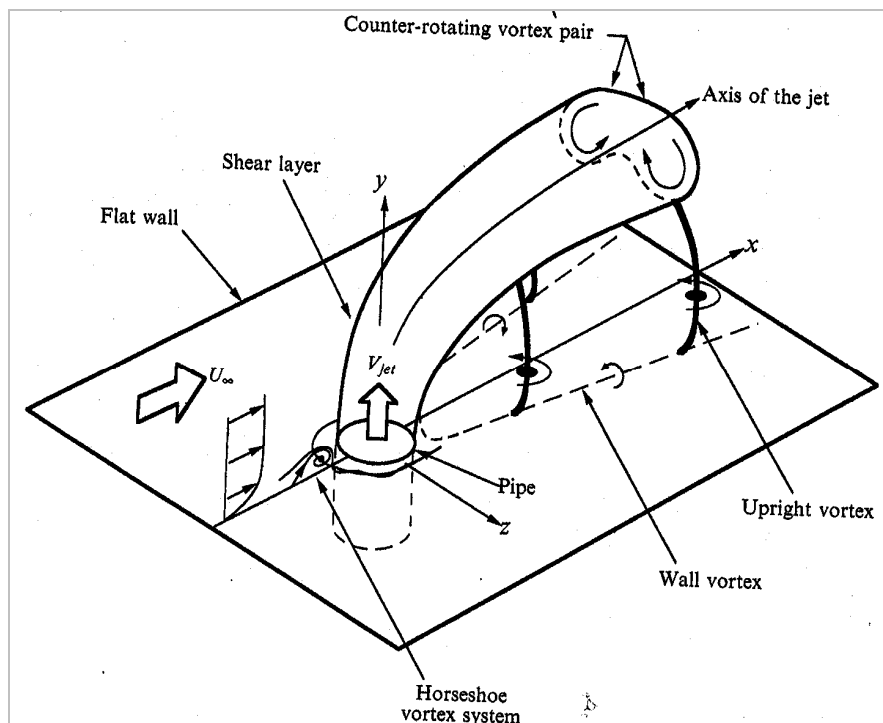


Figure (2. 1) : System of vortices in cross flow; Kelso et al. (1996)

Under these configurations, the oncoming mainstream flow carries along with it the vorticity generated in the boundary layer region of the flow. The annular mixing layer generated in the boundary layer of injection hole flow rolls up after exiting from the hole to form vortex ring. The interaction of these two flows causes these vortices to reorient, to incorporate and to form new vortex systems, leading to a large-scale structure called counter rotating vortex pair 'CVP', (Moussa et al. 1977; Andreopoulos 1984; Kelso et al. 1996; Yuen et al. 2003a). Andreopoulos (1984) has suggested that vertical rings exiting from the hole/pipe carry the vorticity of the same sign as the flow inside the pipe but opposite in sign of the cross stream turbulent flow. These structures are subjected to tilting and stretching on the downstream side of the hole, and break down to turbulence within the first couple of hole diameters downstream of the exit.

### 2.2.1 Flow field at low Reynolds number flow

Figure (2.2) shows an idealized model of the vorticity pattern for the laminar-flow case, proposed by Andreopoulos (1984). It shows the prominent rolling-up of the shear layer at the upstream edge of the jet. Kelso et al. (1996) suggested that the shear layer rolls-up due to Kelvin-Helmholtz like instability. The resulting vortices contribute significantly to the vorticity of CVP. It was mentioned that the separation pattern inside the hole has an important role in the initial roll-up of the CVP immediately downstream of the hole exit. They also reported the presence of a steady vortex at the upstream edge close to jet exit at  $Re_{\infty} = 940$  and  $R = 2.3$ , other than the horseshoe vortex, and referred it as 'hovering vortex', which, as explained, also contributes to the vorticity of CVP. An almost similar kind of a vortex was also mentioned by Guo et al. (2006), who has performed a numerical study based on LES.

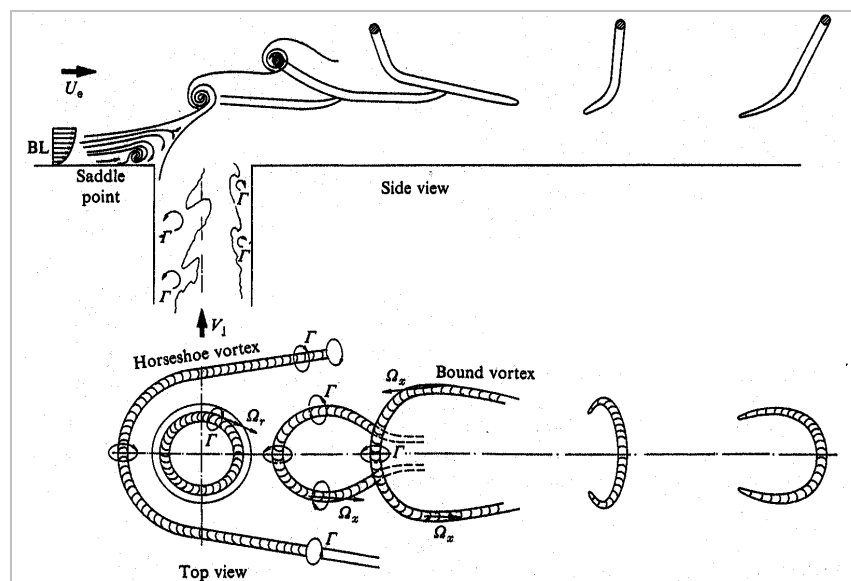


Figure (2. 2): Interpretation of vortex formation and downstream shedding; Andreopoulos (1984).

The presence of the horseshoe vortex system near the upstream edge of the hole is reported to have a minor role in the overall structure. Kelso et al. (1996) has mentioned that the downstream trajectories of the horseshoe vortices at low Reynolds number ( $Re_\infty = \overline{U}_\infty \cdot d / \nu < 1000$ ) holds on average, the vorticity of the same sign as the flat-wall boundary layer, which extends downstream along the flat wall and incorporates into the vortex system of the wake. The horseshoe vortices with vorticity opposite to the flat-wall boundary layer lifted away from the wall behind the jet and merge with the CVP.

### 2.2.2 Flow field at high Reynolds number flow

Kelso et al. (1996) suggested that the global topological features observed in the low Reynolds number ( $440 \leq Re_\infty \leq 2700$  and  $2 \leq R \leq 6$ ) situation also apply to higher Reynolds number flows ( $Re_\infty = 6200$  and  $R = 2.2$ ), while referring to their flow visualization experiments conducted in the water channel for low Reynolds numbers cases and to the wind tunnel measurement for high Reynolds number cases. From higher Reynolds number experiments, Andreopoulos and Rodi (1983) proposed that the cross-stream flow acts like a partial cover over the exit and causes the flow inside the pipe to bend before reaching the exit, which makes the jet to leave mainly from the downstream part of the hole. The covering effect also causes some acceleration, and gives a velocity of the bend-over jet somewhat higher than the freestream velocity.

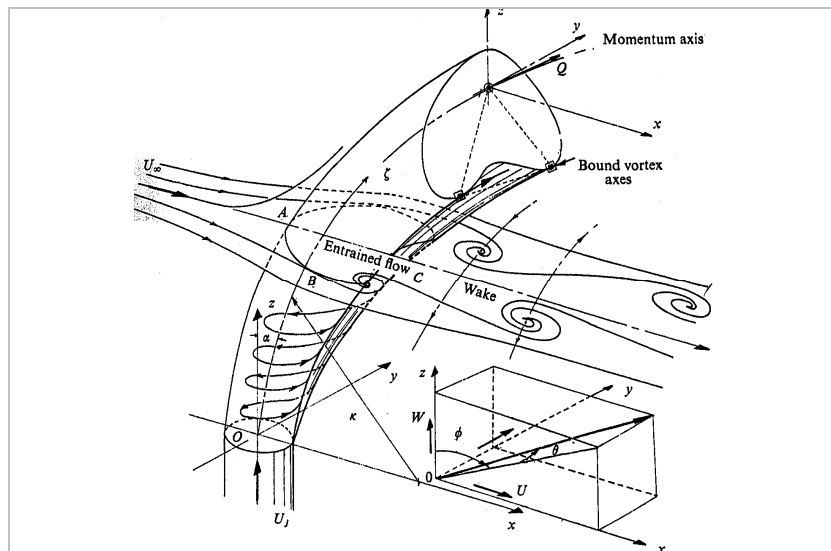


Figure (2. 3): Near field pattern proposed by Moussa et al. (1977)

Moussa et al. (1977) compared the velocity distribution of the cross-stream flow along the leading-edge streamline with that of a flow around a rigid circular cylinder. They observed that as the cross-stream approaches the jet boundary and decelerates, it deflects around the boundary surface with partial mixing with the jet flow. They found that the

distribution of mean velocity was quite similar as for a rigid cylinder of the same cross-section. Figure (2.3) shows their proposed pattern of the interaction of two flows. In the wake region, they noticed that the most of the vorticity issuing from the hole, tilted and stretched by the flow, bundles up into a pair of vortex tubes at the lee surface of the jet. At the interface around the jet, a portion of mean hole vorticity and the additional vorticity generated at the shear layer were described to roll up into periodically shed vortices. They imagined that these two vortex systems are responsible for most of the entrainment of cross-stream flow into the deflected jet and its wake.

Figure (2.4a) and (2.4b) show the difference of the pattern of flow structure generating at low Reynolds number flow ( $R=4$  and  $Re_{\infty}=1600$ ) and at high Reynolds number flow ( $R=4$  and  $Re_{\infty}=2700$ ), obtained from the dye visualization experiments of Kelso et al. (1996). These figures indicate that the regularity of the appearance of the large structure leaving the pipe decreases at high Reynolds numbers, and eddies occupy a wide range of sizes. In both situations, the vortex break down accruing in the CVP (Counter rotating Vortex Pair) on the downstream side near the pipe outlet was referred to occur due to the region of reverse flow. Upright vortices in the wake region (nearly having vorticity in the wall normal direction), were argued to come from the vorticity generated at the flat wall, and links up with the wall vortices and the CVP. They explained that these vortices are formed at high Reynolds number, as the wake region starts to develop unsteady vortices. Some alternative mechanisms for the shedding of the upright vortices in the wake were suggested, because they observed that at high Reynolds number the upright vortex orientation changes from one pattern to another, containing either a pattern similar to classical von Kármán vortex street or in some particular case, of mushroom-like structures where the vortices appeared to be grouped into pairs of opposite circulation.

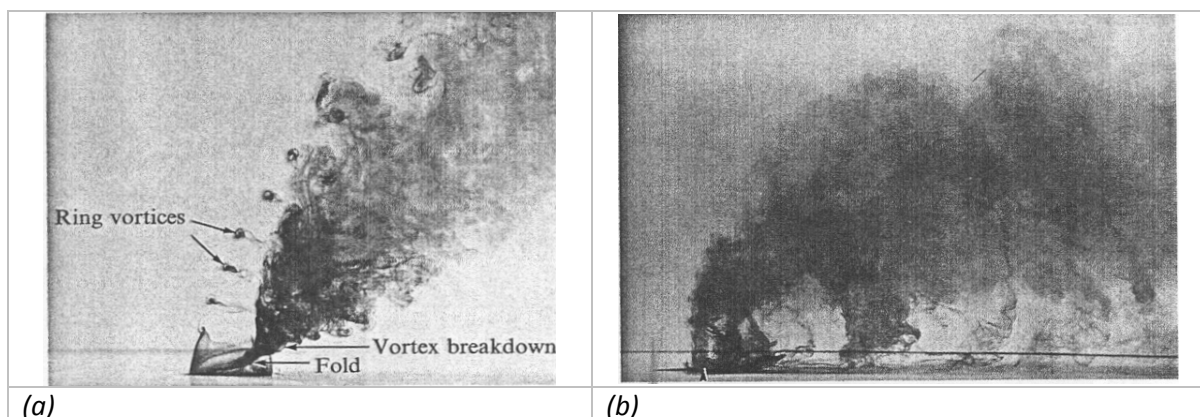


Figure (2. 4): Flow structures generating at (a)  $R=4$  and  $Re_{\infty}=1600$ , (b)  $R=4$  and  $Re_{\infty}=2700$ ; dye visualization by Kelso et al (1996).

### 2.2.3 Development of the flow field in the wake region

The DNS performed by Rudman (1996) and the experimental study of Fric and Roshko (1994) have exclusively described the formation of wake structures of the jet in crossflow. They both concluded that the vortical structures in the wake are formed from the vorticity that originates in the boundary layer of the crossflow wall. Fric and Roshko (1994) studied a large number of cases to figure out the physical phenomena associated with the formation of the wake of a transverse jet, and described the difference in the nature of the wake generated in case of a transverse jet and a solid cylinder. Figure (2.5a) shows a typical well-organized wake structure forming in case of  $R=6$  and  $Re=7600$  (Fric and Roshko 1994), which shows the vortices of alternating signs. A point to be noticed from the given figure is that the wake of the jet is quite close compared to the wake generated in the case of a solid cylinder, which usually shows a wide open near wake due to the early separation on the cylinder. Also, they mentioned that the vortices, even though containing vortices of alternating sign, do not necessarily lie in a well-ordered array as in the Kármán vortex street.

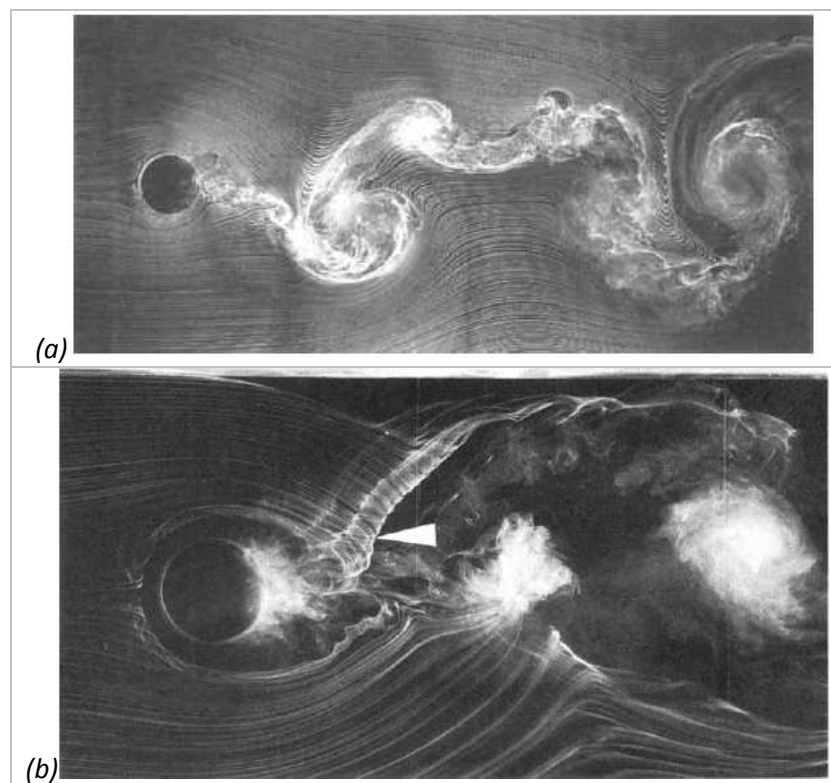


Figure (2.5) : Smoke-Wire results of Fric and Roshko (1994); (a)  $R=6$ ,  $Re=7600$  (with smoke-wire plane at a wall-normal distance of  $0.5D$ ); (b)  $R=4$ ,  $Re=3800$  (with smoke-wire plane at a wall-normal distance of  $0D$ ).

Fric and Roshko (1994) proposed a possible mechanism by which vorticity leaves the wall to enter the wake region. They mentioned that the boundary layer streaklines, located

away from the center and besides those that rolled into the horseshoe vortices, flow around the sides of the jet and then separate on the lee side of the injection hole. These separation events are reported to form on one side of the jet and then on the other in an alternating manner. The Authors mentioned that at lower velocity ratios ( $R \leq 2$ ) the separation regions were found difficult to identify. Figure (2.5b) shows the event of vortical structures rolling up after separation leading to the formation of wake vortices.

## 2.2.4 Shedding frequency of wake structures

The study of the vortical structures in the wake of a transverse jet issuing in a crossflow was performed by Fric and Roshko (1994). For a range of Reynolds numbers and different distances from the leading edge of the crossflow wall to the centre of injection tube, they studied the Strouhal number of the vortical structures convecting past a fixed point in the jet wake, see figure (2.6a). It was concluded that within a range of small variability the periodic shedding of the wake vortices is about ( $St = f * d / \overline{U_\infty} = 0.13$ ) near a velocity ratio of 4, and is about  $St=0.16$  near a velocity ratio of 2. Elsewhere, the level of variability of the  $St$  were relatively significant and fall within  $0.07 < St < 0.18$  for a velocity ratio ranging from 2 to 10. Levi (1983) reported the law of Strouhal number for the periodic phenomena taking place in different flows; including wakes behind cylinders, flapping turbulent plane jets, flow over cavities and Von Karman vortex street. They suggested that the  $St$  is of the order of 0.159, despite of little and no resemblance among these flows. Moussa et al. (1977) observed a shedding frequency of the order of  $St=0.2$ , for a vertical jet issuing in a crossflow. For lower velocity ratios ( $U_i/U_\infty < 5.5$ ) with  $\rho_i/\rho_\infty = 1$ , they considered that the shedding from the jet is dominated by shedding from the solid cylinder, because of the lack of dependence of Strouhal number on Reynolds number ( $Re_\infty = \overline{U_\infty} * d / \nu$ ) and  $U_i/U_\infty$ . Andreopoulos (1984) figured a slightly higher value of Strouhal number ( $St = f * d / \overline{U_\infty}$ ) for jet-in-crossflow, which was about 0.41, figure (2.6b). He found that the  $St$  is independent of jet Reynolds number ( $Re_i$ ), while performing the experiments for different velocity ratios with a constant free-stream Reynolds number ( $Re_\infty$ ). He showed that the jet in the presence of crossflow retains some of the characteristics of the jet issuing into 'still' air, and proposed a strong possibility for sequential shedding of large structures. The DNS performed by Rudman (1996) focused on the formation of wake vortex system for jet-in-crossflow. He mentioned that the Strouhal number ( $St = f * d / \overline{U_\infty}$ ) of the wake vortex system is 0.098, and also suggested that the wake vorticity originates in the upstream boundary layer. Moreover, he suggested for a peak around 0.68 to be associated with Kelvin-Helmholtz roll-up of the jet shear layer.

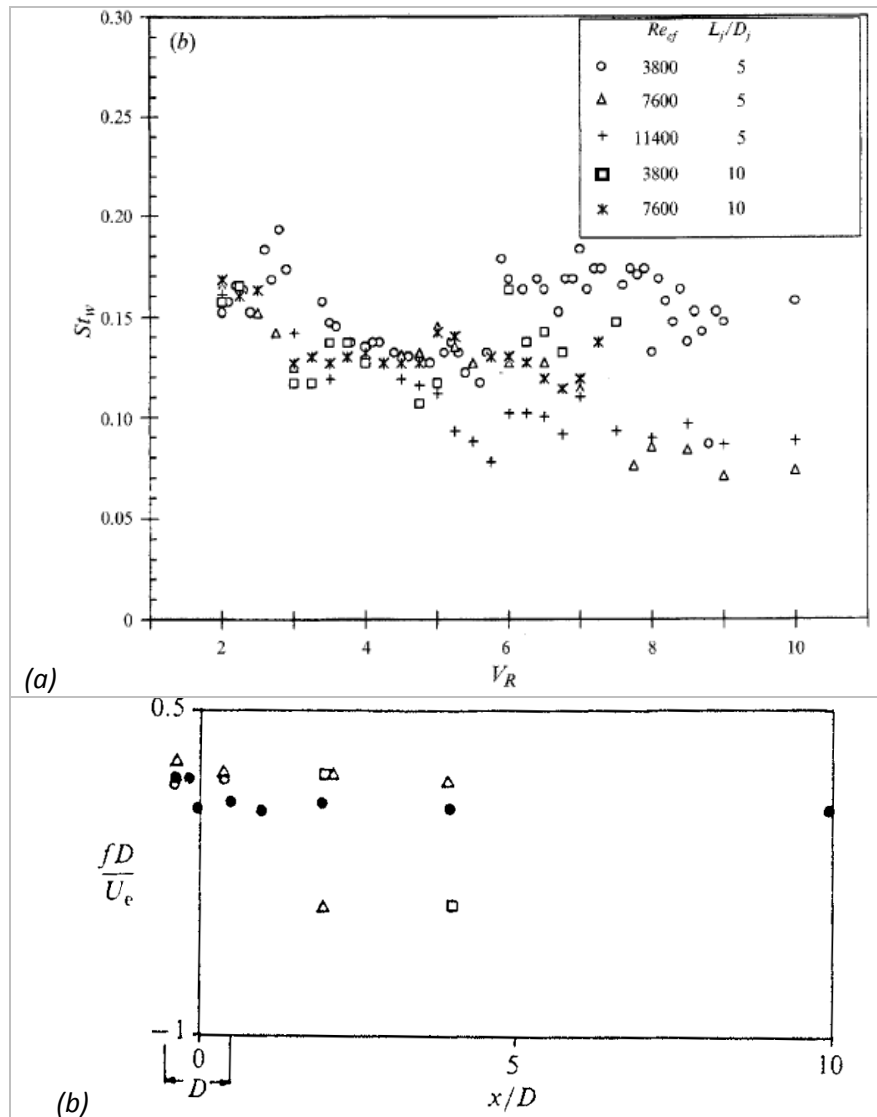


Figure (2. 6): (a) Distribution of  $St$  as a function of velocity ratio; Fric and Roshko (1994), (b) Distribution of  $St$  as a function of downstream distance; empty circle (velocity ratio=0.25), solid circle (0.5), empty triangle (1), empty square (2); Andreopoulos (1984).

### 2.2.5 Influence of a slightly heated jet on the JICF

The heat transfer characteristics of a slightly heated jet issuing perpendicularly into a cold cross-stream has been performed by Andreopoulos (1983). The investigation was primarily based on the estimation of second and third order temperature-velocity correlations in turbulence processes. They suggested that the mean temperature profiles at the jet exit are considerably more nonuniform at Low Velocity Ratio 'LVR' than for Higher Velocity Ratio 'HVR', indicating an early mixing between the cold and hot fluid and suggesting that for LVR turbulent processes are more important in the flow. The nonuniformity in the temperature profile was identical to the mean velocity profile, where the pressure distribution around the exit imposed by the cross stream caused the pipe flow to decelerate at the upwind side and

accelerate at the downstream side. Temperature fluctuations  $\overline{\vartheta^2}$  at the hole exit were indicated to reduce from the upstream side to the downstream side, and were shown to hold higher values for the low Reynolds number condition, figure (2.7a).

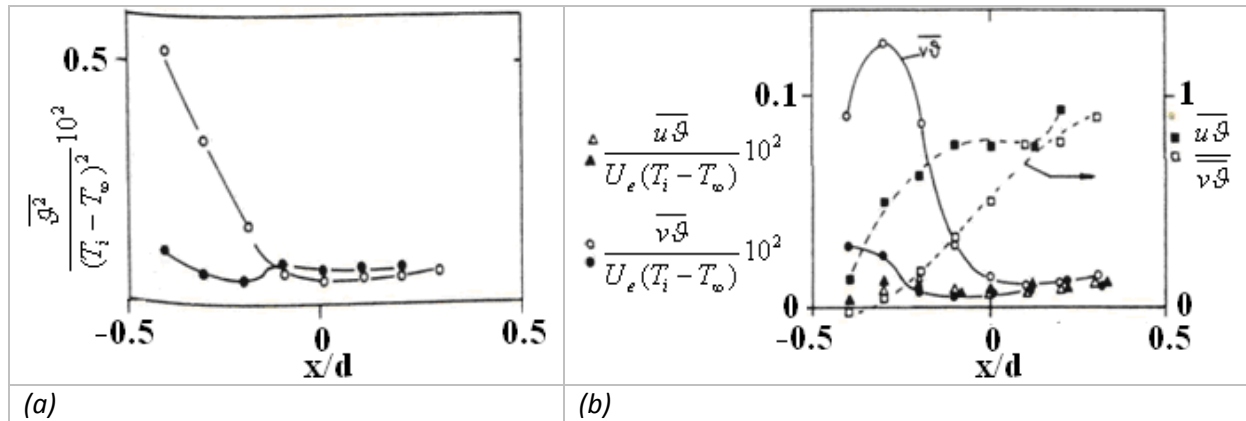


Figure (2. 7): Streamwise distribution at the exit plane of pipe at different Reynolds number,  $R=0.5$ , (a) Temperature fluctuation  $\overline{\vartheta^2}$ , (b) Turbulent heat flux in normal direction  $\overline{v\vartheta}$  and longitudinal direction  $\overline{u\vartheta}$ . Opened symbols:  $Re=20500$ , filled symbols:  $Re=41000$ , (Andreopoulos 1983).

The second-order temperature-velocity correlations or turbulent heat fluxes were reported to contain higher fluxes in normal direction  $\overline{v\vartheta}$ , whereas the fluxes in the longitudinal direction  $\overline{u\vartheta}$  has featured low values almost everywhere on the exit plane, and seemed to change sign close to the upstream edge of the pipe, figure (2.7b). Further it was mentioned that, up to 4 diameters downstream for the case of  $R=0.5$ , the temperature fluctuations and longitudinal and normal turbulence heat fluxes reached a higher values, and further downstream they decay considerably.

## 2.3. Description of aerodynamic and heat transfer of an inclined Jet in crossflow applied to film cooling

### 2.3.1 Aerodynamic description

Film cooling configurations usually use an inclined injection of the coolant jet. An inclined injection not only reduces the turbine aerodynamic losses but also carries the injectant to a larger downstream distance under a similar blowing condition, before diffusing in the bulk flow. The global characteristics of the inclined jet configuration are similar to the normal jet configuration, except for some features of significantly small strength that are not observed so often. As shown in figure (2.1), the usual flow features witnessed in case of a normal jet include;

- The Kelvin-Helmholtz roll-up of jet shear layer

- The formation of counter rotating vortex pair
- The horseshoe vortex system
- The wake region and the reverse flow
- The wall vortex

In case of the inclined jet the strength of the vortex systems is comparatively low. It is to be noted that the cases of film cooling usually require the flow field inspection at lower velocity ratios compared to the normal injection, due to the variety of their practical applications.

The flow field aerodynamics due to the interaction of the two flow streams with oblique injection were studied by (Foucault et al. 1992; Pietrzyk et al. 1989; Dorignac et al. 1992; Lee et al. 1994; Walters and Leylek 2000; Guo et al. 2006; ). Pietrzyk et al (1989) used a short delivery tube ( $L/D=3.5$ ) for the injectant flow and explained the evolution of the downstream flow along with the skewing of the jet exit profile, which settles towards the downstream side at low blowing ratio and moves towards the upstream side at high blowing ratio. Foucault et al. (1992) described the existence of the CVP (Counter Rotating Vortex Pair) for a  $45^\circ$  inclined jet and its influence on both velocity and temperature fields. Dorignac et al. (1992) studied the injectant flow dynamics downstream of a row of holes as a function of blowing ratio for a slightly heated jet flow. The computational results of Walters and Leylek (2000) traced back to the origin of vorticity leading to the CVP for an inclined jet. They also reported the appearance of small reverse flow zones immediately downstream of the trailing edge for a blowing ratio of 1 and a density ratio of 2. They nominated the streamwise vorticity originating from the lateral edges of the hole and the shearing between the jet and the mainstream flow as being the primary sources for developing the counter-rotating-vortex pair (CVP).

Mendez and Nicoud (2006) performed the LES on effusive cooling or full-coverage film cooling, employing a model of multi-perforated wall that contained  $30^\circ$  cylindrical holes of a length of  $4d$ . The descriptions of flow structures given for a blowing ratio of 1.17 have shown the presence of the number of features at different magnitudes of employed  $Q$  criterion. Figure (2.8a) and (2.8b) shows two different views of the flow field, which indicate the following flow structures.

- (1) The pair of counter-rotating vortices (CVP). The two vortices were described to originate from the lateral edges of the hole outlet and their direction of rotation is such that the fluid is pulled away from the wall at the centreline and entrained towards the wall when coming from the sides of the jet.
- (2) The two counter-rotating vortices aligned with the jet were shown to present in the hole itself, which were much less intense than the earlier one.

- (3) A horseshoe vortex much weaker than the one found in case of a normal jet was also shown. Consistently with the fact that the adverse pressure gradient experienced by the primary stream flow is smaller when the jet is inclined.
- (4) A pair of small downstream spiral separation node vortices locating immediately downstream of the hole exit were reported to originate from the wall, where they were almost vertical, and they rapidly reoriented in the direction of the jet.
- (5) A pair of suction vortices was shown near the inlet, originating as the flow enters through the sharp inlet.
- (6) A small streamwise vortices lying beneath the CVP were reported to have a direction of rotation opposite to that of the CVP.

Figure (2.8c) shows author's Q criterion results indicating the flow field dominated by shear layer vortices formed at the upstream face of the jet and also inside the hole.

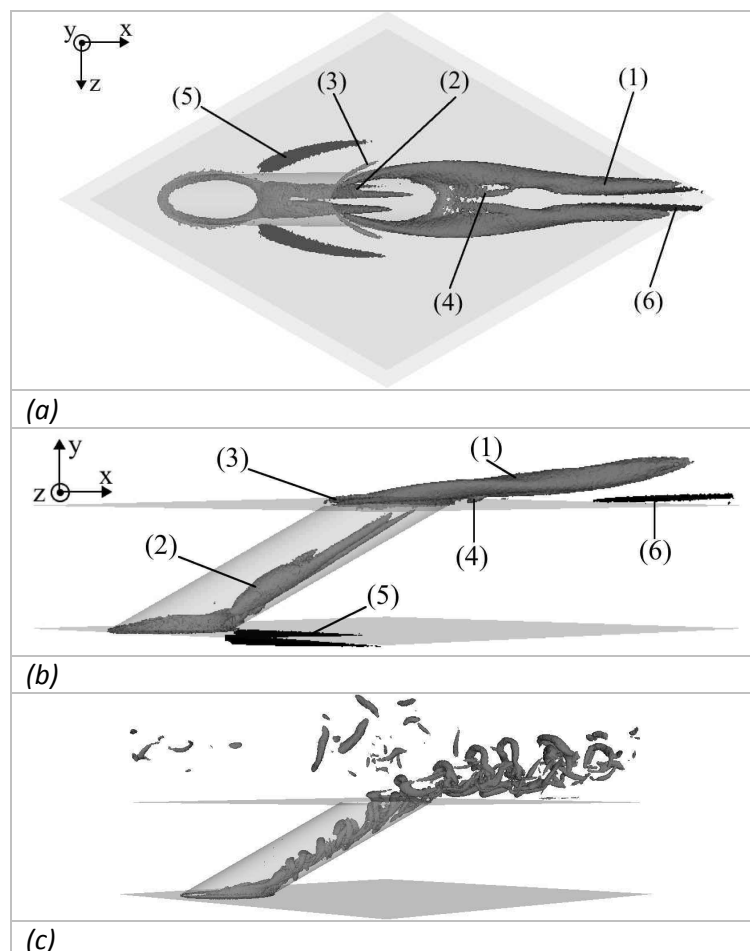


Figure (2. 8): Q-criterion showing flow structures present in the time-averaged field (a) and (b), instantaneous field (c), (Mendez and Nicoud 2006)

Lee et al. (1994) studied both normal and inclined jet cases and reported the disappearance of reverse flow, lesser crossflow entrainment and stronger secondary motion

due to larger pressure gradient in wake region in the case of an inclined jet, compared to a normal jet. They mentioned that the bound vortex region lies much closer to the wall and the induced flow into the wake is much stronger in the inclined injection case than in the normal injection case. The large eddy simulations of an inclined and a normal jet issuing in the cross-stream flow were conducted by Guo et al. (2006). They noticed that the interaction between the mainstream and the jet flow is considerably reduced and the first occurrence of the vortex pair is shifted downstream for inclined jet. Figure (2.9a) and (2.9b) show the distribution of the velocity vector at the lateral plane of  $x/d=0.75$  for a normal jet and an inclined jet respectively. The strength of the streamwise vortex is much higher for the case of a normal jet (the portion of jet flow near the tube exit was not shown for normal jet). In case of streamwise inclined jet, they observed that the separation at the leading edge of the jet hole is suppressed, which follows the vortex formation due to the streamline rollup of the freestream boundary layer due to the initial blockage from the upstream edge of the jet. They also examined the anisotropy of the flow by using the invariant technique, and concluded that the JICF problem possesses a complicated anisotropic turbulence characterises, which is hard to be described by standard one- or two-equation models, especially for the flow field in the separation area downstream of the jet exit.

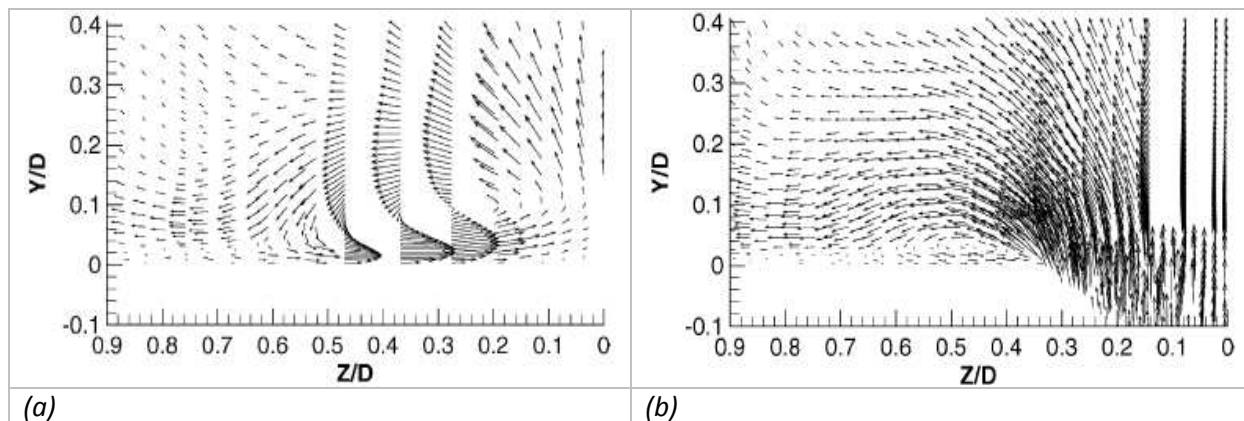


Figure (2. 9): Development of counter rotating vortex pair,  $M=1$  and  $x/d=0.75$ , (a) perpendicular jet, (b) inclined jet; Guo et al. (2006).

## 2.3.2 Thermal description

### 2.3.2.1 Fundamental parameters of film cooling analysis

Sinha & al. (1991a) provided a brief overview of the parameters that influences the film cooling performance of the coolant jet issuing in a crossflow. These include the parameters of the hole geometry and their placement on the injection wall, properties of interacting flows and the parameters of the fluid dynamics. Author summarized these parameters or the

ratio of parameters as follow; coolant to mainstream density ratio ( $D.R.$ ), velocity ratio ( $R.$ ), mass flux ratio ( $M$ ), and momentum flux ratio ( $I$ ).

$$D.R = \frac{\rho_i}{\rho_\infty}; \quad R = \frac{U_i}{U_\infty}; \quad M = \frac{\rho_i U_i}{\rho_\infty U_\infty}; \quad I = \frac{\rho_i U_i^2}{\rho_\infty U_\infty^2} \quad \dots\dots\dots(2. 1)$$

In addition to these, other parameters like free stream boundary layer thickness, turbulent intensity and pressure gradient of mainstream flow are also influential. In order to investigate the film cooling performance near to engine representative conditions, the unsteadiness of actual turbine system influencing the coolant flow rate at the hole exit, their trajectories and the wall coverage are studied with artificially imposed pulsation.

### 2.3.2.2 Geometrical parameters

The dependence of film cooling performance on different geometrical parameters is markedly complex. Various geometric parameter, such as; hole diameter ( $d$ ), hole shape, lateral spacing of holes or pitch ( $P$ ), interspacing of rows ( $S$ ), positioning format of holes (inline/staggered), angle of injection ( $\alpha$ ) and the configuration of injection angle (simple/compound), requires huge database of information for characterization of their impact on the film cooling. Fortunately, presently available literature has already tapped a large number of these conventional configurations. In fairly recent time, some promising designs for injection hole geometry have been proposed. However, manufacturing difficulties and strength factors constraints associated with complex geometrical features impose a certain degree of reluctance on their industrial applications, such as; complex console shaped holes (Sargison et al. 2002), using triangular tabs at hole exit (Nasir et al. 2003).

#### **Shape of jet perforation channel**

The performance of the film cooling system relies significantly on the design of jet perforation channel. As the attributes of jet exit profile plays an important role in establishing the immediate downstream flow. Many kinds of perforation channel are studied in the past. Out of which, Sargison et al. (2002) has compared the most famous ones with his newly proposed model named as 'Console'. Figure (2.10) indicates the author's range of film cooling holes studied.

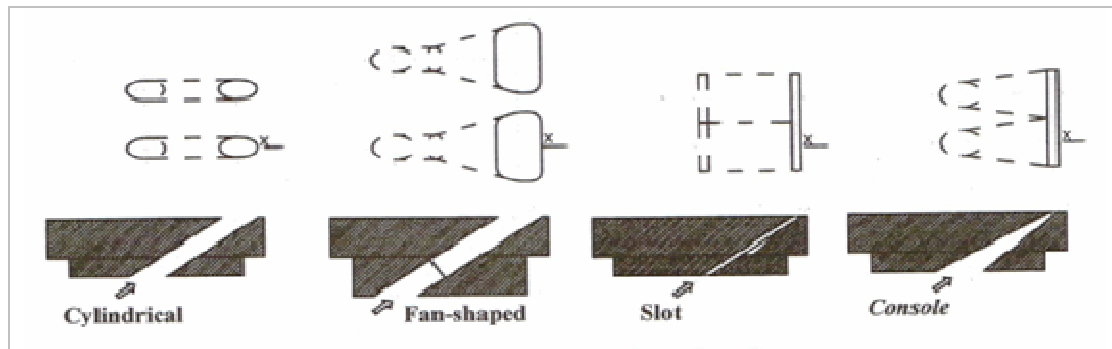


Figure (2. 10): Range of holes studied; Sargison & al. (2002a)

Sargison et al. (2002) compared the cooling performance of a single row of consoles with the typical 35 degree cylindrical, fan-shaped holes and slot, by employing equal throat area per unit width for each type of hole shape. In Figure (2.11a), the laterally averaged adiabatic effectiveness demonstrates that the console approaches towards the slot effectiveness, as does the fan-shaped hole effectiveness. The console laterally averaged heat transfer coefficient is similar to the slot, and higher than the cylindrical and fan-shaped holes, Figure (2.11b). The slot and console do not significantly change the boundary layer flow compared with the case of no film cooling, and hence the heat transfer coefficient is similar. The fan-shaped and cylindrical film-cooling holes appear to thicken the boundary layer and reduce the heat transfer coefficient compared with no film cooling. Author has mentioned that there is an aerodynamic penalty associated with this thickening. While, the aerodynamic loss due to a console is significantly less than for the fan-shaped or cylindrical film cooling holes.

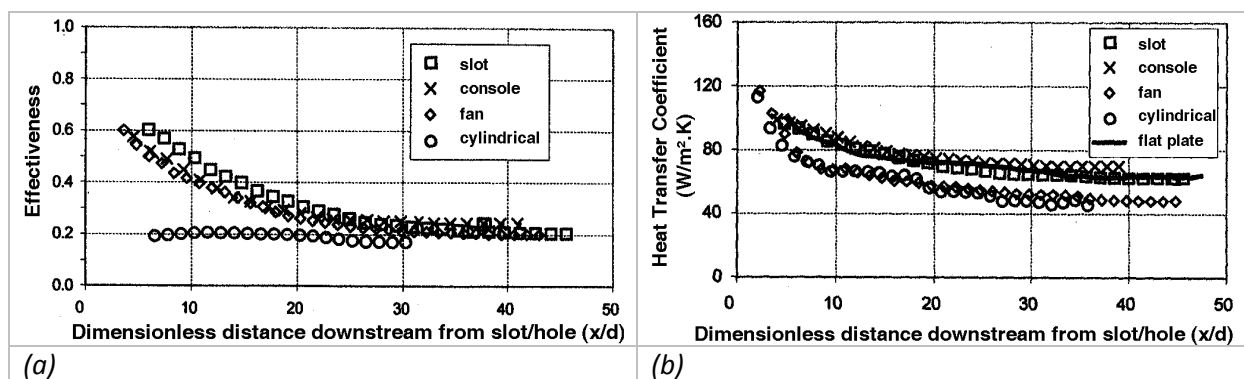


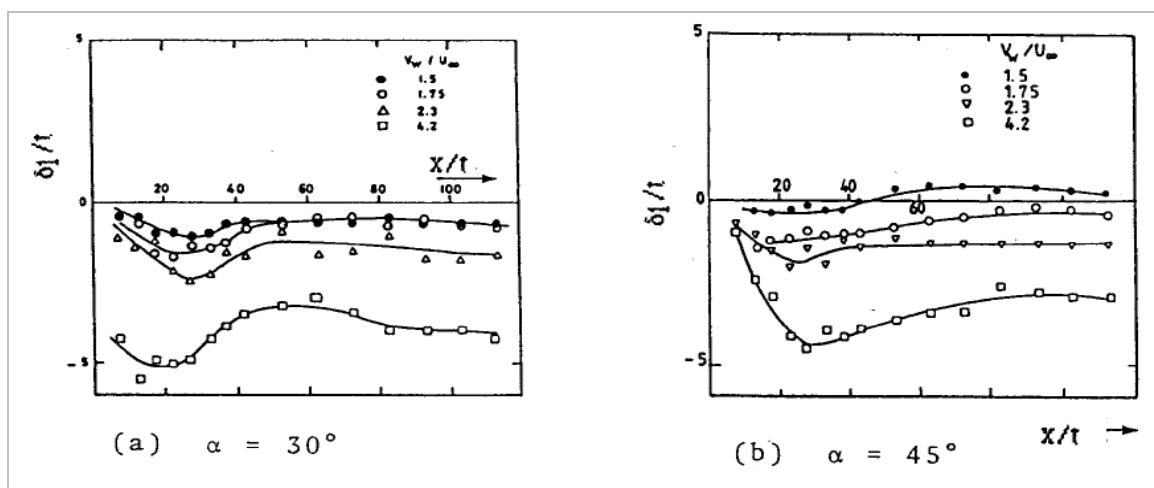
Figure (2. 11): Laterally average adiabatic effectiveness and heat transfer; Sargison et al. (2002)

### Angle of injection

The effect of angle of injection on film cooling is an issue, which is by far the most studied parameter, for various hole shapes and the pattern of their placement. For a simple cylindrical type injection hole or slot, it is widely known through open literature that at the

higher angles the flow tends to lift off from the surface and the wall protection is significantly reduced. For every angle of injection, there exists an optimum blowing ratio (Yuen et al. 2003a). Various investigations on film cooling that employed ' $\alpha$ ' as low as  $0^\circ$  (tangential surface) up to high values of  $90^\circ$  (normal to surface) have been studied, Volchkov et al (1967), Aly (1999), Yuen et al.(3003a, b), Yuen et al.(3005a, b). It may be concluded that a lower angle jet losses a good fraction of momentum during its flow in the vicinity of the wall, while a higher injection angle lifts the jet off the surface and thus reduces the wall coverage.

Aly (1999) observed a general trend for a jet emanating from a thin slot and observed that the ratio of displacement thickness to the slot thickness ( $\delta_1/t$ ) increases by increasing ' $\alpha$ ', and its sign changes from negative to positive somewhere between  $\alpha=45^\circ$  to  $60^\circ$ . The negative ( $\delta_1/t$ ) indicates that the jet did, not only make up for the displacement created by the boundary layer upstream of the slot, but also bring more fluid to the wall vicinity compared with the main stream. This behavior is increased by increasing blowing ratio ' $M$ ' for  $30^\circ$  and  $45^\circ$ , especially in the near downstream of the slot and starts to level towards the far end of the test surface, figure (2.12a) and (2.12b). In the case of higher ' $\alpha$ ' (i.e,  $60^\circ$  and  $90^\circ$ ), ( $\delta_1/t$ ) acquires positive values which increases by increasing ' $\alpha$ ' and/or ' $M$ ', figure (2.12c) and (2.12d). The shown distributions indicate that the jet could not make up for the flow deficiency in the wall region. The incoming main stream pushed the jet towards the surface, which brings more fluid to the wall vicinity, and accordingly ( $\delta_1/t$ ) decreases gradually, until we see that the curve changes its sign in some case, which implies to the reattachment of injectant fluid towards the wall.



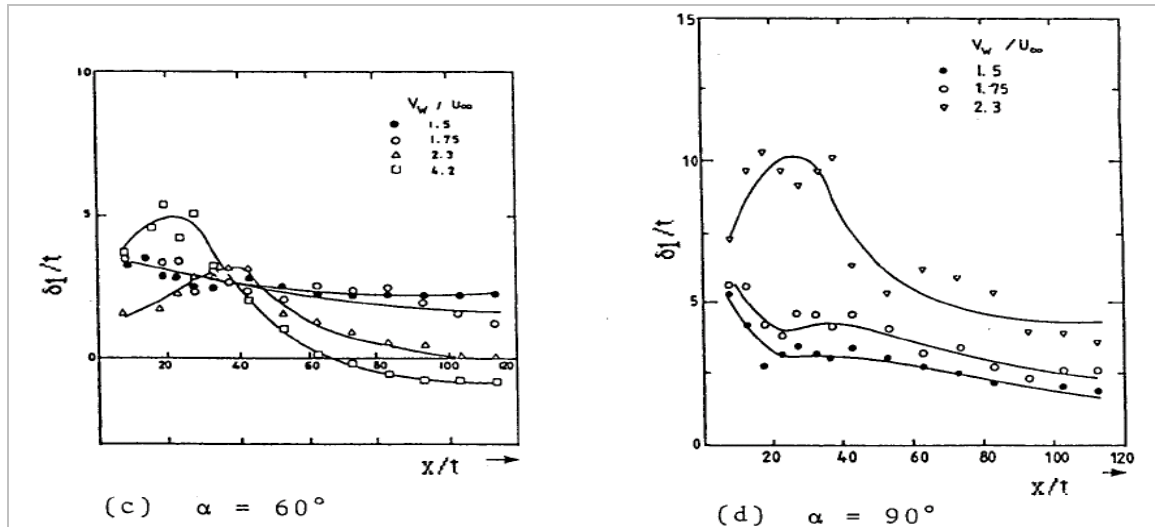


Figure (2.12): Variation of boundary layer displacement thickness in case of different velocity ratios (a) 0 deg, (b) 45deg, (c) 60 deg, (d) 90 degree; Aly (1999).

### **Effect of length to diameter ratio**

The form of exit velocity profile of the secondary jet significantly depends upon the hole length-to-diameter ratios ' $L/d$ ', which generally are responsible for important consequences on film cooling performance. Short length-to-diameter ratios are more representative of turbine actual configurations, such as employed by Pietrzyk et al. (1989) and Walters and Leylek (2000) to an order of ( $L/d=3.5$ ). With short  $L/d$ , the additional vorticities leaving the hole due to the flow separation inside the pipe plays an essential role in the formation of jet structure in the near-field.

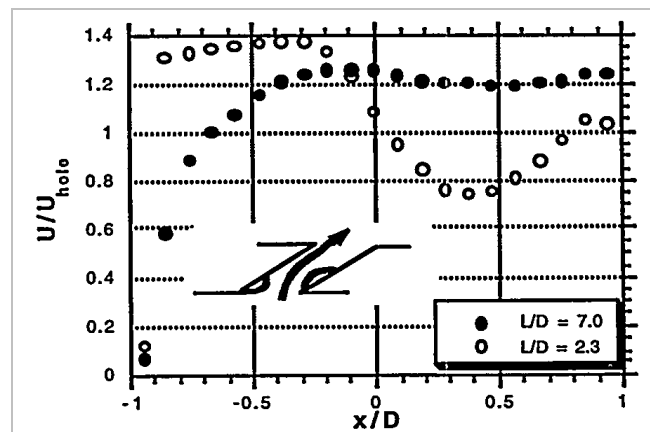


Figure (2.13): Centerline mean velocity profiles at the hole-exit plane with FSTI=12%; Burd et al. (1996).

Burd et al. (1996) studied the influence of free stream turbulence intensity and hole length-to-diameter ratio on film cooling, with a streamwise injection of  $35^\circ$  and velocity and

density ratio equal to 1.0. They suggested that film cooling with low free stream turbulence intensity (FSTI) is more affected to the changes in  $L/d$  than that with high FSTI. Short-hole injection leads to the phenomena of “jetting”, where the coolant ejects further into the freestream and spreads more in the spanwise direction than with long  $L/d$  injection. With jetting, the jet velocity profile is not uniformly distributed across the majority of the plane at which it exits, but is skewed with substantially higher velocities upstream as shown in figure (2.13).

### 2.3.2.3 Influence of aerodynamic parameters on wall heat transfer

#### Blowing ratio

Blowing or mass flux ratio ‘ $M$ ’ is one of the most significant and fundamental film cooling controlling parameter. An early study on the variation of centerline adiabatic effectiveness  $\eta_c$ , Eq. (2.2), with respect to the blowing ratio for cylindrical holes at  $35^\circ$  inclination, and with 3D spacing was realized by Eckert (1970) and extended by Goldstein et al (1974) using shaped holes. Figure (2.14a) and (2.14b) corresponds simultaneously to these studies. At low blowing ratio, close to jet exit in downstream region higher values of adiabatic effectiveness are observed due to larger quantity of the injectant. As, the distance from the point of injection increases the jet structures starts diffusing and the flow is entirely dominated by the mainstream flow characteristics.

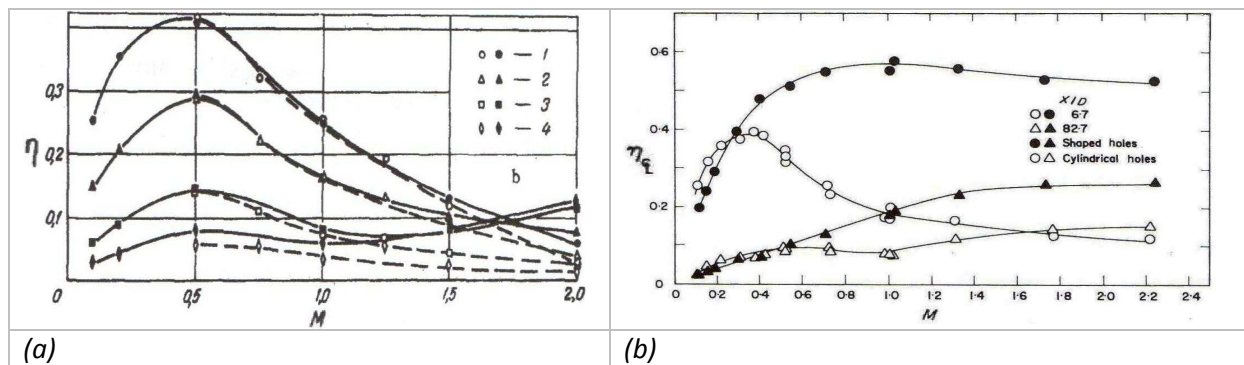


Figure (2. 14) : Centerline effectiveness as a function of blowing rate for injection of air through cylindrical holes at  $35^\circ$  and 3D hole spacing, (a) Empty symbols stands for single hole, solid symbols stands for rows of holes; (1)  $x/D=5.19$ , (2) 11.11, (3) 31.47, (4) 80.67; Eckert (1970), (b) Empty symbols stands for row of cylindrical holes, solid symbols stands for row of shaped holes; (1)  $x/D=6.7$ , (2)  $x/D=82.7$ ; Goldstein et al. (1974).

Figures show that in a range of  $M < 0.5$ , film cooling effectiveness increases and reaches a point after which it started to decrease, the point of highest effectiveness is known as optimum blowing ratio. Optimum blowing ratio changes with secondary jet injection angle. The higher blowing rates lowered the effectiveness, as the coolant jets

penetrated more into the mainstream. However, further downstream the effectiveness tended to increase with the blowing ratio in some cases, where the coolant jets have been reattached to the surface.

$$\eta_c = \frac{(T_{ad} - T_\infty)}{(T_i - T_\infty)} \dots\dots\dots(2. 2)$$

Where,

- $T_\infty$  Mainstream temperature,
- $T_i$  Injection temperature
- $T_{ad}$  Adiabatic wall temperature

**Density Ratio**

The adiabatic wall measurements by Goldstein et al. (1974) and Sinha et al. (1991a) showed that the film-cooling effectiveness strongly depends on the density ratio. For constant momentum flux ratio, jets with higher density ratio will have higher mass flux ratio, which results in greater centerline effectiveness ‘ $\eta_c$ ’. Jessen et al. (2007) studied 30° jets of air and CO<sub>2</sub> emanating from a pipe into a cross-stream boundary layer at different velocity ratio by using PIV technique. They examine the effects of density ratio between coolant and mainstream on the mixing behavior, as well as on cooling efficiency. Their results show that a higher velocity ratio enlarges the size of the recirculation region leading to a more pronounced entrainment of cross-flow fluid into the wake of the jet. Velocity effects dominate the flow field in the vicinity of the jet hole. However, the lateral spreading of the coolant downstream, which is crucial for the cooling efficiency, is strongly increased at a higher density ratio.

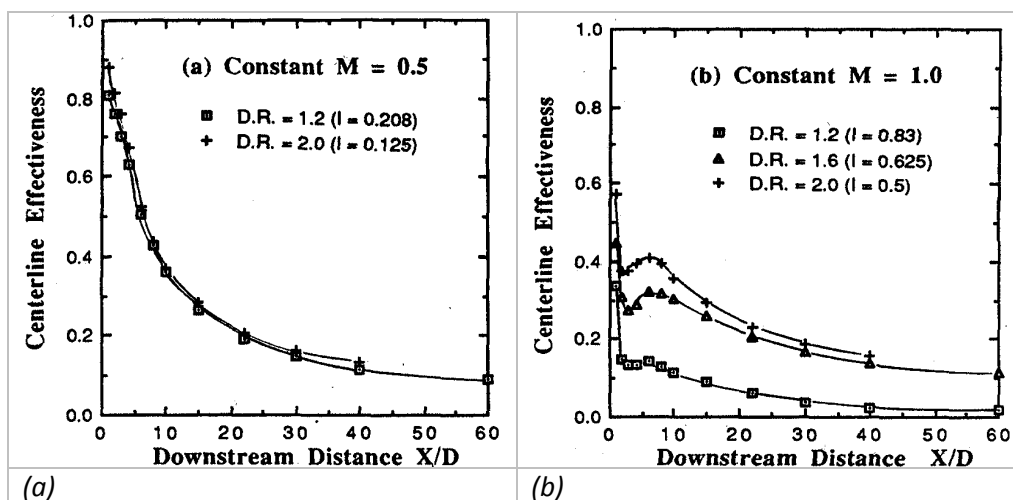


Figure (2. 15): Centerline effectiveness at different density ratio, (a) M=0.5, (b) M=1.0; Sinha et al. (1991a).

Figure (2.15a) and (2.15b) present some results from Sinha et al. (1991a), it is clear that at high blowing ratio ' $\overline{M}$ ' the phenomena of detachment and reattachment occurs. Moreover, higher levels of centerline effectiveness ' $\eta_c$ ' seem to occur at higher density ratio.

### Ratio of momentum flux

Sinha et al. (1991a) deduced from their study of a single row of holes with variable density and blowing ratios, that the flow characteristics downstream of the jet primarily depends on the momentum flux ratio ' $I$ ', as the jet either remains attached to the surface, detaches and then reattaches, or to become fully detached. Their studies were composed of a row of 35 degree jet with a length to diameter ratio ' $L/d$ ' of 3.5 and hole spacing of  $3d$ . At  $I=0.2$ , as shown in figure (2.16a), the jet remain attached and the distribution of ' $\eta_c$ ' is nearly similar in the initial region of  $x/d=10$ , for density ratio ' $DR$ ' of 1.2 and 1.6. At  $I=0.3$ , figure (2.16b) shows that the jet have barely detached. Moreover, the trends of the  $\eta_c$  distributions for  $DR=1.2$  and  $DR=2.0$  seem very similar, but  $\eta_c$  for  $DR=1.2$  is slightly lower than for  $DR=2.0$ . For  $I=0.5$ , figure (2.16c) demonstrates a clear detachment and reattachment that occurs for all density ratios. The level of  $\eta_c$  is consistently lower for  $DR=1.2$  compared to the higher density ratios. They proposed that the reduced levels of  $\eta_c$  for lower density ratios may be attributed to the lower blowing ratio at same momentum flux ratio.

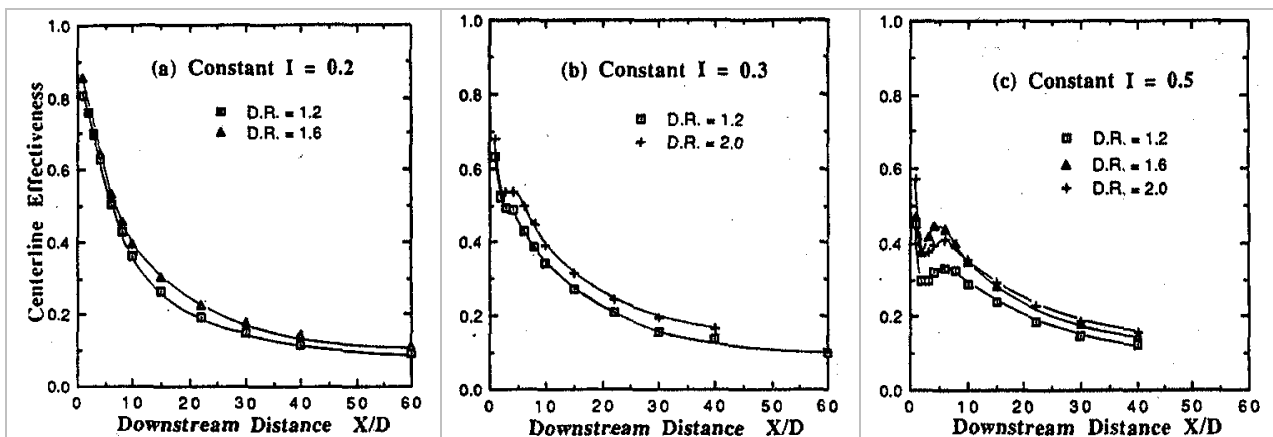


Figure (2. 16): Centerline effectiveness in different cases of constant momentum flux ratio, (a)  $I=0.2$ , (b)  $I=1.3$ , (c)  $I=0.5$ ; Sinha et al. (1991a)

Schmidt et al. (1996) have examined the film cooling effectiveness for different hole geometries as a function of momentum flux ratio ' $I$ '. They studied the behavior of the row of round hole with compound angle ' $CA$ ' at zero degree and 60 degree, and the holes with 15 degree forward expansion and a compound angle at 60°. The injection angle with respect to the test surface was 35 degree in all configurations. The intermediate space between two

holes ‘P’ and length to diameter ratio ‘L/d’ were 3d and 4 respectively. Figure (2.17) shows that the spatially average effectiveness  $\bar{\eta}$  (effectiveness averaged over a particular area, Eq. (2.3)) at low ‘l’ is quite similar for the different geometries.

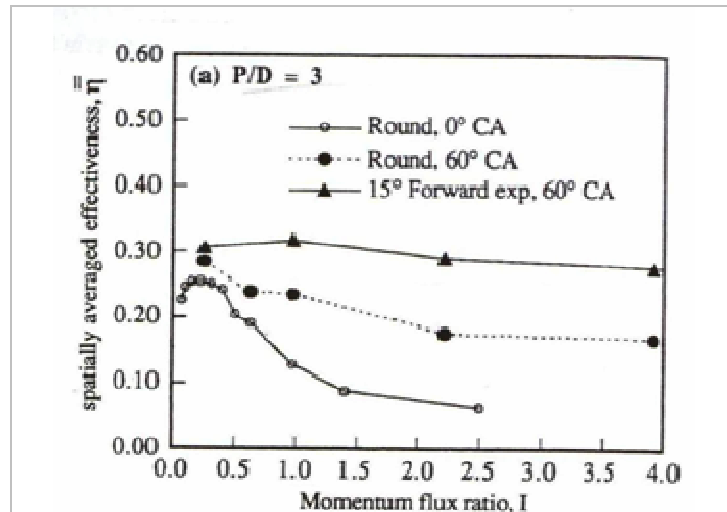


Figure (2. 17): Spatially average effectiveness  $\bar{\eta}$  as a function of Momentum flux ratio for P/D=3; Schmidt et al. (1996).

For the case with compound angle ‘CA’ holes at 60°, the  $\bar{\eta}$  is higher compared with the simple angle hole and the region over which high  $\bar{\eta}$  existed is also increased. The forward expanded exit holes with CA=60° maintained essentially the same level of  $\bar{\eta}$  over the full range tested, with  $0.25 < I < 3.9$ , and were significantly better than the round CA=60° holes at the larger I. For the round CA=60 holes,  $\bar{\eta}$  decreased slightly with increasing I, but still had reasonably good effectiveness at I=3.9.

$$\bar{\eta} = \frac{1}{(x_2 - x_1)(z_2 - z_1)} \int_{z_1}^{z_2} \int_{x_1}^{x_2} \eta(x, z) dx dz \quad \dots\dots\dots(2. 3)$$

**Free-stream turbulent intensity of cross-stream flow**

The effect of free-stream turbulence on the film cooling was studied by Mayhew et al. (2003), Burd et al. (1996), Lebedev et al. (1995), Bons et al. (1995) and Marek et al. (1975). Bons et al. (1995) studied the effects of free stream turbulence intensity along with jet pulsation to mimic the unsteadiness of real gas turbine units. High Free-stream turbulent intensity (FSTI) cases are more influenced by the freestream flow and are characterized by increased mixing downstream of the edges of the film cooling holes, which reduces the film cooling effectiveness (Burd et al. 1996).

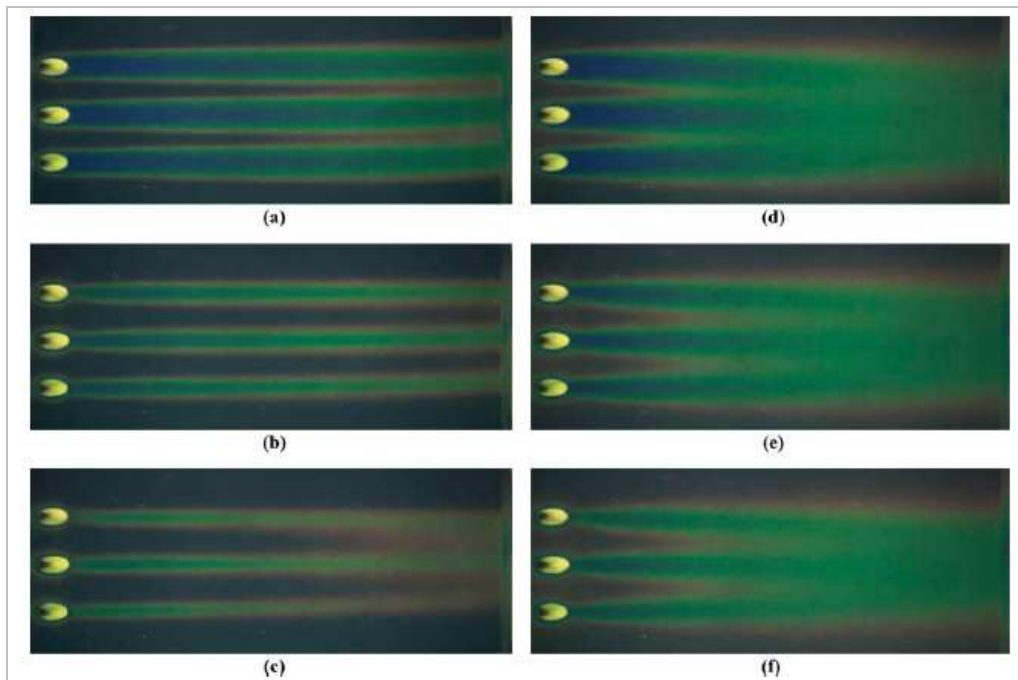


Figure (2. 18): Raw images of model at various blowing rates and low and high freestream turbulence levels: (a)  $M=0.5$ ,  $Tu=0.1\%$ , (b)  $M=1.0$ ,  $Tu=0.1\%$ , (c)  $M=1.5$ ,  $Tu=0.1\%$ , (d)  $M=0.5$ ,  $Tu=10\%$ , (e)  $M=1.0$ ,  $Tu=10\%$ , and (f)  $M=1.5$ ,  $Tu=10\%$ ; Mayhew et al. (2003)

Figure (2.18a-f) shows the raw images of the color pattern achieved with the blowing ratio of  $M=0.5$ , 1 and 1.5, where free-stream flow held the turbulent intensity of  $Tu=0.1\%$  and  $10\%$  in different test configurations (Mayhew et al. 2003). In the array of subfigures given below,  $M$  varies row-wise and  $Tu$  varies column-wise. In low turbulent intensity cases ( $Tu=0.1\%$ ) shown in figure (2.18a-c), a thin black region between the hole are essentially unprotected. This unprotected region increased for  $M=1$  and 1.5 as the liftoff occurs. In high turbulent intensity cases ( $Tu=10\%$ ) shown in figure (2.18d-f), the injectant spreading in the lateral direction increases, which shortened the distance that the cooling air had traveled downstream in the low turbulent intensity case. It was concluded that the high freestream turbulence affects the film cooling effectiveness only slightly for a blowing ratio of  $M=1.5$ , but has significantly detrimental effects for the blowing ratios of  $M=0.5$  and 1.0.

### **Boundary layer thickness of cross-stream flow**

Goldstein et al. (1974) observed that the film cooling effectiveness decreases when the ratio of boundary layer thickness to injection hole diameter ' $\delta/D$ ' increases, although the trend is diminished at large  $\delta/D$ , figure (2.19).

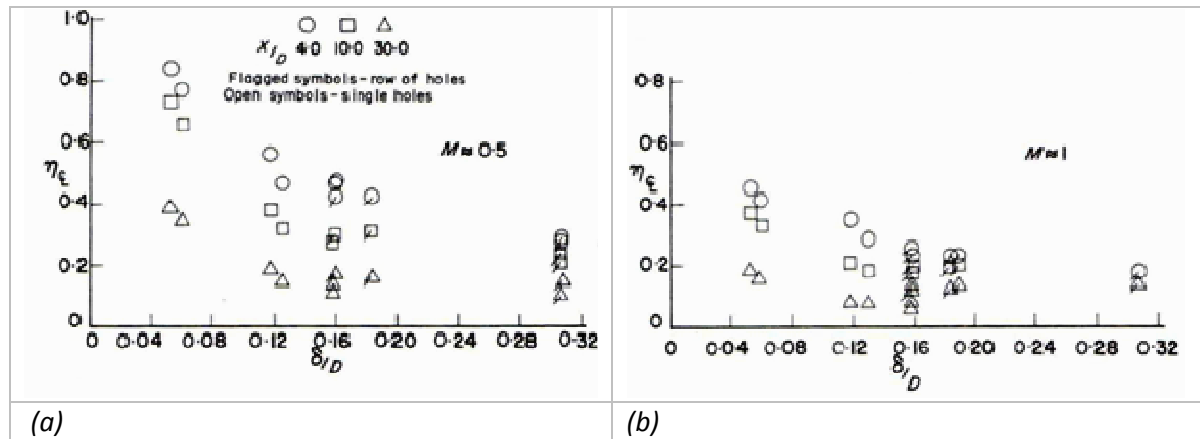


Figure (2. 19): Effect of upstream boundary layer thickness on centerline film cooling effectiveness for air injecting through cylindrical holes (symbols with a mark at the centre stands for single hole, empty symbol stands for a single row of holes) (a)  $M=0.5$ , (b)  $M=1.0$ ; Goldstein et al. (1974).

The decreased in effectiveness has been attributed to the lower mainstream velocity inside the boundary layer, which permits greater penetration of the jet. Author has suggested that at a large distance downstream there should be a greater difference between the results for a single hole and a row of holes due to the merging of the jets from the row of holes. Eriksen et al. (1974) noticed that there were no significant difference between centerline film cooling effectiveness as a function of Reynolds number (using free stream velocity and injection tube diameter ( $Re_D = \rho_\infty U_\infty D / \mu_\infty$ ) and the boundary layer thickness  $\delta/D$  within the limit of  $M \leq 1.0$ , when secondary flow is injected through a single hole or through the row of holes at 35 degree. Moreover, the physical mechanism responsible for the variation of centerline effectiveness was found to be similar as suggested by Goldstein et al. (1974).

## 2.4. Application of periodic velocity boundary limit on flow structure and wall heat transfer

### 2.4.1 Flow from a submerged pulsating jet

The effect of providing pulsation to submerged jet results in the appearance of large coherent structures within shear layer formed between a free jet flow and a surrounding still fluid. Farrington and Claunch (1994) studied the large-amplitude, low-frequency periodic disturbances on a planar jet and reported that the large-amplitude forcing leads to temporal, as well as spatial, velocity gradient in the shear layer. These velocity gradients enhance the natural instability of the jet, leading to early vortex generation. Figure (2.20a) shows that the vortex formation occurred closer to the nozzle as the pulsation Strouhal number is increased, compared to the steady jet case ( $St=0$ ). The size of the formation of coherent structure is influenced by the pulse amplitude and frequency.

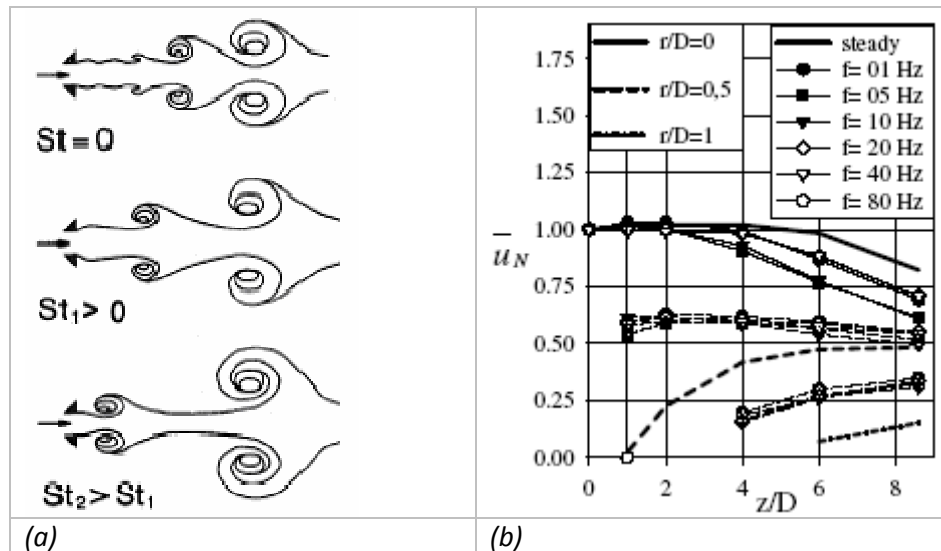


Figure (2. 20) : (a) Effect of pulsations on the development of a non-impinging jet; Farrington and Claunch (1994), (b) Influence of pulsation frequency on axial mean velocity along three radial locations; Hafmann et al. (2007).

Hafmann et al. (2007) reported that the deliverance of pulsation to the jet causes the enhanced entrainment of the air from the surrounding along with a decrease in the jet core velocity. The turbulence intensity in the core jet increased only slightly, also it became more homogeneous in the pulsating jet than in the case of steady jet. Figure (2.20b) demonstrates the evaluation of jet axial mean-velocity with respect to jet axis at three different radial positions, which shows that the length of the core decreases and the diameter of the jet increases, and this is due to the enhanced entrainment of air from the environment into the jet. At low pulsating frequency, flow structure shows nearly the similar distribution as for steady flow, but at higher frequencies the behavior of the flow properties changed significantly from the steady behavior. The critical frequency at which the flow behavior is departed from the quasi-steady behavior, was defined by a critical Strouhal number,  $St_{crit}=0.2$ . With pulsation above  $St_{crit}$ , mean axial velocity profile changed greatly from the one with low pulsating frequency (containing gauss-curve like velocity profile). Turbulence intensity increased compared to the steady and low frequency pulsating jet. The amplitude dampened in the jet, while it remained constant in the low-frequency pulsating jet.

## 2.4.2 Effect of turbine flow unsteadiness on film cooling

In the actual gas turbine system unsteadiness in the flow field influences the heat transfer and surface pressure distribution on the blade. The unsteadiness on the turbine airfoil develops from four different sources: (1) potential flow interactions, (2) shock wave passage, (3) wake passage and (4) random free-stream turbulence from the combustion chamber (Ligrani et al. 1996a, b). The flow, coming from the upstream nozzle guide vanes

locating pretty close to the rotating blades, is subjected to a periodic variation of the potential flow during turbine operation. The flow approaching to the rotor blade with significant periodic variations of pressure field, as well as the wake resulting from the blunt trailing edge of the vane significantly influence the film cooling performance. Moreover, in case of a transonic turbine, additional unsteadiness generated due to the release of shock waves from the vane row further influence the injectant distribution at the wall (Bon et al. 1996). Out of different sources of flow unsteadiness, potential flow interactions and passing shock wave are recognized to have dramatic effect on film cooling, (Ligrani et al. 1996a, b). Both of these unsteadiness results in important variations of the static pressure near turbine airfoil surfaces as blade row moves relative to each other. Film concentrations and film trajectories move to and from the wall with such periodic unsteadiness in the bulk flow, because of instantaneous change in both film flow rate and momentum at the cooling hole exit. The study of Abhari (1996) on the impact of rotor-stator interaction on surface heat transfer of film cooled turbine blades has shown that, on the pressure side of the blade the time average of the unsteady surface heat flux is as much as 230 percent greater than the steady-state prediction, while the reduction reported in the adiabatic film effectiveness is as much as 64 percent. It was considered that the reduction in the adiabatic film effectiveness is attributed to both the change in the time-averaged mass flux out of the film holes as well as the interaction of the coolant with the unsteady external flow.

The study of film cooling flow with externally imposed pulsation are performed with the purpose of characterizing both the effects of turbine unsteadiness on film cooling with frequency range typical to actual turbine, and also to figure out the range of Strouhal number pulsation and the blowing conditions which could possibly deliver a performance improvement in film cooling. The fundamental objectives of the present study correspond to the second category of the pulsating film cooling flow examination.

#### 2.4.2.1 Characterization of turbine unsteadiness through bulk flow pulsation

Studies based on the idea of static pressure pulsation in the far end of the tunnel test section by using an array of rotating shutters is employed by Ligrani et al. (1996a, b, 1997), Sohn et al. (1997), Seo et al. (1998), and Lee et al. (2002). The rotating shutters mechanism allows simulating the aforementioned unsteadiness by varying the injectant flow through the periodic variations of static pressure and streamwise velocity of the bulk flow. It was proposed that the altered time-averaged position of the film and mean-trajectories spreads the same amount of coolant over a larger volume.

Depending upon the magnitude of the coolant Strouhal number " $St_c = 2\pi fL / u_i$ , where;  $f$ =frequency,  $L$ =injection hole length,  $u_i$ =injection velocity", Ligrani et al. (1996a) proposed two distinctly different regimes of film cooling behavior with pulsations, (1) quasi-

steady and (2) non-quasi-steady. They defined a criteria that the  $St_c$  magnitude less than 1-2 corresponds to quasi-steady behavior, and  $St_c$  magnitude greater than 1-2 corresponds to non-quasi-steady behavior, regardless of the magnitude of blowing ratio  $\bar{M}$ . It was further explained that with quasi-steady film behavior, the entire film concentration moves to and from the wall in the continuous stream so that the injectant distribution at each instant of time remained same as the steady distribution. Moreover, in quasi-steady cases, pulsation time periods ( $1/2\pi m$ ) were found longer than the time required for a parcel of injectant to pass into and out of a film cooling hole ( $L/\bar{u}_i$ ). Under non-quasi-steady film behavior, multiple pulsations was expected to imposed on the injectant over the time period required for it to pass through a film cooling hole ( $1/2\pi m < L/\bar{u}_i$ ). In non-quasi-steady condition the injectant film has been found to oscillate in a way different from adjacent portions, which as mentioned, gives a 'wavy' appearance at each instant of time, such that larger injectant accumulations are to be spaced with a distance that the film moved over one pulsation cycle. Figure (2.21) indicates the trend of coolant Strouhal number variation as a function of averaged blowing ratio (Ligrani et al. 1996a).

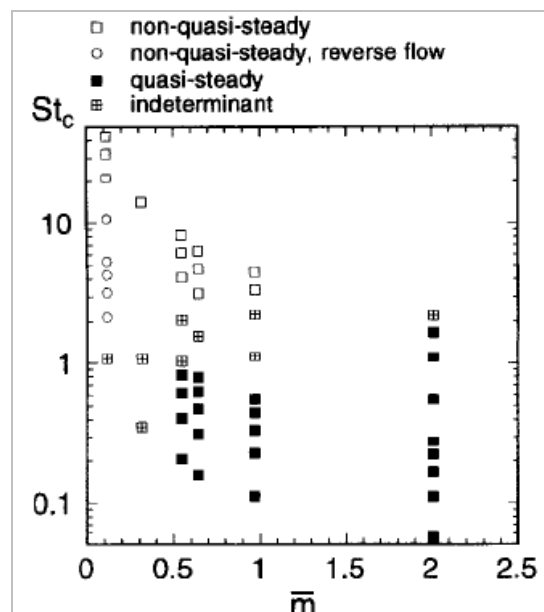


Figure (2. 21): Map illustrating different regimes of pulsating film cooling behavior, (blowing ratio ( $\bar{m}$ ) vs coolant Strouhal number ( $St_c$ )), Ligrani et al. (1996a).

#### 2.4.2.2 Characterization of turbine unsteadiness through injectant flow pulsation

In these studies, the pulsation frequencies are chosen to maintain a condition of injectant flow variation, close to those typically encountered in gas turbine system. Bons et al. (1996) provided the sinusoidal pulsing to the injectant flow by using a loudspeaker placed at one of the wall of the coolant supply plenum. The modulation frequencies of the jet were rather

small and the jet Strouhal number ( $St = f * d / U_{\infty}$ ) varies from 0.0059 to 0.0240. They concluded that the periodic forcing of the film cooling flow results in reduction in the film cooling effectiveness (70% at  $M=0.6$ ), and these reductions in the film effectiveness become progressively smaller as the blowing ratio increased, which was 65% at  $M=0.7$  and 60% at  $M=0.8$ . The reduction in film cooling effectiveness continues up to  $M=1$ . However, at  $M=1.5$  the forcing amplitude was nominally down to 5% of the film flow velocity, which did not modify the results much from the steady conditions.

In contrast to some other numerical studies using a square wave frequency signal (Muldoon and Acharya 2009; Kartuzova et al. 2009), Rutledge et al. (2009) also tested the response of a saw-tooth wave form for the jet pulsation in a CFD analysis of a turbine blade leading edge film cooling. It was shown that the saw-tooth wave input has helped in alleviating the part of initial start-up of the film cooling, causing jet lift-off from the wall for pulsation between  $M=1$  and 0 using square wave input. It was concluded that the performance of study jet with  $\overline{M}=0.5$  stayed superior to the other cases. They mentioned that at low frequency pulsing ( $St = f * d / U_{\infty} < 0.8$ ), the film cooling had performance similar to the time-weighted average performance of the steady jet. The cooling performance was determined in terms of net heat flux reduction ( $NHFR$ ).

$$NHFR = 1 - h/h_0(1 - \eta\theta) \quad \dots\dots\dots(2.4)$$

Where;  $\eta = (T_{ad} - T_{\infty}) / (T_i - T_{\infty})$  and  $\theta = (T_i - T_{\infty}) / (T_w - T_{\infty})$ . For two cases of blowing ratio,  $\overline{M}=0.5$  and 0.25, they reported a deterioration in film cooling performance when pulsing frequency was increased form  $St=0.755$  to 3.04. The trend reversed when the pulsing frequency was raised as high as  $St=6.04$  for the  $\overline{M}=0.5$  case, with significant pulsing effects to extend up to  $x/d=10$ . However, they mentioned that the dynamics of the jet at higher frequency are rather complex.

### 2.4.2.3 Influence of jet Strouhal number pulsation on film cooling effectiveness

Coulthard et al. (2006a) experimentally investigated the effects of jet pulsation on a flat constant heat flux wall containing a row of five cylindrical hole inclined at  $35^\circ$  in streamwise direction. The pulsation was generated by using nine fast response solenoid valves placed between the manifold and plenum, and the pulsation studied in a range of  $St=0.0119$  to 0.1905. Figure (2.22a) and (2.22b) indicates the spanwise-averaged effectiveness for the blowing ratios of 0.5 and 1 (B; symbol for blowing ratio is momentarily shown here). The poor quality of the images does not clearly show the entire range of pulsating frequency cases. However, the observations of the prominent ones can still provide meaningful informations.

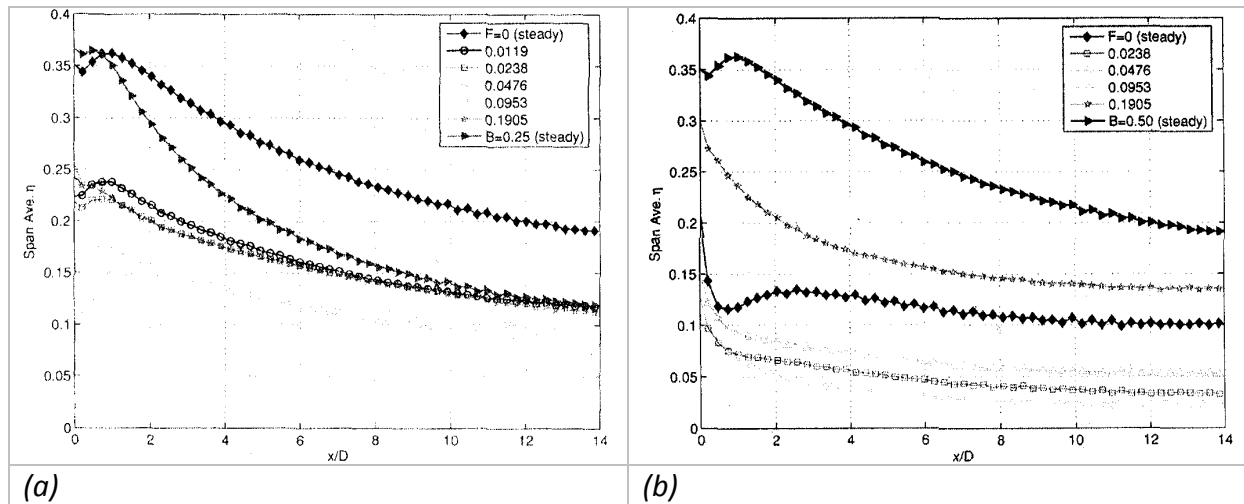


Figure (2.22): Spanwise adiabatic effectiveness, Duty cycle (DC)=0.5 (a)  $B=0.5$ , (b)  $B=1$ ; Coulthard et al. (2006a).

In figure (2.22a), author has shown the steady-state results for  $B=0.25$  and  $0.5$  for the reason of comparison. The steady blowing with  $B=0.5$  delivers higher effectiveness and the curve for  $B=0.25$  approaches to the fairly lowered pulsating jet cases. The lower-frequency pulsating cases had the best film cooling effectiveness because the effect of initial liftoff was reduced compared to the higher-frequency cases. The time duration for initial liftoff remained same for both lower- and higher-frequency cases, but at higher-frequency cases it has occupied a larger fraction of the total cycle time. Thus the time remaining for the steady condition was reduced. In figure (2.22b), author has shown the steady-state results for  $B=0.5$  and  $1$  for the reason of comparison. The pulsed case with  $St=0.1905$  has shown an improved film cooling effectiveness over the steady case, while in other cases of lower frequencies the flow is subjected to significant liftoff and had small effectiveness. At higher frequency the jets were not able to respond fast enough to keep up with the high frequency opening and closing of the valves, and some low momentum fluid left the film cooling holes during the “valve-off” portion of the cycle, resulting in higher effectiveness.

Figure (2.23a) and (2.23b) indicate the spanwise-averaged Stanton number ratio ( $S/S_o$ ) for the blowing ratios ( $B$ ) of  $0.5$  and  $1$  (Coulthard et al. 2006b). In figure (2.23a), author has shown the steady-state results for  $B=0.25$  and  $0.5$  for the reason of comparison. They observed the appearance of a starting vortex at the start of each pulsating cycle, which tends to induce higher mixing and to increase Stanton numbers. At higher frequencies, the number of starting vortices per unit time increases. Lower frequencies provide more time between pulses for the instantaneous Stanton number to drop. Generally, the higher film cooling effectiveness were shown to correspond well to lower Stanton numbers, with  $St=0.1905$

manifesting the highest values among other cases. In figure (2.23b), author has shown the steady-state results for  $B=0.5$  and  $1$  for the reason of comparison. The case of steady  $B=1$  had a 5% higher Stanton number ratio than the corresponding case of  $B=0.5$ . For  $B=1$ , the pulsation caused an increase of 10 to 15% compared to the Stanton number ratio measured under steady-state condition.

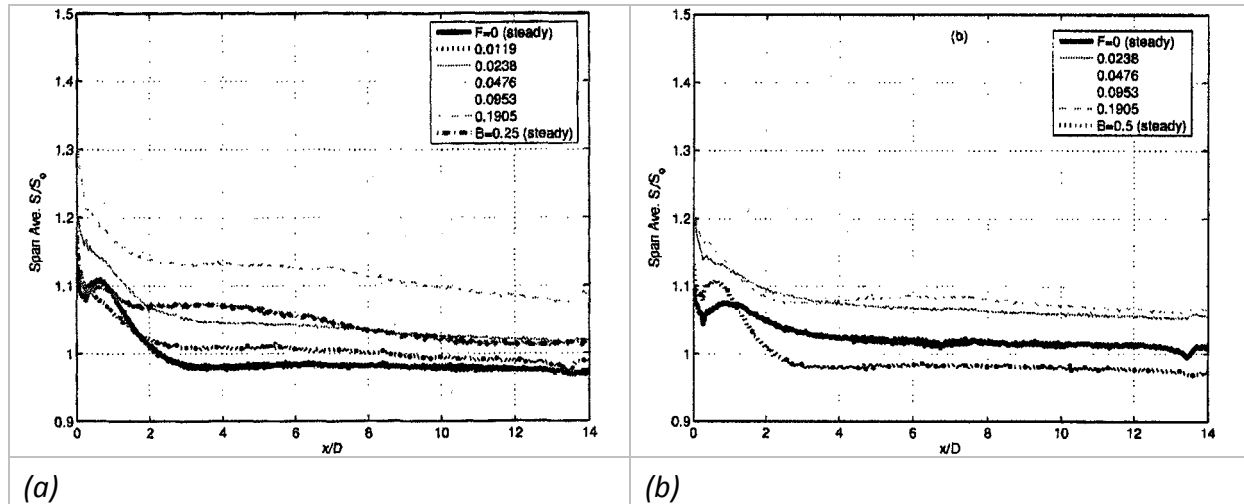


Figure (2. 23): Spanwise Stanton number ratio, (a)  $B=0.5$ , (b)  $B=1$ ; Coulthard et al. (2006b)

Direct Numerical Simulation (DNS) performed by Muldoon and Acharya (2009) has shown some improvement in wall coverage with pulsation. For a single  $30^\circ$  inclined cylindrical jet, they compared the cases of unpulsed and pulsed jet subjected to a wide range of non-dimensionalized frequency ( $St = f * d / U_\infty$ ) varying from 0.004 to 0.32 and signal amplitude with duty cycle (DC) varying from 0.25 and 0.5. Figure (2.24a) and (2.24b) show the instantaneous images of the temperature field  $T = (T - T_c) / (T_h - T_c)$  for the cases of study and pulsed jet flows. These results correspond to the best performance results of the author obtained at ( $\overline{M} = 1.5$ ,  $St=0.32$ ,  $DC=0.5$ ) compared to steady blowing. The recirculation region behind the jet reduced greatly with pulsing, leading to improved film-cooling effectiveness. They mentioned that the enhanced vortex dynamics and induction are the reasons for the greater attachment of the jet to the wall. In the pulsing cases the vortex strength increased to a level that they started to alter the dynamics of the lifted jet and causes early reattachment. These attributes of jet variation with pulsation seems to correspond globally with the attributes of a submerged pulsating jet discussed earlier.

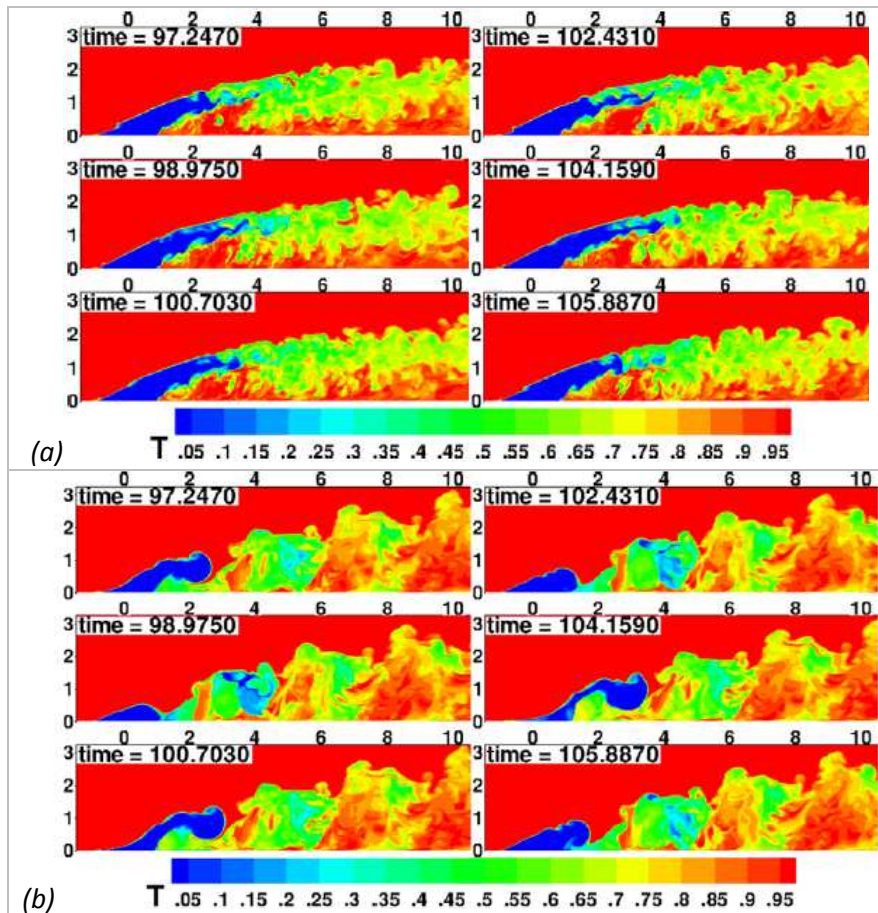


Figure (2. 24): Temperature contour,  $T = (T - T_c)/(T_h - T_c)$  at different times,  $\bar{M} = 1.5$ ,  $z/d = 0$ , (a) unimpulsed case, (b)  $St = 0.32$ , Duty cycle (DC) = 0.5; Muldoon and Acharya (2009).

The computational results of Kartuzova et al. (2009) also indicated an improvement in wall protection as a function of blowing ratio for a cylindrical hole inclined at a  $35^\circ$  in streamwise direction. The injectant was pulsed with a square wave input signal to a non-dimensionalized frequency ( $St = f * d / U_\infty$ ) varying from 0.0119 to 1 and signal amplitude with duty cycle (DC) of 0.5 in cases of nominal blowing ratios  $\bar{M}$  of 0.5 and 1.5. Figure (2.25a) and (2.25b) show the contours of film cooling effectiveness for unimpulsed ( $St = 0$ ) and pulsating ( $St = 0.19$ ) jet cases for  $\bar{M} = 0.5$ . With pulsation film cooling effectiveness is poor, and the injectant flow has considerable variation in the spanwise direction. Figure (2.25c) shows the velocity vectors and contour in the injection tube varying in the cycle of pulsation. The vector field became increasingly complicated as the pulsation started to follow the lower edge of the square wave signal at  $t = 1/2$  of the cycle and most of them acquired a reverse direction.

An interesting observation highlighted by the author is the returning of film cooling effectiveness to the quasi-steady behavior at higher frequency ( $St = 0.38$ ) for  $\bar{M} = 0.5$ , while the pulsation amplitude was constant in all cases. In case of higher frequency pulsation

( $St=0.38$ ), the time-averaged film cooling effectiveness has increased but remained below the steady-state results.

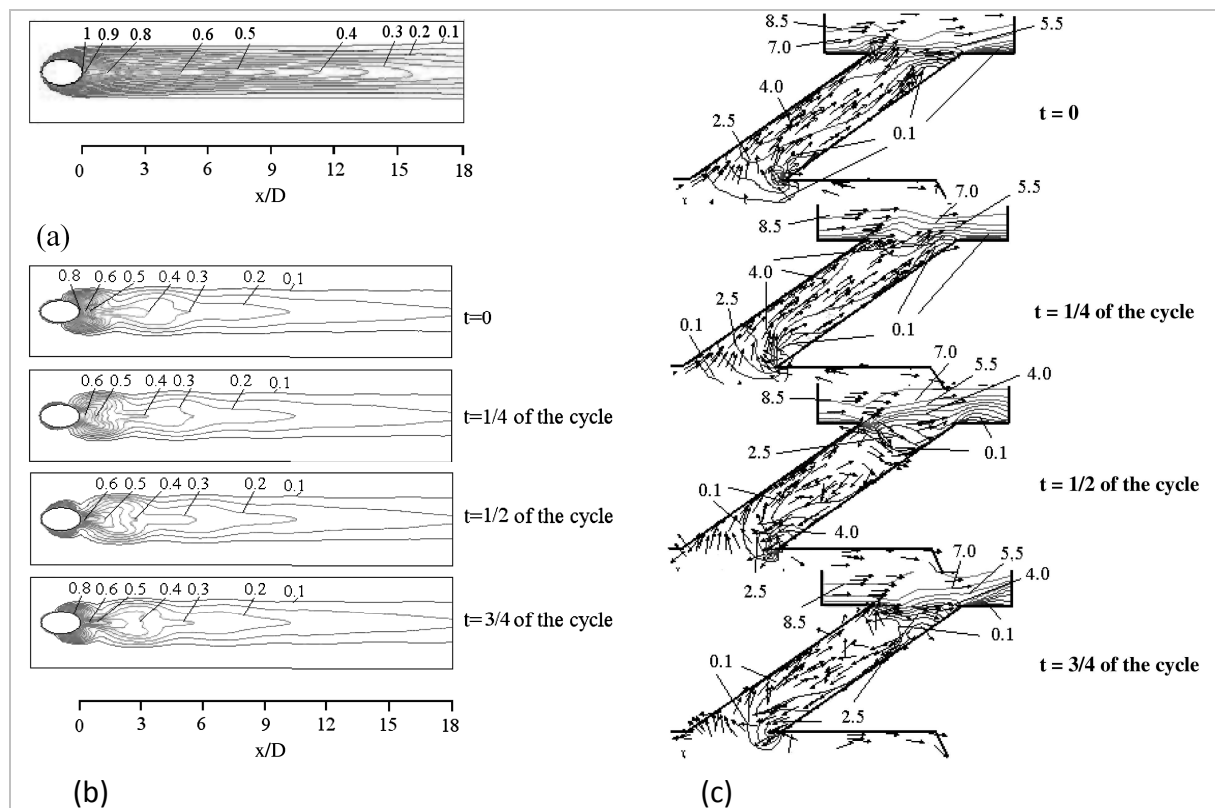


Figure (2. 25): Contours of film cooling Effectiveness,  $\overline{M}=0.5$ , (a) Steady state ( $St=0$ ), (b)  $St=0.19$ , (c) velocity vectors at  $St=0.19$ ; Kartuzova et al. (2009)

Figure (2.26a) shows the results for  $\overline{M}=1.5$  and  $St=0$ , manifesting low effectiveness downstream of the jet, and figure (2.26b) shows the results for  $\overline{M}=1.5$  and  $St=0.38$  where the effectiveness were higher than  $St=0$  at all times of the cycle. In this case the jet broke up due to both the jet liftoff and pulsation. This provided a continuous supply of coolant on the top surface and thus higher effectiveness at all  $x/d$  value.

They mentioned that the overall higher injectant film concentration due to jet pulsation is only achievable at blowing ratios triggering jet lift-off, such as  $\overline{M}=1.5$ . Cooling efficiency at  $St=0.38$  was higher than for  $St=1.0$  and for the steady blowing case. It was conclude that the spatially averaged effectiveness is reduced to 38.12% compared to steady state condition at  $\overline{M}=0.5$ , and increased to 15% for  $\overline{M}=1.5$ .

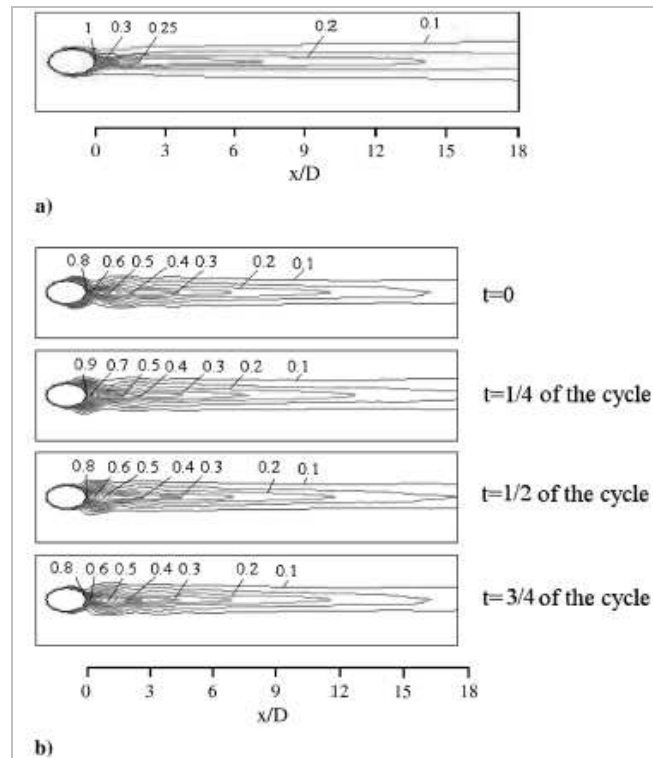


Figure (2. 26): Contours of film cooling Effectiveness,  $\overline{M} = 1.5$ , (a) Steady state ( $St=0$ ), (b)  $St=0.38$ ; Kartuzova et al. (2009).

## 2.5. Conclusion

The review of the aerodynamic characteristics of the jet in cross flow is undertaken for both normal and inclined jet crossflow interaction. The thermal attributes of an inclined jet are reviewed exclusively in the perspective of film cooling. The principle sources of gas turbine flow unsteadiness were discussed, and their effects on film cooling performance were reviewed from the small number of references available through open literature. Generally, it can be concluded that an externally imposed pulsation in a frequency range typical of the actual engine for blowing ratios of  $\overline{M} < 1$  results in the degradation of wall protection by film cooling, compared to the steady condition. However, the phenomena mainly depend on the blowing ratio and the Strouhal number frequency. An improvement in film cooling performance due to jet pulsation was only reported for the blowing ratios triggering jet lift-off, such as  $\overline{M} = 1.5$ .

The review of the available studies focusing on film cooling effectiveness under jet pulsation has shown that this topic is fairly recent. Therefore both aerodynamic and thermal attributes of the flow field require further investigation for a wider range of Strouhal number pulsation, so that the associated phenomena can be understood in a better way.



## 2.6. References

- 1 Abhari RS, "Impact of Rotor-Stator Interaction on turbine Blade film cooling", Journal of Turbomachinery, 118 (1996) 123-133.
- 2 Aly SE, "Injection effect on two dimensional boundary layer", Energy Conversion & Management, 41 (2000) 539-550.
- 3 Andreopoulos J, "Heat transfer measurement in a heated jet-pipe flow issuing into a cold cross steam", Physics of Fluid, 26 (1983) 3201-3210.
- 4 Andreopoulos J, "On the structure of jets in a crossflow", J. Fluid Mech. 157 (1984) 163-197.
- 5 Andreopoulos J, Rodi W, "Experimental investigation of jets in a crossflow", J. Fluid Mech. 138 (1984) 93-127.
- 6 Bons JP, Rivir JB, Mac Arthur CD, Pestian DJ, "The effect of unsteadiness on film cooling effectiveness", Wright Laboratory, WL-TR-96-2096, Jan-1995.
- 7 Brundage AL, Plesniak MW, Ramadhyani S, "Influence of coolant feed direction and hole length on film cooling jet velocity profiles", International Gas Turbine & Aeroengine Congress & Exhibition, Indianapolis, Indiana, June 1999.
- 8 Burd SW, Kaszeta RW, Simon TW, "Measurement in film cooling flows: Hole L/D and turbulence intensity Effects", Gas turbine Heat Transfer Session, 1996 IMECE Conference, Atlanta, GA.
- 9 Coulthard SM, Volino RJ, Flack KA, "Effect of jet pulsing on film cooling-Part 1: Effectiveness and flow-field temperature results", Journal of Turbomachinery, ASME, 129 (2007a) 232-246.
- 10 Coulthard SM, Volino RJ, Flack KA, "Effect of jet pulsing on film cooling-Part 2: Heat transfer results", GT2006-91274, ASME Turbo Expo 2006: Power for land, Sea and Air, May 8-11, (2007b), Barcelona Spain.
- 11 Dorignac E, Vullierme JJ, Delouche E, Garem JH, Leblanc R, "Blowing rate effects on the heat transfer coefficient on a film heated surface at transonic speed", Int. Symposium on

- experimental and computational aerodynamics of internal flow, July 12-15, 1993, Prague.
- 12 Dorignac E, Vullierme JJ, Deniboire P, Foucault E, Bousgarbies JL, "*Thermographie Infrarouge et tomographie laser appliqués à l'étude des films de refroidissement*", 5ème colloque national de visualisation et de traitement d'images en mécanique des fluides, Juin 2-5, 1992, Poitiers.
  - 13 Eckert ERG, "*Gas-to-gas film cooling*", Published in *Inzhenerno-Rizicheskii Zhurnal*, SpringerLink, 19 (1970) 426-440.
  - 14 Eriksen VL, Goldstein RJ, "*Heat transfer and film cooling following injection through inclined circular tubes*", *Journal of heat transfer*, May-1974, 239-245.
  - 15 Farrington RB, Claunch SD, "*Infrared imaging of large-amplitude, low-frequency disturbances on a planer jet*", *AIAA Journal*, 32 (1994) 317-323.
  - 16 Foucault E, Deniboire P, Bousgarbies JL, Vullierme JJ, Dorignac E, "*Etude expérimentale du transfert de chaleur près d'une paroi plane chauffée en présence d'injection multiples (Ecoulement subsonique)*". *Heat transfer and cooling in Gas Turbine-1992*, AGARD-CP-527, paper-4.
  - 17 Fric TF, Roshko A, "*Vertical structure in the wake of a transverse jet*", *J. Fluid Mech.* 279 (1994) 1-47.
  - 18 Goldstein RJ, Eckert E.R.G., "*Effects of hole geometry and density on three-dimensional film cooling*", *Int. J. Heat Mass Transfer*, 17 (1974) 595-607.
  - 19 Guo X, Schröder W, Meinke M, "*Large-eddy simulations of film cooling flows*", *Computers & Fluids* 35 (2006) 587-606.
  - 20 Hofmann HM, Movileanu DL, Kind M, Martin H, "*Influence of a pulsation on heat transfer and flow structure in submerged impinging jets*", *Int. J. heat Mass Transfer*, 50 (2007) 3638-3648.
  - 21 Jessen W, Schröder W, Klaas M, "*Evolution of jets effusing from inclined holes into crossflow*", *International Journal of Heat Fluid Flow* 28 (2007) 1312–1326.

- 22 Kartuzova O, Daniel D, Ibrahim MB, Volino RJ, "*Computational simulation of cylindrical film hole with jet pulsation on flat plates*", Journal of propulsion and power, 25 (2009) 1249-1258.
- 23 Kelso RM, Lim TT, Perry AE, "*An experimental study of round jets in cross-flow*", J. Fluid Mech. 306 (1996) 111-144.
- 24 Lebedev VP, Lemanov VV, Misyura S YA, Terekhov VI, "*Effects of flow turbulence on film cooling efficiency*", Int. J. Heat Mass Transfer, 38 (1995) 2117-2125.
- 25 Lee JS, Jung IS, "*Effect of bulk flow pulsations on film cooling with compound angle holes*", Int. J. Heat Mass Transfer, 45 (2002) 113-123.
- 26 Lee SW, Lee JS, Ro ST, "*Experimental study on the flow characteristics of streamwise inclined jets in crossflow on flat plate*", ASME J. Turbomach, 116 (1994) 97-105.
- 27 Levi E, "*A universal Strouhal law*", ASCE Journal of the Engineering Mechanics Division 109 (3) 718-727.
- 28 Ligrani PM, Ciriello S, Bishop DT, "*Heat transfer, Adiabatic effectiveness, and injectant distribution downstream of a single row and two staggered rows of compound angle film cooling holes*", Journal of Turbomachinery, ASME, 114 (1992) 687-700.
- 29 Ligrani PM, Gong R, Cuthrell JM, "*Bulk flow pulsations and film cooling-I: Injectant behavior*", Int. J Heat Mass Transfer, 39 (1996a) 2271-2282.
- 30 Ligrani PM, Gong R, Cuthrell JM, "*Bulk flow pulsations and film cooling-II: Flow structure and film effectiveness*", Int. J. Heat Mass Transfer, 39 (1996b) 2283-2292.
- 31 Ligrani PM, Gong R, Cuthrell JM, Lee JS, "*Effect of bulk flow pulsations on film cooled boundary layer structure*", Journal of fluid engineering, 119 (1997) 56-66.
- 32 Ligrani PM, Ramsey AE, "*Film cooling from spanwise-oriented holes in two staggered rows*", ASME, 119 (1997) 562-567.
- 33 Marek CJ, Tacina RR, "*Effect of free-stream turbulence on film cooling*", NASA Technical Note, NASA TN D-7958.

- 34 Mayhew JE, Baughn JW, Byerley AR, “*The effect of freestream turbulence on film cooling adiabatic effectiveness*”, *Int. J. Heat and Fluid Flow*, 24 (2003) 669-679.
- 35 Mendez S, Nicoud F, “*Large-eddy simulation of a bi-periodic turbulent flow with effusion*”, *J. Fluid Mech*, 2006.
- 36 Moussa ZM, Trischka JW, Eskinazi S, “*The near field in the mixing of a round jet with a cross-stream*”; *J. Fluid Mech.* 80 (1977) 49-80.
- 37 Muldoon F, Acharya S, “*DNS study of pulsed film cooling for enhanced cooling effectiveness*”, *Int. J. Heat Mass Transfer*, 52 (2009) 3118-3127.
- 38 Nasir H, Acharya S, Ekked S, “*Improved film cooling from cylindrical angled holes with triangular tabs: effect of tab orientations*”, *Int. J. Heat Mass Transfer*, 24 (2003) 657-668.
- 39 Pietrzyk JR, Bogard DG, Crawford ME, “*Hydrodynamic Measurement of jets in crossflow for gas turbine film cooling application*”, *ASME J. Turbomach*, 111 (1989) 139-145.
- 40 Rudman M, “*Simulation of the near field of a jet in a crossflow*”, *Experimental Thermal and Fluid Science*, 12 (1996) 134-141.
- 41 Rutledge JL, King PI, Rivir R, “*CFD Prediction of the frequency dependence of pulsed film cooling heat flux on a turbine blade leading edge*”, *AIAA Paper 2009-0680*, 47<sup>th</sup> AIAA Aerospace Sciences Meeting , Jan 2009, Orlando.
- 42 Sargison JE, Guo SM, Oldfield MLG, Lock GD, Rawlinson AJ, “*A converging slot-hole film-cooling geometry—Part 1: Low-speed flat plate heat transfer and loss*”, *Journal of Turbomachinery*, ASME, 124 (2002a) 453-460.
- 43 Sargison JE, Guo SM, Oldfield MLG, Lock GD, Rawlinson AJ, “*A converging slot-hole film-cooling geometry—Part 2: Transonic nozzle guide vane heat transfer and loss*”, *Journal of Turbomachinery*, ASME, 124 (2002b) 453-460.
- 44 Schmidt DL, Sen B, Bogard DG, “*Film cooling with compound angle holes: Adiabatic effectiveness*”, *Journal of Turbomachinery*, ASME, 118 (1996) 807-813.

- 45 Seo HJ, Lee JS, Ligrani PM, *“The effect of injection hole length on film cooling with bulk flow pulsations”*, Int. J. Heat Mass Transfer, 41 (1998) 3515-3528.
- 46 Sinha AK, Bogard DG, Crawford ME, *“Film cooling effectiveness downstream of a single row of holes with variable density ratio”*, Journal of Turbomachinery, ASME, 113 (1991a) 442-449.
- 47 Sinha AK, Bogard DG, Crawford ME, *“Gas turbine film cooling: Flowfield due to a second row of holes”*, Journal of Turbomachinery, ASME, 113 (1991b) 450-456.
- 48 Sohn DK, Lee JS, *“The effect of bulk flow pulsation on film cooling from the rows of holes”*, Presented at the International Gas Turbine & Aeroengine Congress & Exhibition, Orlando, Florida—2-5 June, 1997.
- 49 Volchkov EP, Zaulichnyi EG, Kutaleladze SS, Leont’ev AL, *“Film cooling by injection into a turbulent boundary layer”*, Journal of Applied Mechanics and Technical Physics, 8 (1967) 103-106.
- 50 Walters DK, Leylek JH, *“A Detailed analysis of film cooling physics: Part 1-Streamwise injection with cylindrical Holes”*, ASME J. Turbomach, 122 (2000) 102-111.
- 51 Yuen CHN, Martinez-Botas RF, *“Film cooling characteristics of a single round hole at various streamwise angles in a crossflow: Part I, Effectiveness”*, Int. J. Heat Mass Transfer, 46 (2003a) 221–235.
- 52 Yuen CHN, Martinez-Botas RF, *“Film cooling characteristics of a single round hole at various streamwise angles in a crossflow: Part II, Heat transfer coefficient”*, Int. J. Heat and Mass Transfer, 46 (2003b) 237–249.
- 53 Yuen CHN, Martinez-Botas RF, *“Film cooling characteristics of rows of round hole at various streamwise angles in a crossflow: Part I, Effectiveness”*, Int. J. Heat and Mass Transfer, 48 (2005a) 4995–5016.
- 54 Yuen CHN, Martinez-Botas RF, *“Film cooling characteristics of rows of round hole at various streamwise angles in a crossflow: Part II, Heat transfer coefficient”*, Int. J. Heat Mass Transfer, 48 (2005b) 5017–5035.



## Table of Contents

3.1	Frame work of experimental measurement .....	55
3.2	Principle hardware components .....	57
3.2.1	Wind tunnel .....	57
3.2.1.1	Test section .....	57
3.2.1.2	Injection plate .....	58
3.2.2	Injection Flow System .....	59
3.2.2.1	Measurement of injection mass flow rate .....	60
3.2.2.2	Heating system for injectant flow .....	61
3.2.2.3	Injectant temperature regulation system .....	61
3.2.2.4	Pulse generation system .....	62
3.3	Velocity measurement systems .....	66
3.3.1	Laser Doppler Anemometry .....	67
3.3.1.1	Descriptions of the measurement scenario .....	67
3.3.1.2	Experimental conditions for LDV measurements .....	67
3.3.1.3	Working principle .....	68
3.3.2	Hot wire Anemometer .....	69
3.3.2.1	Descriptions of the measurement scenario .....	69
3.3.2.2	Experimental conditions for hot wire measurements .....	70
3.3.2.3	Working principle .....	71
3.3.3	Statistical errors in LDV and hot wire measurements .....	72
3.3.4	Time Resolved Particle Image Velocimetry .....	73
3.3.4.1	Descriptions of the measurement scenario .....	73
3.3.4.2	Experimental conditions for TR-PIV measurements .....	75
3.3.4.3	Fundamentals of PIV system .....	77
3.3.4.4	Spatial resolution of PIV system .....	77
3.3.4.5	Statistical errors in TR-PIV measurements .....	78
3.4	Thermal measurements of film cooling configuration .....	79
3.4.1	Infra-red thermography .....	79
3.4.1.1	Descriptions of the measurement scenario .....	79
3.4.1.2	Experimental conditions for TR-PIV measurements .....	83
3.4.1.3	Injection wall heat dissipation system .....	83
3.4.1.4	Infra-red camera .....	84
3.4.1.5	Surface temperature map (without flow) .....	85
3.4.2	Cold wire measurement .....	86
3.4.2.1	Descriptions of the measurement scenario .....	86
3.4.2.2	Experimental conditions for cold wire measurements .....	87
3.4.2.3	Working principle .....	87
3.5	Data treatments .....	88
3.5.1	Phase average description of the flow .....	88
3.5.2	Turbulence description of the flow .....	90
3.5.3	Convective heat transfer coefficient and adiabatic wall temperature .....	94
3.5.3.1	Heat transfer Models .....	94
3.5.3.2	Steady state heat transfer model .....	97
3.5.3.3	Convective heat flux .....	98
3.5.4	Phase averaged description of the temperature field .....	99
3.5.5	Thermal uncertainties .....	100
3.6	Reference .....	103

## Nomenclatures

<b><u>Abbreviations</u></b>	<b><u>Subscripts/superscripts</u></b>
$\rho$	Fluid density (kg/m <sup>3</sup> )
$T$	Temperature (K)
$P$	Pressure (Pa)
$d$	Hole diameter (mm)
$L$	Hole length (mm)
$U$	Streamwise velocity (m/s)
$V$	Normal velocity (m/s)
$W$	Lateral velocity (m/s)
$\overline{M}$	Blowing ratio ( $= \rho_i \overline{U}_i / \rho_\infty \overline{U}_\infty$ )
$u$	Streamwise velocity fluctuation (m/s)
$v$	Normal velocity fluctuation (m/s)
$w$	Lateral velocity fluctuation (m/s)
$\delta$	Boundary layer thickness (mm)
$\delta^*$	Displacement thickness (mm)
$u_\tau$	Friction velocity (m/s)
$U^+$	U normalized by friction velocity ( $= U / u_\tau$ )
$IT$	Turbulent intensity (%)
$\sqrt{u^2}$	x-component of RMS velocity (m/s)
$\sqrt{v^2}$	y-component of RMS velocity (m/s)
$\phi$	Heat flux (W/m <sup>2</sup> )
$\varepsilon$	Emissivity / Energy dissipation rate (m <sup>2</sup> /s <sup>3</sup> )
$\tau$	Transmissivity
$F$	Radiation form factor
$h$	Heat transfer coefficient (W/m <sup>2</sup> .K)
$NHFR$	Net heat flux reduction ( $= 1 - \phi / \phi_o$ )
$\theta$	Non-dimensionalized temperature ( $= (T - T_\infty) / (T_i - T_\infty)$ )
$\eta$	Effectiveness ( $= (T_{ad} - T_\infty) / (T_i - T_\infty)$ )
$R$	Resistance (Ohms)
$t$	Time (s)
$f$	Frequency (1/s)
$K$	Wave number (m <sup>-1</sup> )
$\Lambda$	Integral length scale (mm)
$\lambda$	Taylor micro scale (mm)
$\eta_\varepsilon$	Kolmogorov scale (mm)
$x, y$	Streamwise and normal coordinates (mm)
	$i$ Injectant
	$\infty$ Free-stream
	$ad$ Adiabatic
	$rms$ Root mean square
	$-$ Time-averaged
	$\sim$ Periodic component
	$a$ Amplitude
	$j$ Index number
	$acq$ Acquisition
	$s$ Excitation
	$t$ Thermal

## ***EXPERIMENTAL SETUP AND MEASURING TECHNIQUES***

### **3.1 Frame work of experimental measurement**

The film cooling technique has great implications in the aeronautical industry. It is commonly applied to gas turbine components running under extremely harsh thermal conditions to ensure structural integrity of the material, such as; combustor chamber liner and high pressure turbine blades, figure (3.1). The flow field resulting under these conditions engenders strong coupling of aerodynamic and thermal aspects of the flow.

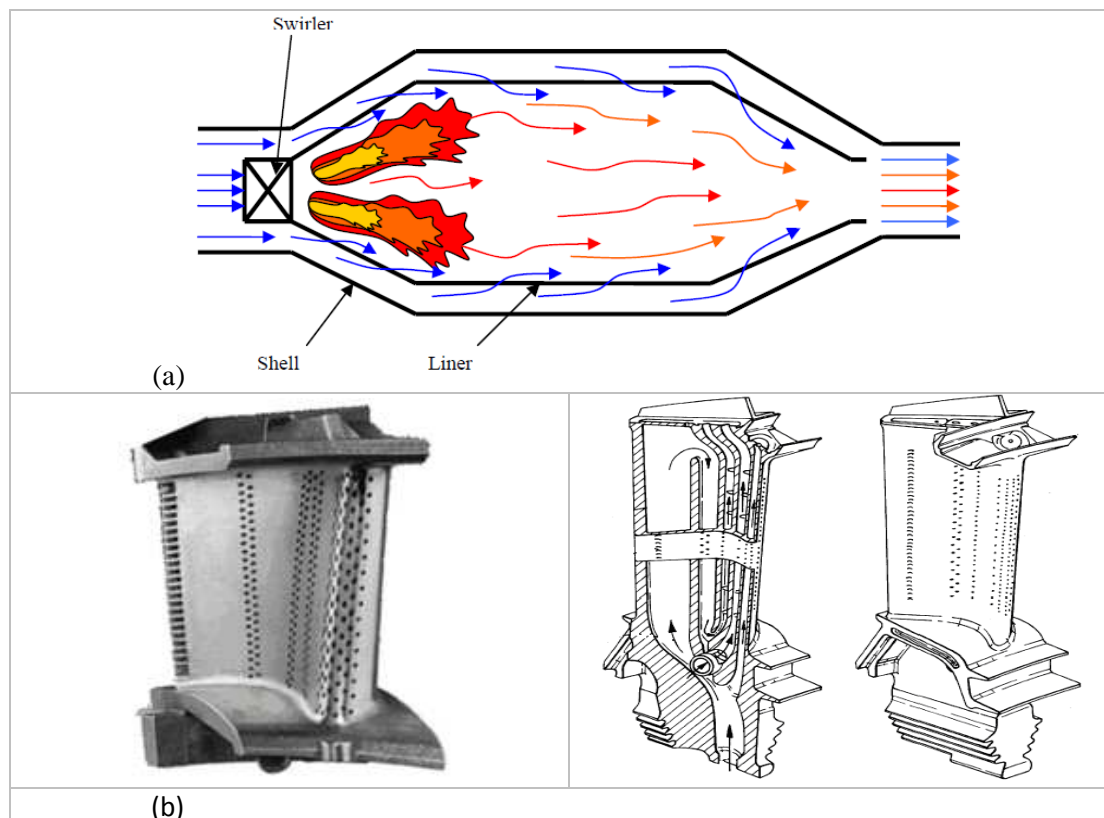


Figure (3.1): Film cooling of (a) Combustion chamber liner; Esposito (2006), (b) Gas turbine blade; Harvey (2003).

An experimental model that allows investigating the inherent characteristics of such configuration primarily consists of a cross-stream interaction of a high temperature mainstream flow and a cold injectant flow issuing from a perforated wall. The thermal conditions encountered under these circumstances are inherently difficult to control in conventional test facilities. To maintain similar fluid properties, some studies have employed extremely cooled injectant fluids; such as the conventional refrigerants, to maintain more or less a realistic density ratios (Teekaram et al. (1989); Ekkad et al. (1998); Saumweber and

Schulz (2004)). However, most of the researches have been performed under modest temperature ranges, and focuses the attributes of fundamental flow structures resulting from crossflow interaction and their ultimate influence on the thermal exchange at the wall by using several nondimensionalised parameters (density ratio (D.R) =  $\rho_i/\rho_\infty$ , velocity ratio (R) =  $U_i/U_\infty$ , blowing ratio (M) =  $\rho_i U_i/\rho_\infty U_\infty$ , momentum ratio (I) =  $\rho_i U_i^2/\rho_\infty U_\infty^2$ ), ratio of boundary layer thickness and hole diameter  $\delta/d$  and freestream turbulent intensity  $u_{rms}/\bar{U}$  etc. A common practice employed to the film cooling experiments is the use of hot fluid stream in wall injection and cooler fluid stream in the mainstream flow (i.e. reversing the input thermal condition of the interacting flows). This approach helps in maintaining the injectant flow temperature to a much higher level compared to the ambient with minor heat loss (Dung 2009; Thibault 2009). Reversing of the inlet flow temperature boundary condition do not vary the actual thermal exchange accruing at the wall as long as the Richardson number expressing the relative importance of gravitational forces over inertia forces remains fairly low, Eq. (3.1).

$$R_i = \frac{g.L.\Delta T}{U_e^2.T} \quad \dots\dots (3.1)$$

The computed value of this number lies within 0.011 to 0.0073 for the entire working range of the present study. This implies that the influence of the buoyancy effect is very small in the present conditions.

A simple scale-up model used to simulate the film cooling problem in the present study includes a mainstream flow and a 30° inclined injectant flow interacting over a flat wall, see figure (3.2). The origin of coordinate system is considered at the center of hole exit plane.

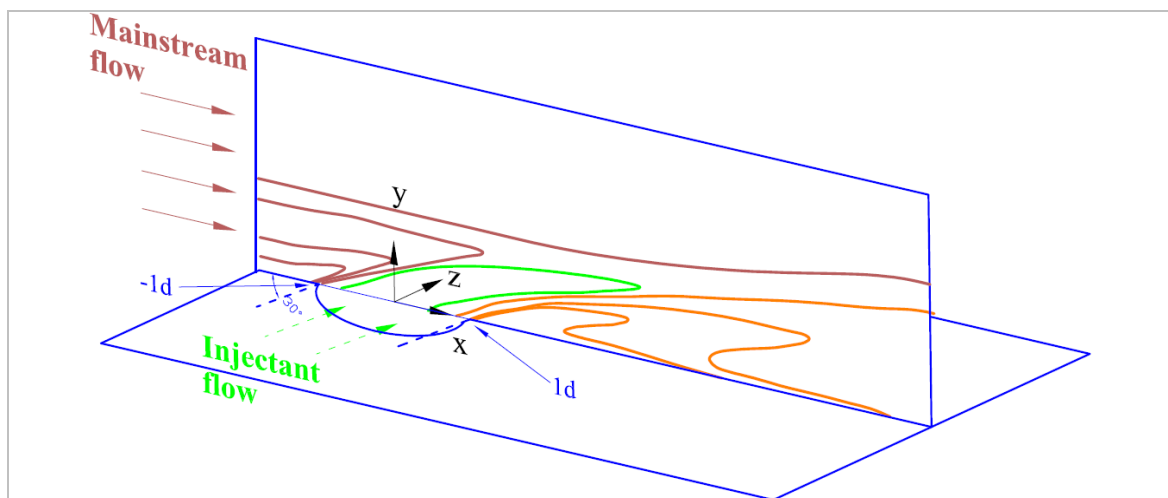


Figure (3.2): Schematic diagram of film cooling configuration.

## 3.2 Principle hardware components

### 3.2.1 Wind tunnel

The film cooling experiments are performed in a subsonic, close-loop wind tunnel equipped with a thermoregulatory system. The circulation of air is achieved by a helical fan, coupled with a 9 kW electric motor having a highest speed of 1500 revolutions per minutes. At the outer side, the entire metallic wall of the tunnel is covered with 9mm thick polyurethane foam. A global view of the wind tunnel is shown in figure (3.3a). The available thermoregulatory unit allows maintaining a desired temperature level by means of an automatic control unit containing a hot source (electric battery) and a quick response refrigeration unit. The system is likely to perform more effectively with lower transition time for a temperature range of 15-25 °C, even if the flow velocity is considerably low, (Dieumegard 2003).

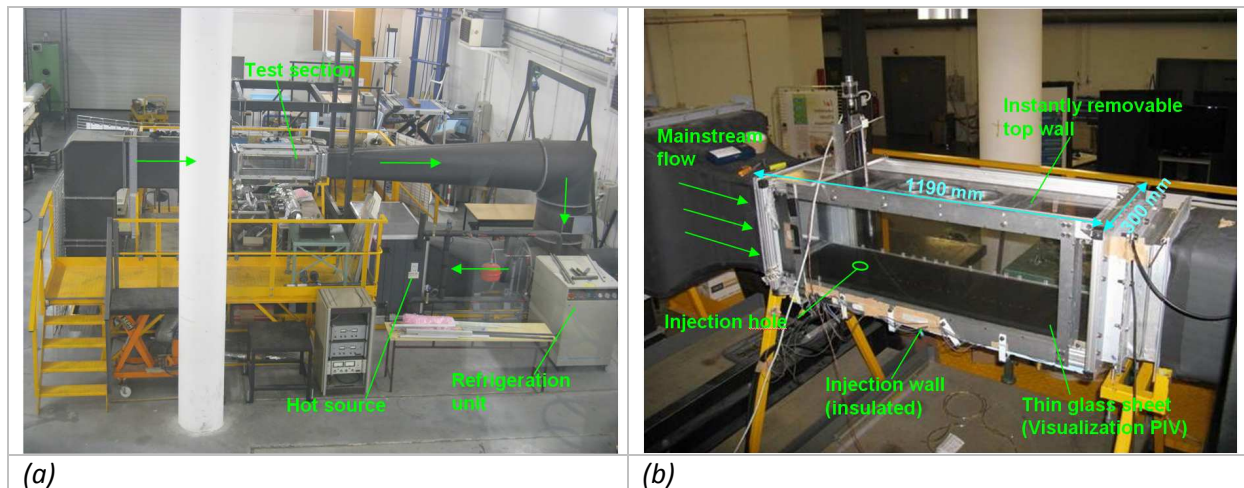


Figure (3.3): (a) Plan of Wind tunnel system; (b) Test section assembly.

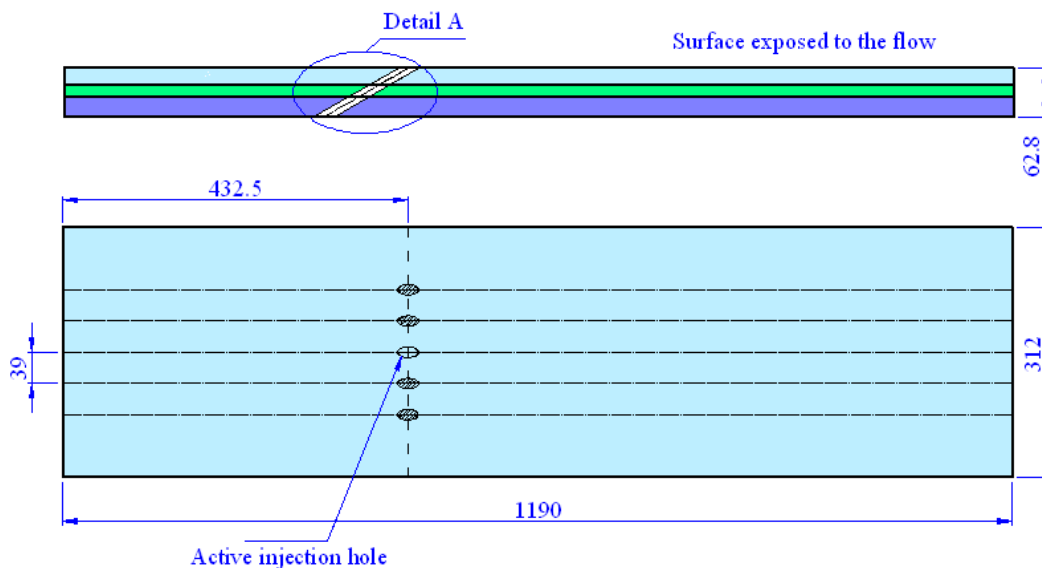
#### 3.2.1.1 Test section

The test section of the wind tunnel has a square cross-section of  $300 \times 300 \text{ mm}^2$  and a length of 1190 mm, as shown in figure (3.3b). It contains different types of wall mounted to a metallic frame. On the upper side, the test section assembly facilitates a rapid exchange of the wall for a desired measurement scheme such as the aerodynamic measurement using PIV, the thermal measurement using an infra-red camera or a hot and cold wire survey. The first configuration for the top wall allows an auxiliary assembly consisting of a thin rectangular frame of aluminum glued with a 5mm ordinary glass sheet to perform PIV experiments with an improved illumination of the desired region. This fixation allows a rapid removal of the upper wall for providing an access for cleaning purposes, which might be required at times while performing PIV measurement with significant seeding of the oil

particles. The other configuration, which allows the placement of a Plexiglas sheet that fits to the dimension with the test section at the upper wall location, provides the access to the hot wire probe to maneuver in both axial and lateral direction by moving a number of centrally placed axially sliding strip measuring  $110 \times 20 \text{ mm}^2$ . The movement of the strips covers an overall area of  $580 \times 110 \text{ mm}^2$ . Thus, hot wire measurement requiring the placement of the probe right over the region of interest is limited to a streamwise distance of  $-5d$  to  $35d$ . Among the other three walls, the two vertical walls lying on each side of the test section have one side of 5mm glass sheet in order to achieve an improved exposure of the region of interest during PIV measurement, while on the other side a Plexiglas sheet is simply screwed on the structure of the test section to achieve a straight forward fixation of the wall. The injection wall lying on the bottom side of the tunnel contains a  $35 \text{ }\mu\text{m}$  copper circuit on the inner side of the wall, followed by a 0.8 mm epoxy layer and a 22 mm Ertalon® plate.

### 3.2.1.2 Injection plate

The injection plate contains a row of 5 circular simple-angled holes inclined at  $30^\circ$  with respect to the mainstream flow. In the present study, only the central hole was used to study the effects of injectant flow pulsation on the ultimate wall coverage. The holes have a diameter,  $d$ , of 13 mm and a length,  $L$ , of  $7.7d$ . The longitudinal position of the holes with respect to the test section inlet is hydro-dynamically fixed to a boundary layer thickness of  $\delta \approx 1d$  and  $0.93d$  under different mainstream conditions. The detail of hole dimension and their respective location on the injection plate is shown in figure (3.4). A small groove shown in the detail view allows a 13 mm (inside diameter) tube to fit inside the injection hole, which is connected with the convergent section of the injectant flow pulsation assembly on the upstream end.



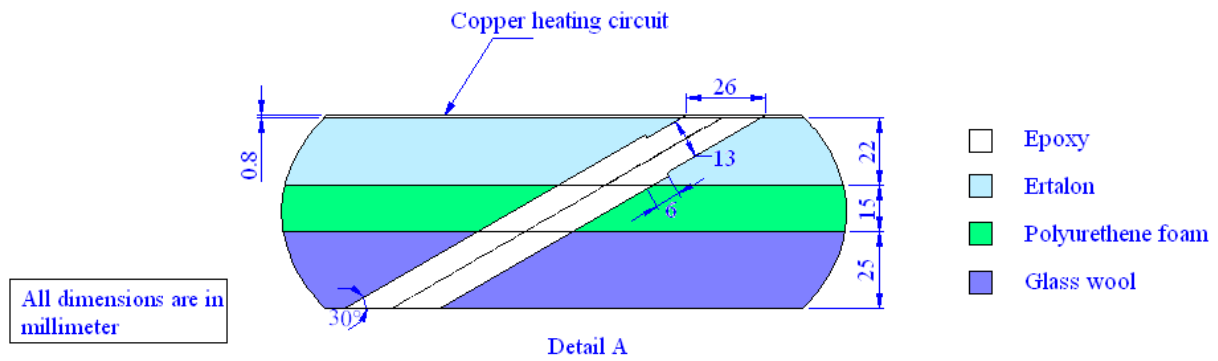


Figure (3.4): Coolant injection wall.

The bottom wall is further covered-up by other insulating materials during the thermal measurements to reduce the heat transfer by conduction to the bottom side. Descriptions of those materials are given in table-3.1.

	Thickness, $e_i$ (mm)	Thermal conductivity, $\lambda_i$ (W/m.K)
Epoxy	0.8	0.32
Ertalon	22	0.3
Polyurethane foam	15	0.037
Glass wool	25	0.035

Table-3.1 : Description of the insulative materials used on the bottom side of the injection plate.

### 3.2.2 Injection Flow System

The configuration of film cooling with an imposed pulsation is analyzed with the injection from a single cylindrical hole. The air required for injection purposes is extracted from the compressed air network. The air is heated by a small heat-dissipating coil controlled with a temperature monitoring probe placed inside a large manifold. The manifold providing a near stagnant condition to the injectant flow is designed to feed a row of five injection holes. In the present study, we are intended to focus on the basic flow attributes constituting as a result of the interaction of the injectant flow issuing from the central hole of the injection row and the boundary layer of the wind tunnel flow, and then want to compare these attributes with the cases of injectant pulsation. The schematic diagram of the injectant flow system is shown in figure (3.5). The flow rate in the supply branch of the injection flow is maintained by an orifice tube. The periodic excitation is introduced by a loudspeaker based pulsation system connected flawlessly with the injection tube at identical diameter.

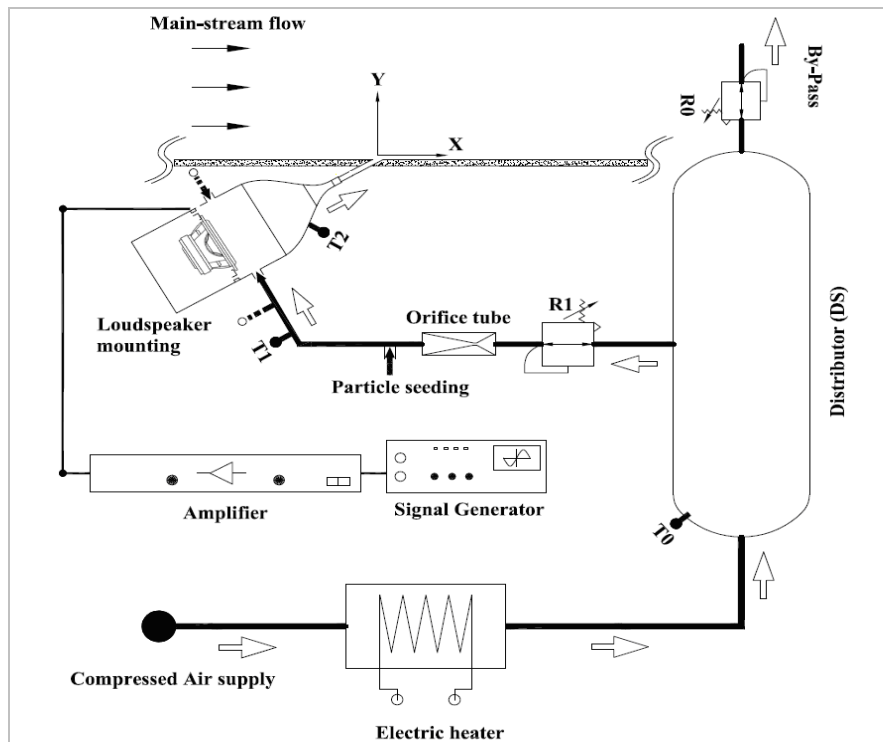


Figure (3.5): Schematic diagram of injection flow system, R(0-1): Pressure Regulator, T0: Temperature Probe PT100, T(1-2) Thermocouple Type-K.

### 3.2.2.1 Measurement of injection mass flow rate

The air is distributed at a constant flow rate with the help of a pressure regulator and an orifice tube connected upstream on the supply branch. The compressed air network delivers significant pressure to the injection system (approx. 7 Bar). The pressure set by the pressure regulator at the inlet of orifice tube chokes the flow at the throat well above the required pressure ratio to provide a constant mass flow rate. The orifice tubes fabricated in the local facility are known to achieve choking condition at a pressure ratio of  $P_1/P_2 \geq 2$ ; where  $P_2$  is the downstream pressure of the orifice tube (it includes the flow pressure at the hole exit and the pressure drop taking place in the various components of supply system locating on the downstream side of the orifice tube), and  $P_1$  is the upstream pressure at the regulator outlet. The orifice tubes are calibrated by using a panel mounted flow calibration unit consisting of rotameters. Figure (3.6) shows an example of the calibration curve obtained for the orifice tubes. The measurement of absolute pressure on the upstream side of the orifice tube is done by a Druck® pressure transducer and the flow temperature is measured by a K-Type thermocouple. Eq. (3.2) determines the flow rate of the injectant fluid with respect to the upstream pressure  $P_u$ , upstream pressure  $T_0$  and throat area  $S$ , where;  $\gamma=1.4$ ,  $R=287 \text{ J/kg} \cdot ^\circ\text{C}$ . The measured signals are acquired and interpreted by a computer program developed on LabVIEW® software.

$$Q = \frac{P_1 S}{\sqrt{T_o}} \cdot \frac{\sqrt{\gamma/R}}{\left(1 + \frac{\gamma-1}{2}\right)^{\frac{\gamma+1}{2(\gamma-1)}}} \quad \dots\dots (3.2)$$

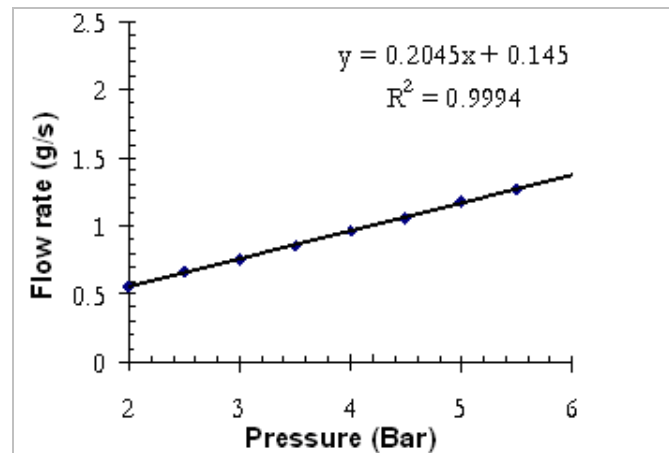


Figure (3.6): Flow rate calibration curve of orifice tube.

### 3.2.2.2 Heating system for injectant flow

The air in the injection flow circuit is heated by a small heating cartridge recovered from a BOSCH's PHG 500-2 type hot air blower. The heating cartridge is coupled with additional metallic attachments fabricated to mount the cartridge in the compressed air environment, as shown in figure (3.7). The heating cartridge consists of a small helical coil heating element, placed inside a 39 mm tube, which is authorized to use up to 300 °C at 240 l/min and 450 °C at 500 l/min according to manufacturer's specification. A bypass system is introduced in the main branch of injection system to protect the heating element from burning off at lower flow rates.

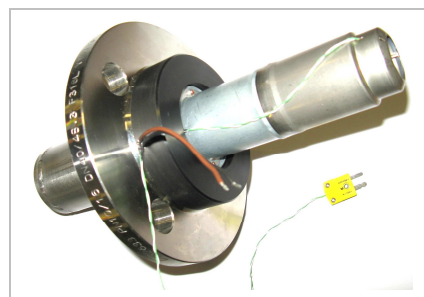


Figure (3.7): Heating cartridge of injectant circuit

### 3.2.2.3 Injectant temperature regulation system

The system of automatic temperature regulation is developed in order to maintain the temperature of the heating cartridge near desired level. Figure (3.8) shows the principle component of the close loop system.

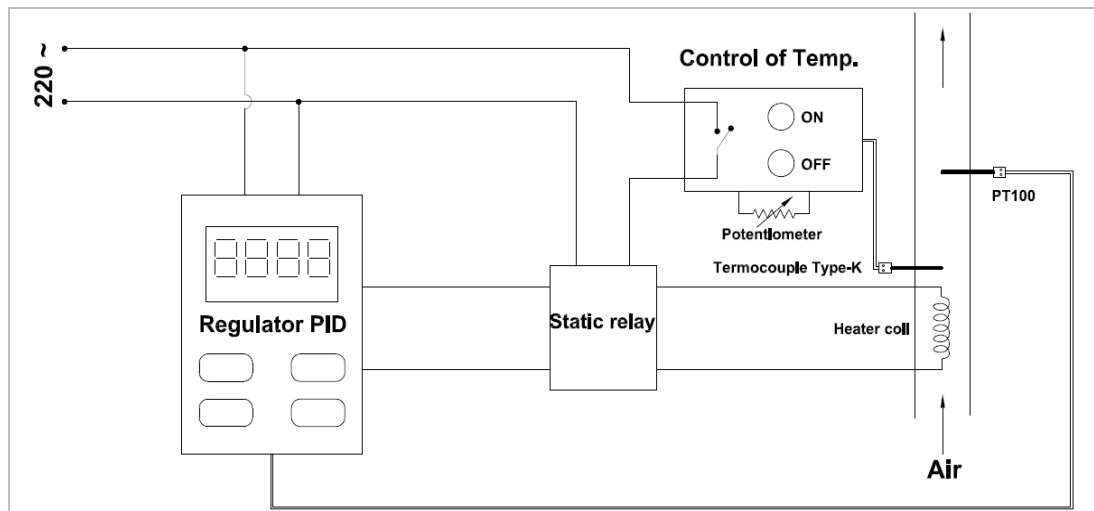


Figure (3.8): Temperature regulation system.

A high sensitivity temperature measuring probe of platinum called PT-100 is placed as feed back sensor and a proportional–integral–derivative controller (PID) controls accordingly the supply of power to the heating coil. A Type-K thermocouple is placed near heating cartridge for reasons of security. Power feed system turns off automatically as the temperature goes past intended security limit. The security system only triggers at an occasion, when the principle system halts to respond properly. Injectant temperatures are regulated to 40 and 60 °C.

### 3.2.2.4 Pulse generation system

The injectant flow is pulsated by acoustic means. A signal generator (ITT Instruments-GX240) is used to generate sinusoidal pulses at a required frequency, while the signal amplitude is controlled by a stereo amplifier (JB SYSTEMS-VX400). The fundamental characteristics of the loudspeaker are given in table-3.2.

Admissible Power (rms)	60 W
Peak Admissible Power	150 W
Nominal Impedance	4 $\Omega$
Resonance Frequency	41 Hz
Emissive surface	86.6cm <sup>2</sup>
X-max linear	+/- 4.5mm
Maximum excursion at peak	+/- 7mm
Recommended cut off frequency	3000 Hz

Table-3.2: Fundamental characteristics of the loudspeaker

The loudspeaker used in the present work is manufactured by ATOHM®, and it has a diameter of 130mm. It offers high excursion capacity for diaphragm movement, which allows obtaining a significant acoustic pressure by imparting a larger displacement to the quantity of air instantaneously appearing at the surface of the moving diaphragm of the loudspeaker. The loudspeaker has a nominal impedance of  $4\Omega$  and a low resonance frequency of 41 Hz. This allows an effective use of the loudspeaker drive with consistently reproducible output during low frequency operation.

### **Loudspeaker cabin**

The loudspeaker is placed in an enclosure, which is used to impart periodic forcing to the incoming injectant flow. This enclosure, which may be called as loudspeaker cabin is mainly consists of two major portions of nearly equal volumes, see figure (3.9). The first one consists of an intermediate cylindrical component named as volume extender and represents a significant portion of the upper side volume. It also contains three air entrance ports symmetrically placed at  $120^\circ$  along the circumference, which allows to discharge the air near the vibrating cone of the loudspeaker. The dynamic pressure of the injectant at the point of entrance is kept fairly low in order to extract maximum benefit of the force generated by the loudspeaker. The upper side volume of the enclosure also includes the convergent which is formed with an area ratio of 171. The second part of the enclosure covers the bottom part of the loudspeaker and represents the bottom side volume. A loudspeaker support ring, an intermediate object used to mount the loudspeaker locates at the interface of the two chambers and has 8 holes of 6 mm diameter near the periphery in order to achieve the air pressure equivalence on both sides of the loudspeaker.

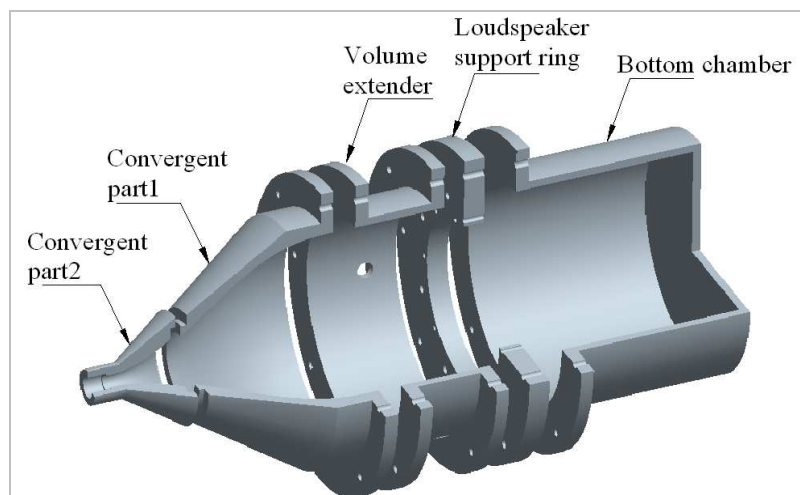


Figure (3.9): Assembly of loudspeaker cabin

A soft woolen material is placed on the inner wall of bottom chamber to absorb the acoustic wave primarily emanating from the rear side of loudspeaker and the resonance of the fixed volume. In order to diminish the lateral velocity component of the flow a honeycomb structure of an average mesh size of 5 mm and a length of 25 mm is placed just upstream of the convergent assembly.

The present objective of flow excitation is a bit different from the usual requirements of the sound based system. Therefore, the exact behavior of the loudspeaker and the resulting acoustic properties of the flow inside the perceived enclosure design are not fully known. The loudspeaker behavior was analyzed by using a well-established sealed-box model, Vanderkooy et al. (2003). The model assumes that the front side of the loudspeaker facing the flow is opened while the volume at the bottom,  $V_b$ , is completely sealed. This relatively simple model with bottom sealed configuration allows having some idea of loudspeaker behavior within the range of practical frequencies. The tests are performed to check the frequency response of the diaphragm excursion capacity,  $X_c$ , and the resulting acoustic pressure. The acoustic pressure generated by the loudspeaker is presented in decibel, dB-SPL (Sound Pressure Level), a way of output representation frequently used for loudspeaker evaluation. In this definition, the output pressure is normalized by the lowest acoustic pressure level sensitive to human ears. This value is around 20  $\mu\text{Pa}$  and roughly equivalent to the sound of a mosquito flying 3 meters away [30]. In order to calculate the loudspeaker response, the input electrical power is considered to be 125 W, which represents an extreme condition for the chosen loudspeaker drive. The distance for observing the radiations emanating from the loudspeaker diaphragm is considered at 1m.

Various values of  $V_b$  are tested to determine a better compromise between chamber volume and output performance for flow excitation. Figure (3.10a) and (3.10b) show that the variation in loudspeaker behavior with  $V_b$  is more pronounced in a region for  $f < 100$  Hz. A large enclosure volume delivers higher acoustic pressure and large diaphragm excursion but their response seems to vary only in the lower frequency domain. In higher frequency domain, the excursion level decreases considerably for all sizes of volumes considered. Therefore, a chamber with large  $V_b$  would not be very effective and would also cost heavily. A casual increment of input electrical power at this point for increasing the amplitude of pulsation could result in a permanent damage of the driver. The two largest volumes considered here ends-up giving the similar response curve for the whole frequency range, which shows that any theoretical increment of  $V_b$  beyond this point doesn't bring any increment in the excursion level. This situation is also referred as an open baffled mounting in box designing for audio system, since  $X_c$  has become independent of  $V_b$ . For existing system, the volume of the loudspeaker bottom chamber is assumed around  $0.0034 \text{ m}^3$  (3.4 liters). This provides us a constant excursion capacity of around  $X_c \approx 4.5$  mm in the low

frequency zone. The linear displacement of this order is sufficient enough to produce significant acoustic pressure for incoming air. The quantity of air excited perfectly over the diaphragm of the loudspeaker at a particular frequency is given by Eq. (3.4), where  $V_d$  is the volume displaced by the loudspeaker and  $S_c$  is the area of radiating surface.

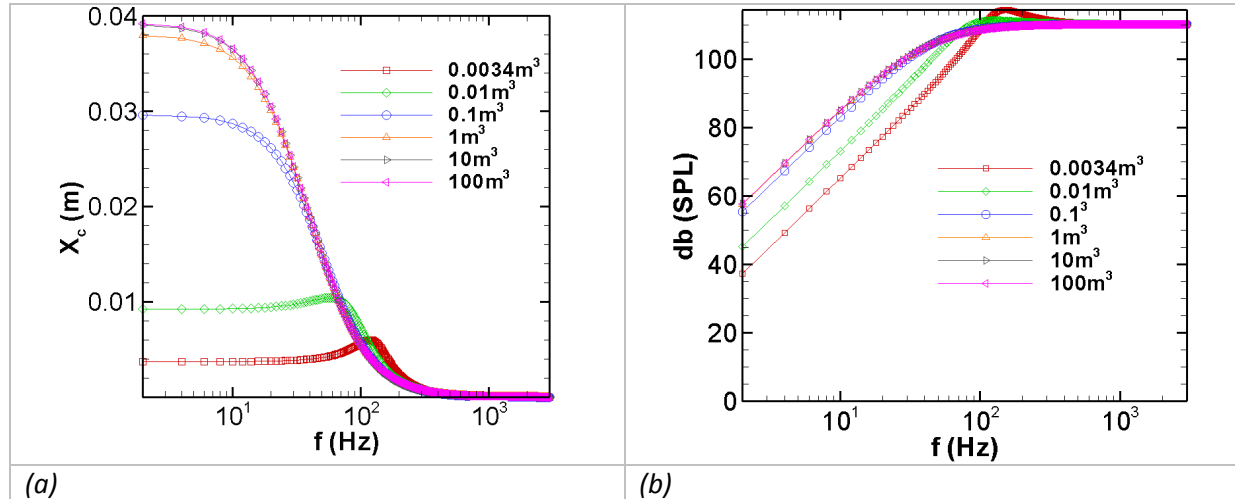


Figure (3.10): Loudspeaker frequency response for different volume of bottom chamber; (a) output excursion level (b) output pressure.

$$V_d = S_c \cdot X_c \quad \dots\dots (3.3)$$

$$\dot{m} = \rho \cdot V_d \cdot f \quad \dots\dots (3.4)$$

### **Convergent section of loudspeaker cabin**

The convergent part is developed by using a fifth order polynomial suggested by Bell & Mehta (1988). An exponential transfer function is used to transform Bell & Mehta's polynomial to a form that carries arbitrary inlet ' $H_i$ ' and outlet ' $H_o$ ' heights, and length ' $l$ '. The flow in a convergent is more vulnerable to separation in the initial part because of improperly designed concave curvature of the wall. At the exit, the convex curvature of the wall has an inherently stabilizing effect on the flow and the presence of usually strong favorable pressure gradient help in avoiding the separation. In Eq. (3.5), the choice of the appropriate exponential coefficient ' $\alpha$ ' ( $0 < \alpha < 1$ ) weakens the effect of the point of inflection in the contour near the inlet, figure (3.11b). The selected coefficient is of the order of 0.7, which was determined in an iterative manner. The formulation given by Eq. (3.5) makes the first arc near inlet to become significantly larger than the second arc close to the exit, as shown in figure (3.11a). This helps in preventing any flow anomaly near the wall. The flow is expected to have a uniform flow profile at the exit because of zero gradient of wall contour maintained at outlet section and as well as at inlet section for an appropriate flow entrance.

$$\xi = \frac{X}{l}$$

$$\eta = -10(\xi)^3 + 15(\xi)^4 - 6(\xi)^5$$

$$h_x = \left[ \eta \left( H_i^{\frac{1}{\alpha}} - H_o^{\frac{1}{\alpha}} \right) + H_i^{\frac{1}{\alpha}} \right]^\alpha \quad \dots\dots (3.5)$$

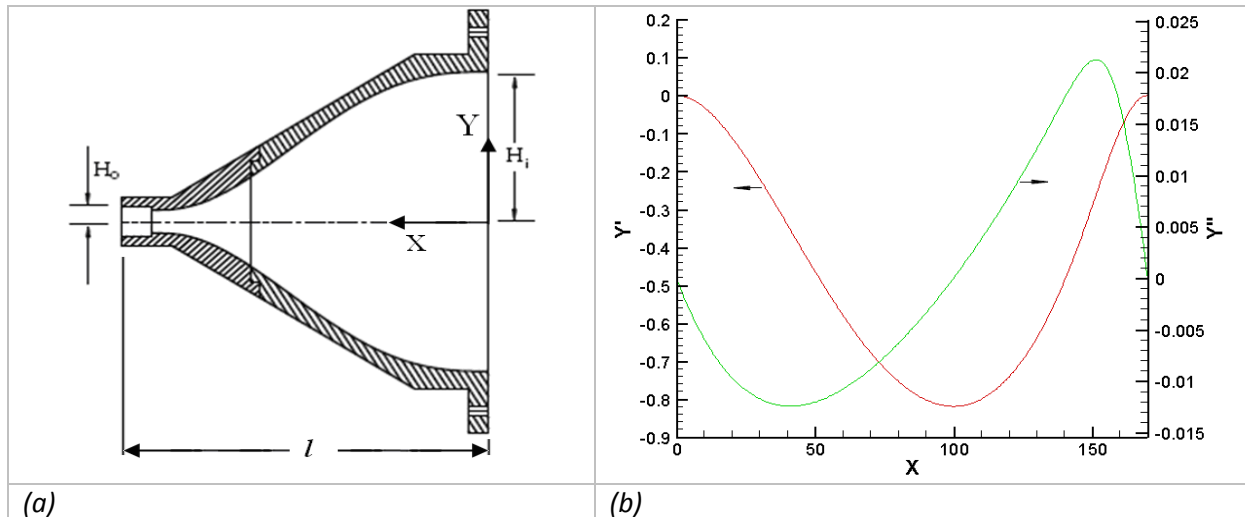


Figure (3.11): (a) Convergent section developed by using fifth order polynomial of Bell & Mehta (1988), (b) First and second order derivative ( $Y'$ ,  $Y''$ ) of the profile.

### 3.3 Velocity measurement systems

The characterization of the upstream flows constituting the boundary conditions for the film cooling experiments was performed by using the system of one-dimensional Laser Doppler Velocimetry 'LDV' for the mean flow characteristics (including mean- and rms-velocities), and a simple hot wire 'HW' for determining turbulent scales and energy spectra at some particular locations of the wind tunnel. During the measurement of wind tunnel flow, injection holes were covered neatly with a tape, and the boundary layer was allowed to evolve smoothly without being interfered at the wall.

The nominal velocity of the jet and the form of jet velocity profiles at the hole exit were later determined by using the system of Particle Image Velocimetry 'PIV' prior to the film cooling experiments, when the required injection system and the other support system for PIV measurement were all in place.

The nature of the pulsing jet forced by a loudspeaker was investigated by a simple hot wire at higher sampling rates to determine the appropriate working amplitude for the whole range of Strouhal number frequency. Later on, the study of film cooling behavior with injectant flow pulsation was performed by using a Time-Resolved PIV system (TR-PIV) for a range of forcing frequencies  $f_s$  and amplitude  $U_a$  constituted previously.

### 3.3.1 Laser Doppler Anemometry

#### 3.3.1.1 Descriptions of the measurement scenario

The assessment of flow uniformity and the evolution of the freestream boundary layer of the wind tunnel flow were performed by the system of LDA-1D of DANTEC®. Figure (3.12) shows the locations of the velocity profiles measurement in wall-normal direction. The measurement grid consists of different streamwise and spanwise location;  $x = -16.8d, -12.9d, -9.1d, -5.2d, -1.4d$  and  $14d$ ; and  $z = -6d, -3d, 0, 3d$  and  $6d$ . Centerline velocities of 5, 8 and 10 m/s, constituting the freestream Reynolds numbers ( $Re = \overline{U}_\infty \cdot \delta / \nu$ ) of 4305, 6681 and 8609 were studied. The required parameters relevant to film cooling include; evolution of boundary layer thickness (which allows determining the location of the injection hole with respect to the mainstream boundary layer), uniformity of oncoming flow, the shape of the velocity profiles, freestream turbulence etc. The early studies revealing the influence of the upstream boundary layer thickness on film cooling effectiveness are reported by Goldstein and Eckert (1974) and Eriksen and Goldstein (1974), whereas the influence of freestream turbulence intensity is examined by Marek and Tacina (1975) and Burd et al. (1996).

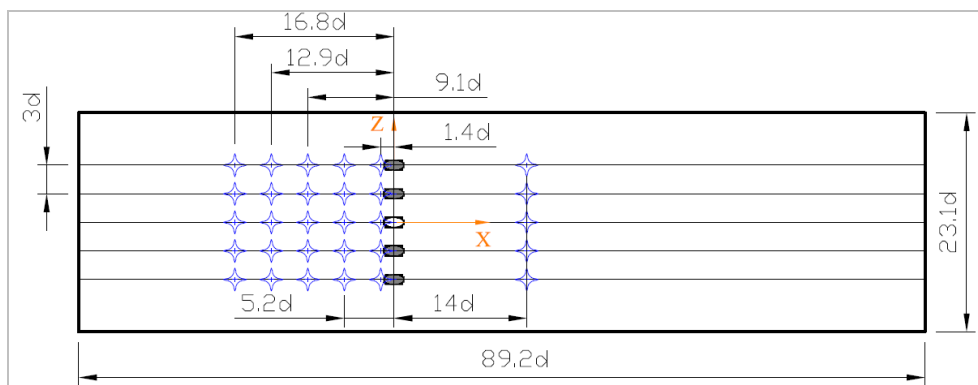


Figure (3.12): Plan of measuring stations for the profile measurement with LDV.

#### 3.3.1.2 Experimental conditions for LDV measurements

The measurement with LDV is conducted to figure out flow uniformity and prospects of boundary layer evolution by measuring velocity profiles at various locations. In order to get precise results, the profile was divided into various zones, where data sampling rate is controlled by defining the appropriate values of signal gain, photomultiplier voltage and upper and lower ranges of expected flow velocity. The ellipsoidal measuring volume measures  $0.2 \times 0.2 \times 3.3 \text{ mm}^3$ , and the diameter of beam waist measures 1.0mm. The system of LDA was used under the following conditions;

Wave length	514.50 nm
No. of fringes	46
Fringe spacing	4.265 $\mu\text{m}$
Beam half angle	3.458 deg
Probe volume (dx*dy*dz)	0.199mm*0.199mm*3.291mm
Focal length of beam expender	600.0mm

Table 3.3: Conditions for LDV measurement.

### 3.3.1.3 Working principle

A Laser Doppler Anemometer is a non-intrusive optical instrument used for the investigation of fluid flow velocities in gases and liquids. The optics of the laser anemometer are able to define a very small measuring volume, which, in combination with a fast and efficient signal processing unit provides excellent spatial and temporal resolution of fluctuating velocities. In LDV measurements, the Doppler effect comes into play due the particle movements. The frequency of incoming laser beam is referred by  $f_i$ , which is interpreted by the moving particle as  $f_p$ , from the moving particle the light is scattered back towards the stationary receiver, which introduces additional Doppler-shift in the frequency of the light reaching the receiver. The frequency of light reaching at the receiver  $f_s$  can be calculated by using the Doppler theory;

$$f_s = f_i \left[ 1 + \frac{U}{c} (e_s - e_i) \right] \quad \text{..... (3. 6)}$$

Where;  $e_s$  and  $e_i$  describe the direction of scattered and incoming light respectively. In the present backscatter LDA system, two laser beams are projected with an angle,  $\theta$ , between them. They intersect at some distance and form dark and bright fringes due to the phenomena of interference of light to constitute the optical measuring volume. Corresponding to each incoming beam, the frequency of light scattered back from the seeding particles towards the receiver on crossing the measuring volume is  $f_{s,1}$  and  $f_{s,2}$ , so the Doppler frequency,  $f_D$ , can be written as;

$$f_D = f_{s,2} - f_{s,1} \quad \text{..... (3. 7)}$$

The velocity component measured by the system would lie in the direction perpendicular to the fringes, which can be shown to be a linear function of the Doppler frequency, where  $\lambda$  is the wavelength of incoming laser beam.

$$u_x = \frac{\lambda}{2 \cdot \text{Sin}((\theta/2))} f_D \quad \text{..... (3. 8)}$$



with LDV, as one of the Reynolds number in hot wire testing is nearly twice as high as the highest Reynolds number studied with LDV. However, these measurements certainly provide some valuable information concerning the variation of the spectra and the turbulent length scales at different Reynolds numbers. It also extends the database regarding the wind tunnel flow characteristics, which can be helpful for the similar experiments that might possibly be performed in the future.

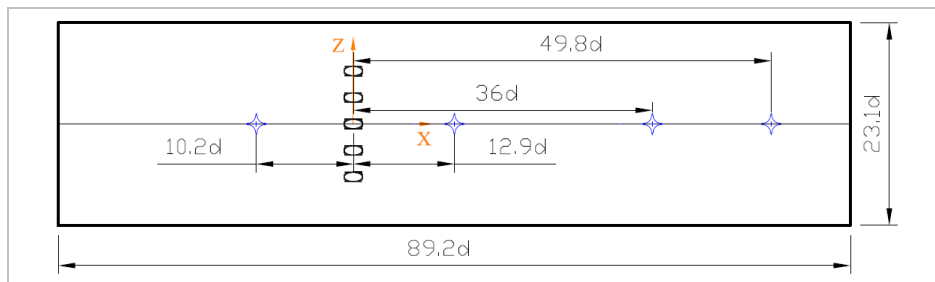


Figure (3.14): Plan of measuring stations for the profile measurement with HW.

### 3.3.2.2 Experimental conditions for hot wire measurements

The hot wire anemometer used is a IFA-300 constant temperature anemometer system, which contains a  $2.5\mu\text{m}$  platinum wire sensor of 1.27 mm length, a IFA-300 signal conditioning unit and a 12 bit PowerDAQ A/D-converter, interfacing between signal conditioning unit and a desktop computer equipped with IFA's THERMALPRO™ software. It also includes a Type-T Thermocouple Module, which was placed in the flow for any correction in the flow velocity with temperature. Hot wire system is calibrated prior to use for the entire working range by a small calibration tunnel located in the laboratory. Tunnel Flow rate is regulated through a precision valve, which is managed by a stepper motor drive. The differential pressure, constituted between the static pressure of the tunnel settling chamber and the ambient provides the calibration tunnel jet velocity. A FC014 Micromanometer is used to monitor the differential pressure against impose flow velocities, at which calibration points are logged.

Sampling frequency	20 kHz
Block size	1024 pts
Size of an acquisition	128 kpts
Acquisition time	6.5536 Sec
Reynolds numbers.	5801 and 18436
Measurement location	-10.2d, 12.9d, 36d and 49.8d

Table-3.4: Conditions for hot wire measurement.

Tunnel allows a differential pressure variation from 0 to 250 mmH<sub>2</sub>O (2452 Pa), which is equivalent to a flow rate of 0 to 69.5 dm<sup>3</sup>.min<sup>-1</sup> (0.00116 m<sup>3</sup>.s<sup>-1</sup>). Hot wire sensor was frequently calibrated to avoid calibration drift error due to the shifting of wire characteristics with time. The details of hot wire working parameters are given in table-3.4.

### 3.3.2.3 Working principle

The working principle of the Constant Temperature Hot Wire Anemometer (CTA) relies on a fact that the probe's resistance is proportional to the temperature of the hot wire. An electronic circuit based on the combination of a Resistance Bridge and a servo amplifier maintains the probe temperature in the fluid by controlling the variation in probe resistance. When a measuring probe is immersed in a fluid flow, the flow passing over it tries to cool the wire. The bridge voltage in response is required to adjust accordingly in order to maintain probe resistance and so to the wire temperature. At thermal equilibrium, the input electrical power is equal to the power lost by convective heat transfer,

$$I^2 R_w = h.A_w(T_w - T_f) \quad \text{..... (3. 10)}$$

Where  $I$  is the input current,  $R_w$  is the resistance of the wire,  $T_w$  and  $T_f$  are the temperatures of the wire and the fluid,  $A_w$  is the projected wire surface area, and  $h$  is the heat transfer coefficient of the wire. The wire resistance  $R_w$  is a function of temperature according to,

$$R_w = R_{ref} [1 + \alpha(T_w - T_{ref})] \quad \text{..... (3. 11)}$$

Where  $\alpha$  is the thermal coefficient of resistance and  $R_{ref}$  is the wire resistance at the reference temperature  $T_{ref}$ . The heat transfer coefficient  $h$  is a function of fluid velocity  $v_f$  according to King's law,

$$h = a + b.v_f^c \quad \text{..... (3. 12)}$$

where  $a$ ,  $b$ , and  $c$  are coefficients obtained from calibration ( $c \approx 0.5$ ). Combining the above three equations allows us to eliminate the heat transfer coefficient  $h$ .

$$a + b.v_f^c = \frac{I^2 R_w}{A_w(T_w - T_f)} \quad \text{..... (3. 13)}$$

$$v_f = \left\{ \frac{1}{b} \cdot \left( \frac{I^2 R_{ref} [1 + \alpha(T_w - T_{ref})]}{A_w(T_w - T_f)} - a \right) \right\}^{1/c} \quad \text{..... (3. 14)}$$

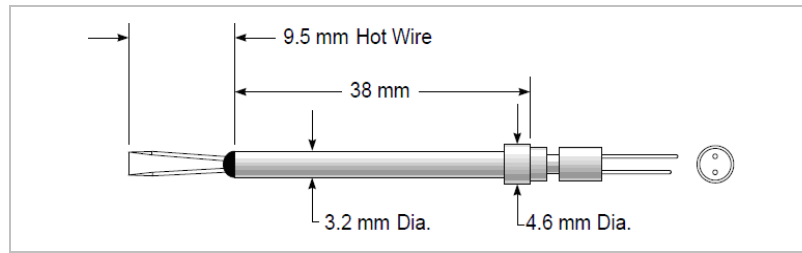


Figure (3.15): TSI IFA-300 hot wire probe.

### 3.3.3 Statistical errors in LDV and hot wire measurements

The uncertainty estimates for measurements are determined by using the estimators of Benedict and Gould (1996) derived for the case of a random process. For a confidence interval of 95%, the statistical errors in the mean and rms values of the streamwise component of velocity are estimated from Eq. (3.15) and (3.16), where  $N$  is the number of independent samples.

$$U\{\bar{U}\} = 1.96 \times \left[ \bar{u}^2 / N \right]^{0.5} \quad \dots\dots (3.15)$$

$$U\{\sqrt{u^2}\} = 1.96 \times \left[ \left\{ \bar{u}^4 - (\bar{u}^2)^2 \right\} / 4N\bar{u}^2 \right]^{0.5} \quad \dots\dots (3.16)$$

The measurements with LDV contain 0.15% and 0.6% error in mean and RMS velocities ( $\bar{u}$  and  $\sqrt{u^2}$ ) measured in the near wall region and 0.05% and 0.8% error in respective velocities for the region lying outside the boundary layer, the number of samples for each location were  $N \approx 50000$ .

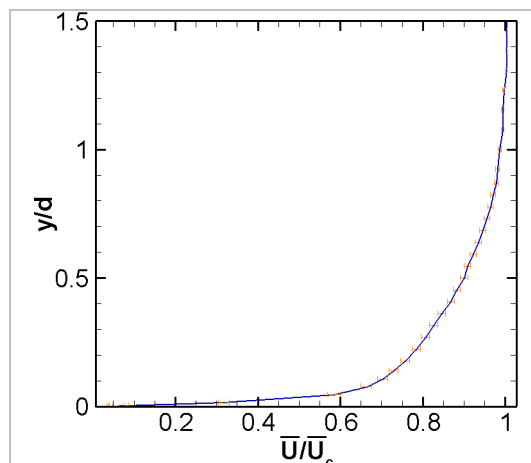


Figure (3.16): Uncertainties in mean velocity measured from LDV,  $Re=8609$ .

In contrast to the measurement of LDV, the hot wire measurements were performed with much larger samples. Therefore the statistical uncertainties of the random samples were found to have pretty small magnitudes.

In the process of characterizing the wind tunnel flow, the nominal values of the statistical error associated with hot wire measurement is 0.05% and 0.36% for  $\bar{u}$  and  $\sqrt{u^2}$  in the near wall region and 0.002% and 0.4% in the respective velocities for the region lying outside the boundary layer. A large number of samples ( $N \approx 128000$ ) were taken to ensure the statistical convergence with a data rate of 20 kHz.

In the process of characterizing the pulsating jet, the nominal values of the random statistical error associated with high resolution temporal measurement using a hot wire is 0.1% and 0.4% for  $\bar{u}$  and  $\sqrt{u^2}$ . A large number of samples ( $N \approx 131000$ ) were taken to ensure the statistical convergence and a high data rate of 40000 Hz for achieving highly time resolved phase averaged velocity results after the post-treatment.

### 3.3.4 Time Resolved Particle Image Velocimetry

The study of the flow aerodynamics is performed to figure out the behavior of the flow field established by the interaction of a crossflow and a pulsating jet. Flow field measurements were performed by Time-resolved Particle Image Velocimetry (TR-PIV), allowing broad temporal and spatial resolution. The study was conducted for the most conventional cases of film cooling ( $\bar{M} = 0.65, 1$  and  $1.25$ ) along with jet pulsation. This study not only present the fundamental attributes of the classically existing structures of the flow field, but also the impact of pulsation on those structures in different cases. The injectant flow is pulsated by a loudspeaker based pulsation system, with pulsation frequencies corresponding to a range of Strouhal numbers ( $St = 0, 0.2, 0.3$  and  $0.5$ ).

#### 3.3.4.1 Descriptions of the measurement scenario

The flow domain captured in TR-PIV measurements is the near field region of high velocity gradient and the intermediate region manifesting the evolution of resulting flow structures. The region of flow examination extends from  $x/d = -1$  to  $6.5$  and from  $y/d = 0$  to  $2.6$  in streamwise and wall-normal directions respectively. By the end of the region of flow examination the shearing effects are expected to reduce considerably. The motorized displacement systems were used for positioning both laser and camera to the desired location. Figure (3.17) gives a global view of the TR-PIV arrangement.

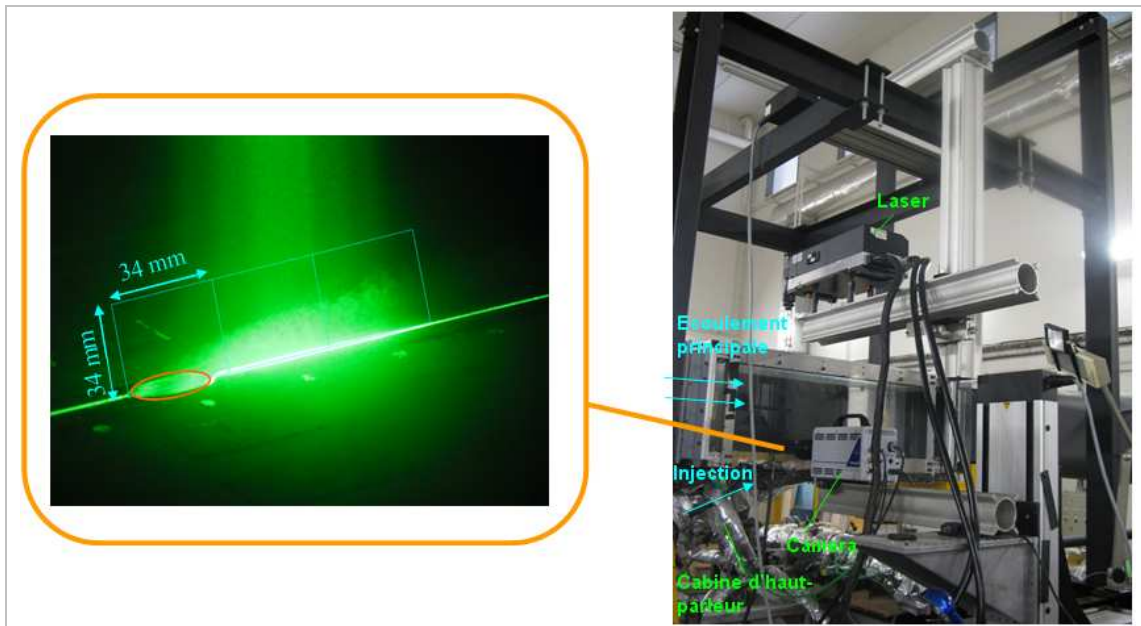


Figure (3.17): Hardware arrangements for TR-PIV measurements.

The main stream flow is seeded by a Puffer-6 (Silver Series) smoke generator while the injectant flow is seeded by grape-seed oil with a particle size of a few microns. The TR-PIV system is comprised of a LaVISION (High Speed Star) camera with a 10-bit C-MOS imaging sensor, maximum resolution of  $1024 \times 1024$  pixels<sup>2</sup> (up to 3000 fps). The flow domain is illuminated by NewWave Pégasus, double-pulsed Nd:YAG Laser ( $\lambda=527$  nm,  $E=2 \times 10$  mJ at 1KHz,  $f=1-10000$  Hz). A LaVISION high speed controller mediates the system for initial data recording in the camera memory and the subsequent transfer to a desktop computer. Both high speed camera and laser were mounted on a precise displacement system to maneuver in streamwise direction with the command initiated from the same computer used for the data acquisition of PIV measurements.

The schematic diagram shown in figure (3.18) indicates the hardware setup used in aerodynamic measurements. The distance of the test wall and the laser optics was about 500mm, and the distance between the measuring plane and the objective of the camera was about 230mm.

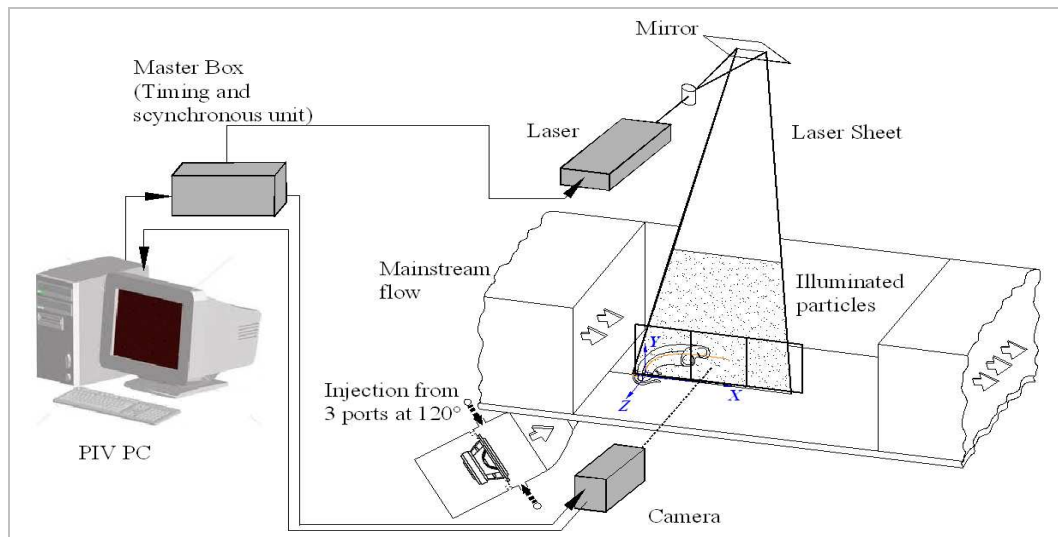


Figure (3.18): Schematic diagram of the hardware setup used for aerodynamic measurements

The measurements are performed for a domain consisting of three  $1024 \times 1024$  pixels<sup>2</sup> consecutive planes with an on-field dimension of  $33.7 \times 33.7$  mm<sup>2</sup> for each plane, as shown in figure (3.19). The vector calculation for the instantaneous velocity field was performed by a LaVISION software package, using the cross-correlation scheme with an ultimate size of interrogation window of  $12 \times 12$  pixel<sup>2</sup> along with 50% overlapping, which gives a  $171 \times 171$  vector domain for each measurement plane.

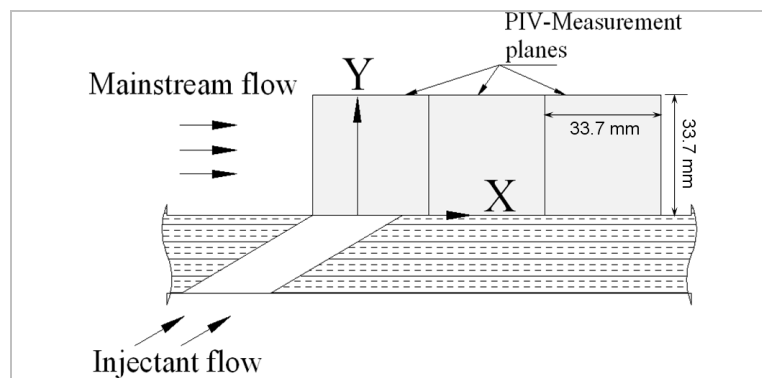


Figure (3.19): Profile locations chosen for the presentation of results in the zone of TR-PIV measurement.

### 3.3.4.2 Experimental conditions for TR-PIV measurements

The hydrodynamic parameters chosen for the study are well-treated and thoroughly analyzed in the open literature. Table-3.5 shows the fundamental parameters encompassing the dynamic conditions of the flow. The choice made for some of the geometrical parameters relies on the available test facility, which was primarily developed to study some basic film cooling configurations with steady blowing (Dieumegard 2003). The development

of the jet pulsation system is based on the range of Strouhal numbers, which are chosen after examining the characteristic frequencies of the turbulent wake vortices reported in the open literature for the case of a normal jet issuing in a crossflow (as described in the Section 2.2.4).

$\overline{U}_\infty$ (m/s)	$Re_\infty = \overline{U}_\infty \delta / \nu$	$Re_i = \overline{U}_i d / \nu$		$\overline{M} = \rho_i \overline{U}_i / \rho_\infty \overline{U}_\infty$		$St = f d / \overline{U}_i$
10	8609	5596	8437	0.65	0.98	0, 0.2, 0.3, 0.5
7.7	6165	8220		1.25		0, 0.2, 0.3, 0.5

Table-3.5: Test conditions.

In all cases of aerodynamic measurements, the injectant to mainstream density ratio ( $\rho_i / \rho_\infty$ ) was set to unity. The relative boundary layer thicknesses ( $\delta / d$ ) at the center of hole exit plane ( $x/d=0$ ) for the mean freestream velocity of 10 and 7.7 m/s are 1.0 and 0.93, the displacement thicknesses ( $\delta^* / d$ ) are 0.146 and 0.11 and the freestream turbulent intensities ( $TI_\infty$ ) are 1.2 % and 1 % respectively (*measurement results for mainstream flow are presented in chapter 4*). The injection plate consists of a cylindrical hole having a diameter,  $d$ , of 13 mm and a length,  $L$ , of  $7.7d$ . The use of a short injection tube ( $L/d \approx 4$ ) and a higher density ratio ( $\rho_i / \rho_\infty \approx 3$ ) are more practical (engine representative) for the study of turbine blades film cooling. The choice of these parameters is based on the characteristics of existing hardware, which seems to have a marginal deviation from the conventional film cooling case. However, numerous studies covering a range of parameters related to both flow dynamics and the geometry of test hardware (including the present ones) are extensively analyzed and published in the open literature, such as; Seo et al. (1998) used a range of length to diameter ratios ( $L/d=1.6, 4$  and  $10$ ) to investigate the effects of bulk flow pulsation in film cooling for a density ratio of 0.93. The effects of density ratio on the wall coverage caused by a refrigerant film were analyzed by Goldstein and Eckert (1974) up to ( $\rho_i / \rho_\infty \approx 3.5$ ). Sinha et al. (1991) examined the film cooling under diverse injection patterns and density ratios ( $\rho_i / \rho_\infty = 1$  and  $2$ ). In the later situation, they maintained the temperature of the air in the injection plenum chamber at 150 K. In the underlying approach focused on analyzing the effects of injectant flow pulsations in a crossflow configuration, the situation is expected to simplify greatly while the densities of interacting flows remain identical. Furthermore, it should be noticed that a higher boundary layer thickness ( $\delta / d > 1$ ) of the oncoming mainstream flow allows the jet to penetrate more in the mainstream and results in a quick diffusion of the turbulence of the injectant fluid. With a boundary layer thickness nearly equal to the diameter of the injection hole, the test condition pertaining to the interaction of a pulsed jet and a mainstream flow appears fairly attractive and is expected to

have important consequences on the formation of coherent structures and their impact on the downstream flow field. For the range of frequencies used for the injectant pulsation, an amplitude giving approximately a constant ratio between streamwise rms velocity and average hole velocity was chosen for all cases.

### 3.3.4.3 Fundamentals of PIV system

The measurement of the velocity field using PIV is based on the ability to accurately record and measure the position of small tracers suspended in the flow as a function of time. The tracer particles have to be illuminated in a plane of the flow at least twice within a short time interval. The light scattered by the particles is recorded either on a single frame or on a sequence of frames and the displacement of the particles is determined through the evaluation of the PIV recordings (Raffel et al. 2007). For the process of evaluation, the digital PIV recording is divided in small subareas called “interrogation areas”. The local displacement vector for the images of the tracer particles of the first and second illumination is determined for each interrogation area by means of auto- and cross-correlation. Dividing the estimated particle displacement by the time scale  $\Delta t$  between the capture of two images gives the average velocity in the sampled region.

$$\vec{V} = \frac{\Delta \vec{d}}{\Delta t} \quad \text{..... (3. 17)}$$

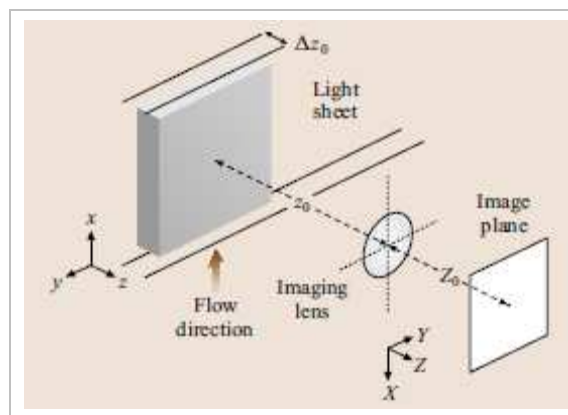


Figure (3.20): Schematic of the optical configuration for PIV imaging, Westerweel (1997).

### 3.3.4.4 Spatial resolution of PIV system

Figure (3.21) shows the one-dimensional cut of the two-dimensional energy spectrum of streamwise and wall-normal components of the velocity fluctuations ( $u, v$ ), which are obtained by using the Matlab 2-dimensional FFT function. The final 2D spectra were obtained from the average of 500 samples. In the present case, particle images are evaluated with an ultimate size of the interrogation window of  $12 \times 12$  pixel<sup>2</sup> and 50% overlapping. The given spectra allow us to have some global estimate of the spatial

resolution of the measuring system. The trend of the spectra shows a cut-off frequency, which sets the limit for the measurable turbulent scales with the present arrangements, as the turbulent scale of energy levels below this range are filtered out in the PIV measurements. Loss of valuable information is also accompanied with the gain due to the filtering of undesirable high frequency noise. The cut-off frequency of  $f=0.1727$  corresponds to 5.78 pixels, which means that the smallest scale treated with current resolution would be of the order of 1.14 mm, while the largest scale would be of the order of 33 mm approximately.

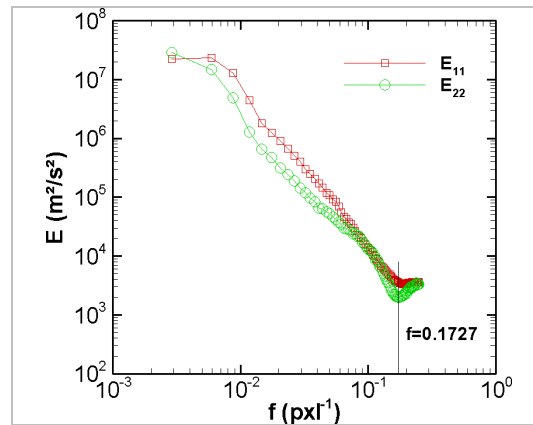


Figure (3.21): One-dimensional cut of the two-dimensional energy spectrum of  $u$ - and  $v$ -components of velocity fluctuations.

### 3.3.4.5 Statistical errors in TR-PIV measurements

For the measurements of TR-PIV, the level of statistical variation in the rms value of streamwise and wall-normal components of velocity fluctuations  $\sqrt{u^2}$ ,  $\sqrt{v^2}$  and their correlation  $\overline{uv}$  are estimated by using Eq. (3.16) and Eq. (3.18). The uncertainty calculations are based on the set of formulae proposed for a general distribution of measured flow variables, which basically suggests that the author's method is capable of taking into account any deviation from the normal distribution (Benedict and Gould 1996).

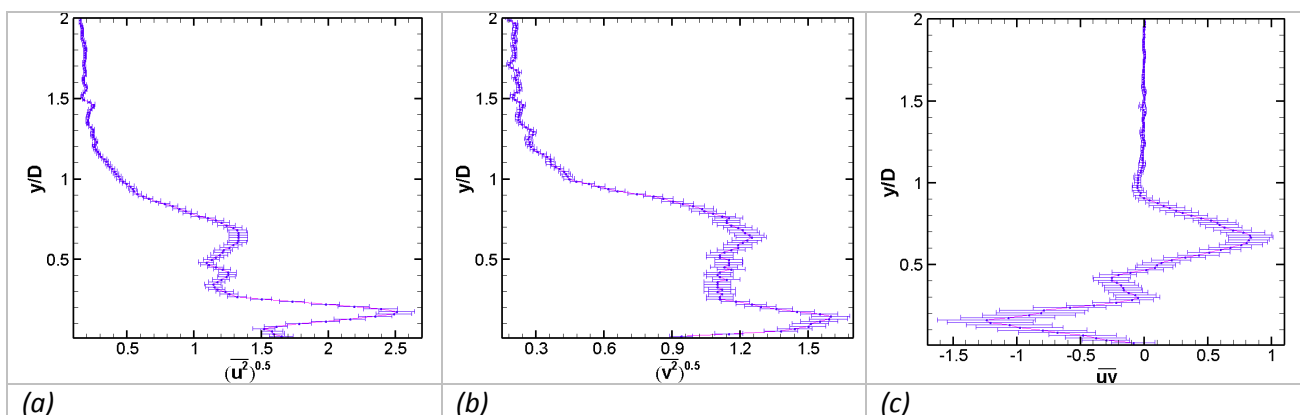


Figure (3.22): Uncertainty estimates of rms value of velocity fluctuations and their correlation,

$\bar{M} = 1.25$  and  $x/D=1.5$ , (a)  $\sqrt{u^2}$ , (b)  $\sqrt{v^2}$  and (c)  $\overline{uv}$ .

$$U\{\overline{uv}\} = 1.96 \times \left[ \frac{\overline{u^2 v^2} - (\overline{uv})^2}{N} \right]^{0.5} \quad \dots\dots (3.18)$$

Figure (3.22) shows the level of uncertainties for an average blowing ratio of 1.25 by a profile locating at  $x/D=1.5$ . The maximum deviation from the respective value of the profile ( $\sqrt{u^2}$ ,  $\sqrt{v^2}$  and  $\overline{uv}$ ) with a confidence interval of 95% are  $\pm 5\%$ ,  $\pm 5\%$  and  $\pm 23\%$  respectively.

### 3.4 Thermal measurements of film cooling configuration

The objective of the thermal measurements was to investigate the effect of externally imposed sinusoidal pulsations of an oblique coolant jet on the coolant protective film, which forms over a constant heat flux wall. The measurement of pressure and temperature at different locations of the injectant delivery system allows us to maintain the required blowing and momentum ratios of the interacting flows through a LabVIEW® program. The assessment of the thermal aspects of the flow field consists of determining the convective heat transfer coefficient and the adiabatic wall temperature by using the technique of infrared thermography. These experiments were undertaken with slight modification to the test section assembly. The blowing ratios ( $\bar{M}$ ) were held at 0.65, 1 and 1.25. The injection fluid was pulsated to a non-dimensionalized frequency ( $St$ ) of 0, 0.2, 0.3 and 0.5. For the cases of pulsation.

#### 3.4.1 Infra-red thermography

##### 3.4.1.1 Descriptions of the measurement scenario

Figure (3.23) indicates the principal hardware arrangements realized to carry out to thermal measurement by the infrared thermography. The camera was placed at a distance of 1m from the object. The movement of the camera was locked in the lateral direction and the movement in the streamwise direction was controlled by a motorized displacement system. The position at the wall is referenced by placing small pieces of low emissivity tape. Thus, the overall domain covered at the wall ranges from  $x/d=-4.5$  to 32.4 and  $z/d=-3$  to 3.

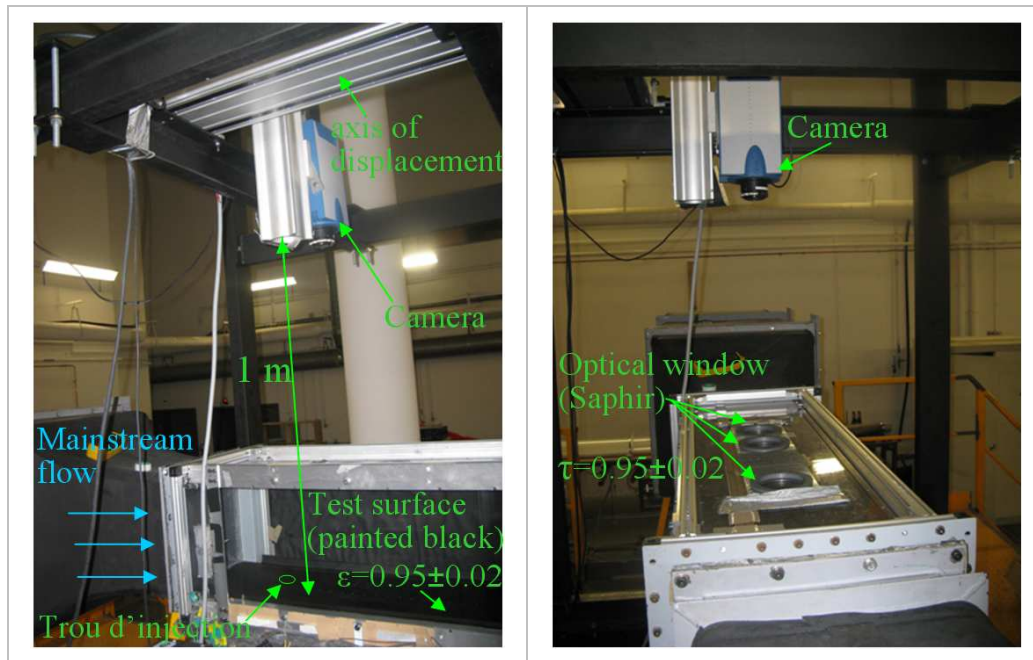


Figure (3.23): hardware arrangements for infrared thermography

Thermography of the test wall is performed by using a Cedip Jade-III infrared camera integrated with a highly functional Altair® software package that contains extended utilities. The measurement setup is constructed to visualize the heated wall across a high transmissivity *Saphir* glass from a vertical distance of 1m, which is the recommended height of the camera given by the manufacturer when using standard calibration files imbedded in the camera memory. It was positioned 3-4 degree off from the vertical axis to avoid the reflection of the radiations from the viewing window.

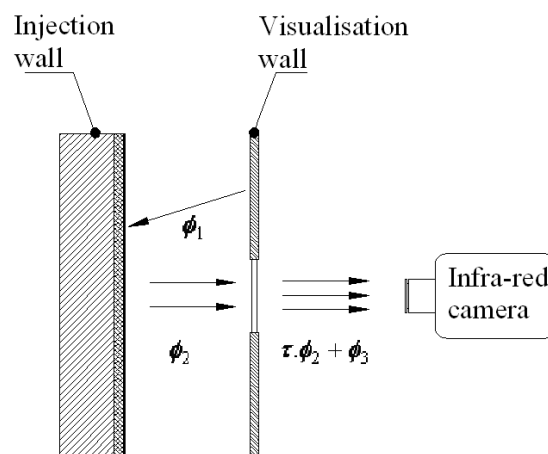


Figure (3.24): Hardware arrangements for infrared thermography, where  $\phi_1$  is the radiative flux emitted by the visualisation wall,  $\phi_2$  by injection wall and  $\phi_3$  by the optical window

An infrared camera measured the oncoming radiative flux in internal units called digital level and converts it to temperature by using the calibration file. The net heat flux reaching at the camera includes a part of heat flux coming from the surrounding walls. A schematic diagram indicating the basic arrangements used for infrared thermography of the injection wall is shown in the figure (3.24).

In order to prepare the camera for wall measurement, the proper definition of the radiometric parameters of the object and the measuring path in the pilot software is extremely important. This includes the emissivity of the wall ( $\varepsilon$ ), the transmissivity of the intermediate medium ( $\tau$ ), the interval of measuring temperature, the distance of the camera from the measuring wall, the atmospheric temperature and the surrounding temperature of the working domain etc. Moreover, the output parameters are required to set for acquiring the field data. Table-3.6 includes some basic parameters used for the measurement of wall temperature. All measurements are performed at steady state condition. The emissivity of the present test wall (painted black) was measured by Dieumegard (2003) under identical arrangements to be ( $\varepsilon \approx 0.95 \pm 0.02$ ). The radiation transmittance of the optical window containing the *Saphir* glass was determined by performing temperature measurements for a particular point at the wall with and without introducing optical window in the radiation path, while both flows were shut off. The first measurement was taken without introducing the optical window in the radiation path and choosing,  $\tau = 100\%$  in the software. The second measurement was taken with optical window, and the value of transmissivity was adjusted in the input menu to match the temperature value in both cases. The repetition of this exercise has resulted in a transmissivity of the order of ( $\tau = 95 \pm 2\%$ ). The composite injection plate contains many K-type thermocouples placed inside the wall. These thermocouples were used to cross check the measurement by the infrared camera.

Sampling rate (Hz)	50
Sampling size (frames)	1000
Emittance (%)	$95 \pm 2$
Transmittance (%)	$95 \pm 2$
Intermediate distance (m)	1
Resolution	320*240

Table-3.6: Operating conditions of Infrared camera

A full domain of wall temperature measured at a particular situation is obtained after assembling the thermal images obtained at nine consecutive positions along the streamwise direction with an overlap of 5mm (0.385d). The final temperature field consists of a region enclosed by  $x/d = -4.5$  to 32.4 and  $z/d = -3$  to 3. The overall view of the surface covered in the

temperature field measurement is shown in figure (3.25a). This surface is covered by traversing both the optical window and the camera in the streamwise direction and keeping the tunnel closed with the help of various plastic strips. For each location of thermal measurement, the intermediate zones contain a region spanning  $5d$  in the streamwise direction, while the two zones at the extremities are registered for only half of its size along the streamwise direction, owing to the views allowed by the present hardware arrangements. The relative position at the wall was figured out by placing the high emissivity tapes, which are placed at a distance of  $2.3d$  from each another. The upper-wall arrangements realized for manoeuvring the optical window in infrared measurement is shown in figure (3.25b).

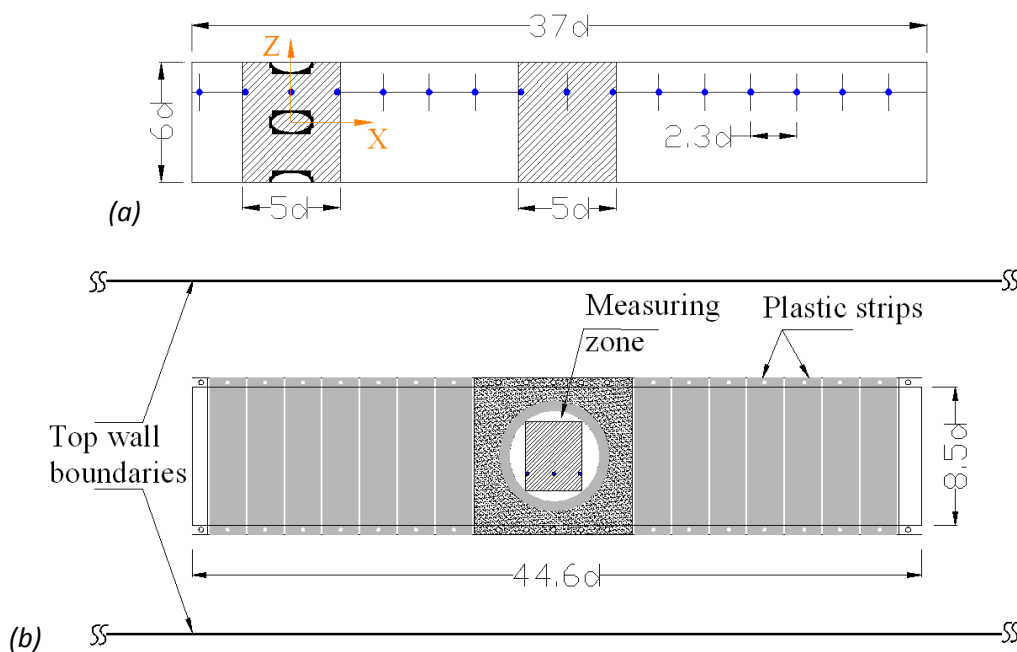


Figure (3.25): (a) View of the wall region investigated for infrared thermography. (b) Upper-wall arrangement realized for manoeuvring the optical window during infrared measurement.

The results are presented by the surface contours and the profiles along the centerline, laterally-averaged and the spatially-averaged parameters of film cooling. Eq. (3.19) recalls the definition of adiabatic film effectiveness, while Eq. (3.20) and (3.21) are referring to the definition used for estimating laterally-averaged and the spatially-averaged quantities respectively.

$$\eta = \frac{(T_{ad} - T_{\infty})}{(T_i - T_{\infty})} \dots\dots\dots(3. 19)$$

$$\bar{\eta} = \frac{1}{1.5d} \int_0^{1.5d} \eta(x, z) dz \dots\dots\dots(3. 20)$$

$$\bar{\eta} = \frac{1}{|(x_2 - x_1)(z_2 - z_1)|} \int_{z_1}^{z_2} \int_{x_1}^{x_2} \eta(x, z) dx dz \quad \dots\dots\dots(3. 21)$$

### 3.4.1.2 Experimental conditions for TR-PIV measurements

Infrared thermography of a constant heat flux wall was performed for the cases of film cooling with and without periodic forcing of the coolant jet. Air temperatures of both mainstream and injectant flows were maintained with the help of a quick response temperature regularity system. Temperature of the wind tunnel flow was always maintained at  $20 \pm 0.2$  °C, while the temperature of the injectant flow was either fixed at  $20 \pm 0.4$  °C or at  $40 \pm 0.4$  °C, corresponding to the two different test conditions ( $T_i/T_\infty = 1$  and 2). The resulting density ratios ( $\rho_i/\rho_\infty$ ) of the interacting flows were 1 and 0.93. The details of measuring conditions are summarized in table-3.7.

$\bar{U}_\infty$ (m/s)	$Re = \bar{U}_\infty \delta / \nu$	$Re = \bar{U}_i D / \nu$		$\rho_i / \rho_\infty$		$\bar{M} = \rho_i \bar{U}_i / \rho_\infty \bar{U}_\infty$		$St = f D / \bar{U}_i$
10	8609	5596	8437	0.93	1	0.65	1	0, 0.2, 0.3, 0.5
7.7	6165	8220		0.93	1	1.25		0, 0.2, 0.3, 0.5

Table -3.7: Test conditions.

In flow configuration bearing a similar temperature for both fluids ( $T_i/T_\infty = 1$ ), the induced convection effects due to the mixing of two flows was analyzed. The other configuration of  $T_i/T_\infty = 2$  enabled us to figure out the spreading of injectant fluid in the mainstream boundary layer by determining the adiabatic effectiveness and the convection heat transfer coefficient of the injectant film.

### 3.4.1.3 Injection wall heat dissipation system

The injection wall used in the present experiment was acquired from a former facility, primarily developed to study higher Reynolds number cases of film cooling. The test wall contains a group of four streamwise running thin copper electrical circuits on the side of the wall facing the flow. The copper tracks have a thickness of 35  $\mu\text{m}$ , a width of 1.8mm and an inter-track space of 0.2mm. The circuits are feed by four separate power supply units of Agilent-E3634A to generate a constant wall flux with a maximum variation of 2%.

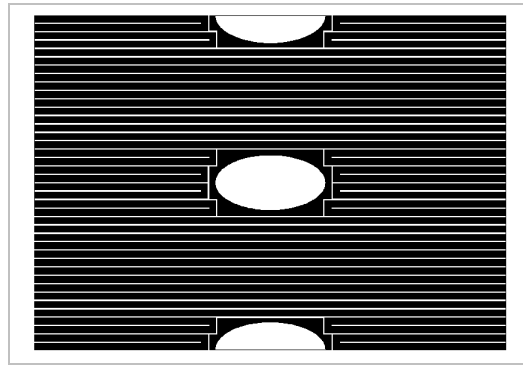


Figure (3.26): Pattern of engraved electrical circuit in the injection hole region.

The generation of heat flux through multiple circuits helps in reducing the variation of electrical resistivity of the heating element, which might be a significant issue with longer streamwise engraved tracks and implies to falling into a condition where the idea of having constant wall heat flux is marginalized greatly. Figure (3.26) shows the pattern of heating circuit realized in the hole region, except for this region the remaining length of the plate is covered with a streamwise running pattern. The measured resistance of each heating circuit is around 14  $\Omega$ .

#### 3.4.1.4 Infra-red camera

The infrared thermography of the constant heat flux wall was performed with a CEDIP Jade MWIR camera, whose sensor matrix is composed of 320\*240 detectors Indium monoantimonide (InSb) and the spectral band ranges from 3.6 to 5.1 microns. The sensor provides a digital signal proportional to the radiative flux received by the test object during a certain integration time. The latter is set automatically by the camera software with the choice of the working range of temperature.

Sensor type	InSb
Resolution	320*240 pixels
Spectral range	3,6 - 5,1 $\mu\text{m}$
Measureable temperature range	-20 $^{\circ}\text{C}$ to +1300
Precision of measurement	+/-2 $^{\circ}\text{C}$ for $T < 100$ $^{\circ}\text{C}$ +/-2 % for $T > 100$ $^{\circ}\text{C}$
Frequency of acquisition	5 - 145 Hz for an image of 320x240 pixels 700 Hz for an image of 160x120 pixels 2800 Hz for an image of 64x123 pixels
Dynamic range	14 bits

Table-3.8 : Characteristics of Infra-red camera.

The sensor array is cooled by a Stirling motor to an operating temperature of 77 K. The overall error is less than 2 °C for the measurement up to 100 °C and equal to 2% for higher temperatures. During testing, the measured temperatures are between 34 and 70 °C. The camera positioning leads to a surface resolution of about  $0.6 \times 0.6 \text{ mm}^2$ . The temperature maps are averaged from a sample of 50 images for 20 s, sampling conducted at a frequency of 50 Hz by keeping one image out of ten to minimize the measurement noise.

The flux arriving from the object is accounted in the internal units of the camera called Digital Level (DL), which is subsequently transformed into temperature with the help of calibration files. The calibration of the camera is performed on a black body producing a uniform temperature and having an emissivity close to unity. Figure (3.27) shows the calibration curve used by the camera to convert the measured digital level to the temperature.

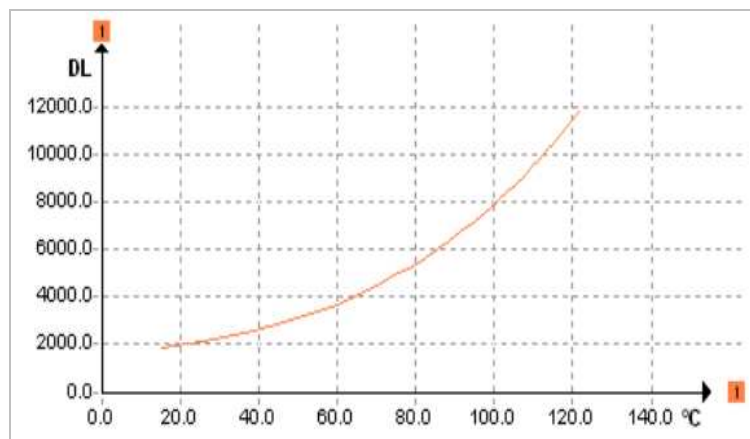


Figure (3.27): Calibration curve of the Infrared camera.

### 3.4.1.5 Surface temperature map (without flow)

The initial test of wall temperature distribution conducted with an Infrared camera at moderate electrical heat flux has shown small variation in the wall temperature. Figure (3.28a) and (3.28b) show the distribution of wall temperature in the absence of tunnel flow for a constant wall heat flux of 333 and 434  $\text{W/m}^2$  respectively.

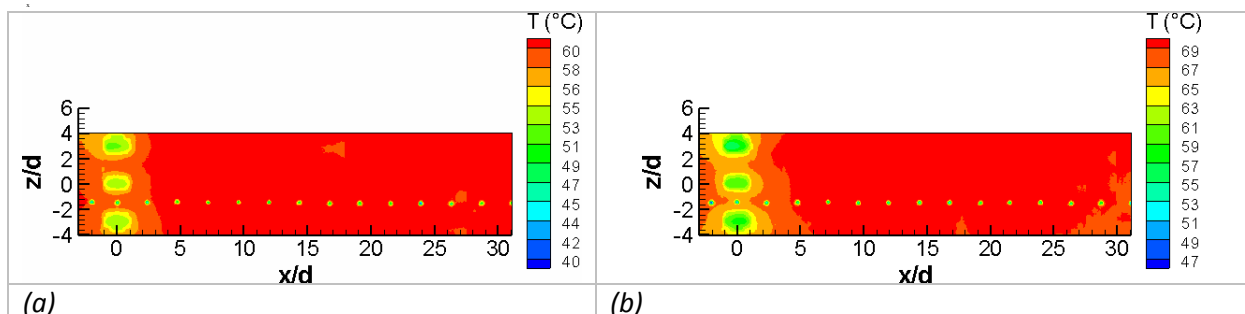


Figure (3.28): Wall temperature distribution in the absence of tunnel flow, (wall region viewed by fluorine glass); (a) 333  $\text{W/m}^2$ , (b) 434  $\text{W/m}^2$ .

The maximum variation observed in the temperature field appears to fall within 2 °C. Keeping in view the small variation in wall temperature, the assumption of constant wall flux can be applied.

### 3.4.2 Cold wire measurement

#### 3.4.2.1 Descriptions of the measurement scenario

The mixing temperatures of the flow field resulting from the interaction of an oncoming mainstream wind tunnel flow and an inclined circular jet issuing at a slightly higher temperature were measured by using a cold wire system. The cold wire measurement enables us to resolve both mean and fluctuating component of the temperature to a higher data rate. It allows us to minimize the inaccuracies associated to low pass filtering of acquired signals. In the cold wire experiments, the temperature ratios of the interacting flows was maintained at  $T_i/T_\infty = 40/40 = 2$ . Figure (3.29) indicates the principal hardware arrangements carried out to conduct cold wire thermometry.

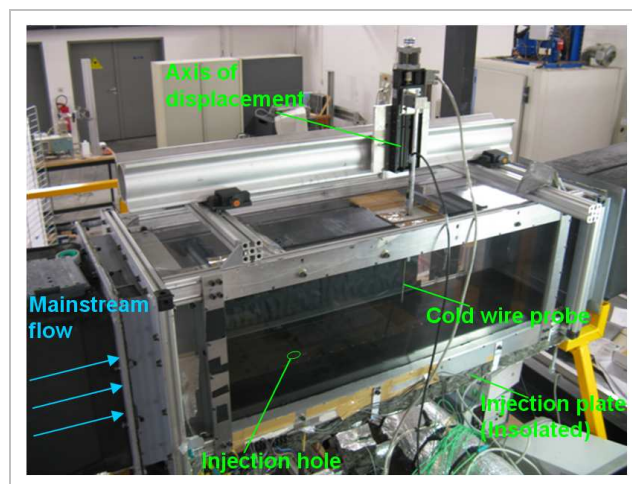


Figure (3.29): Plan of measuring stations for profile measurement with Cold wire.

Due to a significant number of test cases and a large domain of flow variation, the flow domain is divided into five regions, as was considered by Yuen and Martinez-Botas (2003) that is; the upstream region ( $-3d \leq x/d \leq -1d$ ), the immediate region ( $1d \leq x/d \leq 3d$ ), the near field region ( $3d \leq x/d \leq 7d$ ), the intermediate region ( $7 \leq x/d \leq 26d$ ) and the far downstream region ( $x/d \geq 26d$ ). The temperature profiles were measured along the y-axis at a streamwise locations of  $x/d = -1.5, 0, 1.5, 3, 7, 15$  and  $30$ , which lie on a central ( $z/d = 0$ ) and an off-centre ( $z/d = 1.5$ ) plane of the injecting hole. Figure (3.30) shows the plan of measuring stations chosen for cold wire measurement. The choice of different measuring stations seems to cover all important regions of the flow field referred earlier on. The cold



variation of the flow temperature. The variation in wire resistance is in turn transformed into the voltage signal through the cold wire circuit incorporating the resistance bridge. The variation in wire resistance  $R_w$  with respect to the temperature is expressed from Eq. (3.22):

$$R_w = R_{ref} [1 + \alpha(T_w - T_{ref})] \quad \dots\dots (3.22)$$

Where  $\alpha$  is the thermal coefficient of resistance,  $T_w$  is the temperatures of the wire and  $R_{Ref}$  is the wire resistance at the reference temperature  $T_{Ref}$ . In the static regime, the heat transfer by convection, being a predominant mode of heat transfer, is equivalent to the heat generated by Joule's effect (Eq. (3.22)).

$$Nu \lambda_g \pi (T_w - T_g) = \frac{R_{ref}}{l} [1 + \alpha(T_w - T_{ref})] I^2 \quad \dots\dots (3.23)$$

$$\Delta T_{mes} = (T_w - T_g) = \frac{R_{ref}}{l} \frac{[1 + \alpha(T_w - T_{ref})] I^2}{Nu \lambda_g \pi} \quad \dots\dots (3.24)$$

Where  $T_g$  is the temperatures of the gas,  $l$  is the length of probe wire,  $\lambda_g$  and  $Nu$  are the thermal conductivity and the Nusselt number of the gas,  $I$  is the amount of electric current passing through the sensor. In case of a cold wire, a constant of time characterizing the thermal inertia of the wire due to convection  $M_{cv}$  and conduction  $M_{cd}$  were introduced by Paranthoën and Lecordier (1996).

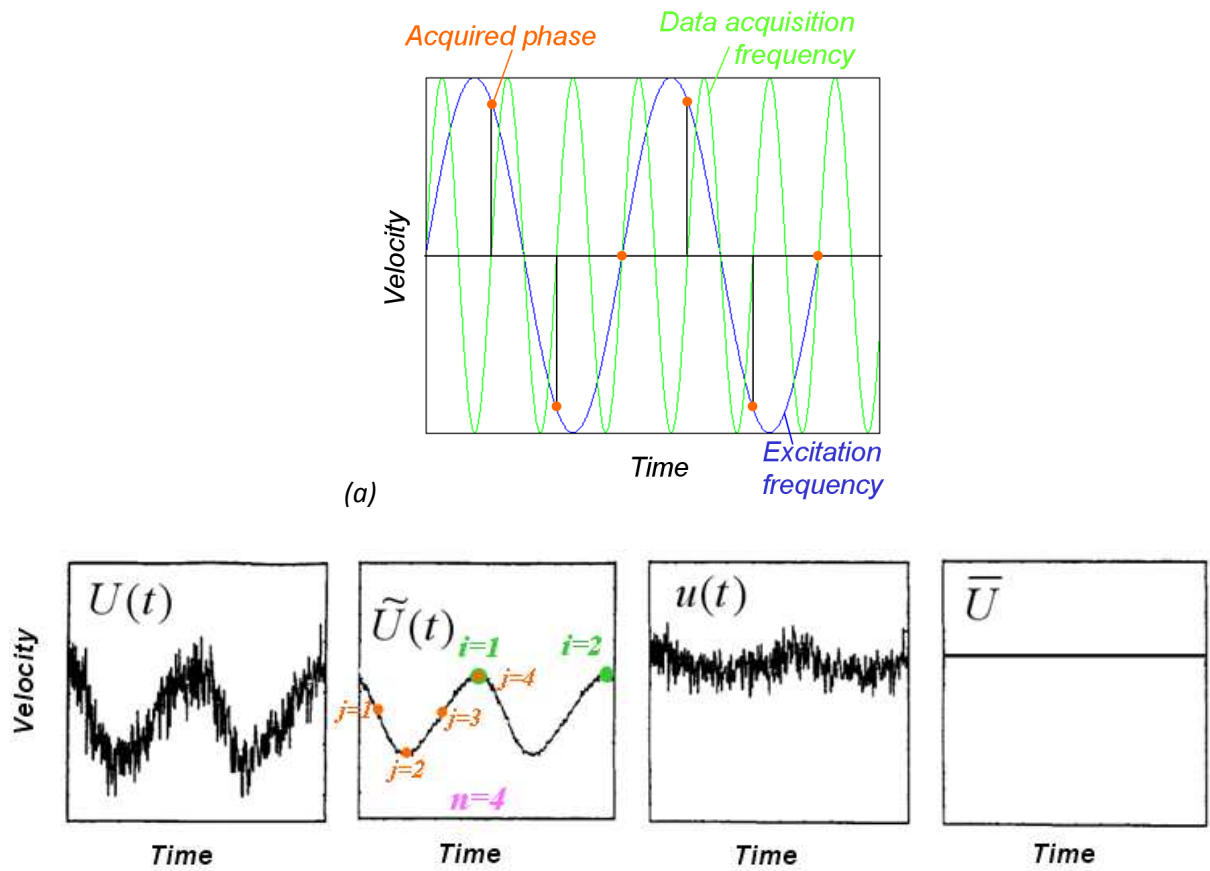
$$M_{cv} = \frac{d^2 \cdot \rho_w \cdot c}{4Nu \lambda_g}; \quad M_{cd} = \frac{l^2}{\pi^2 a_w} \quad \dots\dots (3.25)$$

## 3.5 Data treatments

### 3.5.1 Phase average description of the flow

For the measurement in pulsating cases, the PIV data acquisition frequencies,  $f_{acq}$ , of the particle image were always set as an exact integral multiple of flow excitation frequency  $f_s$  (i.e.  $f_{acq} = n \times f_s$ , where  $n \geq 1$ ). The maximum data acquisition frequency  $f_{acq}$  of the system is restrained by the specified level of PIV spatial resolution. Under this constraint, a maximum possible acquisition frequency being the exact integral multiple of excitation frequency was chosen and used to determine the number of time instants in a period of excitation, see figure (3.31a). For the range of forcing frequency considered, the number of time instants,  $n$ , locked in a period varies from 4 to 10 instants per period. The measured velocity field can be decomposed in the following way (Ligrani et al. 1996-b);

$$U(t) = \bar{U} + \tilde{U}(t) + u(t) \quad \text{..... (3. 26)}$$



(b) Figure (3.31): (a) Schematic description of data acquisition frequency relative to the excitation frequency and the number of phases or time instant in a period of pulsation, (b) Schematic description of the various components of the velocity.

Where,  $U(t)$  is the evolution of instantaneous velocity in time,  $\bar{U}$  is the time average component of velocity,  $\tilde{U}$  is the periodic component of velocity;  $\tilde{U}(t) = U_a \cdot \cos(\omega t + \phi)$  and  $u(t)$  is the fluctuating component of velocity, see figure (3.31b). In the present study, the results for flow parameters are presented with time  $t_j$ , for which the equivalent phase value can be written as,  $\theta_j = 2\pi \cdot (t_j) / T$ . In order to make the velocity field in Eq. (3.26) independent of the periodic term, the data classification in time was performed with a time interval equivalent to the period of data acquisition frequency. This reduces the result into mean and fluctuating components of velocity locked at  $n$  time or phase instants in the period of excitation,

$$U(t_{i,j}) = \bar{U} + u(t_{i,j}); \quad 1 \leq j \leq n \text{ and} \quad \text{..... (3. 27)}$$

$$i = j + (k \cdot f_{acq}) / f_s; \quad k \in \mathbb{N}_0 \quad \text{..... (3. 28)}$$

The application of ensemble averaging over index  $i$  of  $U(t_{i,j})$  provides the averaged phase or time instant quantities at each index of  $j$ . The grouping of phase averaged results along a single index will reduce to;

$$\bar{U}(t_j) = \bar{U} + \tilde{U}(t_j) \quad \text{..... (3. 29)}$$

### 3.5.2 Turbulence description of the flow

#### Taylor Hypothesis

Hot wire measurement permits to obtain local velocity evolution with respect of time. This corresponds to the measurements performed in Eulerian view point, but in general most of the turbulence theory is discussed exclusively from the Lagrangian viewpoint. Therefore, the hypothesis of Taylor is used to link Eulerian measurements to the Lagrangian statistics.

Taylor (1938) made the hypothesis that turbulence has high power at large length scales. Therefore, the advection contributed by the small scale turbulent circulations themselves must be small, compared with the advection produced by the larger integral scales containing most of the energy. The Taylor's hypothesis of frozen-in turbulence applies, only when the advection of a field of turbulence past a fixed point can be taken as being mainly due to the larger, energy containing scales.

$$u(t + \delta t, x_0) \cong u(t, x_0 - \bar{U}\delta t) \text{ and } \frac{\partial}{\partial t} = -\bar{U} \frac{\partial}{\partial x} \quad \text{..... (3. 30)}$$

Taylor's hypothesis holds only if the fluctuation  $u$  remains small in comparison with  $\bar{U}$ . It is estimated by earlier studies that this hypothesis is applicable for the maximum fluctuation rate  $u/\bar{U}$  of 10%. However, according to Antonia et al. (1980) for jets this hypothesis is applicable for a rate of turbulence up to 25%.

#### Energy dissipation rate

The rate at which the energy associated with the bulk motion of the fluid (kinetic energy) is dissipated into molecular motion, due to the action of viscosity, is defined as the energy dissipation rate ( $\varepsilon$ ). The energy dissipation rate for homogenous and isotropic flow is given by Eq. (3.31). This relation permits to calculate  $\bar{\varepsilon}$  from the derivative of fluctuating velocities.

$$\bar{\varepsilon} = 15\nu \overline{\left(\frac{\partial u}{\partial x}\right)^2} \quad \text{..... (3. 31)}$$

Kolmogorov (1941) assumes that the effect of viscosity is negligible in the inertial zone and the flow of energy from the large scale eddies to the small scale eddies is only due to the

energy transfer mechanism dominated by the inertial zone. The turbulence in this situation becomes a function of the rate of dissipation and the size of the structures, and the energy injected from the large scales and dissipated by the small scales occurs at a same rate  $\bar{\varepsilon}$ . For high Reynolds number flow, the dissipation rate can be determined from the structure function like  $S_3(r)$  and  $S_2(r)$ .

$$S_3(r) = \overline{(u(x+r) - u(x))^3} \quad \text{and} \quad S_2(r) = \overline{(u(x+r) - u(x))^2} \quad \dots\dots (3.32)$$

The term  $(u(x+r) - u(x))$  represents the fluctuations of the velocity at the scale “ $r$ ”. The “4/5 law” of Kolmogorov (1941), defined for the inertial domain, is written as;

$$\overline{(u(x+r) - u(x))^3} = -\frac{4}{5} \varepsilon \cdot r \quad \dots\dots (3.33)$$

Also, 
$$\overline{(u(x+r) - u(x))^2} = (\varepsilon \cdot r)^{\frac{2}{3}} \quad \dots\dots (3.34)$$

In present work, results for dissipation rate are calculated by using  $S_3(r)$  structure function. Figure (3.32) indicates the criteria used for determining the  $\bar{\varepsilon}$ . The flat portion of the curve corresponds to the scales existing in the inertial zone with uniform average dissipation rate  $\bar{\varepsilon}$ .

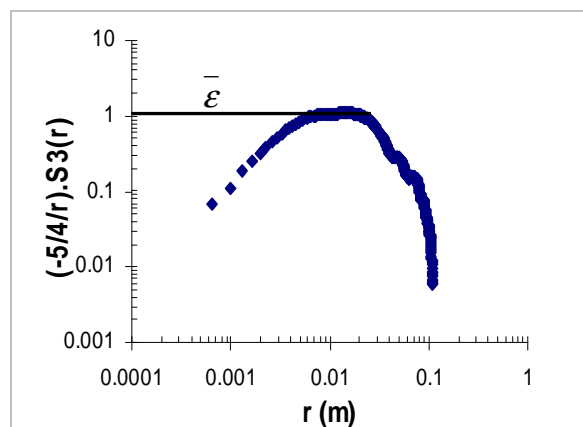


Figure (3.32): Determination of dissipation rate from  $S_3$  structure function.

### **Turbulent length scales**

Kolmogorov length scale ( $\eta_\varepsilon$ ) signifies the size of the smallest eddies in the flow. Its value is closely related to the energy dissipation rate and can be deduced by using;

$$\eta_\varepsilon = \left( \frac{v^3}{\varepsilon} \right)^{\frac{1}{4}} \quad \dots\dots (3.35)$$

Integral length scale ( $\Lambda$ ) represents the energy containing scale. This scale can be estimated from the autocorrelation function. The autocorrelation function can be defined as,

$$\rho(m\Delta t) = \frac{\frac{1}{N-m} \sum_{i=1}^{N-m} (u_i u_{i+m})}{\frac{1}{N} \sum_{i=1}^N u_i^2} \quad \text{..... (3. 36)}$$

Where  $m$  is varied from 0 to  $N-1$ . Theoretically, the integration of the above function from zero to infinity gives the integral time scale. However, sampling time always remains finite in the experiments. Therefore, the integral time scale can be defined as;

$$\tau_\Lambda = \left( \sum_{i=1}^{N-1} \rho(i\Delta t) \right) \Delta t \quad \text{..... (3. 37)}$$

The integral length scale can be obtained by multiplying the local time-averaged velocity with the integral time scale, that is,

$$\Lambda = \bar{U} \cdot \tau_\Lambda \quad \text{..... (3. 38)}$$

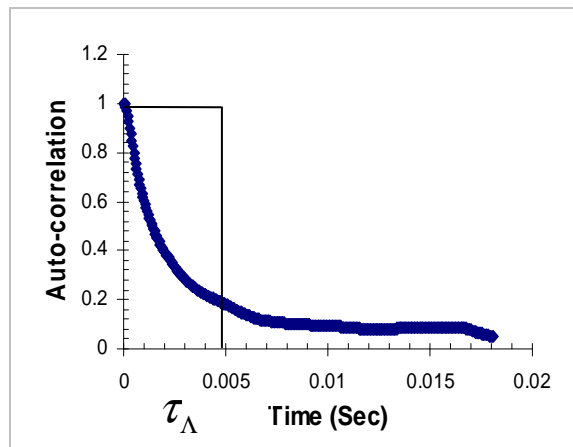


Figure (3.33): Determination of integral time scale from velocity autocorrelation curve.

Another important length scale, which can be obtained from the correlation function, is called Taylor's micro-scales. The correlation function admits an osculating parabolas ( $P$ ) defined by  $\rho = 1 - r^2 / \lambda^2$  in the limit as  $r \rightarrow 0$ . Therefore, Taylor's micro scales can be defines as;

$$\left( \frac{\partial^2 \rho(r)}{\partial r^2} \right)_{r=0} = -\frac{2}{\lambda^2} \quad \text{..... (3. 39)}$$

' $\lambda$ ' is called micro-scale because it is defined by the curvature at the origin of the velocity correlation function, thus depending on the smallest eddies. In isotropic and homogeneous turbulence, it is common to express the dissipation rate ' $\epsilon$ ' as a function of Taylor's micro-scale, considering that the rate of strain of the dissipative scales can be evaluated by  $s \approx u / \lambda$ . Taylor's micro scale can thus be defined as:

$$\lambda^2 = \frac{\overline{u^2}}{\left(\frac{\partial u}{\partial r}\right)^2} \dots\dots (3. 40)$$

And assuming  $\epsilon = 2\nu\overline{\left(\frac{\partial u}{\partial r}\right)^2}$ , the above equation will give:

Thus, 
$$\epsilon = 2\nu\frac{\overline{u^2}}{\lambda^2} \dots\dots (3. 41)$$

This relation shows that the Taylor micro scale characterizes the dissipative phenomena.

In order to determine Taylor micro scale from the graphical method, it is important to define a certain limit for the selection of points from autocorrelation curve to estimate osculation parabola ( $P$ ). This limit is defined by  $0 \leq \rho \leq T$ , where  $T$  is the threshold value, which lies between 0.95 and 0.99.

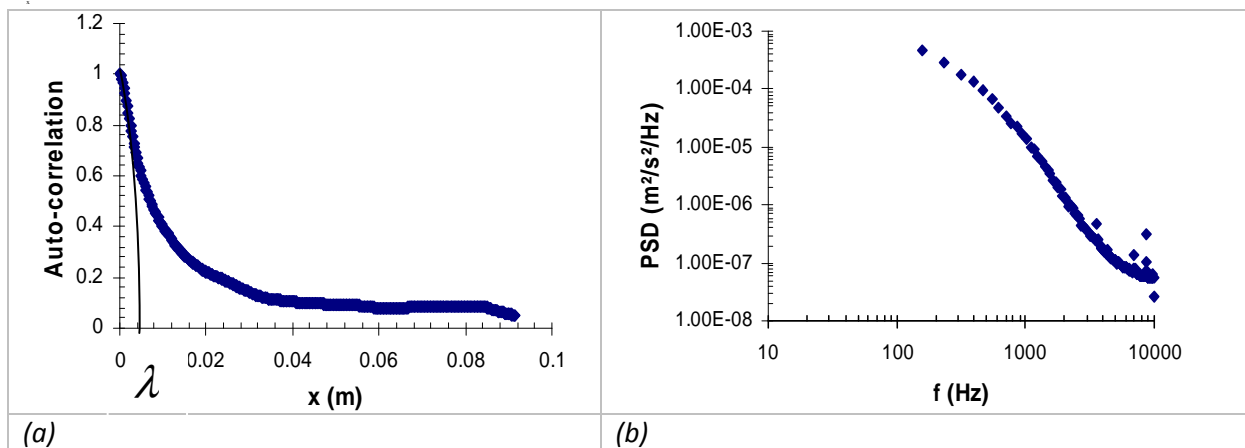


Figure (3.34): (a) Determination of Taylor micro scale from autocorrelation data. (b) Power spectral density of longitudinal velocity fluctuation.

**Energy spectrum and Kolmogorov law**

Kolmogorov (1941) presented the famous “-5/3 law” for the energy spectrum of the intermediate scales, or inertial scale subrange, for high Reynolds number flows (which are ideally homogeneous and isotropic in three velocity dimensions). He derived the form of the

distribution or energy spectrum  $E(k)$  over the inertial subrange simply by dimensional analysis, where  $k$  is the wave number given by  $k^2 = k_x^2 + k_y^2 + k_z^2$ .

$$E(K) = C \cdot \varepsilon^{\frac{2}{3}} \cdot K^{-\frac{5}{3}} \quad \dots\dots (3.42)$$

Where  $C$  is a dimensionless constant, which Kolmogorov and subsequently many others deduced from experimental data to be of the order of 1. In contrast to the above assumptions of Kolmogorov law, our case which is a fairly low turbulent Reynolds number case and might not work well with this constant. Therefore, ' $C$ ' is determined from the available results, since dissipation rate ' $\varepsilon$ ' is constant in the inertial zone [11], so  $A = C \cdot \varepsilon^{\frac{2}{3}}$  can be determined by generating a plot between  $E(K) \cdot K^{\frac{5}{3}} = A$  and  $K$ . The flat part of the curve provides the value of  $A$ , as shown in figure (3.35).

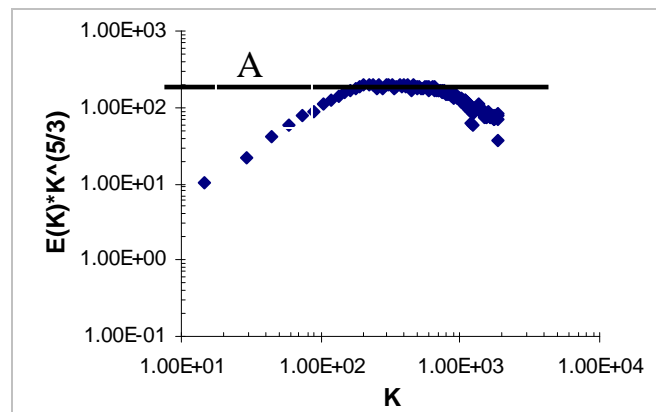


Figure (3.35): Determination of constant for energy distribution equation.

By using this constant in the equation of Kolmogorov spectrum, we can determine the inertial zone in the energy spectrum of the velocity fluctuations.

### 3.5.3 Convective heat transfer coefficient and adiabatic wall temperature

#### 3.5.3.1 Heat transfer Models

The film cooling technique is applied to prevent a direct exposure of the metal surface to the hot stream of gas by the injection of coolant in an appropriate combination of holes geometry and the dynamic parameters of the flow. The surface protection characteristics are explained by both the film cooling effectiveness and the surface heat transfer coefficient. An improved thermal protection requires lower heat transfer coefficient on the wall. The problem of modeling the surface heat transfer includes three different temperatures to play with, which is inherently difficult to handle. In the classical form of convective heat transfer

problem as proposed by Newton, there exists only two temperatures, the free stream temperature  $T_\infty$  and the wall temperature  $T_w$  as shown by Eq. (3.43).

$$\phi_{conv} = h(T_w - T_\infty) \quad \dots\dots (3.43)$$

Film cooling problems include a third temperature, which is the temperature of the bulk fluid downstream of the holes after mixing of the hot combustion gases and the injecting coolant. We call it a reference temperature  $T_{ref}$ , and the heat transfer over the wall surface actually occurs between this temperature and the wall temperature  $T_w$ . The approximation of  $T_{ref}$  is quite difficult as it depends primarily on the mixing of two different flow streams approaching at different temperatures levels. This mixing temperature can be replaced by an adiabatic wall temperature ' $T_{ad}$ ', if the testing wall is made to represent the adiabatic wall condition ( $\phi = 0$ ), Eq. (3.44). The determination of heat transfer from this equation is largely apprehended by the difficulty of determining  $T_{ad}$  and  $h_f$ . Over the years, various methods have emerged in the domain of thermal measurement in order to cope with this difficulty, and both testing conditions and data exploitation techniques are proposed for determining both film reference/adiabatic wall temperature  $T_{ad}$  and wall heat transfer coefficient  $h_f$  over the test surface.

$$\phi_{conv} = h_f(T_w - T_{ad}) \quad \dots\dots (3.44)$$

Mick and Mayle (1988) employed a test condition using a heater foil thermocouple technique under steady state condition. They performed two separate tests to determine, 1) adiabatic wall temperature without supplying power to the surface heater strips, and applying corrections to the temperature measured by the thermocouples placed underneath the test surface, and 2) the coefficient of heat transfer with power supplied to the surface heater strips to maintain a constant heat flux condition. In both cases, the correction for heat loss due to conduction and radiation were taken into consideration. Ligrani et al. (1992), Ligrani et al. (1994) and Saumweber and Schulz (2004) used the concept of linearity in the heat transfer model and described the model by the linear superposition theory. This model is applicable in a condition, when the equation leading to the temperature distribution is homogeneous and linear for flow properties. The author has chosen a free-stream recovery temperature  $T_{r,\infty}$  in place of  $T_\infty$  for convective heat transfer given by Eq. (3.43). By equating Eq. (3.43) and (3.44) following form would be resulted;

$$h = h_f(T_w - T_{ad}) / (T_w - T_{r,\infty}) \quad \dots\dots (3.45)$$

$$h = h_f(1 - \theta\eta) \quad \dots\dots (3.46)$$

Where,  $T_{r,i}$  is the injectant recovery temperature and  $\theta = (T_{r,i} - T_{r,\infty}) / (T_w - T_{r,\infty})$ ,  $\eta = (T_{ad} - T_{r,\infty}) / (T_{r,i} - T_{r,\infty})$ . The above technique requires the information of  $h(\theta)$  at different values of  $\theta$ , which is determined from wall temperature measured at different wall fluxes. The wall temperatures were normally determined by using either infra-red camera or liquid-crystals techniques.

Vedula and Metzger (1991) proposed a transient method using liquid crystals coating to determine both heat transfer coefficient and adiabatic wall temperature by suddenly exposing the testing wall to mainstream and injectant flow, which was initially at thermally uniform condition. The wall temperatures at two different instants of time were used to simultaneously solve the semi-infinite heat conduction equations. Ekkad et al. (2004) implemented the same concept with Infrared thermography and proposed that the IR technique is more robust allowing temperature measurement over a wider range with improved accuracy of both  $h$  and  $\eta$ .

A solution of the three temperature problem based on two heat transfer coefficients was proposed by Teekaram et al. (1989), as given by Eq. (3.47). He modeled the heat transfer by determining the two coefficient  $\alpha$  and  $\beta$  which represent the heat transfer for a situation when  $T_i = T_\infty$  and  $T_w = T_\infty$  respectively. Such modeling leaves the dependency of  $\alpha$  and  $\beta$  on the flow field and makes them independent of thermal boundary conditions. Both  $A$  and  $B$  in Eq. (3.48) are determined by a linear plot of the data generated by varying  $\theta(T_w)$ , where  $k_e$  is thermal conductivity of main flow.

$$\phi = \alpha(T_\infty - T_w) + \beta(T_\infty - T_i) \quad \dots\dots (3.47)$$

$$\phi / \{k_e (T_\infty - T_w)\} = A + B(T_\infty - T_i) / (T_\infty - T_w) = A + B\theta \quad \dots\dots (3.48)$$

The film cooling problem with two heat transfer coefficients for both adiabatic and a non-adiabatic wall cases was studied by Dorignac and Vullierme (1996). A simpler kind of decomposition leading to two coefficients of heat transfer was proposed. The two coefficients  $h_1$  and  $h_2$  were referred as the thermal exchange between mainstream flow and the wall and between wall and jet flow respectively.

$$\phi = h_1(T_w - T_\infty) + h_2(T_w - T_i) \quad \dots\dots (3.49)$$

Both  $h_1$  and  $h_2$  are determined by setting different injection temperatures and a constant wall flux. The treatment of results using linear-regression at two variables provides the values of  $h_1$  and  $h_2$ . The lower values of  $h_1$  was mentioned as a favorable film cooling condition as the level of thermal exchange between mainstream flow and the wall remained low. The authors have also proposed some interesting combinations of these coefficients,

that include  $(h_1 + h_2)/h_0$  and  $(h_1 - h_2)/h_0$ , where  $h_0$  was shown as the heat transfer coefficient without injection. The term  $(h_1 + h_2)/h_0$  indicates the effects of injectant on aerodynamic aspects of the flow when the temperature of injectant and mainstream flows are the same ( $T_\infty = T_i$ ). For a value greater than one, this term actually suggests the stimulation of convective exchange due to the introduction of injectant flow. The term  $(h_1 - h_2)/h_0$  indicates the importance of thermal exchange accruing at the wall in achieving a mean flow temperature due to the interaction of two different flow streams. A negative value identifies the domination of injectant flow in film concentration on the wall.

Another method based on two heat transfer coefficients  $h_{cf}$  and  $h_{2,j}$  is proposed in Messaadi (1992) and Petre et al. (2003). In this model,  $h_{cf}$  was represented by a thermal exchange at iso-energetic condition, ( $T_\infty = T_i$ ). The subscript *cf* stands for cold flow because the chosen temperatures were close to ambient temperature. The resulting equation for the convective heat transfer coefficient would be similar as for two temperatures conditions where the reference temperature is known.

$$h_{cf} = \phi_{conv} / (T_w - T_\infty) \quad \dots\dots (3.50)$$

The second heat transfer coefficient  $h_{2,j}$  was mentioned as the thermal exchange at ( $T_e > T_i$ ). The subscript *2,j* corresponds to the thermal condition at two different mainstream temperatures, which is used to calculate the average heat transfer coefficient  $h_2 = (h_{2,1} + h_{2,2})/2$ . The contribution of these coefficients to convective heat flux was given by;

$$\phi = h_{cf} (\lambda_{c,j} / \lambda_{cf}) (T_{w,j} - T_{\infty,j}) + h_{2,j} (T_{\infty,j} - T_i) \quad \dots\dots (3.51)$$

Where  $\lambda_{cf}$  is the thermal conductivity of air corresponding to cold flow condition and  $\lambda_{c,j}$  is the thermal conductivity of air at a mean temperature  $T_{m,j} = (T_{\infty,j} + T_{w,j})/2$ .

A model based on the infrared measurement of wall temperature at different convective heat fluxes under steady state conditions was adopted by Fenot (2004), Thibault (2009) and Dung (2009). The method consists of a single heat transfer coefficient which is determined simultaneously with adiabatic wall temperature under the conditions when fluid properties remain constant for the range of wall temperature tested. The present study is based on the similar model and the detail description is given in the next section.

### 3.5.3.2 Steady state heat transfer model

The model consists of determining the wall temperature distribution at different convective heat fluxes and employing the linear characteristics of the thermal exchange to specify both the convective heat transfer coefficient and the adiabatic wall temperature. Usually two or

more points are required in order to limit the bias effect for required parameters. Mathematically, this can be written as;

$$T_w = 1/h_f \cdot \phi_{conv} + T_{ad} \quad \dots\dots (3.52)$$

$$T_w = A \cdot \phi_{conv} + B \quad \dots\dots (3.53)$$

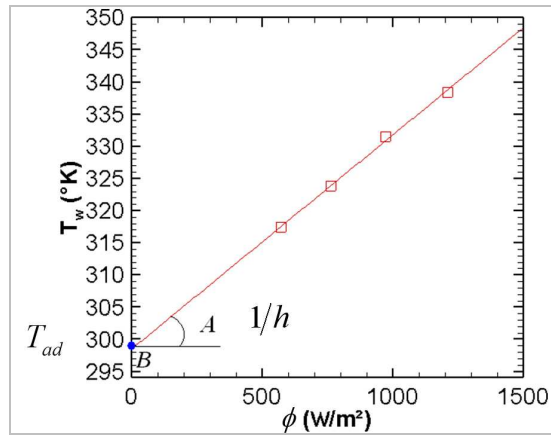


Figure (3.36): Heat transfer model, using a linear fit for four points.

The adiabatic wall temperature  $T_{ad}$  theoretically indicates the thermal equilibrium of the test wall at zero heat flux. In laboratory measurement, this condition is often difficult to achieve. However, with current method  $T_{ad}$  is obtained from the extrapolation of the results following a linear fit. The  $T_{ad}$  is normally expressed in a non-dimensionalized form as shown in Eq. (3.54). This non-dimensionalized term is known as *film cooling effectiveness*.

$$\eta = (T_{ad} - T_{\infty}) / (T_i - T_{\infty}) \quad \dots\dots (3.54)$$

The present form of film cooling effectiveness is adopted by Dorignac and Vullierme (1996) and Fenot (2004). However, a group of authors prefers to use the free-stream recovery temperature  $T_{r,\infty}$  in place of  $T_{\infty}$ . For the flow conditions at low velocities the difference between these two temperatures approaches to zero (Fenot 2004). On the other hand, the approach of using  $T_{\infty}$  is quite simple and straightforward.

### 3.5.3.3 Convective heat flux

The convective heat flux on the wall surface exposed to the flow is calculated by subtracting the factor of heat flux escaping from the wall. The constant heat flux on the wall is generated from a thin layer of copper electrical circuit. The convective heat flux can be obtained by using the energy balance at the wall, as shown in figure (3.37).

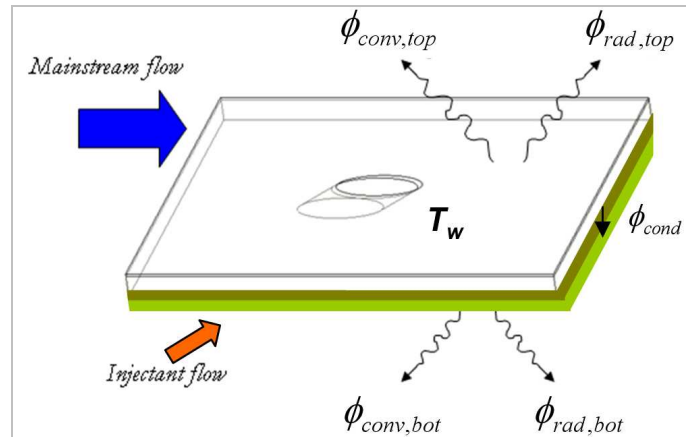


Figure (3.37): Heat transfer model, using a linear fit for four points.

$$\phi_{conv,top} = \phi_{elect} - \phi_{rad,top} - \phi_{cond} \quad \dots\dots (3.55)$$

$$\phi_{cond} = (T_{w,top} - T_{w,bot}) / \sum R_i = \phi_{conv,bot} + \phi_{rad,bot} \quad \dots\dots (3.56)$$

$$\sum R_i = e_{ep} / \lambda_{ep} + e_{ert} / \lambda_{ert} + e_f / \lambda_f + e_{gw} / \lambda_{gw} \quad \dots\dots (3.57)$$

Where;

$\phi_{conv,top}$	= Convective heat flux on the top surface, lying on flow side,	(W.m <sup>-2</sup> )
$\phi_{elect}$	= Electrical heat flux,	(W.m <sup>-2</sup> )
$\phi_{rad,top}$	= Loss of heat flux due to radiation from the top surface,	(W.m <sup>-2</sup> )
$\phi_{cond}$	= Loss of heat flux due to conduction,	(W.m <sup>-2</sup> )
$e_{ep}, \lambda_{ep}$	= Thickness & Thermal conductivity of epoxy,	(m, W.m <sup>-1</sup> .K <sup>-1</sup> )
$e_{ert}, \lambda_{ert}$	= Thickness & Thermal conductivity of Ertalon,	(m, W.m <sup>-1</sup> .K <sup>-1</sup> )
$e_f, \lambda_f$	= Thickness & Thermal conductivity of Polyurethane foam,	(m, W.m <sup>-1</sup> .K <sup>-1</sup> )
$e_{gw}, \lambda_{gw}$	= Thickness & Thermal conductivity of Glass wool,	(m, W.m <sup>-1</sup> .K <sup>-1</sup> )

Radiative and conductive heat fluxes are determined from two different models. The description of the calculation method for both heat fluxes is available in Annex-B.

### 3.5.4 Phase averaged description of the temperature field

With reference to the decomposition given by Ligrani et al. (1996b), the cold wire temperature signal can be decomposed into a time-averaged  $\bar{T}(t)$ , periodic  $\tilde{T}(t)$  and fluctuating  $T'(t)$  component of temperature as given by Eq. (3.58).

$$T(t) = \bar{T} + \tilde{T}(t) + T'(t) \quad \dots\dots\dots(3.58)$$

Since, the cold wire acquires the results at higher data rate, which can be used to obtain the phase-averaged temperature distribution with reasonably fine resolution. The phase-averaged temperature can be determined by using Eq. (3.59)

$$\tilde{T}(j)|_{j=1}^N = \frac{1}{npulse} \sum_{i=1}^{npulse} T(i, j)|_{j=1}^N \quad \dots\dots\dots(3. 59)$$

Where  $i$  corresponds to the number of periods of imposed pulsation hold by the overall time duration of data acquisition and  $j$  is the number of phases in each period where data are sampled.

The post-treatment analysis consists of both time- and phase-averaged temperature, and the rms temperature description, which allows ascertaining the pattern of injectant flow dispersion in the freestream boundary layer. The results for these parameters are presented after normalization. The time- and phase-averaged temperatures are normalized by using the temperatures of the mainstream and injectant flow, as given by Eq. (3.60) and (3.61). The rms temperature is normalized with the mean temperature of the corresponding location of the flow.

$$\bar{\theta} = \frac{(\bar{T} - \bar{T}_\infty)}{(\bar{T}_i - \bar{T}_\infty)} \quad \dots\dots\dots(3. 60)$$

$$\tilde{\theta} = \frac{(\tilde{T} - \bar{T}_\infty)}{(\bar{T}_i - \bar{T}_\infty)} \quad \dots\dots\dots(3. 61)$$

### 3.5.5 Thermal uncertainties

Table-3.10 shows some nominal values of uncertainty for the principal parameters of the thermal measurements. These parameters were obtained from the flow condition set for  $\bar{M} = 1$ ,  $T_i/T_\infty = 2$  under steady blowing ( $St=0$ ). Details regarding the calculation method are given in Annex-E.

$\delta \bar{M} / \bar{M}$ (%)	1.5
$\delta I / I$ (%)	1.4
$\delta \varphi_{rad} / \varphi_{rad}$ (%)	8.6
$\delta \varphi_{cond} / \varphi_{cond}$ (%)	8.3
$\delta \varphi_{elec} / \varphi_{elec}$ (%)	2.2
$\delta \varphi_{conv} / \varphi_{conv}$ (%)	3.5
$\delta h / h$ (%)	6.4
$\delta T_{ad} / T_{ad}$ (%)	1

Table-3.10: Nominal values of uncertainty in case of  $\bar{M} = 1$ ,  $T_i/T_\infty = 2$ .

Figure (3.38) shows an example of the range of estimated errors inducing in final results for  $h$  and  $T_{ad}$ . These curves are generated by using the level of minimum and maximum error in  $h$  and  $T_{ad}$ . The red line locating in the middle represents the nominal values of  $h$  and  $T_{ad}$  without error.

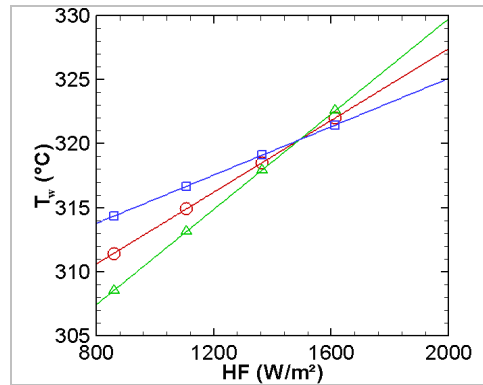


Figure (3.38): Range of estimated errors in  $h$  and  $T_{ad}$ ,  $M=1, T_i/T_\infty=2$

Error contours for both adiabatic wall temperature and convective heat transfer coefficient are shown in figure (3.39). These estimates are based on the flow condition set for  $\bar{M}=1, T_i/T_\infty=2$  under steady blowing ( $St=0$ ).

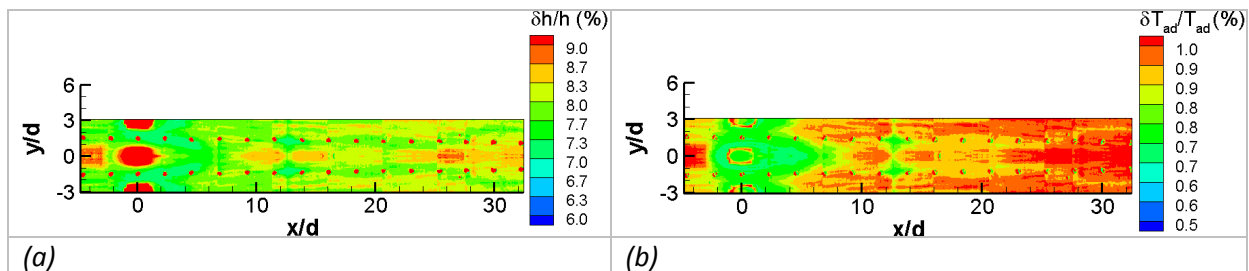


Figure (3.39): Uncertainty in (a) adiabatic wall temperature (b) convective heat transfer coefficient for  $\bar{M}=1, T_i/T_\infty=2$  under steady blowing condition.

The statistical errors in cold wire measurement were determined by using the Eq. (3.15) and (3.16). The mean temperature measured from cold wire is expressed in a non-dimensionalized form given by Eq. (3.60).

$$\bar{\theta} = \frac{(\bar{T} - \bar{T}_\infty)}{(\bar{T}_i - \bar{T}_\infty)}$$

Figure (3.40) shows the uncertainty of non-dimensionalized mean and RMS temperature profiles for the downstream location of  $x/d=1.5$ , under steady blowing ( $\bar{M}=1, T_i/T_\infty=2$ ). The error in  $\bar{\theta}$  also includes the error contribution of freestream and injection temperatures

along with the actual mean temperature measured by the cold wire. The estimated error is about 5% at the location of peak non-dimensionalized mean temperature. The error in  $\bar{T}_{rms}$  is about 0.8% at the location of peak value in the curve.

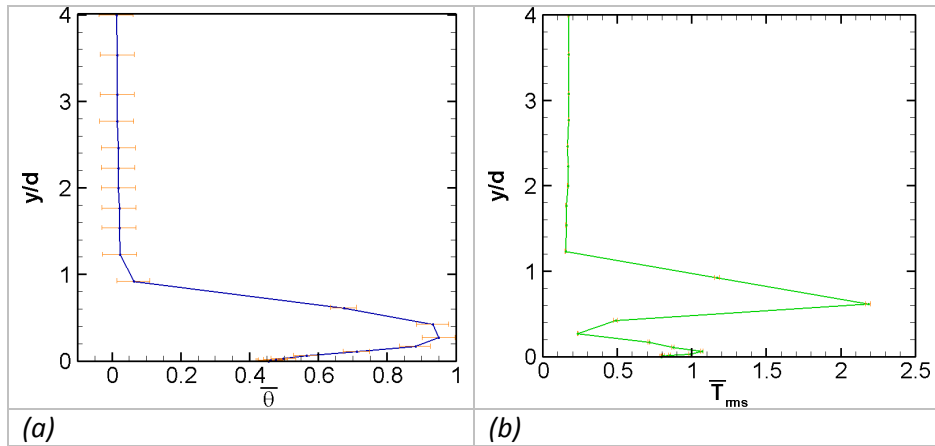


Figure (3.40): Uncertainty in (a) non-dimensionalized mean temperature (b) RMS temperature profile at  $x/d=1.5$ , and steady blowing at  $\bar{M}=1$ ,  $T_i/T_\infty=2$ .

### 3.6 Reference

1. Antonia RA, Satyaprakash BR et Hussain AKMF; "*Measurement of Dissipation Rate And Some Other Characteristics of Turbulent Plane And Circular Jets*", Physics of Fluid, 23 (1980) 695-700.
2. Bell JH, Mehta RD, "*Boundary-layer Prediction for small low-speed contractions*", AIAA Journal, 27 (1989) 372-374.
3. Benedict LH, Gould RD, "*Towards better uncertainty estimates for turbulence statistics*", Exp Fluids, 22 (1996) 129-136.
4. Dieumegard D, "*Etude Experimentale Du Film Cooling Developpe Par Une Range De Cinq Perforations Et Modelisation Des Echanges Convectifs*", Mémoire de Diplôme d'ingénieur, Université de Poitiers- ENSMA, 2003.
5. Dorignac E, Vullierme JJ, "*Etude expérimentale des coefficients d'échange d'un film de refroidissement sur plaque non-athermane: effet de la géométrie d'injection*", Int. J. Heat Mass Transfer, 39 (1996) 1935-1951.
6. Dung HTK, "*Étude du refroidissement d'une paroi concave par l'impact d'un jet bidimensionnel*", Thèse du Doctorat de l'Université de Poitiers, ENSMA, fév. 2009.
7. Ekkad SV, Han JC, Du H, "*Detailed film cooling measurements on a cylindrical leading edge model: Effect of free-stream turbulence and cooling density*", ASME Journal of Turbomachinery, 120 (1998) 799-807.
8. Ekkad SV, Ou S, Rivir RB, "*A transient infrared thermography method for simultaneous film cooling effectiveness and heat transfer coefficient measurements from a single test*", ASME J. Turbomach, 126 (2004) 597-603.
9. Esposito EI, "*Jet Impingement Cooling Configurations For Gas Turbine Combustion*", Thesis of Master of Science, Louisiana State University, August 2006.
10. Fenot M, "*Etude du refroidissement par impact de jets application aux aubes de turbines*", Thèse du Doctorat de l'Université de Poitiers, Déc. 2004.
11. LALIZEL G, "*Caractérisation Expérimentale De L'aérodynamique D'un Jet Annulaire A Très Grand Rapport De Diamètres*", 2004, Thèse de Doctorat de l'Université de Rouen.
12. Harvey NW.; "*Cooling Of Gas-Turbine Engine Aerofoils*", United States Patent, Patent No.: US 6,609,884 B2, Aug 2003.
13. Kolmogorov AN, "*Dissipation of Energy In Locally Isotropic Turbulence*", Dokl. Akad. Nauka SSSR 32 (1941) 16-18.

14. Kolmogorov AN, "On degeneration of isotropic turbulence in an incompressible viscous liquid", *Comptes Rendus (Doklady) de l'Academie des Sciences de l'U.R.S.S.*, ibidem, 31 (1941b) 538–540.
15. Ligrani PM, Ciriello S, Bishop DT, "Heat transfer, Adiabatic effectiveness, and injectant distributions downstream of a single row and two staggered rows of compound angle film cooling holes", *ASME J. Turbomach*, 114 (1992) 687-700.
16. Ligrani PM, Gong R, Cuthrell JM, "Bulk flow pulsations and film cooling-II: Flow structure and film effectiveness", *Int. J. Heat Mass Transfer*, 39 (1996-b) 2283-2292.
17. Ligrani PM, Wigle JM, Ciriello S, Jackson SM, "Film-cooling from holes with compound angle orientation: Part 1—Results Downstream of two staggered rows of holes with 3d spanwise spacing", *ASME J. Turbomach*, 116 (1994) 341-352.
18. Messaadi A, "Etude des échanges convectifs le long d'une paroi à multiperforation incline. Application au refroidissement des parois des chambres de combustion", Thèse du Doctorat de l'Université de Poitiers, Mars 1992.
19. Mick WJ, Mayle RE, "Stagnation film cooling and heat transfer, Including its effect within the hole pattern", *ASME J. Turbomach*, 110 (1988) 66-72.
20. Paranthoën P, Lecordier JC, "Mesures de température dans les écoulements turbulents", *Rev Gén Therm*, Elsevier, 35 (1996) 283-308.
21. Petre B, Dorignac E, Vullierme JJ, "Study of the influence of the number of holes rows on the convective heat transfer in the case of full coverage film cooling", *Int. J. Heat Mass Transfer*, 46 (2003) 3477-3496.
22. Raffel M, Willert CE, Wereley ST, Kompenhans J, "Particle Image Velocimetry 2nd-Edition", Springer, 2007.
23. Saumweber C, Schulz A, "Interaction of film cooling rows: Effects of hole geometry and row spacing on the cooling performance downstream of the second row of holes", *ASME Journal of Turbomachinery*, 126 (2004) 237-246.
24. Taylor GI, "The Spectrum of Turbulence", *Proc. R. Soc. London A* 164: 476, 1938.
25. Teekaram AJH, Forth CJP, Jones TV, "The use of foreign gas to simulate the effects of density ratios in film cooling", *ASME Journal of Turbomachinery*, 111 (1989) 57-62.
26. THIBAUT D, "Étude du refroidissement par impact de jets à travers une paroi mince et avec un écoulement cisailant amont : application aux aubes de turbines", Thèse du Doctorat de l'Université de Poitiers, ENSMA, Déc. 2009.

27. Vanderkooy J, Boers PM, Aarts RM, “*Direct-Radiator Loudspeaker Systems With High-BI*”, Audio Engineering Society 114th Convention Amsterdam, Paper 5742, March 22–25, 2003.
28. Vedula RJ and Metzger DE, “*A method for the simultaneous determination of local effectiveness and heat transfer distribution in three-temperature convection situation*”, ASME Paper No. 91-GT-345, 1991.
29. Westerweel J, “*Fundamentals of digital particle image Velocimetry*”, Meas. Sci. Technol. 8 (1997) 1379-1392.
30. Wikipedia article “*Sound Pressure*” [http://en.wikipedia.org/wiki/Sound\\_pressure](http://en.wikipedia.org/wiki/Sound_pressure).



## Table of Contents

---

4.1	Velocity characterization of wind tunnel flow .....	109
4.1.1	Evolution of mean and rms velocities .....	109
4.1.2	Viscous scales .....	111
4.1.3	Comparison of velocity profiles .....	113
4.1.4	Turbulence intensity .....	113
4.2	Description of turbulence scales and energy spectra.....	114
4.2.1	Energy spectrum.....	114
4.2.2	Turbulence length scale.....	117
4.3	Temperature description of the wind tunnel flow .....	119
4.4	Characterization of injectant flow .....	121
4.4.1	Velocity profiles at the hole exit .....	121
4.4.2	Characterization of pulsation amplitude .....	123
4.5	Energy spectra .....	125
4.6	Comparisons of baseline results .....	126
4.7	Conclusion.....	127
4.8	Reference.....	131

## Nomenclatures

<u>Abbreviations</u>		<u>Subscripts/superscripts</u>	
$\rho$	Fluid density (kg/m <sup>3</sup> )	$i$	Injectant
$T$	Temperature (K)	$\infty$	Free-stream
$d$	Hole diameter (mm)	$ad$	Adiabatic
$U$	Streamwise velocity (m/s)	$rms$	Root mean square
$V$	Normal velocity (m/s)	$-$	Time-averaged
$W$	Lateral velocity (m/s)	$\sim$	Periodic component
$u$	Streamwise velocity fluctuation (m/s)	$a$	Amplitude
$v$	Normal velocity fluctuation (m/s)	$h$	Nominal hole
$w$	Lateral velocity fluctuation (m/s)	$j$	Index number
$\delta$	Boundary layer thickness (mm)	$acq$	Acquisition
$\delta^*$	Displacement thickness (mm)	$s$	Excitation
$M$	Blowing ratio ( $= \rho_i \overline{U}_i / \rho_\infty \overline{U}_\infty$ )	$t$	Thermal
$Re_\infty$	Reynolds number ( $= \overline{U}_\infty \cdot \delta / \nu$ )		
$Re_i$	Reynolds number ( $= \overline{U}_i \cdot d / \nu$ )		
$St$	Strouhal number ( $= f \cdot d / \overline{U}_i$ )		
$u_\tau$	Friction velocity (m/s)		
$U^+$	U normalized by friction velocity ( $= U / u_\tau$ )		
$IT$	Turbulent intensity (%)		
$\sqrt{u^2}$	x-component of RMS velocity (m/s)		
$\sqrt{v^2}$	y-component of RMS velocity (m/s)		
$t$	Time (s)		
$\tau$	Fraction of time period		
$f$	Frequency (Cycles/s)		
$\theta$	Phase (radian)		
$\phi$	Phase shift (radian)		
$\psi$	Angular frequency (radians/s)		
$K$	Wave number (m <sup>-1</sup> )		
$x, y$	Streamwise and normal coordinates (mm)		
$y^+$	Normal coordinate in wall units ( $= y \cdot u_\tau / \nu$ )		
$\Lambda^+$	Integral length scale ( $= \Lambda \cdot u_\tau / \nu$ )		
$\lambda^+$	Taylor micro scale ( $= \lambda \cdot u_\tau / \nu$ )		
$\eta^+$	Kolmogorov scale ( $= \eta \cdot u_\tau / \nu$ )		

## **CHARACTERIZATION OF UPSTREAM FLOWS**

The flow field characteristics of the wind tunnel were assessed by determining the distribution of mean and fluctuating velocities in different streamwise planes by a system of one-dimensional Laser Doppler Velocimetry 'LDV', and a simple hot wire 'HW' for determining turbulent scales and energy spectra at some particular locations of the wind tunnel. This study is performed to qualify the wind tunnel system for onward testing of the film cooling configuration. Flow conditions with different Reynolds numbers based on the centerline boundary layer thickness and mean velocity in the tunnel centre were examined. The study is undertaken to figure out associated mean flow and important turbulence characteristics both inside and outside the boundary layer, to establish a certain database and also a list of possible testing parameters in accordance with film cooling objectives. During the measurement, injection holes were covered neatly by a "scotch" tape, and the boundary layer was allowed to evolve smoothly without interference at the wall. The nominal velocity of the jet and the form of jet velocity profiles at the hole exit were later determined by using the system of Particle Image Velocimetry (PIV). Before starting the study of the phenomena of the interaction between a crossflow and a pulsating jet, some auxiliary measurements were performed with a hot wire anemometer to figure out the behavior of the jet with pulsation. The hot wire survey was performed to determine the appropriate levels of amplitude of the input signal that can be reproduced by the loudspeaker at different frequencies.

### **4.1 Velocity characterization of wind tunnel flow**

#### **4.1.1 Evolution of mean and rms velocities**

The profiles of mean and rms velocities were measured at the central plane along with four other locations lying on each side of the center, as shown in figure (4.1). Each measurement location was progressively distant by a  $3d$  step on each side of the tunnel's longitudinally bisecting plane, also called as mid-span.

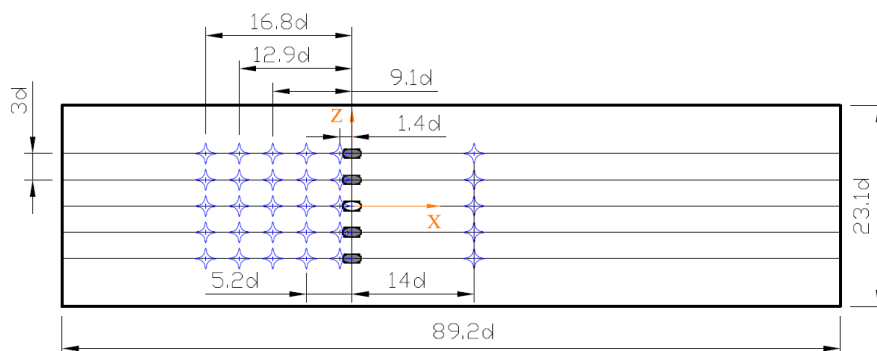
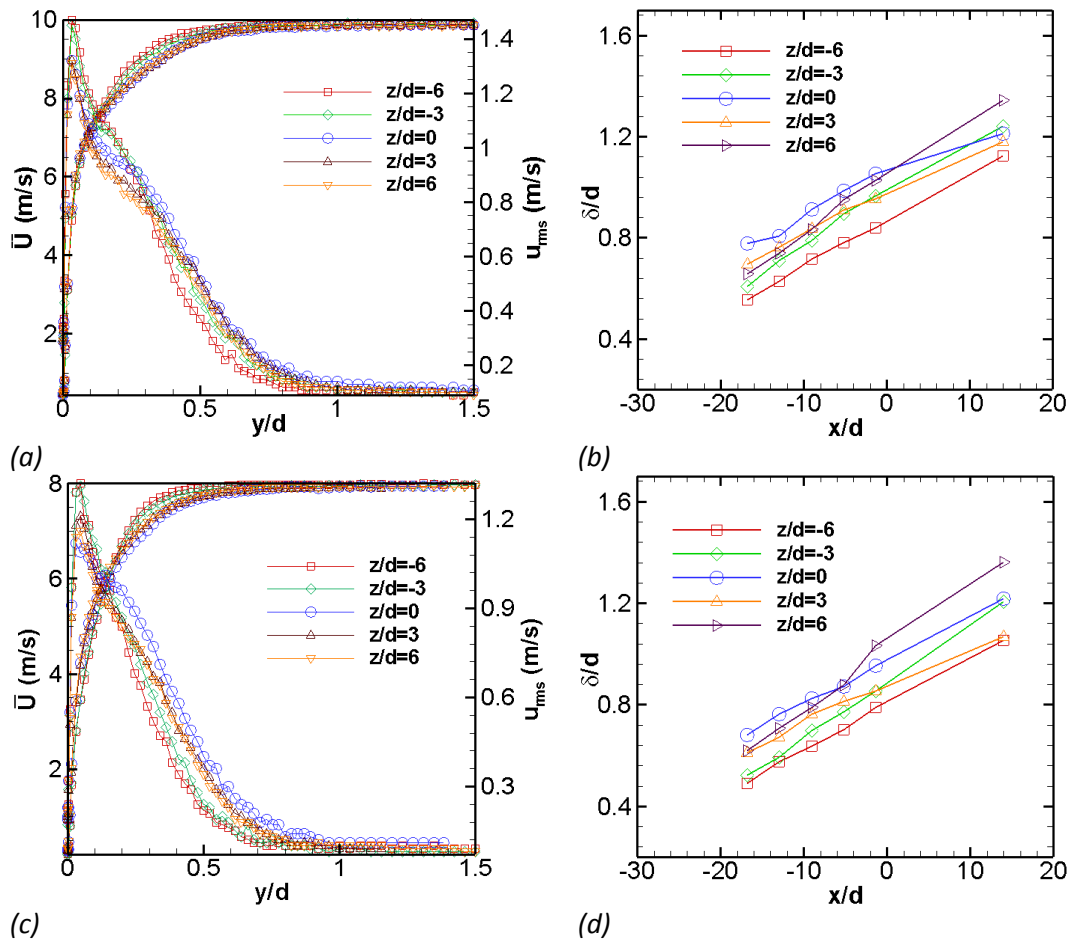


Figure (4.1): Locations of profile measurement with LDV.

The resulting flow fields are quite uniform as shown in figure (4.2a) and (4.2c). Figure (4.2b) and (4.2d) show that the deviations in boundary layer thickness across the mid-span of tunnel test section are in reasonable limits, except for the case with the lowest mean flow velocity ( $5 \text{ m}\cdot\text{s}^{-1}$ ), figure (4.2e) and (4.2f). The thickness of boundary layer corresponds to a wall-normal distance, where  $\bar{U} = 0.99\bar{U}_\infty$ . In the lowest velocity case, the flow along the central plane has been found to evolve much faster than the flow on the lateral extremities. The flow condition below these velocities can not be considered as a reference mainstream condition, as the flow has not been developed evenly in the entire section of the wind tunnel. Such behavior of the flow along the tunnel mid-span was found to hold up to a distance which lies half way down from the inlet. The pattern of evolution of boundary layer thickness is quite similar for 10 and 8  $\text{m}\cdot\text{s}^{-1}$  cases, which shows that the evolution of flow characteristics is reasonably even across the tunnel and thus can be considered as a working condition in film cooling experiment.



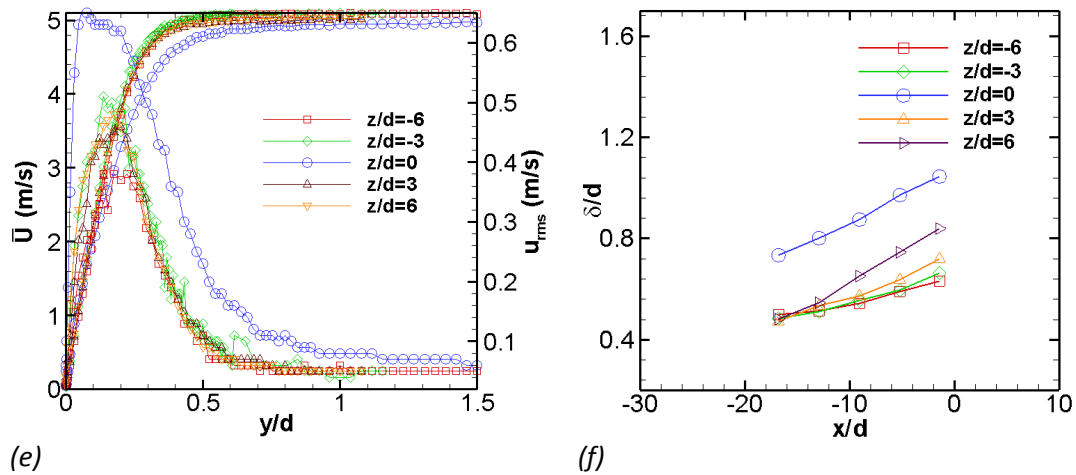


Figure (4.2): Mean and rms velocity profiles (a)  $10 \text{ m.s}^{-1}$ ,  $Re=8609$  (c)  $8 \text{ m.s}^{-1}$ ,  $Re=6681$  and (e)  $5 \text{ m.s}^{-1}$ ,  $Re=4305$ ; Boundary layer thickness (b)  $10 \text{ m.s}^{-1}$ ,  $Re=8609$  (d)  $8 \text{ m.s}^{-1}$ ,  $Re=6681$  and (f)  $5 \text{ m.s}^{-1}$ ,  $Re=4305$ .

The importance of this exercise is based on the fact that in the study of the influence of Strouhal number pulsation for a range of crucial blowing ratios, we want to have the lowest possible velocity in the mainstream flow. So that, the practical difficulty associated with the periodic forcing mechanism could be minimized for higher Strouhal number pulsations cases. In the present study, flow in the mainstream was set to  $10$  and  $7.7 \text{ m.s}^{-1}$  during the final film cooling experiments under periodic pulsation.

#### 4.1.2 Viscous scales

Results of the mean velocity profiles are used to calculate the viscous or inner variables that lead us towards the determination of  $Y^+$ . This scale is used in the subsequent sections for presenting some of the turbulent parameters.

$$y^+ = \frac{u_\tau \cdot y}{\nu} \quad \dots(4.1)$$

Where;  $u_\tau$  is known as friction velocity. Since, the LDV is a non-intrusive technique and it allows fairly close wall measurement. Therefore, we are able to locate a few points of the profile in the viscous sublayer. The linear region of the viscous sublayer allows determining the wall shear stresses from the velocity gradient in wall-normal direction;  $\tau_p = \mu \cdot dU/dy$ , which is used to calculate the friction velocity;  $u_\tau = \sqrt{\tau_p/\rho}$ . Figure (4.3) shows the form of velocity profile normalized in wall units.

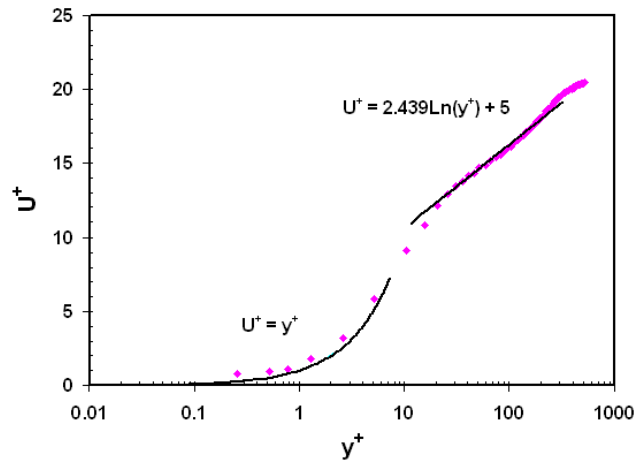


Figure (4. 3): Velocity profile normalized in wall units,  $Re=6681$ .

In case of hot wire measurements, the unavailability of data points in the viscous sub-layer halts the determination of viscous scales directly from the near wall region. The friction velocity is calculated by means of the logarithmic law since plenty of points are available in the logarithmic region. For this purpose, velocity profiles are plotted on semi-log axes, where the logarithmic portion of the velocity profile appears to be linear on the log axis. The points lying in this region can be fitted to a log law and can be used to estimate the  $u_\tau$  by using following the equation;

$$u_\tau = \frac{\kappa}{2.3} \frac{u_2 - u_1}{\log_{10}(y_1) - \log_{10}(y_2)} \quad \dots(4.2)$$

Where;  $\kappa = 0.41$  is an empirical constant, known as von Karman's constant.

As indicated by the above formula that we are required to select only two points on the fitted line to estimate  $u_\tau$  from the logarithmic zone. In figure (4.4) indicates an example of outlined method.

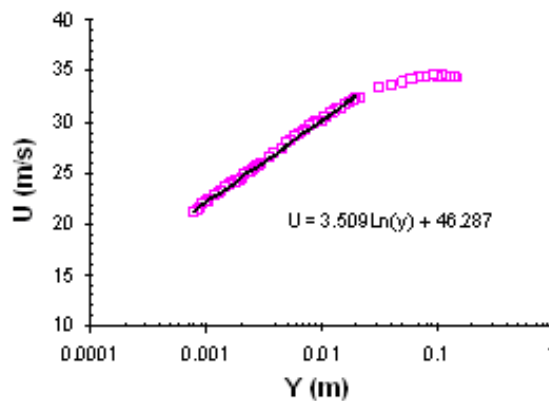


Figure (4. 4): Determination of friction velocity from logarithmic law.

### 4.1.3 Comparison of velocity profiles

For the comparison of results, the velocity profiles obtained on the upstream side ( $x/d=-1.4$ ) of the injection hole and the results given by Kim et al. (1987) from a Direct Numerical Simulation are plotted in figure (4.5). The profiles of streamwise mean and rms velocities, normalized by the friction velocity, appear to be in good agreement with the DNS results.

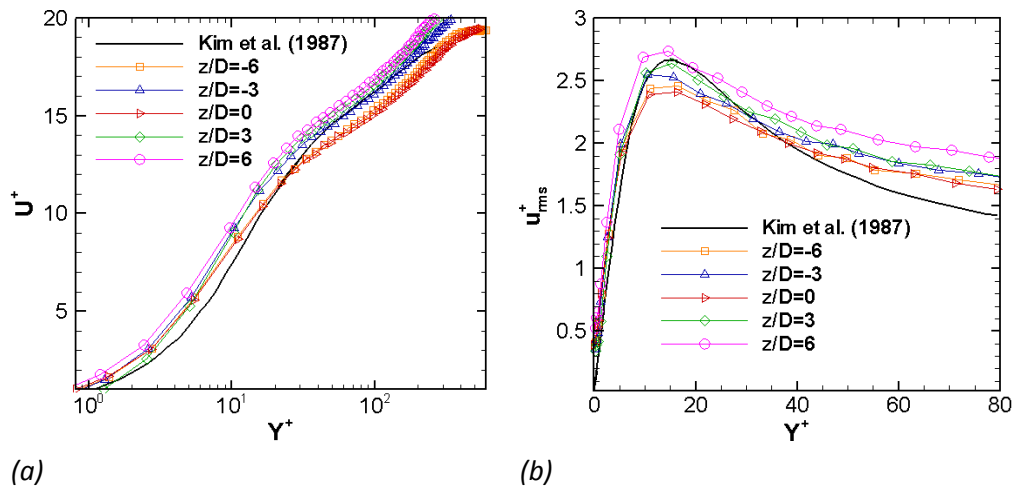


Figure (4. 5): Comparison of (a) mean & (b) RMS velocities normalized with friction velocity, ‘lines with symbol’ present study (LDV), ‘—’ Kim & al. (1987).

### 4.1.4 Turbulence intensity

Figure (4.6) shows the profiles of turbulence intensity measured for different Reynolds number cases at an upstream location of  $x/d=-1.4$ . The nominal values of turbulence intensity for  $Re=4305$ ,  $6681$  and  $8609$  are  $1.3\%$ ,  $1.5\%$  and  $1.2\%$  in the central region of the tunnel. For the case of lowest Reynolds number, the non-uniformity of the profile at  $z/d=0$  is more noticeable than the other cases, figure (4.6a).

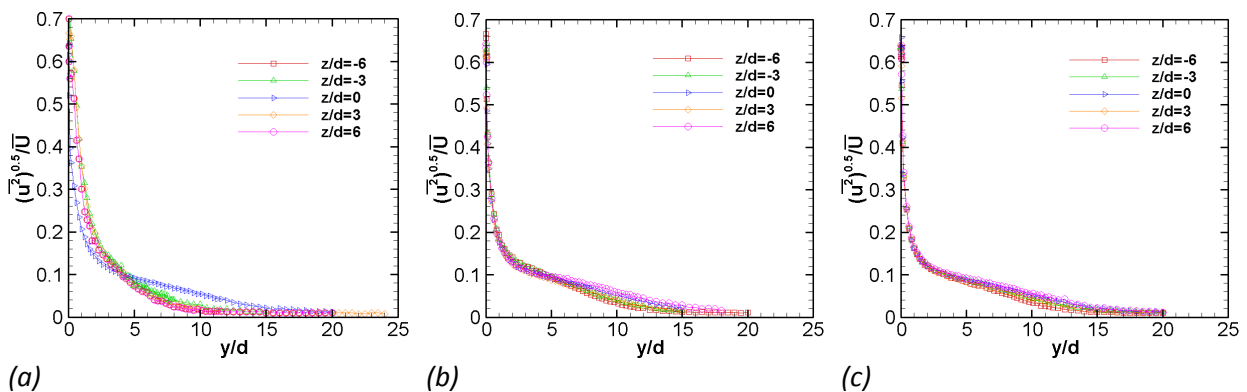


Figure (4. 6): Turbulent intensity (a)  $Re=4305$ , (b)  $Re=6681$  and (c)  $Re=8609$ .

## 4.2 Description of turbulence scales and energy spectra

The low particle density in the near wall region during the LDV measurements results in a lower data rate and thus the temporal resolution of the measuring system reduced greatly. Therefore, the hot wire measurements were performed at a relatively higher data rate to determine energy spectra and turbulent scales at various locations of the wind tunnel, figure (4.7) shows the locations of the profile measurement. The measuring stations are aligned to the central plane ( $z/d=0$ ) and lies on the streamwise position of  $x=-10.2d$ ,  $12.9d$ ,  $36d$  and  $49.8d$ . The freestream Reynolds numbers ( $Re = \overline{U}_\infty \cdot \delta / \nu$ ) were 5801 and 18436.

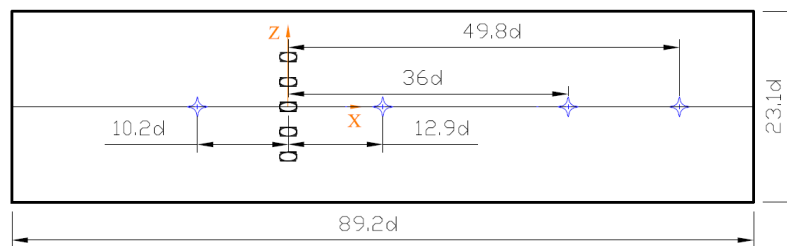


Figure (4. 7): Plan of measuring stations for the profile measurement with hot wire.

### 4.2.1 Energy spectrum

The analyses of the spectral distribution of energy have shown that at higher frequencies few peaks exist. Fluctuation peaks occurring in the higher frequency zones of the spectra are more pronounced in the highly uniform, low turbulence freestream region, where the velocity fluctuations are much smaller compared to the velocity fluctuations occurring in the near wall region. In figure (4.8a), an example of such difference can be observed from the energy spectra estimated for two points located at a wall-normal distance of  $y/d=3.14$  and  $y/d=0.085$  and a downstream distance of  $49.8d$  of the mid-span, and a flow Reynolds number of 5801. Alimpiiev (1975) reported the similar kind of shift in spectra. He observed that in the immediate vicinity of the wall, the spectra are located in the region of large wave number and they are displaced into the region of smaller wave number, as he moved away from the wall. Figure (4.8a) also shows that the lower peaks are observed in the higher frequency domain of larger PSD. This may take place due to the larger turbulent fluctuations results in a certain level of reduction or complete dissolution of such peaks.

Figure (4.8b) shows the energy spectra for different cases of Reynolds number. For a fixed point located near the central region, the energy spectra shows that at higher Reynolds number the energy levels are not only higher but their distribution is also more uniform. The estimated energy spectra have manifested some important peaks in high frequency zone. The exact source of these peaks is not clear. One of a reason that could possibly explain these peaks is the generation of large scale fluid structures somewhere from the tip region of the air blower, which creates periodically fluctuating velocities characterized by a nearly constant Strouhal number. Since, it was noticed that the peak moved towards the high

*“Experimental aerothermal characterization of a pulsating jet issuing in a crossflow:*

*Influence of Strouhal number excitation on film cooling”*

frequency region with the increment in mean flow velocity, as shown in figure (4.8b). For downstream position of 49.8d an increment of Reynolds number from  $Re=5801$  to  $Re=18436$  have produced a displacement of peak from 3594 Hz to 7031 Hz.

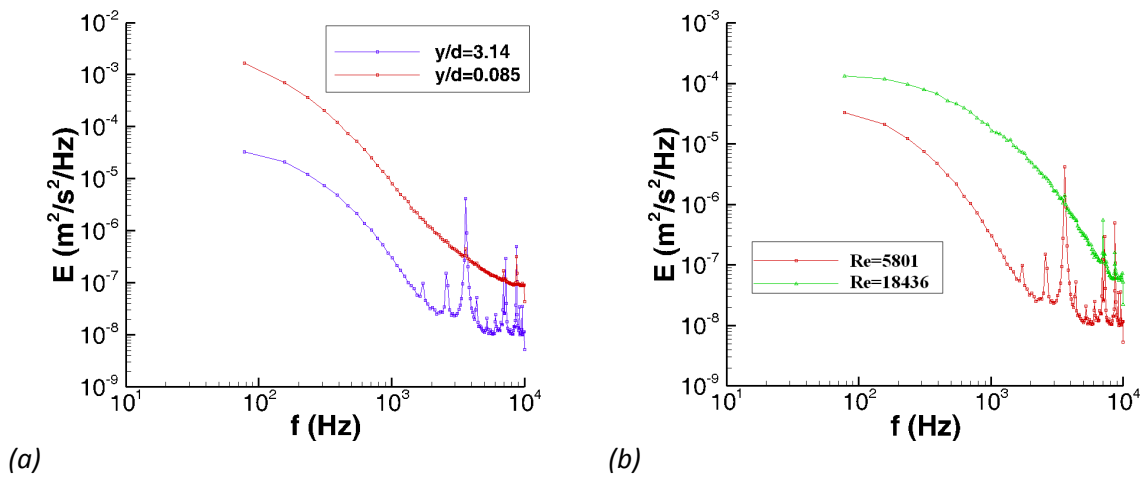
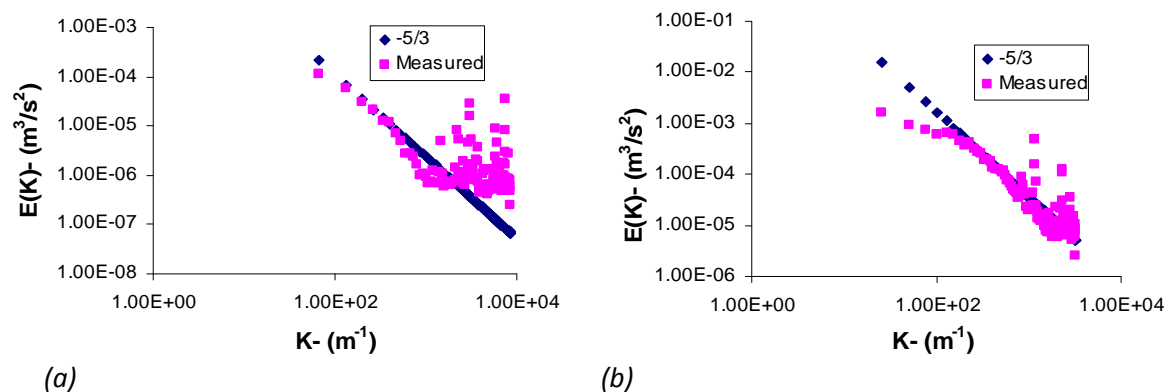


Figure (4. 8): (a) Energy spectrum at  $y/d=0.085$  and  $y/d=3.14$ ; along with flow at  $Re=5801$ , (b) comparison of energy spectrum for different Reynolds numbers;  $Re=5801$  and  $18436$  at  $y/d=0.085$ .

However, this periodicity doesn't exist in the boundary layer region where the turbulence is higher due to the wall shearing. The measurement of both velocity and temperature field at a maximum acquisition frequency being as high as 10 times of the maximum jet excitation frequency will remain unaffected by these frequency peaks.

The energy spectra and the corresponding inertial laws were determined for the points lying at  $y/d=3.14$  and  $x/d=-10.2d, 12.9d, 36d$  and  $49.8d$  for  $Re=5801$  and  $18436$ , see figure (4.9a-4.9h). A survey of the above results shows that the size of the inertial zone increases as the flow Reynolds number is increased. This phenomenon is usually reported by a one-dimensional spectra  $E_{11}(K_1)/(\epsilon\nu^5)^{1/4}$  plotted as a function of Kolmogorov scale  $K_1 \cdot \eta$ , and the variation of spectrum for different Reynolds numbers based on the Taylor scale is shown, see Pope (2000).



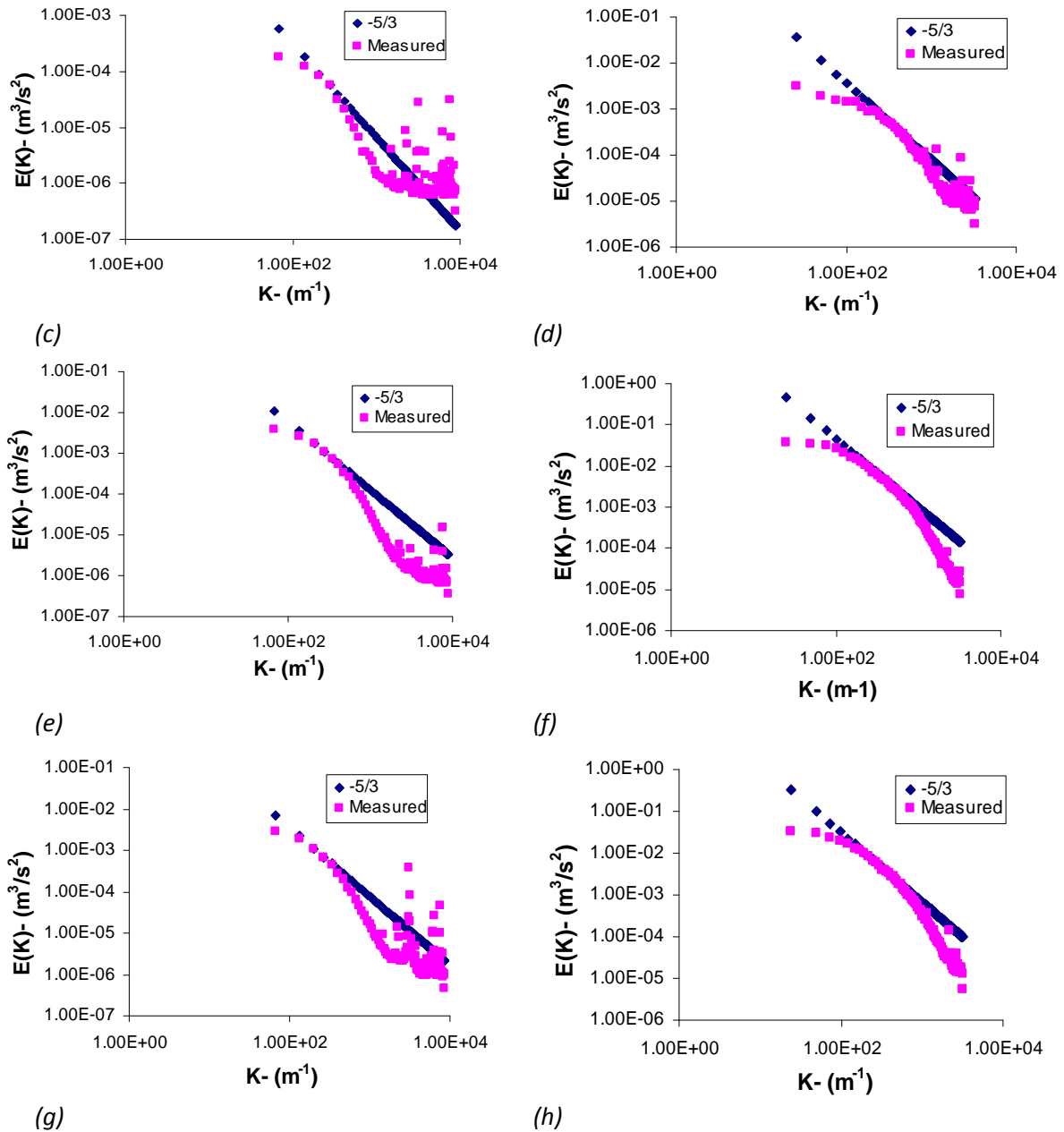


Figure (4. 9): Energy spectra for the case of  $Re=5801$  obtained from  $y/d=3.14$  and  $x/d=;$  (a)  $-10.2d$ , (c)  $12.9d$ , (e)  $36d$  and (g)  $49.8d$ , and for the case of  $Re=18436$  obtained from  $y/d=3.14$  and  $x/d=;$  (b)  $-10.2d$ , (d)  $12.9d$ , (f)  $36d$  and (h)  $49.8d$ .

The elongation of inertial zone is also attributed to the shift of the measuring station along the longitudinal direction. Thus, at each successive plane a small increment in the inertial zone is observed.

## 4.2.2 Turbulence length scale

### Integral length scale

A review of basic turbulent parameters reveals that the flow field is characterized by low turbulence level in the central region. Because of this, the calculation of integral length scales outside the boundary layer is not feasible from the outlined definition, since their implementation carried significant errors or at times provided meaningless outcomes. Results of integral length scale are therefore presented up to a distance of  $y/d=2.38$  normal to the wall for all profiles. The profiles of integral length scale are shown in figure (4.10), which illustrates an increment in the integral length scale with respect to the flow Reynolds number. However, these profiles do not show any clear distinction in scale size with respect to the streamwise distance of the tunnel.

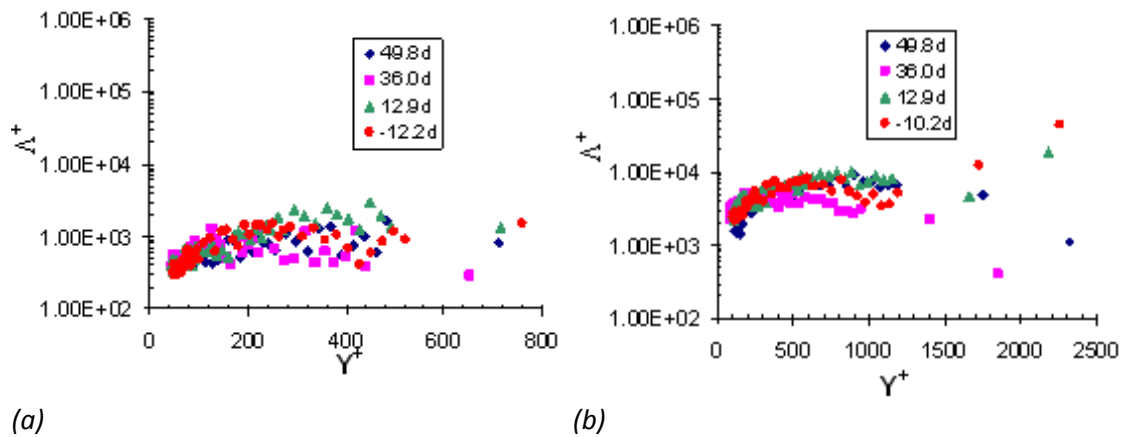


Figure (4. 10): Profiles of integral length scale measured at  $x/d = -10.2d, 12.9d, 36d$  and  $49.8d$  for the Reynolds number cases of (a)  $Re_{\infty} = 5801$  and (b)  $Re_{\infty} = 18436$ .

### Taylor micro scale

The initial assumption adopted for sampling frequency in hot wire measurement is found to be little under estimated as it is found that in the low turbulence central region the autocorrelation curves of longitudinal velocity fluctuation do not provide a sufficient number of points within the defined limits of its threshold value, for constructing the osculating parabolas. So, it becomes difficult to determine the inertial length scale in the central region of the test section from the graphical method. However, in the boundary layer region a sufficient number of points are obtained and the results are estimated with respect to the  $y$ -coordinate at each measuring station lying on the mid-span. It is observed that the velocity fluctuations increase with the increase in the flow Reynolds number, as was noticed by the results of root mean velocity (not presented here). Therefore, at higher flow rates the correlation between fluctuating velocity component is found to be weak within the limit of  $r \rightarrow 0$ , and so the calculation of the Taylor scales at high Reynolds numbers is halted in these

conditions as well. The only results for the Taylor micro scales, which are accessible, are at lowest Reynolds number exercised in the experiment as shown in figure (4.11).

Results depict small gradual increment in the size of the scale towards the edge of boundary layer for all profiles. It is also noticed that the diversity in scale size at different measuring stations is not easy to distinguish.

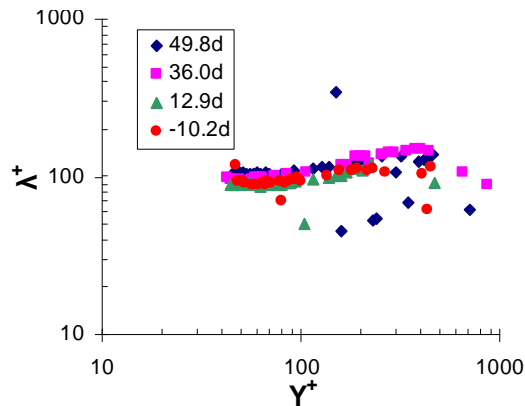


Figure (4. 11): Profiles of Taylor micro scale measured at  $x/d = -10.2d, 12.9d, 36d$  and  $49.8d$  for  $Re_{\infty} = 5801$ .

### Kolmogorov scale

The determination of Kolmogorov scale  $\eta$  is quite a straight forward process, when results of energy dissipation rate are available. The limits for the distribution of profile appear to be similar as mentioned above. A positive shift in the profiles of the Kolmogorov scale are observed for each successively higher Reynolds number, when plotted on the scale of non-dimensionalized wall unit  $Y^+$ . This positive shift is attributed to the increase of friction velocity (velocity associated to the viscous scale), which increases as well with the augmentation of mean flow rate. Also, a slight reduction in scale size is observed with the increment of the distance in x-direction for a region away from the wall. Figure (4.12) shows the variation of smaller scale within the boundary layer.

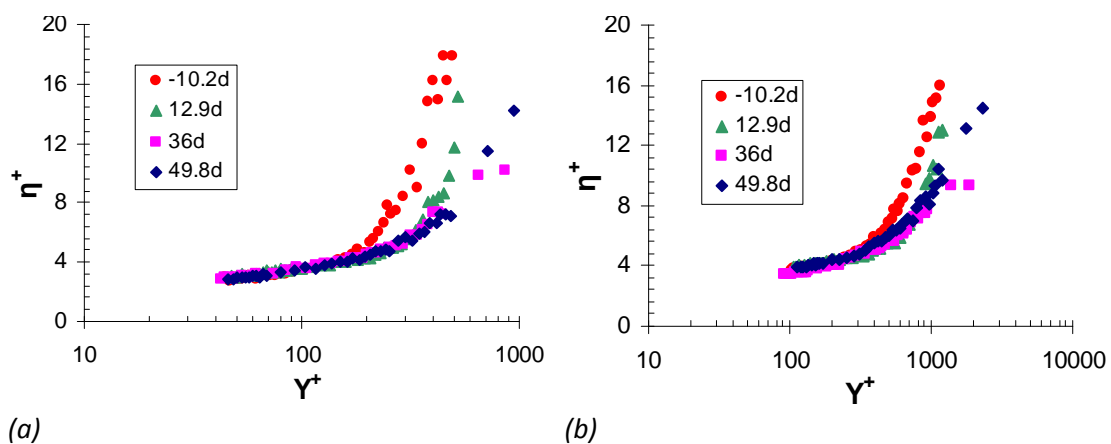


Figure (4. 12): Profiles of Kolmogorov scale measured at  $x/d = -10.2d, 12.9d, 36d$  and  $49.8d$  for the Reynolds number cases of (a)  $Re = 5801$  and (b)  $Re = 18436$ .

### 4.3 Temperature description of the wind tunnel flow

#### Temperature response of the wind tunnel flow

Since the present wind tunnel is equipped with a Thermo-regulatory system, which allows maintaining the temperature in the mainstream flow with the help of an automatic temperature regulation system consisting of hot and cold thermal batteries. Therefore, the temperature response of the mainstream flow was observed to estimate the time required for achieving a uniform temperature field. Figure (4.13a) and (4.13b) show the response of thermal unit of the wind tunnel without and with the implementation of heat flux to the top surface of the test wall. In the heated wall case, the applied heat flux was of the order of  $1512 \text{ W.m}^{-2}$ .

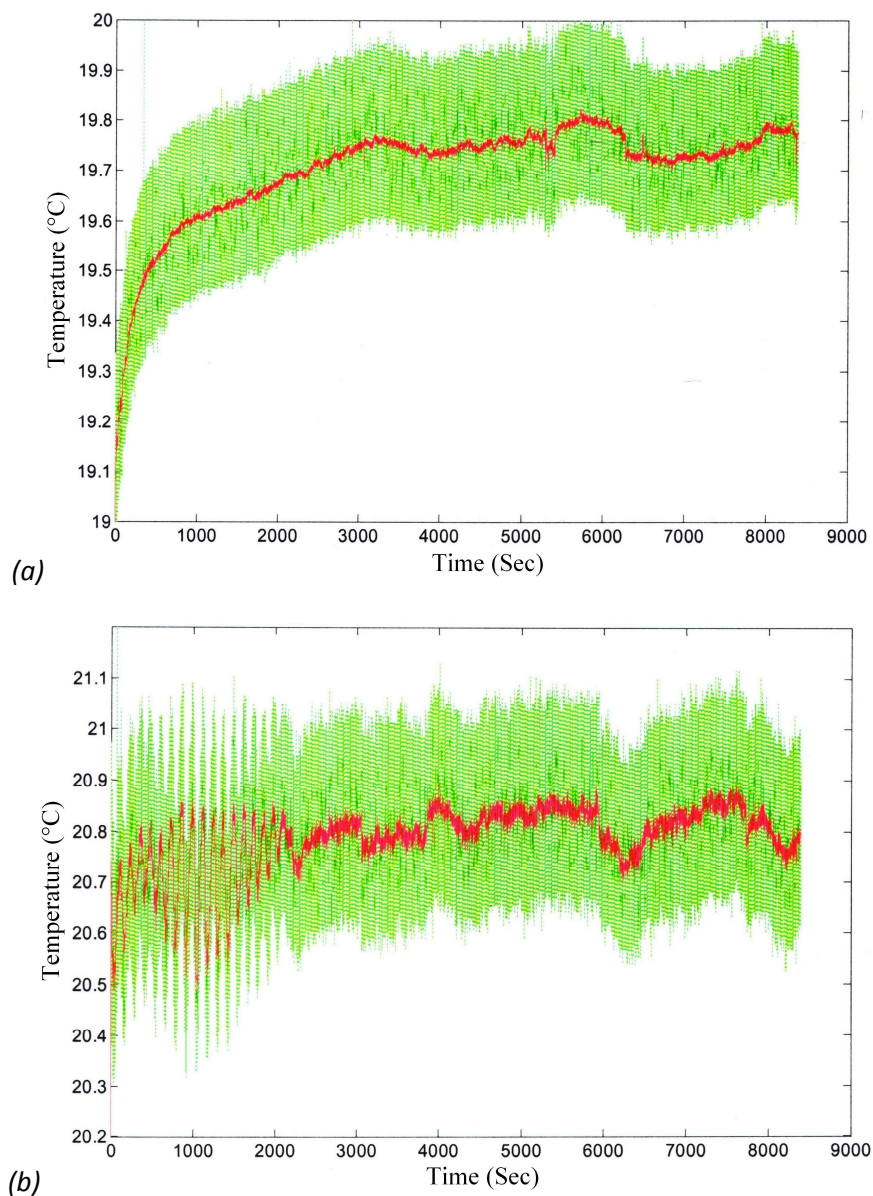
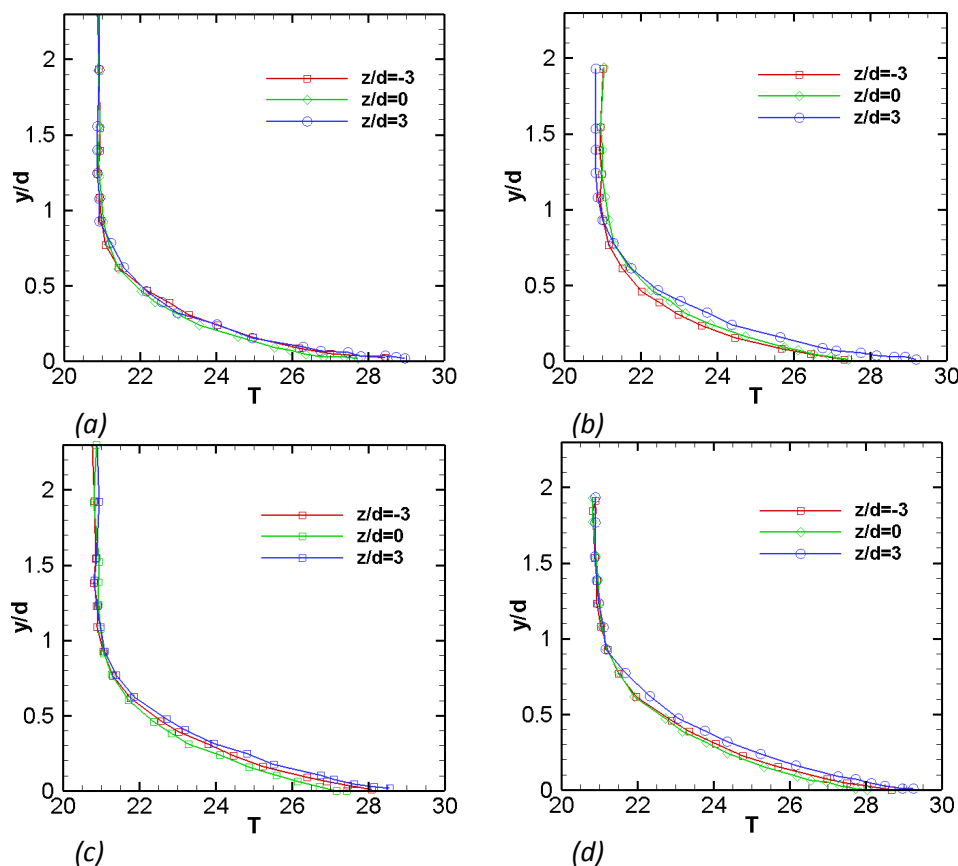


Figure (4. 13): Temperature response measured for a regulation temperature of 20 °C and  $Re=8609$ ,  
(a) without heating of the wall, (b) with heating of the wall.

It was observed that the system attains a uniform temperature in the mainstream flow after one-and-half hours, when the regulation temperature of the wind tunnel flow is set to 20°C. The red line plotted in the middle is showing the running average.

### **Uniformity of Temperature field**

The temperature measurements of the wind tunnel flow were made to determine the uniformity in temperature field developing across the wind tunnel test section. For this purpose, the test wall was heated by supplying a heat flux at  $1512 \text{ W.m}^{-2}$ . The centerline mean velocity of the wind tunnel was set to  $10 \text{ m.s}^{-1}$  ( $\text{Re}=8609$ ), while the regulation temperature for the flow was maintained at  $20 \text{ }^\circ\text{C}$ . The measurement grid consists of different streamwise and spanwise location;  $x=-2d, 0, 2d, 7d, 14d$  and  $28d$ ; and  $z=-3d, 0$  and  $3d$ . The measurements were performed with a T-Type thermocouple, which came as an integrated part of TSI IFA-300 constant temperature anemometer. The signal conditioning unit of TSI was used to acquire primary signals measured in voltages, which were subsequently transformed into temperature from calibration data. The calibration of the thermocouple probe was performed in the wind tunnel test section at two different flow temperatures maintained at the center of the test section.



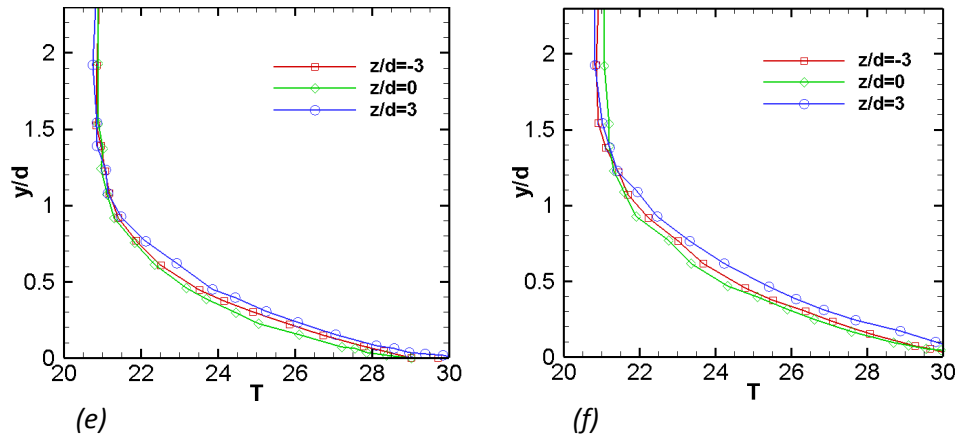


Figure (4.14): Temperature profile measured at different lateral  $z/d=-3, 0$ , and  $3$ , and axial locations of  $x/d=$  (a)  $-2$ , (b)  $0$ , (c)  $2$ , (d)  $7$ , (e)  $14$  and (f)  $28$ .

The temperature of the flow appears quite uniform across the central hole position figure (4.14a-4.14f). The slightly higher value of the flow temperature outside the thermal boundary layer is because of the insertion of additional heat from test wall into the mainstream flow. Figure (4.15a) shows the evolution of thermal boundary  $\delta_t/d$ . The boundary layer thickness corresponds to a wall-normal distance, where  $\bar{T} = 0.99\bar{T}_\infty$ . The maximum deviation in  $\delta_t/d$  from the mid-span values is 6.6% for  $z/d=-3$  and 13% for  $z/d=3$ . Figure (4.15b) is shown to make a qualitative comparison between the evolution of the thermal boundary layer and the aerodynamic boundary layer.

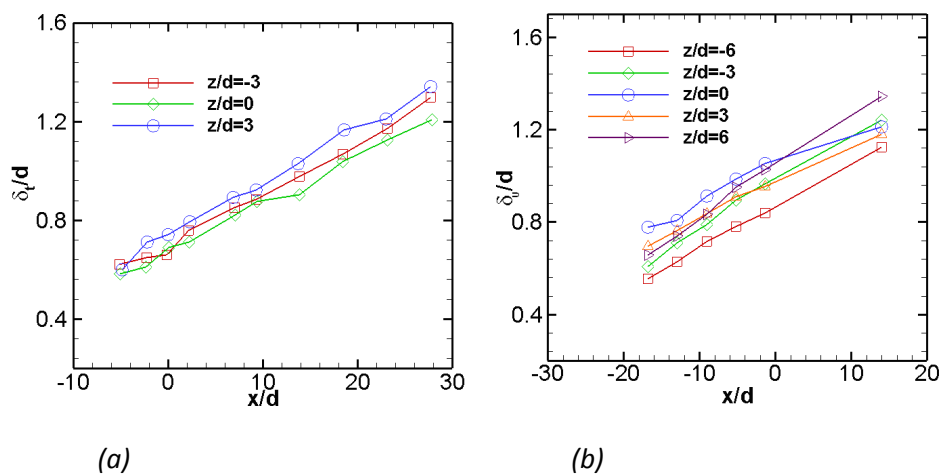


Figure (4.15): (a) Evolution of Thermal boundary along the plans at  $z/d=-3, 0$  and  $3$  (b) Evolution of aerodynamic boundary layer (shown for comparison);  $Re=8609$ .

## 4.4 Characterization of injectant flow

### 4.4.1 Velocity profiles at the hole exit

The profiles of the resultant of mean velocity components  $\sqrt{\overline{U}^2 + \overline{V}^2}$  measured nearest to the hole exit plane are presented in figure (4.16) after normalization by the

“Experimental aerothermal characterization of a pulsating jet issuing in a crossflow: Influence of Strouhal number excitation on film cooling”

nominal hole velocity,  $\overline{U_{nom,h}}$ . The nominal velocity of hole flow,  $\overline{U_{nom,h}}$ , was determined by performing PIV measurements on various lateral planes at the hole exit and then performing the velocity integration along the exit plane, which appears as an elliptical surface for inclined injection. These measurements enable us to fine tune the pressure regulator lying on the upstream side of the injection flow delivery system for required nominal velocity of the jet at the hole exit.

Measurement conditions include the flow from the injection hole only and flow from both mainstream and injection hole at velocities which correspond to the blowing ratio of  $\overline{M}=0.65$  and  $\overline{M}=1$ . A comparison with Seo et al. (1998) is presented to show the change in the form of velocity profiles at the hole exit. The reference case used a hole length to diameter ratio of 10 and an injection angle of  $35^\circ$  comparing to 7.7 and  $30^\circ$  in the present case. The velocity profiles measured along the central plane and near the hole exit ( $y \approx 1$  mm) show an increase in jet velocity, which is larger than the velocity at respective blowing ratio maintained at the hole exit. This is also reported by Pietrzyk et al. (1989) in film cooling measurement, and it is because of the diversion of jet fluid towards the downstream by the mainstream flow. The extra rate of strain and bending causes some acceleration of jet fluid. In the absence of mainstream flow, the maximum in velocity profile appears on the upstream side, which is skewed to the downstream side for the two flow cases. The profile skewness is relatively high for  $\overline{M}=0.65$ , which is pushed slightly back upstream as the blowing ratio rises to 1 (Pietrzyk et al. 1989; Walters and Lylek 2000; Yuen and Martinez-Botas 2003). One of the reasons for such a variation as mentioned in many references is the use of sharp entrance at the tube inlet, which results in flow separation inside the tube. Separation effects become more severe at higher tube velocities. Walters and Lylek (2000) explains the role of streamwise vorticity appearing on the lateral edges of the hole and vertical momentum of the jet in specifying the orientation of the counter-rotating vortex pair along with the shape of velocity profile at the hole exit. In the present case, the injection tube has a length of  $7.7D$  and is connected with a standard fitting on the upstream side, which may have some variation in the flow cross-sectional area and lacks cleanness at the joint interface. This may result in an increase of vorticity emerging from the hole at higher injection flow rate. High vertical momentum and strong streamwise vortices originating from the hole shifts the maximum of jet velocity at the hole exit plane to the upstream side. At low blowing ratio, the resulting velocity distribution is attributed to the formation of a high pressure region on the leading side and low pressure region on the trailing side of the jet, which causes profile skewness towards the downstream side.

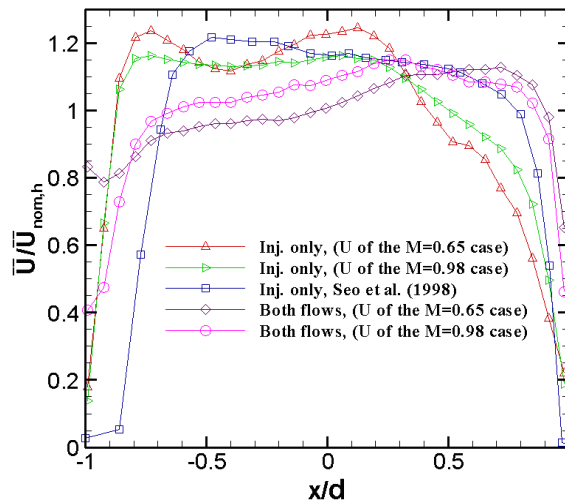


Figure (4. 16): The profiles of resultant of mean velocity components  $\sqrt{(\overline{U}^2 + \overline{V}^2)}$  at hole exit normalized with hole nominal velocity for cases with both flows and the cases without freestream flow (injection only) where the jet velocity corresponds to the cases of  $\overline{M} = 0.65$  and  $\overline{M} = 1$ .

#### 4.4.2 Characterization of pulsation amplitude

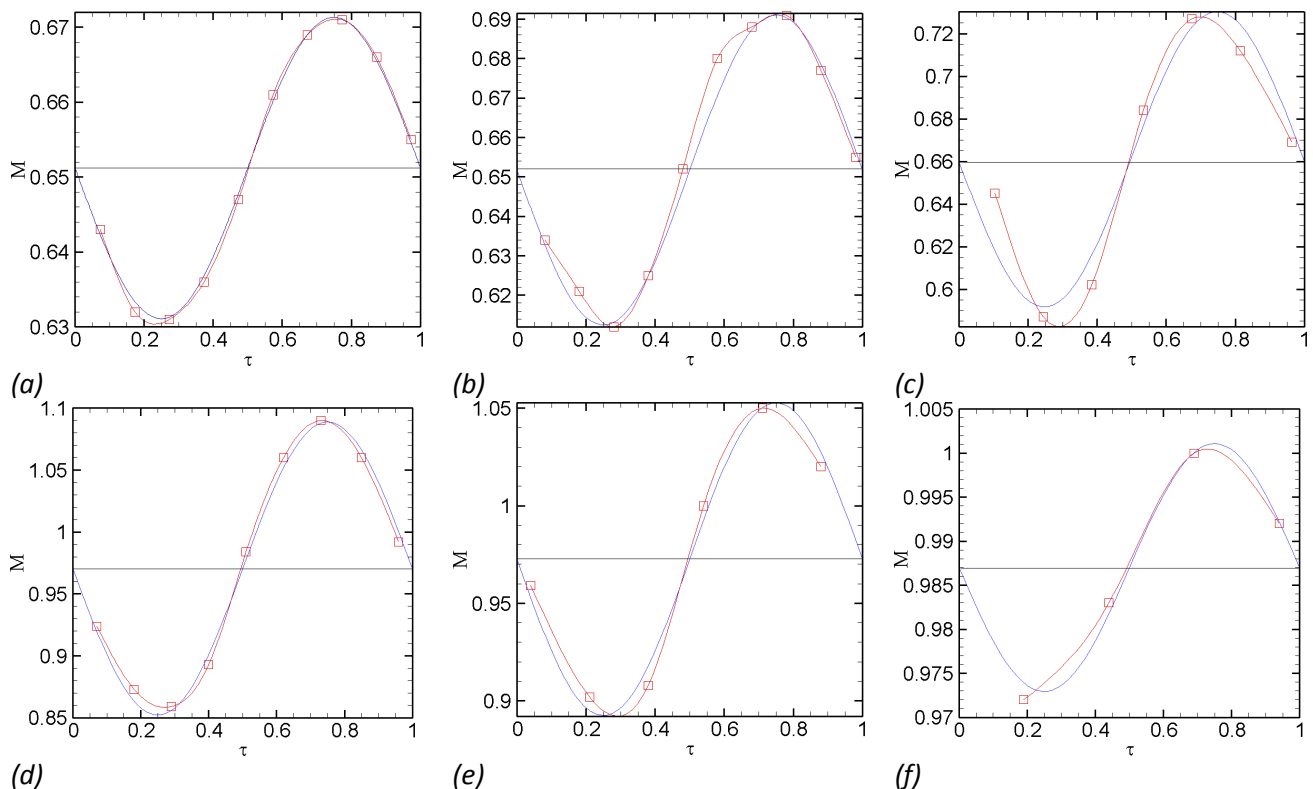
With a loudspeaker based pulsation system, maintaining a constant amplitude for a broad range of frequency is pretty much out of question. Therefore, in order to make some sense for the choice of the amplitude for the entire range of pulsation cases, an initial analysis of the jet, pulsating at the corresponding frequencies was performed by a hot wire anemometer. That study was performed by using a TSI IFA-300 constant temperature hot wire anemometer containing a platinum sensor of 2.5  $\mu\text{m}$  diameter and 1.2 mm length. The measurements at the hole exit plane allow determining the optimum working range of the loudspeaker for a given range of excitation frequencies, considering the limitations of maximum excursion capacity of the loudspeaker diaphragm at high frequencies and the comfortably reproducible pulses at low frequencies, as per the manufacturer's specifications.

For the range of frequencies used for injectant pulsation, an amplitude giving approximately a constant ratio between streamwise rms velocity and average hole velocity was chosen for all cases. A maximum deviation of 13% for the range of pulsating cases belonging to  $\overline{M} = 0.65$ , and a maximum deviation of 14.5% for the range of pulsating cases belonging to  $\overline{M} = 1$  and 1.25 was noticed. For the cases of  $\overline{M} = 1$  and 1.25, the mean velocities of the jet are equivalent. Therefore, the input parameters of pulsation for these cases are identical.

The study of film cooling behavior by using TR-PIV was performed by setting different forcing frequencies  $f_s$  (corresponding to the certain Strouhal number mentioned earlier), and the amplitudes  $U_a$  from the set of pre-established input levels obtained from hot wire analysis. The average/effective blowing ratios,  $\overline{M}$ , were determined by normalizing the

phase-averaged velocities of the jet with the mainstream velocity, while phase-averaged velocities were obtained at different time instants of a period using the data of TR-PIV. The values of phase-averaged velocity at different time instants are estimated by performing the integral averaging of the velocity profile extracted from phase-locked results at the hole exit.

The response of phase-averaged blowing ratios,  $M$ , for the pulsation cases of  $St=0.2$ ,  $0.3$  and  $0.5$  are shown in figure (4.17) along with the actual sinusoidal signal, which gives an effective blowing ratio of  $\overline{M}=0.65$ ,  $1$  and  $1.25$ . The maximum deviation of the signal amplitude increase for the extreme cases of pulsation ( $\overline{M}=0.65$ ,  $St=0.2$ ;  $\overline{M}=1$  and  $1.25$ ,  $St=0.5$ ) as the fluctuating component of the velocity is filtered out. The ratio of velocity amplitude,  $U_a$ , of periodic signal  $\tilde{U} = U_a \cdot \cos(\psi \cdot t + \phi)$  and nominal hole velocity ( $\overline{U}_{nom,h}$ ) is approximately 8% for all cases of  $St=0.3$ . Relative to this level considered as a reference, the deviation of extreme cases of pulsation mentioned above increases as much as 50%. This indicates that at higher frequency cases the periodic displacement of loudspeaker diaphragm is limited because of the inherent characteristics of the loudspeaker. The amplitude of the pulsation remains fairly low even when a significant input voltage is supplied from the amplifier (staying below the threshold value mentioned for a safe operation). Whilst, at low frequency cases turbulence produced in the delivery passage, containing various components like a honeycomb structure, a convergent section and connecting tubes, has dominating effects. It should be noticed that the addition of a honeycomb structure has helped greatly in reducing the turbulence level in the hot wire signal recorded for the issuing jet.



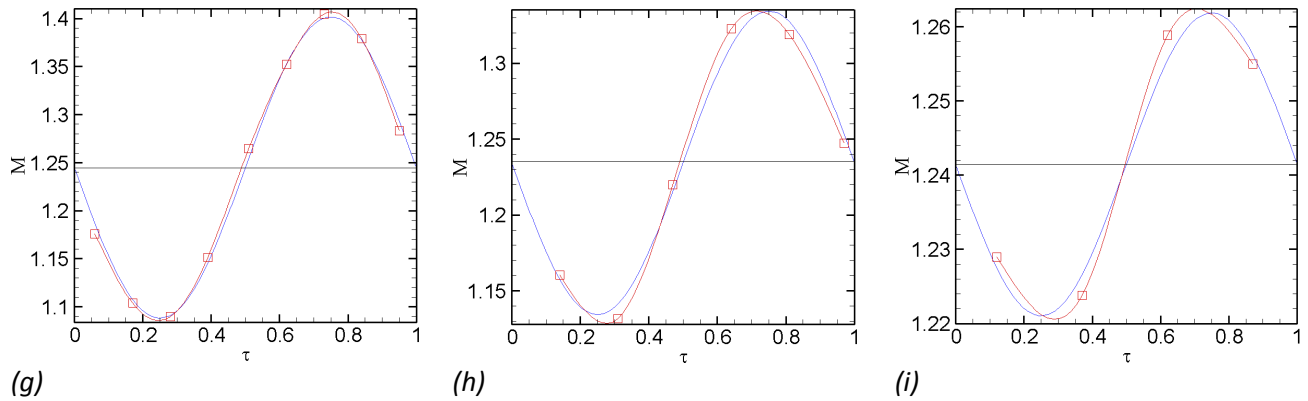


Figure (4. 17): Phased-averaged blowing ratio,  $M$ , of temporal data extracted from  $y/d=0.15$ , giving the averaged blowing ratios of  $\overline{M} = 0.65, 1$  and  $1.25$ .

## 4.5 Energy spectra

The energy spectra of the fluctuating velocity components in streamwise and wall-normal direction are determined in the wake region of the flow, by using the results of TR-PIV. Figure (4.18a-4.18c) corresponds to the range of blowing ratios ( $\overline{M} = 0.65, 1$  and  $1.25$ ) examined with steady blowing. The temporal evolution for each velocity component were obtained from a downstream location of  $x/d=6.4$  and  $y/d=0.23$ . The curve shown in the figures below, indicate a nearly constant Strouhal number peak in the region of jet wake around  $St_\infty = 0.15$ , where the definition of Strouhal number  $St_\infty = f * d / \overline{U}_\infty$  is based on the peak frequency 'f', freestream velocity ' $\overline{U}_\infty$ ', injection tube diameter 'd'. At blowing ratios of  $\overline{M} = 1$  and  $1.25$ , another peak around  $St_\infty = 0.04$  was observed. The practical relevance of this peak to the flow field attributes is unclear. These figures also include the axis of the injection Strouhal numbers to show the location of peak corresponding to that. It should be noticed that to study the effects of imposed pulsation, the input Strouhal number was defined with the mean velocity of the jet and not with mainstream velocity, as in many studies on crossflow interaction. Firstly, this is for a reason that we were intending to keep the mainstream flow nearly constant in order to maintain the boundary layer thickness at the hole exit in all cases and change the jet velocity to study different case of blowing ratio. Secondly, because the mean flow becomes slightly non-uniform laterally at lower velocities, as was shown for 5 m/s earlier on. This halts the analysis of low Strouhal number cases while using mainstream velocities as variable. Therefore, the Strouhal number definition for the unsteady or periodic analysis was based on the jet velocity.

The study of the vortical structure in the wake of a transverse jet issuing in a crossflow was performed by Fric and Roshko (1994). For a range of Reynolds numbers and different distances from the leading edge of the crossflow wall to the centre of injection tube, they studied the Strouhal number of the vortical structures convecting past a fixed point in the jet wake. They concluded that within a range of small variability the periodic shedding of the wake vortices is about ( $St = f * d / \overline{U}_\infty = 0.13$ ) near a velocity ratio of 4, and

is about  $St=0.16$  near a velocity ratio of 2. Elsewhere, the level of variability of the  $St$  were relatively significant and fall within  $0.07 < St < 0.18$  for a velocity ratio ranging from 2 to 10. Levi (1983) reported the law of Strouhal number for the periodic phenomena taking place in different flows; including wakes behind cylinders, flapping turbulent plane jets, flow over cavities and Von Karman vortex street etc. They suggested that the  $St$  is of the order of 0.159, despite of little and no resemblance among these flows.

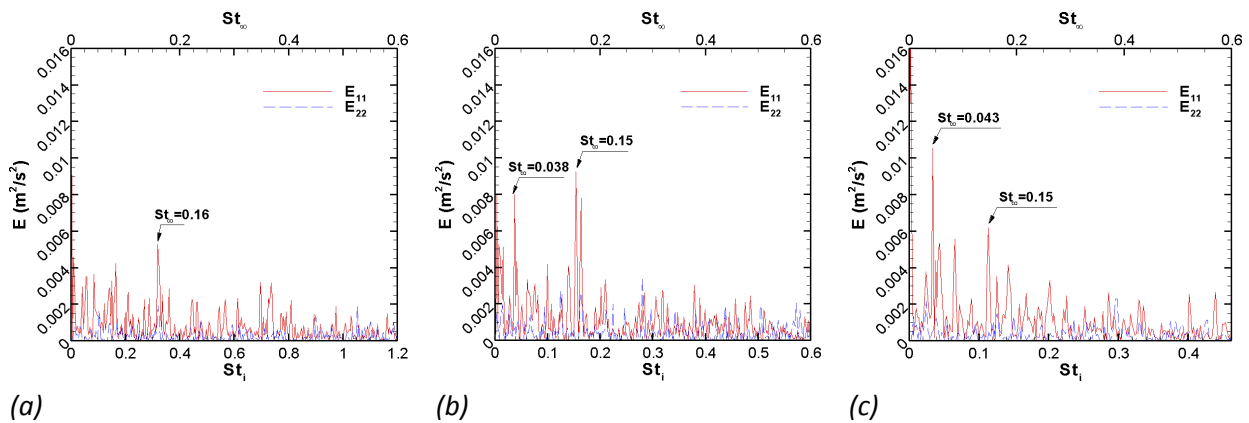


Figure (4. 18): Energy spectrum of  $u$  and  $v$  in different cases of steady blowing with, (a)  $\overline{M} = 0.65$ , (b)  $\overline{M} = 1$  and (c)  $\overline{M} = 1.25$ .

### 4.6 Comparisons of baseline results

Before passing on to the detailed analysis of the flow field both with and without pulsation, few comparisons with the results accessible through open literature are shown to observe the degree of correspondence of some of the benchmark results obtained from the present study (measurements of TR-PIV). The comparison of hot wire results presented by Ligrani et al. (1996-b) with the present study for streamwise velocity  $\overline{U}/\overline{U}_\infty$  and the Reynolds shear stress  $-2\overline{uv}/\overline{U}_\infty^2$  are shown in Figure (4.19a) and (4.19b).

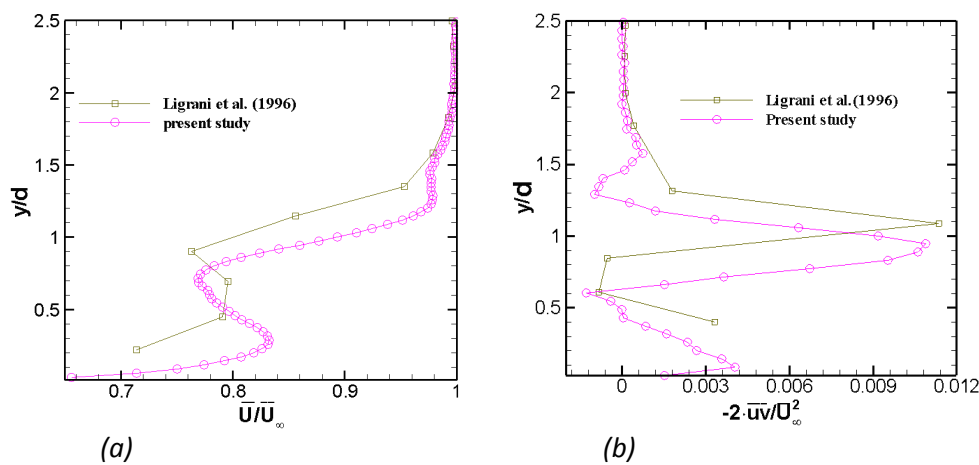


Figure (4. 19): Profile comparison for steady blowing at  $\overline{M} = 1$ ,  $x/d=5.5$ , (a) Streamwise velocity, (b) Reynolds shear stress.

The comparison is made for steady blowing with  $\overline{M} = 1$  and at a downstream location of  $x/d=5.5$ . The slight shift in these profiles is because of higher injection angle and injection Reynolds number ( $Re_i$ ),  $35^\circ$  and 15000, in the reference case and  $30^\circ$  and 8437 in the present study.

Figure (4.20a-4.20b) shows the comparison of streamwise mean velocity profile,  $\overline{U}/\overline{U}_\infty$ , for the steady blowing conditions of  $\overline{M} = 0.65$  and  $\overline{M} = 1$  with the experimental results of Dieumegard (2003). For the comparison shown in figure (4.20a), the injection Reynolds number ( $Re_i$ ) in the reference study is 13129 along with a blowing ratio of  $\overline{M} = 0.5$ , compared to  $Re_i = 5596$  and  $\overline{M} = 0.65$  of the present study. In figure (4.20b), the comparison of two different cases of injection Reynolds number ( $Re_i = 16788$  and  $26258$ ; referred as case 'A' and 'B' in the figure), reported in the reference study for a blowing condition of  $\overline{M} = 1$  is plotted with the presented case of  $\overline{M} = 1$  and  $Re_i = 8437$ . Higher injection Reynolds number in the reference case for  $\overline{M} = 1$  causes a slight increase in streamwise mean velocity profile compared to the profile obtained from the present case. The angle of injection of the jet fluid is identical for both studies, but a slightly thicker boundary layer flow in the reference case allows a deeper penetration of the jet in the mainstream flow compared to the present study.

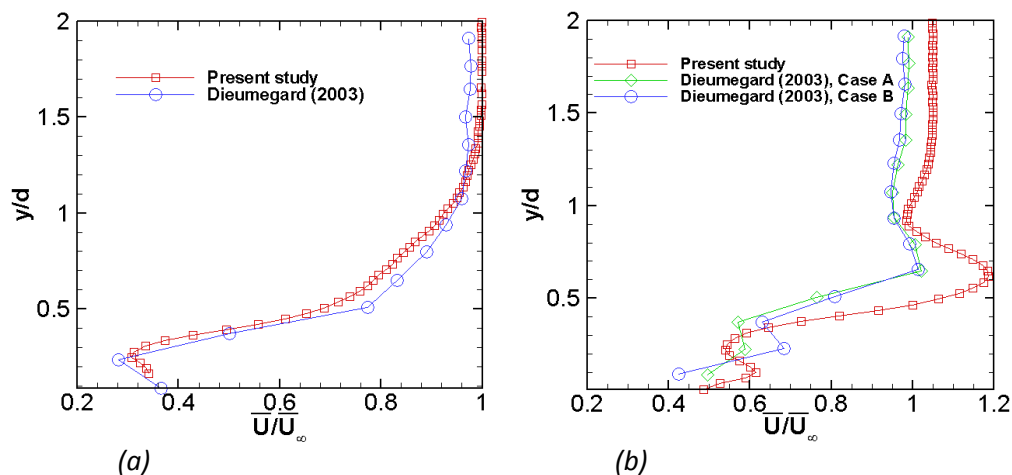


Figure (4. 20): Comparison of streamwise velocity in steady blowing, for a downstream location of  $x/d=2$ , (a)  $\overline{M} = 0.65$  (Present study) and  $\overline{M} = 0.5$  (Reference case), (b)  $\overline{M} = 1$ .

## 4.7 Conclusion

Measurements with Laser Doppler Anemometry were carried out to determine the wind tunnel characteristics in accordance with film cooling measurement. Some fundamental parameters include the evolution of boundary layer thickness, uniformity of incoming flow, the form of the velocity profiles, freestream turbulence etc. The measurements were performed for a freestream Reynolds numbers ( $Re = \overline{U}_\infty \cdot \delta / \nu$ ) of 4305, 6681 and 8609. The

review of different statistical and turbulent flow parameters shows that the flow field contains a substantially uniform flow through out its length and low turbulence level, (turbulence intensity;  $TI \approx 1.1 \pm 0.2\%$  outside the boundary layer).

Hot wire measurements were carried out at the Reynolds numbers of 5801 and 18436 for determining turbulent scales and energy spectra at some particular locations of the wind tunnel. The estimated energy spectra have manifested some important fluctuations in high frequency zone. Exact source of these fluctuations is not clear. One of a reason that could possibly explain these peaks is the generation of large-scale fluid structures somewhere from the tip region of the air blower, which creates periodically fluctuating velocities characterized by a nearly constant Strouhal number. However, this periodicity doesn't exist anymore in the boundary layer region where the turbulence is higher due to the wall shearing. The measurement of both velocity and temperature field at a maximum acquisition frequency being as high as 10 times of the maximum jet excitation frequency will remain unaffected by these frequency peaks.

The temperature regulatory system seems to function well within the defined working range. It is found that the system effectiveness for a process of temperature reduction is relatively higher than a process of temperature augmentation, as far as the temperature settling time is concerned.

The velocity profiles measured along the central plane and near the hole exit show an increase in jet velocity, which is larger than the velocity at respective blowing ratio. This is because of the diversion of jet fluid towards the downstream by the mainstream flow. The extra rate of strain and bending causes some acceleration of the jet fluid. In the absence of mainstream flow, the maximum in velocity profile appears on the upstream side, which is skewed to the downstream side in the presence of both flows. The profile skewness is relatively high for  $\overline{M} = 0.65$ . The profile is pushed slightly back upstream, as the blowing ratio is risen to 1.

An initial study of the pulsating jet was performed by means of hot wire anemometry. For the range of frequencies used for injectant pulsation, an amplitude giving approximately a constant ratio of streamwise rms velocity and average hole velocity was chosen for all cases. The extreme cases of pulsation carry significant variations in the amplitude of pulsation. A maximum deviation of 13% for the range of pulsating cases belonging to  $\overline{M} = 0.65$ , and a maximum deviation of 14.5% for the range of pulsating cases belonging to  $\overline{M} = 1$  and 1.25 were noticed. The filtering of the fluctuating component from the instantaneous measurements widens the level of these deviations.

The energy spectra determined from the wake region of the flow have shown a nearly constant Strouhal number of  $St_{\infty} = 0.15$ . The characteristic frequency related to the dynamics of wake structures is also similar to the one found in many studies. Therefore, we

can expect that the range of Strouhal number pulsation considered here will allow us to characterize the film cooling configuration in an appropriate manner.

The comparison of the baseline results shows that the test rig is properly calibrated, as the present results seems to approach to the previously reported results with reasonable deviations.



## 4.8 Reference

1. Alimpiev AI, Mamonov VN, Mironov BP, *“Energy spectra of velocity pulsation in a turbulent boundary layer on a penetrable plate”*; Plenum Publishing Corporation, 1975.
2. Burd SW, Kaszeta RW, Simon TW, *“Measurement in film cooling flows: Hole L/D and turbulence intensity Effects”*, Gas turbine Heat Transfer Session, 1996 IMECE Conference, Atlanta, GA.
3. Dieumegard D, *“Etude Experimentale Du Film Cooling Developpe Par Une Range De Cinq Perforations Et Modelisation Des Echanges Convectifs”*, Mémoire de Diplôme d’ingénieur , Université de Poitiers- ENSMA, 2003.
4. Eriksen VL, Goldstein RJ, *“Heat transfer and film cooling following injection through inclined circular tubes”*, Journal of heat transfer, May-1974, 239-245.
5. Fric TF, Roshko A, *“Vertical structure in the wake of a transverse jet”*, J. Fluid Mech. 279 (1994) 1-47.
6. Goldstein RJ, Eckert E.R.G., *“Effects of hole geometry and density on three-dimensional film cooling”*, Int. J. Heat Mass Transfer, 17 (1974) 595-607.
7. Levi E, *“A universal Strouhal law”*, ASCE Journal of the Engineering Mechanics Division 109 (3) 718-727.
8. Ligrani PM, Gong R, Cuthrell JM, *“Bulk flow pulsations and film cooling-II: Flow structure and film effectiveness”*, Int. J. Heat Mass Transfer, 39 (1996b) 2283-2292.
9. Kim J, Moin P, Moser R, *“Turbulence statistics in fully developed channel flow at low Reynolds number”*, J. Fluid Mech, 177 (1987) 133-166.
10. Marek CJ, Tacina RR, *“Effect of free-stream turbulence on film cooling”*, NASA Technical Note, NASA TN D-7958, 1975.
11. Pietrzyk JR, Bogard DG, Crawford ME, *“Hydrodynamic Measurement of jets in crossflow for gas turbine film cooling application”*, ASME J. Turbomach, 111 (1989) 139-145.
12. Pope SB, *“Turbulent Flows”*; Cambridge University Press, 2000.
13. Seo HJ, Lee JS, Ligrani PM, *“The effect of injection hole length on film cooling with bulk flow pulsation”*, Int. J. Heat Mass Transfer, 41(1998) 3515-3528.
14. Walters DK, Leylek JH, *“A Detailed analysis of film cooling physics: Part 1-Streamwise injection with cylindrical Holes”*, ASME J. Turbomach, 122 (2000) 102-111.

15. Yuen CHN, Martinez-Botas RF, *“Film cooling characteristics of a single round hole at various streamwise angles in a crossflow: Part I, Effectiveness”*, Int. J. Heat Mass Transfer, 46 (2003) 221-235.

## Table of Contents

---

5.1	Structure involved in the flow dynamics.....	133
5.2	Velocity field.....	137
5.2.1	Time-averaged velocity.....	137
5.2.2	Phase-averaged velocity results.....	141
5.3	Velocity probability density function (PDF).....	144
5.4	Turbulent description, tensor of Reynolds stresses.....	147
5.4.1	Time-averaged normal stresses.....	147
5.4.2	Time-averaged shear stresses.....	151
5.4.3	Phase-averaged shear stresses.....	153
5.4.4	Ratio of phase-averaged rms-velocity components.....	155
5.4.5	Phase-averaged turbulent intensity.....	157
5.5	Tensor of velocity gradient.....	158
5.5.1	Time-averaged vorticity.....	158
5.5.2	Phase-averaged vorticity.....	161
5.5.3	Time-averaged rate of deformation.....	162
5.6	Vortex identification.....	164
5.7	Mass, momentum and energy conservation.....	170
5.7.1	Balance of mass (Continuity equation).....	170
5.7.2	Balance of momentum.....	171
5.7.2.1	Terms of momentum equation, time-averaged results.....	172
5.7.2.2	Convection subterm, phase-averaged results.....	175
5.7.3	Balance of energy.....	176
5.7.3.1	Terms of Energy equation, time-averaged results.....	177
5.7.3.2	Time-averaged turbulent kinetic energy.....	181
5.7.3.3	Phase-averaged production of kinetic energy.....	183
5.7.3.4	Phase-averaged energy dissipation rate.....	184
5.7.3.5	Ratio of time-averaged Production and dissipation ( $P_k/\epsilon_k$ ).....	185
5.8	Conclusion.....	186
5.9	References.....	189

## Nomenclatures

<u>Abbreviations</u>		<u>Subscripts/superscripts</u>	
$\rho$	Fluid density (kg/m <sup>3</sup> )	$i$	Injectant
$P$	Pressure (Pa)	$\infty$	Free-stream
$d$	Hole diameter (mm)	$rms$	Root mean square
$L$	Hole length (mm)	$\bar{\quad}$	Time-averaged
$U$	Streamwise velocity (m/s)	$\sim$	Periodic component
$V$	Normal velocity (m/s)	$a$	Amplitude
$W$	Lateral velocity (m/s)	$h$	Nominal hole
$\bar{M}$	Blowing ratio ( $= \rho_i \bar{U}_i / \rho_\infty \bar{U}_\infty$ )	$j$	Index number
$u$	Streamwise velocity fluctuation (m/s)	$acq$	Acquisition
$v$	Normal velocity fluctuation (m/s)	$s$	Excitation
$w$	Lateral velocity fluctuation (m/s)	$mom$	Momentum
$\delta$	Boundary layer thickness (mm)	$nor$	Normal
$\delta^*$	Displacement thickness (mm)	$sh$	Shear
$Re_\infty$	Reynolds number ( $= \bar{U}_\infty \cdot \delta / \nu$ )	$k$	kinetic energy
$Re_i$	Reynolds number ( $= \bar{U}_i \cdot d / \nu$ )	$x$	$mom, k$
$St$	Strouhal number ( $= f \cdot d / \bar{U}_i$ )		
$\omega$	Vorticity (m/s)		
$\sigma_s$	Rate of deformation (m/s)		
$TI$	Turbulent intensity (%)		
$\sqrt{u^2}$	x-component of RMS velocity (m/s)		
$\sqrt{v^2}$	y-component of RMS velocity (m/s)		
$\overline{uv}$	Reynolds shear stress (m/s) <sup>2</sup>		
$\overline{q^2}$	turbulent kinetic energy (m <sup>2</sup> /s <sup>2</sup> )		
$C_x$	Convection term (m/s <sup>2</sup> )		
$T_x$	Turbulent transport (m/s <sup>2</sup> )		
$D_x$	Diffusion term (m/s <sup>2</sup> )		
$\pi_x$	Pressure gradient (m/s <sup>2</sup> )		
$P_k$	Production of energy (m <sup>2</sup> /s <sup>3</sup> )		
$\mathcal{E}_k$	Energy dissipation rate (m <sup>2</sup> /s <sup>3</sup> )		
$t$	Time (s)		
$T$	Time period (s)		
$\tau$	Fraction of time period ( $= t/T$ )		
$f$	Frequency (Cycles/s)		
$\theta$	Phase (radian)		
$\phi$	Phase shift (radian)		
$\psi$	Angular frequency (radians/s)		
$x, y$	Streamwise and normal coordinates (mm)		

## **STUDY OF THE FILM-COOLED BOUNDARY LAYER FLOW**

### **AERODYNAMICS**

The investigation of the aerodynamic behavior of the flow in the film cooled boundary layer, altering periodically under the influence of injectant pulsation, is studied by using Time Resolved Particle Image Velocimetry 'TR-PIV'. A reasonably high temporal and spatial resolution of TR-PIV allows resolving all significant features of the flow field. The blowing ratios ( $\overline{M}$ ) studied are 0.65, 1 and 1.25. The effect of pulsation is studied at the non-dimensional frequency ( $St$ ) of 0, 0.2, 0.3 and 0.5.

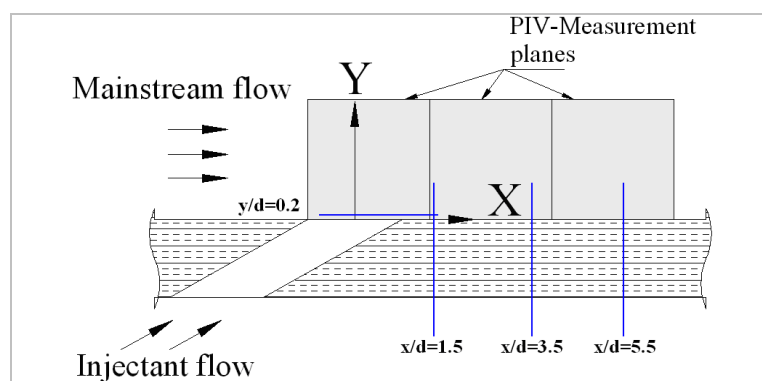


Figure (5. 1): Profile locations chosen for the presentation of results in the zone of TR-PIV measurement.

The time- and phase-averaged results are presented by the two dimensional flow fields and the profiles of concerned parameters. In order to compare different cases of pulsation, the profiles are extracted from the downstream locations of  $x/d=1.5$ , 3.5 and 5.5, and wall-normal location of  $y/d=0.2$ , as mentioned in the figure (5.1).

### **5.1 Structure involved in the flow dynamics**

The instantaneous images of the flow field shown in figure (5.2a-c) are obtained by sticking together the images of separate planes, standing for the blowing ratios of  $\overline{M}=0.65$ , 1 and 1.25 in steady blowing (flow direction is from left to right). In the following figures, the absence of tracer particle in the injectant flow allows us to visualize some basic attributes of the injectant jet issuing in the mainstream flow. It is evident that the jet flow in case of  $\overline{M}=0.65$  stays close to the wall, while for  $\overline{M}=1$  and 1.25, it moves slightly away due to the increase of jet momentum. It can also be observed that the growing of the coherent vortices is more organized for  $\overline{M}=1$  than the rest of the cases. On the bottom side of the jet, the interaction of the wake structures with the lower boundary of the jet and the entrainment of mainstream flow make the formation of vortices somewhat different from the one expected

for the case of a free jet issuing from the injection hole at a similar flow rate. The wake effects are appeared to be dominant in case of  $\overline{M} = 1.25$ .

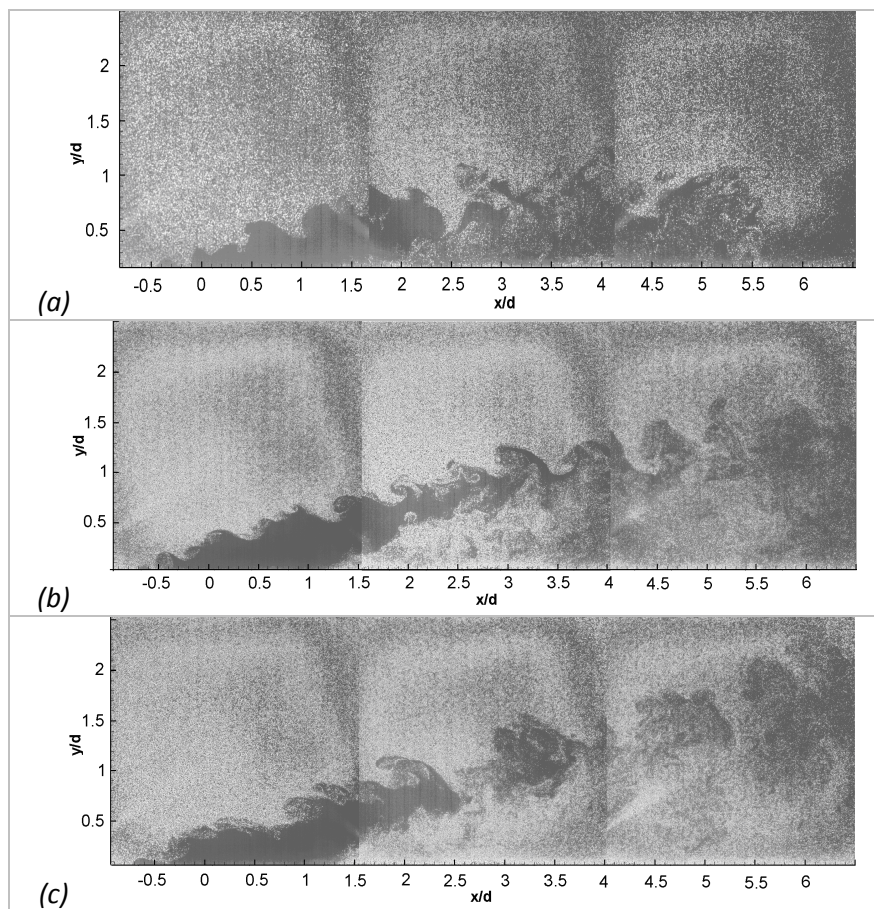


Figure (5. 2): Instantaneous images of the flow filed, (a)  $\overline{M} = 0.65$ , (b)  $\overline{M} = 1$  and (c)  $\overline{M} = 1.25$ .

To visualize some general characteristics of the near-field interaction of the two flows, the vector field obtained from cross-correlation algorithm is plotted in figure (5.3) for a flow configuration of  $\overline{M} = 1.25$  and  $St=0$ , where the jet effects prevail larger than the other cases of steady blowing.

Some important features of the “jet-in-crossflow” can surely be identified here, such as; the contribution of the boundary layer vorticity of the oncoming flow rolling up at the shear layer along with the tube vortices to form the large counter rotating vortex pair (CVP), which greatly influences the wall coverage of the injectant fluid. Experimental studies performed by Foucault et al. (1992) and Dorignac et al. (1992) featured the existence of CVP in a crossflow configuration using an oblique jet. The attributes of the flow field resulting due to the immediate interaction of two flows control the dynamics of the CVP. Walters and Leylek (2000) have mentioned a strong dependence of the near-field interaction on the ultimate distribution of the injectant flow in the downstream region.

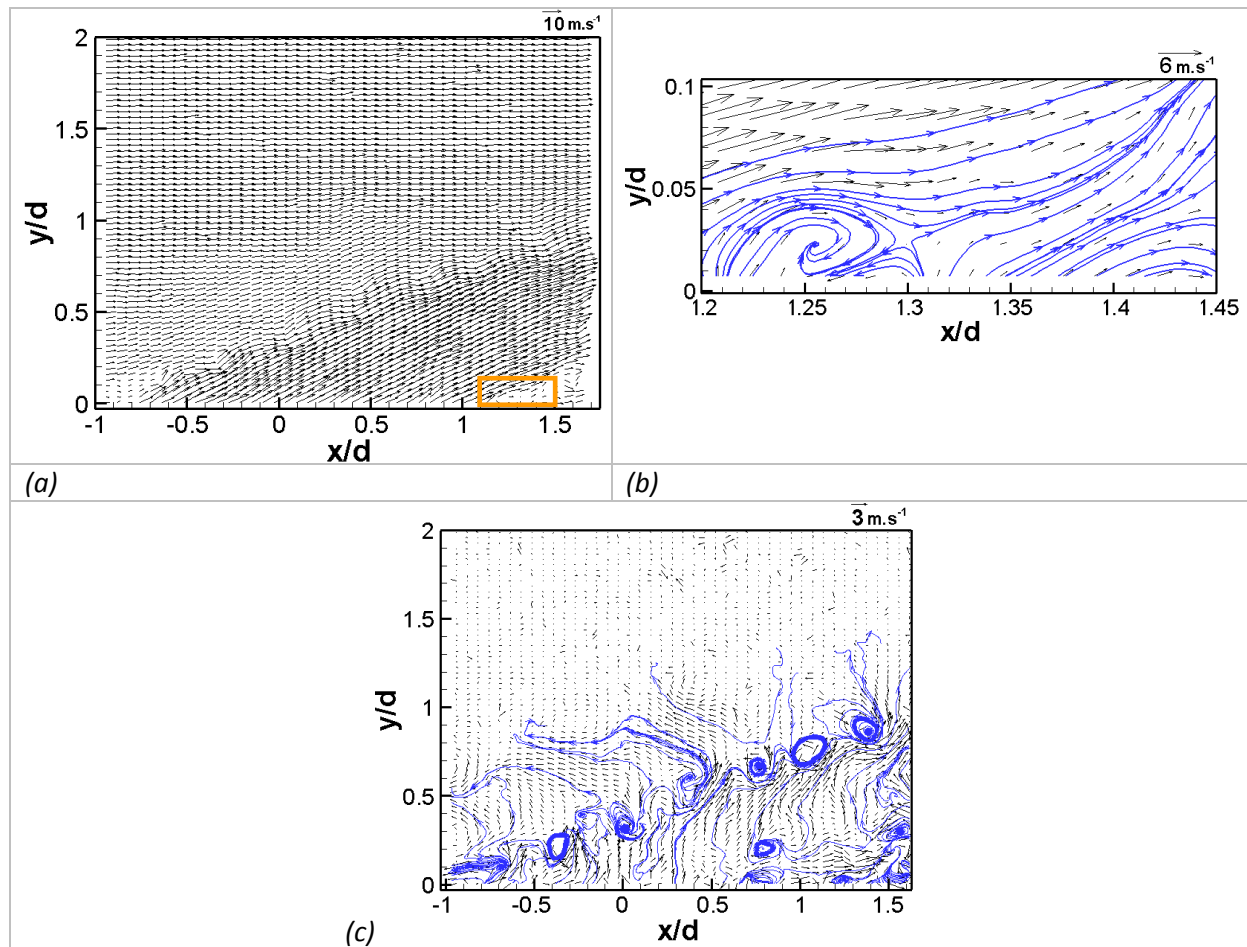


Figure (5. 3): (a) Vector field of instantaneous velocity, (b) Zoom-in region of vector field shown in (a), and (c) Vector field of fluctuating velocities,  $\overline{M} = 1.25$ ,  $St = 0$ .

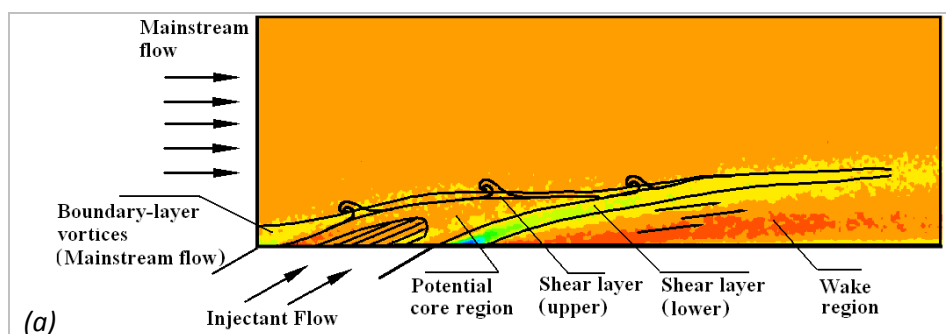
Figure (5.3b) shows the detailed view of the instantaneous velocity field obtained from the near downstream region of the trailing edge of the hole, which shows the initiation of a small wake region. The instantaneous image given here is randomly chosen from the database. The size of the wake region may vary due to the slight unsteady variations in the dynamics of the upstream flows. Walters and Leylek (2000) have reported the existence of small reverse flow region for an oblique jet issuing at  $35^\circ$ .

The fluctuating field shown in figure (5.3c) indicates the formation of vortices at the upstream edge of the jet due to the rolling-up of the shear layer very close to the exit of jet fluid. For a vertical jet issuing into a cross-stream flow, Kelso et al (1996) referred to the rolling of the shear layer as a consequence of the Kelvin-Helmholtz like instability, which consistently produces these vortices at the leading edge. The entrainment of the cross-stream flow towards the jet and to its wake region is evident from the streamlines of the fluctuating velocity components. Moussa et al. (1977) suggested that the two vortex systems generated at the upstream interface of the two flows and the other one bounded to the lee surface of the jet were responsible for most of the entrainment of crossflow into the

deformed jet and its wake. The lateral motion of the mainstream flow occurring in the wake region is expected to increase with the increase of blowing ratio.

A complete scenario for the flow field can be build in the light of a number of interpretations proposed in the open literature (Lee et al. 1994 ; Walters and Leylek 2000; Kelso et al 1996; Andreopoulos 1984), as well as the prior understanding of the flow behavior implied from the present study. The vertical structure ejecting from the tube comprises of the vorticity generating in the boundary layer of the injection tube. Interaction of these vortices with the vorticity generating in the boundary layer of mainstream flow takes place in the area of jet boundary. With the interaction, a strong shear layer is form in the region of the interface of two flows. The unstable shear layer in this region rolls-up due to the Kelvin-Helmholtz like instability and contributes to the formation of CVP (Counter-Rotating Vortex Pair). Near the trailing edge, the vorticity generated along the circumference of the injection tube tilts and stretches slightly due to the acceleration of the jet flow close to the trailing edge of the hole. In this region, the piling up of these vortices results in a bound vortex, which interacts with the mainstream flow entraining into a relatively low pressure region lying underneath the jet. The mainstream flow entrained below the jet moves towards the central plan of the jet and deforms the bound vortex to the kidney shape vortex system. This kidney shape vortex determines the major attributes of jet-in-crossflow and also influences the ultimate distributions of the jet fluid in the wall region. Flow configurations allowing higher lateral/secondary motions underneath the jet actually result in the lowering of wall coverage.

Figure (5.4a-c) shows the schematic diagram of the flow field for different cases of blowing ratios. Various zones highlighted in the diagram will be referred frequently in the forthcoming discussion in order to describe the flow field behavior for various cases. The most significant regions include the upper and lower shear layer, wake region and the potential core of the jet. The colors codes belonging to the mean vorticity filed are shown to highlight the different zones of the flow field and only give a qualitative description.



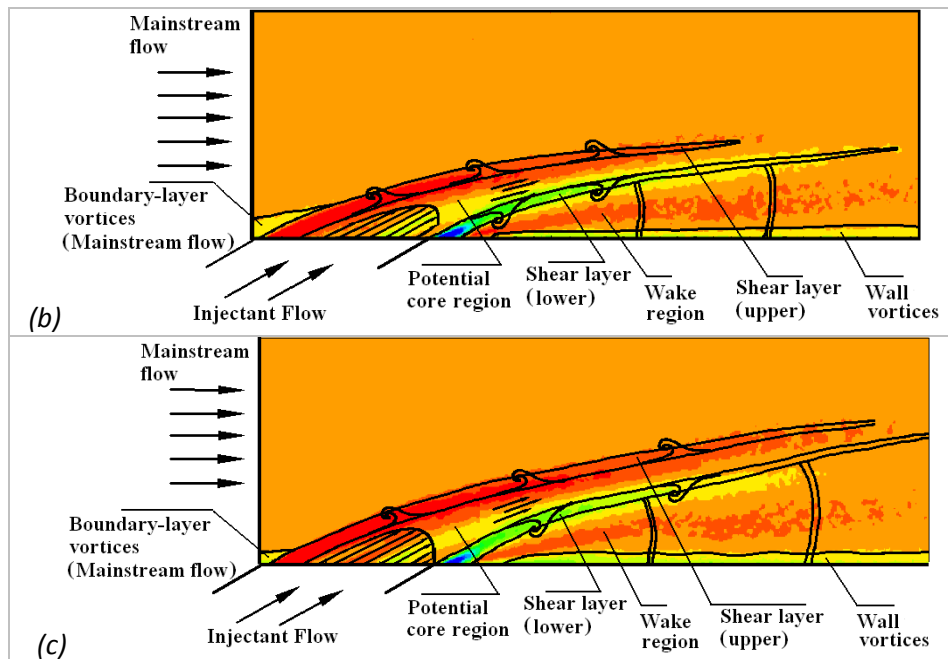


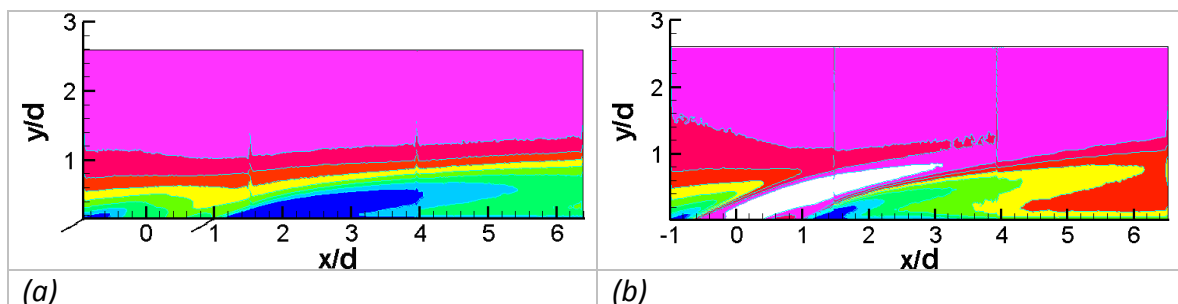
Figure (5. 4): (a) Schematic diagram representing the various region of the flow field in steady blowing, (a)  $\overline{M} = 0.65$ ,  $\overline{M} = 1$  and  $\overline{M} = 1.25$ .

## 5.2 Velocity field

### 5.2.1 Time-averaged velocity

Figures (5.5a-c) show the variation in mean streamwise velocity fields at different blowing ratios in a steady/continuous blowing condition. The distribution of injectant in the near wall region is more important in the case of  $\overline{M} = 0.65$  as the injectant penetrates less into the freestream than for  $\overline{M} = 1$  and 1.25. The phenomenon of higher jet penetration due to large momentum ratio was referred to “Jetting” in many studies (Burd et al. 1996; Walters and Leylek 2000).

The flow between the bottom side of the jet and the wall is linked with a number of complex activities, including the presence of a low pressure region as a result of the initial blockage offered by the flow of the leading surface of the jet and the subsequent ingestion of mainstream flow interacting with the wake and wall vortices. The mean flow field provided here can be considered as benchmark results to compare against the ones with pulsation.



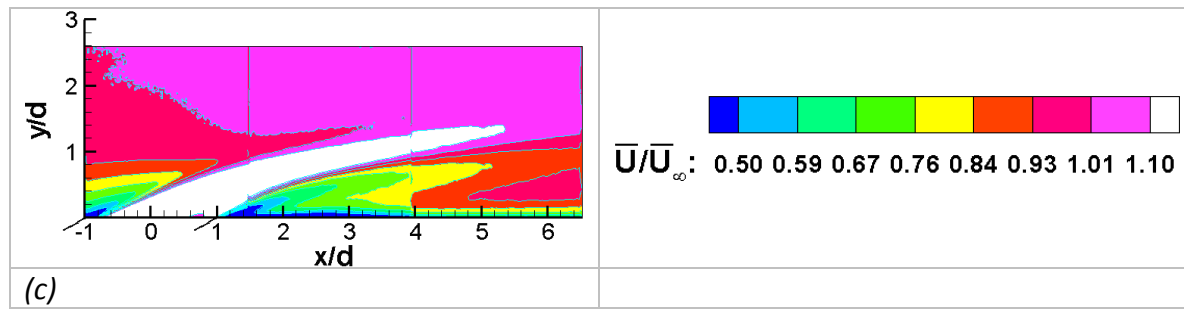
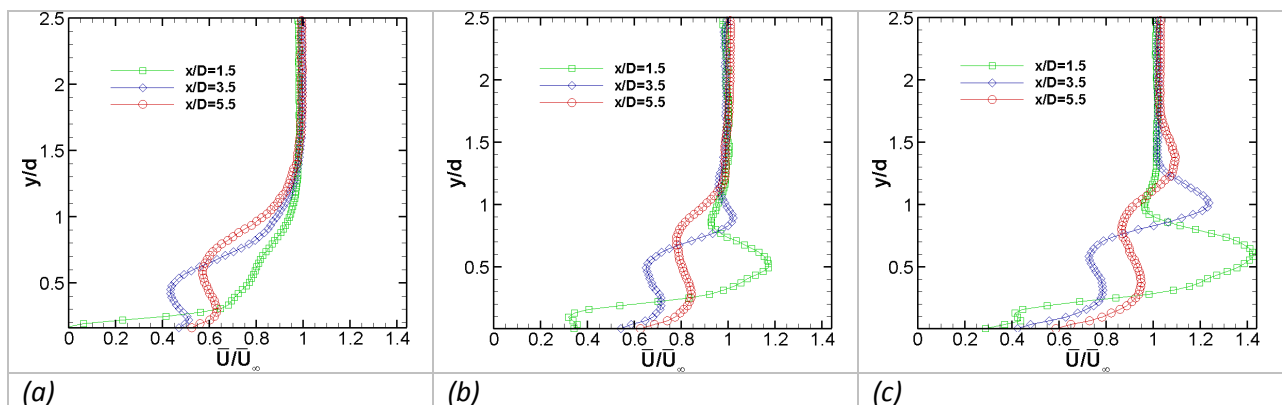


Figure (5. 5): Velocity field  $\overline{U}/\overline{U}_\infty$  without pulsation, (a)  $\overline{M} = 0.65$ , (b)  $\overline{M} = 1$ , (c)  $\overline{M} = 1.25$ .

The flow characteristics as a function of average blowing ratio  $\overline{M}$  under steady blowing ( $St=0$ ) are shown by the profiles of time-averaged streamwise and wall-normal components of velocity at different streamwise positions of  $x/d=1.5$ , 3.5 and 5.5 in figure (5.6a-f).

For  $\overline{M} = 0.65$ , figure (5.6a) shows that the injectant flow at  $x/d=1.5$  remains completely attached to the wall and the velocity profile show no obvious sign of shearing between two flows (i.e. appears similar to one of a turbulent boundary layer). At the downstream positions, the jet lifts off slightly from the wall and the shear layer due to the interaction of the high speed free-stream and relatively low speed injectant flow becomes evident.

For the case with  $\overline{M} = 1$ , figure (5.6b) shows higher penetration of the jet in the mainstream flow. The near downstream profile shows an increment of injectant flow velocity slightly above the wall in the potential core region of the jet. More downstream, the jet trajectory follows a continuous lift-off with  $x/d$ . At  $x/d=3.5$ , the first peak near the wall appears due to the entrainment of the mainstream flow, and the second peak lying at the upper wall-normal distance appears due to the presence of potential core region of the jet. At  $x/d=5.5$ , the upper peak of velocity seems to vanish completely.



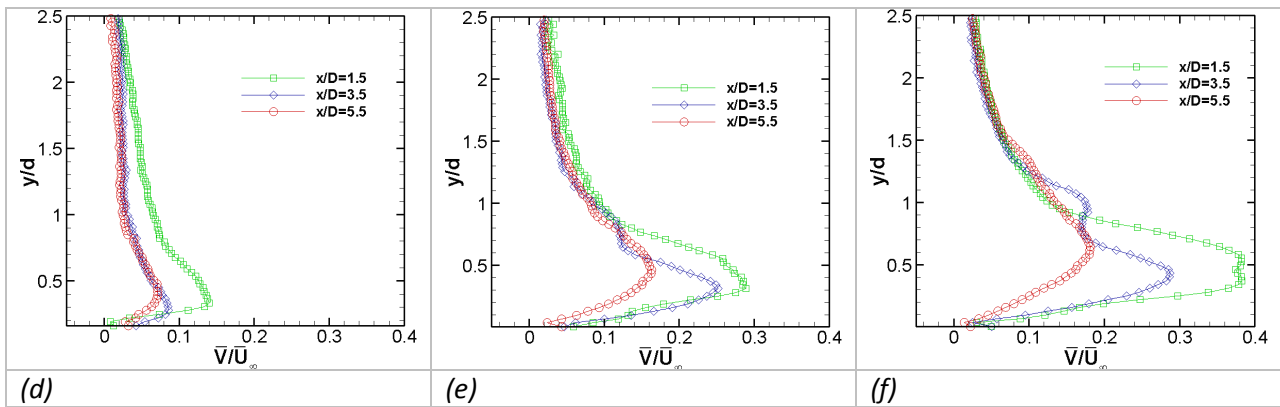


Figure (5. 6): Velocity profiles obtained from steady blowing cases ( $St=0$ ), lying at  $x/d=1.5, 3.5$  and  $5.5$ , (a)  $\bar{M} = 0.65$ ,  $\bar{U}/\bar{U}_\infty$ , (b)  $\bar{M} = 1$ ,  $\bar{U}/\bar{U}_\infty$ , (c)  $\bar{M} = 1.25$ ,  $\bar{U}/\bar{U}_\infty$ , (d)  $\bar{M} = 0.65$ ,  $\bar{V}/\bar{U}_\infty$ , (e)  $\bar{M} = 1$ ,  $\bar{V}/\bar{U}_\infty$ , (f)  $\bar{M} = 1.25$ ,  $\bar{V}/\bar{U}_\infty$ .

For  $\bar{M} = 1.25$ , the eminent lifting-off of the jet body is quite obvious due to the higher vertical momentum of the jet, as shown in figure (5.6c). The higher penetration of jet causes greater ingestion of mainstream flow into the low pressure field.

Figure (5.6d-f) shows the profile of time-averaged wall-normal component of the velocity for the cases of  $\bar{M} = 0.65, 1$  and  $1.25$  respectively. In all cases, the velocity profile obtained from the near downstream region ( $x/d=1.5$ ) has a higher velocity than the other downstream profiles. For most of the cases, the trend of variation exhibits only one peak in positive direction for these profiles, which shows that the changes in the vertical component of the velocity with respect to the vertical coordinate is comparatively lower than for the horizontal component of the velocity.

For the cases of  $\bar{M} = 1$  and  $1.25$ , the profiles at  $x/d=3.5$  show a second peak, which seems to correspond well with the upper peak of streamwise velocity component. However, the larger peaks lying near the wake region have slight difference in their respective heights. Lee et al. (1994) has mentioned that the flow field in the vertical direction is also influenced by the secondary motion of the mainstream flow induced in the wake region. They have shown that for  $\bar{M} = 2$  and  $\rho_i/\rho_\infty = 1$ , the inward flow towards the jet symmetry plane, developing below the jet, reaches a maximum velocity level of about half of the freestream velocity at  $x/d=2$  and decreases while moving downstream. Therefore, one might consider the lateral movement of the mainstream flow a possible reason for such differences. Furthermore, the maximum of these two peaks is completely opposite to the two peaks observed for the streamwise velocity.

Figure (5.7a-f) shows the comparison of time-averaged streamwise components of velocity for different Strouhal numbers in the cases of different blowing ratios ( $\bar{M} = 0.65, 1$  and  $1.25$ ), increasing column-wise in the array of subfigures. The results shown in figure (5.7a-c) and

figure (5.7d-f) are obtained from  $x/d=3.5$  and  $x/d=5.5$  of the central plane ( $z/d=0$ ). The comparison shown for  $\overline{M}=0.65$  in figure (5.7a) and figure (5.7d) indicates that the higher Strouhal number pulsation ( $St=0.5$ ) causes some significant disturbances in the steady flow pattern of the jet, compared to what is caused in lower pulsation cases. At  $x/d=3.5$ , the pulsation at  $St=0.5$  causes relaxation of about 19% in  $\overline{U}/\overline{U}_\infty$  with respect to the peak lying at the lower edge of the jet boundary under steady blowing at  $\overline{M}=0.65$ , while at  $x/d=5.5$ , it is about 13%. Similarly, for  $\overline{M}=1$  and  $\overline{M}=1.25$ , it is about 6% and 10% for  $St=0.2$  at  $x/d=3.5$ . This difference decreases gradually as the flow evolves in the downstream direction.

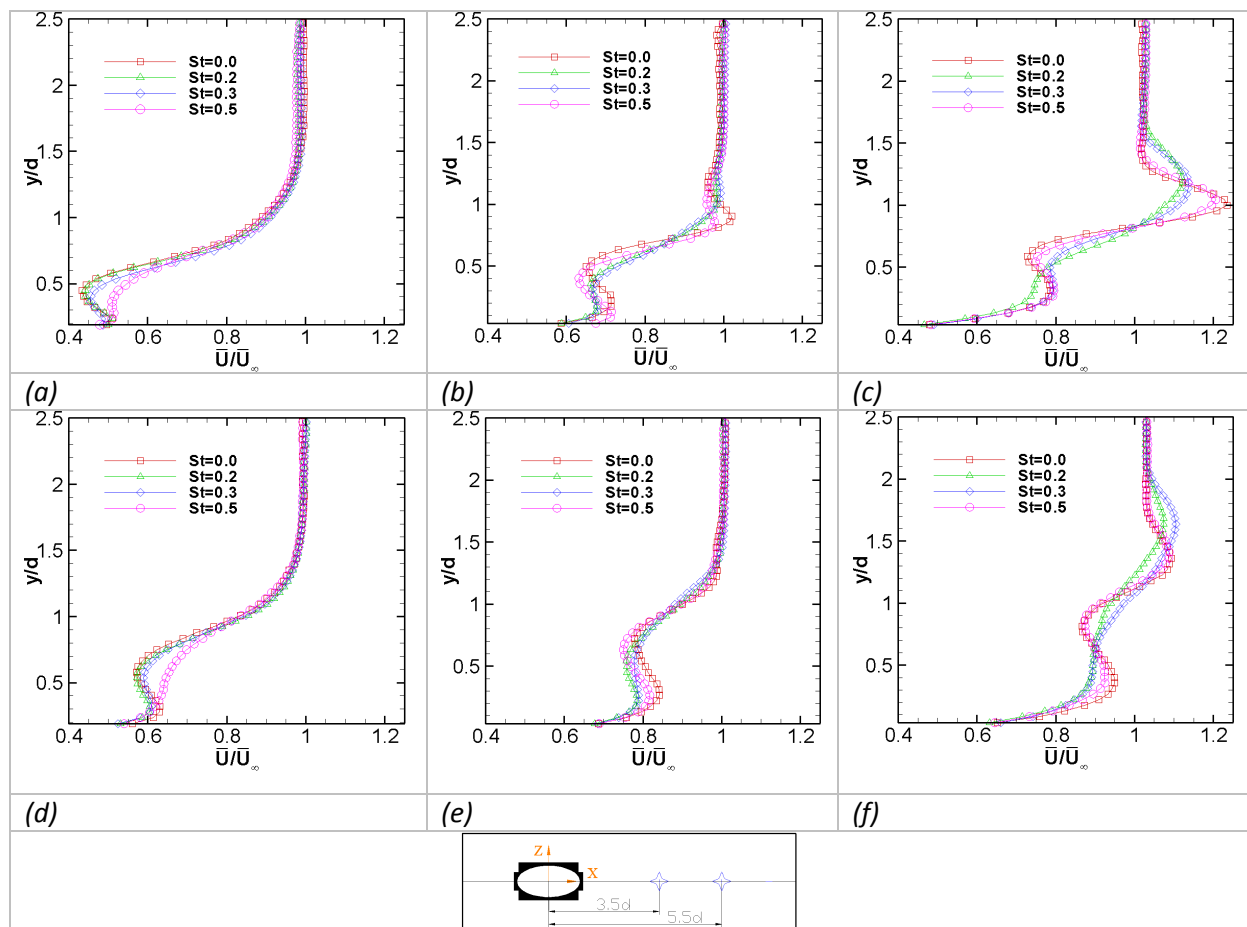


Figure (5. 7) : Comparison of time-averaged profiles of  $\overline{U}/\overline{U}_\infty$ , lying at  $x/d=3.5$  and  $5.5$  of the hole central plane ( $z/d=0$ ), for different  $St$  (0, 0.2, 0.3 and 0.5) examined under a range of  $\overline{M}$  (0.65, 1 and 1.25), while  $\overline{M}$  increasing column-wise and  $x/d$  increasing row-wise.

In steady blowing at  $\overline{M}=0.65$ , the injectant stays quite close to the wall and forms a fairly strong shear layer due to the interaction of the jet and the crossflow at the location of the lower jet boundary. The periodic variation of injectant flow rate at higher Strouhal number pulsation causes the instantaneous variation in the jet trajectory evolving along the downstream flow. Such variation reduces the time-averaged velocity gradient in the shearing region of the flow field for  $\overline{M}=0.65$ . For the cases of  $\overline{M}=1$  and  $1.25$ , the jet tends

to lift-off from the wall and a relatively stronger bound vortex forms, allowing a larger secondary motion of the mainstream flow underneath the jet. The time-averaged flow with  $St=0.2$  and  $0.3$  is expected to reduce the strength of shear layer and the bound vortex system, which bears a strong possibility of improving the flow of injectant fluid close to the wall, compared to the steady flow condition.

It can also be observed that the reduced peak and increased level of variations in the wall-normal direction also expected to increase the lateral distribution of the injectant fluid, as the CVP grows somewhat uniformly all over the circumference, and is also asymmetric across the central plan ( $z/d=0$ ).

### 5.2.2 Phase-averaged velocity results

The application of injectant flow pulsation in a film cooled turbulent boundary layer seems to bear some important consequences, compared to the normal behavior with continuous blowing. Figure (5.8a-d) shows a general mechanism of flow modification through the distribution of phase-averaged streamwise velocity  $\overline{U}/\overline{U}_\infty$  for  $\overline{M}=1$  and  $St=0.2$  over different times of a pulsating cycle. It is evident from the first image at time  $t/T=0.19$  that the jet flow tends to lift significantly from the wall due to the initial acceleration and bears a flow field underneath of relatively low speed. This region referring to as the wake region seems to be accompanied with shedding of wake structures at imposed frequencies, which is cited more clearly in the later time instant. From the computational analysis of steady flows, Walters and Leylek (2000) hypothesized that the fluid in the wake belongs to the jet flow. In that case, the periodically passing wake structures can also improve the time-averaged injectant distribution at the wall.

From figure (5.8b), it can be observed that the periodic pulsation at  $t/T=0.41$  causes a splitting of the jet body at a streamwise distance of  $x/d=3.85$  (zone labeled as 'A' in figure (5.8b)), which is followed by widening of the wake region under jet inertia (zone labeled as 'B' in figure (5.8b)). At this instant, the main stream flow also appears to be ingested a bit inside the hole. At  $t/T=0.63$ , the injectant flow re-originates from the hole but remains covered by the mainstream flow. The near wall flow in the downstream region exhibits the shedding of vortices in wake region. The downstream movement of these structures is coupled with a subsequent growth and velocity changes. At  $t/T=0.86$ , the acceleration of injectant flow approaches toward a point of maximum blowing with the consistent development of the flow in the wake region. The injectant flow trajectory under these effects moves towards and away from the wall under pulsating effects, which promises to improve the relative concentration of injectant compared to that of steady blowing.

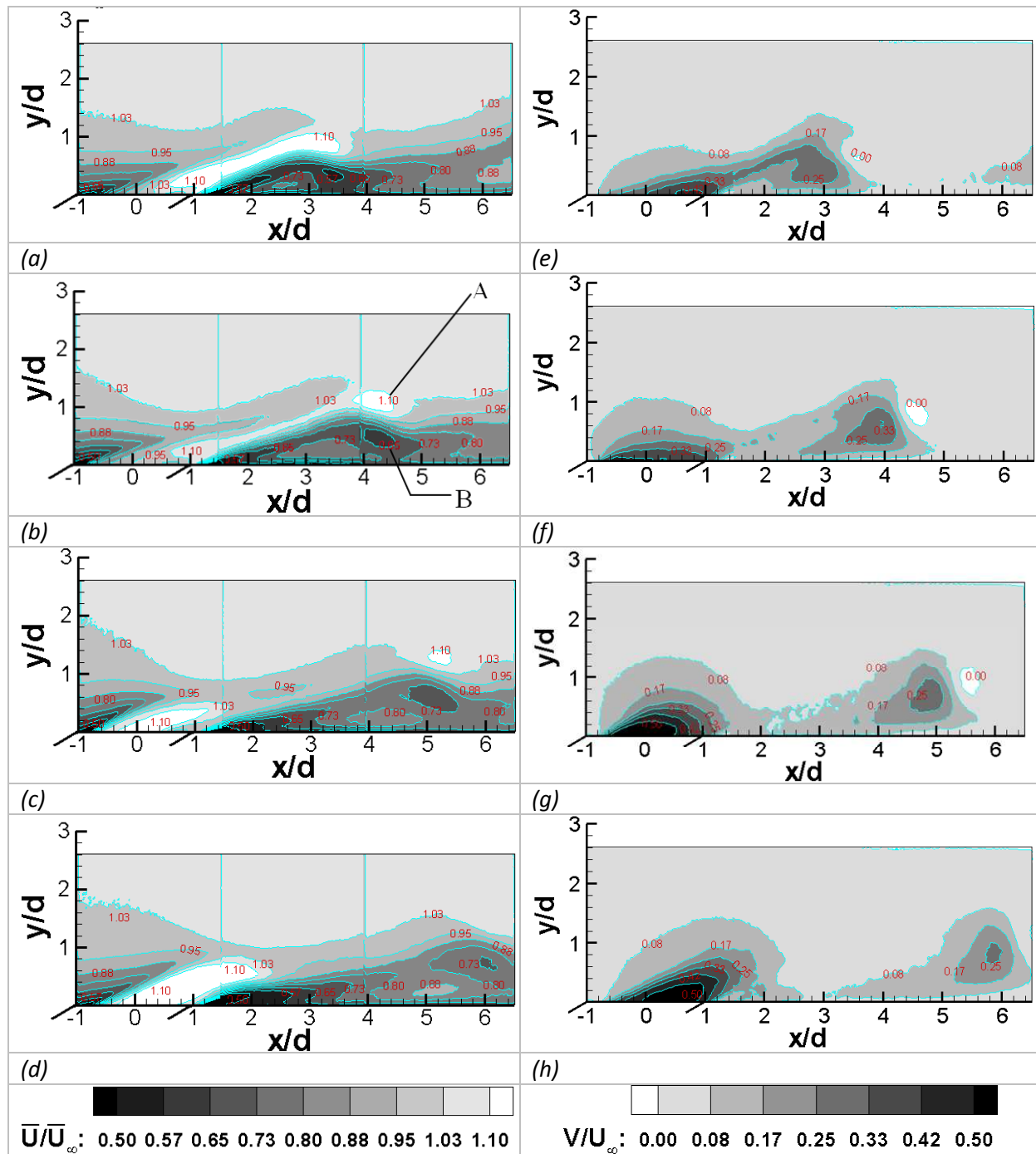


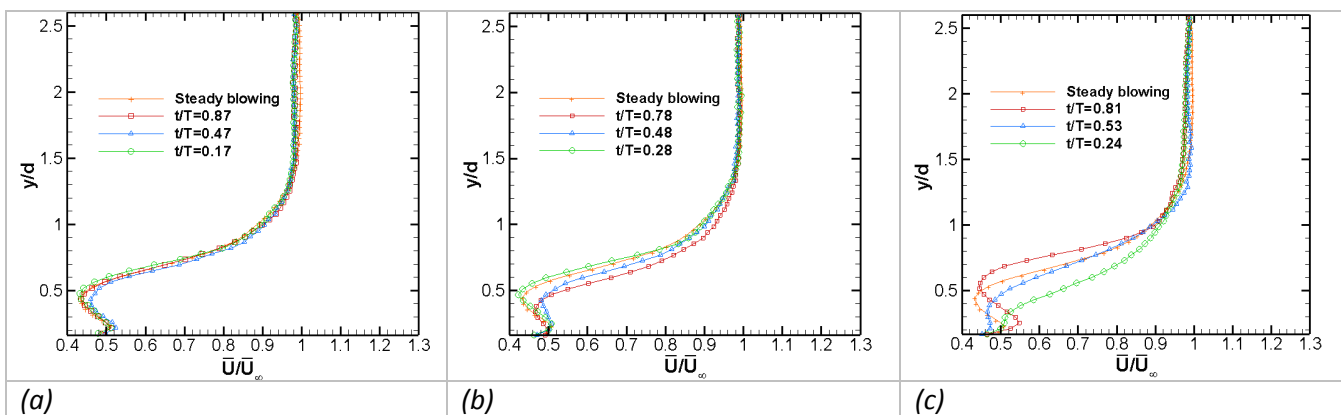
Figure (5. 8): Distribution of the components of phase-averaged velocity at  $\bar{M} = 1$  and  $St = 0.2$ ;  $\bar{U}/\bar{U}_\infty$ , (a)  $t/T = 0.19$ , (b)  $t/T = 0.41$ , (c)  $t/T = 0.63$  and (d)  $t/T = 0.86$ ;  $\bar{V}/\bar{U}_\infty$ , (e)  $t/T = 0.19$ , (f)  $t/T = 0.41$ , (g)  $t/T = 0.63$  and (h)  $t/T = 0.86$ .

Figure (5.8e-h) shows the distribution of phase-averaged wall-normal velocity component  $\bar{V}/\bar{U}_\infty$  for  $\bar{M} = 1$  and  $St = 0.2$  over different times of a pulsating cycle. The evolution in time shows the growing of the vertical component of the velocity from the hole exit, and the event of collapsing on the reversing of jet flow rate.

The flow field variations due to the imposed injectant flow pulsation for the whole range of experimental conditions are shown through the profiles of streamwise component of velocity locating at  $x/d=3.5$ , figure (5.9a-i). The times shown in figures were determined from the phase orientation observed 2 mm above the hole exit. The phase orientation of the number of point locked in a period changes with the spatial location. However, the pattern of temporal variation of the flow remains periodic all over. It is also reminded that the number of average time instants is not constant for all  $\overline{M}$  and  $St$  studied.

For  $\overline{M}=0.65$ , the profiles of  $\overline{U}/\overline{U}_\infty$  is shown in figure (5.9a-c) for  $St=0.2, 0.3$  and  $0.5$ , respectively, which shows that the pulsation causes periodic variations in jet trajectory and that the profile of phase averaged velocity seems to lie above and below the steady blowing case. The zone of crosswise variation extends considerably with the increase of  $St$  for  $\overline{M}=0.65$ . It should be noticed that some instants of jet flow belonging to the upper part of pulse cycle may cause the instantaneous uplifting of the jet which would lead to the increased entrainment of near wall flow or a poorer wall coverage against cross-stream flow compared to the steady blowing situation.

At  $\overline{M}=1$ , the jet lifted-off further from the wall, and significant variations in velocity profile across the steady flow situation are observed in figure (5.9d-e). At the higher excitation of  $St=0.5$ , the modifications imposed on the flow do not have sufficient time to acquire the overall effects produced in one pulsation cycle, meanwhile the next period starts. Therefore, modifications produced in a particular period could not diffuse around a great deal within a given time span and so the effects are not fully established, see figure (5.9f). The resulting flow field exhibits a rippling jet trajectory with short pulsating span and a trend of frequent splitting (the case of high frequency excitation will be described more comprehensively through vorticity field in a forthcoming section).



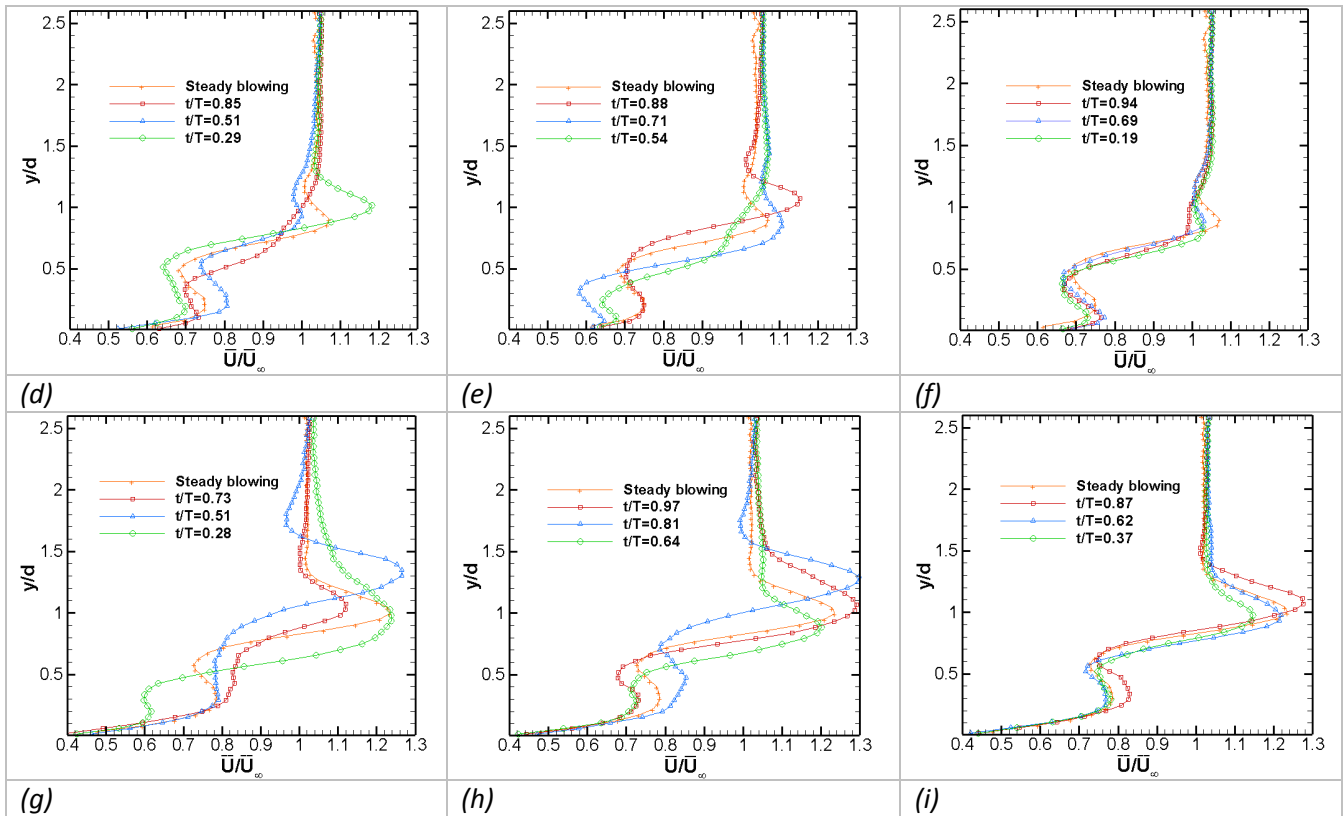


Figure (5. 9): Velocity profiles  $\bar{U}/\bar{U}_\infty$  with pulsation at  $x/d=3.5$ . (a)  $\bar{M}=0.65$ ,  $St=0.2$ , (b)  $\bar{M}=0.65$ ,  $St=0.3$ , (c)  $\bar{M}=0.65$ ,  $St=0.5$ , (d)  $\bar{M}=1$ ,  $St=0.2$ , (e)  $\bar{M}=1$ ,  $St=0.3$ , (f)  $\bar{M}=1$ ,  $St=0.5$ , (g)  $\bar{M}=1.25$ ,  $St=0.2$ , (h)  $\bar{M}=1.25$ ,  $St=0.3$ , (i)  $\bar{M}=1.25$ ,  $St=0.5$

At  $\bar{M}=1.25$ , as shown in figure (5.9g-i), the zone of variation across the highly uplifted steady flow profile is the one which is greater than all other cases for both  $St=0.2$  and  $0.3$ . Also, the significant jet acceleration on the downstream side with higher injectant flow rate appears to be more detrimental at the instant, which lies on the upper part of the pulsation period. However, the combination of activities such as higher lift-off and the collapsing of jet at low frequency pulsation exhibit some interesting consequences on the far-end.

### 5.3 Velocity probability density function (PDF)

The influence of pulsation on the distribution of fluctuating velocities is investigated by determining the Probability density function (PDF) in different cases of pulsation. Figure (5.10a-f) shows the PDF of both streamwise and wall-normal components of fluctuating velocities obtained from a location of  $x/d=3$  and  $y/d=0.2$ , where blowing ratios ( $\bar{M}=0.65$ , 1 and 1.25) increase column-wise in the array of subfigures, and the subfigures in rows represent the PDF of  $u$  and  $v$  respectively. At the given location, as well as at a downstream location of  $x/d=6$  and  $y/d=0.5$  (see Annex C), the observed distributions of  $u$  and  $v$  differ only slightly from the Gaussian distribution. For a Gaussian distribution the values of skewness

and flatness are 0 and 3. In the physical sense, a negative skewness signifies the occasional passage of large negative velocity fluctuations from the point of observation than the positive velocity fluctuations passing more frequently at relatively lower magnitudes, and vice-versa for a positive skewness. A higher value of flatness factor usually implies that more of the variability is due to a few extreme differences from the mean, rather than most of modest differences from the mean. A higher flatness factor suggests an intermittent behavior of the flow, which can be noticed from a sharp peak and a heavy tail in the PDF.

For  $\overline{M} = 0.65$ , the trends of the PDF show a slight positive skewness for  $u$  and a slight negative skewness for  $v$  with an order of magnitude of 0.53 and -0.45, as well as a maximum flatness of 4.2 and 4.4 for  $St = 0.3$ .

For  $\overline{M} = 1$ , the skewness is nearly zero for  $u$ , and it has small negative values for  $v$  with a maximum of -0.34 for  $St = 0.3$ . Moreover, the flatness factor seems to reduce a little bit for  $St = 0.2$  and  $0.3$  than the case of  $St = 0$  and  $St = 0.5$ . The values of flatness factor are nearly similar for the fluctuations of both  $u$  and  $v$  in the cases of  $St = 0.2$  and  $0.3$ , and are about 2.6 and 2.8. These lower values of the flatness factor mean more uniform and less extreme deviations from the mean. In such cases, the PDF features a lower and broader central peak and a shorter and thinner tail than the normal distribution.

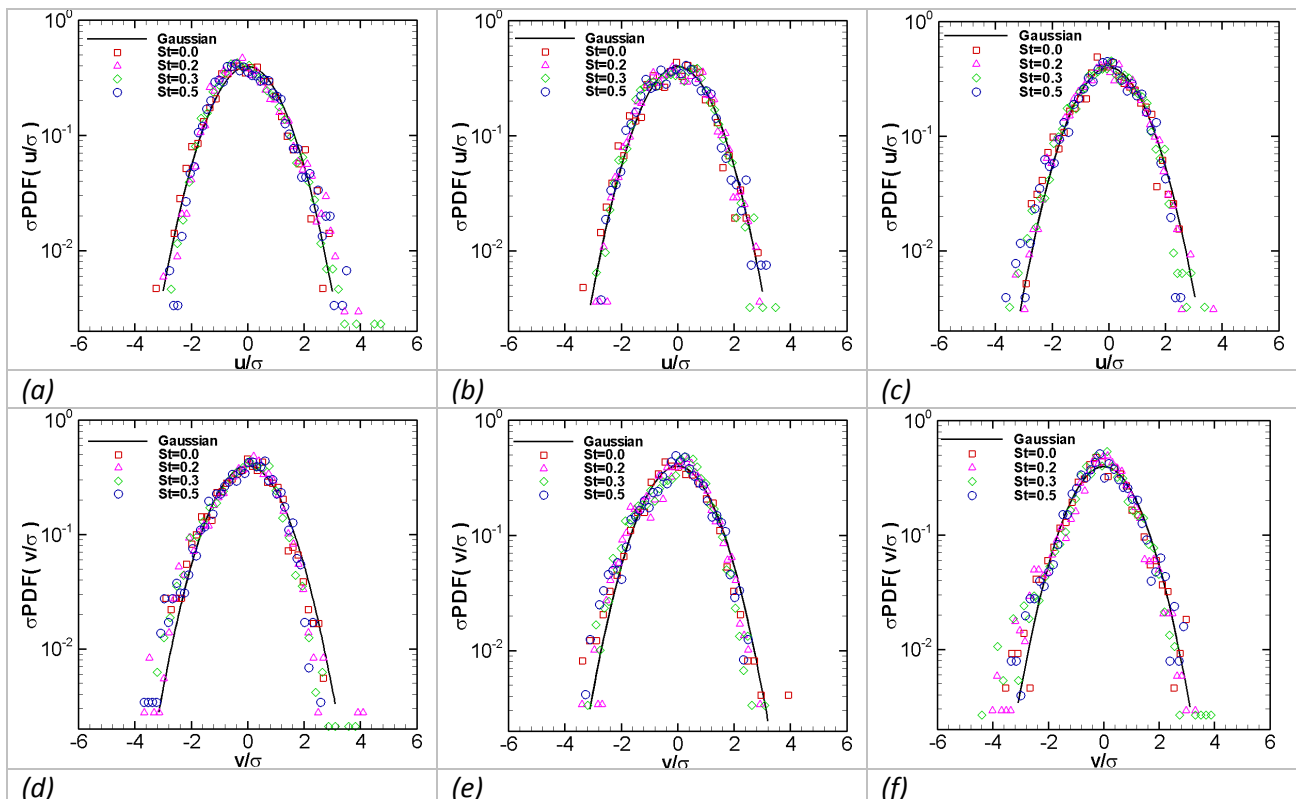


Figure (5. 10): Comparison of PDF for different  $St$  at  $x/d=3$  and  $y/d=0.2$ , in the array of subfigures blowing ratios ( $\overline{M} = 0.65, 1$  and  $1.25$ ) increases column-wise, and the PDF of  $u$  and  $v$  belongs to the first and second row.

At  $\overline{M} = 1.25$ , the PDF for both  $u$  and  $v$  shows slight negative skewness in all cases of  $St$ , with skewness for  $u$  to be nearly zero and  $-0.3$  for  $v$  at  $St=0.3$ . Also at  $St=0.3$ , the flatness factor is maximum at  $4.2$  for  $v$ . The pulsation at  $St=0.2$  and  $0.3$  seems to increase the flatness factor slightly compared to the cases of  $St=0$  and  $St=0.5$  for  $v$ .

Figure (5.11a-c) shows the PDF of both streamwise and wall-normal components of fluctuating velocities obtained from a location at  $x/d=3$ ,  $y/d=1.5$ , where blowing ratios ( $\overline{M} = 0.65, 1$  and  $1.25$ ) increase column-wise in the array of subfigures, and the subfigures in rows represent the PDF of  $u$  and  $v$  respectively. The coordinates of the point chosen for the PDF roughly lies near the zone of the upper jet boundary. At this location, the PDF seems to vary significantly from the Gaussian distribution. Near the jet boundary the flatness becomes higher in all cases, irrespective of the pulsation. At  $\overline{M} = 0.65$ , the PDF shows a negative skewness for  $u$  and a positive skewness for  $v$ . The maximum value of the flatness factor is about  $7.3$  at  $St=0.5$  for  $u$  and  $9.6$  for  $v$  at  $St=0.2$ . The values of the skewness factor in the corresponding cases are  $-0.6$  and  $1.03$ .

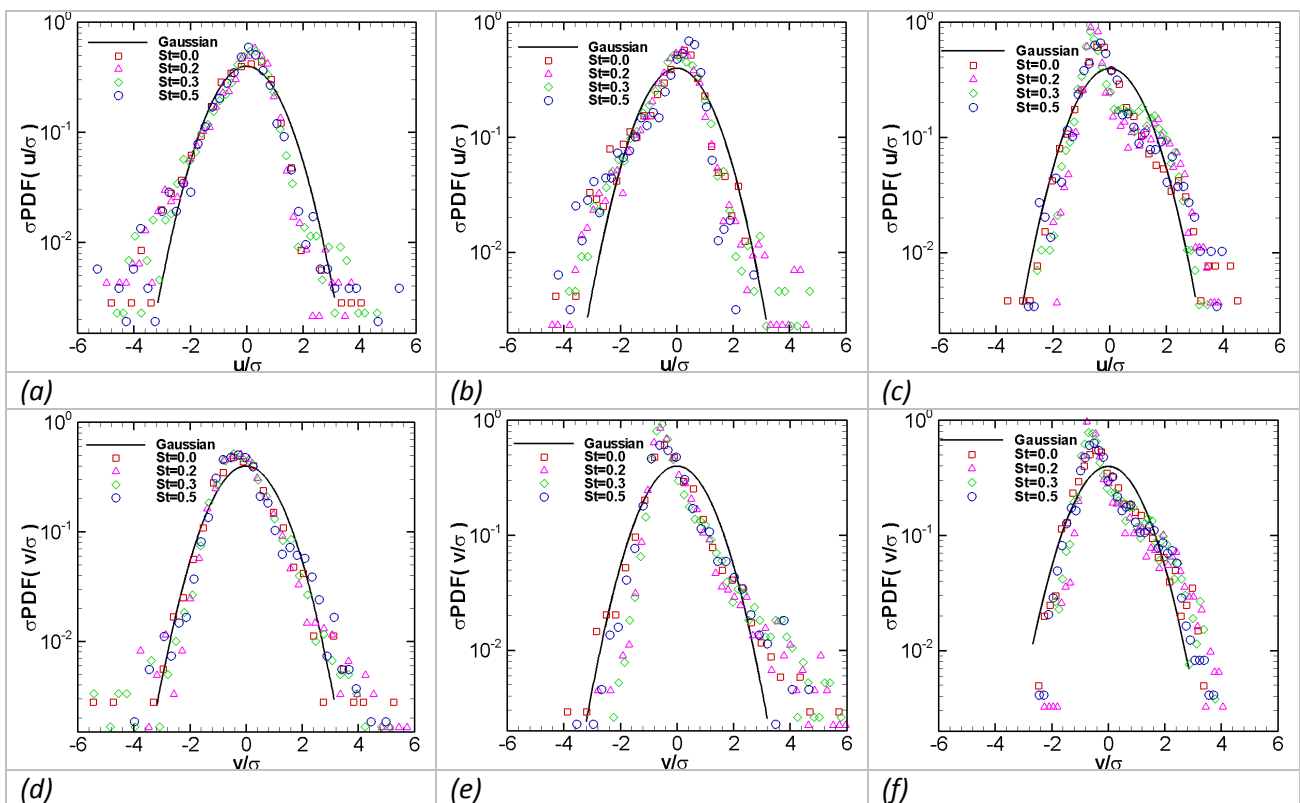


Figure (5. 11): Comparison of PDF for different  $St$  at  $x/d=3$  and  $y/d=1.5$ , in the array of subfigures blowing ratios ( $\overline{M} = 0.65, 1$  and  $1.25$ ) increases column-wise, and the PDF of  $u$  and  $v$  belongs to the first and second row.

The global attributes of the PDF do not change much for  $\overline{M}=1$ , as it still exhibits a small negative skewness for  $u$  of about -0.3 and maximum flatness of 6, as well as a positive skewness of 2.4 and a flatness of 11 for  $v$  in case of  $St=0.2$ .

For  $\overline{M}=1.25$ , the flatness of the PDF increases for  $v$  at  $St=0.2$  and  $0.3$  similarly as for the other blowing ratios, while the skewness becomes positive for both  $u$  and  $v$ . The higher values of the skewness are about 1.3 and 1.48, along with the values for the flatness factor of 3.9 and 4.8 for  $u$  and  $v$  respectively at  $St=0.2$ . It is interesting to note that the flatness factor for  $v$  at  $\overline{M}=1.25$  are slightly lower than the  $\overline{M}=0.65$  and 1.

## 5.4 Turbulent description, tensor of Reynolds stresses

The study of the tensor of Reynolds stresses gives an idea of how correlations of fluctuating velocities with zero time lag vary locally in the flow domain. In the present case with two dimensional results, only four out of the nine components of the tensor can be determined (i.e.  $\overline{u^2}$ ,  $\overline{v^2}$ ,  $\overline{uv}$  and  $\overline{vu}$ ). The characteristics of the fluctuating field are presented in the form of turbulence intensity for the normal stress components, which are obtained by normalizing the rms values of velocity fluctuations either with the mean velocity of the mainstream flow or with the local velocity of the mean flow. The normalization of the normal stress components with the mean velocity of the mainstream flow does not change the trend of a profile and allows us to observe the actual pattern of these components, while the normalization with local mean velocity accounts for the local variations incorporating the variations of both rms and mean velocity fields. At the end, the results for the shear stress component are presented after the normalization with the mean mainstream velocity.

### 5.4.1 Time-averaged normal stresses

Figures (5.12a-c) and (5.12d-f) show the variation in the profiles of time-averaged normal stress components  $u$  and  $v$  for steady blowing ratios of  $\overline{M}=0.65$ , 1 and 1.25 at the downstream locations of  $x/d=1.5$ , 3.5 and 5.5. The profiles for both streamwise and wall-normal rms velocity components located in the near downstream region ( $x/d=1.5$ ) of the hole exit show an initial higher magnitudes of stresses closer to the wall in most of the cases, which seems to lie in the mixing layer region of the lower boundary of the jet. As the distance in the wall-normal direction increases, we observe some reduction in the stress level in the inner part of the jet. Further away from the wall, a peak in the region of the upper jet boundary is observed. More downstream, the peak near the upper boundary of the jet becomes less prominent. These peak regions are more prominent for the streamwise component of the rms velocity, especially when comparing the trend of the downstream profiles. This indicates that the diffusion of the wall-normal rms component of the velocity increases across the jet, as we move farther downstream.

It can be observed that the stress levels when normalized with the corresponding velocities of the mainstream flow show small differences between the streamwise and wall-normal components. One can expect that the normalization of these components with the local mean velocity of the flow would show significant differences for all blowing ratios.

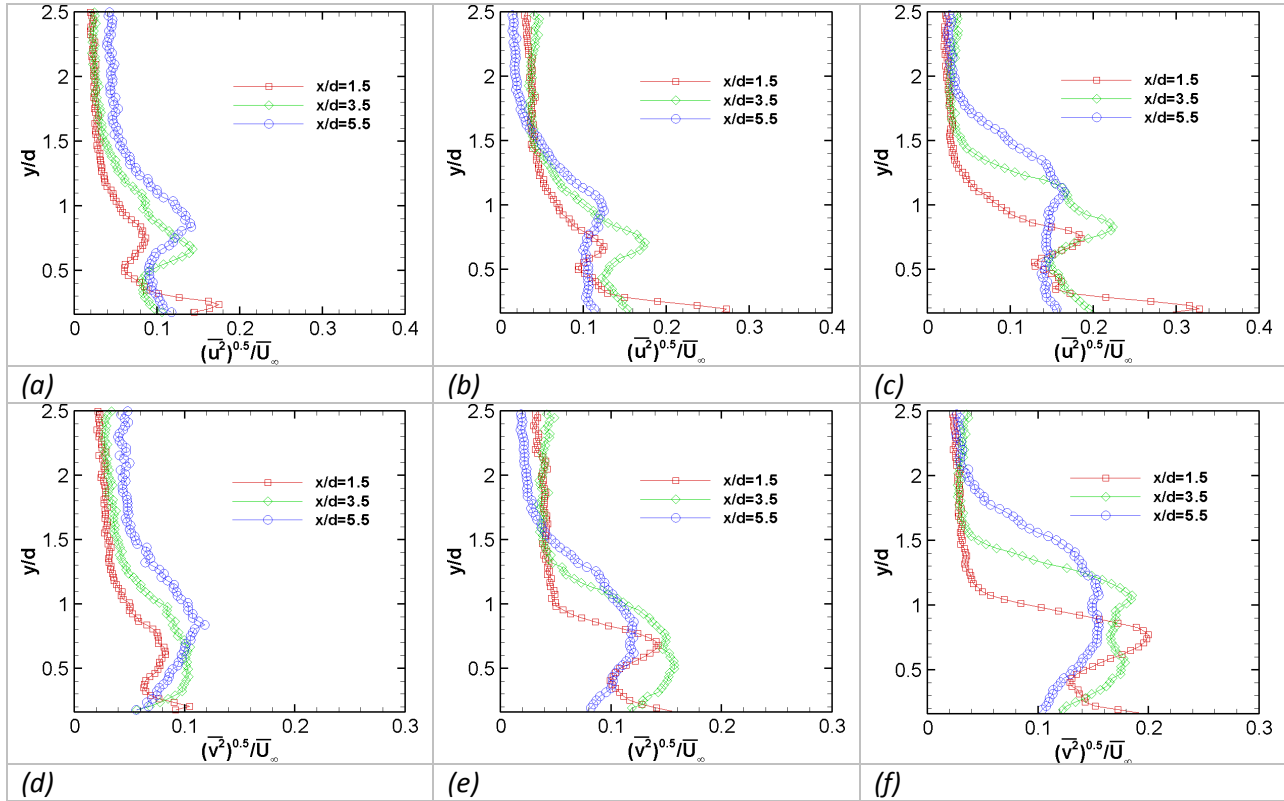


Figure (5.12): Comparison of time-averaged profiles of  $\left(\overline{u^2}\right)^{0.5}/\overline{U_\infty}$  and  $\left(\overline{v^2}\right)^{0.5}/\overline{U_\infty}$  in continuous blowing, lying at the downstream locations of  $x/d=1.5$ ,  $3.5$  and  $5.5$  of central plane ( $z/d=0$ ), for different  $\overline{M}$  ( $0.65$ ,  $1$  and  $1.25$ ), with  $\overline{M}$  increasing column-wise, and the  $u$  and  $v$  fluctuating component of velocity belong to the first and second row in the array of subfigures.

Figure (5.13a-f) shows the comparison of the time-averaged streamwise components of turbulent intensity for different Strouhal numbers in the cases of different blowing ratios ( $\overline{M}=0.65$ ,  $1$  and  $1.25$ ), increasing column-wise in the array of subfigures. The results shown in figure (5.13a-c) and figure (5.13d-f) are obtained for  $x/d=3.5$  and  $x/d=5.5$  of the central plane ( $z/d=0$ ). From these figures, it can be noticed that the effects of pulsation are more prominent for the blowing condition of  $\overline{M}=1.25$ . The large span variation of the injectant trajectory along the wall-normal direction causes the time-averaged streamwise component of turbulence intensity to become more uniform, as the values in the peak region level-off slightly followed by an increase in both upper and lower region for  $St=0.2$ , and only in the upper region for  $St=0.3$ , with respect to lower boundary of the jet. It indicates that the pulsating case of  $St=0.3$  does not significantly alter the flow field lying between the jet and the wall, from the one for steady conditions, similarly as noted for  $St=0.5$ . Pulsation at  $St=0.2$

“Experimental aerothermal characterization of a pulsating jet issuing in a crossflow: Influence of Strouhal number excitation on film cooling”

and 0.3 causes the jet pulsating effect to propagate through out the domain considered in the wall-normal direction.

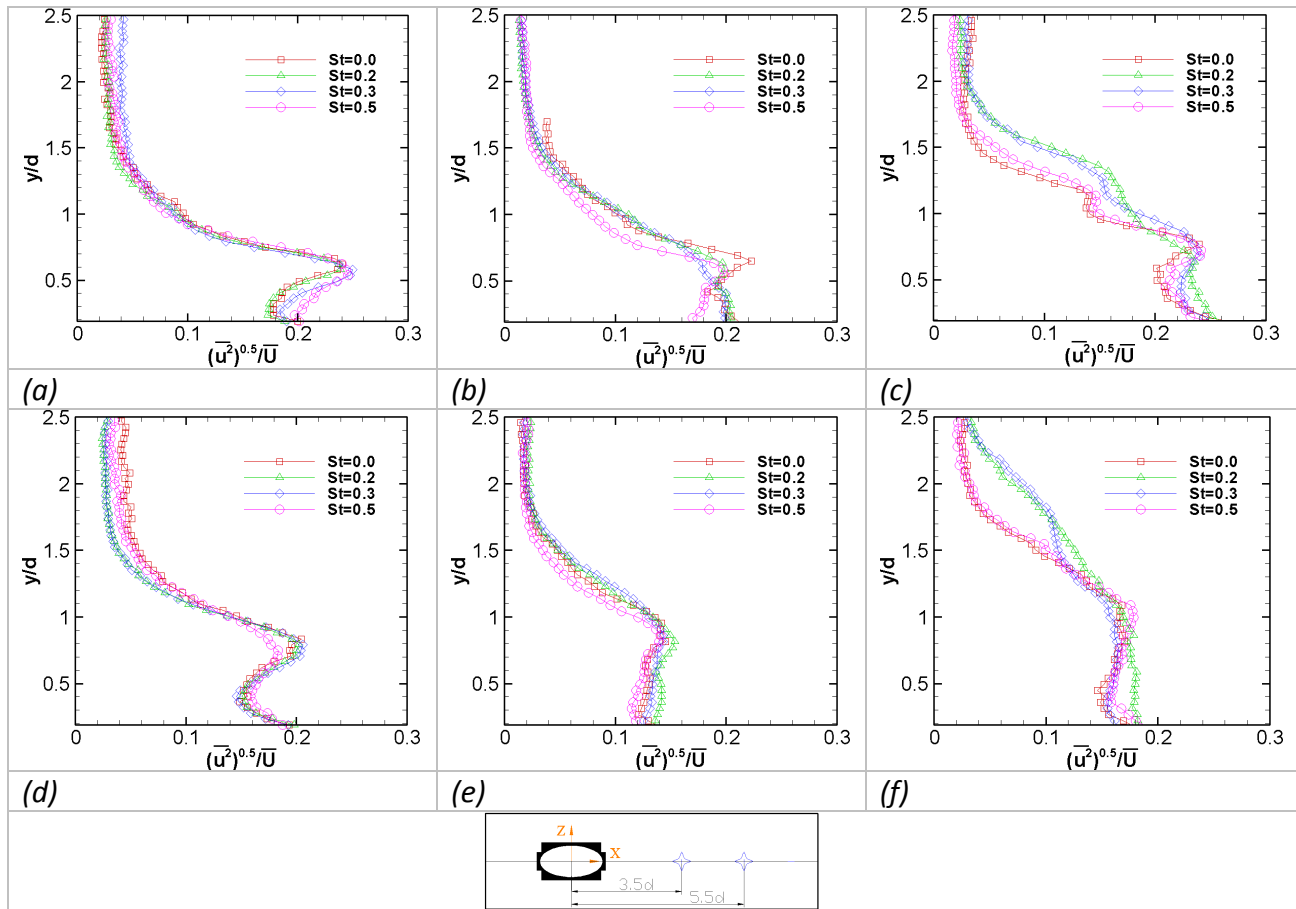


Figure (5.13): Comparison of time-averaged profiles of  $(\overline{u^2})^{0.5}/\overline{U}$ , lying at  $x/d=3.5$  and  $5.5$  of the hole central plane ( $z/d=0$ ), for different  $St$  (0, 0.2, 0.3 and 0.5) examined under a range of  $\overline{M}$  (0.65, 1 and 1.25), while  $\overline{M}$  increasing column-wise and  $x/d$  increasing row-wise.

Figure (5.14a-f) shows the comparison of the time-averaged wall-normal components of turbulence intensity for different Strouhal numbers in the cases of different blowing ratios. The locations of the profiles are similar as for the streamwise stresses mentioned in figure (5.14). The distributions of the turbulence intensity based on local mean velocity component have shown that the turbulence intensity in wall-normal direction is fairly high compared to the streamwise direction and turbulence intensity of the velocity fluctuations in wall-normal direction normalized by the mean freestream velocity.

At a blowing ratio of  $\overline{M}=0.65$ , the peak values of the turbulence intensity appear to be higher than the other cases for each downstream location, because of the normalization by lower mean velocities in wall-normal direction. Furthermore, the pulsation at  $St=0.5$  results in an increase of turbulence intensity at the lower-end of the profile located below the jet.

For  $\overline{M} = 1$ , the profiles peaks are less intense near the region of the jet boundary and a small increase seems to take place throughout the length of profile for the cases of  $St=0.2$  and  $0.3$ .

In the case of  $\overline{M} = 1.25$ , the profile becomes a bit more uniform across the expected boundary of the jet. Some significant turbulence produced in the upper region is probably due to the interaction of the mainstream flow and the systematically collapsing jet fluid. The turbulence fluctuation may also be induced by the periodically pulsing injectant flow while passing through the tube during the moments of instantaneously high blowing ratio. In the moment of higher blowing ratio, the turbulence produced in the tube might be higher as well (Pietrzyk et al. 1989).

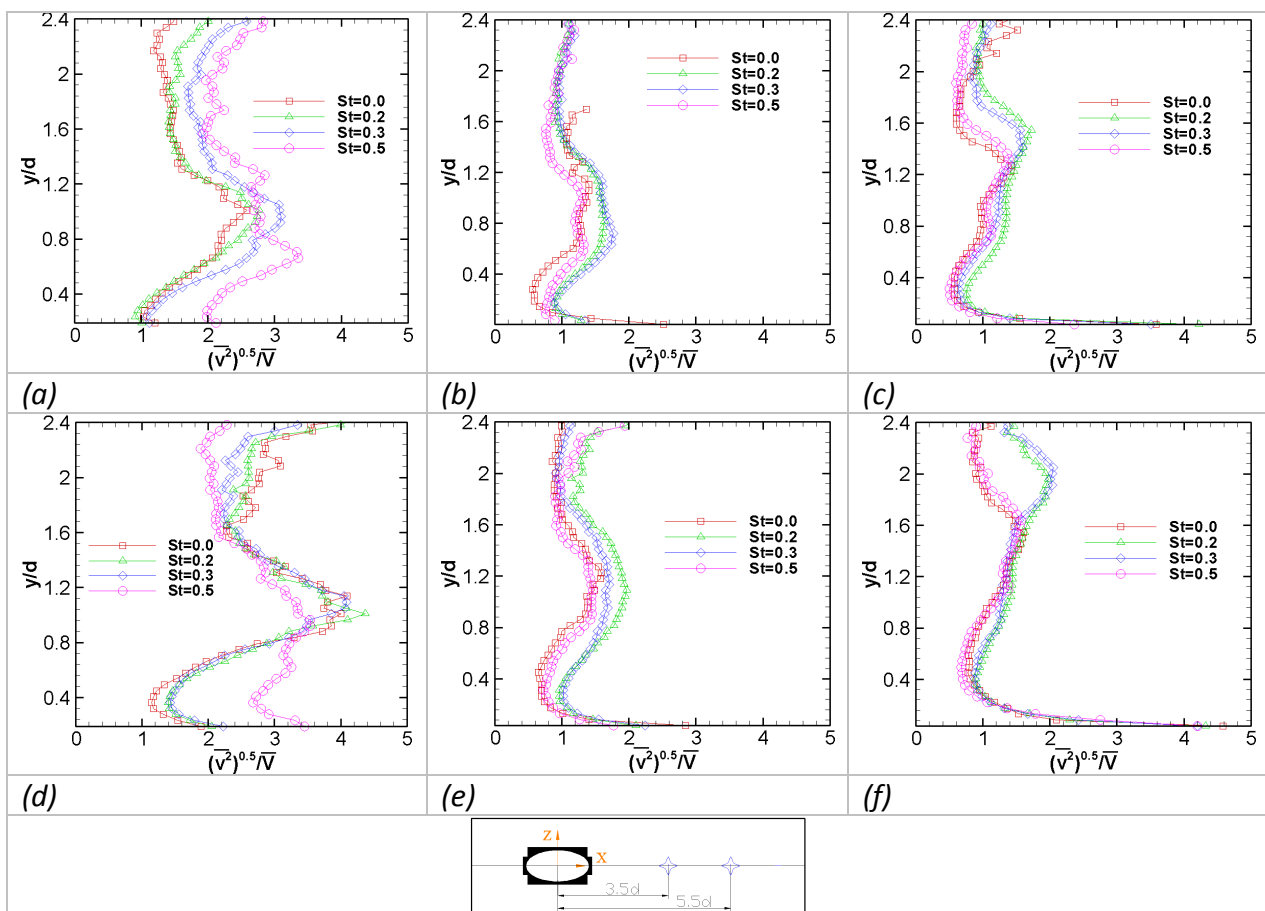


Figure (5. 14): Comparison of time-averaged profiles of  $(\overline{v^2})^{0.5} / \overline{V}$ , lying at  $x/d=3.5$  and  $5.5$  of the hole central plane ( $z/d=0$ ), for different  $St$  ( $0, 0.2, 0.3$  and  $0.5$ ) examined under a range of  $\overline{M}$  ( $0.65, 1$  and  $1.25$ ), while  $\overline{M}$  increasing column-wise and  $x/d$  increasing row-wise

The effects of freestream turbulence on the ultimate wall coverage were studied by Burd et al. (1996) and Brundage et al. (1999). It is generally admitted that with higher freestream turbulence intensity the mixing of the interacting flow streams increases, which reduces the film cooling effectiveness. However, the cases where turbulence intensity

“Experimental aerothermal characterization of a pulsating jet issuing in a crossflow: Influence of Strouhal number excitation on film cooling”

increases due to the nature of the interaction of two flows are somewhat different. Bons et al. (1995) also reported an increase in streamwise rms velocity with pulsation. In those experiments, the modulation frequencies ( $St = f * d / U_{\infty}$ ) of the jet were 0.0059 to 0.024, and blowing ratios  $\bar{M}$  were 0.7 to 1.0 for a constant freestream turbulence intensity of 0.7%.

## 5.4.2 Time-averaged shear stresses

The Reynolds shear stress profiles as a function of average blowing ratio  $\bar{M}$  with steady blowing ( $St=0$ ) are shown for different streamwise positions  $x/d=1.5, 3.5$  and  $5.5$  in figure (5.15).

For  $\bar{M}=0.65$ , figure (5.15a) shows that the shear stress correlation is relatively high in the vicinity of the wall for a near downstream profile at  $x/d=1.5$ , compared to  $x/d=3.5$  and  $5.5$ . On the downstream, the jet attains the position of maximum shear stress at a vertical distance which is slightly higher compared to the respective  $\bar{U}/\bar{U}_{\infty}$  profiles. This is consistent with the other two cases,  $\bar{M}=1$  and  $\bar{M}=1.25$ , indicating the interface between jet and freestream flows. The maximum positive shear stress values for  $x/d=3.5$  and  $5.5$  are 0.012 and 0.013 at  $y/d=0.63$  and  $0.85$  respectively. The effects of shear stresses are negligible above  $y/d=1.35$ .

At  $\bar{M}=1$ , figure (5.15b) shows that the higher jet momentum causes the low velocity region between the jet and the wall to become large for  $x/d=1.5$ , and a highest positive shear stress of 0.032 is attained at  $y/d=0.18$ . The shear stress becomes zero in the core and again reaches a maximum negative value of -0.015 in the upper jet boundary area ( $y/d=0.68$ ). For other downstream profiles, at  $\bar{M}=1$ , the shear stress is lower because of the loss of momentum of the jet fluid. The location of the maximum shear stress on the bottom side is shifted to  $y/d=0.71$  and  $0.91$  respectively. The flow field sees almost negligible shearing effect beyond  $y/d=1.5$  on the upper boundary.

At  $\bar{M}=1.25$ , figure (5.15c) shows that the higher vertical momentum of the jet further widens the low velocity zone underneath the jet due to increasing lift-off. In this situation, the velocity profile at the hole exit, which is normally skewed towards the downstream edge due to the flow pressure distribution effects at low blowing ratio is pushed towards the upstream edge due to increase of jet momentum and the influence of injection tube vortices (Walters and Leylek 2000), see figure (4.16). This causes an increment in maximum negative value of shear stress at the upper side to -0.029 at  $y/d=0.76$  for the near downstream profile at  $x/d=1.5$  and subsequently for other profiles at  $x/d=3.5$  and  $5.5$  to -0.023 and -0.0064 at  $y/d=1.15$  and  $1.55$  respectively. The effects of shear stress are insignificant above  $y/d=1.9$ . At a higher blowing ratio, the upper side of the jet is expected to be a zone where the upstream boundary layer vortices of the mainstream flow interact with vorticity ejecting from the hole and later form some coherent counter rotating entity due to the rolling up of the shear layer and the tilting of the jet in streamwise direction. On the

lower side of the jet, the uplifting of the jet, entrainment of mainstream flow and wake activity cause an increase in the mixing of two flows locally (Kelso et al. 1996; Walters and Leylek 2000).

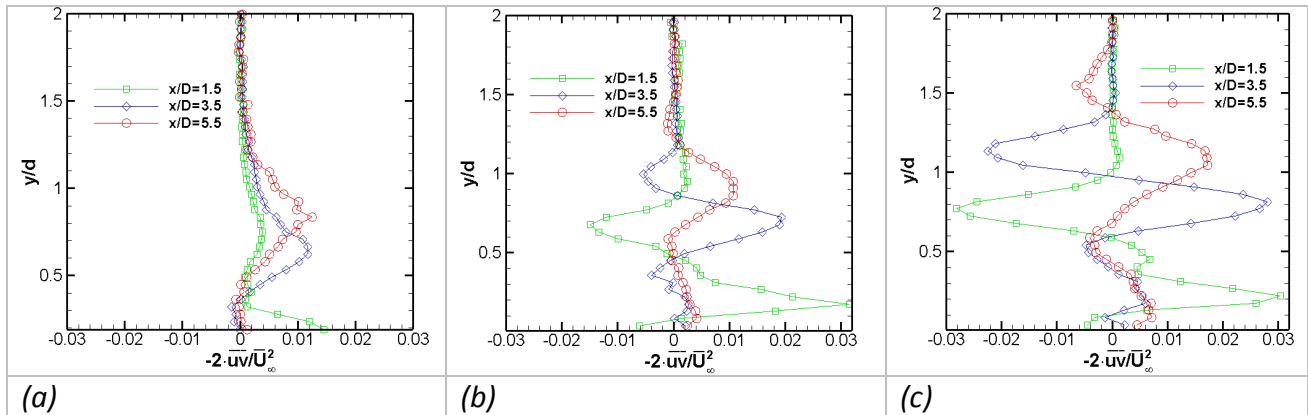


Figure (5. 15): Reynolds shear stress profiles  $-2\overline{uv}/U_{\infty}^2$  obtained from steady blowing cases ( $St=0$ ), lying at  $x/d=1.5, 3.5$  and  $5.5$ , (a)  $\overline{M} = 0.65$ , (b)  $\overline{M} = 1$ , (c)  $\overline{M} = 1.25$ .

Figure (5.16a-f) shows the Strouhal number based comparison of the time-averaged shear stress profiles for different blowing ratio. The results shown in figure (5.16a-c) and figure (5.16d-f) are obtained from  $x/d=3.5$  and  $x/d=5.5$  of the central plane ( $z/d=0$ ). It can be observed that the shear stress level increases with increase of pulsation Strouhal number at  $\overline{M} = 0.65$ . At  $x/d=3.5$ , the pulsation at  $St=0.5$  compared to steady blowing causes an increase of about 66% in the peak value of  $-2\overline{uv}/U_{\infty}^2$  lying at the lower boundary of the jet. The pulsating conditions of  $St=0.2$  and  $0.3$  have dominant effects for  $\overline{M} = 1$  and  $1.25$ . The large span movement of the jet trajectory at  $St=0.2$  and  $0.3$  drifts the peak region of the profile slightly away from their respective locations for steady blowing, and thus broaden the zone of their variation. There is also an increase in peak values for the lately mentioned pulsation cases. The relative difference between the velocities of two flows, varying periodically, might cause a slight increase in their peak levels. At  $x/d=3.5$ , the increase in shear stresses observed for  $\overline{M} = 1$  is only about 20% and 30% for  $St=0.2$  and  $0.3$ , while it is fairly high for  $\overline{M} = 1.25$  to about 114% and 93% for  $St=0.2$  and  $0.3$  near the lower boundary of the jet. The flow field loses its momentum with the evolution in the downstream, and that reduces the shearing stresses for the profiles lying on the downstream station.

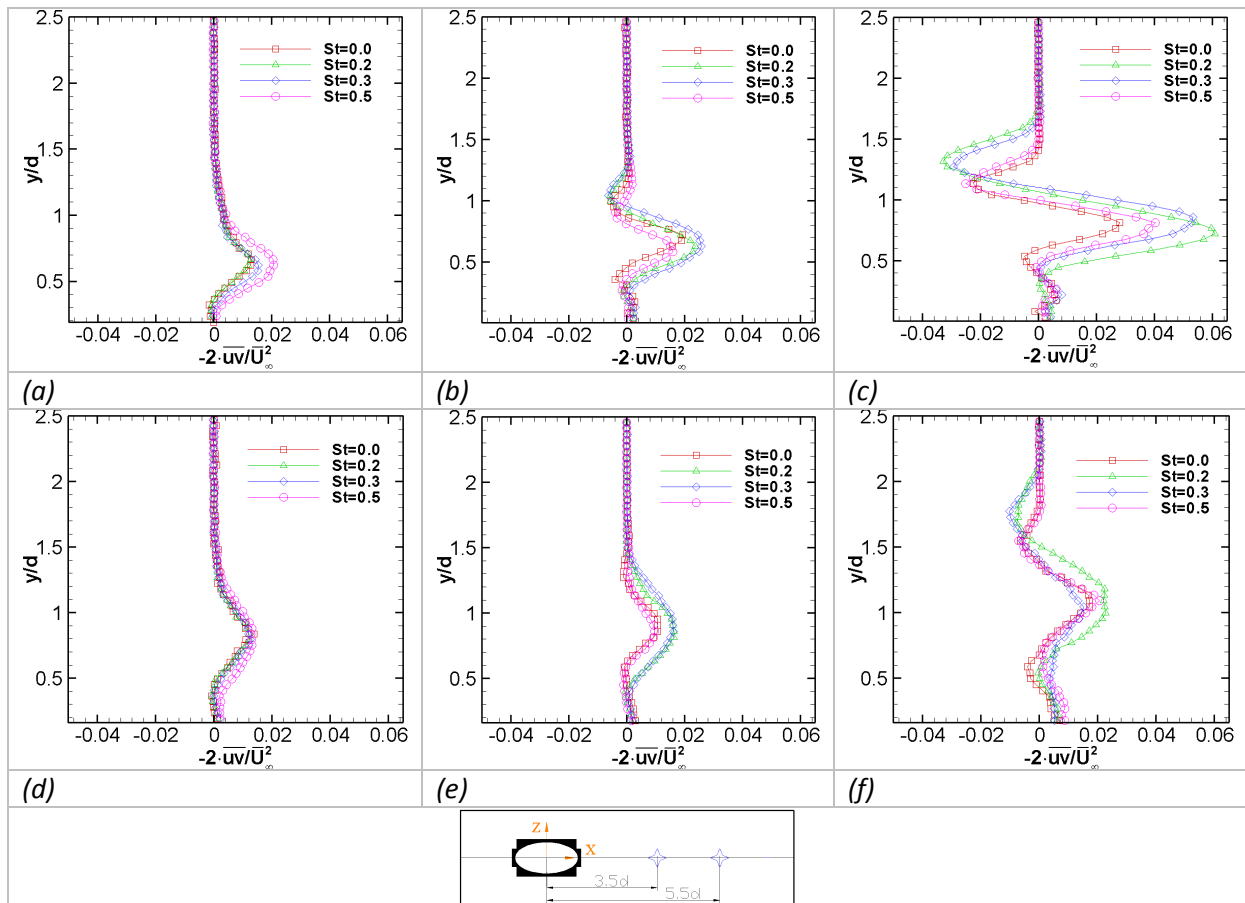


Figure (5. 16): Comparison of time-averaged profiles of  $-2\overline{uv}/U_\infty^2$ , lying at  $x/d=3.5$  and  $5.5$  of the hole central plane ( $z/d=0$ ), for different  $St$  (0, 0.2, 0.3 and 0.5) examined under a range of  $\overline{M}$  (0.65, 1 and 1.25), while  $\overline{M}$  increasing column-wise and  $x/d$  increasing row-wise.

### 5.4.3 Phase-averaged shear stresses

Figure (5.17a-d) shows the distribution of flow Reynolds shear stress  $-2\overline{uv}/U_\infty^2$  at different times for  $\overline{M}=1$  and  $St=0.2$ . The contours seem to contain three different types of shear flow zones. The first one is due to the upper boundary of the jet and is negative, the second one is due to the lower boundary of the jet and is positive and the last one which originates from the near downstream location of the hole and also has negative shear stresses. The former is the wake flow region which appears to shed downstream with a certain periodic variation of injectant flow rate. For the first instant at  $t/T=0.19$ , the injection velocity is high and the overall jet body moves away from the wall and allows the development of a wake region under it. At  $t/T=0.41$ , the jet trajectory bends down a bit due to initiation of the lower half of the pulsation period causing a reduction in injectant flow. Such bending towards the wall then triggers splitting of wake vortices. At  $t/T=0.63$ , the wake structure moves further downstream and part of the fluid with negative shear splits up followed by the splitting of the zone with positive shear. At the same time, flow at the hole exit begins to rise. At

$t/T=0.86$ , the parts of fluid with positive and negative shears seems to move in succession down in the shedding zone.

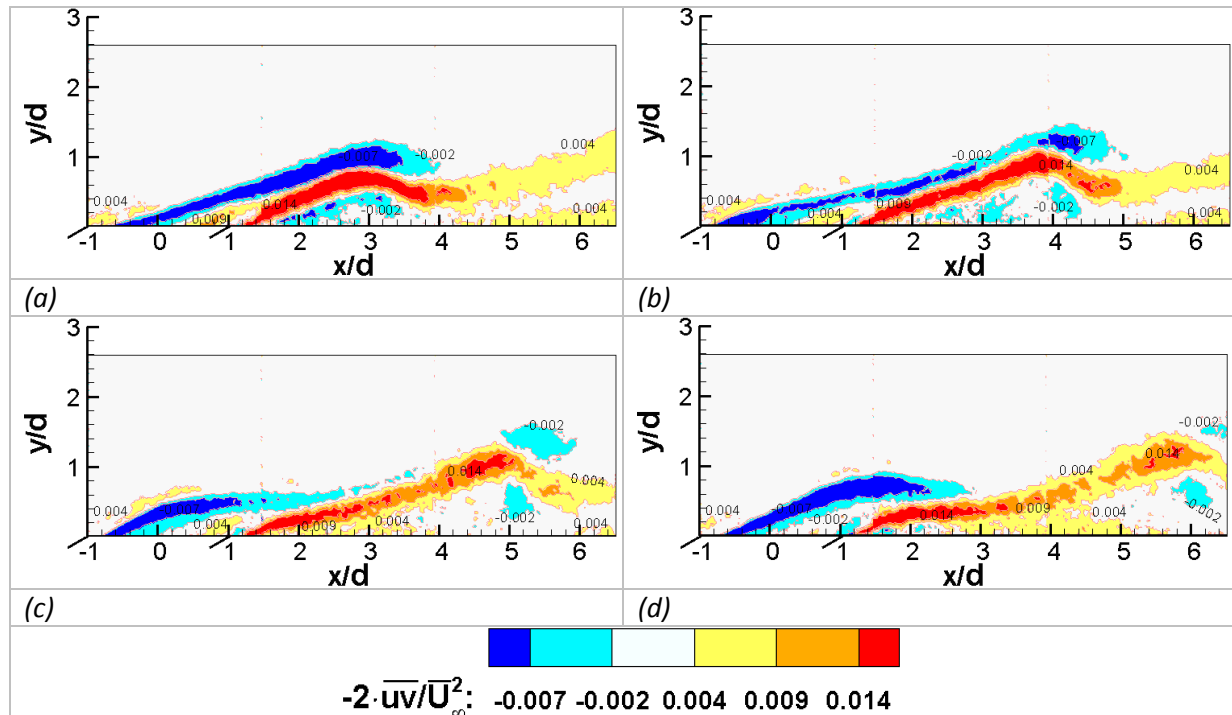


Figure (5. 17): Reynolds shear stress distribution  $-2\overline{uv}/U_{\infty}^2$ ,  $\overline{M}=1$ ,  $St=0.2$ ; (a)  $t/T=0.19$ , (b)  $t/T=0.41$ , (c)  $t/T=0.63$  and (d)  $t/T=0.86$ .

In figure (5.18a-i), the variations in the flow field due to injectant flow pulsation are presented by the shear stress profiles at  $x/d=3.5$  for the range of blowing ratio and Strouhal number considered. Figures (5.18a-c) show the variation in shear stresses at  $\overline{M}=0.65$  for  $St=0.2$ ,  $0.3$  and  $0.5$ . It can be observed that the variation along the vertical direction amplifies with an increase in  $St$ , especially for  $St=0.5$ . The portion with negative stresses is considerably low for both  $St=0.2$  and  $0.3$ , and merely exists for  $St=0.5$ . At  $\overline{M}=1$ , figures (5.18d-f) show that the periodic variations with higher lift-off carries large influences in the shear affected zone compared to the previous case. At higher frequencies the effect of pulsation are not fully established under short time duration of successive pulses and the resulting variation in shear stresses are comparatively low across the steady flow profile. The part of negative shearing stresses is particularly high for  $\overline{M}=1.25$ , as shown in figure (5.18g-i). This is due to the slight shift in velocity profile at hole exit towards the upstream. Also, the ambit of spatial variation for shear stress is even larger for the range of  $St$  considered. These effects make the jet highly unstable due to high lift-off and jet movement in larger span under low pulsing condition could easily lead to an early break down. However, broken jet with higher momentum of fluctuating velocity component established at jet boundary able to bring some part of injectant flow in the near wall region in following the periodic variation

of jet trajectory and increase the presence of injectant flow on average basis compared to the steady blowing. As one can expect that the shear stresses can play a dominant role in the mean momentum transfer by turbulent motion from the jet boundary.

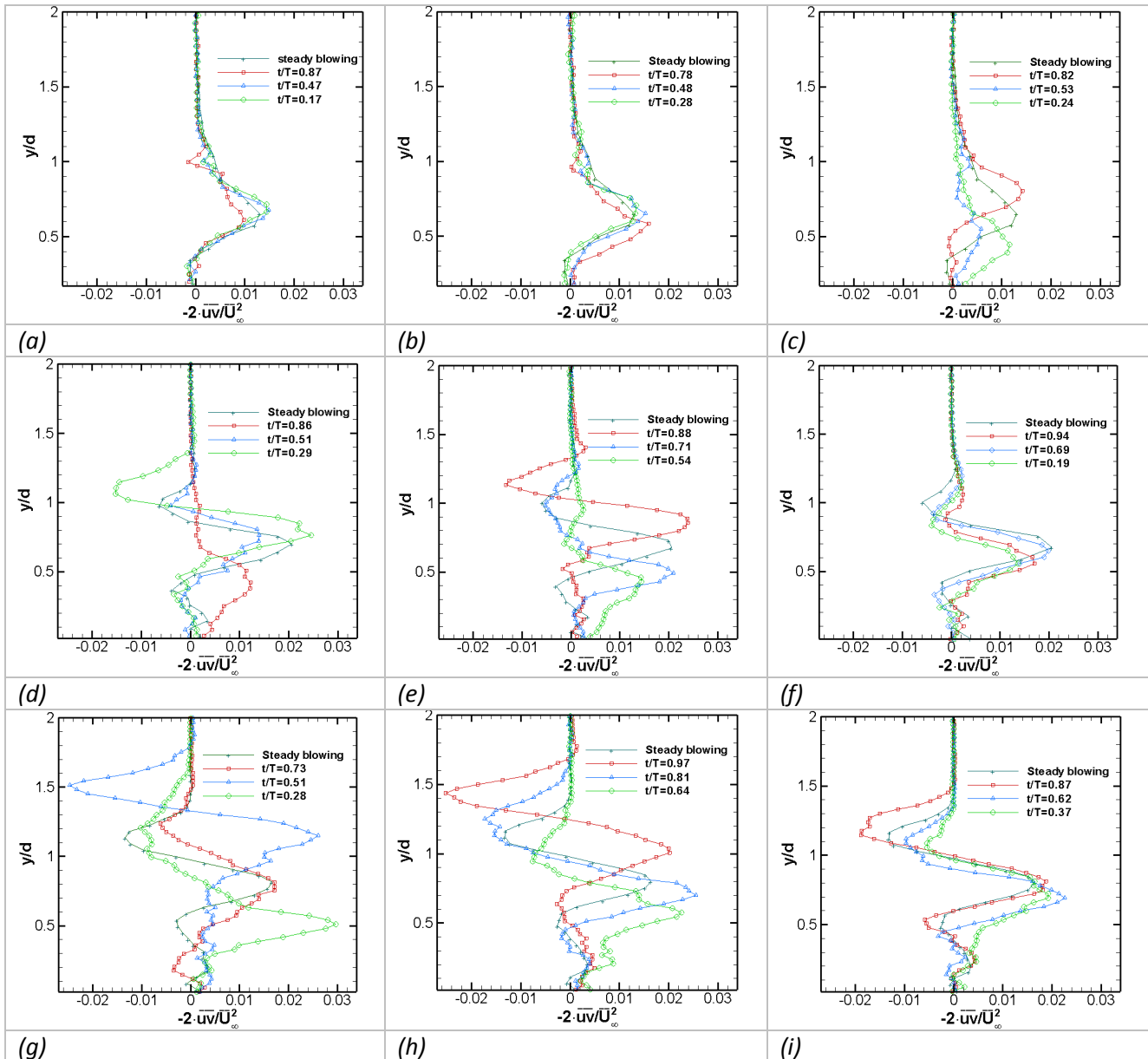


Figure (5. 18): Reynolds shear stress profiles  $-2\overline{uv}/U_\infty^2$  with pulsation at  $x/d=3.5$ , (a)  $\overline{M}=0.65$ ,  $St=0.2$ , (b)  $\overline{M}=0.65$ ,  $St=0.3$ , (c)  $\overline{M}=0.65$ ,  $St=0.5$ , (d)  $\overline{M}=1$ ,  $St=0.2$ , (e)  $\overline{M}=1$ ,  $St=0.3$ , (f)  $\overline{M}=1$ ,  $St=0.5$ , (g)  $\overline{M}=1.25$ ,  $St=0.2$ , (h)  $\overline{M}=1.25$ ,  $St=0.3$ , (i)  $\overline{M}=1.25$ ,  $St=0.5$ .

#### 5.4.4 Ratio of phase-averaged rms-velocity components

Figures (5.19a-d) show the relative importance of normal stresses in different sections of the flow field formed at  $\overline{M}=1$  and  $St=0.2$  by presenting a ratio of the RMS quantities of velocity fluctuation  $R' = \sqrt{\overline{u^2}}/\sqrt{\overline{v^2}}$ . This term generally gives an idea of global isotropy/anisotropy in a given flow. The contour plot seems to indicate three different zones of increased importance

in the flow field. The first one is the zone containing a part of upstream flow and the upper and lower jet boundary with a magnitude greater than one  $\sqrt{u^2} > \sqrt{v^2}$ , second one constitutes the inner part of jet where values are less than one  $\sqrt{u^2} < \sqrt{v^2}$ , and the third zone lies below the jet in the wake region again with values less than one. At the first instant,  $t/T=0.19$ , the zone of the jet potential core dominated by the normal component  $\sqrt{v^2}$  appears to extend in the downstream direction with accelerating jet. The part of flow lying below the jet also with  $\sqrt{u^2} < \sqrt{v^2}$  seems to emerge just after the emergence of the jet and lasts until its splitting in following the induced periodic variation of injectant flow. At  $t/T=0.41$ , the jet starts to bend towards the wall and the development of the flow in the downstream side brings the zones of low stress ratio close to each other in the near wall region. As the development of the wake slightly lags the growing of the jet in the downstream flow, so there is a part of jet with low streamwise stresses which moves a bit ahead of the point where the flow from two different regions with low streamwise stresses meet. Such movement is also visible in later instants  $t/T=0.63$  and  $0.86$ . The sequence of images shows that splitting of the wake occurs due to a reversing of the lift-off event, while for jet, at re-initiation after the falling of injectant flow rate.

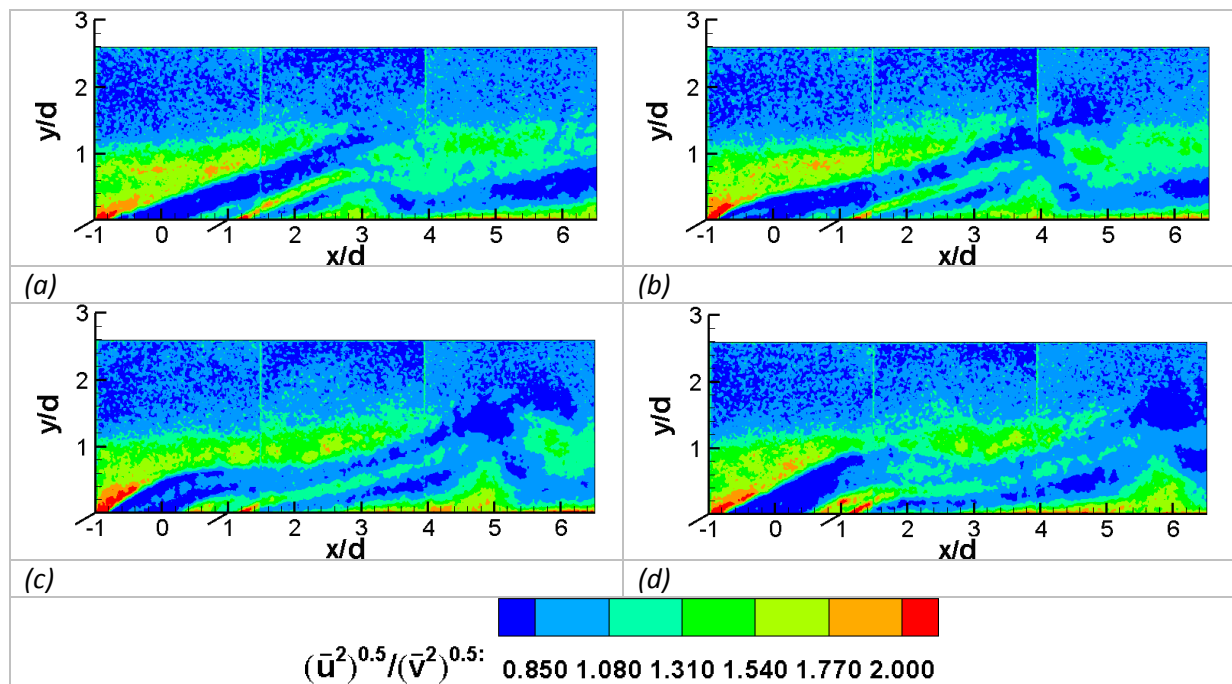


Figure (5. 19): Distribution of Reynolds normal stress ratio  $\sqrt{u^2}/\sqrt{v^2}$ ,  $\bar{M} = 1$  and  $St=0.2$ , (a)  $t/T=0.19$ , (b)  $t/T=0.41$ , (c)  $t/T=0.63$  and (d)  $t/T=0.86$ .

The stresses in the wall region lying on the downstream side of the hole seem to be dominated by streamwise stresses and also appear to move in accordance with the variation in the jet due to induced pulsation. It can be noticed that the pulsing of injectant with a

mean blowing ratio leading to separation is able to reorient the injectant close to the wall during the lower part of pulsing cycle.

### 5.4.5 Phase-averaged turbulent intensity

The evolution of phase-averaged turbulent intensity at different time instants is shown in figure (5.20a-d) for  $\overline{M} = 1$  and  $St=0.2$ . The estimation of the turbulent intensity is based on the ratio of the resultant of rms-velocity components and the resultant of mean velocity components, as shown in Eq. (5.1).

$$TI = \frac{\sqrt{(u_{rms}^2 + v_{rms}^2)}}{\sqrt{(U^2 + V^2)}} \dots\dots\dots(5. 1)$$

Based on this definition, the present parameter can be named as overall/total turbulent intensity just to differentiate it from the previously estimated quantities of the turbulence level. In the present case, the pulsation seems to cause significant periodic variations of the flow in the wake region, as the jet emerges and attains a higher blowing ratio during different time instants of the period of pulsation. The region lying near the upstream edge of the injection tube is considered to have higher turbulent intensities than the mainstream boundary layer flow because of the combined effect of a partial blockage offered by the jet and the interaction of vorticity coming from the mainstream boundary layer and those ejecting from the hole.

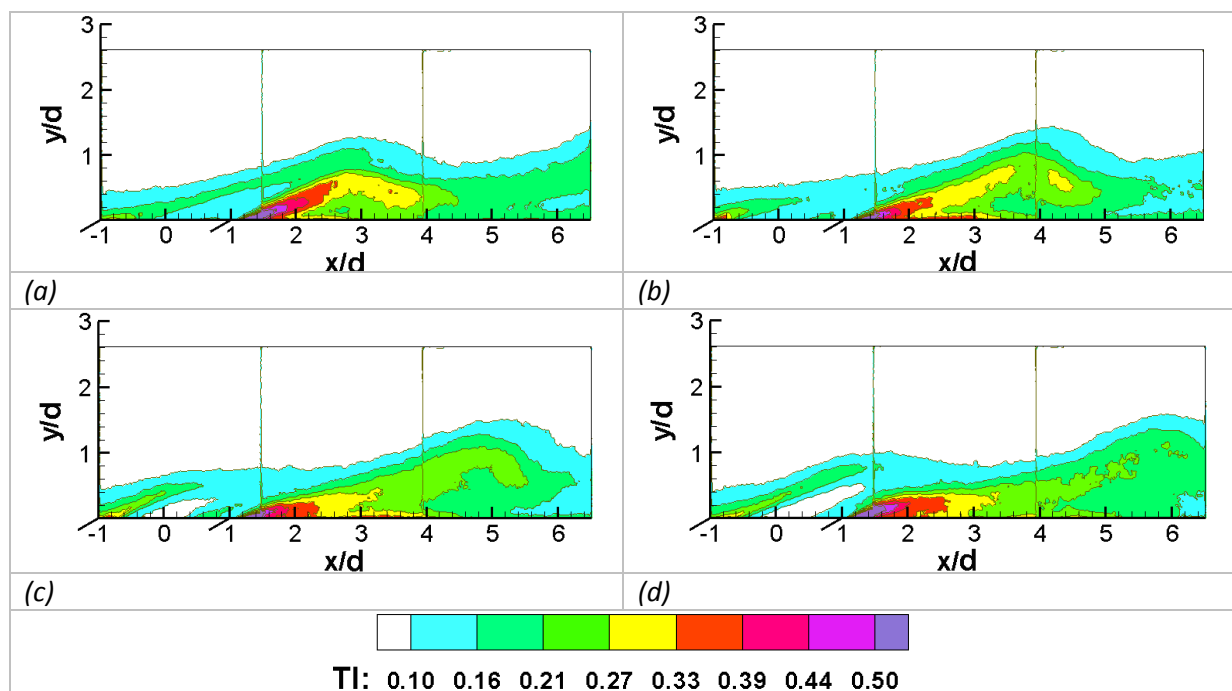


Figure (5. 20): Distribution of overall turbulence intensity (TI),  $\overline{M} = 1$  and  $St=0.2$ , (a)  $t/T=0.19$ , (b)  $t/T=0.41$ , (c)  $t/T=0.63$  and (d)  $t/T=0.86$ .

In the present study, the upstream region of the hole was not chosen for detail analysis, as no significant turbulence was observed during the initial testing. However, a small portion of the upstream edge of the jet shows some higher turbulence level immediately after the interaction of two flows. The contour for turbulent intensity are plotted between 10 to 50% to clearly indicate the rising of jet fluid in the sequence of images obtained at different time instants. However, the noted turbulent intensity of the jet fluid is about 7% in the potential core region lying close to the jet exit.

## 5.5 Tensor of velocity gradient

The tensor of velocity gradient describes the kinematics of a volume element deforming in the flow. For a three dimensional coordinate system, the whole array of the tensor of velocity gradient can be written as,

$$\begin{pmatrix} \frac{\partial U}{\partial x} & \frac{\partial V}{\partial y} & \frac{\partial W}{\partial z} \\ \frac{\partial U}{\partial x} & \frac{\partial V}{\partial y} & \frac{\partial W}{\partial z} \\ \frac{\partial U}{\partial x} & \frac{\partial V}{\partial y} & \frac{\partial W}{\partial z} \end{pmatrix} \dots\dots\dots(5.2)$$

Due to the limitation of the present results obtained by using a 2D TR-PIV system, we are only left with four terms locating on the upper-left corner of the tensor array. These informations can be used to define both symmetric and asymmetric part of the tensor, which are respectively the rate of deformation,  $\sigma_s$ , and the rotation (vorticity),  $\omega_z$ , as given by Eq. (5.3) and Eq. (5.4).

$$\sigma_s = \frac{1}{2} \left( \frac{\partial U}{\partial y} + \frac{\partial V}{\partial x} \right) \dots\dots\dots(5.3)$$

$$\omega_z = \frac{1}{2} \left( \frac{\partial V}{\partial x} - \frac{\partial U}{\partial y} \right) \dots\dots\dots(5.4)$$

### 5.5.1 Time-averaged vorticity

The time-averaged vorticity profiles shown in figure (5.21a-c) are obtained from the flow configuration of  $\overline{M} = 0.65, 1$  and  $1.25$  under steady blowing. In most of the cases except  $\overline{M} = 0.65$ , the near downstream profile ( $x/d=1.5$ ) indicates one peak of negative vorticity and one peak of positive vorticity, which corresponds to the shearing region at the upper and lower boundary of the jet.

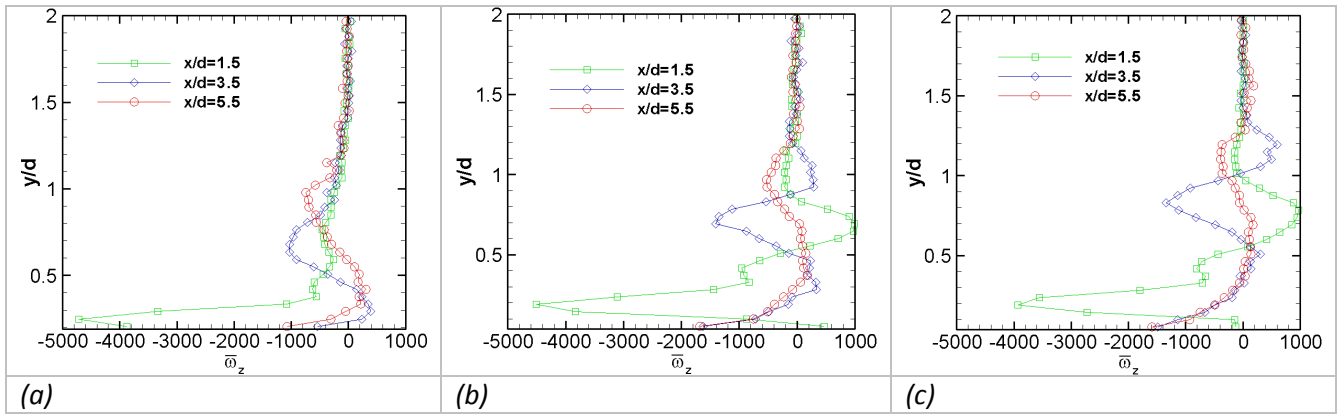


Figure (5. 21): Profiles of time-averaged vorticity  $\overline{\omega_z}$  obtained from steady blowing cases ( $St=0$ ), lying at  $x/d=1.5, 3.5$  and  $5.5$ , (a)  $\overline{M} = 0.65$ , (b)  $\overline{M} = 1$ , (c)  $\overline{M} = 1.25$ .

In case of  $\overline{M} = 0.65$ , the shearing at the upper boundary of the jet at  $x/d=1.5$  is not found to be significant. At the downstream distance of  $x/d=3.5$ , flow in the wake region has already become prominent, which lifts gradually from the wall as the flow evolve in the downstream region. The profile at  $x/d=3.5$  obtains a slight positive vorticity in the region of wake flow after departing from a negative vorticity, and then shows a peak of negative vorticity at the lower boundary of the jet. The secondary movement of the mainstream flow, proceeding in the lateral direction underneath the wake, produces negative vorticity at the wall. Pietrzyk et al. (1989) indicated the lateral influx of mainstream fluid below the jet from the vector field of mean velocity, showing negative velocity gradient for a blowing ratio of  $\overline{M} = 0.5$  and  $\rho_i/\rho_\infty = 1$ , while fixing the injection angle at  $35^\circ$ . In case of higher blowing ratios,  $\overline{M} = 1$  and  $1.25$  a third peak of positive vorticity emerges due to the shearing at the upper boundary of the jet. At the final post selected in the downstream flow ( $x/d=5.5$ ), these peaks started to become less prominent due to the loss of momentum of the jet fluid. Pietrzyk et al. (1989) studied the evolution of the flow field up to a far downstream region ( $x/d=30$ ), and mentioned that the magnitude of the velocity gradient decays faster than the  $\overline{uv}$  shear stress.

From the present 2D results obtained from the TR-PIV, the dynamics of the flow in the wake region can not be understood properly. Kelso et al. (1996) has proposed some possible ways for the shedding of vorticity generating at the flat wall in case of a high Reynolds number ( $Re=d.U_\infty/\nu$ ) flow. They mentioned that the orientation of vortex shedding may change from one pattern to another, containing either a pattern similar to classical von Kármán vortex street or in some particular case, of mushroom-like structures where the vortices appear to be grouped into pairs of opposite circulation. As far as the dynamics of the wake region of an oblique jet is concerned, not much of a detail was actually found in the open literature.

The time-averaged vorticity profiles shown in figure (5.22a-f) are obtained from the flow configuration of  $\overline{M} = 0.65, 1$  and  $1.25$ . The results shown in figure (5.22a-c) and figure (5.22d-f) are obtained from  $x/d=3.5$  and  $x/d=5.5$  of the central plane ( $z/d=0$ ). Comparison of different Strouhal number cases have shown some distinctive variation in the flow characteristics, especially for  $\overline{M} = 1$  and  $1.25$  compared to steady blowing. For the blowing ratio of  $\overline{M} = 0.65$ , the pulsation at  $St=0.5$  causes some significant variation in the flow field generating underneath the jet. As, the peaks for the flow in both wake region and at the lower boundary of the jet is reduced considerably, which is roughly about 38% of the peak value lying at the lower boundary of the jet in steady blowing. Similarly, for  $\overline{M} = 1$ , this is about 59% and 70% for  $St=0.2$  and  $0.3$ , and for  $\overline{M} = 1.25$  is about 75% and 57% for  $St=0.2$  and  $0.3$  at  $x/d=3.5$ . The reduction of vorticity at the jet boundary, lower than the vorticity developing in the steady blowing cases of  $\overline{M} = 1$  and  $1.25$ , reduces the strength of CVP on the time-averaged basis during the pulsation at  $St=0.2$  and  $0.3$ . This reduces the level of turbulence generating near the wall and finally the thermal exchange, as it will be presented next.

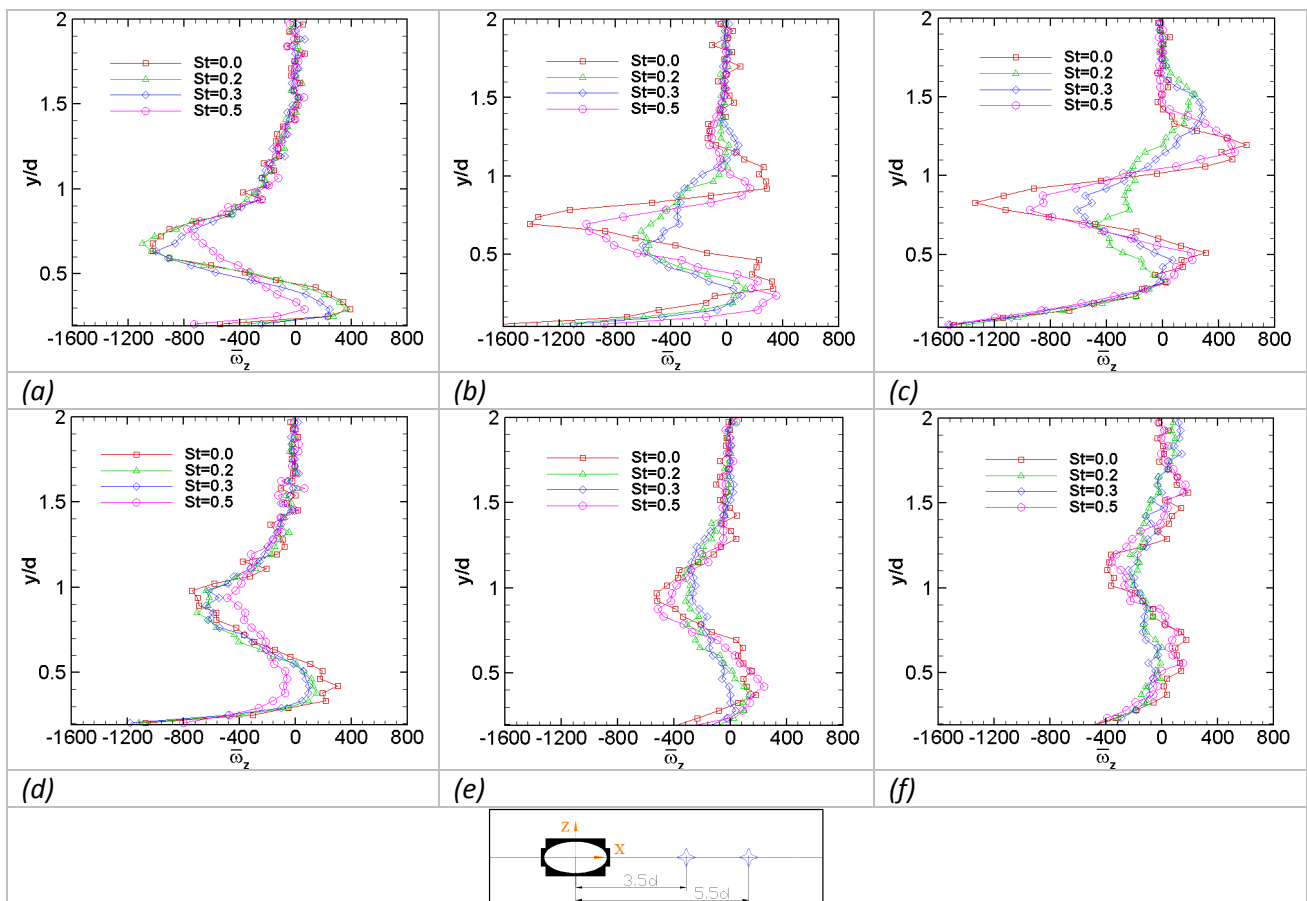


Figure (5. 22): Comparison of time-averaged profiles of  $\overline{\omega}_z$ , lying at  $x/d=3.5$  and  $5.5$  of the hole central plane ( $z/d=0$ ), for different  $St$  (0, 0.2, 0.3 and 0.5) examined under a range of  $\overline{M}$  (0.65, 1 and 1.25), while  $\overline{M}$  increasing column-wise and  $x/d$  increasing row-wise.

### 5.5.2 Phase-averaged vorticity

The contours of vorticity distribution along the width of injection plate is shown for  $\overline{M}=1.25$  and  $St=0.5$  in figure (5.23a-d). The present case represents the detrimental aspect of pulsation at higher Strouhal number, while the jet is significantly lifted against the wall. It can be observed that the different zones with pertinent vorticity are consistent with the previous discussion, as the variation in upper and lower jet boundary and the zone of wake evolve in a similar way except for the variations leading to collapsing of the jet which appear to take place much more rapidly. The trajectory of injectant in the downstream direction shows small rippling effects as the adjacent pulsation cycles do not allow the flow to establish fully on the periodic effects. The zone of dominant vorticity lies on the lower jet boundary and appears to sustain longer under jet pulsation. These effects promote the mixing rate locally and drive them out to influence the flow in the near wall region. The distribution of injectant on the downstream side in such cases are less effective in terms of wall coverage as the coolant trajectory with frequent feeding of broken jet contents in downstream flow always seem to orient away from the wall.

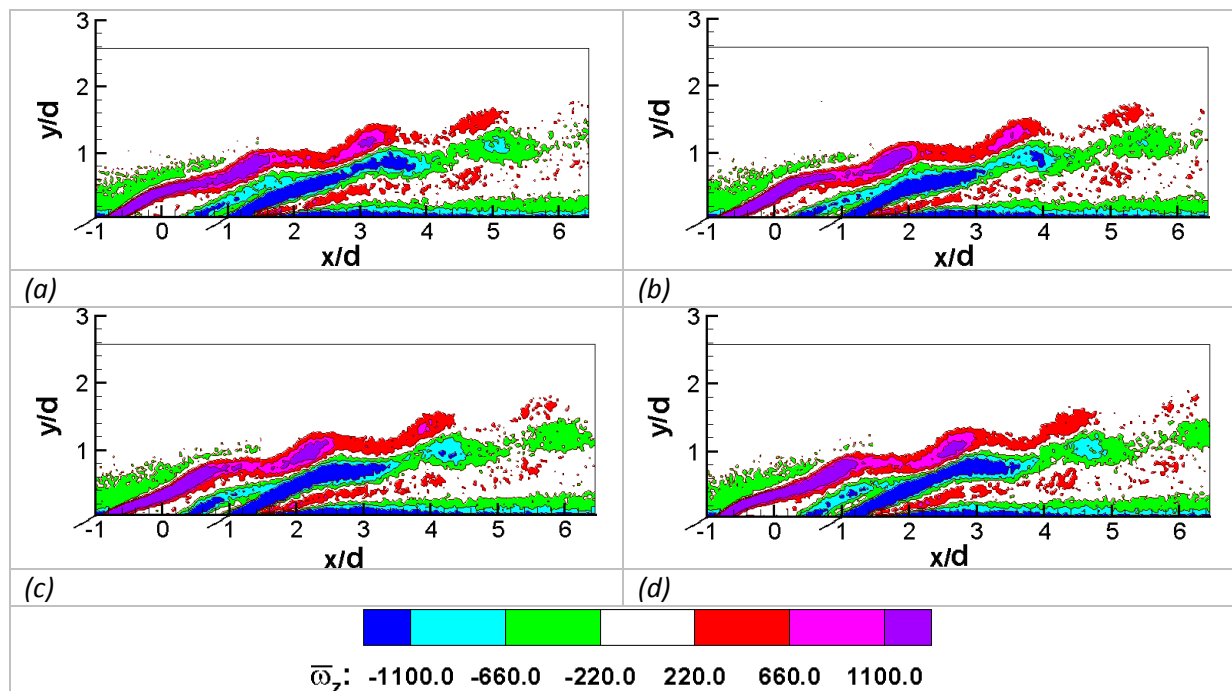


Figure (5. 23): Vorticity distribution,  $\overline{\omega}_z$ ,  $\overline{M}=1.25$ ,  $St=0.5$ ; (a)  $t/T=0.25$ , (b)  $t/T=0.5$ , (c)  $t/T=0.75$  and (d)  $t/T=1.0$ .

These figures also feature an additional vorticity contour emerging from the downstream edge of the injection tube, which is common in all other cases as well. The vorticity emerging from the injection tube is always higher near the downstream edge, and they seem to incorporate with the vorticity of the jet boundary on each side. Pietrzyk et al. (1989) using short injection tube ( $L/d=3.5$ ) have suggested the presence of a separation “Experimental aerothermal characterization of a pulsating jet issuing in a crossflow: Influence of Strouhal number excitation on film cooling”

region inside the tube, which controls the vorticity level generating from the tube. They mentioned that these vorticities have significant influence on the turbulence field, establishing outside the hole at different blowing ratios.

### 5.5.3 Time-averaged rate of deformation

The time-averaged rate of deformation shown in figure (5.24a-c) are obtained from the flow configuration of  $\overline{M}=0.65, 1$  and  $1.25$  under steady blowing. For  $\overline{M}=0.65$ , the near downstream profile shows a positive peak due to the shear layer forming at the lower boundary of the jet, where the wake region is just initiated. For all cases of  $\overline{M}$ , the region of maximum rate of deformation always falls-out very close to the downstream edge of the hole. Kelso & al (1996) inferred from his experiments using a vertical jet in a crossflow that vortex break down occurs in the CVP near the pipe outlet due to the region of reverse flow. In the present case, any possibility of the existence of a reverse flow region is only limited to the case of higher blowing ratio. Moreover, under the current spatial resolution of the PIV, the evaluation of this region might possibly a bit inadequate as well. Therefore, a small region of substantial deformation existing near the jet outlet in almost every case requires more explanations. The flow field also features a maximum turbulence level in this region. It is usually acknowledged that the vorticity ejecting from the pipe deforms near the trailing edge due to the bending and the initial acceleration of the pipe flow and later on interacts with the mainstream flow. The mainstream flow entraining below the jet and moving towards the central plan of the jet could not be incorporated in the movement of CVP, as later is not fully established. For a  $35^\circ$  jet interacting with the mainstream flow at  $\overline{M}=1$  and  $\rho_i/\rho_\infty = 1$ , Lee et al. (1994) found that the CVP established fully after a streamwise distance of  $x/d=2$  that can incorporate and balance out the flow moving in with the secondary motion of the mainstream flow into the dynamics of CVP. The overall effect tied up with both the turbulent characteristics of jet flow at the hole exit and the entrainment of mainstream flow in that region, and might be considered a reason of increased rate of deformation. In the downstream flow, the maximum positive peak of the each profile always stays at the lower boundary of the jet. Apart from a streamwise distance of  $x/d=3.5$ , different regions of significant importance has already established in the flow field, and exhibits the zones of pronounced rate of deformation. The apparent peaks in the profiles correspond to three different regions of the flow field, which are the region of wake and the upper and lower boundary of the jet, as mentioned from the vorticity field.

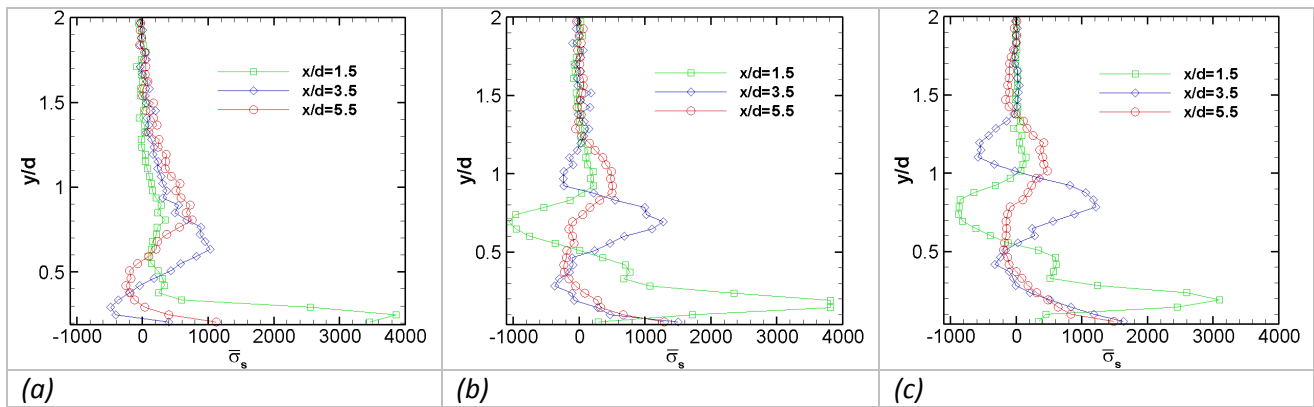
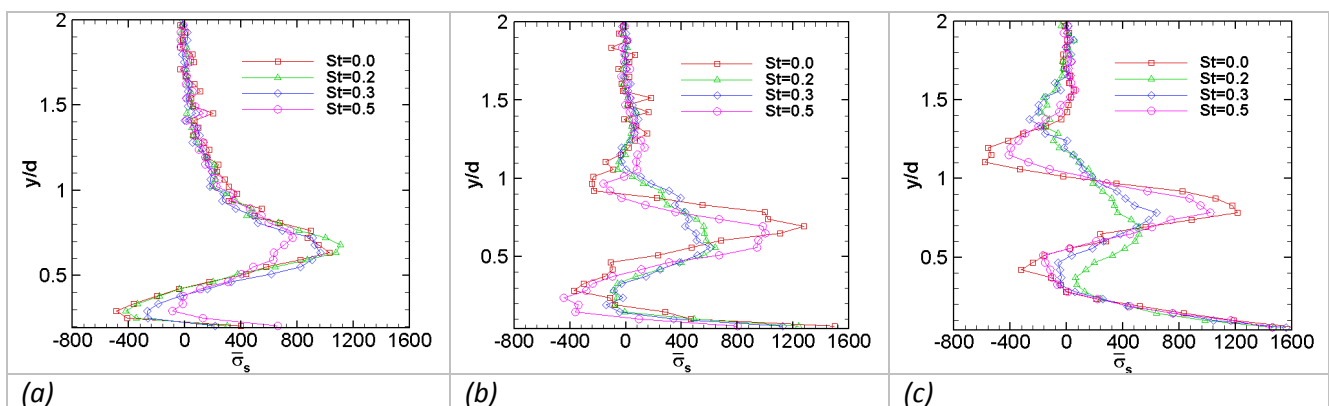


Figure (5. 24): Profiles of time-averaged rate of deformation  $\bar{\sigma}_s$  obtained from steady blowing cases ( $St=0$ ), lying at  $x/d=1.5, 3.5$  and  $5.5$ , (a)  $\bar{M}=0.65$ , (b)  $\bar{M}=1$ , (c)  $\bar{M}=1.25$ .

The profiles of time-averaged rate of deformation shown in figure (5.25a-f) are obtained from the flow configuration of  $\bar{M}=0.65, 1$  and  $1.25$ . The results shown in figure (5.25a-c) and figure (5.25d-f) are obtained from  $x/d=3.5$  and  $x/d=5.5$  of the central plane ( $z/d=0$ ). Comparison of different Strouhal number cases shows that the effect of imposed pulsation becomes significant as the blowing ratio increases. The steady blowing at  $\bar{M}=0.65$  maintains the flow of injectant fluid close to the wall. This results in a certain pattern of injectant distribution and the rate of deformation in the wake of the flow field and the lower boundary of the jet. Any modification from this condition due to imposed pulsation fails to maintain the similar distribution of the injectant fluid, as the wall is often presented to a situation where the flow rate of the injectant flow becomes much smaller compared to the mainstream flow, leading to a drastically low blowing ratio. In that case, the injectant flow loses its momentum much rapidly when flowing downstream at the wall. From the point of view of film cooling that actually indicates the lowering of the capacity of wall coverage. At higher blowing ratio of  $\bar{M}=1$  and  $1.25$ , the rate of deformation is more evolved in the boundary region of the jet. Under these conditions, the lowering of the rate of deformation at jet boundary on time-average basis for  $St=0.2$  and  $0.3$  weakens the strength of jet structure drawing the injectant flow away from the wall.



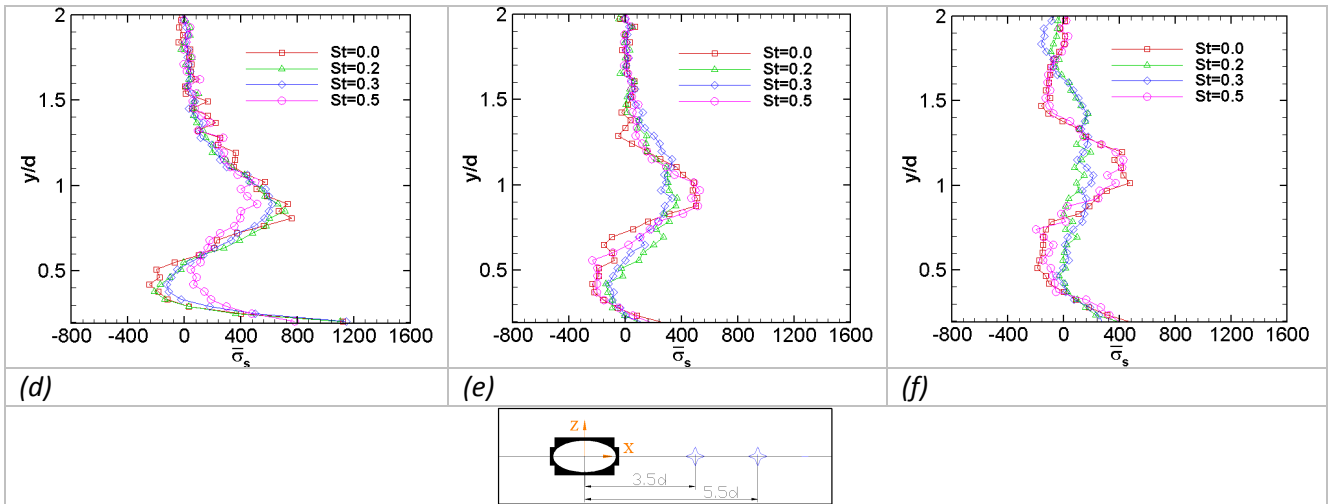


Figure (5. 25): Comparison of time-averaged profiles of  $\overline{\sigma_s}$ , lying at  $x/d=3.5$  and  $5.5$  of the hole central plane ( $z/d=0$ ), for different  $St$  (0, 0.2 0.3 and 0.5) examined under a range of  $\overline{M}$  (0.65, 1 and 1.25), while  $\overline{M}$  increasing column-wise and  $x/d$  increasing row-wise.

### 5.6 Vortex identification

The criteria of vortex identification based on a scalar functions,  $\Gamma_1$ , as proposed by Graftieaux et al. (2001), allows us to characterize the locations of the centre of the large-scale vortex.

$$\Gamma_1(P) = \frac{1}{S} \int_{M \in S} \frac{(PM \wedge U_M) \cdot z}{\|PM\| \|U_M\|} dS = \frac{1}{S} \int_S \sin(\theta_M) ds \dots\dots\dots(5. 5)$$

Where S is a two dimensional area surrounding P, M lies in S and z is the unit vector normal to the measurement plane.  $\theta_M$  represents the angle between the velocity vector  $U_M$  and the radius vector PM.  $\Gamma_1$  is a dimensionless scalar, with  $|\Gamma_1|$  bounded by 1. This bound is reached at the location of the vortex center if the vortex is axisymmetrical. Thus, the scalar function  $\Gamma_1$  provides a way to quantify the streamline topology of the flow in the vicinity of P and the rotation sign of the vortex.

Figures (5.26a-c) show the distribution of  $\overline{\Gamma_1}$  for steady blowing at  $\overline{M}=0.65, 1$  and  $1.25$ . Contours of  $\overline{\Gamma_1}$  give a good representation of the development of vortical structures resulting due to the oblique interaction of two flows. However, the contour legend shown in the figure contains fairly low values. There may be two reasons for that, the first one is due to the averaged representation of the results, where the value of  $\Gamma_1$  is averaged over a fixed location containing both lower and higher values resulting due to the instantaneous variation of the flow, and the second one is due to the fact that the main large-scale counter rotating vortex pair has vorticity in the direction of jet axis, which gradually bend to attain an

orientation parallel to the streamwise direction, as the flow evolves. The present view contains the relatively small-scale vortices linked with the vorticity of CVP. It can be seen that the mainstream flow covers the jet partially on the upstream side and the jet bending towards the streamwise direction, exits the hole with higher velocity near the downstream edge. This is indicated by the small portion of the upstream edge, which is dominated by the presence of mainstream flow. For  $\overline{M} = 0.65$ , the rolling of shear layer near the upstream edge of the jet is much lesser than the cases of  $\overline{M} = 1$  and  $\overline{M} = 1.25$ , as the interaction between two flows is less intense. The wake region lying underneath the jet is also smaller in size with a minor movement away from the wall. On the other hand, the flow at  $\overline{M} = 1.25$  is attributed with significant rolling of the shear layer and sizeable wake region lifting away from the wall pretty early in the downstream flow. It is important to note that the sign of the vortices in different regions of the flow are also distinguishable. The instantaneous field of  $\Gamma_1$  contains the vortices of different sign all over the domain. However the average field only shows the sign of vortex rotation most probable of that region. The sign of vortices generating in the boundary layer of the mainstream flow also experiences a partial blockage offered by the jet at the point of upstream interface, which may lead to a vortex system wrapping around the jet from the upstream side, usually referred as horseshoe vortices. However no clear indications of a strong and organized vortex system were detected during the initial testing performed with a 34 mm<sup>2</sup> region upstream of the hole along the center plane.

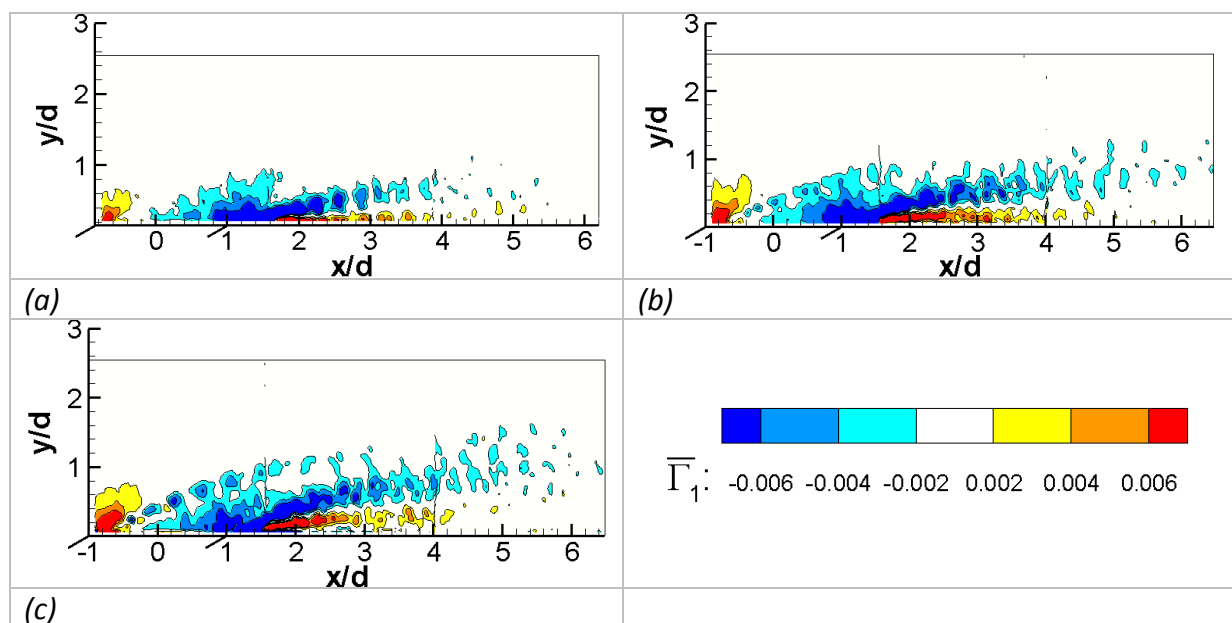


Figure (5. 26): The variation of  $\overline{\Gamma}_1$  computed for steady blowing, (a)  $\overline{M} = 0.65$ ; (b)  $\overline{M} = 1$ ; (c)  $\overline{M} = 1.25$ .

The signs of the upstream vortices, which off course do not tell much about the strength of their vorticity globally matches with the vorticity in the wake region for  $\overline{\Gamma}_1$  field.

The experimental study of jet-in-crossflow performed by Fric and Roshko (1994), as well as the DNS performed by Rudman (1996), suggested that the wake vorticity actually originates in the boundary layer of mainstream flow. Therefore, we might consider that the sign of rotation of the vorticity lying in the wake region are correct.

The effect of jet pulsation on the flow structures are visualized by using the  $\overline{\Gamma}_1$  scalar function. Figure (5.27a-c) shows the effect of pulsation at different times of pulsation period at  $St=0.2$  and  $\overline{M}=0.65$ . Pulsation seems to induce the mixing of the flows, pertaining to the wake region and the jet. However, the pulsation in this case seems to have minor influences on the flow distribution pattern, because the jet remains attached to wall over a significant length. At  $\overline{M}=0.65$  and  $St=0.3$ , as shown in figure (5.27d-f), the jet starts collapsing systematically after covering a certain distance at the wall during each period of pulsation. Such discontinuity in the injectant flow has adverse effects on the film cooling. At  $St=0.5$  and  $\overline{M}=0.65$ , the collapsing of the jet starts to take place much more rapidly and the flow evolving in the downstream contains large accumulations of jet and wake flows passing in alternate fashion, as shown in figure (5.27g-i). The vorticity locating near the upstream edge of the hole is expected to incorporate to the vorticity of the wake region during the flow evolution in the downstream region. At higher blowing ratio of  $\overline{M}=1$  and the jet pulsing at  $St=0.2$ , the increased jet momentum ends up carrying the jet flow to a higher wall-normal distance, before long it collapse, as shown in figure (5.28a-c). Under this configuration, the wall coverage is improved during the time span in which blowing ratio is lower than the mean value, as well as due to the lower entrainment of the mainstream flow responsible for a secondary motion at the wall in steady blowing case. At  $\overline{M}=1$  and  $St=0.3$ , figure (5.28d-f) shows early collapsing of the jet, and the large accumulations of the jet and the wake flow are spaced with short intermediate distances. At  $\overline{M}=1$  and  $St=0.5$ , the variations produced with pulsation could not established fully under short time span available between the successive periods and the flow tends to have a rippling jet trajectory of short pulsing spans, as shown in figure (5.28g-i). At  $\overline{M}=1.25$  and  $St=0.2$ , periodic variations of the jet flow spans over a larger distance in the wall-normal direction due to a most significant injectant flow rate than the accompanying blowing ratios, as shown in figure (5.29a-c). In case of  $\overline{M}=1.25$  and  $St=0.3$  shown in figure (5.29d-f), the more compact formation of alternate vorticity, as well as more clearer signs of the upstream vorticity incorporating with the vorticity of the wake are observed. At  $\overline{M}=1.25$  and  $St=0.5$ , as shown in figure (5.29g-i), the resulting flow field exhibits more frequent splitting of the jet and short span variations in the wall-normal direction like  $\overline{M}=1$  and  $St=0.5$ . This case, among the other cases of Strouhal numbers has a trajectory of segmented jet flow a bit similar to the one found in steady blowing.

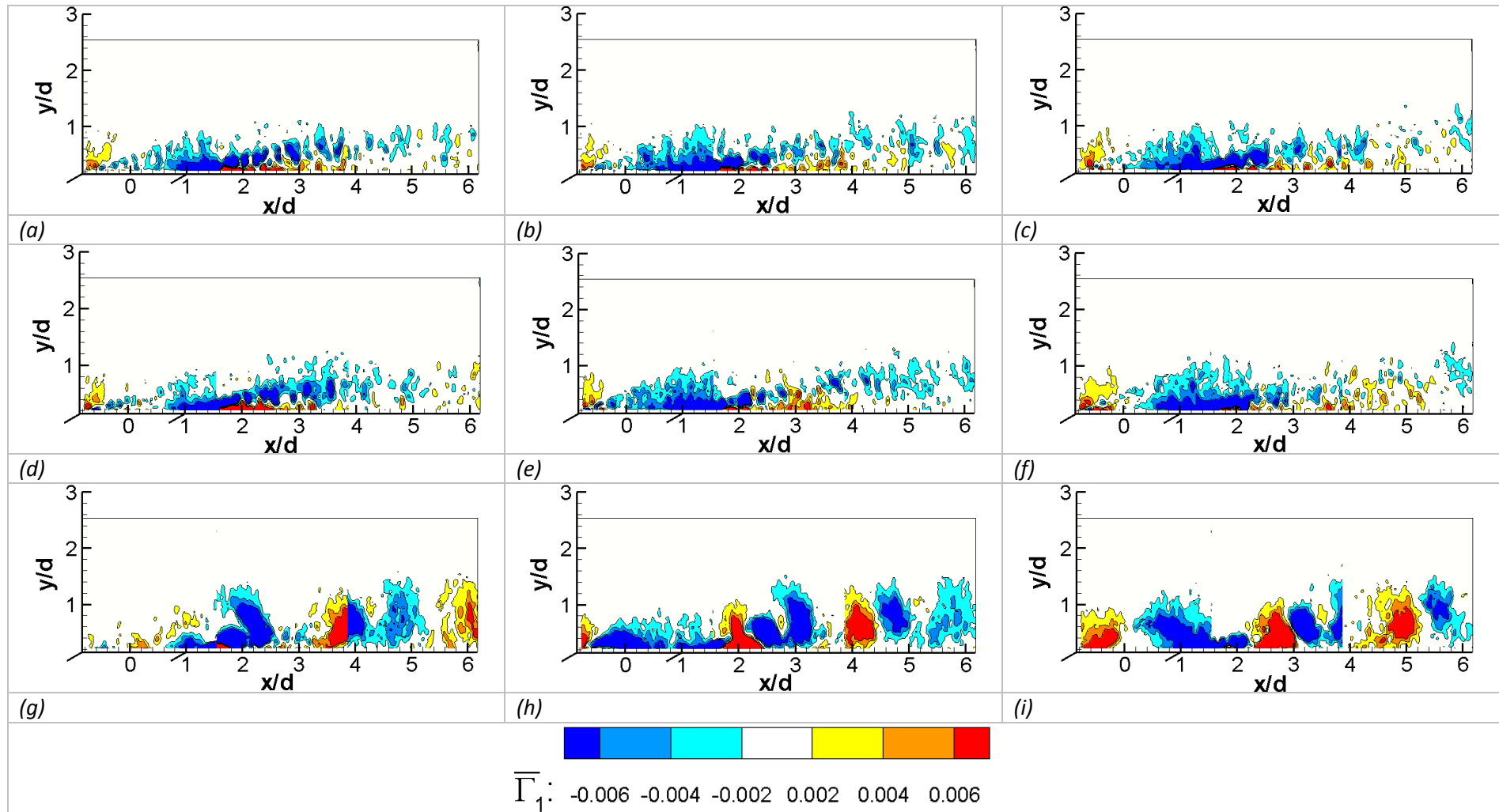


Figure (5. 27):  $\bar{\Gamma}_1$  at different time instants, for  $\bar{M} = 0.65$  and (a)  $t/T=0.1, St=0.2$ ; (b)  $t/T=0.36, St=0.2$ ; (c)  $t/T=0.66, St=0.2$ ; (d)  $t/T=0.1, St=0.3$ ; (e)  $t/T=0.38, St=0.3$ ; (f)  $t/T=0.68, St=0.3$ ; (g)  $t/T=0.12, St=0.5$ ; (h)  $t/T=0.38, St=0.5$ ; (i)  $t/T=0.67, St=0.2$ .

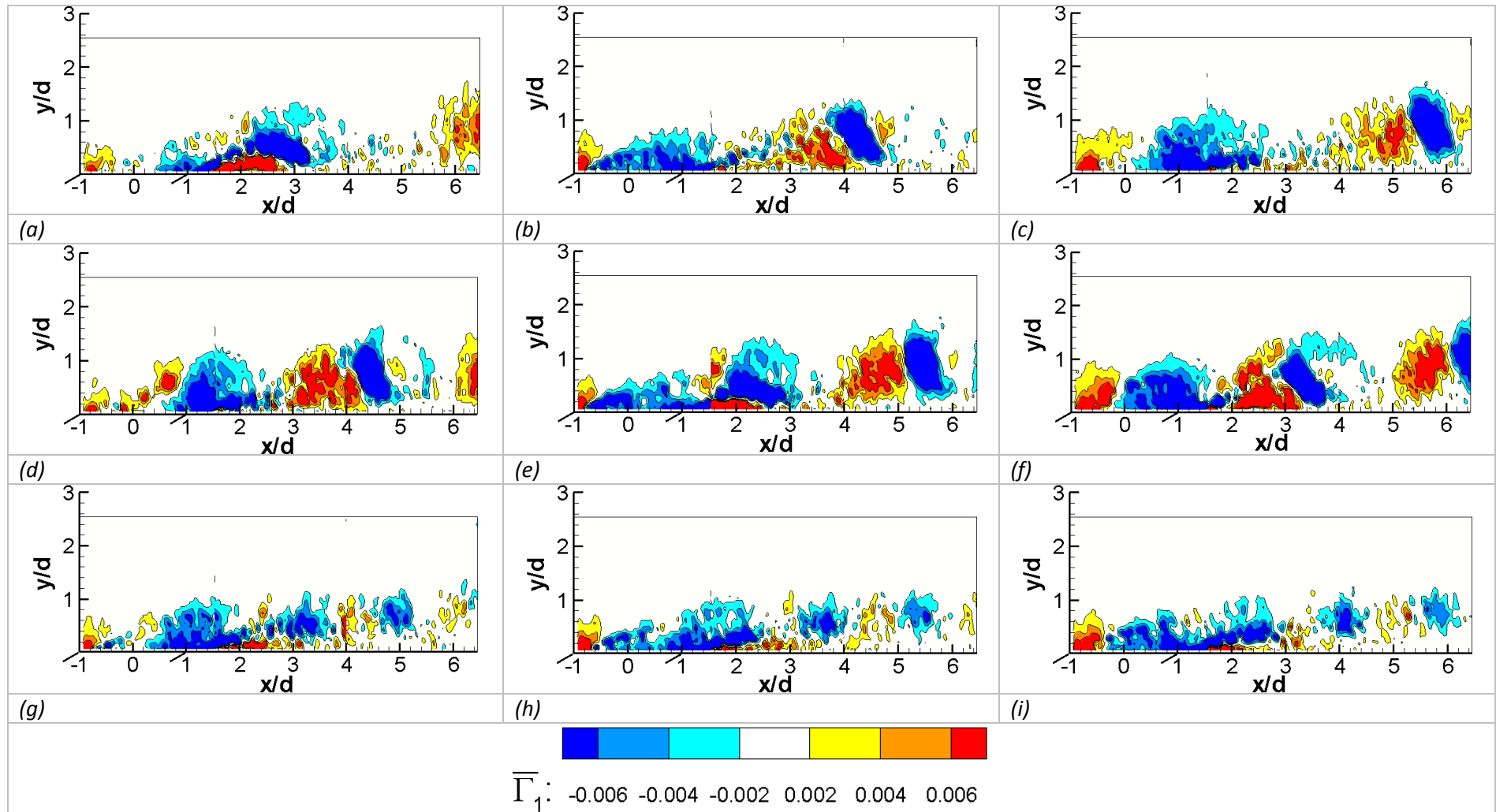


Figure (5. 28):  $\overline{\Gamma}_1$  at different time instants, for  $\overline{M} = 1$  and (a)  $t/T=0.07$ ,  $St=0.2$ ; (b)  $t/T=0.4$ ,  $St=0.2$ ; (c)  $t/T=0.73$ ,  $St=0.2$ ; (d)  $t/T=0.04$ ,  $St=0.3$ ; (e)  $t/T=0.38$ ,  $St=0.3$ ; (f)  $t/T=0.71$ ,  $St=0.3$ ; (g)  $t/T=0.19$ ,  $St=0.5$ ; (h)  $t/T=0.44$ ,  $St=0.5$ ; (i)  $t/T=0.69$ ,  $St=0.2$ .

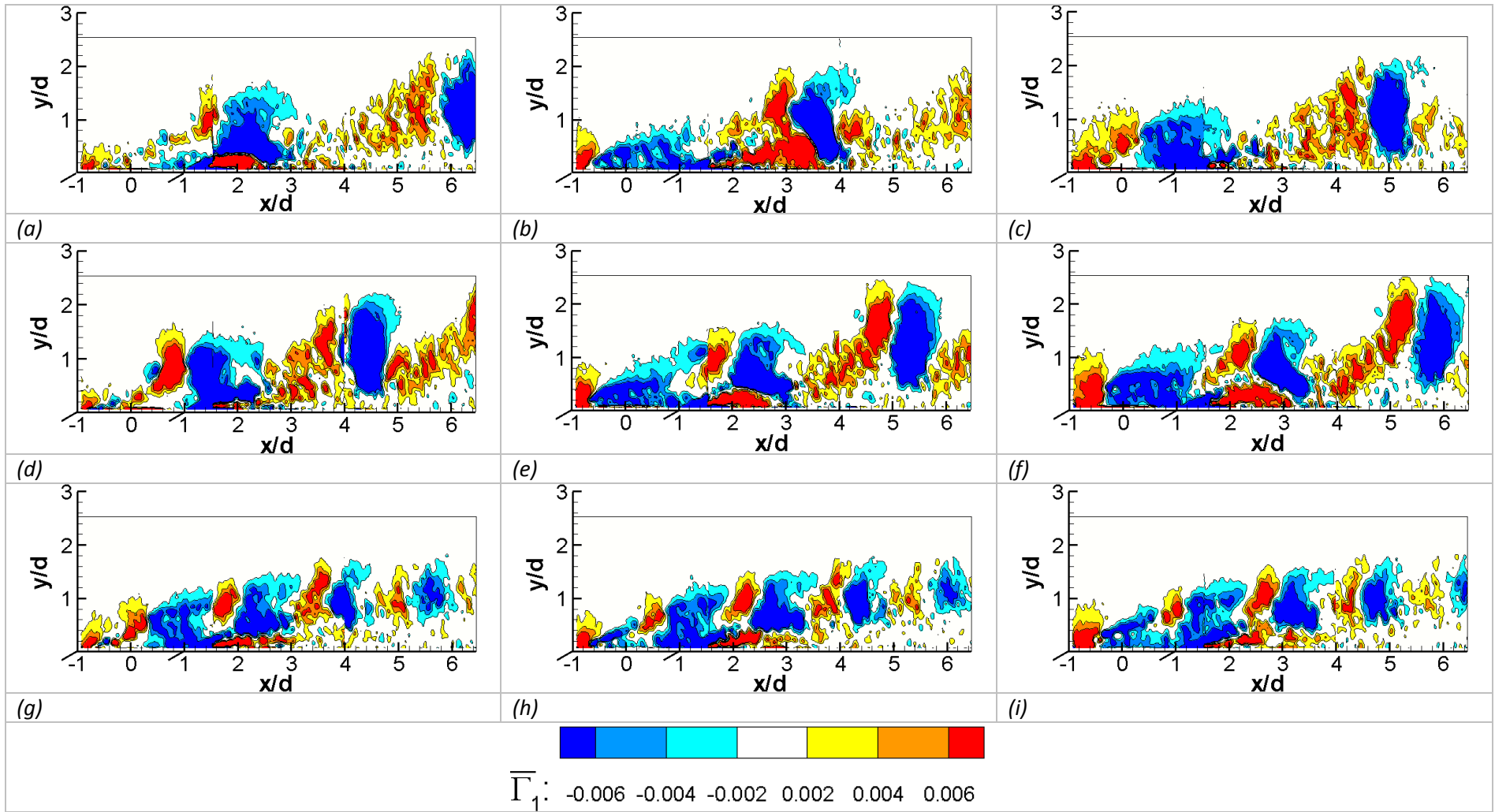


Figure (5. 29):  $\bar{\Gamma}_1$  at different time instants, for  $\bar{M} = 1.25$  and (a)  $t/T=0.06$ ,  $St=0.2$ ; (b)  $t/T=0.39$ ,  $St=0.2$ ; (c)  $t/T=0.73$ ,  $St=0.2$ ; (d)  $t/T=0.14$ ,  $St=0.3$ ; (e)  $t/T=0.47$ ,  $St=0.3$ ; (f)  $t/T=0.64$ ,  $St=0.3$ ; (g)  $t/T=0.12$ ,  $St=0.5$ ; (h)  $t/T=0.37$ ,  $St=0.5$ ; (i)  $t/T=0.62$ ,  $St=0.2$ .

## 5.7 Mass, momentum and energy conservation

### 5.7.1 Balance of mass (Continuity equation)

The gradient of the lateral component of the velocity ( $\partial W/\partial z$ ) can not be determined directly from the usual PIV results. However, it can be calculated by using the continuity equation along with few simplifications. The assumption of steady and incompressible flow is used to simplify the Eq. (5.6). As the Mach number of the interacting flows is quite low ( $Ma \ll 1$ ), and they are statistically stationary. Therefore, the simplified form of equation can be used to determine the velocity gradient in the unknown direction. Sum of the gradients of velocity components known through the measurements is called as the divergence of velocity.

$$\frac{\partial \rho}{\partial t} + \nabla \cdot (\rho \vec{v}) = 0 \quad \dots\dots\dots(5.6)$$

$$\nabla \cdot \vec{v} = \frac{\partial U}{\partial x} + \frac{\partial V}{\partial y} + \frac{\partial W}{\partial z} = 0 \quad \dots\dots\dots(5.7)$$

The estimate of the divergence of velocity allows us to figure out the phenomena of dilatation ( $\nabla \cdot \vec{v} > 0$ ) or contraction ( $\nabla \cdot \vec{v} < 0$ ) taking place in the flow field. However, the unavailability of the lateral component of the velocity and the assumption of  $\nabla \cdot \vec{v} = 0$  used for the determination of the gradient of the remaining component of the velocity would certainly halts the access to those informations.

#### **Time-averaged divergence of velocity**

The profiles of time-averaged divergence of velocity for different steady blowing ratios,  $\overline{M} = 0.65, 1$  and  $1.25$  are shown in figure (5.30a-c). The divergence of velocity shows the three dimensional nature of the flow. The trend of these profiles shows that the divergence of velocity or simply the divergence increases with the increase of blowing ratio. In general, the profiles of divergence seem to contain a negative peak in almost every case. The negative values of the lateral velocity component may suggest a higher value at the central plane, which is likely to reduce while moving away in the lateral direction. At a blowing ratio of  $\overline{M} = 0.65$ , the profile at the near downstream region ( $x/d=1.5$ ) shows that the divergence of velocity is higher near the lower boundary of the jet, and the weaker wake region possesses much lower values. In case of higher blowing ratios ( $\overline{M} = 1$  and  $1.25$ ), the divergence is high in a region lying between the wake and the lower boundary of the jet. At  $x/d=3.5$ , a region with higher divergence seems to lie in the wake region, also extending up to the lower boundary of the jet. At the final downstream station ( $x/d=5.5$ ), the three-dimensional characteristics seem to smooth out a bit, and the profiles have considerably weak divergence level at the lower boundary of the jet.

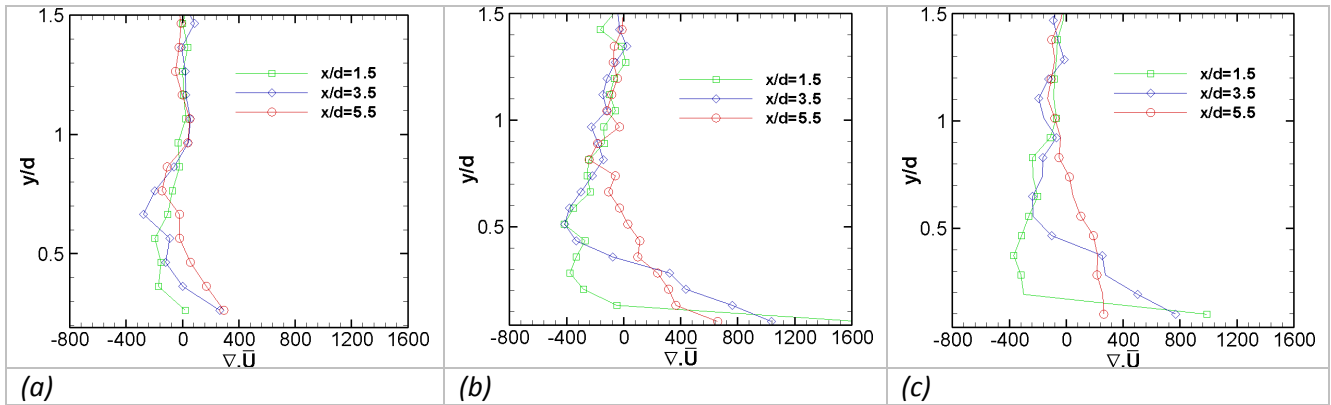


Figure (5. 30): Time-averaged profiles of divergence of velocity  $\nabla \cdot \bar{U}$  obtained from steady blowing cases ( $St=0$ ), lying at  $x/d=1.5, 3.5$  and  $5.5$ , (a)  $\bar{M} = 0.65$ , (b)  $\bar{M} = 1$ , (c)  $\bar{M} = 1.25$ .

### 5.7.2 Balance of momentum

The assessment of the different terms of momentum equation allows us to compare the role of these terms in the crossflow configuration and the trend of variation for these terms in case of different blowing ratios. The mean transport of momentum given by Eq. (5.8) is obtained after applying the Reynolds decomposition ( $U = \bar{U} + u$ ) to the instantaneous momentum equation.

$$\frac{\partial \bar{U}_i}{\partial t} + \bar{U}_j \cdot \frac{\partial \bar{U}_i}{\partial x_j} + \frac{\partial}{\partial x_j} \cdot (\overline{u_i v_j}) + \frac{1}{\rho} \cdot \frac{\partial \bar{P}}{\partial x_i} = \nu \cdot \frac{\partial^2}{\partial x_j \partial x_j} \bar{U}_i \quad \dots\dots\dots(5. 8)$$

In steady condition, different terms in the above equation are determined by using the results of TR-PIV, except the terms of pressure gradient. The term of pressure gradient can be determined from the difference of other terms. Different subterms of Eq. (5.8) can be described as follow;

- the subterms of convection corresponding to the spatial derivatives in each direction

$$C_{mom,x} = \bar{U} \left( d\bar{U} / dx + d\bar{V} / dx \right)$$

$$C_{mom,y} = \bar{V} \left( d\bar{U} / dy + d\bar{V} / dy \right)$$

- gradient of shear and normal stress component of Reynolds stresses

$$T_{mom,sh} = d\bar{uv} / dx + d\bar{uv} / dy$$

$$T_{mom,nor} = d\bar{u}^2 / dx + d\bar{v}^2 / dy$$

- Viscous diffusion and pressure gradient

$$D_{mom} = \nu(d^2\bar{V}/dx^2 + d^2\bar{U}/dy^2)$$

$$\pi_{mom} = 1/\rho.(d\bar{P}/dx + d\bar{P}/dy)$$

In the next section, different terms and subterms of momentum equation are presented after normalization. A star symbols used as a superscript over the symbol of any particular term indicates that the term is divided by  $\bar{U}_\infty^2/d$  for non-dimensionalization.

### 5.7.2.1 Terms of momentum equation, time-averaged results

The profiles of different quantities of momentum equation are shown in figure (5.31), for a steady blowing case of  $\bar{M} = 1$ . Figure (5.31a) contains the profiles of the subterms of momentum convection ( $C_{mom,x}^*$ ,  $C_{mom,y}^*$ ) and the total convection  $C_{mom}^*$ , as well as gradient of shear and normal stress component of Reynolds stresses ( $T_{mom,sh}^*$ ,  $T_{mom,nor}^*$ ) and the total of them  $T_{mom}^*$ . These profiles are obtained from a downstream location of  $x/d=1.5$  and  $z/d=0$ . The region, in which the peaks for various curves are found, is the region of large velocity gradient lying at the lower boundary of the jet. The peaks in the profiles of the gradient of Reynolds stresses lie slightly below this region. The contribution of the normal component of the gradient of Reynolds stresses is higher than the one because of shearing. On the other hand,  $C_{mom,x}^*$  is slightly higher than  $C_{mom,y}^*$  as the velocity gradient in  $C_{mom,x}^*$  is a multiplier of  $\bar{U}$ .

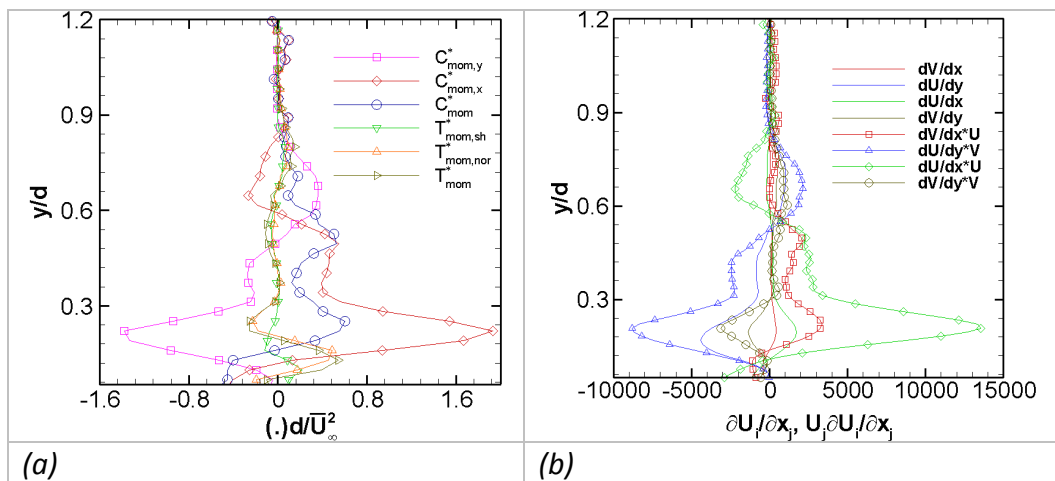


Figure (5. 31): (a) Profiles of the Subterms of momentum equation; (b) Contribution of different velocity gradients and the respective convection subterms; for  $\bar{M} = 1$  and  $St=0$  and a downstream location of  $x/d=1.5$  and  $z/d=0$ .

In order to understand the rule of different velocity gradient and the trend of individual terms of convection, a plot for various gradients is shown in figure (5.31b). It shows that in the lower boundary region of the jet,  $d\bar{U}/dy$  and  $d\bar{V}/dy$  have higher peaks of negative values, while the peak for  $d\bar{U}/dy$  being the dominant one. The other velocity

gradients ( $d\bar{U}/dx$  and  $d\bar{V}/dx$ ) have comparatively small positive peaks. Multiplication of these velocity gradients with the corresponding component of the local time-averaged velocity (derived from the tensor notation) provides a large positive peak for  $\bar{U}.d\bar{U}/dx$ .

The profiles of different terms of momentum equation are shown in figure (5.32a-f), for the steady blowing of  $\bar{M} = 0.65, 1$  and  $1.25$  ( $\bar{M}$  increasing row-wise in the array of subfigures). Figure (5.32a), (5.32c) and (5.32e) show the trends of the profiles extracted from  $y/d=0.2$  and  $z/d=0$ . Similarly, the profiles extracted from the near-field region of  $x/d=1.5$  and  $z/d=0$  are shown in figure (5.32b), (5.32d) and (5.32f). In case of  $\bar{M} = 0.65$ , the profiles shown in figure (5.32a) contain some initial peaks in the region lying upstream of the hole centre, which corresponds to the shearing region at the leading edge of the hole. At the downstream region, profile indicates some initial part of the developing wake region, which shows slight increment in both convection and the gradient of Reynolds stress. These profiles exhibit a change of sign along the length and thereby indicate the location of upper and lower boundary of the jet. In cases of higher blowing ratios ( $\bar{M} = 1$  and  $1.25$ ), the region of lower boundary of the jet is attributed by the higher variations and more prominent peaks, as shown in figure (5.32c) and (5.32e).

For  $\bar{M} = 0.65$ , figure (5.32b) shows that the contribution of the gradient of Reynolds stresses to the transfer of mean momentum is quite small compared to the convection term, which is basically due to the falling of the net value of the final sum, as the components of stress terms nearly level out each other. For  $\bar{M} = 1$ , the profile of convection term initially departing from a negative value shows a first peak near the lower boundary of the jet and then it shows a second peak in the potential core region, where the streamwise component of time-averaged velocity is maximum. The negative value of the profile below the jet is due to  $d\bar{U}/dx$ . The convection term seems to remain positive for a wall-normal distance superior than  $x/d \approx 0.2$ . The term representing the gradient of Reynolds stresses contains a negative and a positive peak roughly in the region of wake and the lower boundary of the jet. For  $\bar{M} = 1.25$ , the trend of the variation of profile shows that the locations of higher peaks of the convection and the Reynolds stress gradient are nearly identical to the flow filled regions observed for  $\bar{M} = 1$ . However, the peak in the potential core region is not so prominent for the convection term.

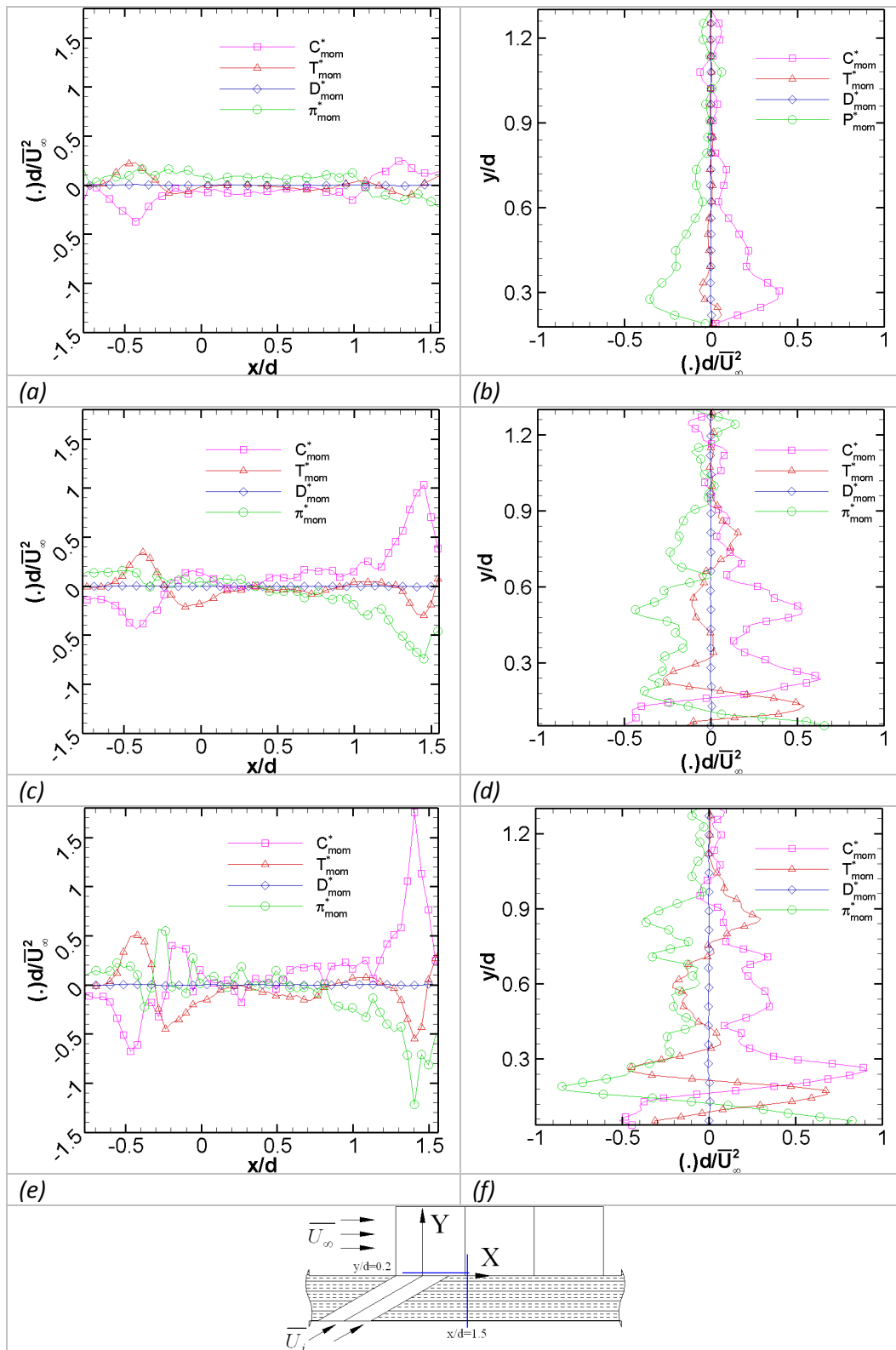


Figure (5. 32): Profiles of the subterms of momentum equation lying at, (a)  $y/d=0.2$  and (b)  $x/d=1.5$  for  $M = 0.65$ , (c)  $y/d=0.2$  and (d)  $x/d=1.5$  for  $M = 1$ , and (e)  $y/d=0.2$  and (f)  $x/d=1.5$  for  $M = 1.25$ .

### 5.7.2.2 Convection subterm, phase-averaged results

Figure (5.33a-f) shows the comparison of time-averaged results of the convection subterm,  $(C_{mom,y}^* = \overline{V}(d\overline{U}/dy + d\overline{V}/dy))$ , for different Strouhal numbers cases studied for different configurations of blowing ratio. The profiles are obtained from the downstream location of  $x/d=3.5$  and  $5.5$  of the central plane ( $z/d=0$ ) to show the comparisons of different pulsing cases in figure (5.33a-c) and figure (5.33d-f) respectively. At a downstream location of  $x/d=3.5$ , the different regions of the flow interpreted from these profiles corresponds well with the profiles of vorticity. For  $\overline{M}=0.65$ , the pulsation seems to have only minor effects on the convection term of momentum transport, and only the pulsation at  $St=0.5$  causes some reduction near the lower boundary of the jet. At the blowing ratio of  $\overline{M}=1$  and  $1.25$ , the case of steady blowing ( $St=0$ ) at  $x/d=3.5$  has superior peaks than the other cases of pulsation. Moreover, the value of  $C_{mom,y}^*$  situating at the upper and lower boundary of the jet and the wake region reduces greatly with the pulsation at  $St=0.2$  and  $0.3$  compared to the case of steady blowing and the case of  $St=0.5$ .

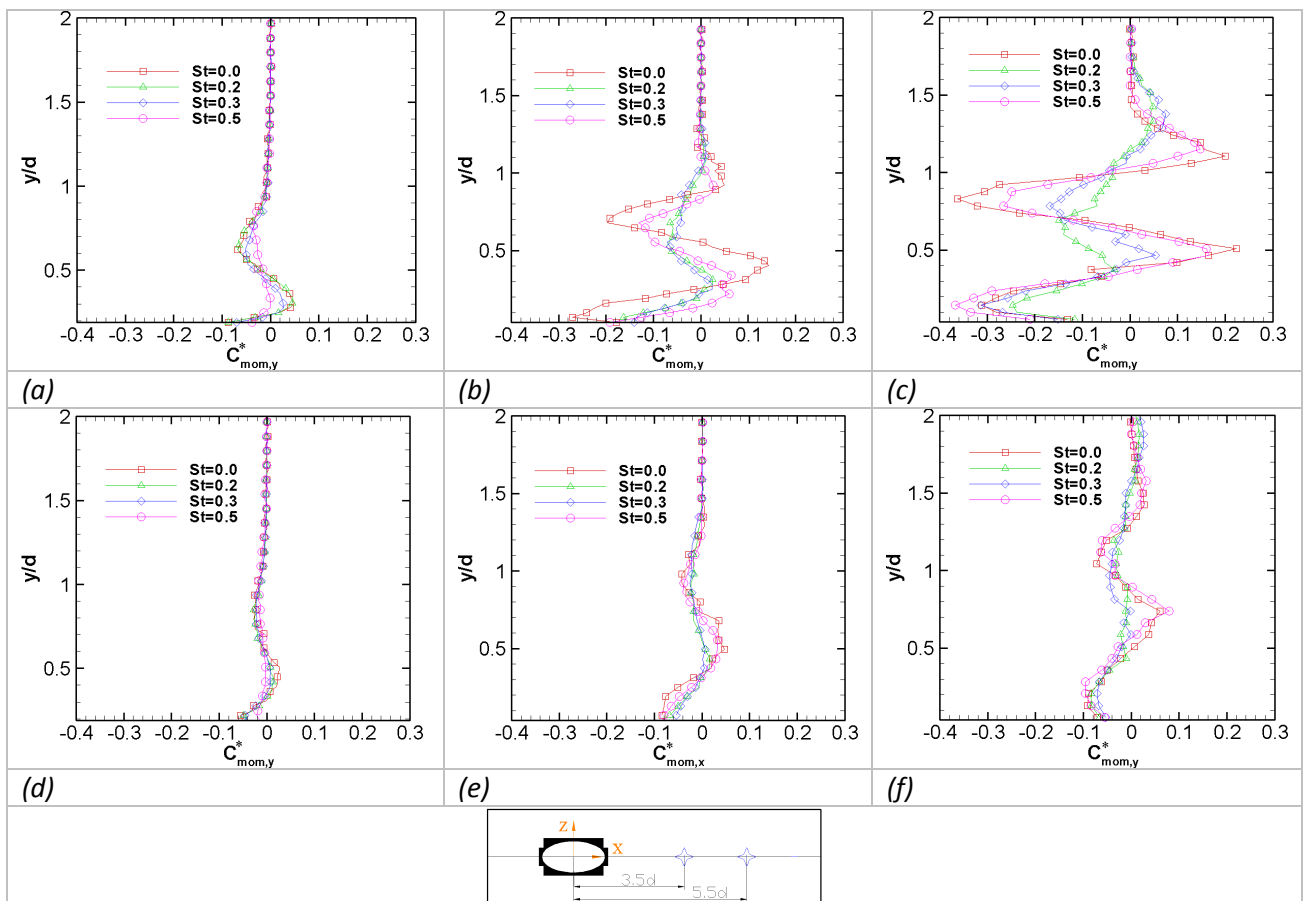


Figure (5. 33): Comparison of the profiles of  $C_{mom,y}^* = \overline{V}(d\overline{U}/dy + d\overline{V}/dy)$  lying at  $x/d=3.5$  and  $5.5$  of the hole central plane ( $z/d=0$ ) for different  $St$  (0, 0.2, 0.3 and 0.5) examined under a range of  $\overline{M}$  (0.65, 1 and 1.25), while  $\overline{M}$  increasing column-wise and  $x/d$  increasing row-wise.

The decrease in  $C^*_{\text{mom},y}$  at the lower boundary of the jet is about 65% and 78% for  $\overline{M}=1$  and  $\overline{M}=1.25$  at  $St=0.2$  compared to steady blowing. At downstream location of  $x/d=5.5$ , an overall reduction of  $C^*_{\text{mom},y}$  in the regions of pertinent velocity gradient seems to occur much rapidly.

### 5.7.3 Balance of energy

The assessment of the different terms of the equation of turbulent kinetic energy and energy balance performed in the most critical zones of the flow allows us to compare the rule of these terms in the crossflow configuration and the trend of the variation of these terms in case of different blowing ratios. Eq. (5.9) indicates the balance of energy transport under steady flow condition.

$$\overline{U}_i \cdot \frac{\partial(0.5\overline{q^2})}{\partial x_i} + \frac{\partial}{\partial x_i} \left( \frac{1}{2} \overline{u_i q^2} \right) + \frac{\partial}{\partial x_i} \left( \frac{1}{\rho} \overline{P u_i} \right) + (\overline{u_i v_j}) \cdot \left( \frac{\partial \overline{U}_j}{\partial x_i} \right) + \overline{\varepsilon} = 0 \quad \dots\dots\dots(5.9)$$

The pressure term in the above equation is determined by the difference of other terms. The turbulent kinetic energy is defined as;  $\overline{q^2} = \overline{u^2} + \overline{v^2} + \overline{w^2}$ . The unknown rms-velocity in the transverse direction of the flow ( $\overline{w^2}$ ) is determined by using the approximation of  $\overline{w^2} = (\overline{u^2} + \overline{v^2})/2$ . This approximation was previously used by Cutler and Johnston (1989), and Fernando and Smits (1990) in the two dimensional study of the turbulent boundary layer involving an adverse pressure gradient, where measurements were performed by using crossed-wire anemometer. Cutler and Johnston (1989) studied the relaxation of the turbulent boundary layer downstream of separation and reattachment, which were simulated in a wind tunnel by placing a rectangular fence in the upstream boundary layer. As, in the preset study, the measurements of the flow field are only limited to the central plane. Therefore, the implementation of the assumption, followed in the reference articles, looks somewhat reasonable. According to the set of results available in the present experiments, the tensor notations can be used to derive various subterms of the energy equation.

- subterms of convection

$$C_{k,x} = \overline{U} / 2 \cdot d(\overline{q^2}) / dx$$

$$C_{k,y} = \overline{V} / 2 \cdot d(\overline{q^2}) / dy$$

- subterms of turbulent transport

$$T_{k,x} = 1/2 \cdot d(\overline{u \cdot q^2}) / dx$$

$$T_{k,y} = 1/2.d(\overline{v.q^2})/dy$$

- subterms of pressure transport

$$\pi_{k,x} = 1/\rho.d(\overline{u.p})/dx$$

$$\pi_{k,y} = 1/\rho.d(\overline{v.p})/dy$$

- subterms of production

$$P_{k,sh} = \overline{uv}(d\overline{U}/dy + d\overline{V}/dx)$$

$$P_{k,nor} = \overline{u^2}.d\overline{U}/dx + \overline{v^2}.d\overline{V}/dy$$

- term of rate of dissipation

$$\varepsilon_k = \overline{v.\omega_z^2}$$

In the next section, different terms and subterms of energy equation are presented after normalization. A star symbols used as a superscript over the symbol of any particular term indicates that the term is normalized by using  $\overline{U_\infty^3}/d$ .

### 5.7.3.1 Terms of Energy equation, time-averaged results

The profiles of different quantities of energy equation are shown in figure (5.34), for a steady blowing condition of  $\overline{M} = 1$ . Figure contains the profiles of the subterms of convection corresponding to the spatial derivative in each direction ( $C^*_{k,x}$ ,  $C^*_{k,y}$ ) and the total convection  $C^*_k$ , as well as the subterms of production that are multiple of turbulent shear stress ( $P^*_{k,sh}$ ) and the subterms of production that are multiple of turbulent normal stress ( $P^*_{k,nor}$ ) along with the total production ( $P^*_k$ ). The profiles are obtained from a downstream location of  $x/d=1.5$  and  $z/d=0$ . Figure (5.34) shows that the peak values of different convection term lie at a similar distance from the wall, while the peak of the total production term,  $P^*_k$ , lies at a slightly lower height. Higher wall-normal location of the peak of convection term is possibly due to the mean velocities, which are the multiplier of the convection term, and are maximum in the internal region of the jet flow. There is also a slight difference in the peak value of the production subterms pertaining to the normal and shear stresses. It shows that  $P^*_{k,sh}$  is higher in the lower part of mixing layer region. The peak of  $P^*_{k,nor}$  seems to correspond better to the location of lower boundary of the jet specified from the criteria of vorticity. It should be noticed that the peak of  $P^*_{k,nor}$  is higher than  $P^*_{k,sh}$ . Andreopoulos and Rodi (1984) have also observed such trends in case of a vertical jet issuing into a cross-stream flow with a blowing ratio of  $\overline{M} = 0.5$ . They particularly highlight the zone near the upstream edge of the hole exit for such results. They reasoned out that having

$d\bar{W}/dz$  an order of magnitude higher than the  $d\bar{U}/dy$  and  $d\bar{V}/dx$  produces considerable turbulent energy due to the lateral divergence of the flow in the upstream part of the edge of the exit. For the profiles shown in figure (5.34), the contribution of the  $P_{k,nor}^*$  to the overall production in the peak region is 62%. Furthermore, it can be noticed that the normal-stress production have negative value below the jet due to  $d\bar{U}/dx$ , see figure (5.31b). Results of Andreopoulos and Rodi (1984) also indicate a small region of negative production for a profile lying at  $x/d=4$  and  $z/d=0$ .

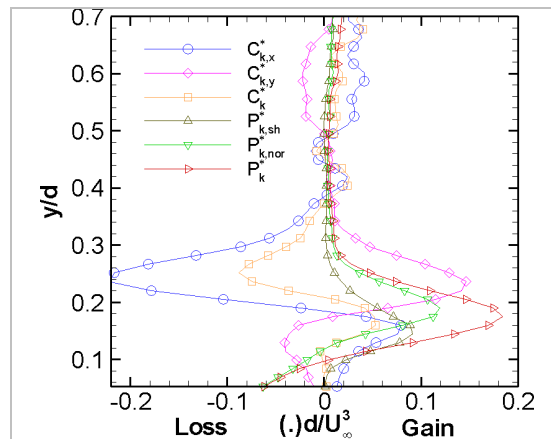


Figure (5. 34): Profiles of the subterms of energy equation for  $\bar{M} = 1$  and  $St=0$ , lying at a location of  $x/d=1.5$  and  $z/d=0$

Due to strong three-dimensional characteristics of the flow, it is hard to characterize the relative importance of the normal- and shear-stress production in different regions of the flow. The energy balance shown in the present study, only gives a tentative picture of the energy transport, as the data in the third dimension of the flow is not available. A qualitative comparison of the present results with Andreopoulos and Rodi (1984), and Muppidi and Mahesh (2007) is not always consistent because of the lack of information of the flow in the third dimension, as well as the difference in the configuration of injectant flow, since the jet is issuing perpendicularly to the mainstream flow in the given references. The energy equation applied to the plane of symmetry ( $z/d=0$ ) by Andreopoulos and Rodi (1984) includes an additional term for normal stress production  $(\overline{w^2} - \overline{v^2}).d\bar{W}/dz$  compared to the present study, which produces significant energy near the upstream edge of the hole in their case. Moreover, to obtain the energy dissipation rate, they used the spectra of velocity fluctuation, as well as the difference of the other terms to compare the results of dissipation rate. However, in the present case, the rate of dissipation was determined by calculating the root-mean-square of the vorticity in the lateral direction of the flow,  $\varepsilon_k$ .

In order to look at the dominance of the shear-stress production as was mentioned earlier, the percentage of normal-stress production with respect to the shear-stress production is shown in figure (5.35a) and (5.35b). It can be observed that the region

containing dominant production due to shear-stress locating near the upstream edge of the jet and the mixing layer region lying at the bottom of the jet seems comparatively wider for the lower blowing ratio ( $\bar{M} = 0.65$ ). The regions with dominant  $P_{k,nor}^*$  are actually blanked in the figures.

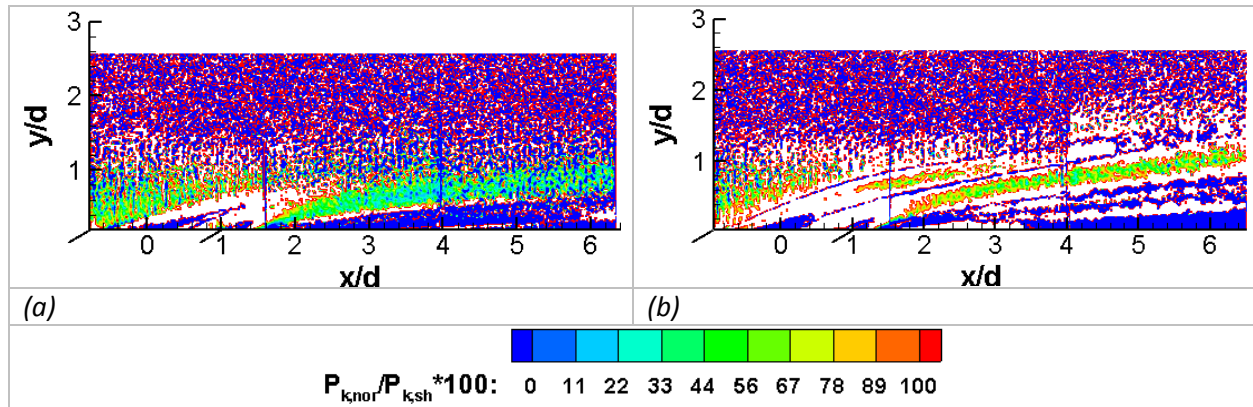
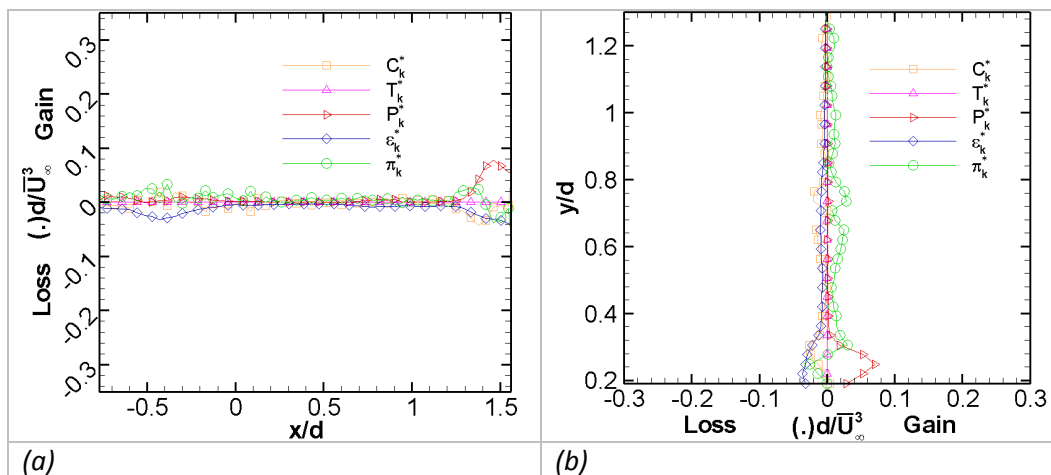


Figure (5. 35): Percentage of normal-stress production with respect to the shear-stress production in steady blowing ( $St=0$ ), (a)  $\bar{M} = 0.65$  and (b)  $\bar{M} = 1$ .

The profiles of different terms of energy equation are shown in figure (5.36a-f), for the steady blowing of  $\bar{M} = 0.65, 1$  and  $1.25$  ( $\bar{M}$  increasing row-wise in the array of subfigures). Figure (5.36a), (5.36c) and (5.36e) show the profile extracted from  $y/d=0.2$  and  $z/d=0$ . The profiles extracted from the near-field region of  $x/d=1.5$  and  $z/d=0$  are shown in Figure (5.36b), (5.36d) and (5.36f). For  $\bar{M} = 0.65$ , the profiles shown in Figure (5.36a) and (5.36b) indicate that the role of the turbulent transport is considerably small compared to the other terms. The peak in horizontal profile locating near the upstream edge of the hole corresponds to the leading edge boundary of the jet. On the lee side of the hole, the production of energy dominates and the transport of energy due to the convection term stays comparatively low. The maximum of the production of turbulent kinetic energy always locates near the lee side of the hole in all cases. Andreopoulos and Rodi (1984) has shown that at the downstream region of  $x/d=4$  the shear-stress production is considerably higher than the normal stress, for  $\bar{M} = 0.5$ . However in the present results, all these term decays quite rapidly even at the downstream location of  $x/d=3.5$ . The peak value of the total production at  $x/d=3.5$  is only 14% of the peak value measured at  $x/d=1.5$ . At the downstream location of  $x/d=1.5$ , the shear-stress production is slightly higher than the normal-stress production, and the contribution of the  $P_{k,sh}^*$  to the overall production in the peak region is 60%. For  $\bar{M} = 1$ , the profiles shown in Figure (5.36c) and (5.36d), as well as for  $\bar{M} = 1.25$ , shown in Figure (5.36e) and (5.36f) indicate that the convection is bit intermittent at the jet boundary lying near the upstream edge of the hole. At the downstream location of  $x/d=1.5$ , the peak value of the normal-stress production is higher than the peak value of

shear-stress production, because of  $d\bar{U}/dy > d\bar{U}/dx$  and  $\overline{uv}.d\bar{U}/dy < \overline{u^2}.d\bar{U}/dx$ . However, at the lower side of the mixing layer, the shear-stress production is higher than the normal-stress production. The contribution of the  $P_{k,sh}^*$  to the overall production in the peak region is 38% and 26% for  $\bar{M} = 1$  and 1.25 respectively. Moreover, in the mixing layer region, the total production is roughly about 2.4 times the dissipation, compared to 1.5 mentioned by Andreopoulos and Rodi (1984). With different approximations mentioned above, a rough estimate for  $(\overline{w^2} - \overline{v^2}).d\bar{W}/dz$  was found to be 5%, 10% and 10% of the peak value of normal-stress production for  $\bar{M} = 0.65, 1$  and 1.25 respectively, at a streamwise location of  $x/d=1.5$ .

The qualitative similarities found in the behavior of the present flow and the reference flow are the appearance of peak of production and dissipation term at the upstream edge of the jet and at the region of mixing layer lying at the bottom of the jet, as well as the appearance of higher normal-stress production compared to the shear-stress production at various regions (see figure (5.35) for details). One of the inconsistencies between the present results and the reference (Muppidi and Mahesh 2007) is the role of turbulent transport, which appears significantly small compared to the other terms in the present study. In the reference article, this term is shown to be significant on the center streamlines (such as;  $x/d=0.11$  and  $y/d=3.22$ , with origin at the hole centre) and less important on the jet edge, while employing a vertical jet and a blowing ratio of 5.7 in his study.



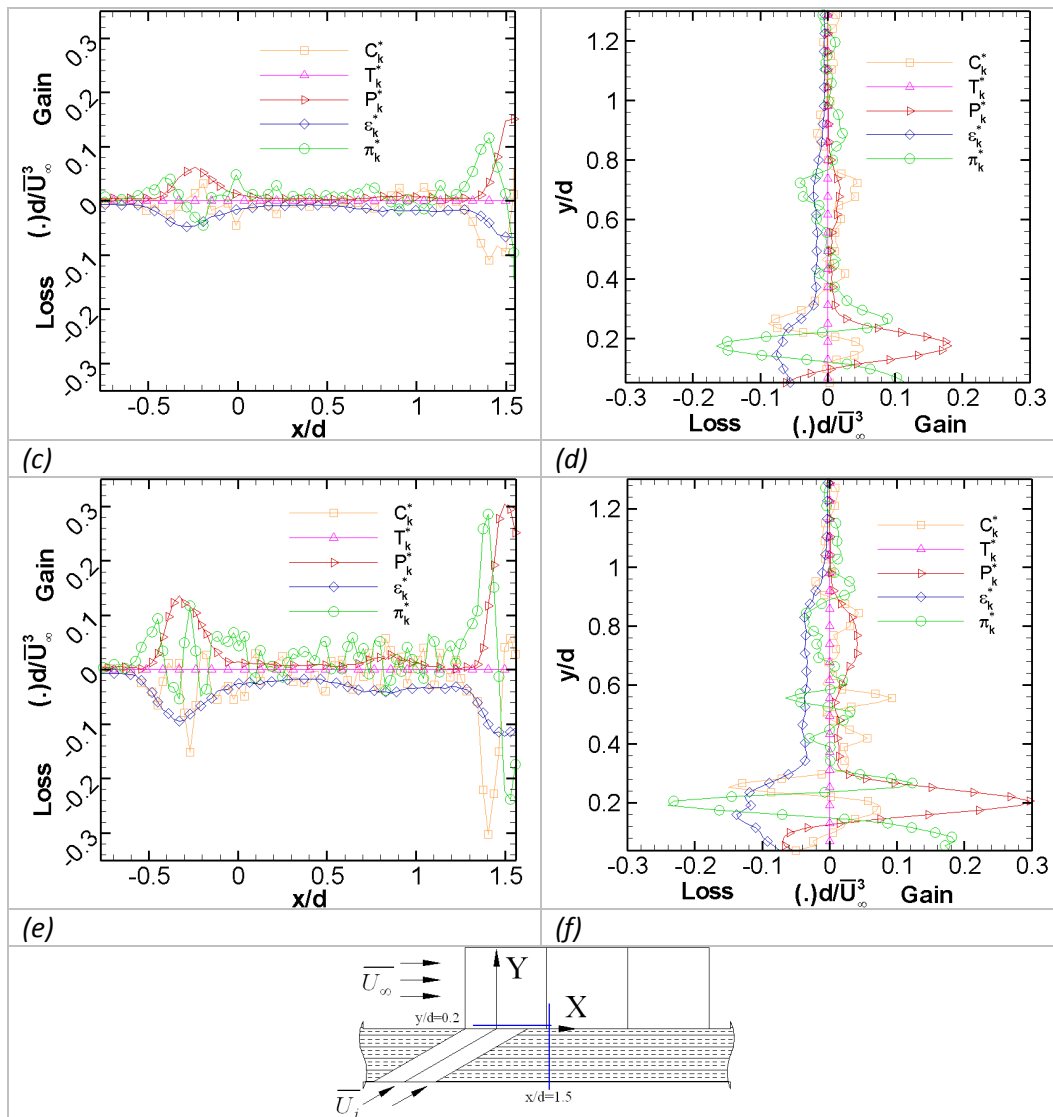


Figure (5. 36): Profiles of the subterms of energy equation lying at, (a)  $y/d=0.2$  and (b)  $x/d=1.5$  for  $\bar{M} = 0.65$ , (c)  $y/d=0.2$  and (d)  $x/d=1.5$  for  $\bar{M} = 1$ , and (e)  $y/d=0.2$  and (f)  $x/d=1.5$  for  $\bar{M} = 1.25$ .

### 5.7.3.2 Time-averaged turbulent kinetic energy

Figure (5.37a-i) presents the comparison of time-averaged turbulent kinetic energy  $\overline{q^2}/(2\overline{U_\infty^2})$  (where;  $\overline{q^2} = 1.5(\overline{u^2} + \overline{v^2})$ ) for different Strouhal numbers cases studied for the flow configuration of different blowing ratios,  $\bar{M} = 0.65, 1$  and  $1.25$ . The profiles are obtained from the downstream location of  $x/d=1.5, 3.5$  and  $5.5$  of the central plane ( $z/d=0$ ), and show the comparisons of different pulsing cases in figure (5.37a-c), figure (5.37d-f) and figure (5.37g-i) respectively. It can be observed that the pulsation influences the distribution of  $\overline{q^2}/(2\overline{U_\infty^2})$  greatly at some particular Strouhal numbers. For  $\bar{M} = 0.65$ , the level of turbulent kinetic energy due to the pulsation induces only slightly at  $St=0.5$ . The increase in turbulent kinetic energy below the jet seems to influence the flow in the wake region. At  $x/d=1.5$ , an increase of about 39% in  $\overline{q^2}/(2\overline{U_\infty^2})$  is observed with respect to the peak lying at

the lower edge of the jet boundary under steady blowing, while at  $x/d=5.5$ , such increase in  $\overline{q^2}/(2\overline{U_\infty^2})$  almost seems to level out to the value of steady blowing. The amount of energy generated due to turbulence becomes significant as the blowing ratio increases, covering the region across the jet boundaries and the wake region.

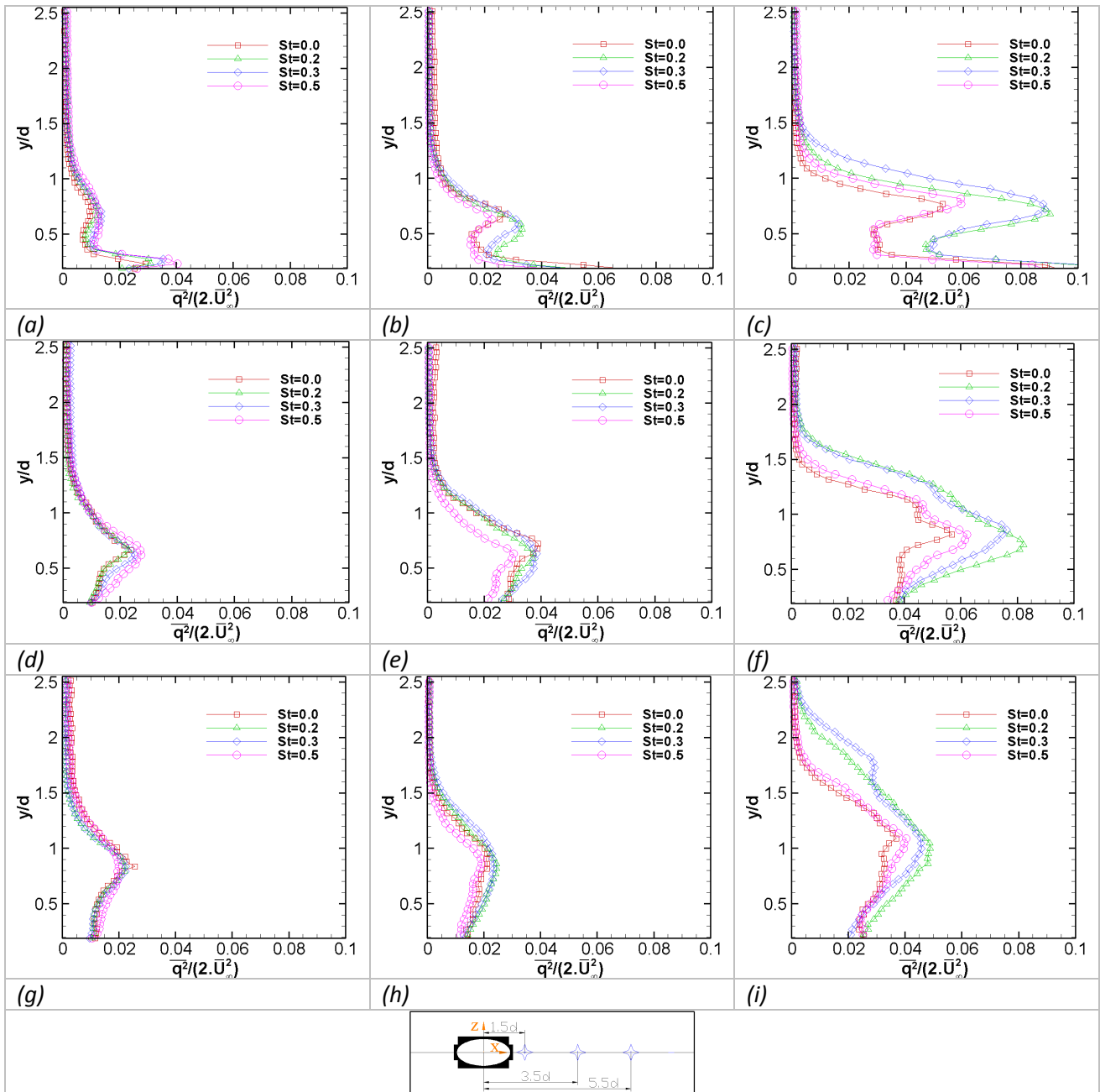


Figure (5. 37): Comparison of time-averaged profiles of  $\overline{q^2}/(2\overline{U_\infty^2})$ , lying at  $x/d=1.5, 3.5$  and  $5.5$  of the hole central plane ( $z/d=0$ ), for different  $St$  ( $0, 0.2, 0.3$  and  $0.5$ ) examined under a range of  $\overline{M}$  ( $0.65, 1$  and  $1.25$ ), while  $\overline{M}$  increasing column-wise and  $x/d$  increasing row-wise.

At  $\overline{M}=1$  and  $St=0.2$ , the increase in  $\overline{q^2}/(2\overline{U_\infty^2})$  compared to steady blowing is roughly about 50% at  $x/d=1.5$ , which decreases to about 16% at the downstream location of

“Experimental aerothermal characterization of a pulsating jet issuing in a crossflow: Influence of Strouhal number excitation on film cooling”

$x/d=5.5$  for the peak value lying near the lower boundary of the jet. Moreover, for a case of  $\overline{M}=1.25$  and  $St=0.3$ , it is roughly about 56 % at  $x/d=1.5$  and about 30 % at  $x/d=5.5$ . The pulsing effects seem to sustain longer for  $\overline{q^2}/(2\overline{U_\infty^2})$  in case of higher blowing ratio.

### 5.7.3.3 Phase-averaged production of kinetic energy

Figure (5.38a-d) shows the distribution of the production of turbulent energy at different times of the period of pulsation, for  $St=0.2$  and  $\overline{M}=1$ . The zone of the higher rate of turbulent production always located at the region of strong shear layer, which undergoes a change of strength in following periodic variations of injectant flow rate. In the wake region, the contours of negative production can also be observed, which are predominantly of lower magnitudes. The region of lower jet boundary always delivers higher production rate. At the time instant of  $t/T=0.41$ , the region of maximum production extends up to  $x/d \approx 4$  in the downstream flow. Since, the pulsation cases with lower  $St$  increase both normal- and shear-stresses in the regions of jet boundaries and the wake. Therefore, some important variation in the distribution of the production also takes place, which includes an increase of the local value of positive production and the variation in the length of the zone of negative production primarily governed by the mean velocity gradients closer to the wall. At this instant, the peak value of production at  $x/d=3$  is increased by 24% compared to the case of steady blowing.

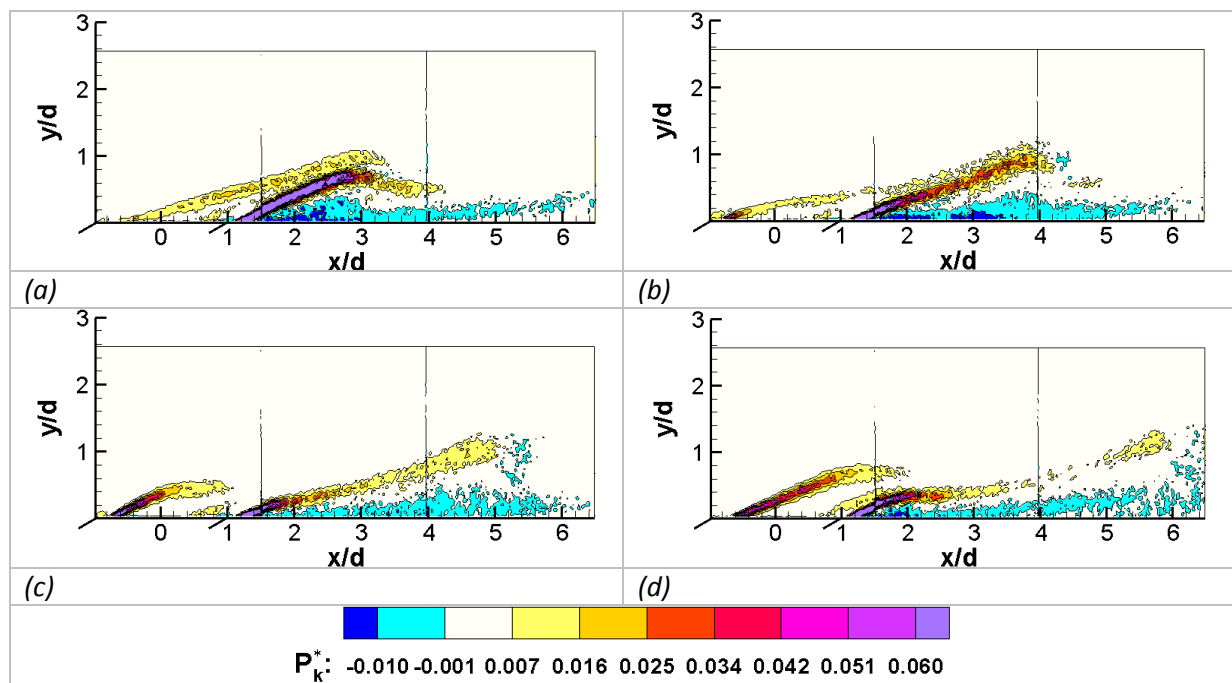


Figure (5. 38): Production of turbulent kinetic energy  $P_k^*$ ,  $\overline{M}=1$ ,  $St=0.2$ ; (a)  $t/T=0.19$ , (b)  $t/T=0.41$ , (c)  $t/T=0.63$  and (d)  $t/T=0.86$ .

At  $t/T=0.63$ , the injectant flow starts to reoriginate from the hole and the flow on the downstream side have lower Reynolds stresses levels, which gives lower production in all significant regions of the flow. At this instant, the instantaneous blowing ratio of the interacting flows is smaller than the average blowing ratio. Finally at  $t/T=0.86$ , the increase in jet velocity, approaching towards the maximum causes deeper penetration of the jet in the mainstream. This increases the velocity gradients establishing between two flows as well as the Reynolds stresses to give higher production of turbulent kinetic energy.

#### 5.7.3.4 Phase-averaged energy dissipation rate

Figure (5.39a-d) shows the distribution of energy dissipation rate  $\varepsilon_k$  at different time of the period of pulsation, for  $St=0.2$  and  $\overline{M}=1$ . In the figure below,  $\varepsilon_k$  is drawn with contour legends similar to ones shown in the figure (5.38) for production term (except the negative ones). It can be observed that the energy dissipation due to viscous effects covers a wider area of the flow field, with most significant of that seems to lie near the boundary region of the jet and in the wake region of the flow field. The region of highest dissipation always locates at the lower boundary of the jet, which also undergo a change of size with the periodic variation.

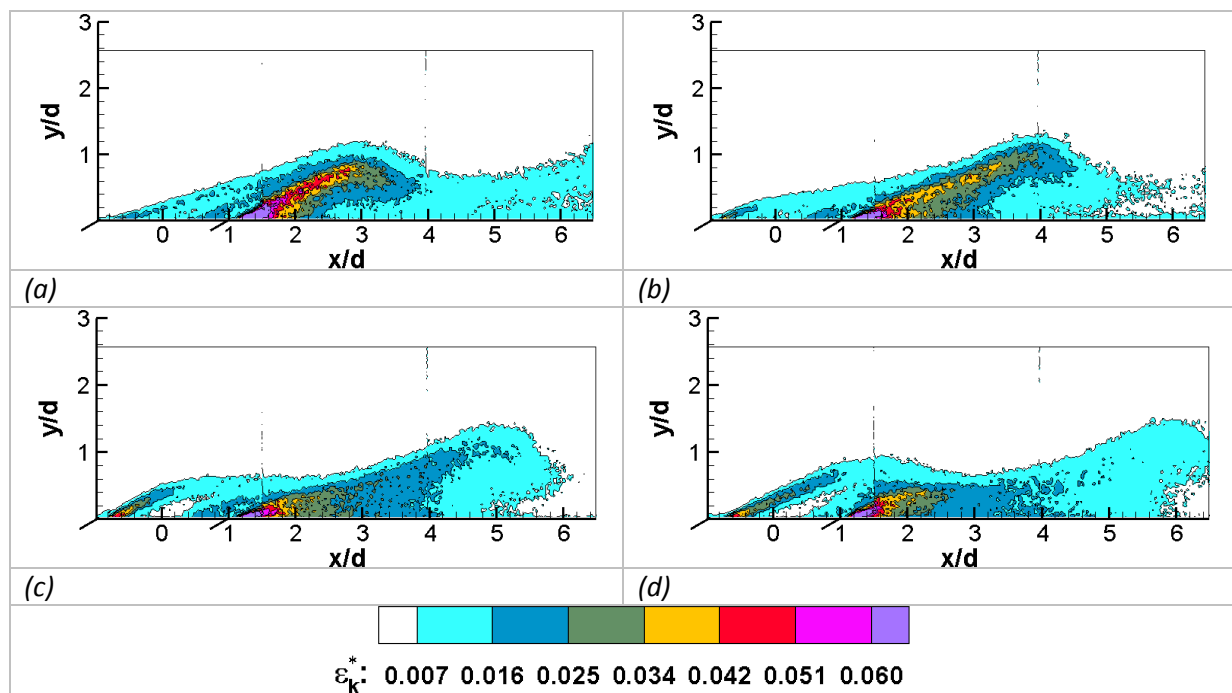


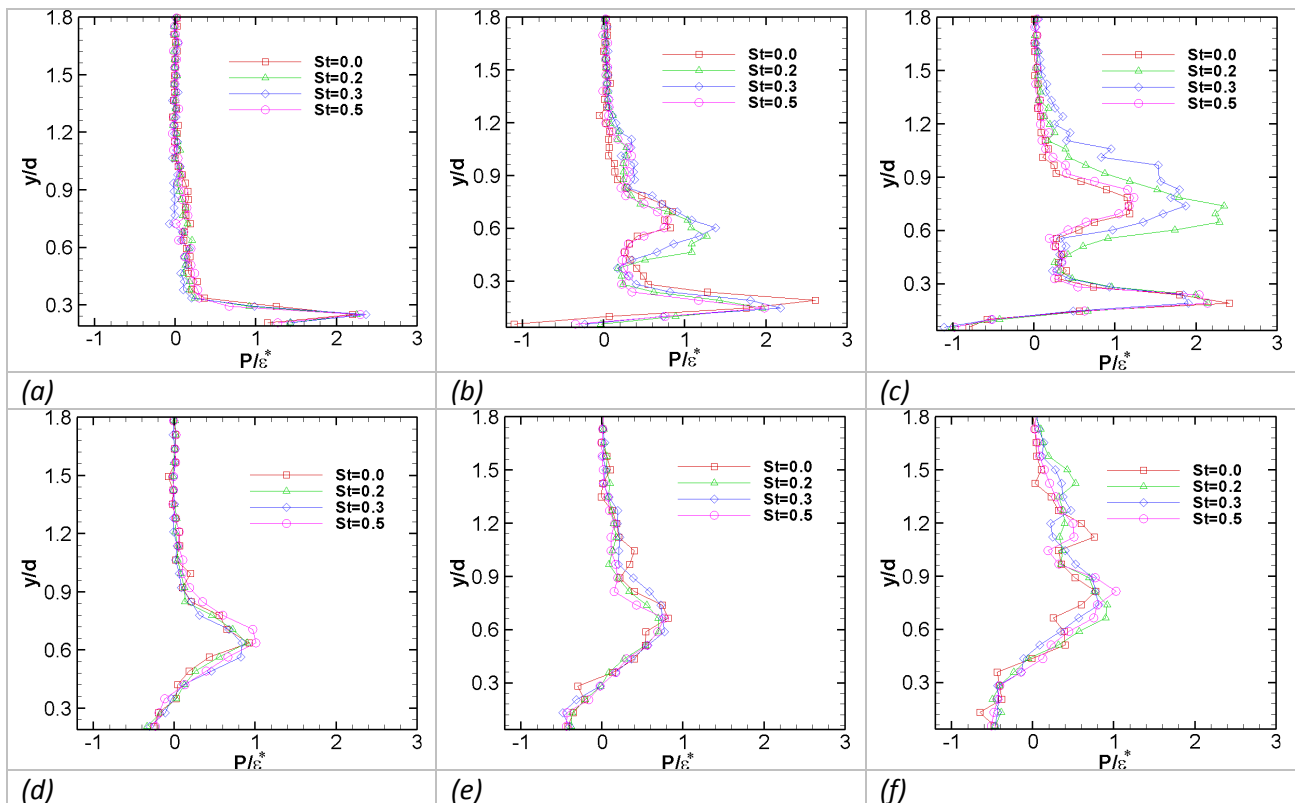
Figure (5. 39): Distribution of energy dissipation rate,  $\varepsilon_k^*$ ,  $\overline{M}=1$ ,  $St=0.2$ ; (a)  $t/T=0.19$ , (b)  $t/T=0.41$ , (c)  $t/T=0.63$  and (d)  $t/T=0.86$ .

At the time instants of  $t/T=0.63$  and  $0.86$  shown in figure (5.39c) and (5.39d), the dissipation in the core region of the jet is considerably low, similarly as the other terms of energy transport. These are the time instants, where the jet is growing again and the region

of substantial dissipation is only limited to a small downstream distance from the streamwise edges of the hole. At the final time instant, the shear layer and thus the zone of higher dissipation become slightly parallel to the wall.

### 5.7.3.5 Ratio of time-averaged Production and dissipation ( $P_k/\epsilon_k$ )

Figure (5.40a-i) shows the comparison of the ratio of time-averaged production and the rate of dissipation ( $P_k/\epsilon_k$ ) for different Strouhal number cases studied for different blowing ratios,  $\overline{M} = 0.65, 1$  and  $1.25$ . The profiles are obtained from the downstream location of  $x/d=1.5, 3.5$  and  $5.5$  of the central plane ( $z/d=0$ ), and show the comparisons of different pulsating cases in figure (5.40a-c), figure (5.40d-f) and figure (5.40g-i) respectively. For  $\overline{M} = 0.65$ , no significant variation is observed for pulsation cases of different Strouhal numbers. Some increase in  $P_k/\epsilon_k$  is observed for  $\overline{M} = 1$  and  $1.25$  at  $x/d=1.5$ , which is not so significant at other downstream stations. Pulsation at  $St=0.2$  and  $0.3$  increases the peak values locating nearly in the region of upper jet boundary. The increase in  $P_k/\epsilon_k$  is due to the combined effect of slight increase in production and slight decrease in dissipation, as we have seen that the terms of Reynolds stress become more uniform with a slight decrease near the lower boundary of the jet and a slight increase in the upper and lower part of the profile, while the gradient of velocity decreasing in all regions of significant shear. At peak region, the increase in  $P_k/\epsilon_k$  compared to steady blowing is about 24% and 33% for  $St=0.2$  and  $0.3$  at the blowing ratio of  $\overline{M} = 1$ , while it is about 85% and 42% for  $St=0.2$  and  $0.3$  at the blowing ratio of  $\overline{M} = 1.25$ .



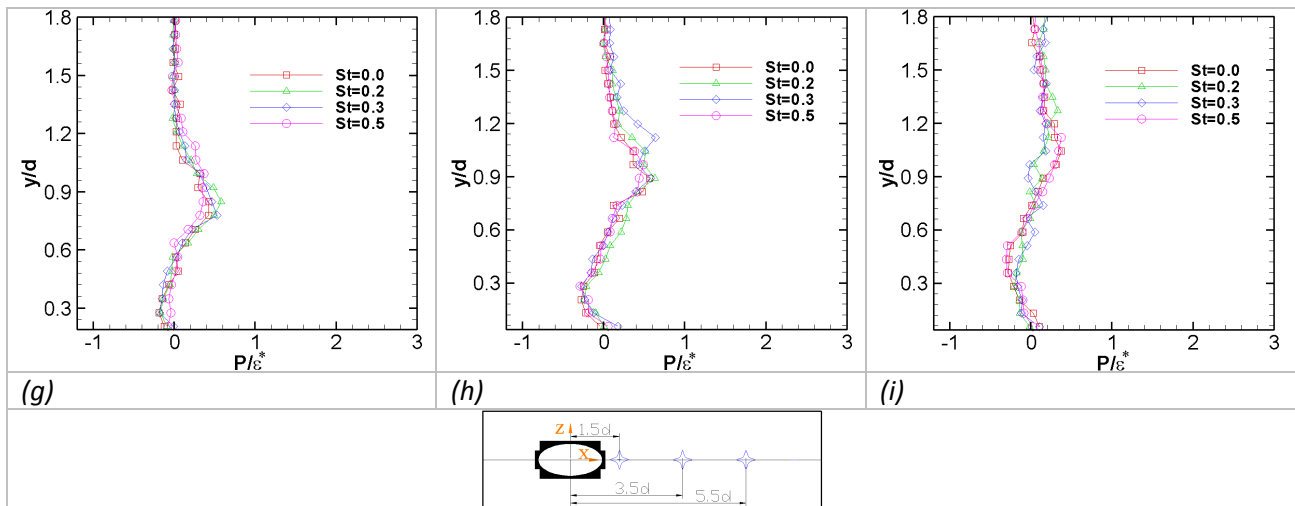


Figure (5. 40) : Comparison of time-averaged profiles of  $P_w/\epsilon_w$  lying at  $x/d=1.5, 3.5$  and  $5.5$  of the hole central plane ( $z/d=0$ ), for different  $St$  (0, 0.2 0.3 and 0.5) examined under a range of  $\overline{M}$  (0.65, 1 and 1.25), while  $\overline{M}$  increasing column-wise and  $x/d$  increasing row-wise.

## 5.8 Conclusion

This investigation has shown the effects of jet pulsation in a complex configuration of jet in crossflow. Both time- and phase averaged velocity distributions and turbulent characteristics are presented. The balance mass, momentum and turbulent kinetic energy are used to determine the role of different terms and subterms influencing the flow field. The synthesis of the phase-averaged results has shown that the periodic forcing and lift-off attributed to large spatial variations in jet trajectory, which leads to events like: jet splitting and shedding of the wake. It was observed that jet splitting under induce pulsation causes the flow in the wake region to shed in succession. Pulsing of injectant at lower Strouhal numbers ( $St=0.2$  and  $0.3$ ) with a mean blowing ratio leading to separation is able to reorient the injectant close to the wall during the lower part of pulsing cycle. The most influencing feature of the flow, the large Counter-Rotating Vortex Pair (CVP) develops primarily due to the existence of streamwise vorticity and the shear layer (Walters and Leylek 2000; and Guo et al. 2006), which controls the dynamics of the flow in the near wall region and thus the wall coverage. Although, the presence of the streamwise vorticity was never shown in the present study due to the lack of measurement in the lateral planes, but it is well reported and recognized in the available literature. The synthesis of the time-averaged results has shown that the blowing ratio of  $\overline{M} = 0.65$  and the pulsing case of  $St=0.5$ , as well as the blowing ratio of  $\overline{M} = 1$  and  $1.25$  and the pulsing cases of both  $St=0.2$  and  $0.3$  have some distinctive and vital influences of the Strouhal number pulsation. It was observed that the pulsation in these cases reduced the velocity gradient in the intense shearing regions of the flow field, and also increases both Reynolds normal and shear stresses. The decrease in velocity gradient, shown by rate of deformation and vorticity results, causes a decrease in the strength of CVP in the

cases of high blowing ratios and the resulting secondary movement of the mainstream flow blew the jet that induce local mixing. The Reynolds stresses on the other hand increases due to the collapsing of the jet fluid and its propagation in the wall-normal direction due to large periodic variation of jet trajectory. The turbulence fluctuation may also be induced by the tube at instantaneously high blowing ratio (Pietrzyk et al. 1989).

It can be concluded that pulsation brings some improvement in wall coverage only at higher blowing ratios and low frequency of excitation, where the injectant propagating with periodically varying trajectory could bring part of injectant flow in close proximity of the wall and improved injectant coverage compared to steady blowing. At  $\overline{M} = 0.65$ , pulsation at  $St = 0.5$  was found particularly detrimental for wall coverage compared to steady blowing conditions, because in this situation, flow of the injectant over the wall is no longer continuous, and the smooth distribution of coolant is significantly compromised. At  $\overline{M} = 1$  and  $\overline{M} = 1.25$  the low frequency shedding has ample time to readjust jet position in the near wall region in following the downstream variation of jet trajectory. However, at higher pulsation rates, jet variations due to back-by-back cycles of excitation and continuous induction of early jet splitting direct the jet flow away from the wall.

The physics of the flow can be further unveiled after the investigation of thermal aspects of the flow field by using the technique of infrared thermography for determining the parameters of wall coverage and a cold wire survey for analyzing the mixing of two flows interacting with a slight temperature difference.



## 5.9 References

1. Andreopoulos J, "On the structure of jets in a crossflow", J. Fluid Mech. 157 (1984) 163-197.
2. Andreopoulos J, Rodi W, "Experimental investigation of jets in a crossflow", J. Fluid Mech. 138 (1984) 93-127.
3. Bons JP, Rivir JB, Mac Arthur CD, Pestian DJ, "The effect of unsteadiness on film cooling effectiveness", Wright Laboratory, WL-TR-96-2096, Jan-1995.
4. Brundage AL, Plesniak MW, Ramadhyani S, "Influence of coolant feed direction and hole length on film cooling jet velocity profiles", International Gas Turbine & Aeroengine Congress & Exhibition, Indianapolis, Indiana, June 1999.
5. Burd SW, Kaszeta RW, Simon TW, "Measurement in film cooling flows: Hole L/D and turbulence intensity Effects", Gas turbine Heat Transfer Session, 1996 IMECE Conference, Atlanta, GA.
6. Cutler AD, Johnston JP, "The relaxation of a turbulent boundary layer in an adverse pressure gradient", J. Fluid Mech. 200 (1989) 367-387.
7. Dieumegard D, "Etude Experimentale Du Film Cooling Developpe Par Une Range De Cinq Perforations Et Modelisation Des Echanges Convectifs", Mémoire de Diplôme d'ingénieur, Université de Poitiers- ENSMA, 2003.
8. Dorignac E, Vullierme JJ, Deniboire P, Foucault E, Bousgarbies JL, "Thermographie Infrarouge et tomographie laser appliqués à l'étude des films de refroidissement", 5ème colloque national de visualisation et de traitement d'images en mécanique des fluides, Juin 2-5, 1992, Poitiers.
9. Fernando EM, Smits AJ, "A supersonic turbulent boundary layer in an adverse pressure gradient", J. Fluid Mech. 211 (1990) 285-307.
10. Foucault E, Deniboire P, Bousgarbies JL, Vullierme JJ, Dorignac E, "Etude expérimentale du transfert de chaleur près d'une paroi plane chauffée en présence d'injection multiples (Ecoulement subsonique)". Heat transfer and cooling in Gas Turbine-1992, AGARD-CP-527, paper-4.

11. Fric TF, Roshko A, "Vertical structure in the wake of a transverse jet", J. Fluid Mech. 279 (1994) 1-47.
12. Goldstein RJ, Eckert E.R.G., "Effects of hole geometry and density on three-dimensional film cooling", Int. J. Heat Mass Transfer, 17 (1974) 595-607.
13. Graftieaux L, Michard M, Grosjean N, "Combining PIV, POD and vortex identification algorithms for the study of unsteady turbulent swirling flows", Meas. Sci. Technol. 12 (2001) 1422-1429.
14. Guo X, Schröder W, Meinke M, "Large-eddy simulations of film cooling flows", Computers & Fluids 35 (2006) 587-606.
15. Kelso RM, Lim TT, Perry AE, "An experimental study of round jets in cross-flow", J. Fluid Mech. 306 (1996) 111-144.
16. Lee SW, Lee JS, Ro ST, "Experimental study on the flow characteristics of streamwise inclined jets in crossflow on flat plate", ASME J. Turbomach, 116 (1994) 97-105.
17. Mendez S, Nicoud F, "Large-eddy simulation of a bi-periodic turbulent flow with effusion", J. Fluid Mech, 2006.
18. Moussa ZM, Trischka JW, Eskinazi S, "The near field in the mixing of a round jet with a cross-stream"; J. Fluid Mech. 80 (1977) 49-80.
19. Muppidi S, Mahesh K, "Direct numerical simulation of round turbulent jets in crossflow", J. Fluid Mech. 574 (2007) 59-84.
20. Pietrzyk JR, Bogard DG, Crawford ME, "Hydrodynamic Measurement of jets in crossflow for gas turbine film cooling application", ASME J. Turbomach, 111 (1989) 139-145.
21. Rudman M, "Simulation of the near field of a jet in a crossflow", Experimental Thermal and Fluid Science, 12 (1996) 134-141.
22. Seo HJ, Lee JS, Ligrani PM, "The effect of injection hole length on film cooling with bulk flow pulsation", Int. J. Heat Mass Transfer, 41(1998) 3515-3528.

23. Sinha AK, Bogard DG, Crawford ME, "Gas turbine film cooling: Flowfield due to a second row of holes", Journal of Turbomachinery, ASME, 113 (1991b) 450-456.
24. Walters DK, Lylek JH, "A Detailed analysis of film cooling physics: Part 1-Streamwise injection with cylindrical Holes", ASME J. Turbomach, 122 (2000) 102-111.



## Table of Contents

---

6.1	Steady blowing (No pulsation).....	196
6.2	Unsteady blowing (with pulsation) .....	199
6.2.1	Case-A .....	199
6.2.2	Case-B .....	201
6.2.3	Case-C .....	202
6.2.4	Case-D .....	204
6.2.5	Case-E .....	205
6.2.6	Case-F.....	205
6.3	Centerline and laterally-averaged effectiveness.....	206
6.4	Centerline and laterally-averaged heat transfer coefficient.....	207
6.5	Comparison of results.....	210
6.6	Spatially-averaged effectiveness and heat transfer coefficient .....	212
6.7	Net heat flux reduction (NHFR).....	213
6.8	Conclusion.....	216
6.9	References .....	217

**Nomenclatures**

<b><u>Abbreviations</u></b>		<b><u>Subscripts/superscripts</u></b>	
$\rho$	Fluid density (kg/m <sup>3</sup> )	$i$	Injectant
$T$	Temperature (K)	$ad$	Adiabatic
$d$	Hole diameter (mm)	$\infty$	Free-stream
$L$	Hole length (mm)	$o$	Without injection
$U$	Streamwise velocity (m/s)	$rms$	Root mean square
$V$	Normal velocity (m/s)	$-$	Laterally-averaged
$u$	Streamwise velocity fluctuation (m/s)	$=$	Spatially-averaged
$v$	Normal velocity fluctuation (m/s)	$\sim$	Periodic component
$\delta$	Boundary layer thickness (mm)	$j$	Index number
$\delta^*$	Displacement thickness (mm)	$s$	Excitation
$\overline{M}$	Blowing ratio ( $= \rho_i \overline{U}_i / \rho_\infty \overline{U}_\infty$ )	$w$	Wall
$Re_\infty$	Reynolds number ( $= \overline{U}_\infty \cdot \delta / \nu$ )		
$Re_i$	Reynolds number ( $= \overline{U}_i \cdot d / \nu$ )		
$St$	Strouhal number ( $= f \cdot d / \overline{U}_i$ )		
$IT$	Turbulent intensity (%)		
$\phi$	Heat flux (W/m <sup>2</sup> )		
$\varepsilon$	Emissivity		
$\tau$	Transmissivity		
$h$	Heat transfer coefficient (W/m <sup>2</sup> .K)		
$Stan$	Stanton number ( $h / c_p \cdot \rho \cdot U$ )		
$NHFR$	Net heat flux reduction ( $= 1 - \phi / \phi_o$ )		
$\theta$	Non-dimensionalized temperature ( $= (T - T_\infty) / (T_i - T_\infty)$ )		
$\eta$	Effectiveness ( $= (T_{ad} - T_\infty) / (T_i - T_\infty)$ )		
$t$	Time (s)		
$f$	Frequency (Cycles/s)		
$x, y$	Streamwise and normal coordinates (mm)		

## **STUDY OF WALL HEAT TRANSFER IN FILM-COOLED BOUNDARY LAYER FLOW**

The principal objective of thermal measurements was to investigate the effect of externally imposed sinusoidal pulsations of an oblique jet on the formation of the injectant film over an adiabatic wall, which was otherwise exposed to a thermally uniform mainstream flow. Both the temperature and the mass flow rate of the injecting air were controlled prior to its entrance in the loudspeaker enclosure. The blowing ratios of the corresponding flows were held at  $(\overline{M} = \rho_i u_i / \rho_\infty u_\infty = 0.65, 1 \text{ and } 1.25)$ . The injection fluid was pulsed to a non-dimensionalized frequency of  $St = f \cdot d / \overline{U}_i = 0, 0.2, 0.3 \text{ and } 0.5$ . The thermal aspects of injectant film were figured out by determining the convective heat transfer coefficient and the adiabatic wall temperature. These parameters were determined by using the technique of infrared thermography. The Injectant coverage at the wall has been presented by non-dimensionalizing the adiabatic wall temperature, usually called as adiabatic effectiveness.

$$\eta = \frac{(T_{ad} - T_\infty)}{(T_i - T_\infty)} \quad \dots\dots\dots(6. 1)$$

The descriptions of the injection plate and the mainstream boundary layer flow at the point of injection are given in Section 3.2.1.2 and Section 3.3.4.2.

Before starting the analysis of the film cooling parameters, a few important features of the flow field, which were discussed previously in the section of aerodynamic analysis, are recalled here. The schematic diagrams shown in figure (6.1a) and (6.1b) provide a general description of the flow field for both unpulsed and pulsating film cooling cases. The averaged flow structures appearing in the steady blowing case or the systematic variations occurring in the unsteady blowing (pulsating case) will help to explain the flow field attributes in the thermal analysis.

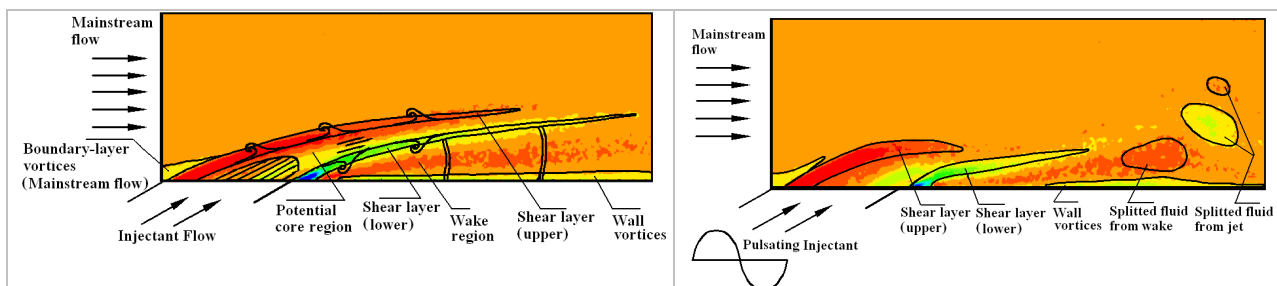


Figure (6. 1): Schematic diagram giving a general description of flow structures, (a) unpulsed (b) pulsating film cooling cases

The steady blowing case of higher jet momentum results in the lifting of the jet from the wall, as indicated by figure (6.1a). The highly lifted jet tends to break up into large fluid packets that feed into the downstream at a regular basis, as shown in figure (6.1b).

## 6.1 Steady blowing (No pulsation)

The contours of adiabatic effectiveness and convective heat transfer coefficient are shown in figure (6.2a-f). In these cases, the temperature of mainstream flow  $T_\infty$  was maintained at  $20 \pm 0.2$  °C and the temperature of the injecting flow  $T_i$  was at  $40 \pm 0.4$  °C. The results for adiabatic wall temperature  $T_{ad}$  and convective heat transfer coefficient  $h$  are presented in a non-dimensionalized form. The non-dimensionalized form of adiabatic wall temperature is called as adiabatic film-cooling effectiveness, Eq. (6.1), which signifies to the capacity of wall coverage offered by the injectant film. The convective heat transfer coefficient of the film cooled boundary layer is non-dimensionalized with a convective heat transfer coefficient determined from the conventional case of flow over a flat-plate ( $h_o$ ). The experiments of flat plate heat transfer cases were performed with mainstream velocities equivalent to the corresponding blowing ratios ( $\overline{U}_\infty = 10, 7.7$  m/s), while injection holes were neatly covered with a black tape. The term  $h/h_o$  signifies the relative increase in the convective heat transfer coefficient due to the blowing of injectant fluid in the freestream boundary layer.

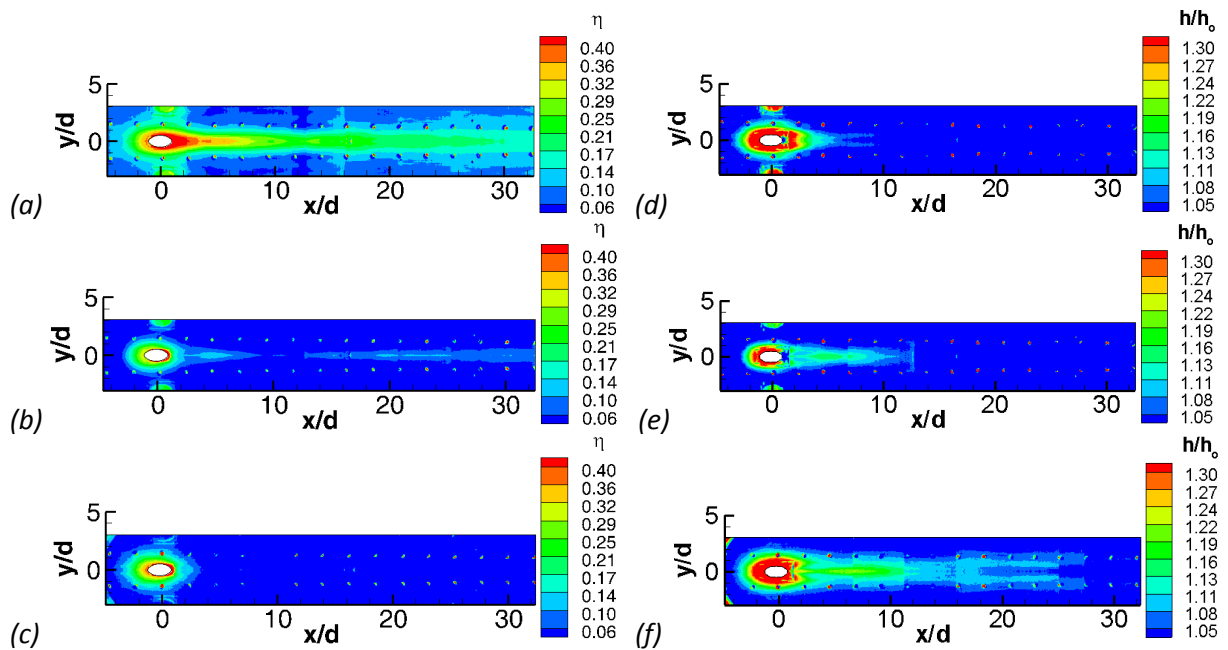


Figure (6. 2): Steady blowing results for Adiabatic effectiveness: (a)  $\overline{M} = 0.65$ , (b)  $\overline{M} = 1$ , (c)  $\overline{M} = 1.25$  and convective heat transfer coefficient: (d)  $\overline{M} = 0.65$ , (e)  $\overline{M} = 1$ , (f)  $\overline{M} = 1.25$ ,

The effectiveness is maximum for the case of  $\overline{M} = 0.65$ , as shown in figure (6.2a), which decreases gradually with the increment of blowing ratio, figure (6.2a-c). The minimum value

of effectiveness is encountered for the case of  $\bar{M} = 1.25$ , which is roughly less than 6% in the region lying on the downstream side of the hole, as shown in figure (6.2c). At higher blowing ratios, the jet flow diffuses early in the mainstream flow due to the outward orientation of the jet trajectory, which reduces the wall coverage. On the other hand, the heat transfer coefficient increases with the increase of blowing ratio and holds maximum contour levels for  $\bar{M} = 1.25$ , see figure (6.2f). The increase in heat transfer coefficient is related to the tendency of lifting-off of the jet from the wall due to a higher vertical momentum, which creates a high pressure region at the leading side and a low pressure region on the trailing side of the jet. On the trailing side, the flow field establishing below the jet usually called as wake region induces turbulence due to the entrainment of mainstream flow. The entrainment increases with the blowing ratio, which boosts-up the mixing of interacting flow locally and thus increases the convection rate. Bons et al. (1996) proposed that the lift-off of the coolant promotes the pumping of freestream flow down to the plate surface by the pair of counter rotating vortices of the film.

Analyses of the film cooling problem under steady blowing have been widely performed and published in the open literature for various configurations of issuing jet and test parameters of the interacting flows (including the present ones). A comparison of baseline results obtained from the infrared thermography of the test wall in steady blowing conditions is shown in figure (6.3a) and (6.3b). The experimental conditions of various authors cited for comparison are shown in Table-6.1. The profiles are obtained from the central plane ( $z/d=0$ ) for a streamwise distance varying from ( $x/d=0$  to 32).

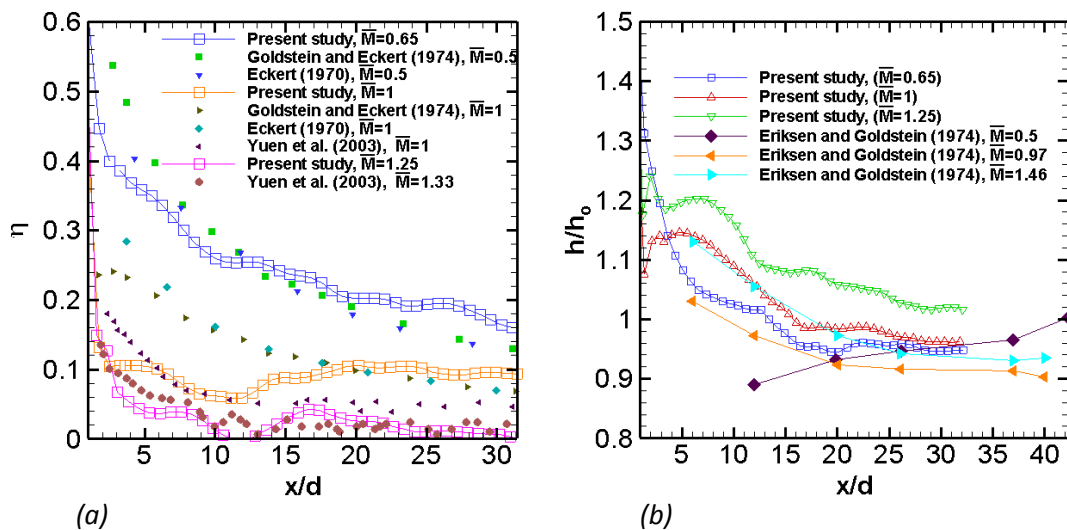


Figure (6. 3): Comparison of the cases of steady blowing at  $T_i/T_\infty = 2$ , (a) adiabatic effectiveness, (b) Convective heat transfer coefficient.

The comparison of the results shows that the adiabatic effectiveness determined for  $\bar{M} = 0.65$  and  $\theta = 30^\circ$  in the present study corresponds well with the results of Eckert (1970), and Goldstein and Eckert (1974) given for  $\bar{M} = 0.5$  and  $\theta = 35^\circ$ . For  $\theta = 35^\circ$ , blowing at  $\bar{M} = 0.5$  is referred as optimum blowing in several references, which means that the injectant flow rate and its trajectory provide an optimum coverage under these conditions (Eckert 1970). In the present case, slightly higher blowing ratio compared to the reference cases seems to compensate for the loss of jet momentum in the vicinity of wall, which leads to early diffusion of the injectant flow due to the slightly lower angle of injection.

For  $\bar{M} = 1$ , the comparison of present measurement with Eckert (1970), and Goldstein and Eckert (1974) shows some significant difference. The difference in Reynolds numbers, which are 17000 and 22000 compared to the 8609 in the present study, and the angle of injection, which is  $35^\circ$  compared to  $30^\circ$  in the present study explicate the difference of dynamic conditions for these cases. However, the comparison with Yuen et al. (2003a) seems to correspond well up to  $x/d=13$ , beyond this location some increase in adiabatic effectiveness is observed for the present results. The reason for such an increase in effectiveness is the turning of the jet fluid back towards the wall after an initial lift-off. The adiabatic effectiveness for  $\bar{M} = 1.25$  appears fairly close to the results of Yuen et al. (2003a) given for  $\bar{M} = 1.33$ . At an injection angle of  $30^\circ$  and the set of flow dynamic parameters, the increase in blowing ratio beyond the present one is expected to have a very small impact on the effectiveness, as the results seem to approach towards zero due to the early diffusion in the mainstream flow.

	Present study			Yuen et al. (2003)		Goldstein and Eckert (1974)		Eckert (1970)		Eriksen and Goldstein (1974)		
	0.65	1	1.25	1	1.33	0.52	1.04	0.5	1	0.5	0.97	1.46
$\bar{M} = \rho_i \bar{U}_i / \rho_\infty \bar{U}_\infty$	0.65	1	1.25	1	1.33	0.52	1.04	0.5	1	0.5	0.97	1.46
Plane z/d	0	0	0	0	0	0	0	0	0	0	0	0
Angle of injection, $\theta$ (deg.)	30	30	30	30	30	35	35	35	35	35	35	35
$\delta^*/d$	0.146	0.146	0.11	0.150	0.150	0.159	0.158	0.124	0.124	0.171	0.171	0.171
$Re_D = \frac{\rho_\infty U_\infty d}{\mu_\infty}$	8609	8609	6629	8563	8563	17700	18300	22000	22000	22000	22000	22000

Table-6.1: Description of the fundamental test conditions of the film cooling experiments referred for comparison.

The variation in convective heat transfer coefficient along the central plane seems to have a similar trend as for the results of Eriksen and Goldstein (1974). Generally, a slight shift

*“Experimental aerothermal characterization of a pulsating jet issuing in a crossflow: Influence of Strouhal number excitation on film cooling”*

towards higher values is noticed for these profiles as the blowing ratios increases in the present study. In the reference case, the heat transfer coefficient increases slightly for  $\overline{M} = 0.5$  on far downstream region.

In light of these results, we can conclude that both the test-rig and the methodology of determining the parameters of wall protection are reasonably good for the subsequent assessments of periodic effects of the jet on the thermal exchange occurring at the wall.

## 6.2 Unsteady blowing (with pulsation)

The effects of injectant flow pulsation on the thermal exchange at the wall resulting from the interaction of a mainstream and an injectant flow for two different cases of upstream temperature ratios ( $T_i/T_\infty = 1$  and 2) are analyzed. The effects of pulsation are presented by the 2-dimensional distribution of the characteristic film cooling parameters,  $(\eta, h/h_o)$ , and then the profiles of centerline, spanwise and spatially-averaged quantities are presented in the line up sections.

List of different cases studied for the range of Strouhal number pulsation of the film cooling jet are shown in Table-6.2.

Case-A	$\overline{M} = 0.65; T_i/T_\infty = 2$
Case-B	$\overline{M} = 1; T_i/T_\infty = 2$
Case-C	$\overline{M} = 1.25; T_i/T_\infty = 2$
Case-D	$\overline{M} = 0.65; T_i/T_\infty = 1$
Case-E	$\overline{M} = 1; T_i/T_\infty = 1$
Case-F	$\overline{M} = 1.25; T_i/T_\infty = 1$

Table -6.2: Description of test cases studied with pulsation.

### 6.2.1 Case-A

Figure (6.4a-d) shows the distribution of adiabatic effectiveness with respect to Strouhal numbers for a blowing ratio of  $\overline{M} = 0.65$  and a temperature ratio of  $T_i/T_\infty = 2$ . The effectiveness is maximum for a case of steady blowing ( $St=0$ ), as shown in figure (6.4a). The imposition of sinusoidal pulsation results in a gradual decline of effectiveness with the increase of Strouhal number. In the cases of pulsation, the flow of the injectant over the wall is no longer continuous, and it is also characterised by the downstream movement of spatially accumulated mass of injectant fluid in the form of packets during each period of pulsation. This either causes an occasional detachment or leaves a weak concentration of the injectant, which flows at the wall in regular intervals. At  $St=0.5$ , the smooth distribution

of coolant in the near wall region is significantly compromised, and the film effectiveness is found to be inferior compared to the other cases.

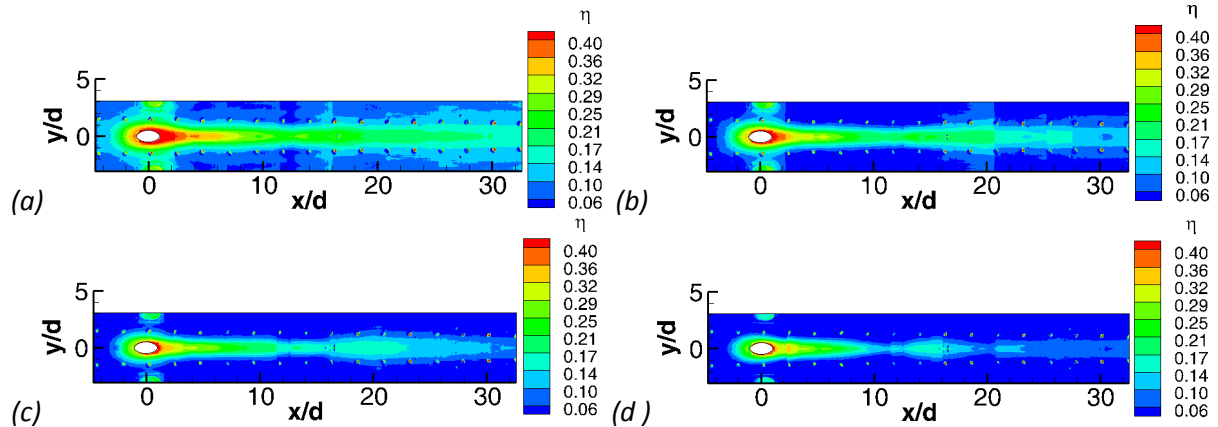
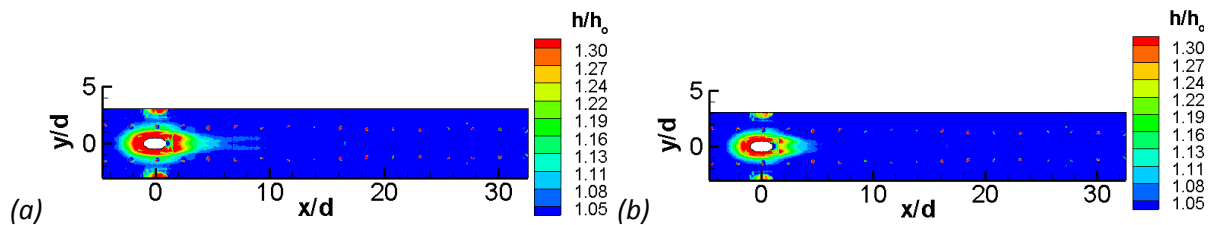


Figure (6. 4): Adiabatic effectiveness estimated for  $\overline{M} = 0.65$  and  $T_i/T_\infty = 2$ , (a)  $St=0$ , (b)  $St=0.2$ , (c)  $St=0.3$  and (d)  $St=0.5$ .

The distribution of convective heat transfer coefficient with respect to Strouhal number for a blowing ratio of  $\overline{M} = 0.65$  and a temperature ratio of  $T_i/T_\infty = 2$  is shown in figure (6.5a-d). The implementation of jet pulsation does not seem to produce any significant difference in convective heat transfer coefficient. The injectant flow under these conditions remains attached to the wall over a significant distance, and the wake region merely exiting on the trailing side of the jet has a minor role for inducing the turbulence at the wall. The flow field is characterized by a weaker entrainment of mainstream flow and thus results in lower local convection coefficient. The fields of convective heat transfer also feature the presence of a pair of symmetric tines about the central plane ( $z/d=0$ ) in some cases, which are believed to be caused by kidney vortices associated with the film cooling jets. Coulthard et al (2006) called them as “fork-tines” in the precedence of earlier studies. They use a row of five streamwise injection holes in film cooling with jet pulsation and showed their existence in various cases of unpulsed and pulsed jets film cooling. Generally, the lateral spreading of these tines increases with the increase of blowing ratio.



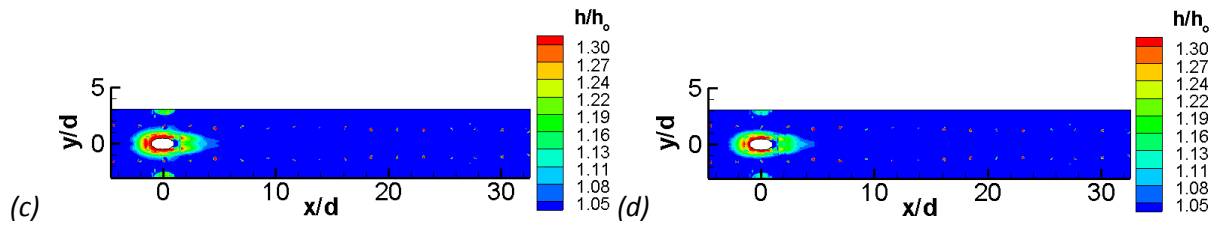
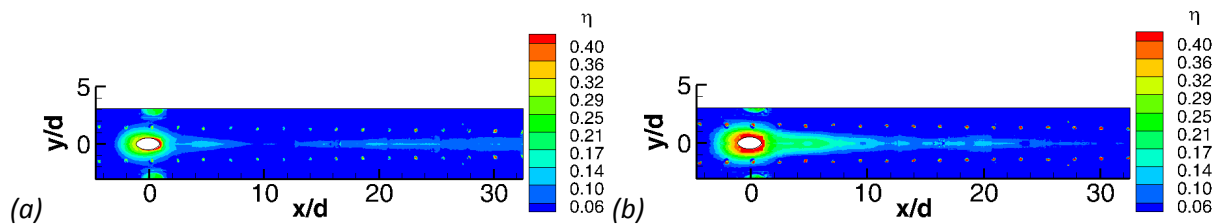


Figure (6. 5): Convective heat transfer coefficient estimated for  $\bar{M} = 0.65$  and  $T_i/T_\infty = 2$ , (a)  $St=0$ , (b)  $St=0.2$ , (c)  $St=0.3$  and (d)  $St=0.5$ .

### 6.2.2 Case-B

Jet pulsation in film cooling seems to have some improvement in adiabatic effectiveness for a flow configuration of  $\bar{M} = 1$  and  $T_i/T_\infty = 2$  in certain frequency range. Figure (6.6a-d) shows the variation in adiabatic effectiveness as a function of Strouhal numbers. For the set of Strouhal number excitation examined here, some noticeable improvement in adiabatic effectiveness is observed for  $St=0.2$ , which corresponds to the lowest level of pulsation considered here, see figure (6.6b). At  $\bar{M} = 1$ , the jet tends to lift-off from the wall in a normal situation, when no pulsation is applied ( $St=0$ ). The pulsation causes the periodic variation of injectant flow rate at the hole exit, which also results in a periodic variation in actual blowing ratio. The fraction of time in the period of pulsation pertaining to the flow at low blowing ratio improves the distribution of injection flow in the near wall region by lowering the jet trajectory towards the wall. This causes an instantaneous improvement in the wall coverage on a regular basis during each period of pulsation. However, during the lower part of the pulsation period, where the injectant flow rate is minimum, the mainstream flow is also ingested a little bit inside the injection hole. The other interesting event is the collapsing of jet body occurring at higher blowing ratio, as was observed in the part of the aerodynamic analysis earlier on. It occurs with the reduction of injectant flow rate after attaining a maximum value. This event takes place much more frequently at higher pulsation cases, such as for  $St=0.5$ . Under these conditions, collapsing of the jet leads the trajectory of downstream convecting jet flow to attain an outward orientation more or less similar as in steady blowing, which reduces the amount of injectant fluid flowing in conjunction to the wall on average bases.



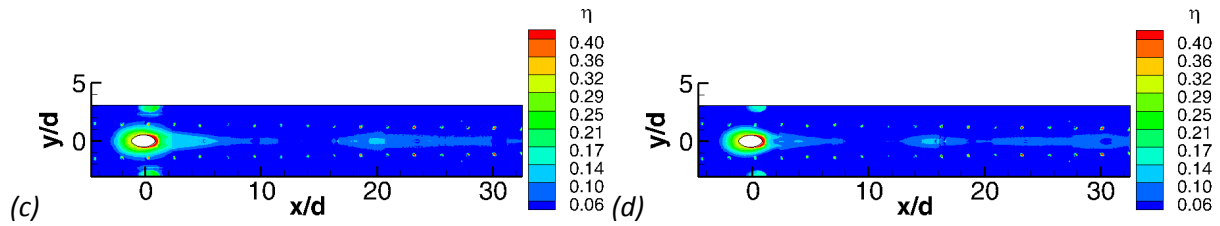


Figure (6. 6): Adiabatic effectiveness estimated for  $\overline{M} = 1$  and  $T_i/T_\infty = 2$ , (a)  $St=0$ , (b)  $St=0.2$ , (c)  $St=0.3$  and (d)  $St=0.5$ .

Figure (6.7a-d) shows the distribution of convective heat transfer coefficient for  $\overline{M} = 1$  and  $T_i/T_\infty = 2$ . In steady blowing situation, the measured heat transfer coefficient is higher than the case of  $\overline{M} = 0.65$  and  $T_i/T_\infty = 2$ , because of superior entrainment of mainstream flow in present configuration. For the case of  $St=0.2$ , the pulsation allows the reorientation of the jet trajectory towards the wall during the time span leading to the formation of low blowing ratio injectant film, whilst the event in the period of pulsation causing the collapsing of the jet and the passing of turbulent wake structures in the neighborhood of the wall causes an increase in the convective heat transfer coefficient. At higher Strouhal number cases, the turbulent wake structures do not have significant time to grow over the period of pulsation and travel along the wall before diffusing fully in the mainstream flow. Therefore, the heat transfer coefficient roughly stays at the same order of magnitude as was found in steady blowing.

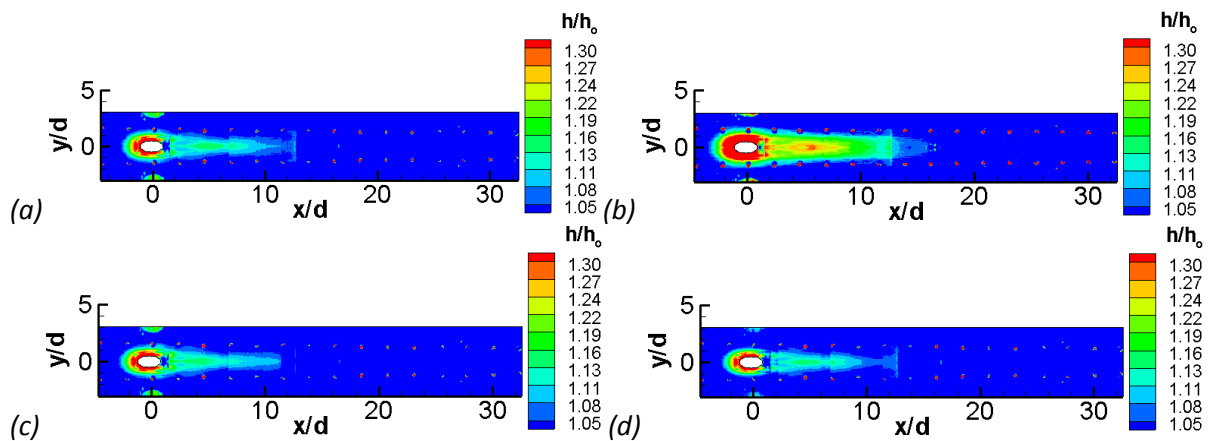


Figure (6. 7): Convective heat transfer coefficient estimated for  $\overline{M} = 1$  and  $T_i/T_\infty = 2$ , (a)  $St=0$ , (b)  $St=0.2$ , (c)  $St=0.3$  and (d)  $St=0.5$ .

### 6.2.3 Case-C

Figure (6.8a-d) shows the variation in injectant flow distribution for  $\overline{M} = 1.25$  and  $T_i/T_\infty = 2$ . Figure (6.8a) represents the case of steady blowing, which shows that the effectiveness of injectant distribution on the downstream side of the hole has the lowest values due to

ascending of the injectant fluid away from the wall. For the present blowing ratio, some signs of an upstream horse-shoe vortex wrapping around the jet flow are also observed. This vortex system evolves due to the intense blockage offered by the upstream side of the jet on the interaction between the two flows. Low frequency pulsations cause an increase in effectiveness, as can be observed for the cases of  $St=0.2$  and  $0.3$  compared to steady blowing. The time-span associated to the lower part of the pulse cycle is expected to improve wall coverage with the reduction of blowing ratio. Also, the higher momentum jet fluid pulsating at  $St=0.3$  is able to improve the lateral dispersion of the injectant fluid, as shown in figure (6.8c). The distribution of adiabatic effectiveness on the near downstream region of the hole indicates superior lateral spreading of injectant flow for  $St=0.3$  compared to the pulsation at  $St=0.2$ .

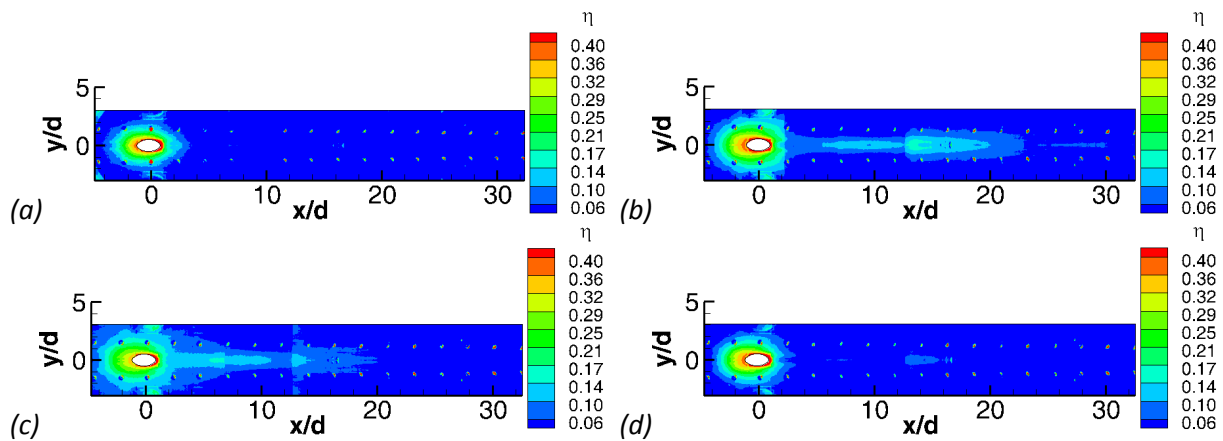


Figure (6. 8): Adiabatic effectiveness estimated for  $\overline{M} = 1.25$  and  $T_i/T_\infty = 2$ , (a)  $St=0$ , (b)  $St=0.2$ , (c)  $St=0.3$  and (d)  $St=0.5$ .

For  $\overline{M} = 1.25$ , the pulsation at  $St=0.3$  allows larger mass of injectant fluid to flow in the neighborhood of the wall, compared to the case of  $\overline{M} = 1$  and  $St=0.3$ . In a higher Strouhal number case ( $St=0.5$ ), the effects of pulsation are not fully established within the short time duration of successive pulses. In the resulting scenario, the jet trajectory stays away from the wall and carries over a trend of frequent splitting. The injectant fluid diffuses more quickly under such effects.

The distributions of heat transfer coefficient for the range of Strouhal number pulsation in a flow configuration of  $\overline{M} = 1.25$  and  $T_i/T_\infty = 2$  are shown in figure (6.9a-d). Under steady blowing, the fields of heat transfer coefficient possesses higher magnitudes compared to the other two cases of smaller blowing ratios, since the development of wider wake region permits greater ingestion of mainstream flow. For the pulsation cases of  $St=0.2$  and  $0.3$ , an increase in convective coefficient has been observed. The passing of the turbulent wake structure ejected from the near downstream region of the hole mainly contributes to the

increment in heat transfer coefficient. The pulsation at  $St=0.5$  does not allow the injectant flow to developed fully on the variations produced in one period while the second period starts-off. The spreading characteristics of the jet in the resulting flow field are affected by the time restrain and so the growth of the wake structures remains comparatively immature.

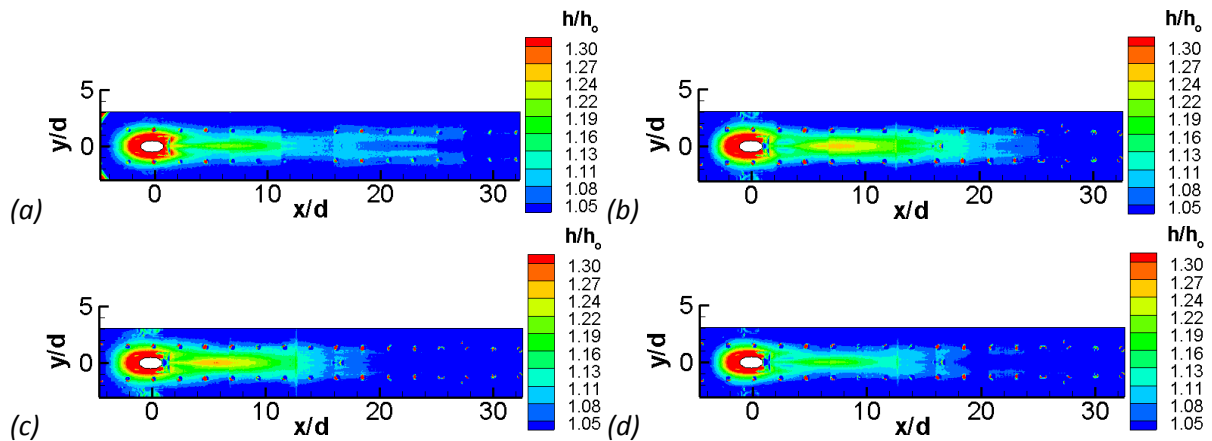


Figure (6. 9): Convective heat transfer coefficient estimated for  $\overline{M} = 1.25$  and  $T_i/T_\infty = 2$ , (a)  $St=0$ , (b)  $St=0.2$ , (c)  $St=0.3$  and (d)  $St=0.5$ .

#### 6.2.4 Case-D

In the configuration of film cooling while both mainstream and injecting flows are introduced at a similar temperature ( $T_i = T_\infty = 20$  °C), the changes in convective heat transfer coefficient due to injectant blowing in the mainstream boundary layer is examined. Figure (6.10a-d) shows the variation of convective heat transfer coefficient as a function of Strouhal number for the flow configuration of  $\overline{M} = 0.65$  and  $T_i/T_\infty = 1$ .

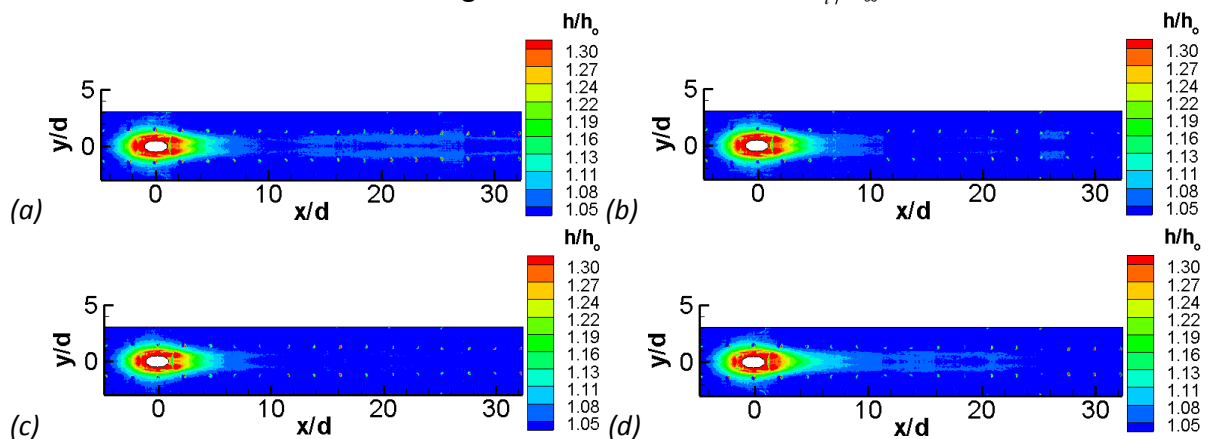


Figure (6. 10): Convective heat transfer coefficient estimated for  $\overline{M} = 0.65$  and  $T_i/T_\infty = 1$ , (a)  $St=0$ , (b)  $St=0.2$ , (c)  $St=0.3$  and (d)  $St=0.5$ .

In present case, the state of convective exchange at the wall is slightly different compared to the previous case of  $T_i/T_\infty = 2$  because of some disparity in the properties of injectant fluid. The injectant flow with slightly higher density promises to increase the convective heat transfer coefficient of the resulting film. Under steady blowing at  $\bar{M} = 0.65$ , the trajectory of injectant flow stays adjacent to the wall. The imposition of pulsation perturbs the rate of injectant flow passing smoothly at the wall and induces the splitting of jet body at higher Strouhal number pulsing, which extenuates the injectant capacity of wall coverage. The presence of symmetric fork-tines described earlier can also be observed in case of steady blowing and the pulsation case of  $St=0.5$ .

### 6.2.5 Case-E

Figure (6.11a-b) shows the variation of convective heat transfer coefficient as a function of Strouhal number for the flow configuration of  $\bar{M} = 1$  and  $T_i/T_\infty = 1$ . The distribution of convective heat transfer in different cases of pulsation alters only slightly. However, a minor increase in convective heat transfer coefficient can be observed for the pulsation at  $St=0.2$  compared to the other cases, which is similar to the observations made in the previous configuration of  $T_i/T_\infty = 2$ . The low Strouhal number case of  $St=0.2$  causes an increase in convective coefficient due to the passing of strong turbulent wake structures in the neighbourhood of the wall.

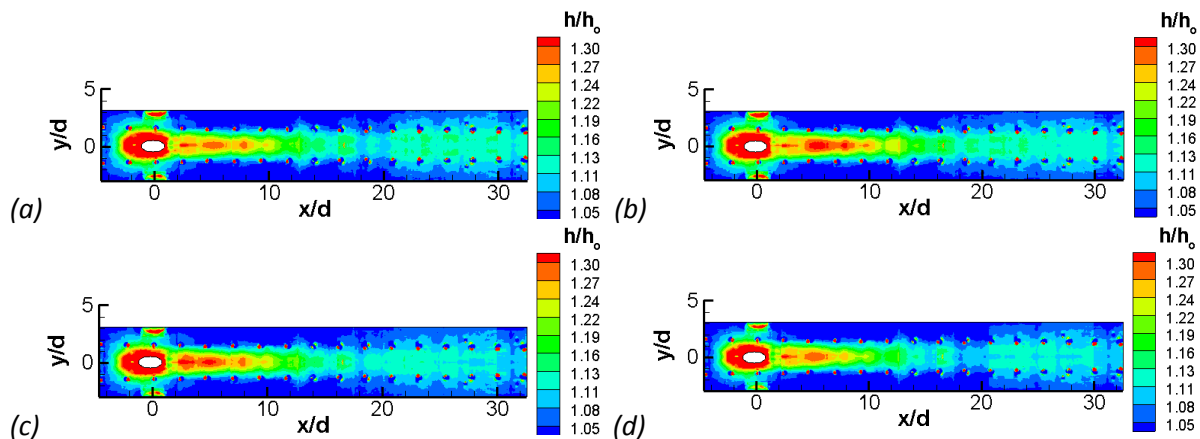


Figure (6. 11): Convective heat transfer coefficient estimated for  $\bar{M} = 1$  and  $T_i/T_\infty = 1$ , (a)  $St=0$ , (b)  $St=0.2$ , (c)  $St=0.3$  and (d)  $St=0.5$ .

### 6.2.6 Case-F

Figure (6.12a-b) shows the variation of convective heat transfer coefficient as a function of Strouhal number for the flow configurations of  $\bar{M} = 1.25$  and  $T_i/T_\infty = 1$ . The distribution of convective heat transfer coefficient is slightly higher for the present cases compared to what have been observed in the corresponding cases of previous configuration ( $T_i/T_\infty = 2$ ). The pulsation causes an increase in the convection rate for the two lower Strouhal number cases

( $St = 0.2$  and  $0.3$ ) relative to steady blowing across the central plan extending roughly up to  $x/d=10-12$ . However, the pulsation case of  $St=0.5$  exhibits a reduction in convective coefficient.

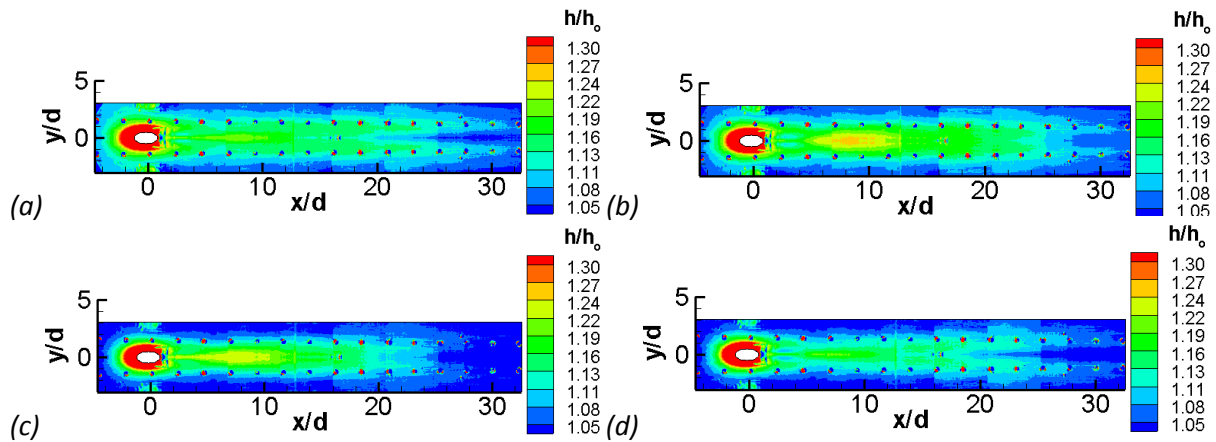


Figure (6. 12): Convective heat transfer coefficient estimated for  $\overline{M} = 1.25$  and  $T_i/T_\infty = 1$ , (a)  $St=0$ , (b)  $St=0.2$ , (c)  $St=0.3$  and (d)  $St=0.5$ .

### 6.3 Centerline and laterally-averaged effectiveness

The profiles of centerline adiabatic effectiveness obtained from a lateral plane of  $z/d=0$  are shown in figure (6.13a-c). These results compare the effects of pulsation on the wall coverage for different blowing ratios examined with a fixed temperature ratio of  $T_i/T_\infty = 2$ . Figure (6.13a) shows that for  $\overline{M} = 0.65$ , the effectiveness of wall coverage seems to reduce in a sequential order as the Strouhal number increases. At a streamwise distance of  $x/d \approx 25$ , the drops noted in the pulsating cases compared to the steady blowing are 26%, 36% and 51% for Strouhal numbers of 0.2, 0.3 and 0.5. In these cases, the pulsation resulting in the periodic variation of injectant flow rate at the hole exit appears quite detrimental for the wall coverage. The profiles for laterally-averaged effectiveness are estimated by integrating the crosswise profiles of the effectiveness bounded by ( $z/d=0$  and  $1.5$ ), Eq. (6.2). The downstream positions chosen for crosswise profiles can be given as;  $(x/d)_n=(n-1)*3$ ; where  $n=1,2,3,\dots$ ). For  $\overline{M} = 0.65$  the profiles for laterally-averaged effectiveness are shown in figure (6.13d), which indicates a downward gradient of adiabatic effectiveness up to  $x/d \approx 14$  and a relatively uniform coolant distribution thereafter. For  $\overline{M} = 1$ , the centerline and laterally-averaged effectiveness are shown in figure (6.13b) and figure (6.13e). The pulsation at  $St=0.2$  increases the wall protection up to a distance of  $x/d \approx 15$  compared to other cases. In this case, the jet tends to lift-off from the wall and then reattaches as it advances downstream. In the region beyond  $x/d \approx 15$ , the centerline effectiveness for different pulsation cases does not show any distinctive behaviour compared to steady blowing. For  $\overline{M} = 1.25$ , the centerline and laterally-averaged effectiveness are shown in

figure (6.13c) and figure (6.13f). It can be observed that the pulsation at  $St=0.2$  offers maximum effectiveness beyond a streamwise distance of  $x/d \approx 10$ , which seems to level-off after a distance of  $x/d \approx 25$ . Pulsation at  $St=0.3$  also results in an increase of wall coverage, compared to the case of  $St=0$  and  $0.5$ . Figure (6.13f) shows that the spread of injectant is most efficient in the lateral direction within a few diameters downstream of the hole for the case of  $St=0.3$ .

$$\bar{\eta} = \frac{1}{1.5d} \int_0^{1.5d} \eta(x, z) dz \tag{6.2}$$

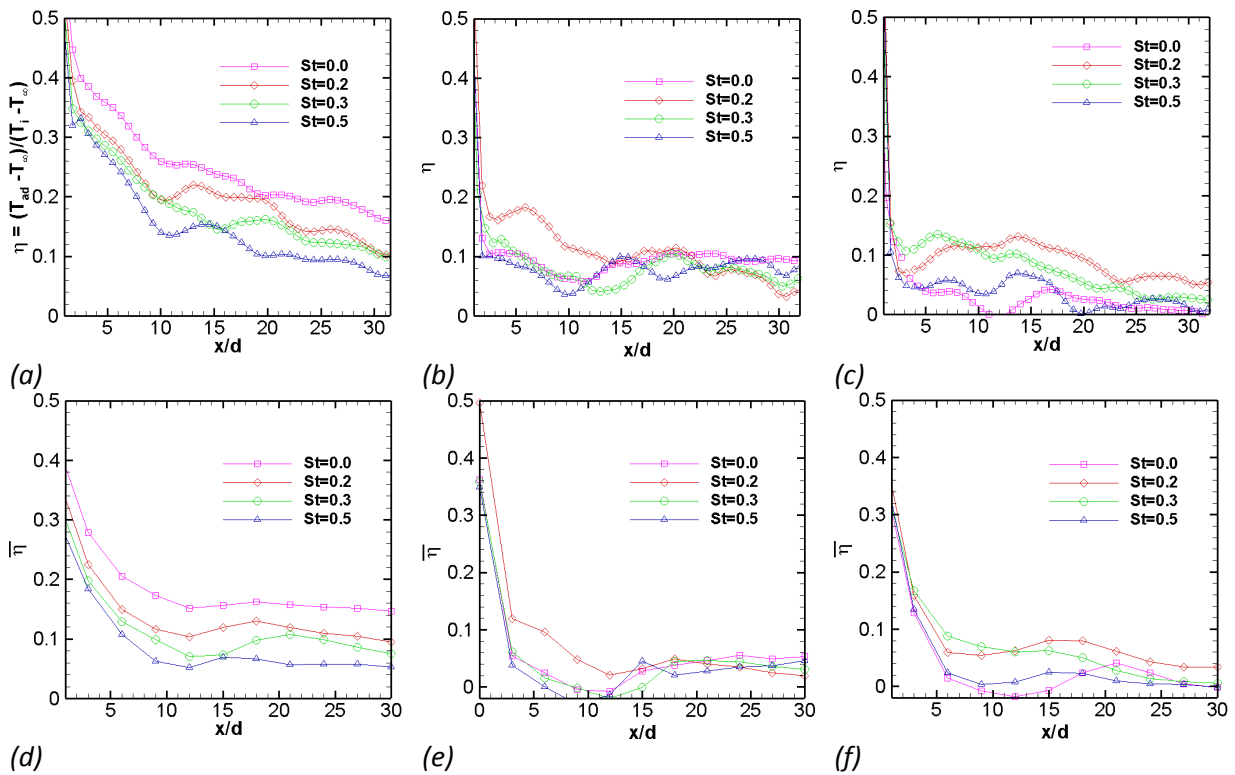


Figure (6. 13): Film cooling at  $T_i/T_\infty = 2$ , centerline effectiveness: (a)  $\bar{M} = 0.65$ , (b)  $\bar{M} = 1$ , (c)  $\bar{M} = 1.25$ , and laterally-averaged effectiveness: (d)  $\bar{M} = 0.65$ , (e)  $\bar{M} = 1$ , (f)  $\bar{M} = 1.25$ .

### 6.4 Centerline and laterally-averaged heat transfer coefficient

Comparisons of centreline and laterally-averaged convective heat transfer coefficient for the range of Strouhal numbers are shown in figure (6.14a-f), incorporating each configuration of film cooling bearing different blowing ratios and a fixed temperature ratio of  $T_i/T_\infty = 2$ . In all cases, the region for the increase in heat transfer due to the blowing of injectant flow roughly extends up to a distance of  $x/d \approx 20$ , beyond this location the role of the injectant blowing in the film cooling configuration relative to the case of flat plate convection is somewhat insignificant. A similar trend for the distribution of heat transfer coefficient was

also reported by Eriksen and Goldstein (1974), Sen et al. (1996) and Yeun and Martinez-Botas (2003). Generally, they concluded that for a cylindrical hole injection, the centerline heat transfer coefficient has little influence of the blowing ratio, for  $\overline{M} \leq 2$ . The region of the flow field mostly influenced by the injectant blowing was the near downstream region of the hole ( $x/d \approx 10-15$ ). For  $30^\circ$  injection, Yeun and Martinez-Botas (2003) suggested a maximum increase of about 40% very close to the downstream edge of the hole. In the present cases, the effects of film cooling were shown to level out to the case of conventional boundary layer flow ( $h/h_0=1$ ) after a streamwise distance of  $x/d \approx 20-25$ .

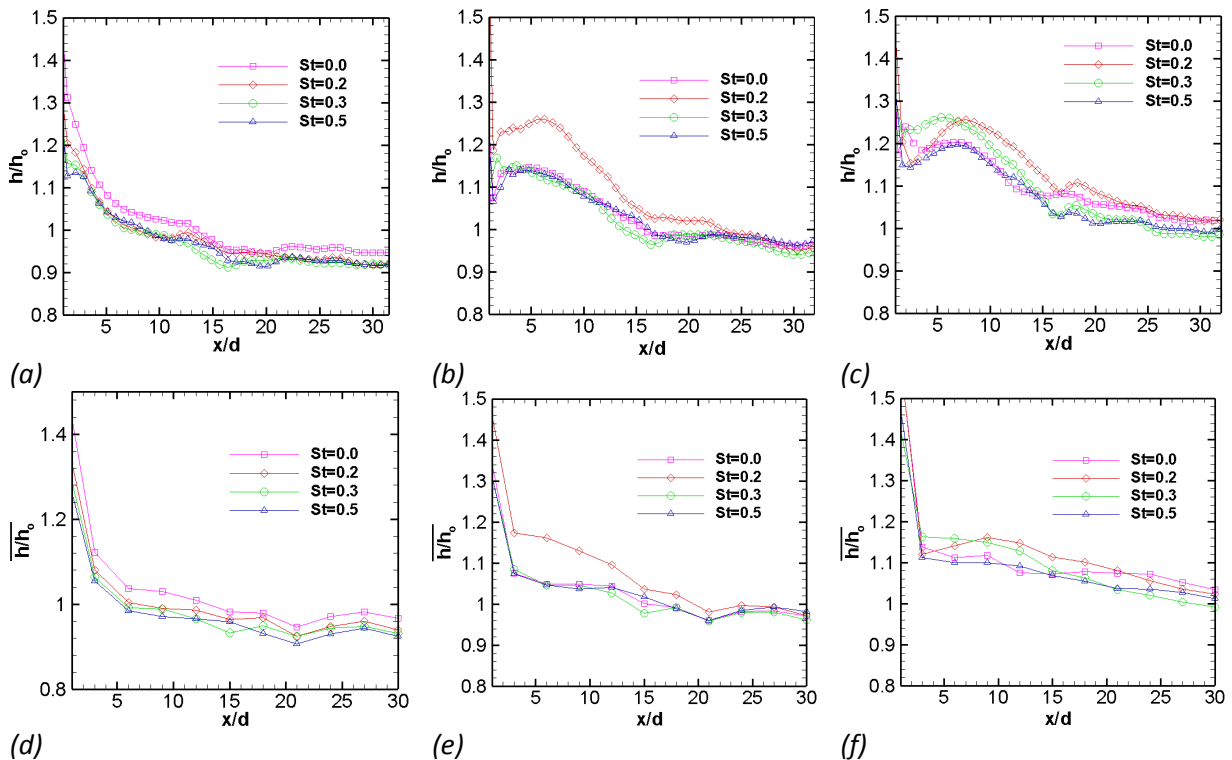


Figure (6. 14): Film cooling at  $T_i/T_\infty = 2$ , centreline heat transfer coefficient (a)  $\overline{M} = 0.65$ , (b)  $\overline{M} = 1$ , (c)  $\overline{M} = 1.25$ , and laterally-averaged heat transfer coefficient (d)  $\overline{M} = 0.65$ , (e)  $\overline{M} = 1$ , (f)  $\overline{M} = 1.25$ .

For  $\overline{M} = 0.65$ , different cases of pulsation do not have a significant impact on the convective coefficient, and the steady blowing case appears marginally superior to the other cases. Beyond the intermediate downstream distance of approximately  $x/d \approx 13$  some decrease in the convective coefficient lower than  $h/h_0=1$  is observed. The centerline convective heat transfer coefficient profiles for  $\overline{M} = 1$  indicate a distinctive rise with pulsation at  $St=0.2$ , as shown in figure (6.14b). In the cases of higher blowing ratio, a steep trajectory of the jet accompanied with the low frequency pulsations boosts the convective coefficient nearly up to a streamwise distance of  $x/d \approx 24$  for  $\overline{M} = 1$ . Similarly, this distance extends nearly up to  $x/d \approx 16$  for  $St=0.2$  and up to  $x/d \approx 14$  for  $St=0.3$  at a blowing ratio of

$\bar{M} = 1.25$ . The pulsation at  $St=0.3$  also increase the convection coefficient in the lateral direction up to  $x/d \approx 7$  for  $\bar{M} = 1.25$ , see figure (6.14f).

In figures (6.14b) and (6.14c), the rise of heat transfer coefficient in the near downstream region of the hole for the case of  $\bar{M} = 1$  and 1.25 is linked with the significantly higher turbulence region lying just downstream of the injection hole and with the passing of turbulent wake structures in the cases of pulsation, as was previously observed in the section of aerodynamic analysis. Since, the zone of aerodynamic measurement was only extended up to  $x/d=6.5$ . Therefore, the approximate distance to which these strong turbulent effects persist before diffusing in the mainstream flow was actually remained unknown from the aerodynamic results. An increase in the heat transfer coefficient in the immediate downstream region of the hole was also shown in Gritsch et al. (2000). They suggested a monotonic increase in the heat transfer with respect to  $x/d$  for low blowing ratio cases ( $\bar{M} \leq 1.25$ ) and a monotonic decrease in heat transfer for high blowing ratio cases ( $\bar{M} \geq 1.75$ ). In the reference article, an increase of 8% from  $x/d=2$  to 6 was shown for laterally-averaged heat transfer coefficient under steady blowing at  $\bar{M} = 1$ , while using a single  $30^\circ$  streamwise cylindrical hole, see figure (6.15). However, in present study, the estimation of laterally-averaged heat transfer coefficient with large number of crosswise profiles has not shown a similar trend as was found in the reference article. Under these conditions, the present study has shown an increase of 6% in the centerline heat transfer coefficient as shown in figure (6.14b). The disagreement between these two results may be because of the difference in the flow conditions, which include the Reynolds number  $Re_d$  (75000 against 8609), the boundary layer thickness  $\delta/d$  (0.5 against 1) and the turbulent intensity of the oncoming freestream boundary layer (2% against 1.2%).

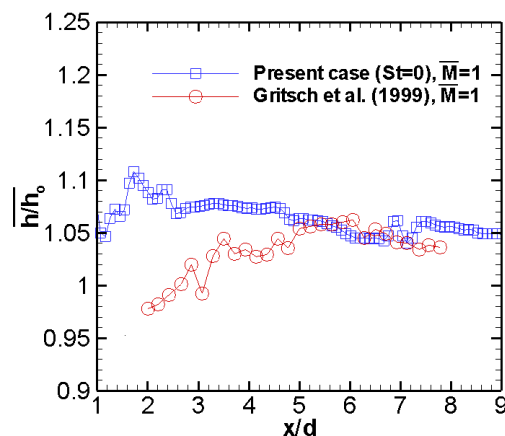


Figure (6. 15): Comparison of the laterally-averaged heat transfer coefficient in the immediate downstream region.

The variation in centerline and laterally-averaged convective heat transfer coefficient for different pulsing conditions are shown in figure (6.16a-f). These results compare the effects of pulsation on the convective heat transfer coefficient for different blowing ratios examined

*“Experimental aerothermal characterization of a pulsating jet issuing in a crossflow: Influence of Strouhal number excitation on film cooling”*

with a fixed temperature ratio of  $T_i/T_\infty = 1$ . It was generally observed that, when the jet flow becomes slightly dense then the variation in the convection coefficient due to the pulsation of injectant flow further narrows down. As shown in figure (6.16a), the variation in convective coefficient with Strouhal number for  $\bar{M} = 0.65$  remains quite small, as well as for the case of  $\bar{M} = 1$  in figure (6.16b). For  $\bar{M} = 1$ , the pulsation case of  $St=0.2$  remains slightly superior to the rest of the cases for the thermal exchange. However, at higher blowing ratio ( $\bar{M} = 1.25$ ), the effect of pulsation becomes more clearer, and the pulsation at  $St=0.2$  and  $0.3$  show orderly increasing of heat transfer coefficient as was observed previously. This trend is evident from the centerline and laterally-averaged results shown in figure (6.16c) and (6.16f) respectively.

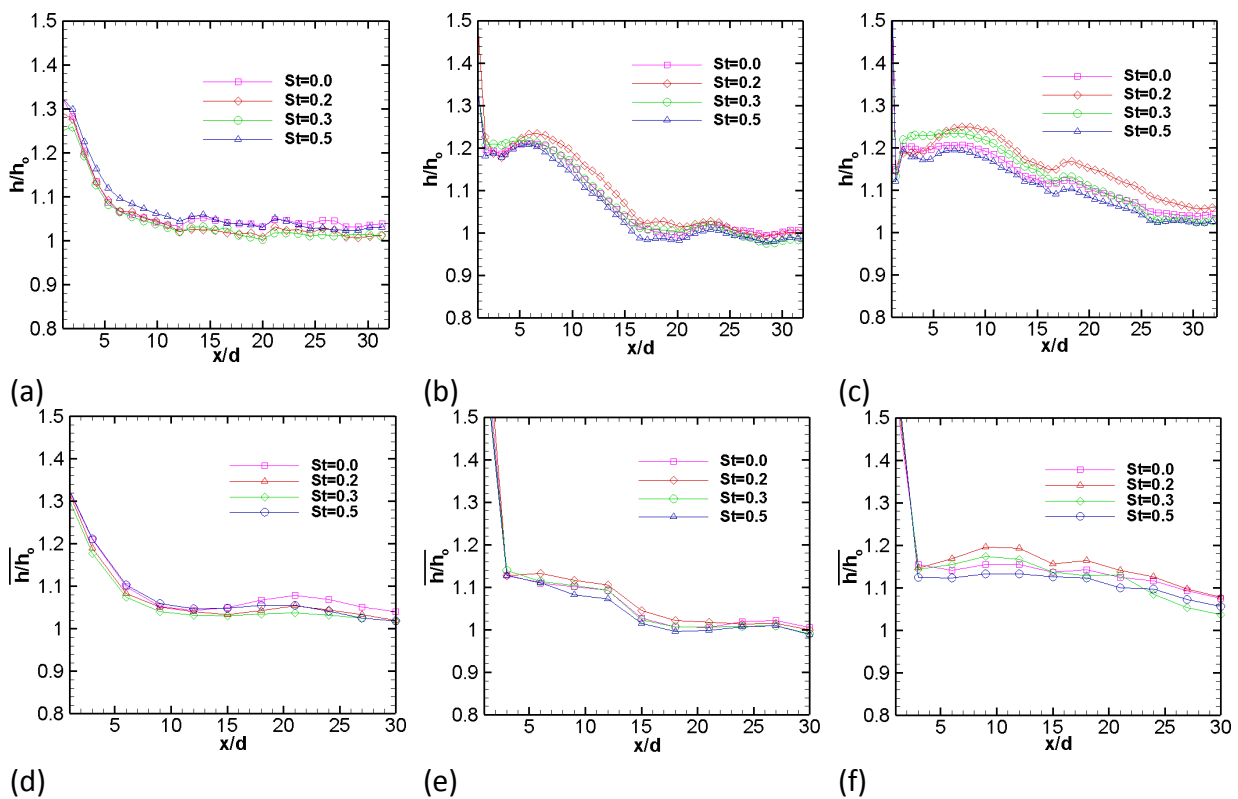


Figure (6. 16): Film cooling at  $T_i/T_\infty = 1$ , centreline heat transfer coefficient (a)  $\bar{M} = 0.65$ , (b)  $\bar{M} = 1$ , (c)  $\bar{M} = 1.25$ , and laterally-averaged heat transfer coefficient (d)  $\bar{M} = 0.65$ , (e)  $\bar{M} = 1$ , (f)  $\bar{M} = 1.25$ .

## 6.5 Comparison of results

The study of the thermal aspects of the film cooling flow involving a pulsating jet is a fairly recent issue. Therefore, the number of both experimental and numerical studies contributing to the variety of conditions relevant to both the characteristics of the interacting flow and the parameters of the imposed pulsation are only few in numbers. The potential of jet pulsation for the improvement in wall coverage was examined by Coulthard

et al. (2007). They use a row of 35° cylindrical hole placed 3d apart to study a range of blowing ratio (0.25, to 1.5) and the range of Strouhal numbers ( $St = fd/U_\infty$ ; 0.0119 to 0.1905). They mentioned that the higher frequency pulsations generally tend to result in lower effectiveness in the cases when the flow remains attached to the wall. For steady blowing cases with jet liftoff; such as for  $\overline{M} = 1$ , the high-frequency pulsation helps to increase film cooling effectiveness due to the injection of lower coolant mass flow during a significant fraction of the pulse cycle. More recently, the Direct Numerical Simulation (DNS) conducted by Muldoon and Acharya (2009) has shown some improvement in wall coverage with pulsation ( $M=1.5$ ,  $St=0.32$ , Duty-Cycle=50%) compared to steady blowing of the jet using a single cylindrical hole with 30° injection. The computational results of Kartuzova et al. (2009) also indicated an improvement in wall protection as a function of blowing ratio for an injection from a 35° cylindrical hole. They mentioned that the overall higher injectant film concentration with jet pulsation is only achievable at the blowing ratios triggering jet lift-off, such as  $\overline{M} = 1.5$ . At  $\overline{M} = 1.5$ , they observed higher cooling efficiency with  $St=0.38$  than for  $St=1.0$  and for the steady blowing case.

The heat transfer experiments performed by Coulthard et al. (2006) have focused the effect of injectant flow pulsation in film cooling. The resulting effects were explained by presenting the Stanton number ratio for a range of Strouhal numbers ( $St = fd/U_\infty = 0.0119$  to 0.1905), which were studied for a range of blowing ratio (0.25 to 1.5). The chosen Strouhal numbers in the reference are relatively low compared to the present study and are studied for a row of 5 cylindrical holes. However, these results can help in making a qualitative assessment of the resulting flow field to compare the general attributes of the injectant film. They concluded that the pulsing generally tends to increase Stanton number ratio and decrease the effectiveness. The heat flux ratio depends most strongly on film cooling effectiveness.

The comparisons with relevant cases found in the literature are shown in figure(6.17a-b). The comparisons between the results of the present study and the above mentioned references are limited to only a few cases due to the existing disparity among the dynamic parameters and the fluid properties of both the oncoming boundary layer and the jet flow.

Figure (6.17a) shows the comparison of centerline adiabatic effectiveness given by Muldoon and Acharya (2009) for  $\overline{M} = 0.75$  and  $St=0.32$  and the present study for  $\overline{M} = 0.65$  and  $\overline{M} = 1$  with pulsation at  $St=0.3$ . For a similar Strouhal number, the profile of adiabatic effectiveness obtained from the reference case is found to be on the intermediate level compared to the ones determined from the present study, where the profile determined for  $\overline{M} = 0.65$  is found to be slightly closer to the reference case. Figure (6.17b) shows the comparison of centerline Stanton number ( $Stan/Stan_0$ ) for  $\overline{M} = 1$  and  $St=0.2$ . The calculated

values of centerline Stanton number is slightly higher within an axial distance of  $x/d = 4$  to 12, compared to the findings of Coulthard et al. (2006).

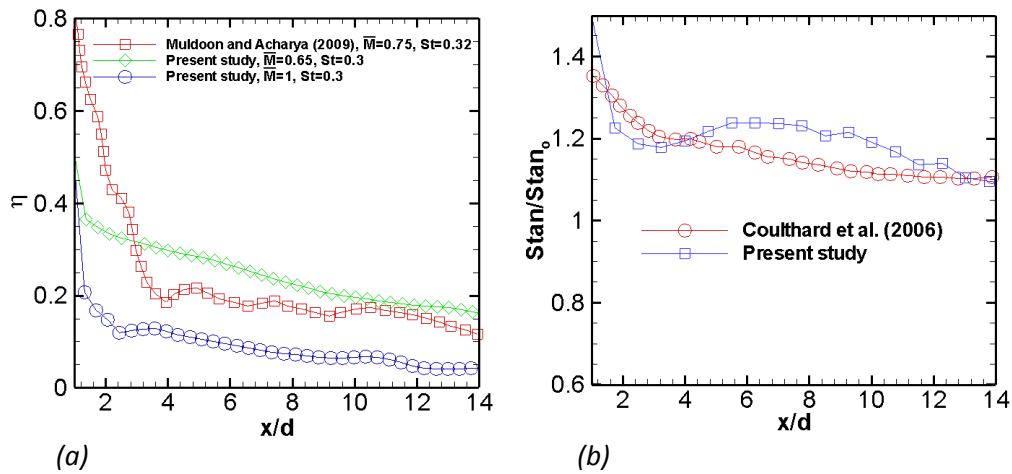


Figure (6. 17): Comparison of Film cooling parameters blowing at  $T_i/T_\infty = 2$ , (a) centreline adiabatic effectiveness (b) centreline Stanton number

## 6.6 Spatially-averaged effectiveness and heat transfer coefficient

The spatially-averaged results are estimated to figure out the average response of the flow field within a certain region. The area confined for calculating the integral-average of any particular quantity is formed by  $x/d=0$  to 30 and  $z/d=0$  to -1.5, as shown in figure (6.18). The set of equations used for determining spatially-averaged effectiveness and normalized heat transfer coefficient are given by Eq. (6.3) and Eq. (6.4).

$$\bar{\eta} = \frac{1}{|(x_2 - x_1)(z_2 - z_1)|} \int_{z_1}^{z_2} \int_{x_1}^{x_2} \eta(x, z) dx dz \quad \dots\dots\dots(6. 3)$$

$$\overline{h/h_o} = \frac{1}{|(x_2 - x_1)(z_2 - z_1)|} \int_{z_1}^{z_2} \int_{x_1}^{x_2} h/h_o(x, z) dx dz \quad \dots\dots\dots(6. 4)$$

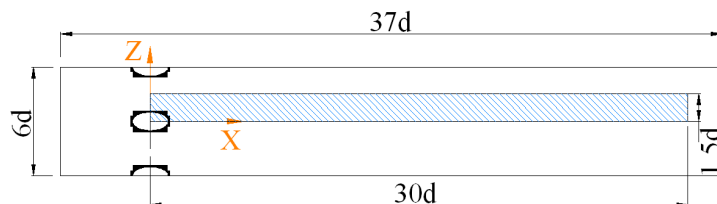


Figure (6. 18): Wall zone for estimating spatially-averaged results.

The spatially-averaged effectiveness and heat transfer coefficient as a function of Strouhal number are plotted in figure (6.19a) and (6.19b). It can be observed that the film

cooling cases with  $\bar{M} = 0.65$  results in the highest effectiveness and the lowest convective coefficient for the entire range of pulsation. The pulsation causes a consistent downward gradient in effectiveness for  $\bar{M} = 0.65$ , and the linear regression curve fitting provides a gradient of  $-1/5$  with a correlation coefficient of  $R^2 = 0.9887$ . The spatially-averaged heat transfer coefficient for  $\bar{M} = 0.65$  with linear fitting provides a correlation coefficient of  $R^2 = 0.9485$  and a gradient of  $-1/10$ . Data from any other case do not deliver a modest value of  $R^2$  for linear fitting. It can also be observed that the effectiveness at  $\bar{M} = 0.65$  and  $St = 0.5$  is quite comparable to the pulsation case of  $St = 0.2$  for both  $\bar{M} = 1$  and  $\bar{M} = 1.25$ , as effectiveness for these cases are only 14% and 9% lower than for  $\bar{M} = 0.65$ .

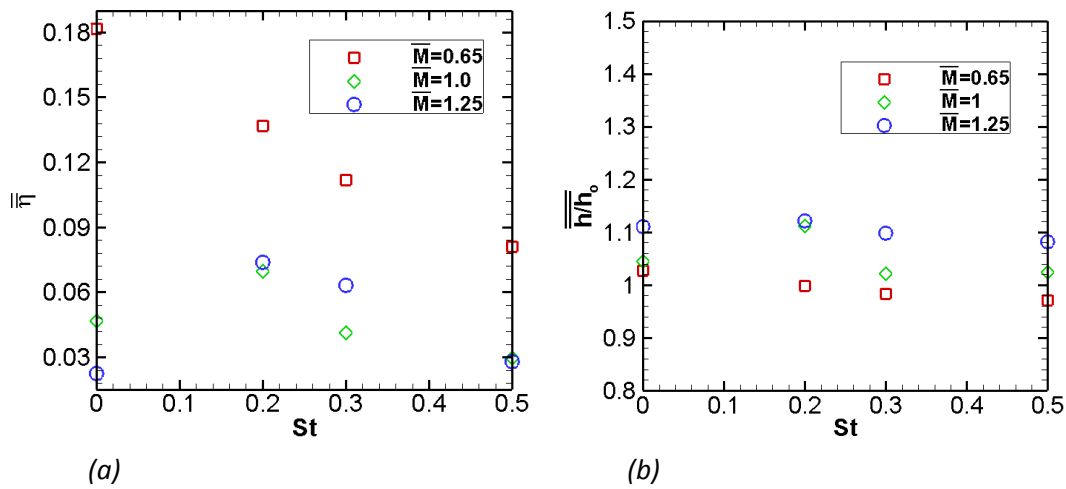


Figure (6. 19): Comparison of different cases of pulsation,  $T_i/T_\infty = 2$ , (a) spatially-averaged effectiveness, (b) spatially-averaged heat transfer coefficient

### 6.7 Net heat flux reduction (NHFR)

The ultimate gains of film cooling technique can be determined by accounting a function combining both adiabatic effectiveness and convective heat transfer coefficient, i.e.;  $f(\eta, h/h_o)$ . Sen et al. (1996) presented a term called Net Heat Flux Reduction (NHFR) to account for the required function, which is simply a ratio of reduction in heat transfer to the wall with film cooling and heat transfer to the wall without film cooling, as given by Eq. (6.5).

$$NHFR = 1 - \phi/\phi_o \tag{6.5}$$

By replacing the terms of heat fluxes without film cooling;  $\phi_o = h_o(T_w - T_\infty)$  and with film cooling;  $\phi = h(T_w - T_{ad})$  in the above equation, one would end up getting the following form;

$$NHFR = 1 - h/h_o(1 - \eta\theta) \tag{6.6}$$

Where;  $\eta = (T_{ad} - T_{\infty}) / (T_i - T_{\infty})$  and  $\theta = (T_i - T_{\infty}) / (T_w - T_{\infty})$ . The first dimensionless parameter is the adiabatic effectiveness mentioned previously, while the second one,  $\theta$ , is generally called as dimensionless temperature ratio in quite a figurative way and can be obtained in different ways for computing NHFR. The technique of infrared measurement as described above requires to register the wall temperature at different wall fluxes. The measured wall temperatures can be used to calculate  $\theta$ , as well as NHFR by using Eq. (6.6) corresponding to each case. The variation of NHFR plotted as a function of  $\theta$  can be used to compare different cases of film cooling as shown by Gritsch et al. (2000). Most often, the NHFR or a heat flux ratio is calculated by using the engine representative value of gas turbine blade film cooling, as was maintained by Mick and Mayle (1988), Sen et al. (1996), Gritsch et al. (2000) and Coulthard et al. (2006). For film cooled turbine blades a typical value of  $\theta = 1.6$  is usually employed.

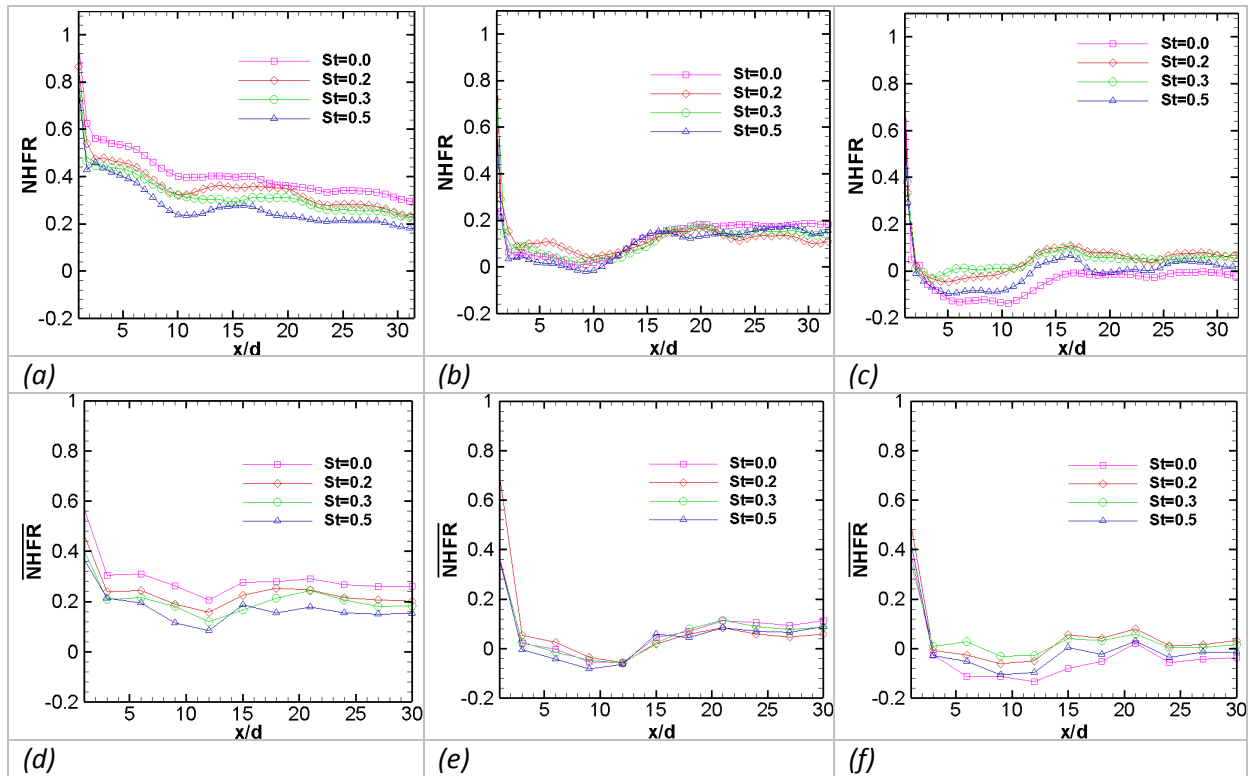


Figure (6. 20): Film cooling at  $T_i/T_{\infty} = 2$ , centreline NHFR (a)  $\bar{M} = 0.65$ , (b)  $\bar{M} = 1$ , (c)  $\bar{M} = 1.25$ , and laterally-averaged NHFR (d)  $\bar{M} = 0.65$ , (e)  $\bar{M} = 1$ , (f)  $\bar{M} = 1.25$ .

The centreline Net Heat Flux Reduction (NHFR) for different cases of pulsation is shown for different blowing ratios and a constant temperature ratio of  $T_i/T_{\infty} = 2$  in figure (6.20a-f). It can be observed from figure (6.20a) that the net effect of employing a pulsating injectant flow in a film cooling configuration of  $\bar{M} = 0.65$  is the performance reduction of injectant wall coverage. The overall performance in case of  $\bar{M} = 1$  is lower than for  $\bar{M} = 0.65$ ,

either the case of steady blowing or the case of pulsing flows. Film cooling performance is higher with  $St=0.2$  than the rest of the cases for  $\bar{M} = 1$  nearly up to a streamwise distance of  $x/d \approx 10$ . Apart from this location, a slight increase in the performance is regarded as a probable cause of the jet turning towards the wall after losing a fraction of its momentum, prior to the moment when the downstream injectant flow is taken over by the dynamics of mainstream flow. The film cooling performance in case of  $\bar{M} = 1.25$  is the lowest than all other cases of blowing ratios. The negative NHFR value indicates an inefficient use of injectant flow, as the thermal exchange is boosting up here due to the increase in convective coefficient. However, pulsation improves the overall film cooling performance compared to steady blowing for  $\bar{M} = 1.25$ .

The variation of spatially-averaged NHFR as a function of Strouhal number is shown in figure (6.21). It can be observed that the film cooling case with  $\bar{M} = 0.65$  delivers higher performance in both steady blowing and in pulsating cases compared to other blowing ratios. At  $\bar{M} = 1$ , pulsation at  $St=0.2$  increases both the adiabatic effectiveness and convective heat transfer coefficient. Therefore, there is no net-gain in the film cooling performance. However, an increase of 36 % is achieved with pulsation at  $St=0.3$ . For  $St=0.2$ , film cooling performance is nearly similar for both  $\bar{M} = 1$  and  $\bar{M} = 1.25$ .

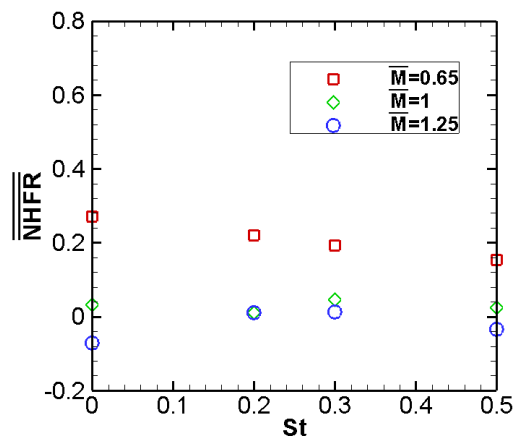


Figure (6. 21): Film cooling at  $T_i/T_\infty = 2$ , spatially-averaged NHFR.

The net effect of pulsation compared to the respective case of steady blowing is listed in Table-6.3 for a range of blowing ratios considered for film cooling investigation. At  $\bar{M} = 0.65$ , the film cooling performance is reduced by 18.8 %, 28.9 % and 43.1 % due to pulsing at  $St=0.2$ , 0.3 and 0.5 respectively. At  $\bar{M} = 1$ , the film cooling performance is reduced by 65.7 % and 25.9% for  $St=0.2$  and 0.5, while the performance is increased by 35.8 % for  $St=0.3$ . At  $\bar{M} = 1.25$ , the performance is increased by 116.2 %, 117.4 % and 53.2 % for pulsing at  $St=0.2$ , 0.3 and 0.5 respectively.

	<b>St=0.2</b>	<b>St=0.3</b>	<b>St=0.5</b>
$\overline{M} = 0.65$	-18.8 %	-28.9 %	-43.1 %
$\overline{M} = 1$	-65.7 %	35.8 %	-25.9 %
$\overline{M} = 1.25$	116.2%	117.4 %	53.2 %

Table-6.3: Performance Budget of different pulsing cases of film cooling compared to the respective steady blowing cases.

## 6.8 Conclusion

The effect of injectant flow pulsation on film cooling performance was studied by using the technique of infrared thermography. The results for adiabatic effectiveness, convective heat transfer coefficient and the Net Heat Flux Reduction (NHFR) are presented. In steady blowing, the film cooling effectiveness was superior for the blowing ratio of  $\overline{M} = 0.65$ , while the convective heat transfer was superior for the blowing ratio of  $\overline{M} = 1.25$ . For  $\overline{M} = 0.65$ , the effectiveness has reduced consistently in an orderly manner with the induction of injectant flow pulsation, whereas the convective heat transfer coefficient has not shown significant variations with pulsation. The overall performance given by NHFR has also shown a consistent decline with the pulsation at different Strouhal numbers for  $\overline{M} = 0.65$ . The case of  $\overline{M} = 1$  have shown a noticeable increase in film cooling effectiveness as well as in heat transfer coefficient for  $St=0.2$  compared to the other cases. However, the overall performance has shown that these factors leveled off for  $St=0.2$ , and only some improvement is observed for the case of  $St=0.3$ . For  $\overline{M} = 1.25$ , an increase in film cooling effectiveness and convective heat transfer coefficient was observed for  $St=0.2$  and  $0.3$  compared to  $St=0$  and  $0.5$ . The NHFR have shown an increase in all cases compared to steady blowing. Among these, the pulsing at  $St=0.2$  and  $0.3$  have resulted in nearly similar improvement in film cooling performance, while the film cooling performance with pulsation at  $St=0.5$  was found to be nearly half of them.

## 6.9 References

1. Bons JP, Rivir JB, Mac Arthur CD, Pestian DJ, "The effect of unsteadiness on film cooling effectiveness", Wright Laboratory, WL-TR-96-2096, Jan-1995.
2. Coulthard SM, Volino RJ, Flack KA, "Effect of jet pulsing on film cooling-Part II: Heat transfer results", ASME Turbo Expo 2006: Power for Land, Sea and Air, Barcelona, May 8-11 2006.
3. Coulthard SM, Volino RJ, Flack KA, "Effect of jet pulsing on film cooling-Part I: Effectiveness and flow-field Temperature results", ASME, Journal of Turbomachinery, 129 (2007) 232-246.
4. Dieumegard D, "Etude Experimentale Du Film Cooling Developpe Par Une Range De Cinq Perforations Et Modelisation Des Echanges Convectifs", Mémoire de Diplôme d'ingénieur, Université de Poitiers- ENSMA, 2003.
5. Eckert ERG, "Gas-to-gas film cooling", Published in Inzhenerno-Rizicheskii Zhurnal, SpringerLink, 19 (1970) 426-440.
6. Eriksen VK, Goldstein RJ, "Heat transfer and film cooling following injection through inclined circular tubes", ASME, Journal of heat transfer, (1974) 239-245.
7. Goldstein RJ, Eckert ERG, "Effects of hole geometry and density on three-dimensional film cooling", Int. J. Heat Mass Transfer, 17 (1974) 595-607.
8. Gritsch M, Schulz A, Wittig S, "Film-cooling holes with expanded exits: near hole heat transfer coefficients", Int. J. Heat Mass Transfer, 21 (2000) 146-155.
9. Kartuzova O, Danila D, Ibrahim M, "Computational simulation of cylindrical film hole with jet pulsation on flat plates", Journal of propulsion and power, 25 (2009) 1249-1258.
10. Mick WJ, Mayle RE, "Stagnation film cooling and heat transfer, including its effect within the hole pattern", ASME, Journal of Turbomachinery, 110 (1988) 66-72.
11. Muldoon F, Acharya S, "DNS study of pulsed film cooling for enhanced cooling effectiveness", Int. J. Heat Mass Transfer, 52 (2009) 3118-3127.
12. Sen B, Schmidt DL, Bogard DG, "Film cooling with compound angle holes: Heat transfer", ASME, Journal of Turbomachinery, 118 (1996) 800-806.
13. Yuen CHN, Martinez-Botas RF, "Film cooling characteristics of a single round hole at various streamwise angles in a crossflow: Part 1 effectiveness", Int. J. Heat Mass Transfer, 46 (2003a) 221-235.
14. Yuen CHN, Martinez-Botas RF, "Film cooling characteristics of a single round hole at various streamwise angles in a crossflow Part II: heat transfer coefficients", Int. J. Heat Mass Transfer, 46 (2003b) 237-249.



## Table of Contents

---

7.1	Validation of cold wire thermometry to measure fluctuating temperature distribution.....	221
7.2	Temperature distribution in the central plane ( $z/d=0$ ).....	226
7.2.1	Comparison of the cases of different blowing ratio (steady blowing) .....	226
7.2.2	Comparison of the cases of different Strouhal numbers .....	227
7.3	Temperature distribution at off-centre plane ( $z/d=1.5$ ).....	234
7.3.1	Comparison of the cases of different blowing ratio (steady blowing) .....	235
7.3.2	Comparison of the cases of different Strouhal numbers .....	236
7.4	Skewness and flatness factor.....	242
7.5	Conclusion.....	245
7.6	References .....	247

## Nomenclatures

<u>Abbreviations</u>		<u>Subscripts/superscripts</u>	
$\rho$	Fluid density (kg/m <sup>3</sup> )	$i$	Injectant
$T$	Temperature (K)	$ad$	Adiabatic
$d$	Hole diameter (mm)	$\infty$	Free-stream
$L$	Hole length (mm)	$o$	Without injection
$U$	Streamwise velocity (m/s)	$rms$	Root mean square
$V$	Normal velocity (m/s)	$-$	Laterally-averaged
$u$	Streamwise velocity fluctuation (m/s)	$=$	Spatially-averaged
$v$	Normal velocity fluctuation (m/s)	$\sim$	Periodic component
$\delta$	Boundary layer thickness (mm)	$j$	Index number
$\delta^*$	Displacement thickness (mm)	$s$	Excitation
$\overline{M}$	Blowing ratio ( $= \rho_i \overline{U}_i / \rho_\infty \overline{U}_\infty$ )		
$Re_\infty$	Reynolds number ( $= \overline{U}_\infty \cdot \delta / \nu$ )		
$Re_i$	Reynolds number ( $= \overline{U}_i \cdot d / \nu$ )		
$St$	Strouhal number ( $= f \cdot d / \overline{U}_i$ )		
$IT$	Turbulent intensity (%)		
$\phi$	Heat flux (W/m <sup>2</sup> )		
$\varepsilon$	Emissivity (m <sup>2</sup> /s <sup>3</sup> )		
$\tau$	Transmissivity		
$h$	Heat transfer coefficient (W/m <sup>2</sup> .K)		
$NHFR$	Net heat flux reduction ( $= 1 - \phi / \phi_o$ )		
$\theta$	Non-dimensionalized temperature ( $= (T - T_\infty) / (T_i - T_\infty)$ )		
$\eta$	Effectiveness ( $= (T_{ad} - T_\infty) / (T_i - T_\infty)$ )		
$t$	Time (s)		
$f$	Frequency (Cycles/s)		
$x, y$	Streamwise and normal coordinates (mm)		

## **STUDY OF THE FILM-COOLED BOUNDARY LAYER FLOW TEMPERATURE**

A Cold wire survey was performed to figure out the temperature distribution of the flow field resulting from the interaction of a mainstream boundary-layer and a slightly heated injectant flow. Prior to their mixing, the temperature of the mainstream flow was maintained at  $20 \pm 0.2$  °C and the temperature of injectant was maintained at  $40 \pm 0.4$  °C. The surrounding walls of the wind tunnel test section including the injection wall were at room temperature. Cold wire measurements allow us to determine the level to which injectant flow “mixes” with the mainstream flow in different cases of blowing ratio ( $\overline{M} = 0.65, 1$  and  $1.25$ ) and Strouhal number pulsation ( $St = 0, 0.2, 0.3$  and  $0.5$ ).

Before starting the analysis of the film cooling parameters, a few important features of the flow field, which were discussed previously in the section of aerodynamic analysis, are recalled here. The schematic diagrams shown in figure (7.1a) and (7.1b) provide a general description of the flow field for both unpulsed and pulsating film cooling cases. The averaged flow structures appearing in the steady blowing case or the systematic variations occurring in the unsteady blowing (pulsating case) will help to explain the flow field attributes in the thermal analysis. The steady blowing case of higher jet momentum results in the lifting of the jet from the wall, as indicated by figure (7.1a). The highly lifted jet tends to break up into large fluid packets that feed into the downstream at a regular basis, as shown in figure (7.1b).

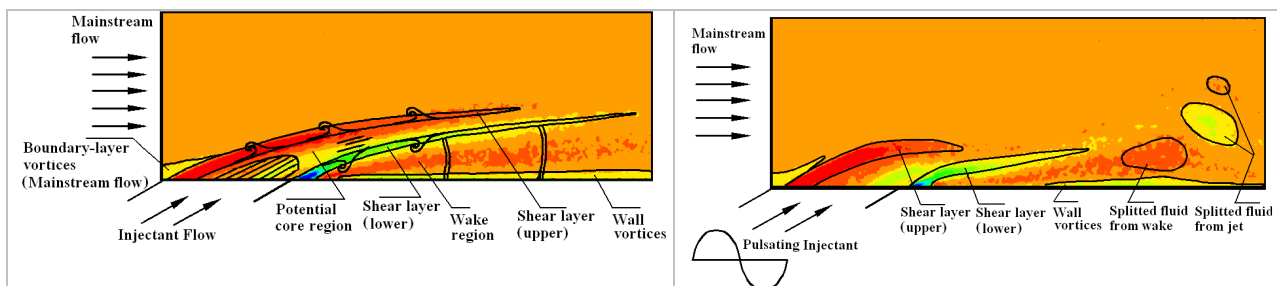


Figure (7. 1): Schematic diagram giving a general description of flow structures, (a) unpulsed (b) pulsating film cooling cases

### **7.1 Validation of cold wire thermometry to measure fluctuating temperature distribution**

The operational frequencies are verified by determining the power spectral density (PSD) from the cold wire results at  $y/d \approx 2$  and  $x/d \approx 30$  for both the central ( $z/d=0$ ) and off-centre plane ( $z/d=1.5$ ), as shown in figure (7.2a) and (7.2b). A band pass filter was introduced for a frequency range of 200-500 Hz by using Matlab® library filter. An order of

30 was chosen iteratively for filter design, which helped in clearing the noise from instantaneous temperature results ahead of calculating the PSD. The peak of 230 Hz is corresponding to the velocity pulsation generated by loudspeaker at  $St=0.3$  for  $M=1$ .

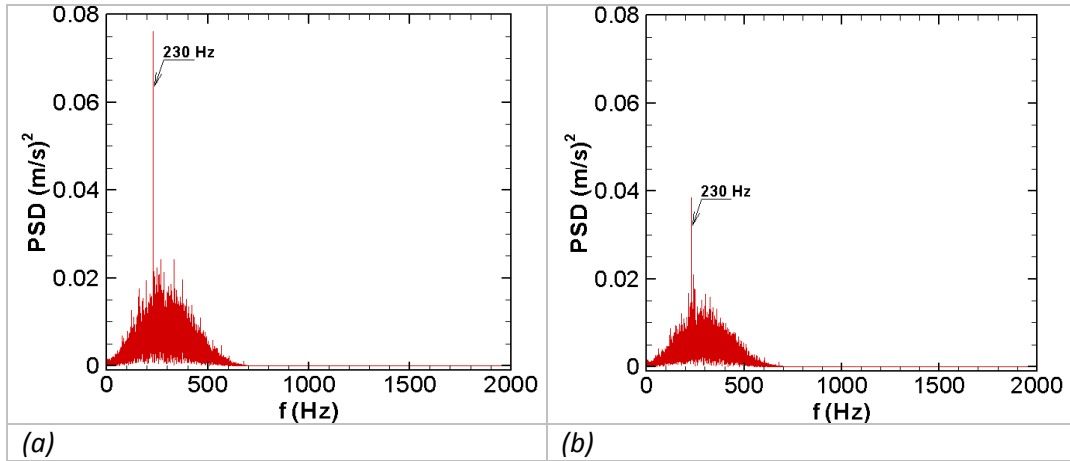


Figure (7. 2): PSD obtained from the cold wire results with probe positioned at  $y/d \approx 2$ ,  $x/d \approx 30$  along the lateral plane; (a)  $z/d=0$ , (b)  $z/d=1.5$ , for  $M=1$  and  $St=0.3$ .

Figure (7.3) shows the comparison of time-averaged temperature profiles with the results of Kohli et al. (1998) in case of steady blowing. The blowing ratio and injection angle in the reference case is 0.4 and  $35^\circ$  compared to 0.65 and  $30^\circ$  of present study. The mean temperature profiles obtained from Kohli and Bogard (1998) are appeared closer to the wall, which can be explained by the difference in blowing ratio.

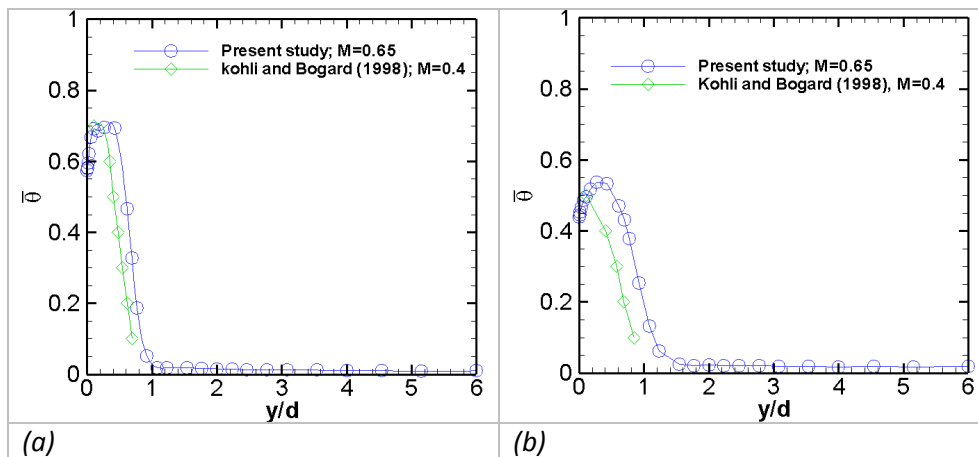


Figure (7. 3): Comparison of time-averaged temperature profiles in steady blowing, (a)  $x/d=3$ ,  $z/d=0$ , (b)  $x/d=7$ ,  $z/d=0$ .

This phase average decomposition has been applied to time-resolved temperature signals measured at  $x/d=30$ . Figure (7.4) shows the location of points used for determining the phase-averaged temperature distribution. These points lies on the wall-normal distance of

$y/d=0.77$  and 2 of both central and off-centre plane and a streamwise distance of  $x/d=30$ . These locations were chosen to verify the influence of the periodic variation of jet velocity at the largest downstream distance considered for profile measurements. If this is the case, this means that at shorter distances, turbulent mixing does not completely damp out the pulsation imposed initially.

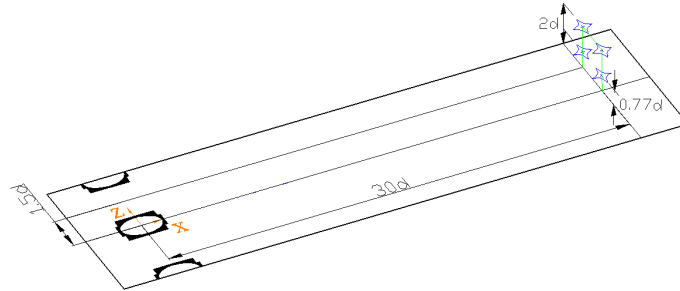


Figure (7. 4): Location of points for determining the phase-averaged temperature results, wall normal locations of  $y/d=0.77$  and 2, lying at  $x/d=30$  and  $z/d=0$

Figure (7.5a-i) shows the evolution of the phase-averaged temperature in a period of pulsation (where time is normalized by the pulsation period), for points lying at the central plane of the tunnel ( $z/d=0$ ). In spite of small amplitude shown in these figures, the evolution of mean temperature seems to follow the imposed periodic pulsation quite well for most of the cases. This allows us to conclude that the cold wire system is able to capture the temperature variations generated with pulsation. Periodic evolutions of the phase averaged temperatures are observed for all the case studied. The cases of  $St=0.5$  shown in Figure (7.5f) and Figure (7.5i) result in a less organized periodic evolution of the mean temperature is just because of the relative decline in the presence of injectant fluid in these regions. The observed levels of variations are less than  $6^{\circ}\text{C}$  (at maximum) in comparison with the initial temperature difference between the hot flow ( $40^{\circ}\text{C}$ ) and the cold flow ( $20^{\circ}\text{C}$ ).

Figure (7.6a-i) shows the evolution of the phase-averaged temperature in a period of pulsation for points lying at the off centre plane. These measurements can provide important informations regarding the lateral spreading of the injectant fluid, as a well organized periodic trend of the mean temperature signals to the larger presence of the injectant fluid. It can be observed that for  $\overline{M} = 0.65$  the lateral spreading of the injectant is poor for all cases of Strouhal numbers. However, for  $\overline{M} = 1$ , the lateral distribution of injectant fluid is improved in the cases of  $St=0.2$  and  $0.3$ . For  $\overline{M} = 1.25$ , the lateral distribution of injectant is increased for  $St=0.2$  compared to the other cases of pulsation.

According to these comparisons, we can conclude that the cold wire measurements is capable to measure both mean and rms temperature distributions of the flow resulting with the jet pulsation, and thus it can provide the basis to compare the cases of different Strouhal numbers.

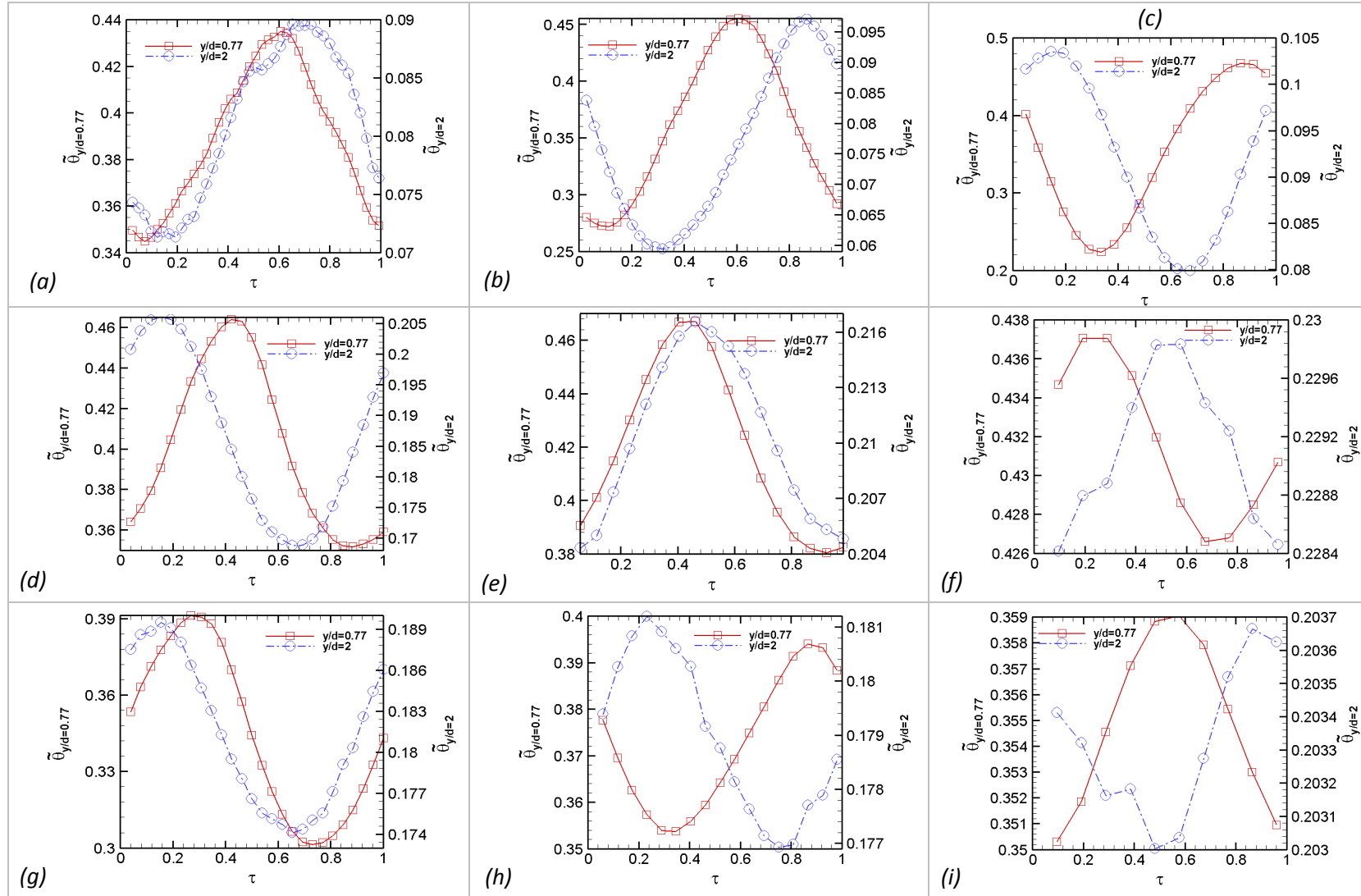


Figure (7. 5): Phase-averaged temperature of the points located at  $x/d=30, z/d=0$  and a perpendicular distance from the wall of  $y/d=0.77$  and  $y/d=2$ , (a)  $\bar{M} = 0.65, St=0.2$ , (b)  $\bar{M} = 0.65, St=0.3$ , (c)  $\bar{M} = 0.65, St=0.5$ , (d)  $\bar{M} = 1, St=0.2$ , (e)  $\bar{M} = 1, St=0.3$ , (f)  $\bar{M} = 1, St=0.5$ , (g)  $\bar{M} = 1.25, St=0.2$ , (h)  $\bar{M} = 1.25, St=0.3$ , (i)  $\bar{M} = 1.25, St=0.5$ .

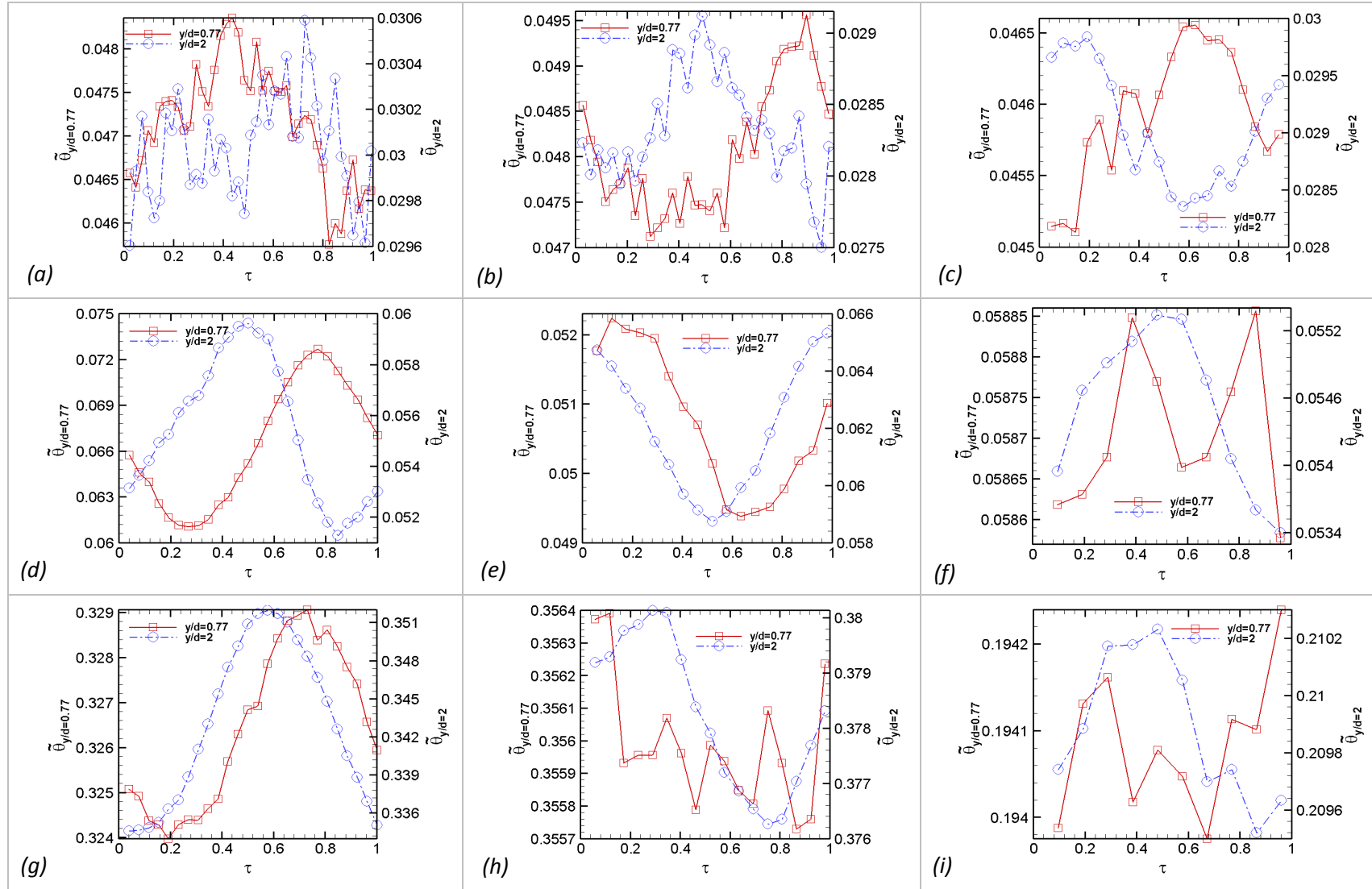


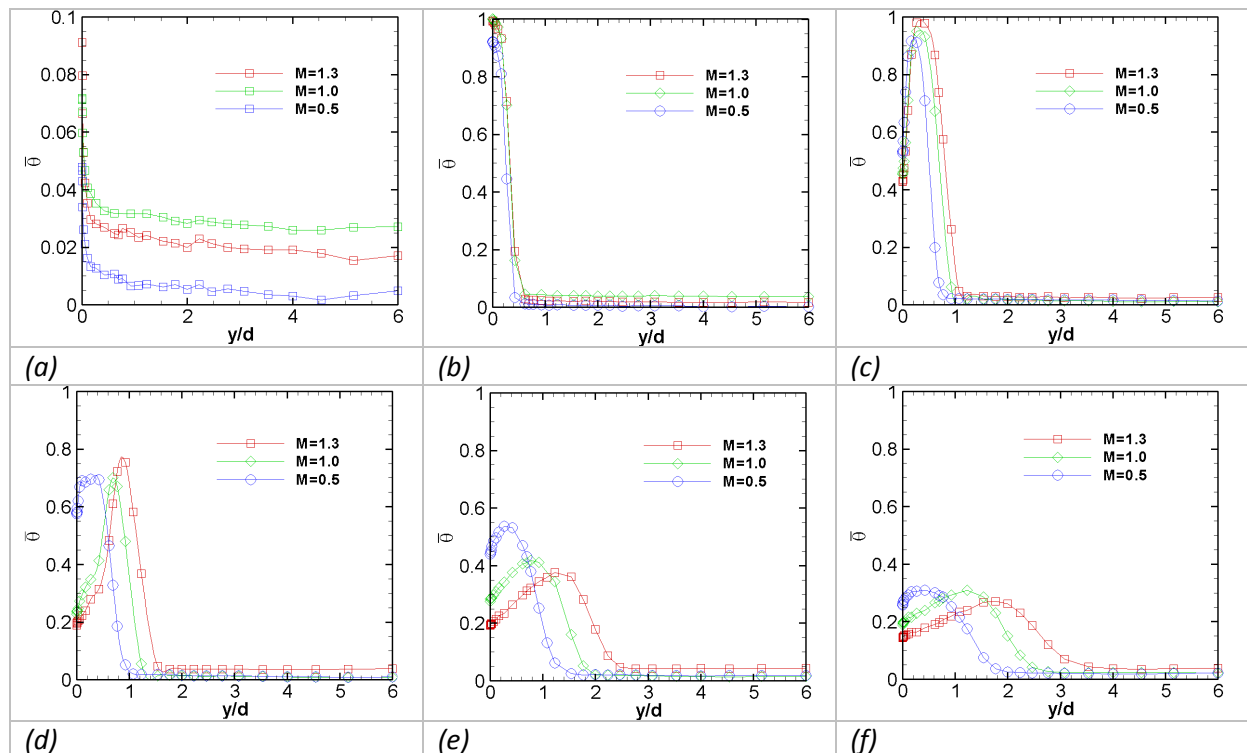
Figure (7. 6): Phase-averaged temperature of the points located at  $\bar{x}/d=30, \bar{z}/d=1.5$  and a perpendicular distance from the wall of  $y/d=0.77$  and  $y/d=2$ , (a)  $\bar{M} = 0.65, St=0.2$ , (b)  $\bar{M} = 0.65, St=0.3$ , (c)  $\bar{M} = 0.65, St=0.5$ , (d)  $\bar{M} = 1, St=0.2$ , (e)  $\bar{M} = 1, St=0.3$ , (f)  $\bar{M} = 1, St=0.5$ , (g)  $\bar{M} = 1, St=0.2$ , (h)  $\bar{M} = 1, St=0.3$ , (i)  $\bar{M} = 1, St=0.5$ .

## 7.2 Temperature distribution in the central plane ( $z/d=0$ )

Cold wire measurements in the central plane ( $z/d=0$ ) are performed to analyze the interaction of two flows affecting the injectant capacity of wall coverage for different blowing ratios maintaining a constant temperature ratio of  $T_i/T_\infty = 40/20 = 2$ . The temperature field is also analyzed to determine the patterns of injectant distribution in the mainstream flow subjecting to the pulsation at different Strouhal numbers.

### 7.2.1 Comparison of the cases of different blowing ratio (steady blowing)

The variation in time-averaged temperature profiles corresponding to different streamwise positions locating at the central plane of the injection hole ( $z/d=0$ ) are shown in figure (7.7a-g) for different cases of blowing ratios in study blowing ( $St=0$ ). Time-averaged temperature profile measured from the upstream side of the injection hole ( $x/d = -1.5$ ) is slightly higher for  $\bar{M} = 1$  compared to  $\bar{M} = 1.25$ , figure (7.7a). The slightly higher temperature in the wall region for both  $\bar{M} = 1$  and  $1.25$  is probably because of a weak vortex forming on the upstream edge of the jet with the obstruction of mainstream flow (see section 5.6).



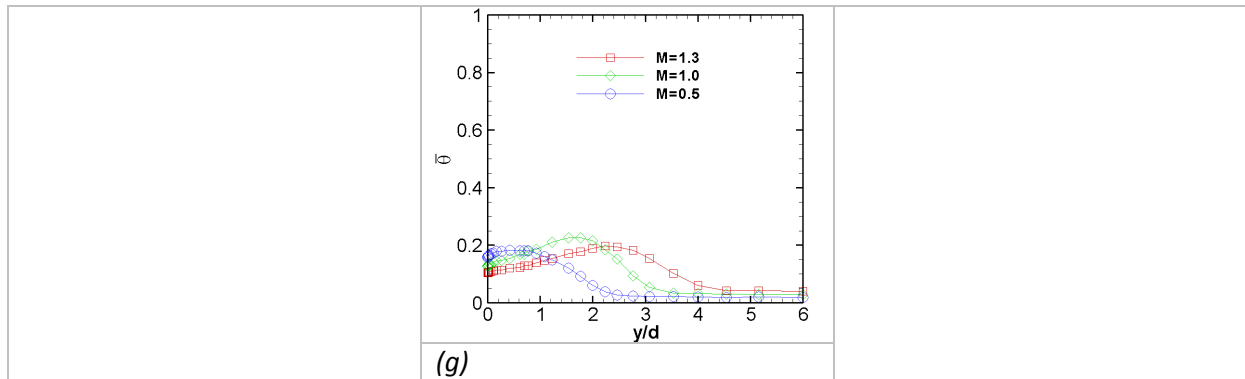


Figure (7. 7): Comparison of time-averaged profiles obtained from different blowing ratios under steady blowing (a)  $x/d=-1.5$ , (b)  $x/d=0$ , (c)  $x/d=1.5$ , (d)  $x/d=3$ , (e)  $x/d=7$ , (f)  $x/d=15$  and (g)  $x/d=30$ .

The temperature profiles shown in figure (7.7b-g) show a smooth increase in the thickness of hot film layer due to the growing of the jet structures with the downstream distance. On the downstream side of the hole ( $3 < x/d < 30$ ), these profiles show a more obvious distinction for the results acquired at different blowing ratios, as the successive increase in the profile thickness corresponds to the increasing of blowing ratio. At  $x/d=30$ , the mean temperature is only equal to 0.2, which is caused by the mixing between hot and cold flows.

At present, only the comparisons among different blowing ratios for the case of steady blowing are presented. Since, the other cases with pulsation possess a similar trend so their results are included in the Annex-D.

## 7.2.2 Comparison of the cases of different Strouhal numbers

### CASE 1: $M=0.65$

The comparisons of time-averaged temperature profiles in different cases of Strouhal numbers for  $\overline{M} = 0.65$  are shown in figure (7.8a-g). At the present blowing ratio, applying pulsation to the injectant flow only slightly influences the time-averaged results because the injectant fluid flows closer to the wall during most of the time in the period. Except, for the occasion when the discharge of injectant flow is maximum and a slight instantaneous lift-off from the wall takes place. At the present situation, a clear indication of the effect of pulsation is only noticeable after a certain downstream distance where the pulsation effect has grown up considerably. Apart from a downstream distance of  $x/d=3$ , it can be observed that the increase in pulsation Strouhal number reduces the temperature level of the flow measured in the near wall region. For  $St=0.3$  and  $0.5$ , the decrease in peak value of the profile is 8 % and 19 % for  $St=0.5$  compared to steady blowing. Bons et al. (1996) also noticed the decrease in temperature for blowing ratios less than 1. This signifies the lack of injectant flow in that region, as the injectant flow is carrying a superior temperature. This is also coherent with the findings of adiabatic effectiveness estimated from the experiments of

*“Experimental aerothermal characterization of a pulsating jet issuing in a crossflow: Influence of Strouhal number excitation on film cooling”*

infrared thermography, showing a continuous decrease in effectiveness with the increase of  $St$ , (see figure (6.13)).

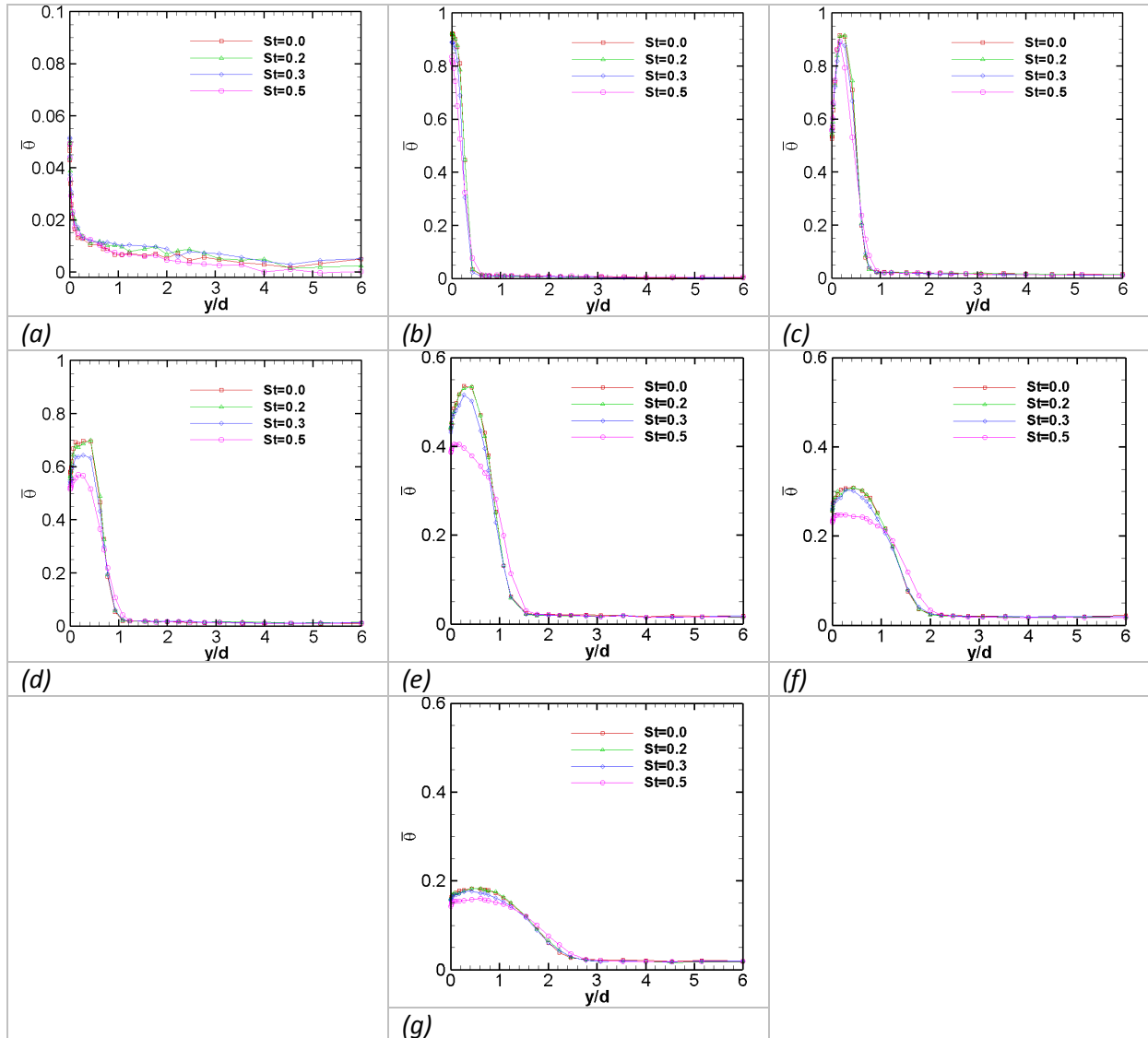
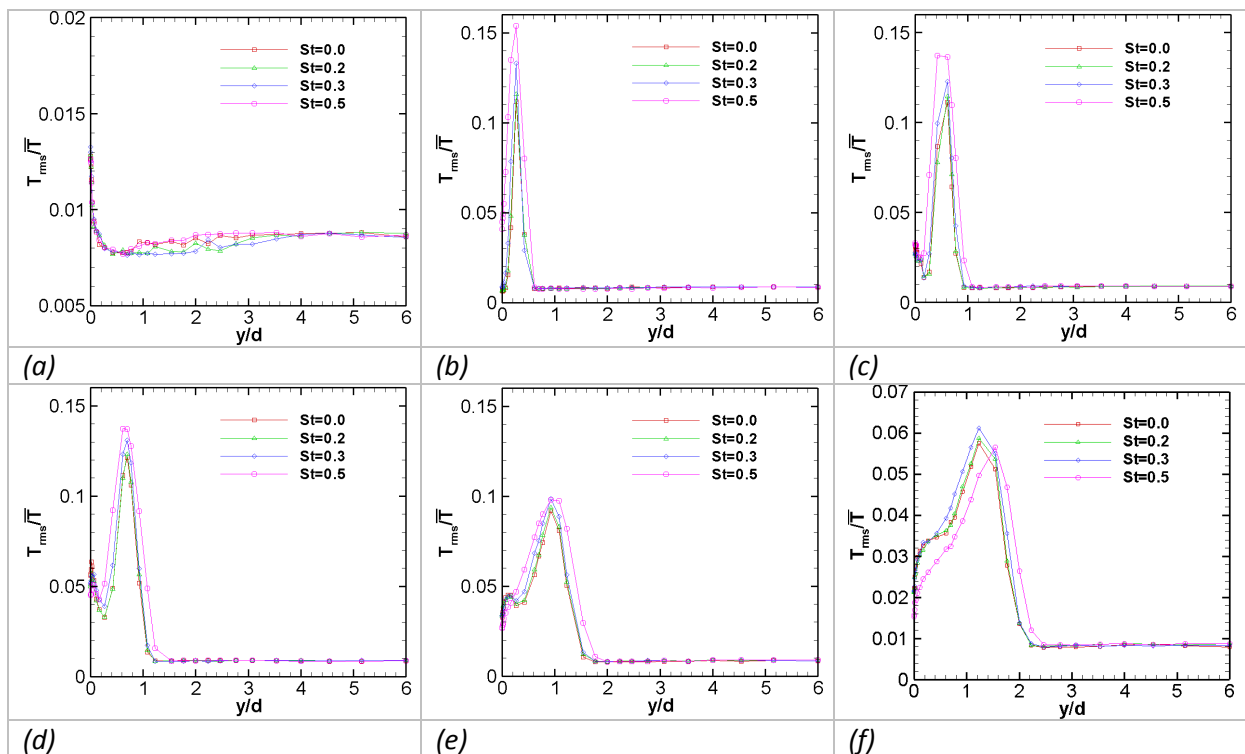


Figure (7. 8): Comparison of time-averaged profiles obtained at different Strouhal number with a blowing ratio of  $\overline{M} = 0.65$ , (a)  $x/d=-1.5$ , (b)  $x/d=0$ , (c)  $x/d=1.5$ , (d)  $x/d=3$ , (e)  $x/d=7$ , (f)  $x/d=15$  and (g)  $x/d=30$ .

This phenomenon of temperature reduction with the application of pulsation decreases gradually to the steady blowing case with the increase of downstream distance. Near the upper jet boundary, the mean temperature is higher for  $St=0.5$  compared to the other cases of pulsation.

The comparisons of rms temperature profiles for  $\overline{M} = 0.65$  and different cases of Strouhal number are shown in figure (7.9a-g). At  $x/d=-1.5$ , very near the wall, rms temperature is greater. This is caused by the recirculation zone localized upstream the hole. The

recirculation zone is unstable and causes strong mixing between hot and cold flows characterized by high rms values. For  $x/d \geq 3$ , two peaks of rms temperature exist, corresponding to the two mixing layers in the flow. The closest to the wall has lower peak. This implies to the mixing of the jet and the mainstream flow bearing a large temperature gradient near the upper boundary. The effects of pulsation on rms results do not look significant for the rms results either, except for the case of higher Strouhal number ( $St=0.5$ ). Nevertheless, pulsation generally seems to increase the rms value of fluctuating temperature with the Strouhal number at all downstream position with the exception of last two measuring positions, where the pulsation at  $St=0.5$  has lower rms values than the rest of the cases in the near wall region. This may happen, because of a hypothetical reason that higher pulsation causes an increase in the diffusion of laterally fluctuating component of the injectant flow, which will exhaust the jet momentum slightly earlier than for the other cases. This hypothesis can be verified by performing detail measurements of temperature distribution in the lateral region. At  $x/d=3$ , the increase in peak value of the rms temperature compared to  $St=0$  case is of the order of 8 % and 13 % for  $St=0.3$  and 0.5 respectively.



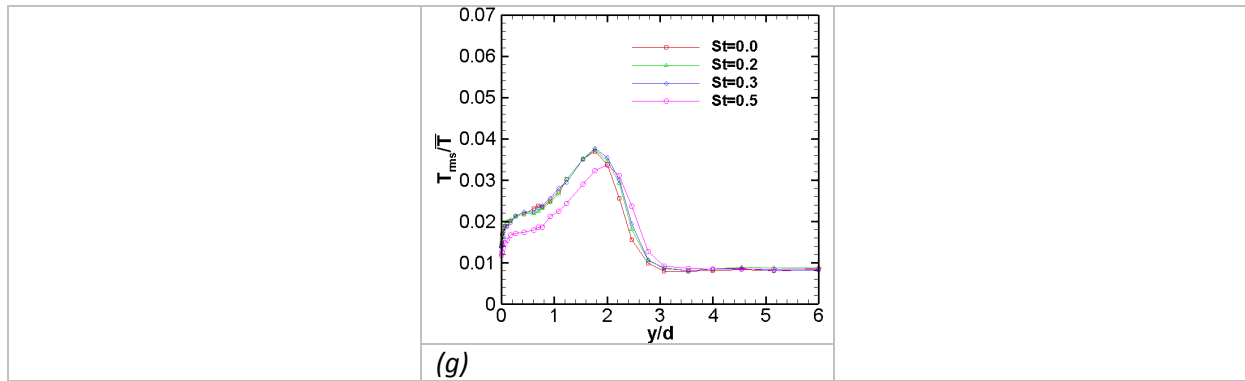
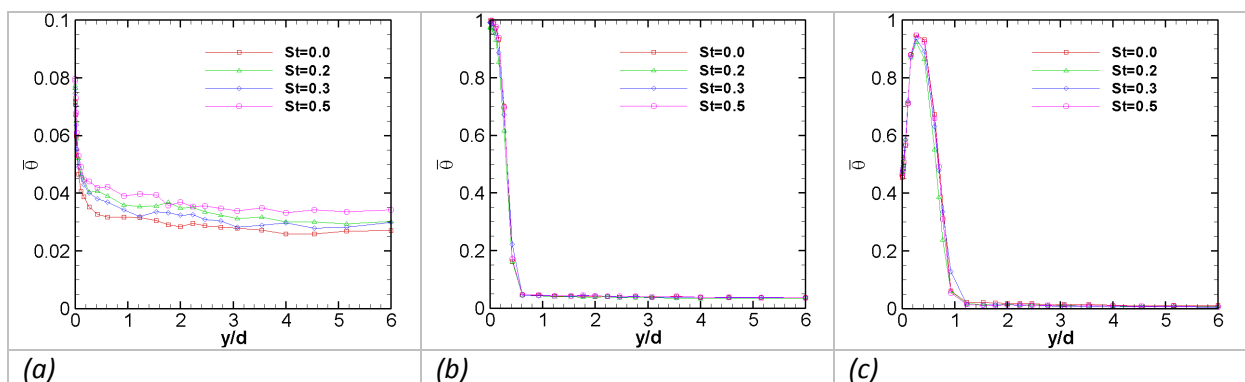


Figure (7. 9): Comparison of rms profiles obtained at different Strouhal number with a blowing ratio of  $\bar{M} = 0.65$ , (a)  $x/d=-1.5$ , (b)  $x/d=0$ , (c)  $x/d=1.5$ , (d)  $x/d=3$ , (e)  $x/d=7$ , (f)  $x/d=15$  and (g)  $x/d=30$ .

### CASE 2: $M=1$

The comparisons of time-averaged temperature profiles in different cases of Strouhal number for  $\bar{M} = 1$  are shown in figure (7.10a-g). In the preceding sections, it was mentioned that the blowing ratio leading to the event of jet lift-off in steady flow cases causes a reduction in wall protection, while pulsation under these cases provides an opportunity to achieve some gain in wall cooling. In the present case, the temperature fields resulting from the interaction of two different temperatures and similar velocity fluids have diverse characteristics for the applied Strouhal number pulsations. Pulsation at  $St=0.2$  slightly improves the wall coverage, characterized by higher  $\bar{\theta}$  value near the wall. The net increase in the flow of injectant fluid in the vicinity of the wall can be observed apart from a streamwise distance of  $x/d = 7$ . The increase in the near wall value of the profile due to pulsation at  $St=0.2$  is of the order 10% at  $x/d=15$ . The pulsation at  $St=0.3$  on the other hand does not seem to contribute much to the wall coverage.



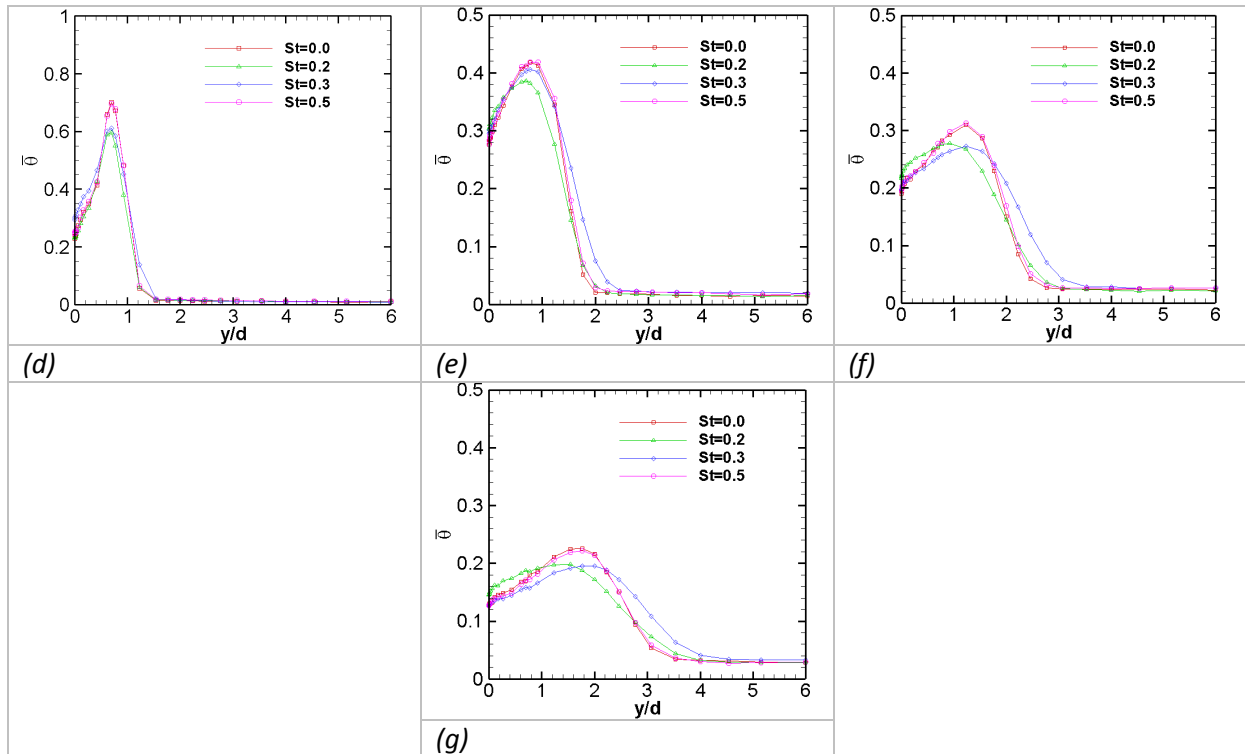
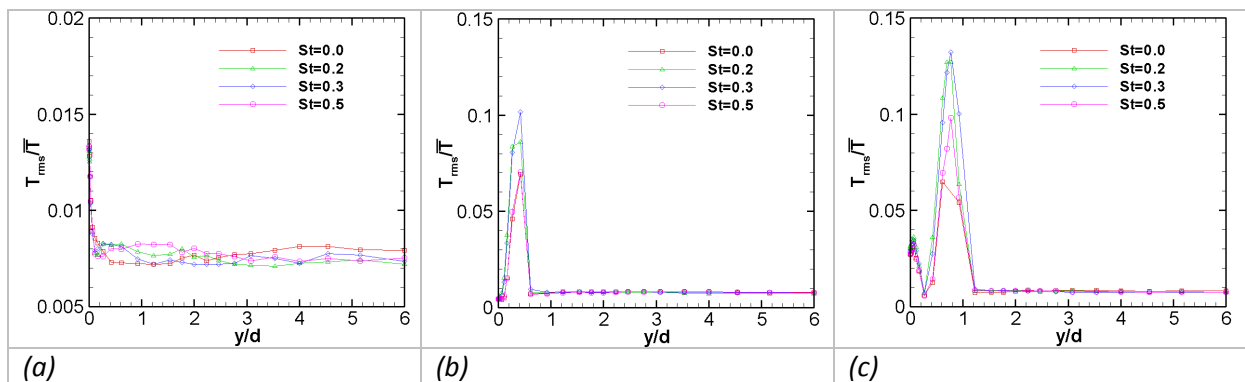


Figure (7. 10): Comparison of time-averaged profiles obtained at different Strouhal number with a blowing ratio of  $\overline{M} = 1$ , (a)  $x/d=-1.5$ , (b)  $x/d=0$ , (c)  $x/d=1.5$ , (d)  $x/d=3$ , (e)  $x/d=7$ , (f)  $x/d=15$  and (g)  $x/d=30$ .

The comparisons of rms temperature profiles in different cases of Strouhal number for  $\overline{M} = 1$  are shown in figure (7.11a-g). It is to be noted that the increase in temperature fluctuation in the near wall region tends to increase the mixing which is not desirable in case of film cooling. The pulsation at intermediate values of Strouhal number  $St=0.2$  and  $0.3$  clearly have higher rms values than for  $St=0$  (steady blowing) and  $St=0.5$ .



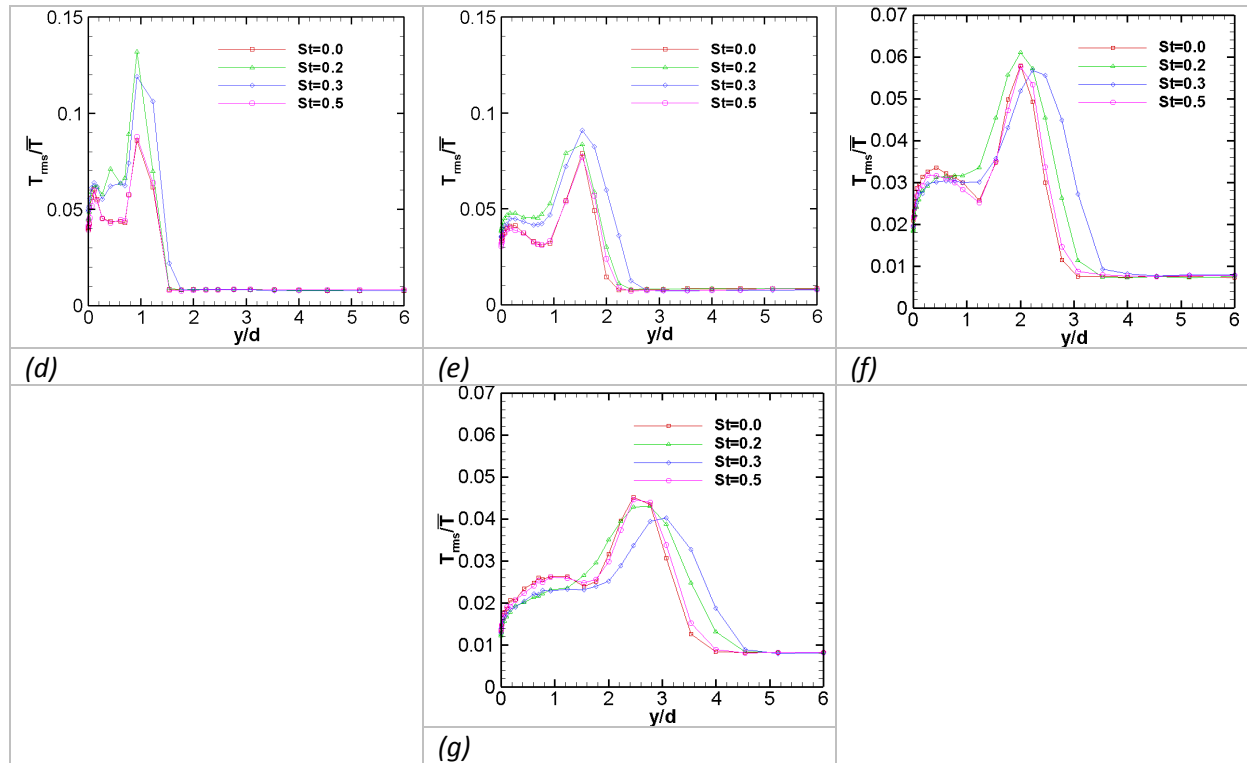


Figure (7. 11): Comparison of rms profiles obtained at different Strouhal number with a blowing ratio of  $\overline{M} = 1$ , (a)  $x/d = -1.5$ , (b)  $x/d = 0$ , (c)  $x/d = 1.5$ , (d)  $x/d = 3$ , (e)  $x/d = 7$ , (f)  $x/d = 15$  and (g)  $x/d = 30$ .

At the hole centre ( $x/d = 0$ ), the increase in peak value of the rms temperature compared to the case  $St=0$  is of the order of 22 % and 43 % for  $St=0.2$  and  $0.3$  respectively. These cases of pulsation with distinctive effect are not only increasing the rms results in the near wall region, which is liable to boost the heat transfer, but also causing a similar increment in the region of upper boundary of the jet which will increase the mixing of jet with the mainstream flow. A somewhat similar trend was also seen for rms velocity fluctuations, (section 5.4.1).

### CASE 3: $M=1.25$

The comparisons of time-averaged temperature profiles in different cases of Strouhal number for  $\overline{M} = 1.25$  are shown in figure (7.12a-g). Pulsation under these condition seems to increase the presence of injectant near the wall for both  $St=0.2$  and  $0.3$  cases. The indication of the presence of the injectant flow very near the wall becomes evident after a streamwise distance of  $x/d = 7$ . In favorable cases of pulsation ( $St=0.2$  and  $0.3$ ), the time-averaged temperature profiles become more uniform (less steep) compared to the two other cases of  $St=0$  and  $0.5$ , as pulsations increase the time-averaged temperature in both near wall and upper boundary region of the jet along with some reduction to occur in the peak values. At downstream distance of  $x/d = 15$ , the decrease in peak value of the time-averaged temperature compared to the case  $St=0$  is of the order of 16 % and 11 % for  $St=0.2$

and 0.3 at a wall normal distance of  $1.8d$ . In case of  $St=0.3$ , the pulsation seems to influence the distribution of temperature profile up to a vertical distance of  $y/d = 5.2$  in evolving down to the far most measuring position, which is superior than the rest of the cases.

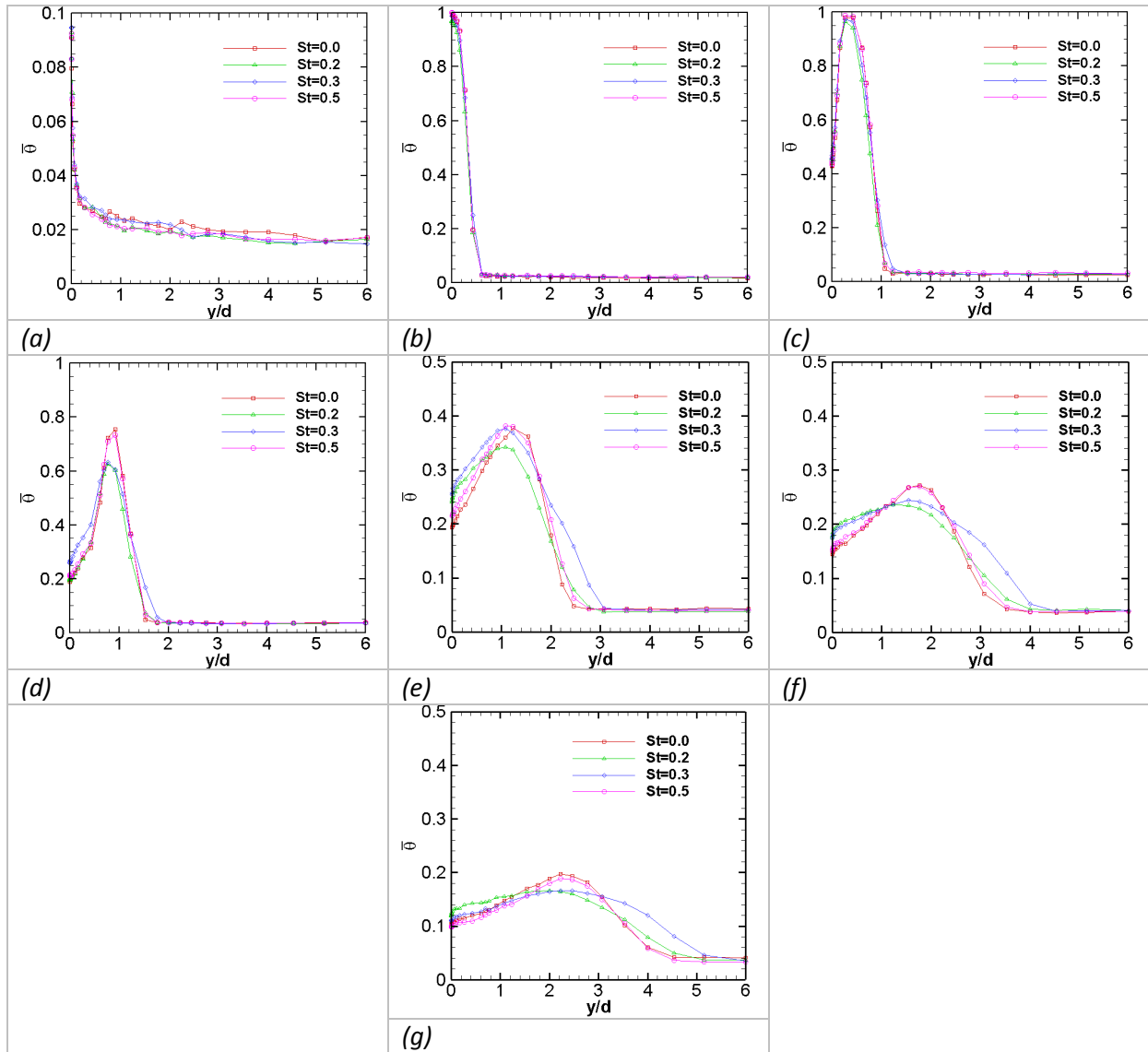


Figure (7. 12): Comparison of time-averaged profiles obtained at different Strouhal number with a blowing ratio of  $\overline{M} = 1.25$ , (a)  $x/d = -1.5$ , (b)  $x/d = 0$ , (c)  $x/d = 1.5$ , (d)  $x/d = 3$ , (e)  $x/d = 7$ , (f)  $x/d = 15$  and (g)  $x/d = 30$ .

The comparisons of rms temperature profiles in different cases of Strouhal number for  $\overline{M} = 1.25$  are shown in figure (7.13a-g). The variations in rms results are somewhat similar to the one found in case of  $\overline{M} = 1$ . It can be observed that the response of rms temperature results for  $St=0$  (steady blowing) and  $St=0.5$  are quite identical, while for the cases of  $St=0.2$  and  $0.3$ , an increase can be observed throughout the profile until a downstream position around  $x/d = 7$ . At the hole centre ( $x/d = 0$ ), the increase in peak value of the rms temperature compared to  $St=0$  is of the order of 37 % and 45 % for  $St=0.2$  and  $0.3$

respectively. Beyond the position of  $x/d = 7$ , the pulsation effect produced in different Strouhal number cases becomes nearly equivalent to the steady blowing case in a flow region lying underneath the jet.

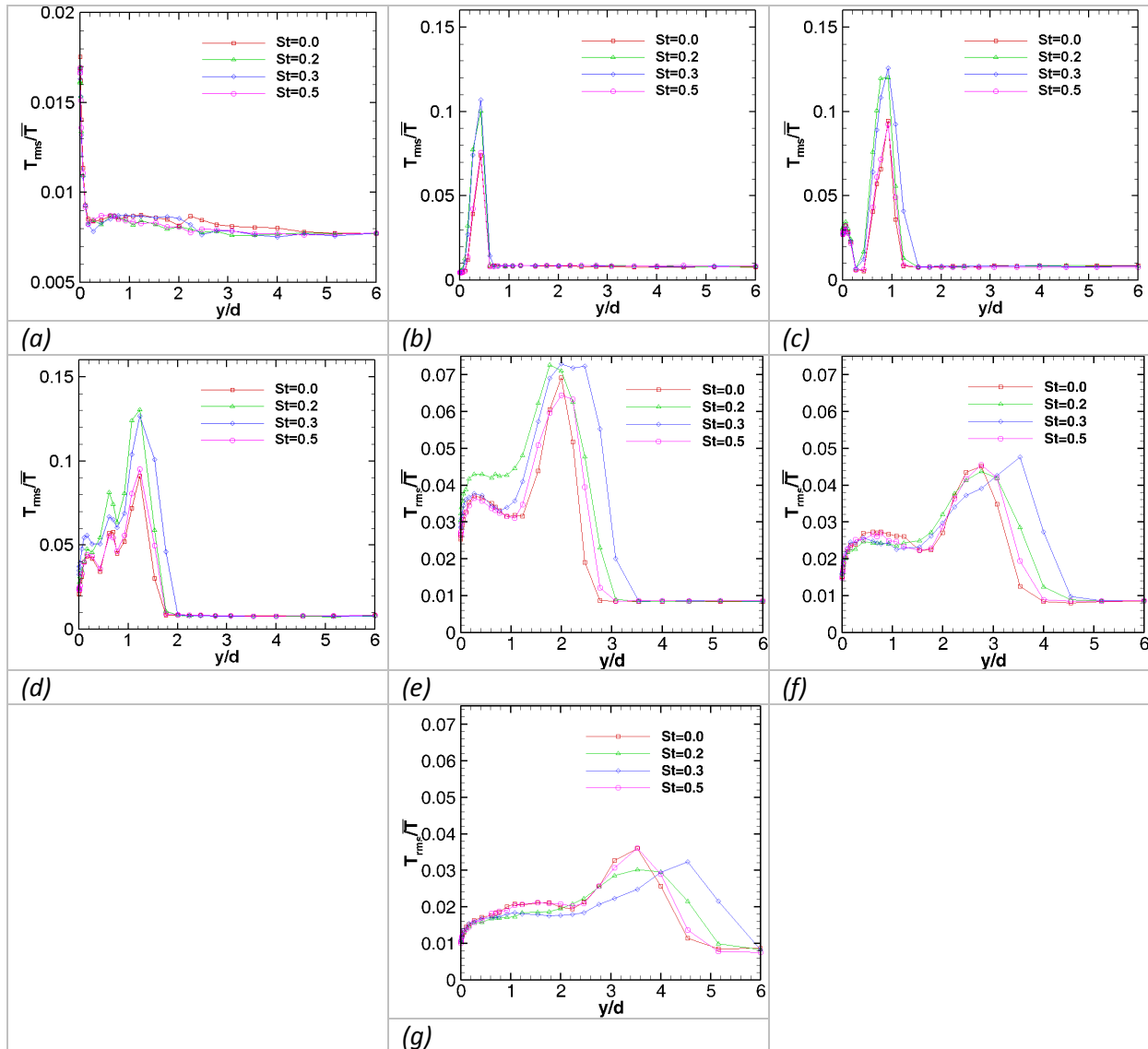


Figure (7. 13): Comparison of rms profiles obtained at different Strouhal number with a blowing ratio of  $\bar{M} = 1.25$ , (a)  $x/d = -1.5$ , (b)  $x/d = 0$ , (c)  $x/d = 1.5$ , (d)  $x/d = 3$ , (e)  $x/d = 7$ , (f)  $x/d = 15$  and (g)  $x/d = 30$ .

### 7.3 Temperature distribution at off-centre plane ( $z/d = 1.5$ )

The measurements at  $z/d = 1.5$  are performed to figure out the level of injectant distribution in the lateral direction for different blowing ratios maintaining a constant temperature ratio of  $T_i/T_\infty = 40/20 = 2$ . The temperature field is also analyzed to determine the patterns of injectant distribution varying due to the periodic forcing of the jet.

### 7.3.1 Comparison of the cases of different blowing ratio (steady blowing)

The variation in time-averaged temperature profiles at different streamwise positions locating at a lateral plane of  $z/d=1.5$  are shown in figure (7.14a-g) for the cases of steady blowing ( $St=0$ ) with different blowing ratios. It can be observed that the lateral spreading of the injectant flow for the present blowing ratios remains nearly insignificant within the downstream region extending up to  $x/d=7$ . At the downstream positions of  $x/d=15$  and 30, the variation in time-averaged temperature profiles shows a clear and obvious distinction among the results acquired for different blowing ratios, as the successive increase in the profile thickness corresponds to the increase of blowing ratio. In the case of higher blowing ratio, the presence of jet fluid is recognized roughly up to a wall-normal distance of  $y/d=4.5$ .

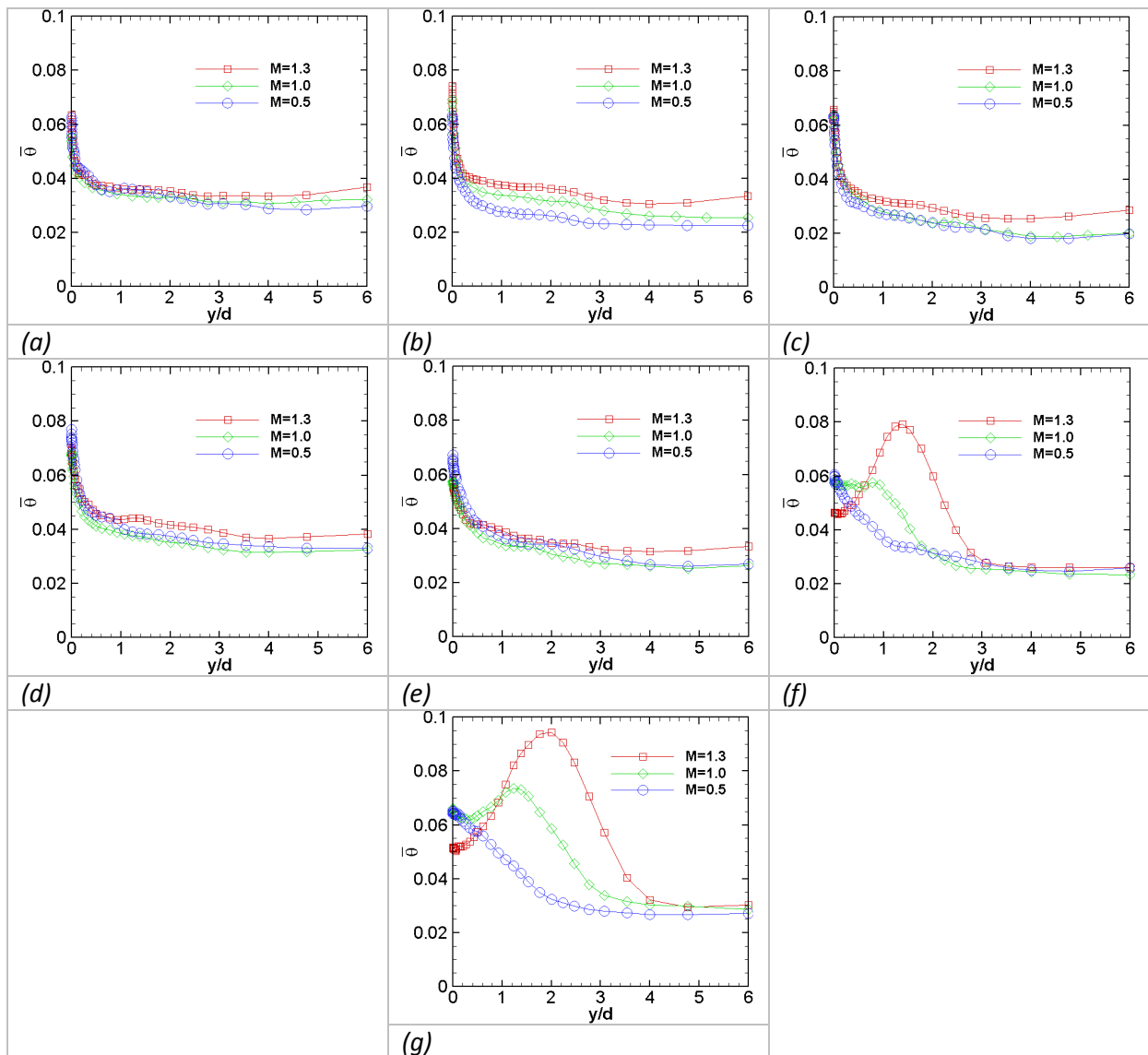
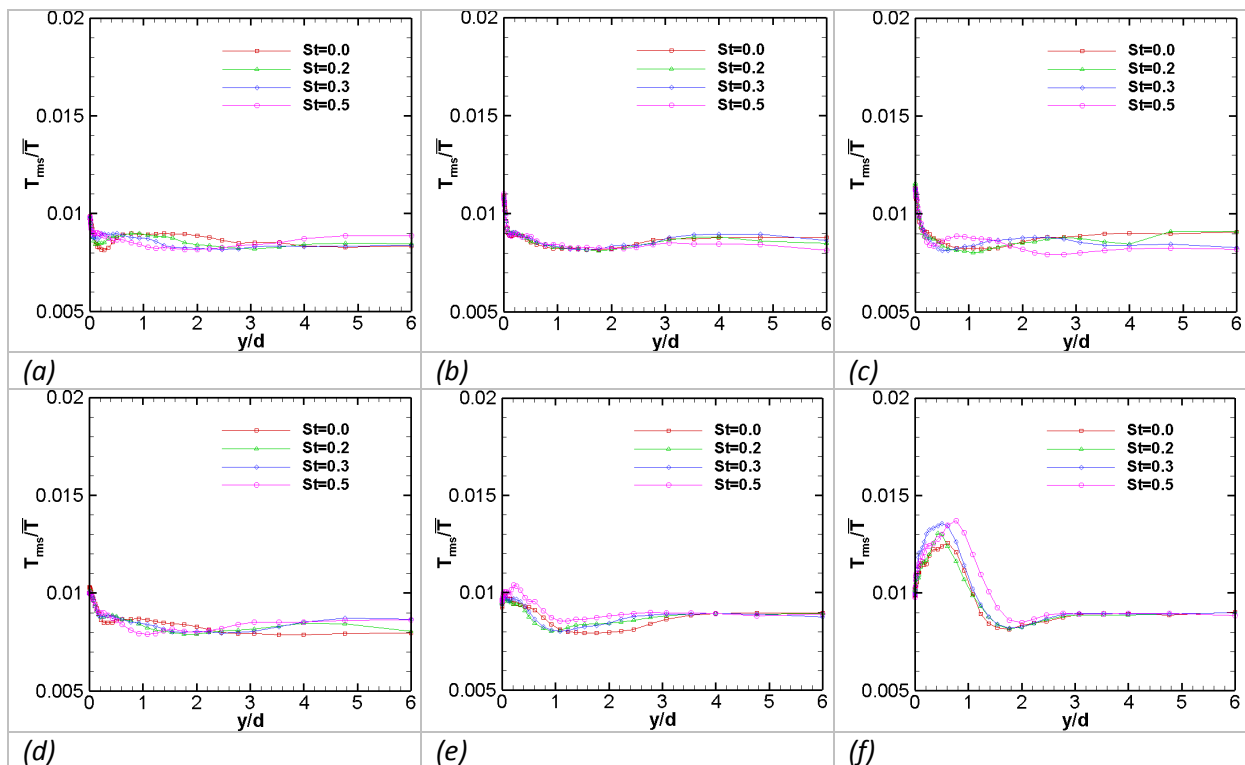


Figure (7. 14): Comparison of time-averaged profiles obtained from different blowing ratios under steady blowing (a)  $x/d=-1.5$ , (b)  $x/d=0$ , (c)  $x/d=1.5$ , (d)  $x/d=3$ , (e)  $x/d=7$ , (f)  $x/d=15$  and (g)  $x/d=30$ .



This shows the minor influence of the injectant fluid in these regions. An increase in the thermal boundary layer with respect to the streamwise distance indicates the evolution of mainstream flow in the region alongside of the injectant flow, which seems to remain unaffected before the downstream location of  $x/d=15$ . For the present blowing ratios, the pulsations do not seem to cause a distinct variation along the lateral plane of  $z/d=1.5$ . For the immediate downstream profile of  $x/d=1.5$ , some increase in the lateral spreading of injectant is noticed for the case of  $St=0.2$  and  $0.3$ , which is not so distinct for the results at other locations.

The comparisons of rms temperature profiles in different cases of Strouhal number for  $\overline{M} = 0.65$  are shown in figure (7.16a-g). It can be observed that the periodic forcing of the jet induces the temperature fluctuation and the rms temperature. Results obtained from the lateral plane of  $z/d=1.5$  start to show these effects apart from a streamwise distance of  $x/d=7$ , which causes a slight lifting of the jet and also increases the spreading of the injectant fluid. However, in the location of the peak value, these effects always remain very small with a maximum increase of 13% at  $x/d=15$  for  $St=0.5$ , compared to the steady blowing case. The pulsation at  $St=0.5$  causes an increase in the spreading of the turbulent fluctuations in the region of the upper boundary of the jet.



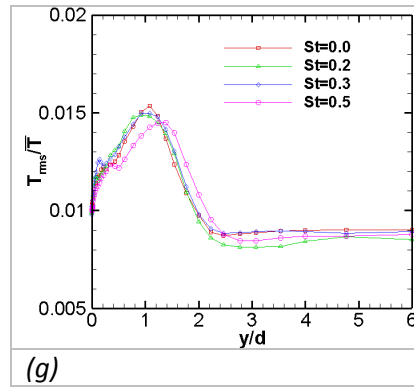
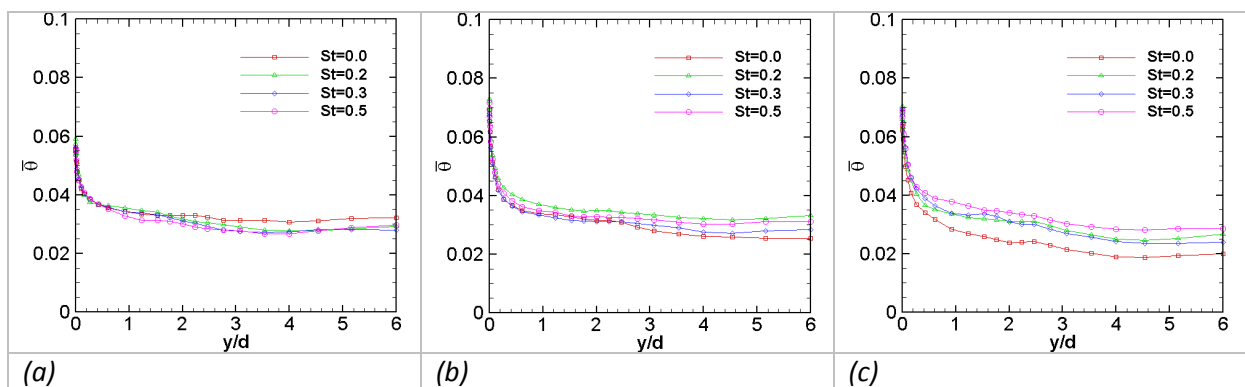


Figure (7. 16): Comparison of rms profiles obtained at different Strouhal number with a blowing ratio of  $\overline{M} = 0.65$ , (a)  $x/d=-1.5$ , (b)  $x/d=0$ , (c)  $x/d=1.5$ , (d)  $x/d=3$ , (e)  $x/d=7$ , (f)  $x/d=15$  and (g)  $x/d=30$ .

### CASE 2: $M=1$

The comparisons of time-averaged temperature profiles for different cases of Strouhal number for  $\overline{M} = 1$  are shown in figure (7.17a-g). The spreading of the injectant flow at steady blowing condition does not seem to have significant influence on the form of time-averaged temperature profile before a streamwise distance of  $x/d = 7$ , which may signify to the absence of injectant fluid in this region. Therefore, the small variations detected in different cases of pulsation are rather unimportant for the upstream positions located before  $x/d = 7$ . The Pulsation at  $St=0.2$  slightly improves the wall coverage due to the net increase in the flow of injectant fluid close to the wall, which is more evident from the profiles measured at  $x/d = 15$ . It is to be noted that these observations are somewhat coherent with the findings of the measurements performed in the central plane carrying superior concentration of hot injectant fluid, where the measurement uncertainty were much smaller compared to the mean temperatures values.



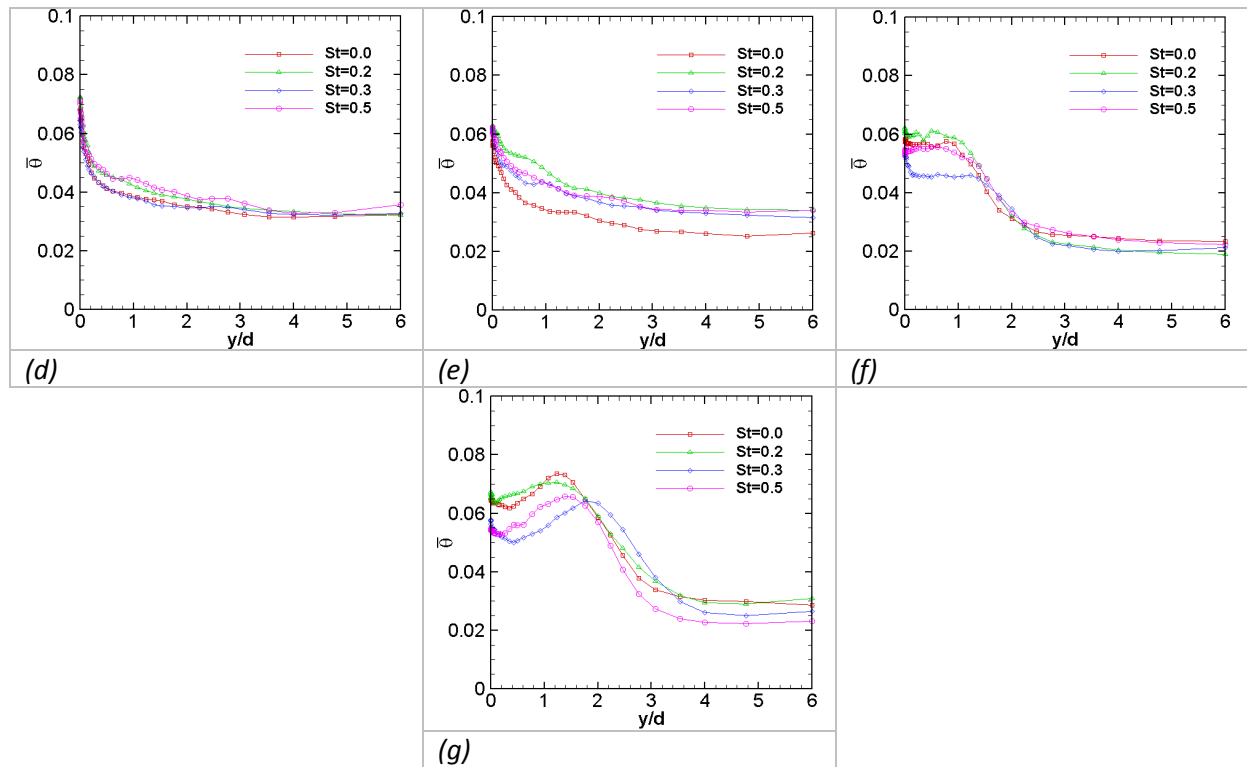


Figure (7. 17): Comparison of time-averaged profiles obtained at different Strouhal number with a blowing ratio of  $\overline{M} = 1$ , (a)  $x/d=-1.5$ , (b)  $x/d=0$ , (c)  $x/d=1.5$ , (d)  $x/d=3$ , (e)  $x/d=7$ , (f)  $x/d=15$  and (g)  $x/d=30$ .

The comparisons of the rms temperature profiles in different cases of Strouhal number for  $\overline{M} = 1$  are shown in figure (7.18a-g). The variations of the rms results measured at different locations show that the influence of pulsation on the locally fluctuating temperature field along  $z/d=1.5$  becomes pronounced, when the injectant flow in steady blowing starts to modify the rms profile due to the lateral diffusion. The pulsation at  $St=0.2$  and  $0.3$  induces temperature fluctuations at  $x/d=7$ , which were also superior in the corresponding cases measured at  $z/d=0$ . At  $x/d=7$ , the increase in rms temperature is of the order of 76 % and 35 % for  $St=0.2$  and  $0.3$ , compared to  $St=0$ , at a wall-normal position of  $y/d=0.6$ . For the pulsation at  $St=0.5$ , the zone for spatial variation of the jet trajectory moving toward and away from the wall reduces on the far-end, because the adjacent pulsation cycles do not allow the flow to establish fully on the periodic effects.

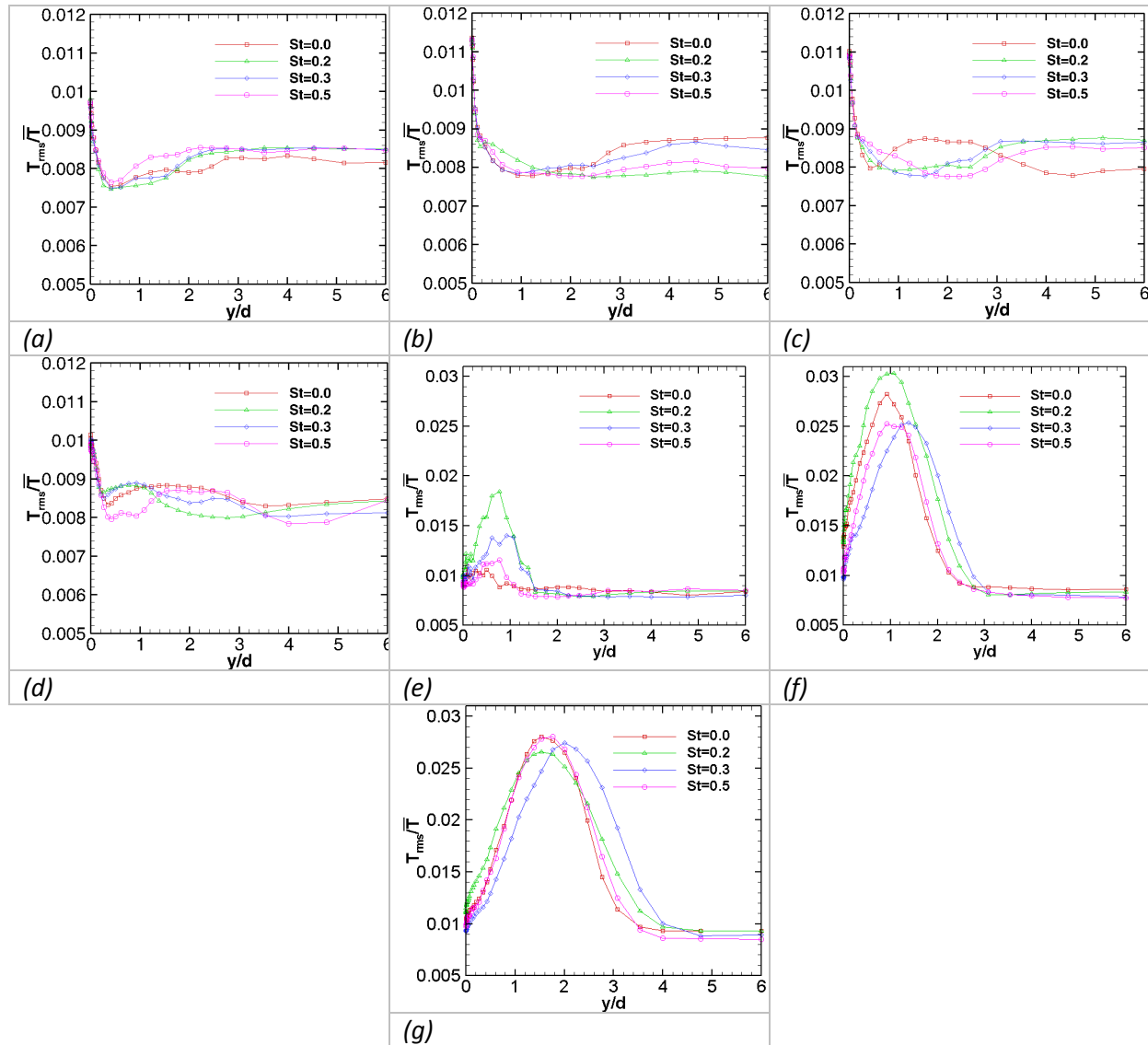


Figure (7. 18): Comparison of rms profiles obtained at different Strouhal number with a blowing ratio of  $\overline{M} = 1$ , (a)  $x/d=-1.5$ , (b)  $x/d=0$ , (c)  $x/d=1.5$ , (d)  $x/d=3$ , (e)  $x/d=7$ , (f)  $x/d=15$  and (g)  $x/d=30$ .

### CASE 3: $\overline{M}=1.25$

The comparisons of time-averaged temperature profiles for different cases of Strouhal number for  $\overline{M} = 1.25$  are shown in figure (7.19a-g). For the present blowing ratio, the injectant flow tends to lift-off significantly from the wall. Pulsation under these condition seems to increase the injectant spreading for both  $St=0.2$  and  $0.3$  at the lateral plane of  $z/d=1.5$ , since the presence of injectant flow becomes obvious at a streamwise distance of  $x/d=7$ , similarly as in case of  $\overline{M} = 1$ . At  $x/d=7$ , the increase in time-averaged temperature is of the order of 38 % and 89 % for  $St=0.2$  and  $0.3$  at a wall-normal position of  $y/d=1.2$  compared to  $St=0$ . Due to higher lift-off, both the cases of  $St=0.2$  and  $0.3$  cause an increase in the spreading of injectant flow near the upper boundary of the jet and a decrease of injectant flow in the near wall region for the measuring locations lying on  $x/d=30$ . The

injectant distribution in the present case is different from the previous case of  $\overline{M} = 1$ , where only the pulsation at  $St=0.3$  causes an increase in the diffusion of the injectant flow in the upward direction.

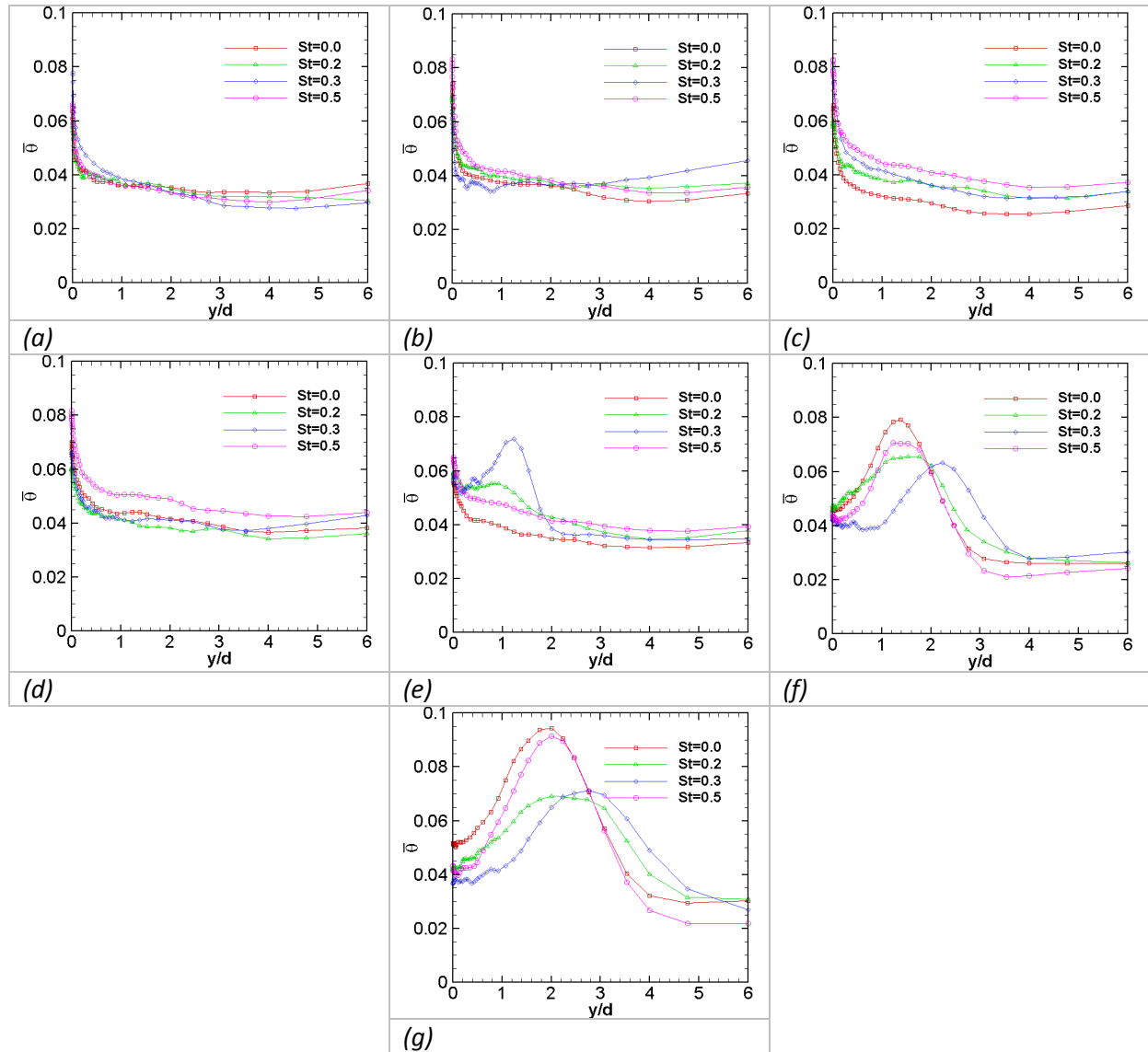


Figure (7. 19): Comparison of time-averaged profiles obtained at different Strouhal number with a blowing ratio of  $\overline{M} = 1.25$ , (a)  $x/d=-1.5$ , (b)  $x/d=0$ , (c)  $x/d=1.5$ , (d)  $x/d=3$ , (e)  $x/d=7$ , (f)  $x/d=15$  and (g)  $x/d=30$ .

The comparisons of rms temperature profiles for different cases of Strouhal number for  $\overline{M} = 1.25$  are shown in figure (7.20a-g). Because of the higher lift-off, the corresponding jet structures have an opportunity to grow larger in the downstream flow as mentioned previously, which stimulates the lateral spreading of rms temperature fluctuations. The resulting variations in rms profiles along  $z/d=1.5$  appear to be more significant for the present blowing ratio compared to the case of  $\overline{M} = 1$ . For the pulsating cases of  $St=0.2$  and  $0.3$ , an evident increase in rms temperature is observed at the downstream position of

$x/d = 7$ . At this location, the increase in rms temperature is of the order of 90 % and 173 % for  $St=0.2$  and  $0.3$  at a wall-normal distance of  $y/d=1.1$  compared to  $St=0$ .

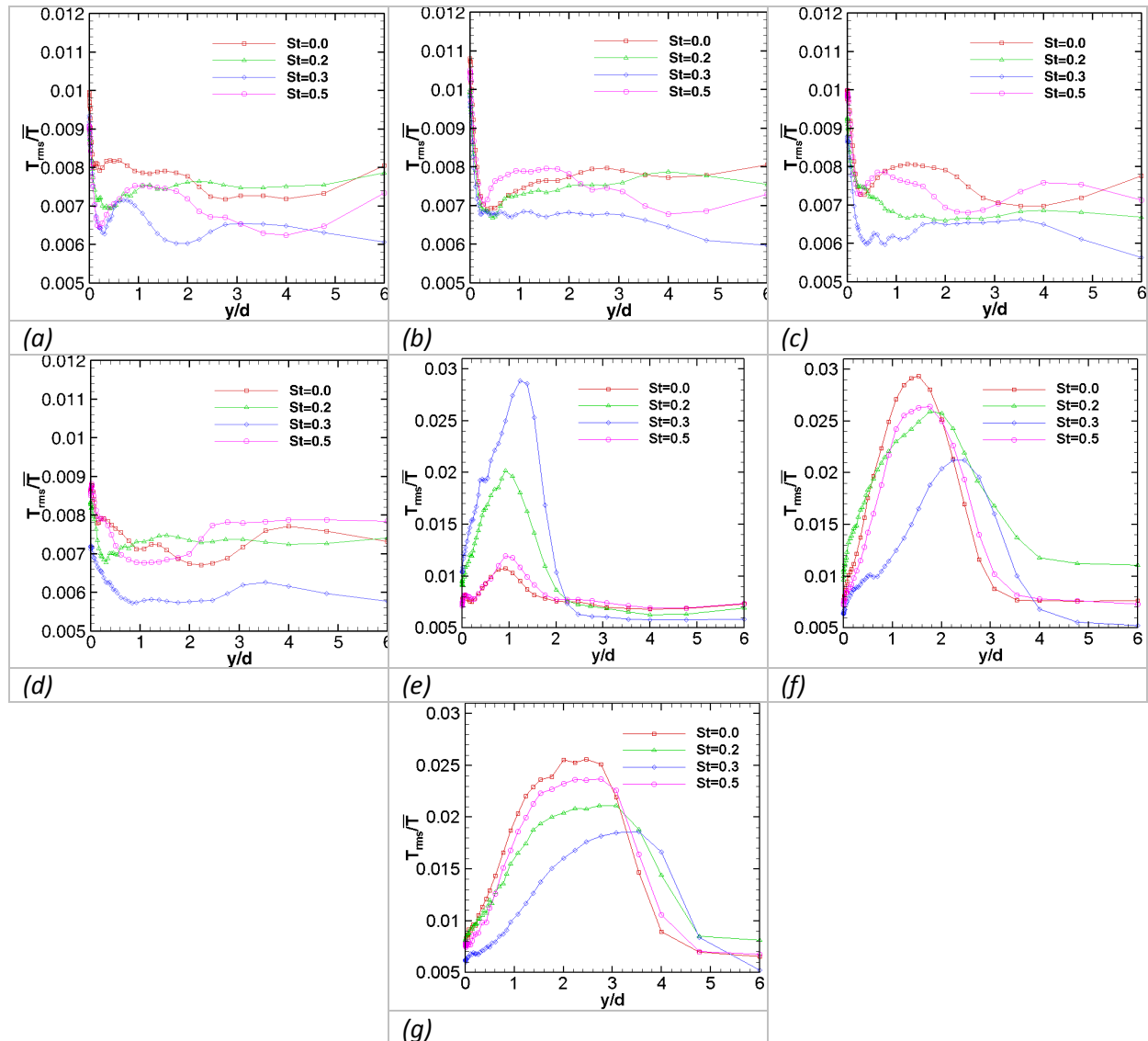


Figure (7. 20): Comparison of rms profiles obtained at different Strouhal number with a blowing ratio of  $\overline{M} = 1.25$ , (a)  $x/d=-1.5$ , (b)  $x/d=0$ , (c)  $x/d=1.5$ , (d)  $x/d=3$ , (e)  $x/d=7$ , (f)  $x/d=15$  and (g)  $x/d=30$ .

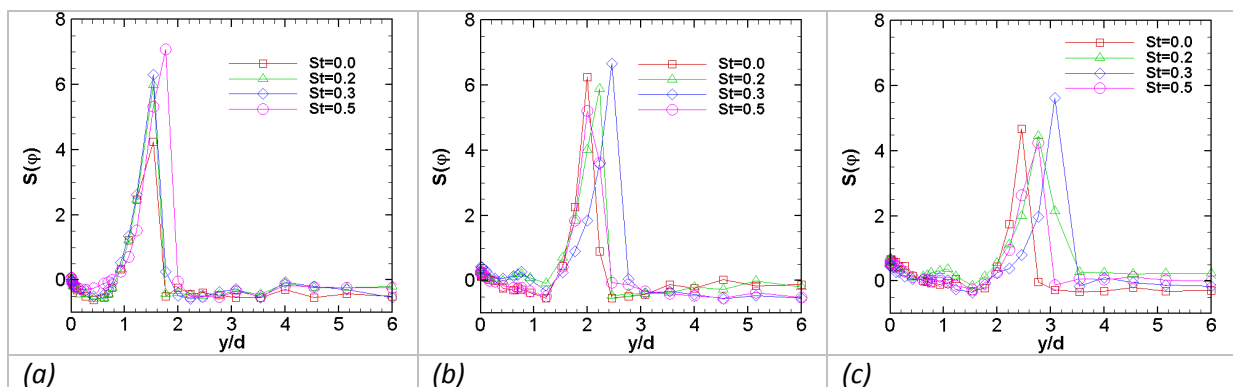
For the downstream positions of  $x/d=15$  and  $x/d=30$ , the rms temperature profiles resulting at  $St=0.2$  and  $0.3$  indicate a higher upwards shift, which signifies an increase in the diffusion of fluctuating temperature of injectant flow in the upward direction.

## 7.4 Skewness and flatness factor

The previous analysis of cold wire measurements has been limited to several averaged and rms temperature results, which do not provide any information regarding the distribution of the temperature fluctuation. Therefore, an analysis based on the skewness and flatness

factor is undertaken for the flow configuration of  $T_i/T_\infty = 40/20 = 2$ . The results for different blowing ratios and Strouhal numbers are compared for the downstream locations of  $x/d = 7$  and 30 of the central plane ( $z/d=0$ ). The skewness and flatness for a Gaussian distribution are 0 and 3 respectively.

Figure (7.21a-f) shows some higher peak for the skewness factor. A value higher than 0 of skewness factor means that the distribution of temperature fluctuations mostly consists of the low temperature fluctuations coming from to the cold mainstream fluid, while the occurrence of high temperature fluctuation pertaining to the hot injectant are less frequent. The peak in skewness profiles correspond to the upper boundary of the jet, while there is no such peak showing up near the lower boundary. This is due to the fact that the flow on the bottom side of the jet has small temperature gradient with the jet fluid at the central plane; either because of the jet fluid flowing near the wall and cover it fully at low blowing ratio or because of some higher turbulent mixing occurring in the wake region at higher blowing ratios resulting in an intermediate temperature. Width of the region lying between the wall and the wall-normal location apart from which skewness rises to attain the peak value increases with the increase of blowing ratio and the downstream distance. The values of skewness in this region indicate a relatively higher probability for the occurrence of high temperature fluctuation primarily of the mixed flow, while the low temperature fluctuations of cold mainstream flow pass less frequently. The interference of low temperature fluctuation increases, as the blowing ratio is increased. The pulsation at  $St=0.5$  displaces the peak skewness slightly away from the wall for  $\bar{M} = 0.65$ , similarly at  $St=0.3$  and 0.2 for blowing ratio of  $\bar{M} = 1$  and 1.25. For  $\bar{M} = 1$  and 1.25, the pulsation case of  $St=0.3$  is appeared to be more influential than  $St=0.2$  and causes a significant shift in the skewness profile above on the vertical axis for each downstream locations, thus referring to the large spatial variation for the injectant trajectory.



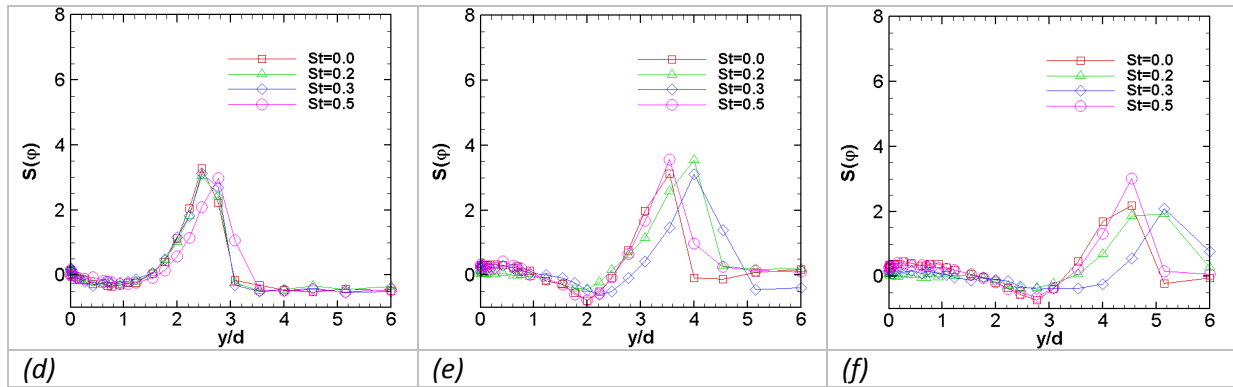


Figure (7. 21): Comparison of the skewness factor of temperature fluctuation for different Strouhal numbers at  $x/d=7$  and  $z/d=0$ , (a)  $\overline{M} = 0.65$ , (b)  $\overline{M} = 1$  and (c)  $\overline{M} = 1.25$ ; and at  $x/d=30$  and  $z/d=0$  (d)  $\overline{M} = 0.65$ , (e)  $\overline{M} = 1$  and (f)  $\overline{M} = 1.25$

The flow has a highly flatness factor in the upper boundary region, as indicated by the figure (7.22a-f). A value of the flatness factor greater than 3 implies that the fluctuations are often larger than the variance of the distribution and that the fluctuations have an intermittent character (Soldati and Banerjee 1998). The peak of flatness factor occurs nearly at the same wall-normal distance as for the skewness factor in different cases of pulsation. Furthermore, the presence of lower boundary of the jet also becomes slightly visible.

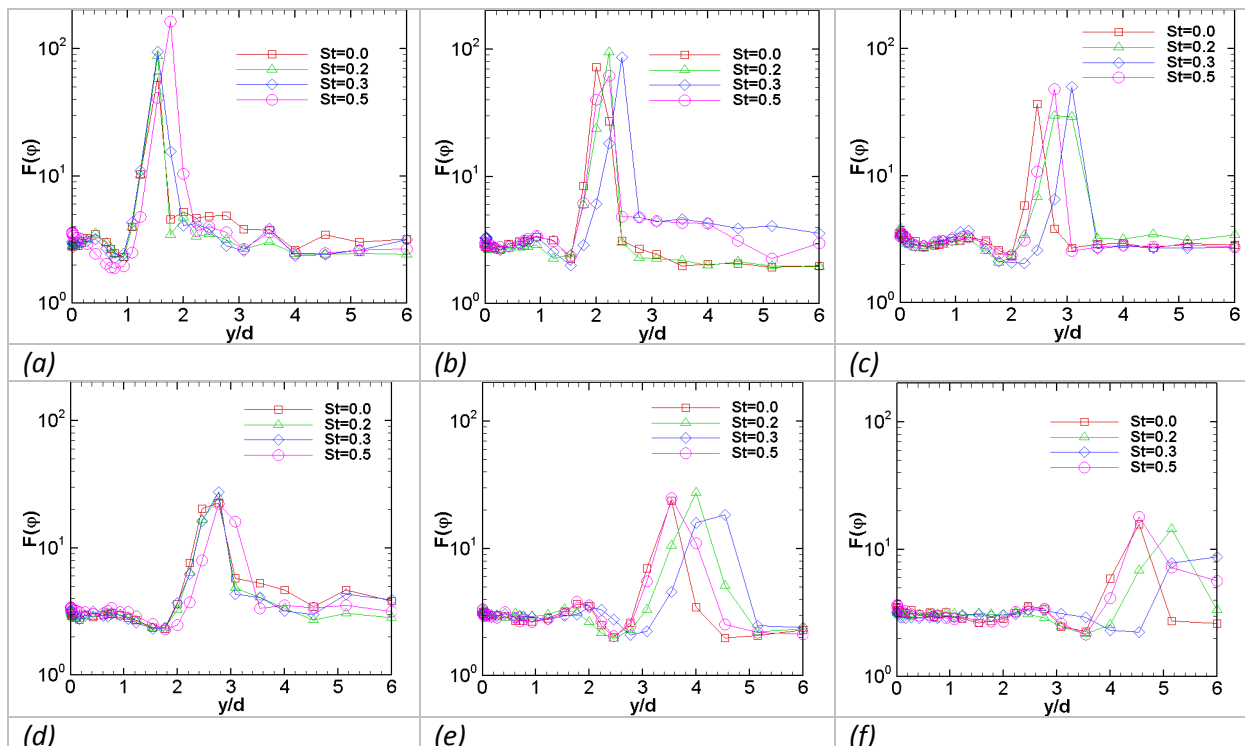


Figure (7. 22): Comparison of the flatness factor of temperature fluctuation for different Strouhal numbers at  $x/d=7$  and  $z/d=0$ , (a)  $\overline{M} = 0.65$ , (b)  $\overline{M} = 1$  and (c)  $\overline{M} = 1.25$ ; and at  $x/d=30$  and  $z/d=0$  (d)  $\overline{M} = 0.65$ , (e)  $\overline{M} = 1$  and (f)  $\overline{M} = 1.25$

## 7.5 Conclusion

The cold wire measurements were conducted for different blowing ratios and Strouhal number pulsations in the configuration of film cooling to figure out the spreading of injectant fluid in the mainstream flow. The variations of the temperature field were analyzed by determining the time- and phase-averaged temperatures, rms temperature, and the skewness and flatness factors.

In the central plane ( $z/d=0$ ), the spread of the injectant fluid was smaller for  $\overline{M} = 0.65$ , compared to  $\overline{M} = 1$  and 1.25. It was noticed that the increase in pulsation Strouhal number reduces the time-averaged temperature measured in the near wall region for  $\overline{M} = 0.65$ , which indicates the decline of wall coverage. However, the rms temperature showed some increase at  $St=0.3$  and 0.5. For  $\overline{M} = 1$ , the pulsation at  $St=0.2$  slightly improves the wall coverage due to the net increase in the flow of injectant fluid in the vicinity of the wall in the central plane ( $z/d=0$ ). The pulsation at  $St=0.3$  on the other hand did not seem to contribute much to the wall coverage, but increased the lateral spreading of the injectant fluid, whereas rms values increased for both  $St=0.2$  and 0.3 compared to  $St=0$  (steady blowing) and  $St=0.5$ . The pulsation effects appeared to reduce for far-end locations. In the case of  $\overline{M} = 1.25$ , the spreading of the injectant was larger than all other cases of steady blowing. On the other hand, the pulsation at  $St=0.2$  and 0.3 increased the presence of injectant near the wall as well as the rms fluctuations with highest lateral diffusion at  $St=0.3$ .

At the off-centre plane of  $z/d=1.5$ , the temperature profiles measured in the last two stations have shown some indication of the presence of injectant flow for the case of  $\overline{M} = 0.65$ . In these cases, pulsations did not seem to cause a significant impact on the flow field. For  $\overline{M} = 1$ , the pulsation at  $St=0.2$  has slightly improved the wall coverage in the lateral plane of  $z/d=1.5$ , which became evident at the downstream location of  $x/d=7$  for both time-averaged and rms temperatures. The pulsation at  $St=0.3$  increased the lateral spreading higher than for  $St=0.2$ . At  $z/d=1.5$ , the measurements for the blowing ratio of  $\overline{M} = 1.25$  have shown superior temperature levels in steady blowing. The pulsation has shown an increase in lateral diffusion at  $St=0.2$  and 0.3. Due to higher lift-off, both cases of  $St=0.2$  and 0.3 cause an increase in the spreading of injectant flow near the upper boundary of the jet and a decrease of injectant flow in the near wall region for the measuring location lying on  $x/d=30$ .

The phase-averaged results have shown that the presence of injectant at a lateral distance of  $z/d=1.5$  decreased sharply for  $\overline{M} = 0.65$ , while the pulsation did not bring any improvement in the situation. The case of  $\overline{M} = 1$  have indicated higher concentration of injectant with  $St=0.2$  and 0.3 compared to  $St=0.5$  at  $z/d=1.5$ , while the blowing ratio of  $\overline{M} = 1.25$  have shown the higher concentration of injectant for  $St=0.2$  only.

The favorable cases of pulsation were found to be  $St=0.2$  and  $0.3$ , while the blowing ratios were  $\overline{M} = 1$  and  $1.25$ . At  $\overline{M} = 0.65$ , the pulsations appear to cause degradation in the wall coverage.

## 7.6 References

- 1 Bons JP, Rivir JB, Mac Arthur CD, Pestian DJ, *"The effect of unsteadiness on film cooling effectiveness"*, Wright Laboratory, WL-TR-96-2096, Jan-1995.
- 2 Kohli A, Bogard DG, *"Fluctuating thermal field in the near-hole region for film cooling flows"*, ASME, Journal of Turbomachinery, 120 (1998) 86-91.
- 3 Ligrani PM, Gong R, Cuthrell JM, *"Bulk flow pulsations and film cooling-I: Injectant behavior"*, Int. J Heat Mass Transfer, 39 (1996a) 2271-2282.
- 4 Ligrani PM, Gong R, Cuthrell JM, *"Bulk flow pulsations and film cooling-II: Flow structure and film effectiveness"*, Int. J. Heat Mass Transfer, 39 (1996b) 2283-2292.
- 5 Seo HJ, Lee JS, Ligrani PM, *"The effect of injection hole length on film cooling with bulk flow pulsation"*, Int. J. Heat Mass Transfer, 41(1998) 3515-3528.
- 6 Soldati A, Banerjee S, *"Turbulence modification by large-scale organized electrohydrodynamic flows"*, Physics of Fluids, 10 (1998) 1742-1756.
- 7 Yuen CHN, Martinez-Botas RF, *"Film cooling characteristics of a single round hole at various streamwise angles in a crossflow: Part I, Effectiveness"*, Int. J. Heat Mass Transfer, 46 (2003a) 221-235.



## **CONCLUSION AND PERSPECTIVE**

### **8.1. Conclusion**

In this study the effect of injectant flow pulsation on the film cooling behavior was studied experimentally. The average blowing ratios ( $\overline{M}$ ) were 0.65, 1 and 1.25. The periodic variations in injectant flow were provided by a loudspeaker based pulsation system to non-dimensionalized excitation frequency ( $St$ ) of 0, 0.2, 0.3 and 0.5. Both aerodynamic and thermal aspects of the flow were studied, using the advanced measuring techniques incorporating; Time-resolved PIV, Infrared thermography, Hot- and cold-wire.

In the part of aerodynamic analysis, both time- and phase averaged velocity distributions and turbulent characteristics are presented. The large Counter-Rotating Vortex Pair (CVP) controls the dynamics of the flow in the near wall region and thus the wall coverage.

The synthesis of the phase-averaged results has shown that the periodic forcing and lift-off attributed to large spatial variations in jet trajectory, which lead to events like: jet splitting and shedding of the wake. It was observed that jet splitting under induced pulsation causes the flow in the wake region to shed in succession. Pulsation of injectant at lower Strouhal numbers ( $St=0.2$  and  $0.3$ ) with a mean blowing ratio leading to separation is able to reorient the injectant close to the wall during the lower part of the pulsation cycle.

The synthesis of the time-averaged results has shown that the blowing ratio of  $\overline{M}=0.65$  and the pulsation case of  $St=0.5$ , as well as the blowing ratios of  $\overline{M}=1$  and  $1.25$  and the pulsation cases of both  $St=0.2$  and  $0.3$  have some distinctive and vital influence. It was observed that the pulsation in these cases reduced the velocity gradient in the intense shearing regions of the flow field, and increased both Reynolds normal and shear stresses. The decrease in velocity gradient, shown by rate of deformation and vorticity results, causes a decrease in the strength of CVP in the cases of high blowing ratios and the resulting secondary movement of the mainstream flow blew the jet that induces local mixing. The Reynolds stresses on the other hand increase due to the collapsing of the jet fluid and its propagation in the wall-normal direction due to the large periodic variation of jet trajectory. The turbulent fluctuations are also expected to increase inside the tube at instantaneously high blowing ratio, since the injectant flow undergoes an instantaneous variation of flow rate due to induced pulsating effects. It can be concluded that pulsation brings some improvement in wall coverage only at higher blowing ratios and low excitation frequency, where the injectant propagating with a periodically varying trajectory could bring part of injectant flow in close proximity of the wall and improve injectant coverage compared to steady blowing. At  $\overline{M}=0.65$ , the pulsation at  $St=0.5$  was found particularly detrimental for wall coverage compared to steady blowing conditions, because in this situation, the flow of the injectant over the wall is no longer continuous, and the smooth distribution of coolant is

significantly compromised. At  $\overline{M}=1$  and  $\overline{M}=1.25$  the low shedding frequency has ample time to readjust the jet position in the near wall region in following the downstream variation of jet trajectory. However, at higher pulsation rates, the jet variations due to back-by-back cycles of excitation and continuous induction of early jet splitting direct the jet flow away from the wall.

In the part of the thermal analysis using infrared thermography, the results for adiabatic effectiveness, convective heat transfer coefficient and Net Heat Flux Reduction (NHFR) are presented. For steady blowing, the film cooling effectiveness was superior for the blowing ratio of  $\overline{M}=0.65$ , while the convective heat transfer was superior for the blowing ratio of  $\overline{M}=1.25$ .

For  $\overline{M}=0.65$ , the effectiveness was reduced consistently in an orderly manner with the induction of injectant flow pulsation, whereas the convective heat transfer coefficient did not show significant variations with pulsation. The overall performance given by NHFR has also shown a consistent decrease with the pulsation at different Strouhal numbers for  $\overline{M}=0.65$ , and film cooling performance is reduced by 18.8 %, 28.9 % and 43.1 % due to pulsation at  $St=0.2$ , 0.3 and 0.5 respectively.

The case of  $\overline{M}=1$  has shown a noticeable increase in film cooling effectiveness as well as in heat transfer coefficient for  $St=0.2$  compared to the other cases. However, the overall performance has shown that these factors leveled off each other for  $St=0.2$ , and only some improvement is observed for the case of  $St=0.3$ . At  $\overline{M}=1$ , the film cooling performance (NHFR) is reduced by 66 % and 26% for  $St=0.2$  and 0.5, while the performance is increased by 36 % for  $St=0.3$ .

At the blowing ratio of  $\overline{M}=1.25$ , an increase in film cooling effectiveness and convective heat transfer coefficient was observed for  $St=0.2$  and 0.3 compared to  $St=0$  and 0.5. The NHFR has shown an increase in all cases compared to steady blowing. The performance is increased by 116 %, 117 % and 53 % for pulsating at  $St=0.2$ , 0.3 and 0.5 respectively.

In the part of flow temperature analysis by coldwire measurement, variations of the temperature field were analyzed by determining the time- and phase-averaged temperatures, rms temperature, and skewness and flatness factors to figure out the spreading of injectant fluid in the mainstream flow.

In the central plane ( $z/d=0$ ), the upward lifting of the jet was higher for  $\overline{M}=1$  and 1.25 compared to  $\overline{M}=0.65$  in steady blowing. With the pulsation, the time-averaged temperature measured in the near wall region was reduced for  $\overline{M}=0.65$ , while some increase was observed for  $\overline{M}=1$  and 1.25 in the pulsating cases  $St=0.2$  and 0.3. The reduction of the time-averaged temperature suggests the lowering of wall coverage. The rms fluctuations generally increase with the increase of excitation frequency in all cases.

In the off-centre plane at  $z/d=1.5$ , the spreading of the injectant was found quite low for  $\overline{M}=0.65$  and the pulsation did not appear to deliver any improvement in the given scenario.

For the cases of  $\overline{M} = 1$  and 1.25, the higher jet momentum lifted the jet from the wall, which moved the location of the peak temperature value of the profile slightly higher on the vertical scale, compared to  $\overline{M} = 0.65$ . The pulsation at  $St=0.2$  and  $0.3$  increases the lateral spreading of the injectant fluid for both  $\overline{M} = 1$  and 1.25.

## 8.2. Perspective

The flow configuration of film cooling constitutes inherently complex turbulent flow structures. The characterization of the strong coupling between the aerodynamic and thermal aspects of the flow requires comprehensive measurements of a large flow domain. The following steps can be taken to improve our understanding.

Three dimensional measurements of the velocity field significantly resolved in both time and space will allow us to visualize the pertinent flow structures ascertaining the phenomena of wall coverage. For film cooling, a very interesting quantity is the correlation  $\overline{uw}$ , indicating the lateral spreading of the injectant flow. Furthermore, these measurements will give us a more comprehensive picture of the variations taking place with jet pulsation.

Study of a broad range of pulsation amplitude for Strouhal number cases of higher importance, such as  $St=0.2$  and  $0.3$  will allow us to understand the impact of pulsation amplitude on the wall coverage in an appropriate manner.

Simultaneous measurements of both velocity and temperature data will allow us to study the correlations between them, which will indicate the coupling between the fields of temperature and velocity fluctuations.



## Annex-A

### Fundamental descriptions of P.I.V.

#### Evaluation of particle images

To estimate the displacement function 'd' using a statistical approach based on localized interrogation windows, a spatial cross-correlation as given by Willert and Gharib (1991) is employed to the discrete interrogation areas. The function f and g denote the grey intensity distributions of the interrogation areas. The displacement d is obtained as the position of the maximum in the correlation table.

$$\phi_{fg}(m, n) = \frac{\sum_{i,j=1}^M f(i, j) \cdot g(i-m, j-n)}{\sum_{i,j=1}^M (f(i, j))^2 \cdot \sum_{i,j=1}^M (g(i, j))^2} \quad \dots\dots\dots(A. 1)$$

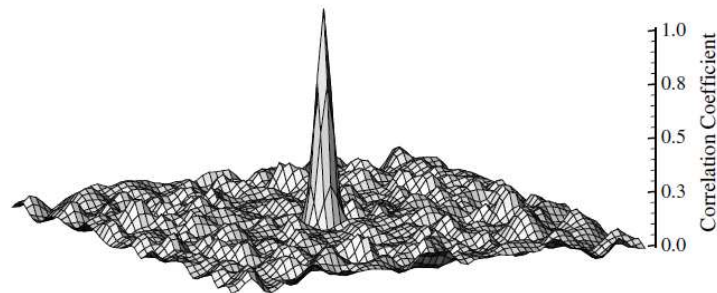


Figure (A.1): Statistical approach for determining cross-correlation of particle images, Raffel et al. (2007).

The fast alternative to the direct application of the algebraic cross-correlation operator is the FFT based algorithm. In which, the tedious two-dimensional correlation process of above equation can be reduced to computing two two-dimensional FFT's with equal sized samples of the image. This is followed by a complex-conjugate multiplication of the resulting Fourier coefficients. The inverse Fourier transformation produces the actual cross-correlation plane, which has the same spatial dimensions  $N \times N$ , as the two input samples.

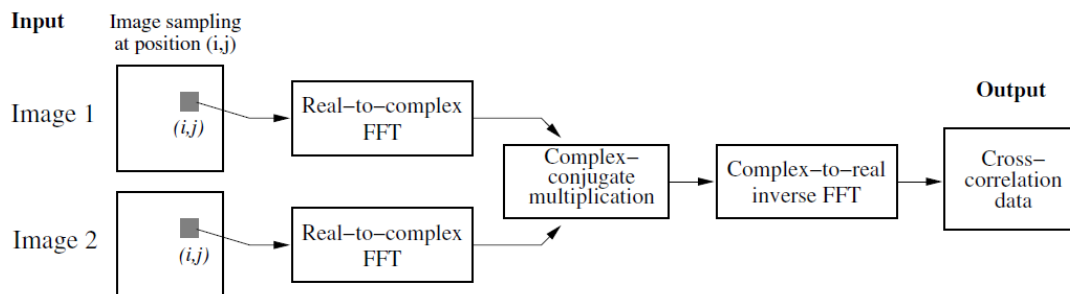


Figure (A.2): FFT based approach for determining cross-correlation of particle images, Raffel et al. (2007)

### **Dynamic range**

The lower end of the dynamic range is determined by the requirement that the corresponding displacement can be distinguished from the noise level. The minimum and maximum detectable displacement are denoted with  $\Delta X_{\min}$  and  $\Delta X_{\max}$ . The maximum measurable displacement is normally expressed as the in-plane displacement should not exceed one-quarter of the interrogation window size  $D$ ; i.e.,  $\Delta X_{\max} \leq D/4$ . The velocity dynamic range can be written as Eq. (A.2), (Tropea et al. 2007). The dynamic range can be increased with a larger window size, but this causes a reduction of spatial resolution.

$$\frac{\Delta X_{\max} - \Delta X_{\min}}{\Delta X_{\min}} = \frac{D}{4\Delta X_{\min}} - 1 \quad \dots\dots(A. 2)$$

In PIV the spatial resolution is limited toward the large scales by the length of the field and towards the small scales by the interrogation window size, (Foucaut and Stanislas 2002). To compensate for the loss of vector field resolution, overlapping of interrogation area is often used, as illustrated in the figure (A.3) for a horizontal and vertical overlapping of 50%.

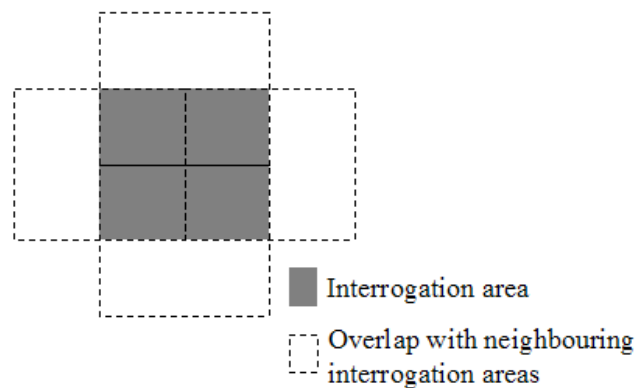


Figure (A.3): Overlapping technique of image evaluation.

The cross-correlation will increase the vector map resolution in both directions by providing a new vector in the intermediate location of two windows. This process not only increases the spatial resolution of the measuring domain but also reduces the loss of particle pair from the images recorded between the times of successive illuminations of the flow field.

### **Common sources of errors**

In spite of being a significantly important utility for fluid dynamic experiments, the measuring technique based on PIV also contains various sources of error that can endure a

significant impact under inadequate operating condition and the complex flow situations. Allano et al (1998) explain that the noise origins can be classified into four categories:

- Physical (light sheet profile, particle optical and dynamical characteristics)
- Specificity of the flow (velocity gradient, out-of-plane motion, wall reflection, seeding homogeneity etc)
- Instrumental (camera and digitizer)
- Analysis method (Peak fitting, algorithm)

Moreover, Willert and Gharib (1991) indicated that the PIV is incapable of taking into account the curvature of the particle trajectory between two successive images, the loss of informations are evidently non-trivial. At the present time, commercially available PIV systems offers highly capable software packages, which help in coping with large number of issues affecting the measurement accuracy. However, it is quite often to encounter flow field artifacts in the form of inconsistent vectors after the evolution of PIV images. The visual inspection of calculated velocity field allows pointing out those velocity vectors clearly out of the local velocity pattern with considerable variation in both magnitude and the direction. These vectors are referred as spurious vector or outliers. The local error associated with an outlier is usually quite high (10 or 100 times), than the typical error associated to the cross-correlation measurement noise. There probability is always higher at the edges of the image, approaching interfaces and in regions with a large velocity gradient. The spurious vectors can be eliminated by using some validation algorithm; such as “Local neighborhood validation algorithm”, which identifies and replaces an erroneous vector by comparing it with the neighborhood vectors lying within a defined region (MxM). The PIV images may also suffered with strong impression of background image. Filtering of background noise can be done by subtracting the average particle image from all other images recorded on a same run.

### **Diameter of Particles**

The velocity measurement by PIV is based on the assumption that the primary particles perfectly follow the flow between each illumination. The choice of particles and their seeding is very crucial to the PIV measurement. A proper kind of tracer should not alter the flow dynamics or the fluid property, as well as should not be liable to interaction among each other (Westerweel 1997). In reality, the concept of ideal tracer admits a certain degree of approximation. The particle size must be small enough to follow the flow properly but not too small to scatter insignificant amount of light (typically, should be superior to the length of incident wave). In case of gases, a good compromise in size is about 1-5 microns (krawczynski 2006).

Beside the actual size of the particles, the size of particle image is also very critical for the detection of correlation peak. As the inadequate particle image diameter in PIV measurement produce measurement biases in the cross-correlation evaluation. When the particle images become too small, the displacement estimate tend to be biased and exhibits a periodic pattern with pixel intervals in the displacement histogram of PIV data. This error is usually termed as peak locking. The particle image diameter can be increased during the recording process by various means. A relatively simple and common practice to mitigate these effects is to increase the sampling rate during the recording process or perhaps defocusing the particle image slightly (Raffel et al. 2007).

### **Effect of particle image density**

The aim of optimizing PIV is to maximize the probability of detecting the displacement-correlation peak. In the process of particle image evaluation, the probability of a valid displacement detection increases when more particle image pairs enter in the correlation calculation.

- Usually a large particle image density is desirable, as the number of image pairs captured in an interrogation window itself depends on effective particle image density and on the factors expressing in-plane displacement (the in-plane loss of pairs) and out-of-plane displacement (the out-of-plane loss of pairs). Particle image density has also a direct influence on the measurement uncertainty in a process of particle image evaluation.
- The inadequately large particle image density could lead to some undesirable effects, such as fluid opacity (due to multiple particle scattering) and multiphase effects (i.e., increase of the apparent fluid viscosity and particle to particle interactions). Therefore a more practical approach is to accept a small fraction of spurious vectors, typically about 5% (Tropea et al. 2007) and rely on the post-treatment phase for the removal and replacement of these vectors.

### **Estimation of the location of correlation peak**

The particle displacement corresponds to the location of the peak correlation value found in the correlation table. Willert and Gharib (1991) mentioned that the majority of the error between the true displacement and the measured displacement is a result of two factors.

- The estimation of the correlation peak through interpolation from three points in either direction introduces a certain amount of error.
- The randomly spaced particle images within the sampling region can only yield displacement vectors for their respective locations. This means that especially if the

seeding density is low, the average displacement vector obtained within the sampling region is only unbiased if there is no velocity gradient, that is all particles move with the same velocity.

This location of peak correlation is the integer value, multiple of the number of pixels. The sub-pixel interpolation, such as Gauss interpolation function given by Willert and Gharib (1991), with particle image size superior to 2 pixels allows improving the precision of the location of the correlation peak.

### **Loss of particle pair**

An important problem associated with PIV measurement is the loss of particle pair due to *out-of-plane motion* of the tracer particle, that is the tracer particle that enter or leave the light sheet between the two exposures, and due to the *in-plane motion*, that is the tracer particles that enter or leave the interrogation domain between the two exposures (Tropea et al. 2007). The loss of particle reduces the correlation peak and thus introduces a bias to the estimation of actual particle displacement. It is usually considered that a minimum of 10 particle pair should be located in the correlating windows to ensure better correlation peaks, (krawczynski 2006). The loss of particle can be reduce by adjusting the time delay between two exposure in a way that the maximum displacement should remain less than 20-30% of the size of interrogation window (Rouland 1994). The loss can also be reduced by the overlapping of interrogation areas.

## **Reference**

1. Allano D, Lecordier B, Lecordier JC, Trinité M, "Qualification d'une chaîne de mesure PIV digitale source de bruit et estimation des erreurs", 6 Congrès francophone de vélocimétrie Laser (Saint-Louis), 1998.
2. Foucaut JM, Stanislas M, "Some considerations on the accuracy and frequency response of some derivative filters applied to particle image Velocimetry vector fields", Meas. Sci Technol. 13 (2002) 1058-1071.
3. Howell JR, Siegel R, "Thermal radiation heat transfer, vol-II; Radiation exchange between surfaces and in Enclosures", National aeronautics and space administration, 1969.
4. krawczynski JF, "La structure de champ de vitesse dens un réacteur à jets opposes, Caractérisation du mélange turbulent", Thèse du Doctorat de l'Université de Rouen, 2006.
5. Raffel M, Willert CE, Wereley ST, Kompenhans J, "Particle Image Velocimetry 2nd-Edition", Springer, 2007.

6. Rouland E, "Etude et développement de la technique de vélocimétrie par intercorrélation d'images de particules. Application aux écoulements en tunnel hydrodynamique." Thèse de Doctorat de l'Université de Rouen, 1994.
7. Tropea C, Yarin AL, Foss JF, "Springer Handbook of Experimental Fluid Mechanics", Ch-5: Velocity, Vorticity and Mach Number, Springer, 2007.
8. Westerweel J, "Fundamentals of digital particle image Velocimetry", Meas. Sci. Technol. 8 (1997) 1379-1392.
9. Willert C E, Gharib M, "Digital particule image velocimetry", Experiments in Fluids, 10 (1991) 181-193.

## **Annex-B**

### **Radiative heat flux**

The radiative heat transfer from the top surface of test plate is estimated from two different methods. The first one considers the radiative exchange occurring between two gray bodies.

$$\phi_{rad,top} = \sigma(T_w^4 - T_m^4) / (1/\epsilon_w + 1/\epsilon_m - 1) \quad \dots\dots (B.1)$$

Where;

$\epsilon_w$  = Emissivity of test wall black painted.

$\epsilon_m$  = Emissivity of surrounding walls of the test section.

$T_w$  = Temperature of test wall surface normally measured by Infra-red camera, (K)

$T_m$  = Temperature of surrounding walls of the test section, (K)

For the sake of simplicity the terms for radiation form-factor and the ratio of respective surface areas are considered as unity. The total fraction of thermal exchange between the test section and both the inlet and outlet plane is around 13 %.

The second method takes into account the thermal exchange occurring among the number of participating surfaces. In this method, the test surface locating on the bottom side of the test section was divided into number of small elements that carry a local surface temperature mapped through infrared measurement. The temperature field consisting of the nodal results was converted into element results and each element was considered as a participating surface. The remaining three walls of the test section along with both inlet and outlet planes were each considered as independently participating surface at ambient temperature. The form-factor in present case was determined by using the theory of radiative exchange taking place between a differential element and a finite area (Howell and Siegel 1969), which can be expressed from Eq. (B.2). From figure (B.1) it can be observed that the capacity of viewing one surface from the other and vice versa is basically depends on their respective angle constituted between the line joining their centers and their surface normals which would change along with the distance  $S$  between two surfaces due to the tracking of differential element at the finite surface  $A_2$ . In the present situation, the finite surfaces  $A_2$  are represented by the wind tunnel test section's left wall, top wall, right wall, inlet plane and outlet plane at ambient temperature and the  $dA_1$  are elements of heated test surface. The radiant energy leaving from one surface and reaching to all visible surfaces can be described by the conservation law given by Eq. (B.3).

$$F_{d1-2} = \int_{A_2} \frac{\cos \beta_1 \cdot \cos \beta_2}{\pi S^2} dA_2 \quad \dots\dots (B.2)$$

$$\sum_{j=1}^n F_{i-j} = 1 \quad \dots\dots (B. 3)$$

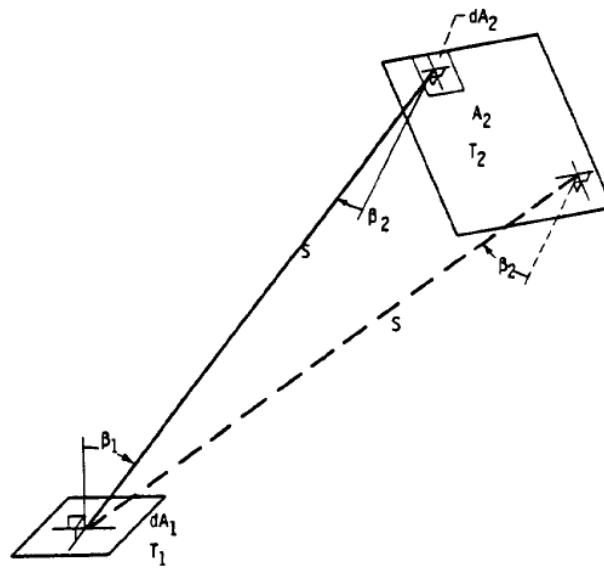


Figure (B.1): Radiant interchange between differential element and finite area; Howell and Siegel (1969).

The estimation of radiative exchange among various surfaces is based on the radiosity method. This method accounts for the radiant flux leaving a surface due to self emittance and due to the reflection of energy fraction coming from other surface, see figure (B.2). The radiosity 'B' for a surface 'i' is given by Eq. (B.4). The test plate constituting the bottom wall of the wind tunnel is heated up to 70 °C at maximum. Therefore, the surrounding walls are supposed to receive a radiant energy that lies in the lower infrared region of the spectrum, notably the wavelength of an order of 8.2  $\mu\text{m}$  (wave length corresponding to the energy peak described by Wien's displacement law;  $T = 2298(\mu\text{m}.K)/\lambda_{\text{max}}$ ). Under this condition the ordinary grade of glass-sheet can be considered as opaque and so the transmissivity is zero. The application of Eq. (B.4) to all participating surfaces is resulted in a matrix of huge mass, which often becomes impossible to solve due to the limitation of computer memory, because the number of elements on the test wall resulting from the infra-red measurements are quite high. The results are estimated after reducing the number of indices in both streamwise and in cross-stream direction by performing surface-clustering at the test wall, where each cluster is formed by a particular number of neighboring elements and carries the mean temperature value. In present example, clusters comprising of six elements in each direction were chosen, which gave 157\*43 participating surfaces for the test wall and five other surfaces due to the surrounding walls and the inlet and outlet of the test section, each of them were considered as single finite surface. Figure (B.3) indicates a general concept of the aforementioned descriptions. The number of variables in the radiosity matrix is equal to

the square of the number of participating surfaces, which was around 45.6e6 for present example.

$$B_i = (1 - \epsilon_i) \sum_{j=1}^n B_j F_{i-j} + \epsilon_i \sigma T_i^4 \quad \text{..... (B. 4)}$$

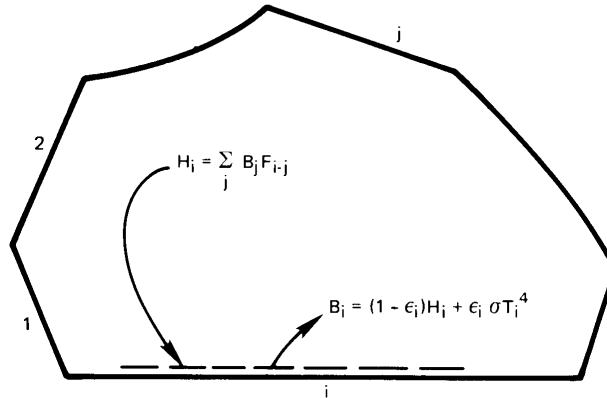


Figure (B.2): Multi-reflection model based on radiosity, Lienhard (2002)

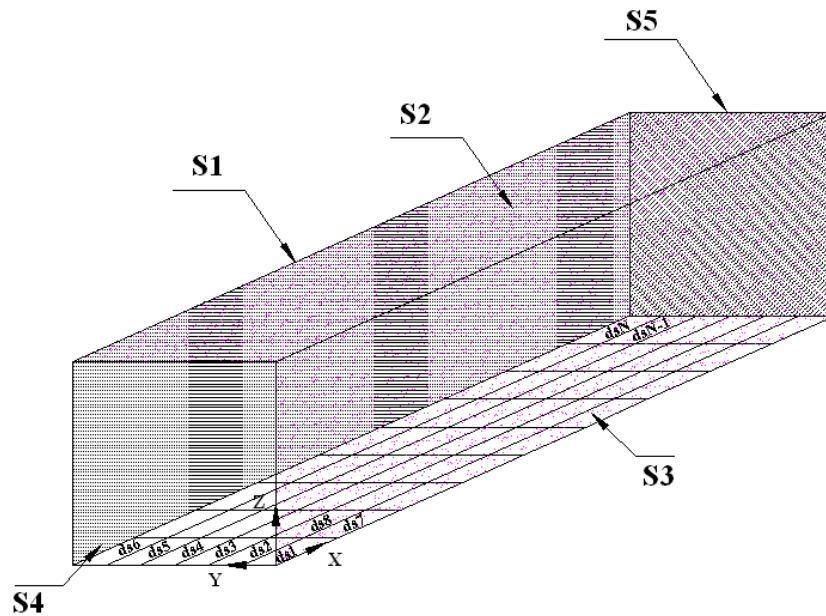


Figure (B.3): Multi-reflection method

Figure (B.4) shows the exchange of radiative heat flux due to multi-reflective model and a radiative exchange model for two grey surfaces (given by Eq. (B.1)). Heat transfer at different conditions has shown a maximum difference in overall radiative loss from the test surface of 4.3%. Although, the local variation could be higher between these two cases. The local maximum in the downstream region of the wall is identical to the temperature field and related to a certain degree of non-uniformity in the wall surface temperature. These results show that the estimation of heat flux from the simpler approach considering radiative exchange between two grey surfaces is not quite absurd. The comparison of two

methods have shown that the detail model requires a huge computational recourse and time to determine the loss of radiative flux from the test surface which could be difficult to implement if large number of test cases are required to be studied. While, the simpler approach is much quicker to implement, also the process of clustering degrades the precision level of the calculation.

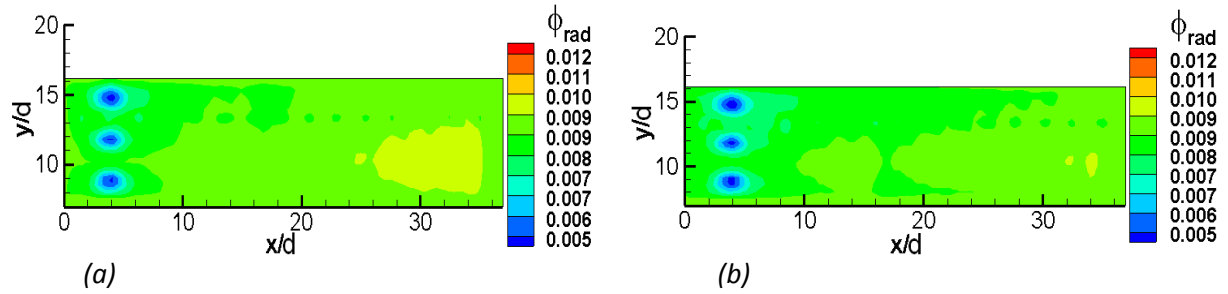


Figure (B.4): radiative flux leaving the test surface; (a) multi-reflective model, (b) simple gray exchange model.

### **Conductive heat flux**

The conductive heat losses from rear side of wall are minimized by using various layers of insulative materials. The bottom wall contains a 35  $\mu\text{m}$  copper circuit on the flow side, which is followed by a 0.8 mm epoxy layer and 22 mm Ertalon<sup>®</sup> plate. The bottom side of the wall is further overlaid by 15 mm polyurethane foam and a 25 mm glass wool insulation that contains the aluminum foil on the external side. The over-insulated bottom wall reduces the temperature gradient significantly at the outer surface. Thus, the conduction loss can also be estimated by using one dimensional heat transfer law comprising of thermal resistance for each material and the temperature difference between the upper wall and the ambient, as given below.

$$\phi_{cond} = (T_{w,top} - T_{w,bot}) / \sum R_i$$

	Thickness $e_i$ (mm)	Thermal conductivity $\lambda_i$ (W/m.K)
Epoxy	0.8	0.32
Ertalon	22	0.3
Polyurethane foam	15	0.037
Glass wool	25	0.035

Table-B.1: thermal conductivity of insulating materials

In order to determine a global estimate of the conductive heat loss from the bottom and the lateral faces of the insulated wall, a three dimensional conduction program was written on the Matlab<sup>®</sup> and the wall flux normal to each surface was estimated. Figure (B.5) shows the temperature distribution in a simple rectangular block consisting of the layer of different

materials in the absence of the injection holes. The top surface is bounded by a region surveyed in infra-red analysis, since the temperature load applied on the top surface are obtained from infra-red measurements. The lateral faces of the walls are considered adiabatic, and the bottom face is considered for going through a small natural convection. The loss of conductive heat flux from the lateral sides is about  $2 \pm 0.5$  % of the input electrical flux, and the loss from the bottom side is also seemed to fall into the similar range of variation ( $2 \pm 0.5\%$ ).

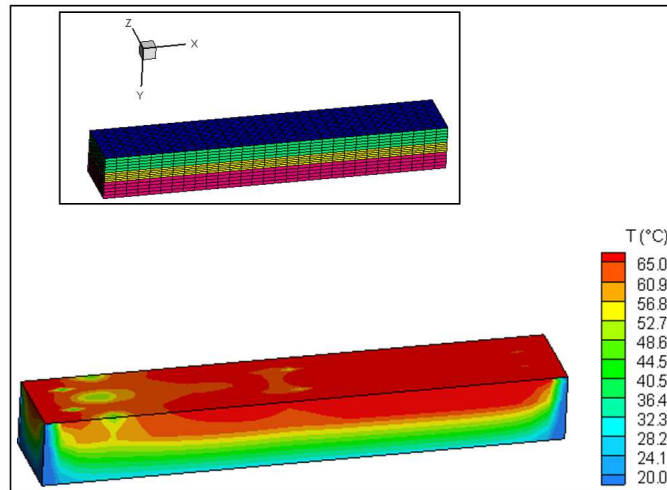


Figure (B.5): 3D analysis of conductive heat transfer.

### 3.1 Reference

1. Lienhard JH IV, Lienhard JH V, "A Heat Transfer Textbook 3rd-Edition", Ch-8: Radiative heat transfer, Published by Phlogiston Press, 2002.
2. Howell JR, Siegel R, "Thermal radiation heat transfer, vol-II; Radiation exchange between surfaces and in Enclosures", National aeronautics and space administration, 1969.



## Annex-C

### Probability density function (PDF) of velocity fluctuations ( $u,v$ )

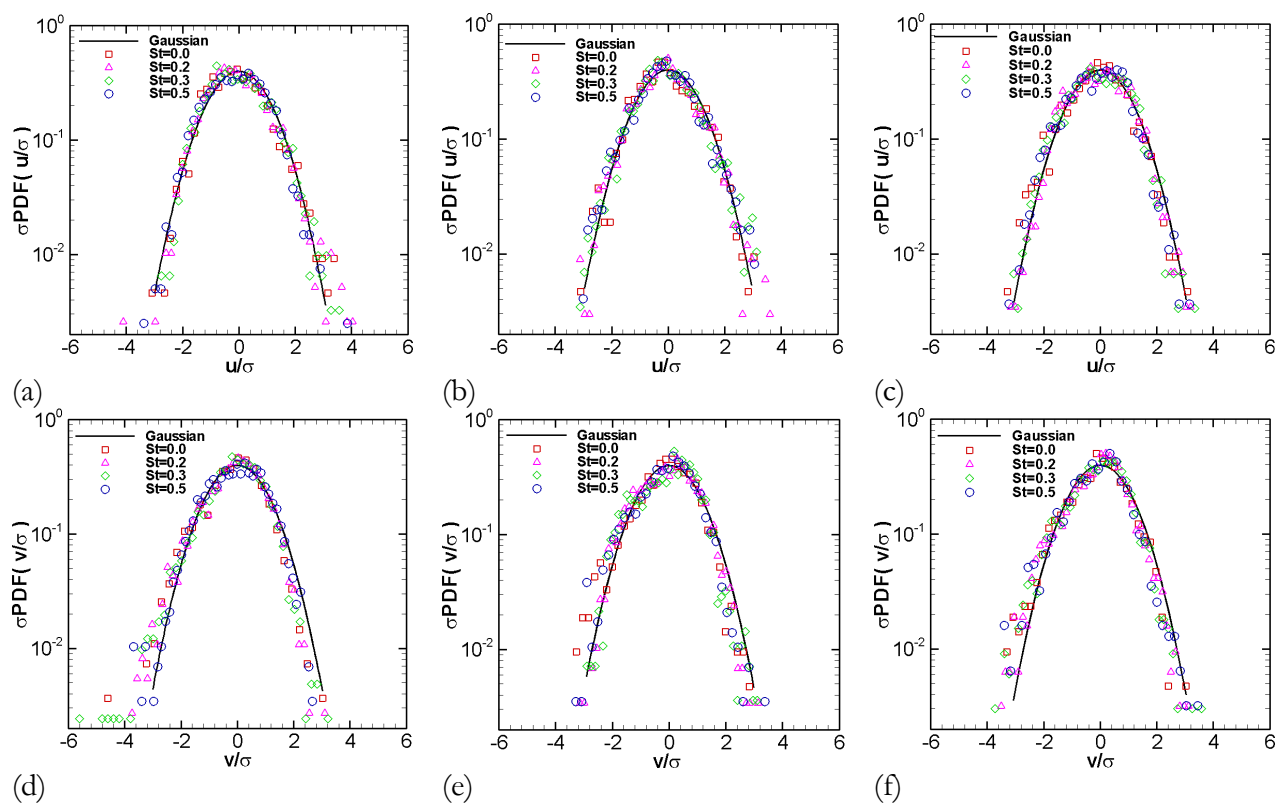


Figure (C.1): Comparison of PDF for different  $St$  at  $x/d=6$  and  $y/d=0.5$ , in the array of subfigures blowing ratios ( $\overline{M} = 0.65, 1$  and  $1.25$ ) increases column-wise, and the PDF of  $u$  and  $v$  belongs to the first and second row.



## Annex-D

### Coldwire measurements

#### Streamwise temperature distribution ( $z/d=0$ )

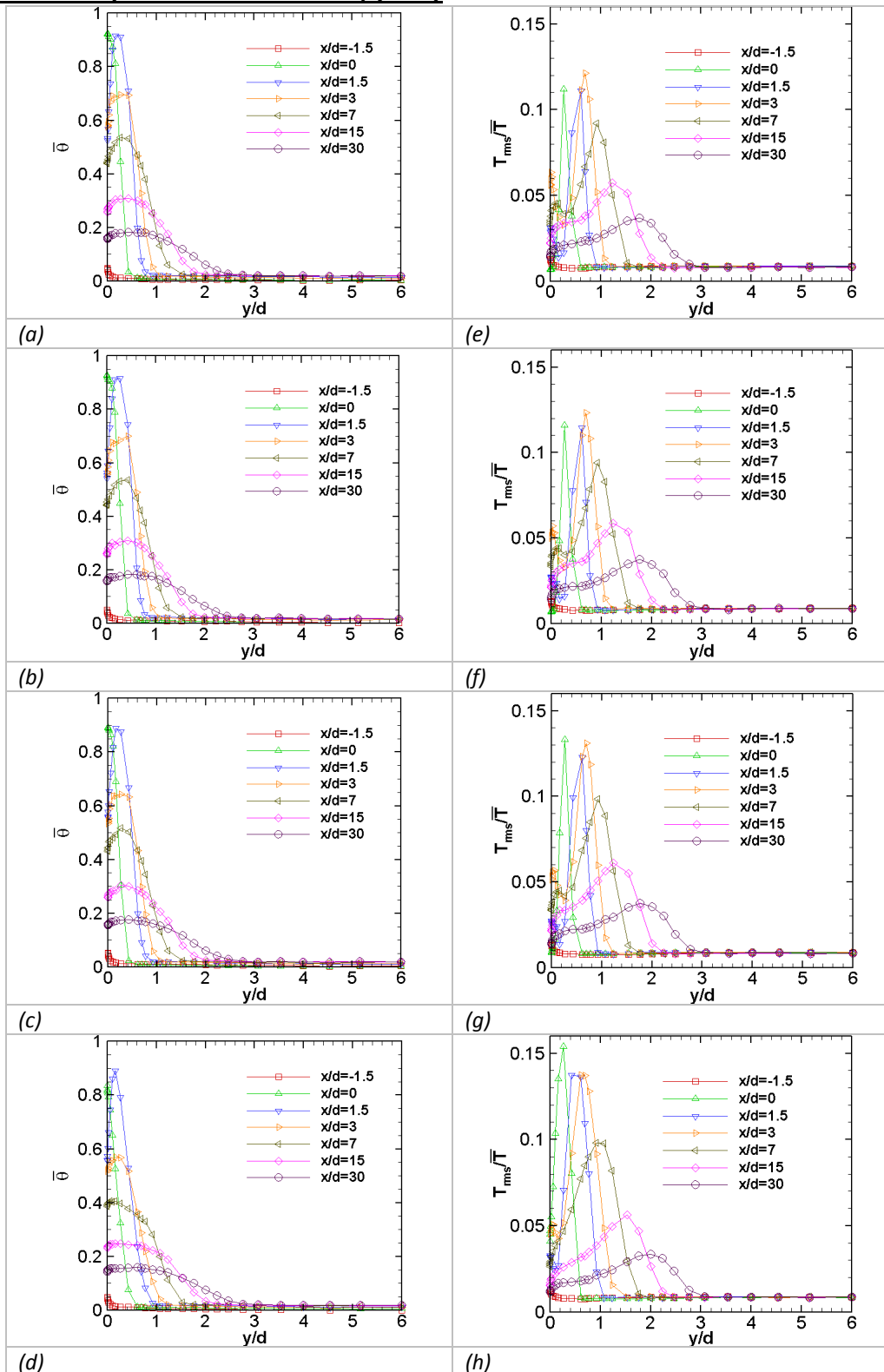


Figure (D. 1) Time-averaged temperature profiles (a)  $St=0$ , (b)  $St=0.2$ , (c)  $St=0.3$  and (d)  $St=0.5$ , and rms temperature profiles (e)  $St=0$ , (f)  $St=0.2$ , (g)  $St=0.3$  and (h)  $St=0.5$ , for a blowing ratio of  $\bar{M} = 0.65$ .

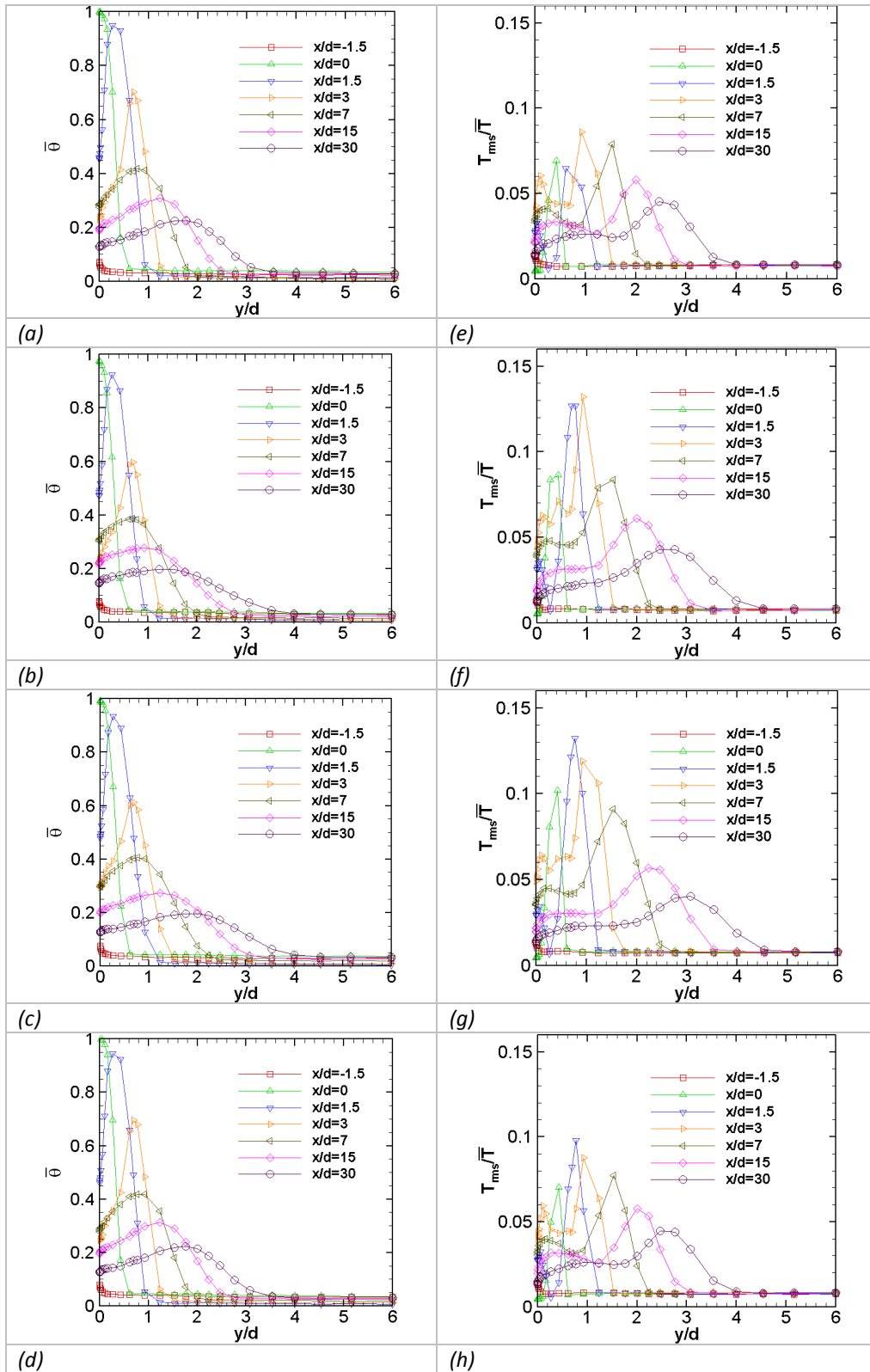


Figure (D. 2): Time-averaged temperature profiles (a)  $St=0$ , (b)  $St=0.2$ , (c)  $St=0.3$  and (d)  $St=0.5$ , and rms temperature profiles (e)  $St=0$ , (f)  $St=0.2$ , (g)  $St=0.3$  and (h)  $St=0.5$ , for a blowing ratio of  $\bar{M} = 1$ .

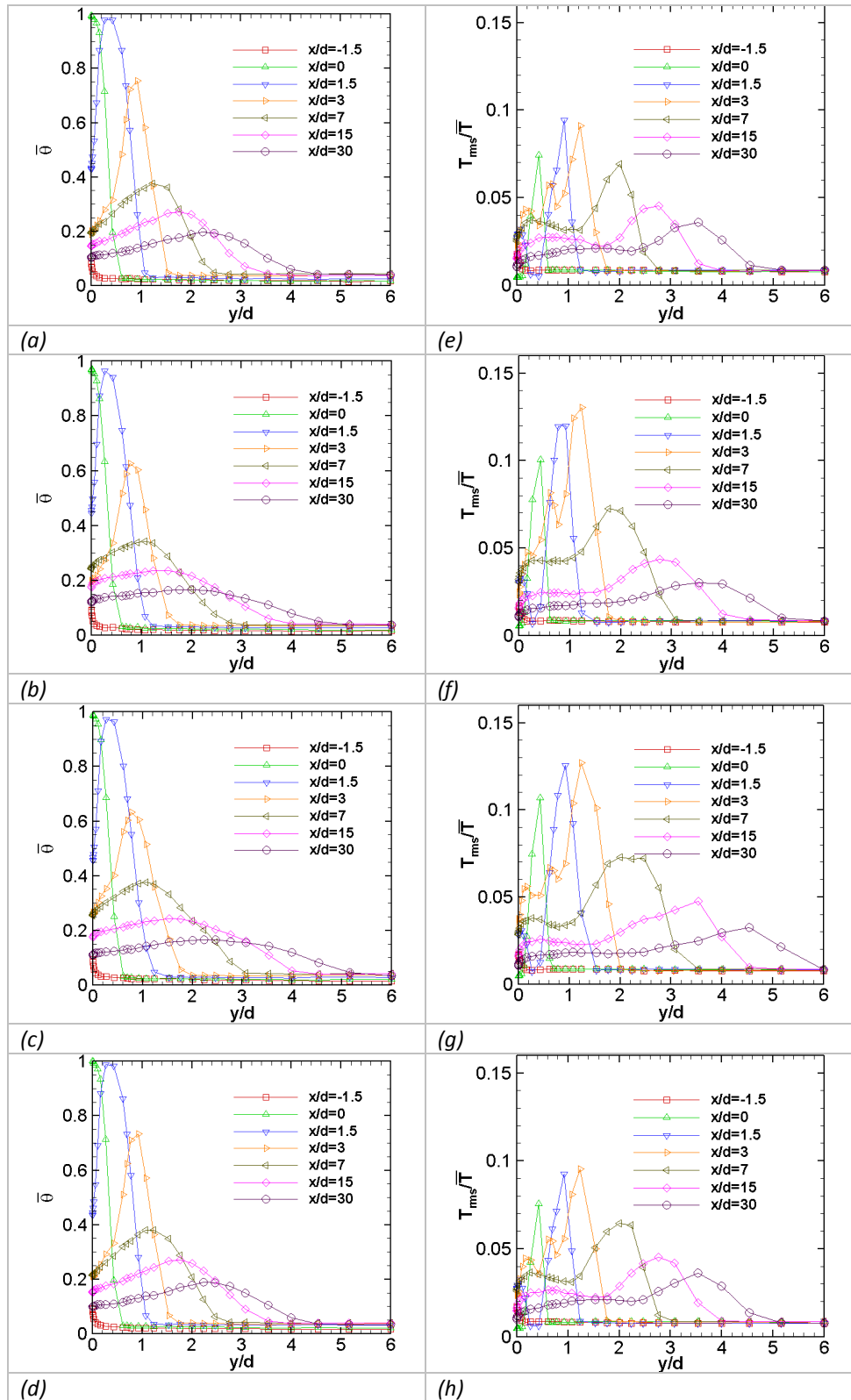


Figure (D. 3): Time-averaged temperature profiles (a)  $St=0$ , (b)  $St=0.2$ , (c)  $St=0.3$  and (d)  $St=0.5$ , and rms temperature profiles (e)  $St=0$ , (f)  $St=0.2$ , (g)  $St=0.3$  and (h)  $St=0.5$ , for a blowing ratio of  $\overline{M} = 1.25$ .

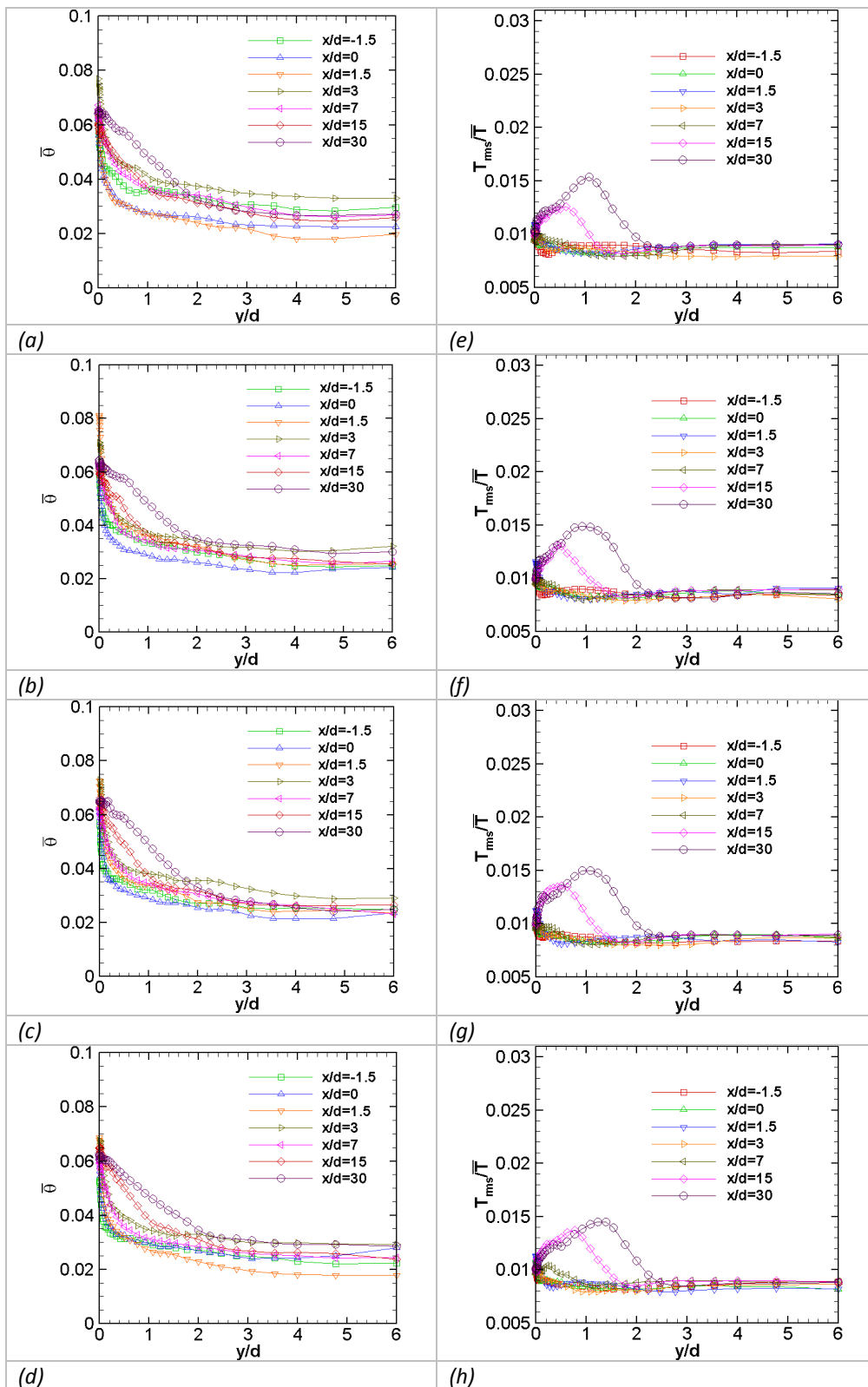
**Streamwise temperature distribution ( $z/d=1.5$ )**

Figure (D. 4): Time-averaged temperature profiles (a)  $St=0$ , (b)  $St=0.2$ , (c)  $St=0.3$  and (d)  $St=0.5$ , and rms temperature profiles (e)  $St=0$ , (f)  $St=0.2$ , (g)  $St=0.3$  and (h)  $St=0.5$ , for a blowing ratio of  $\bar{M} = 0.65$ .

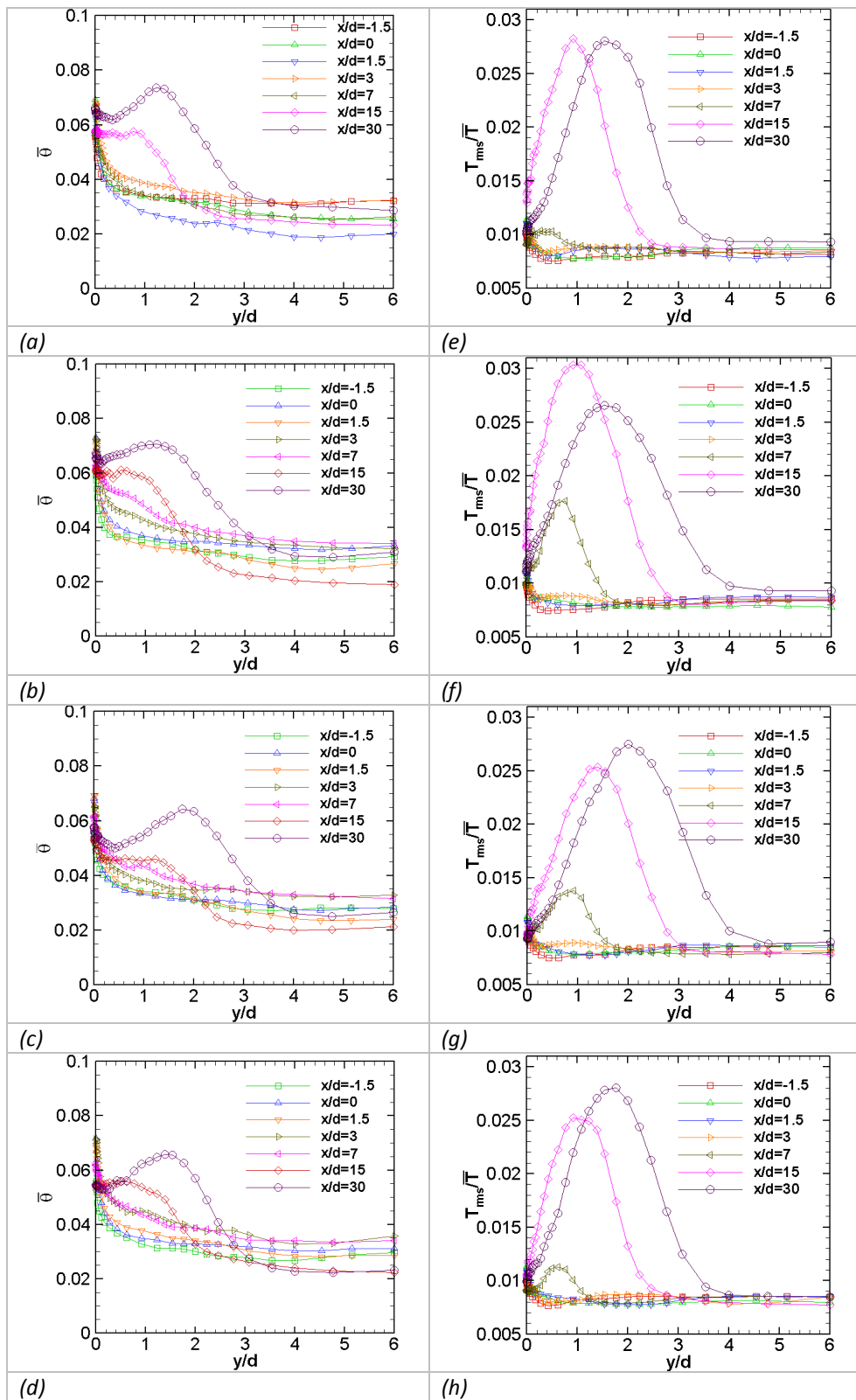


Figure (D. 5): Time-averaged temperature profiles (a)  $St=0$ , (b)  $St=0.2$ , (c)  $St=0.3$  and (d)  $St=0.5$ , and rms temperature profiles (e)  $St=0$ , (f)  $St=0.2$ , (g)  $St=0.3$  and (h)  $St=0.5$ , for a blowing ratio of  $\overline{M} = 1$ .

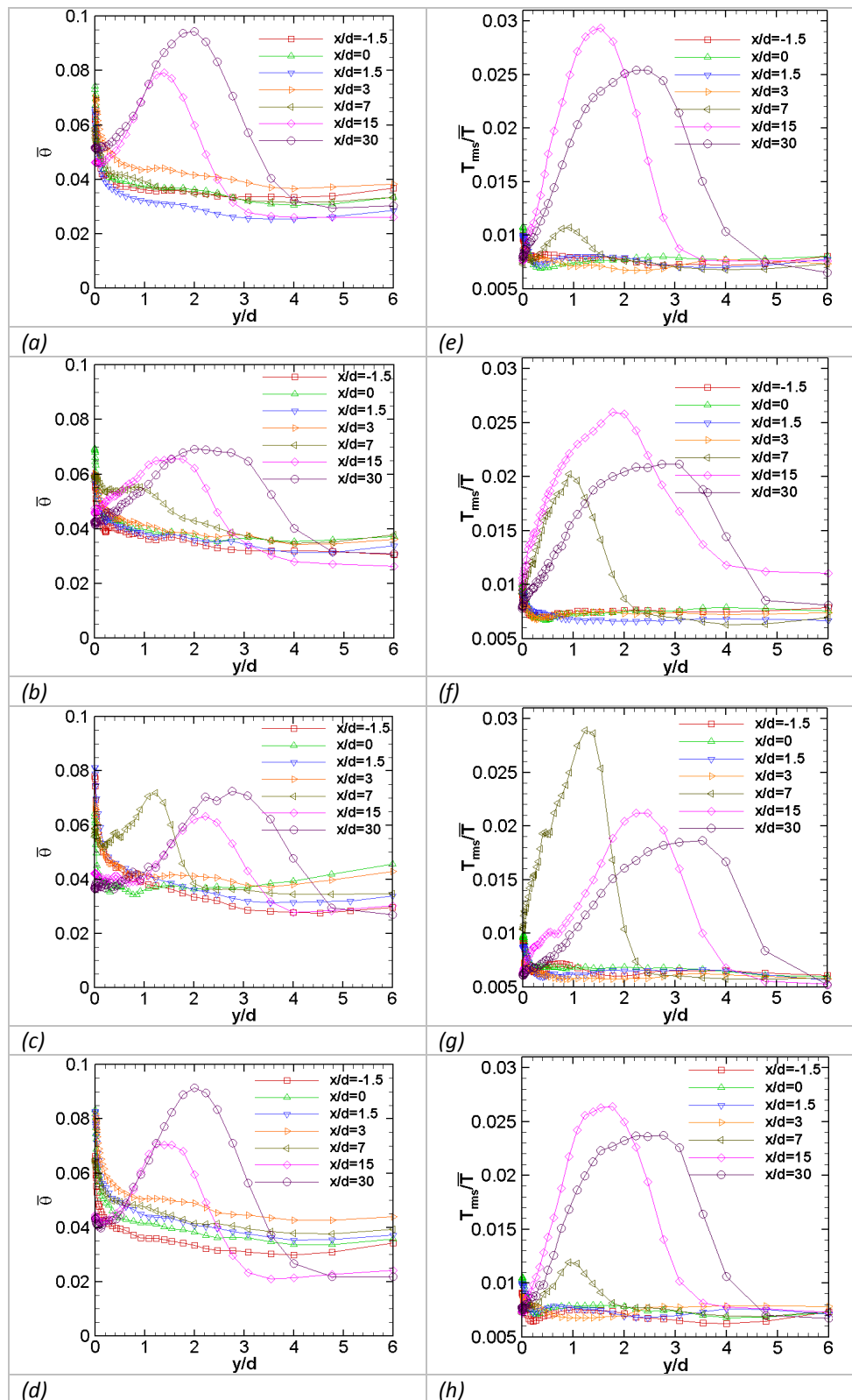


Figure (D. 6): Time-averaged temperature profiles (a)  $St=0$ , (b)  $St=0.2$ , (c)  $St=0.3$  and (d)  $St=0.5$ , and rms temperature profiles (e)  $St=0$ , (f)  $St=0.2$ , (g)  $St=0.3$  and (h)  $St=0.5$ , for a blowing ratio of  $\bar{M} = 1.25$ .

### Comparison of the cases of different blowing ratio

$z/d=0$  and  $St=0.2$

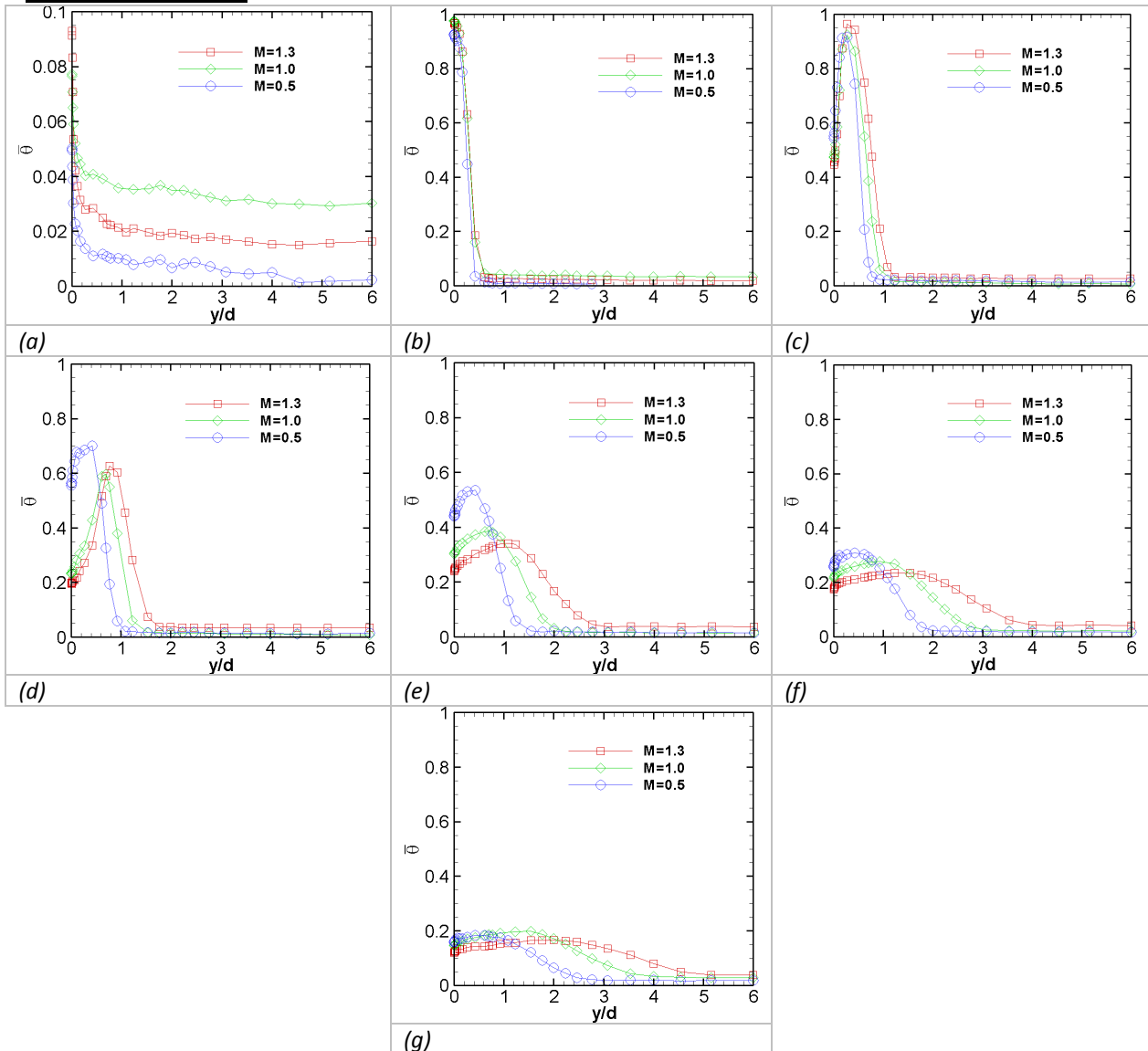
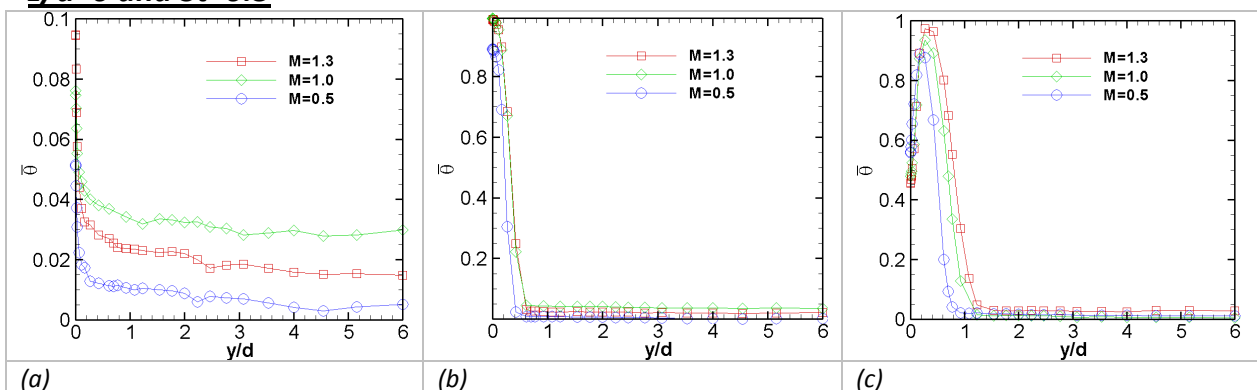


Figure (D. 7): Comparison of time-averaged profiles for different blowing ratios,  $z/d=0$  and  $St=0.2$ , (a)  $x/d=-1.5$ , (b)  $x/d=0$ , (c)  $x/d=1.5$ , (d)  $x/d=3$ , (e)  $x/d=7$ , (f)  $x/d=15$  and (g)  $x/d=30$ .

$z/d=0$  and  $St=0.3$



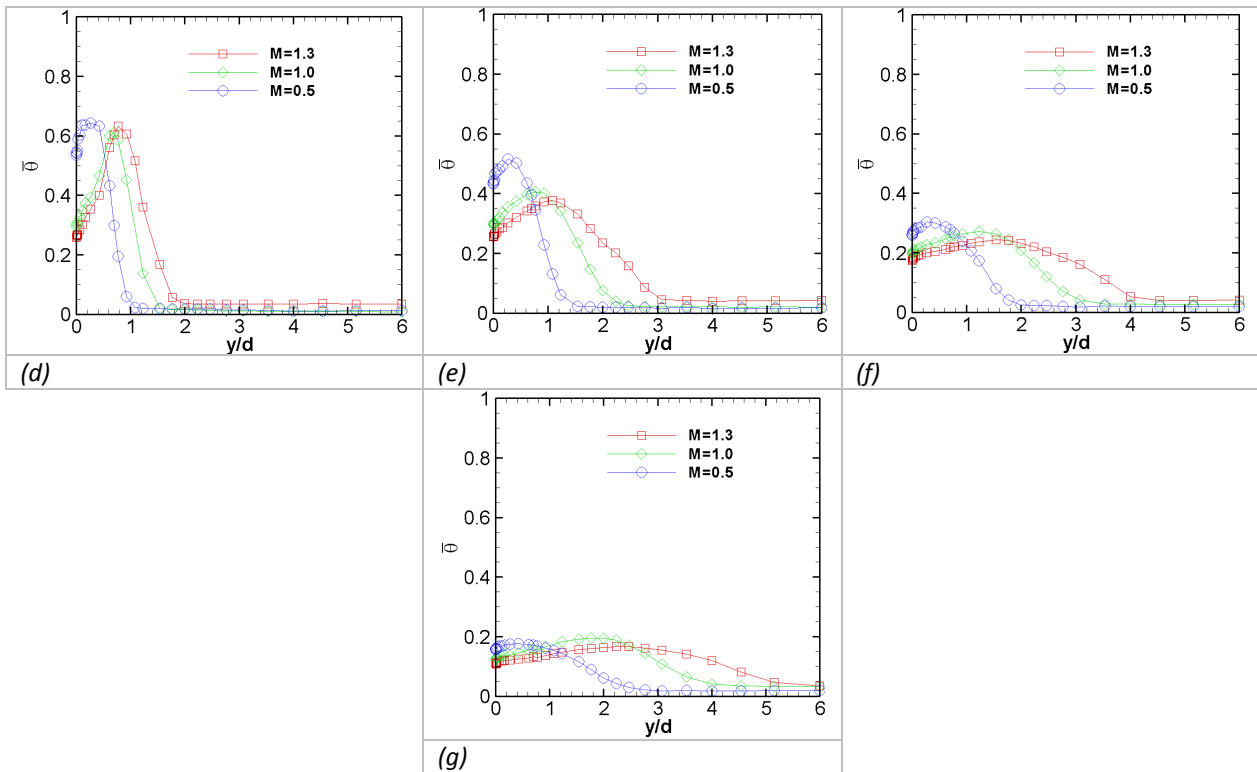
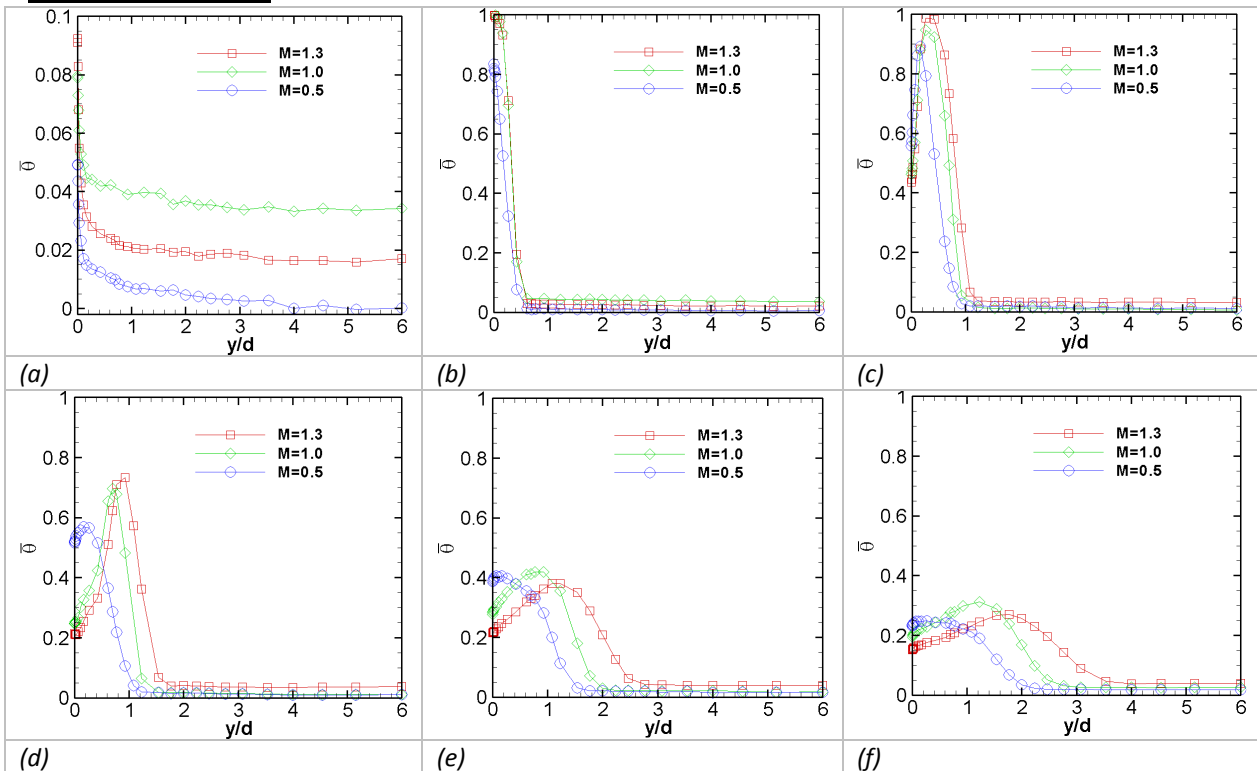


Figure (D. 8): Comparison of time-averaged profiles for different blowing ratios,  $z/d=0$  and  $St=0.3$ , (a)  $x/d=-1.5$ , (b)  $x/d=0$ , (c)  $x/d=1.5$ , (d)  $x/d=3$ , (e)  $x/d=7$ , (f)  $x/d=15$  and (g)  $x/d=30$ .

### $z/d=0$ and $St=0.5$



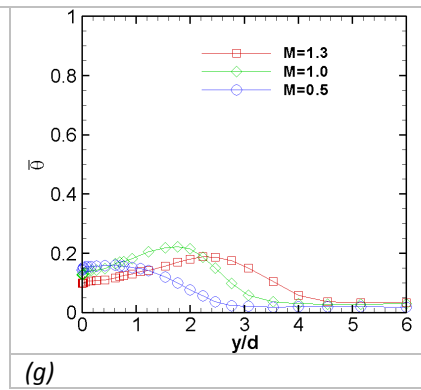


Figure (D. 9): Comparison of time-averaged profiles for different blowing ratios,  $z/d=0$  and  $St=0.5$ , (a)  $x/d=-1.5$ , (b)  $x/d=0$ , (c)  $x/d=1.5$ , (d)  $x/d=3$ , (e)  $x/d=7$ , (f)  $x/d=15$  and (g)  $x/d=30$ .

### $z/d=1.5$ and $St=0.2$

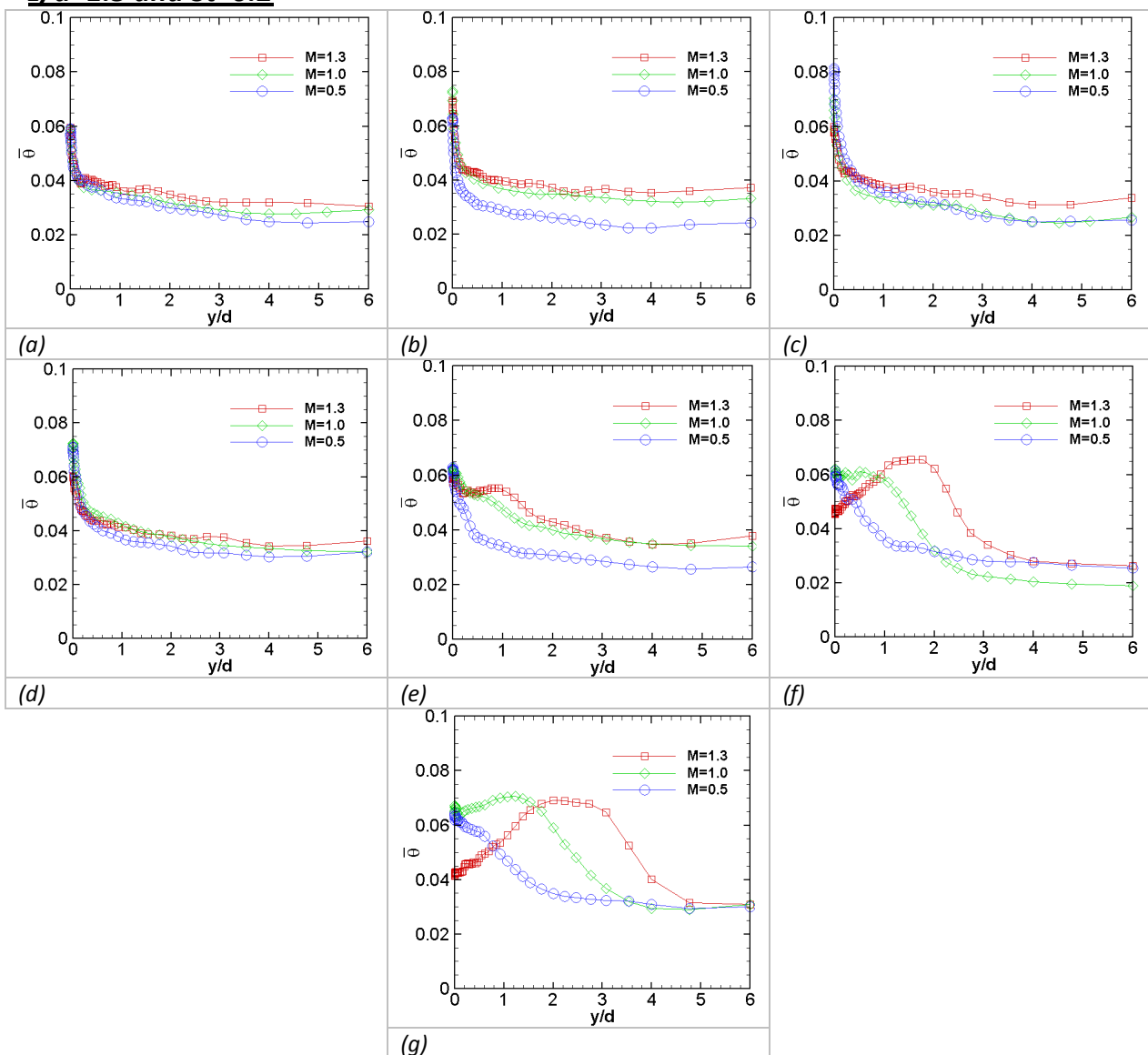


Figure (D. 10): Comparison of time-averaged profiles for different blowing ratios,  $z/d=1.5$  and  $St=0.2$ , (a)  $x/d=-1.5$ , (b)  $x/d=0$ , (c)  $x/d=1.5$ , (d)  $x/d=3$ , (e)  $x/d=7$ , (f)  $x/d=15$  and (g)  $x/d=30$ .

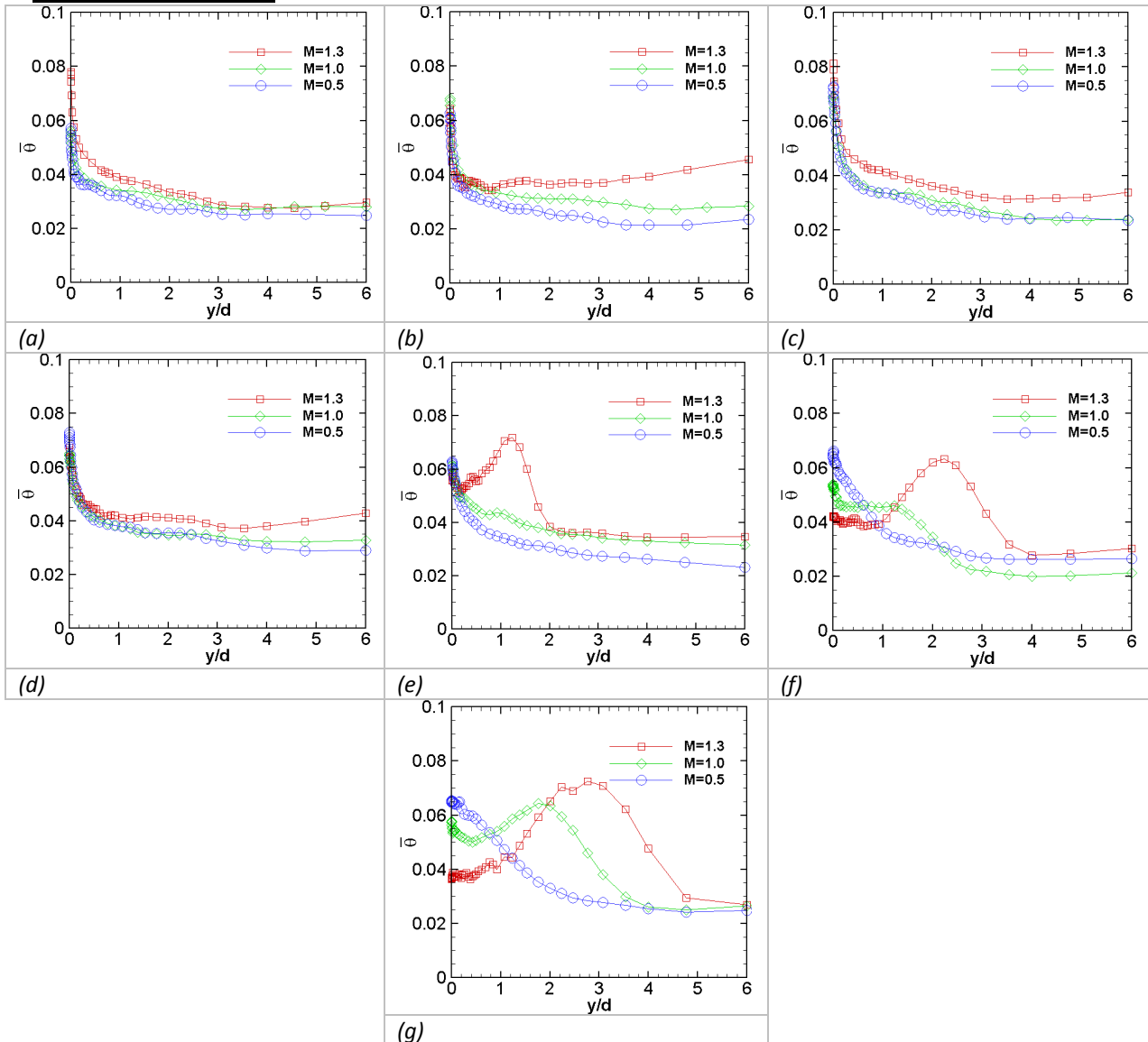
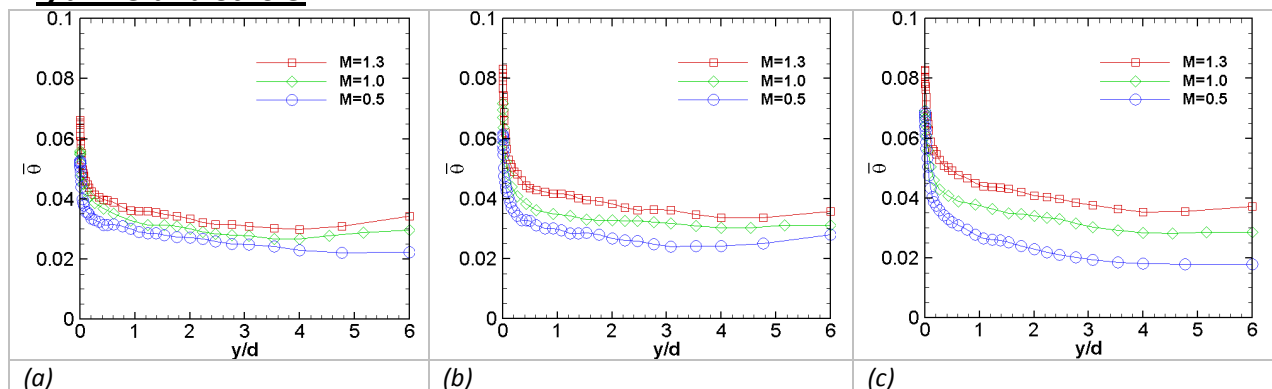
**$z/d=1.5$  and  $St=0.3$** 

Figure (D. 11): Comparison of time-averaged profiles for different blowing ratios,  $z/d=1.5$  and  $St=0.3$ , (a)  $x/d=-1.5$ , (b)  $x/d=0$ , (c)  $x/d=1.5$ , (d)  $x/d=3$ , (e)  $x/d=7$ , (f)  $x/d=15$  and (g)  $x/d=30$ .

 **$z/d=1.5$  and  $St=0.5$** 

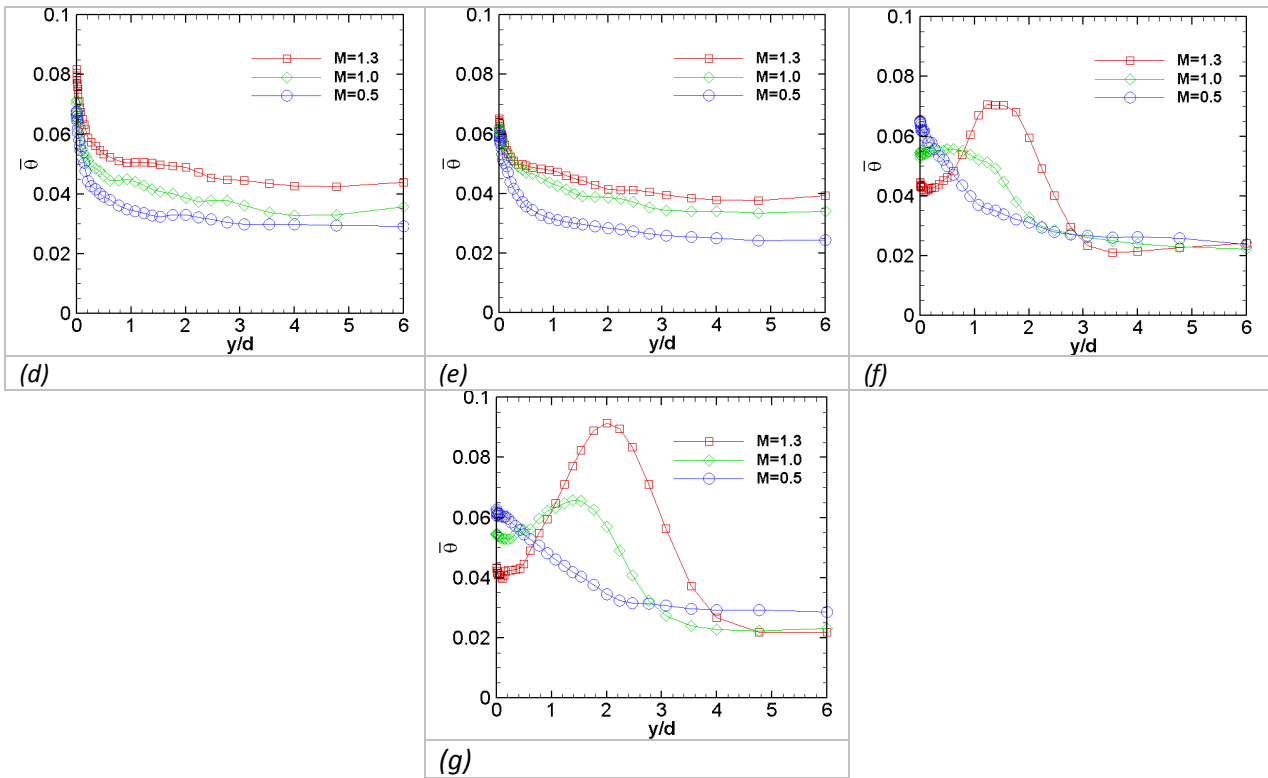


Figure (D. 12): Comparison of time-averaged profiles for different blowing ratios,  $z/d=1.5$  and  $St=0.5$ , (a)  $x/d=-1.5$ , (b)  $x/d=0$ , (c)  $x/d=1.5$ , (d)  $x/d=3$ , (e)  $x/d=7$ , (f)  $x/d=15$  and (g)  $x/d=30$ .



## Annex-E

### Thermal Uncertainties

The uncertainty of a measured quantity is determined from the residual error remained after all kind of correction applied to the measured quantity. The major sources of errors are the fixed and random errors. Fixed errors constitute the errors arriving from equipment accuracy mentioned by the manufacturer, calibration error, data acquisition and data treatment process, which may produce any offset from the actual or mean value of the measured quantity. The random error is an error which changes during the time of one complete measurement. For thermal measurements, both kinds of errors are taken into account by using root-sum-square technique proposed by Kline and McClintock (1953). The method consists of determining the sensitivity coefficient for estimating parameter  $Y$  with respect of each measured quantity  $X_i$  along with the uncertainty interval for all independent quantities. For example, uncertainty for a parameter  $Y$  depending on many variable (such as;  $Y = Y(X_1, X_2, X_3, \dots, X_n)$ ) can be written as follow;

$$\delta y(x_i) = \left\{ \sum_{i=1}^N \left( \frac{\partial Y}{\partial X_i} \cdot \delta X_i \right)^2 \right\}^{1/2} \quad \dots\dots (E. 1)$$

Moffat (1988) referred these error as *bias* and *precision errors* and elaborated them in case of a multiple point measurement. The precision error associated to the random variation of measured quantity was defined as  $tS_{(N)}/(N)^{0.5}$ , where  $S_{(N)}/(N)^{0.5}$  is the standard deviation of the sample mean with  $N$  number of samples and  $t$  is the student's  $t$  multiplier determined from the student's  $t$ -distribution table as a function of given degree of freedom ( $N-1$ ) and desired confidence interval (such as; 95%). The use of  $t$ -distribution is advantageous in case of limited number of observations, where estimated mean is not the actual mean of the population. An interesting attribute of  $t$ -distribution is that the distribution is independent of both mean and standard deviation and only depends on the degree of freedom of the measured sample, which tends to give normal distribution with larger number of observations. In case of multiple point measurement the precision error for a measured variable can be represented as;

$$X_i = X_i(\text{measured}) \pm \frac{tS_{(N)}}{\sqrt{N}} \quad \dots\dots (E. 2)$$

Moffat (1988) mentioned that the overall error for a particular variable  $X$  can be given by Eq. (E.3), where  $B_x$  and  $S_x$  are the overall bias and precision errors estimated from the root-sum-square calculations.

$$(U_x)_{0.95} = \left\{ (B_x)^2 + (tS_x)^2 \right\}^{1/2} \quad \dots\dots (E. 3)$$

In order to determine the overall error in present case, the set of equations for the parameters of interest are identified and then the uncertainty interval for all independent variable along with the sensitivity coefficient for these parameters is estimated. The blowing ratio for two obliquely interacting air streams can be written as,

$$M = \frac{\rho_i U_i}{\rho_\infty U_\infty} \quad \dots\dots (E. 4)$$

The velocities in the above equation are the function of other variables, and can be replaced with the linear relations determined from initial study of the wind tunnel flow and calibration process of the orifice tube. Replacing  $U_i$  in above equation with the equivalent flow rate ( $Q_i/\rho_i S_i$ ) and further writing it in terms of injection Pressure  $P_i$  by using the calibration curve of the orifice tube ( $Q = a_i.P_i + b_i$ ), as well as replacing the wind tunnel velocity  $U_\infty$  with the blower fan rotational speed  $RPM$ , by using a linear relation of ( $U_\infty = a_\infty.RPM + b_\infty$ ) in Eq. (E.4);

$$M = \frac{(a_i.P_i + b_i).R.T_\infty}{S_i.P_\infty.(a_\infty.RPM + b_\infty)} \quad \dots\dots (E. 5)$$

$$\delta M = \left\{ \left( \frac{\partial M}{\partial P_i} \delta P_i \right)^2 + \left( \frac{\partial M}{\partial P_\infty} \delta P_\infty \right)^2 + \left( \frac{\partial M}{\partial T_\infty} \delta T_\infty \right)^2 + \left( \frac{\partial M}{\partial RPM} \delta RPM \right)^2 \right\}^{0.5} \quad \dots\dots (E. 6)$$

Uncertainty in momentum ratio can be determined by elaborating the velocity terms in a similar fashion and determining the derivative of 'I' with respect to all independent variables along with their respective uncertainty intervals. The uncertainty in  $I$  is dominated by the error of injection temperature.

$$I = \frac{\rho_i U_i^2}{\rho_\infty U_\infty^2} \quad \dots\dots (E. 7)$$

$$I = \frac{(a_i.P_i + b_i)^2.R^2.T_i.T_\infty}{P_i.S_i^2.P_\infty.(a_\infty.RPM + b_\infty)} \quad \dots\dots (E. 8)$$

$$\delta I = \left\{ \left( \frac{\partial I}{\partial P_i} \delta P_i \right)^2 + \left( \frac{\partial I}{\partial P_\infty} \delta P_\infty \right)^2 + \left( \frac{\partial I}{\partial T_i} \delta T_i \right)^2 + \left( \frac{\partial I}{\partial T_\infty} \delta T_\infty \right)^2 + \left( \frac{\partial I}{\partial RPM} \delta RPM \right)^2 \right\}^{0.5} \quad \dots (E. 9)$$

The error in overall heat flux generated at the wall relies on the voltage  $V$  and current  $C$  readings of the DC power supply. Therefore, the uncertainty in electrical heat flux would primarily depend on the error span observed for these variables. The error estimates for electrical heat flux determined from Eq. (E.11) represents the same probability of encompassing the actual value as for the constituent variables ( $V$  and  $C$ ).

$$\phi_{elec} = \frac{V.C}{S} \quad \dots\dots (E. 10)$$

$$\delta\phi_{elec} = \left\{ \left( \frac{\partial\phi_{elec}}{\partial V} \delta V \right)^2 + \left( \frac{\partial\phi_{elec}}{\partial C} \delta C \right)^2 \right\}^{0.5} \quad \dots\dots (E. 11)$$

The radiative heat transfer model governs the thermal exchange between the test wall and the surrounding walls.  $T_m$  and  $\varepsilon_m$  is the temperature and emissivity of the surrounding walls. The uncertainty interval of wall temperature  $T_w$  measured by the infrared camera is determined by the root-sum-square of both fixed and random errors. The error in  $\varepsilon_w$  is estimated by using the data of the thermocouples placed inside the test plate. This data is extrapolated to the wall temperature facing the flow and the corresponding radiative flux is determined. The radiative flux obtained from the extrapolated thermocouple temperature and from the infrared measurement are used to determine both  $\varepsilon_w$  and its error level by applying the uncertainty of the constituent temperature terms.

$$\phi_{rad} = \sigma \frac{(T_w^4 - T_m^4)}{(1/\varepsilon_w + 1/\varepsilon_m - 1)}$$

$$\delta\phi_{rad} = \left\{ \left( \frac{\partial\phi_{rad}}{\partial T_w} \delta T_w \right)^2 + \left( \frac{\partial\phi_{rad}}{\partial T_m} \delta T_m \right)^2 + \left( \frac{\partial\phi_{rad}}{\partial \varepsilon_w} \delta \varepsilon_w \right)^2 \right\}^{0.5} \quad \dots\dots (E. 12)$$

The accuracy of uncertainty estimate for conductive heat flux is slightly compromised because of the lack of reliable values of uncertainty intervals for the thermal conductivity of various materials. The uncertainty calculation is based on  $T_w$ ,  $T_{bot}$  and  $\lambda_{ert}$ , which are the temperature of the top, bottom surface of the injection wall and the thermal conductivity of ertalon. The uncertainty interval of  $\lambda_{ert}$  was obtained by referring to the earlier laboratory experiments, which is of the order of 5% (Dorignac and Vullierme 1996).

$$\phi_{cond} = \frac{(T_w - T_{bot})}{\sum R_i} \quad \dots\dots (E. 13)$$

$$\delta\phi_{cond} = \left\{ \left( \frac{\partial\phi_{cond}}{\partial T_w} \delta T_w \right)^2 + \left( \frac{\partial\phi_{cond}}{\partial T_{bot}} \delta T_{bot} \right)^2 + \left( \frac{\partial\phi_{cond}}{\partial \lambda_{ert}} \delta \lambda_{ert} \right)^2 \right\}^{0.5} \quad \dots\dots (E. 14)$$

The uncertainty in convective heat flux will depend on the error level determined for other fluxes, and the error in convective heat flux will simply be equal to the square-root of the sum of error-square of other fluxes.

$$\phi_{conv} = \phi_{elec} - \phi_{rad} - \phi_{cond} \quad \dots\dots (E. 15)$$

$$\delta\phi_{conv} = \left\{ \left( \frac{\partial\phi_{conv}}{\partial\phi_{elec}} \delta\phi_{elec} \right)^2 + \left( \frac{\partial\phi_{conv}}{\partial\phi_{rad}} \delta\phi_{rad} \right)^2 + \left( \frac{\partial\phi_{conv}}{\partial\phi_{cond}} \delta\phi_{cond} \right)^2 \right\}^{0.5} \quad \text{..... (E. 16)}$$

$$\delta\phi_{elec} = \left\{ \delta\phi_{elec}^2 + \delta\phi_{rad}^2 + \delta\phi_{cond}^2 \right\}^{0.5} \quad \text{..... (E. 17)}$$

The uncertainty intervals for different independent quantities are shown in table-E.1. These intervals are obtained from different sources including the previous measurements and manufacturer's specification.

	fixed error	random error
$\delta T_e$ (K)	1	0.1
$\delta T_i$ (K)	1	0.1
$\delta T_w$ (IR-camera) (K)	2	0.03
$\delta P_e$	-	0.8 %
$\delta P_i$	-	0.8 %
$\delta \varepsilon_p$	0.038	-
$\partial\lambda_{ert}$	5%	-

Table-E.1: Uncertainty interval of primary variables

Heat transfer coefficient and adiabatic wall temperature are determined from the coefficients of linear regression, which is obtained by fitting the data of convective heat transfer coefficient and the wall temperature. Uncertainty in these parameters include the uncertainty caused by inherent errors of the corresponding data set, as well as the error contribution due to the deviation of estimated regression coefficients from the actual ones. The uncertainty induced by the process of curve-fitting is determined by assuming the errors to follow the normal distribution. Since, the number of available observations is rather limited. Therefore, the deviation in estimated regression coefficient can be determined by using the t-statistics [4, 5].

$$\hat{\varepsilon}_i = T_{p,i} - T_{ad} - 1/h \cdot (\phi_{conv,i}) \quad \text{..... (E. 18)}$$

$$s_{(1/h)} = \sqrt{\frac{1}{(n-2)} \cdot \frac{\sum_{i=1}^n \hat{\varepsilon}_i^2}{\sum_{i=1}^n (\phi_{conv,i} - \bar{\phi}_{conv})^2}} \quad \text{..... (E. 19)}$$

$$s_{(T_{ad})} = \sqrt{\frac{1}{n(n-2)} \cdot \sum_{i=1}^n \hat{\varepsilon}_i^2 \cdot \frac{\sum_{i=1}^n \phi_{conv,i}^2}{\sum_{i=1}^n (\phi_{conv,i} - \bar{\phi}_{conv})^2}} \quad \text{..... (E. 20)}$$

The deviation for each coefficient ( $1/h$  and  $T_{ad}$ ) can be given as  $1/h \pm s_{(1/h)} \cdot t$  and  $T_{ad} \pm s_{(T_{ad})} \cdot t$ , where  $t$  is the student's t-multiplier determined corresponding to (n-2) degree

of freedom and 95% confidence interval. The uncertainty contribution ( $\delta T'_{ad}$  and  $\delta h'$ ) due to the inherent errors of data set can be determine by solving ( $T_w = 1/h_f \cdot \phi_{conv} + T_{ad}$ ) for required sensitivity coefficient and applying the technique of root-sum-square with uncertainty interval determined previously for  $T_w$  and  $\phi_{conv}$ . The overall uncertainty for both coefficients is given Eq. (E.21) and Eq. (E.22).

$$\delta T_{ad} = \left\{ (\delta T'_{ad})^2 + (t \cdot s_{(T_{ad})})^2 \right\}^{1/2} \quad \dots\dots (E. 21)$$

$$\delta h = \left\{ (\delta h')^2 + (t \cdot s_{(1/h)})^2 \right\}^{1/2} \quad \dots\dots (E. 22)$$

## References

1. Dorignac E, Vullierme JJ, "Etude expérimentale des coefficients d'échange d'un film de refroidissement sur plaque non-athermane: effet de la géométrie d'injection", Int. J. Heat Mass Transfer, 39 (1996) 1935-1951.
2. Kline, S.J., and McClintock F. A., "Describing Uncertainties in Single-Sample Experiments," Mechanical Engineering, 75 (1953) 3-8.
3. Moffat RJ, "Describing the uncertainties in experimental results", Experimental thermal and fluid science, 1 (1988) 3-17.
4. Wikipedia article "Simple linear regression", [http://en.wikipedia.org/wiki/Simple\\_linear\\_regression](http://en.wikipedia.org/wiki/Simple_linear_regression).
5. Wikipedia article "Student's t-distribution", [http://en.wikipedia.org/wiki/Student%27s\\_t-distribution](http://en.wikipedia.org/wiki/Student%27s_t-distribution).



# *Experimental time-resolved study of the interaction between a pulsating injectant and a steady cross-flow: aerodynamics of film cooling*

*Q. Sultan, G. Lalizel, M. Fénot & E. Dorignac*

**Experiments in Fluids**  
Experimental Methods and their Applications to Fluid Flow

ISSN 0723-4864

Exp Fluids  
DOI 10.1007/  
s00348-011-1144-9

A21023 348 Research Journal

# Experiments in Fluids

37  
5

Experimental Methods and their Applications to Fluid Flow

 Springer

Volume 37 · Number 5 · November 2004

**Originals**

Choi Y-D, Nishino K, Kurokawa J, Matsui J:	PIV measurement of internal flow characteristics of very low specific speed semi-open impeller	617
Takamasa T, Hazuku T, Fukamachi N, Tamura N, Hibiki T, Ishii M:	Effect of gravity on axial development of bubbly flow at low liquid Reynolds number	631
Brunet P, Gauthier G, Limat L, Vallet D:	Structure and dynamics of a bidimensional pattern of liquid columns	645
Bertola V:	Drop impact on a hot surface: effect of a polymer additive	653
Gharbi D, Bertin H, Omari A:	Use of a gamma ray attenuation technique to study colloid deposition in porous media	665
Johnstone A, Uddin M, Pollard A, Heenan A, Finlay WIE:	The flow inside an idealised form of the human extra-thoracic airway	673
Holland KT, Green AW, Abelev A, Valent PJ:	Parameterization of the in-water motions of falling cylinders using high-speed video	690
Tariq A, Panigrahi PK, Muralidhar K:	Flow and heat transfer in the wake of a surface-mounted rib with a slit	701
Sumner D, Heseltine JL, Dansereau OJP:	Wake structure of a finite circular cylinder of small aspect ratio	720

(Continuation on cover page IV)

  
0723-4864(200411)37:5:1-B

Indexed in Current Contents

  
Online First  
Immediately Online  
springerlink.com  
Fast, free, and reliable

**Your article is protected by copyright and all rights are held exclusively by Springer-Verlag. This e-offprint is for personal use only and shall not be self-archived in electronic repositories. If you wish to self-archive your work, please use the accepted author's version for posting to your own website or your institution's repository. You may further deposit the accepted author's version on a funder's repository at a funder's request, provided it is not made publicly available until 12 months after publication.**

# Experimental time-resolved study of the interaction between a pulsating injectant and a steady cross-flow: aerodynamics of film cooling

Q. Sultan · G. Lalizel · M. Fénot · E. Dorignac

Received: 22 June 2010 / Revised: 8 June 2011 / Accepted: 8 June 2011  
© Springer-Verlag 2011

**Abstract** A test rig incorporating the injection from a single cylindrical hole with an inclination of  $30^\circ$  to a thermally uniform mainstream flow was used for determining variations in flow structures due to injectant pulsation. The average blowing ratios ( $\overline{M}$ ) were 0.65, 1, and 1.25. The periodic variations in injectant flow were rendered by a loudspeaker-based pulsation system to nondimensionalized excitation frequency ( $St$ ) of 0, 0.2, 0.3, and 0.5. Pulsation resulting in a close-wall orientation of injectant fluid compared with steady blowing bearing outward orientation was only observed in few cases. At  $\overline{M} = 0.65$ , jet fluid remains aligned and covers a significant part of the wall under steady blowing. At higher blowing ratios, pulsation induces large spatial variations in the jet trajectory, collapsing of the jet body, and the shedding of wake structures due to the periodic variation of injection flow rate. It was found that the pulsation improves wall coverage of the injectant fluid under low frequency excitation as the separation of the jet from the wall becomes evident ( $\overline{M} = 1$  and 1.25).

## Abbreviations

$\overline{M}$  Blowing ratio ( $=\rho_i u_i / \rho_\infty u_\infty$ )  
 $\rho$  Fluid density ( $\text{kg/m}^3$ )

$D$  Hole diameter (mm)  
 $St$  Strouhal number ( $=f \cdot D / \overline{U}_i$ )  
 $U$  Streamwise velocity (m/s)  
 $V$  Normal velocity (m/s)  
 $u$  Streamwise velocity fluctuation (m/s)  
 $v$  Normal velocity fluctuation (m/s)  
 $u_\tau$  Friction velocity (m/s)  
 $U^+$   $U$  normalized by friction velocity ( $=U/u_\tau$ )  
 $IT$  Turbulent intensity (%)  
 $\delta$  Boundary layer thickness (mm)  
 $\delta^*$  Displacement thickness (mm)  
 $\sqrt{\overline{u^2}}$  X-component of RMS velocity (m/s)  
 $\sqrt{\overline{v^2}}$  Y-component of RMS velocity (m/s)  
 $\overline{uv}$  Reynolds shear stress ( $\text{m/s}^2$ )  
 $t$  Time (s)  
 $T$  Period of pulsation (s)  
 $f$  Frequency (Cycles/s)  
 $\theta$  Phase (radian).  
 $\phi$  Phase shift (radian)  
 $\omega$  Angular frequency (radians/s)  
 $x, y$  Streamwise and normal coordinates (mm)  
 $y^+$  Normal coordinate in wall units ( $=y \cdot u_\tau / \nu$ )

## Subscripts/superscripts

$i$  Injectant  
 $\infty$  Free-stream  
 $rms$  Root mean square  
— Time-averaged  
 $\sim$  Periodic component  
 $a$  Amplitude  
 $h$  Nominal hole  
 $j$  Index number  
 $acq$  Acquisition  
 $s$  Excitation

Q. Sultan (✉) · G. Lalizel · M. Fénot · E. Dorignac  
Département Fluides, Thermique et Combustion,  
Axe COST, Institute Pprime, ENSMA-University  
of Poitiers-CNRS UPR 3346, 1, Avenue Clément ADER,  
BP 40109, 86961 Futuroscope Chasseneuil Cedex, France  
e-mail: qaiser.sultan@let.ensma.fr

E. Dorignac  
e-mail: eva.dorignac@ensma.fr

## 1 Introduction

The development of high efficiency gas turbine engine is essentially coupled with efficient wall cooling and lower consumption of compressor bleed air. The requirement of efficient film cooling ensuring extended wall coverage involves design innovation and delicate modification in existing systems including injection hole shape (Sargison et al. 2002), arrangement of rows (Sinha et al. 1991; Ligrani et al. 1992; Foucault et al. 1992), optimal blowing and momentum ratios of injectant and free-stream flow (Eckert 1970; Goldstein and Eckert 1974; Yuen and Martinez-Botas 2003), injection hole position (Goldstein and Eckert 1974; Eriksen and Goldstein 1974), and characteristics of both free-stream (Marek and Tacina 1975; Burd et al. 1996) and injectant flow at the hole exit (Burd et al. 1996; Brundage et al. 1999). Physical interpretations of formation of the complex vortex system due to interaction of a jet and a cross-stream flow were addressed in the studies of Moussa et al. (1977), Andreopoulos (1983, 1985), and Kelso et al. (1996). Figure 1 shows a system of potential vortices in cross-flow as proposed by Kelso et al. (1996). Andreopoulos (1985) investigated turbulence processes subjected to extra rates of strain resulting from streamwise curvature, lateral divergence and longitudinal accelerations, and the formation of a dominant vortical structure, widely known as Counter-Rotating Vortex Pair “CVP”. Kelso et al. (1996) gave a topological description of the flow field and highlighted the role of the principle vortex system “CVP” for jet in cross-flow. They elaborated on the influence of vorticity originating from the pipe flow and initial rolling and folding of the shear layer contributing to the formation of the CVP along with the notions of downstream shedding as a function of Reynolds number ( $Re = U_\infty \cdot D/\nu$ ). In the downstream region, Moussa et al. (1977) observed a similarity in the shedding characteristics of a rigid cylinder and the obstruction caused by the

leading surface of the jet at similar cross-sections. The relative significance of turbulent process in a cross-flow configuration with flows submitting different velocity ratios was reported by Andreopoulos (1983) in the case of a slightly heated jet. He showed that the flow conditions with a low velocity ratio indicate an immediate mixing between the two fluids, as the pressure distribution around the exit hole imposed by the cross-stream causes the pipe flow to decelerate at the upwind side and accelerate at the downwind side of the hole.

The flow field aerodynamics due to the interaction of the two flow streams with oblique injection was studied in Foucault et al. (1992), Pietrzyk et al. (1989), Dorignac et al. (1992, 1993), Lee et al. (1994), and Walters and Leyelek (2000). Pietrzyk et al. (1989) used a short delivery tube ( $L/D = 3.5$ ) for injectant flow and explained the evolution of downstream flow along with the skewing of jet exit profile, which settles toward the downstream side at low blowing ratio and moves toward the upstream side at high blowing ratio. Foucault et al. (1992) described the existence of the CVP for a  $45^\circ$  inclined jet and its influence on both velocity and temperature fields. Dorignac et al. (1992) studied the injectant flow dynamics downstream of a row of holes as a function of blowing ratio for a slightly heated jet flow. Lee et al. (1994) studied both normal and inclined jet cases and reported the disappearance of reverse flow, lesser cross-flow entrainment, and stronger secondary motion due to larger pressure gradient in wake region in the case of an inclined jet, compared with a normal jet. The computational results of Walters and Leyelek (2000) traced back to the origin of vorticity leading to the CVP for an inclined jet. They also reported the appearance of small reverse flow zones immediately downstream of the trailing edge for a blowing ratio of 1 and a density ratio of 2.

Film cooling behavior under periodic excitation is a fairly recent issue. Studies based on the idea of static pressure pulsation in the tunnel were employed by Ligrani et al. (1996a, b, 1997) and Seo et al. (1998) to mimic the unsteadiness of actual turbine flow. They mentioned that the periodic variations of static pressure and streamwise velocity in the bulk flow caused the film concentrations and film trajectories to move toward and from the wall, due to the instantaneous changes in both flow rate and momentum at the coolant hole exit. Ligrani et al. (1996a) identified different regimes of film cooling behavior as a function of Strouhal number excitation, referring to them as “quasi-steady”, “non-quasi-steady”, and “non-quasi-steady with reversing flow”. Bons et al. (1996) pulsed the injectant flow by using a loudspeaker with modulation frequencies being close to those typically encountered in gas turbine engine. They concluded that the periodic forcing of the film cooling flow results in reduction in the film cooling effectiveness (70% at  $M = 0.6$ ). The reduction in the film

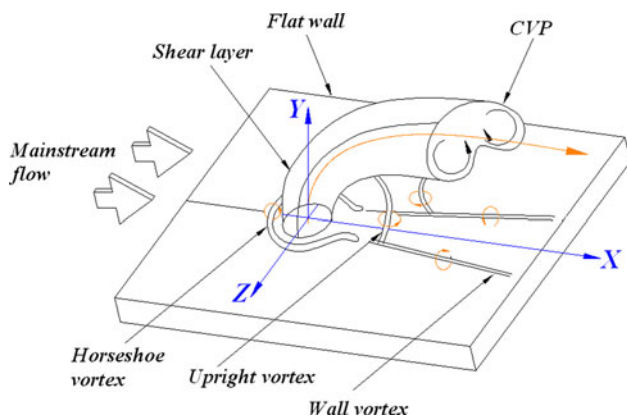


**Fig. 1** Vortices in cross-flow

effectiveness was reported to become progressively smaller as the blowing ratio increased, i.e., 65% at  $M = 0.7$  and 60% at  $M = 0.8$ . Rutledge et al. (2009) studied the response of square wave and saw-tooth wave forms for the jet pulsation in a CFD analysis of a turbine blade leading edge film cooling. It was shown that the saw-tooth wave input has helped in alleviating the part of initial start-up of the film cooling, causing jet lift-off from the wall for pulsation between  $M = 1$  and 0 using square wave input. They mentioned that at low frequency pulsing ( $St = f \times D/U_\infty < 0.8$ ), the film cooling had performance similar to the time-weighted average performance of the steady jet. For the blowing ratio of  $\bar{M} = 0.5$  and 0.25, they reported a deterioration in film cooling performance when pulsing frequency was increased from  $St = 0.755$ – $3.04$ . The trend reversed when the pulsing frequency was raised to  $St = 6.04$  for the case of  $\bar{M} = 0.5$ , but remained inferior to the performance of steady  $\bar{M} = 0.5$  jet. Direct Numerical Simulation “DNS” conducted by Muldoon and Acharya (2009) has shown some improvement in wall coverage with pulsation ( $M = 1.5$ ,  $St = 0.32$ , Duty-Cycle = 50%) compared with steady blowing of the jet using a single cylindrical hole and  $30^\circ$  injection. The computational results of Kartuzova et al. (2009) also indicated an improvement in wall protection as a function of blowing ratio for a cylindrical hole injection. They mentioned that the overall higher injectant film concentration with jet pulsation is only achievable at blowing ratios triggering jet lift-off, such as  $M = 1.5$ . Cooling efficiency at  $St = 0.38$  was higher than for  $St = 1.0$  and for the steady blowing case.

A review of the available literature has shown that the film cooling effectiveness is mainly dependent on the upstream conditions constituting the blowing and momentum ratio of interacting flows and the Strouhal number frequency of pulsation. In order to understand more about the act of pulsation in a complex situation of cross-flow, an experimental investigation of the aerodynamic aspects of the flow incorporating a pulsating jet was undertaken. The flow structure variation at the hole exit and the downstream distribution of injectant over a range of Strouhal numbers excitation are presented and briefly discussed from the perspective of cross-flow interaction and film cooling. These objectives were met by using a time-resolved PIV system for a range of blowing ratios and Strouhal numbers on the central plan of the tunnel

( $z/D = 0$ ). However, a large number of experiments were previously conducted on separate occasions to figure out characteristic of wind tunnel flow by using a 1D-LDV system and also by a hot-wire system to study the jet for suitable pulsating conditions.

## 2 Experimental setup

The film cooling experiment was performed in a low speed, closed-loop thermoregulatory wind tunnel system. The test section is comprised of a  $300 \times 300 \text{ mm}^2$  cross-section extending up to a distance of 1,190 mm in the streamwise direction. The mainstream flow velocities were set either to 10 or to 7.7 m/s as required to attain the average blowing ratio ( $\bar{M}$ ). The injection plate consists of a cylindrical hole having a diameter,  $D$ , of 13 mm and an undisturbed length,  $L$ , of  $7.7D$ . The hole is drilled at an angle of  $30^\circ$  with respect to streamwise direction. The study is performed at blowing ratios of  $\bar{M} = 0.65, 1, \text{ and } 1.25$  along with Strouhal numbers of  $St = 0, 0.2, 0.3, \text{ and } 0.5$ . The ratio of injectant to mainstream density ( $\rho_i/\rho_\infty$ ) was always set to unity. The boundary layer thickness ( $\delta/D$ ) at the center of hole exit plane ( $x/D = 0$ ) for the mean free-stream velocity of 10 and 7.7 m/s are 1.0 and 0.93, the displacement thickness ( $\delta^*/D$ ) are 0.146 and 0.11 and the free-stream turbulent intensity ( $IT_\infty$ ) are 1.2 and 1%, respectively. Details of measuring conditions are summarized in Table 1. The use of a short injection tube and higher density ratio is more practical (engine representative) for the study of turbine blades film cooling. The choice of these parameters is based on the characteristics of existing hardware, which seems to have a marginal deviation from the conventional film cooling case. However, numerous studies covering a range of parameters related to both flow dynamics and the geometry of test hardware (including the present ones) are extensively analyzed and published in the open literature for steady blowing. Seo et al. (1998) used a range of length-to-diameter ratios ( $L/D = 1.6, 4, \text{ and } 10$ ) to investigate the effects of bulk flow pulsation in film cooling for a density ratio of 0.93. The effects of density ratio on the wall coverage caused by a refrigerant film were analyzed by Goldstein and Eckert (1974) for a density ratio as high as  $\rho_i/\rho_\infty \approx 3.5$ . Sinha et al. (1991) studied film cooling under the diverse injection pattern and two cases of density ratio ( $\rho_i/\rho_\infty = 1 \text{ and } 2$ ), where the temperature of

**Table 1** Test conditions

$\bar{U}_\infty$ (m/s)	$Re = \bar{U}_\infty \cdot \delta/\nu$	$Re = \bar{U}_i \cdot D/\nu$		$\bar{M} = \rho_i \bar{U}_i / \rho_\infty \bar{U}_\infty$		$St = f \cdot D / \bar{U}_i$
10	8,609	5,596	8,437	0.65	1	0, 0.2, 0.3, 0.5
7.7	6,165	8,220		1.25		0, 0.2, 0.3, 0.5

air in injection plenum chamber was maintained to 150 K for higher density ratio. In the underlying approach focused on analyzing the effects of injectant flow pulsation in a cross-flow configuration, situation is greatly simplifies as the density of interacting flows remains the same. Higher boundary layer thickness ( $\delta/D > 1$ ) of oncoming mainstream flow allows the jet to penetrate more in the mainstream and results in a quick diffusion of the turbulence of injectant fluid. With boundary layer thickness nearly equal to the diameter of injection hole, test condition pertaining to the interaction of a pulsed jet and a mainstream flow appears fairly attractive and expected to have important consequences on the formation of coherent structures and their impact on the downstream flow field. For the range of frequencies used for injectant pulsation, an amplitude giving approximately a constant ratio of streamwise rms velocity and average hole velocity was chosen for all cases.

The flow field characteristics over the flat injection wall of the wind tunnel test section were initially investigated in both the streamwise and cross-streamwise directions by a DANTEC 1-D-Laser Doppler Anemometer 'LDA' in the absence of injectant flow. The profiles of streamwise mean and rms velocity components normalized by friction velocity ( $U^+, u_{rms}^+$ ) are presented in Fig. 2. The velocity profiles obtained from the upstream side of the injection hole ( $x/D = -1.5$ ) and different lateral positions at ( $z/D = -6, -3, 0, 3, 6$ ) show that the flow is laterally uniform and is in good agreement with the DNS results of Kim et al. (1987) accounting for a turbulent channel flow. The statistical uncertainty estimates for these measurements are determined by using the estimators of Benedict and Gould (1996) derived for the random process. The statistical errors in the mean and rms values of streamwise component of velocity for a confidence interval of 95% are estimated from (1) and (2). N is the number of independent samples. The measurements of LDV contain 0.15 and 0.6% error in mean and rms velocities ( $\bar{U}$  and  $\sqrt{u^2}$ ) measured in

the near wall region and 0.05 and 0.8% error in respective velocities for the region lying outside the boundary layer, the number of statistical samples for each location were ( $N \approx 50,000$ ).

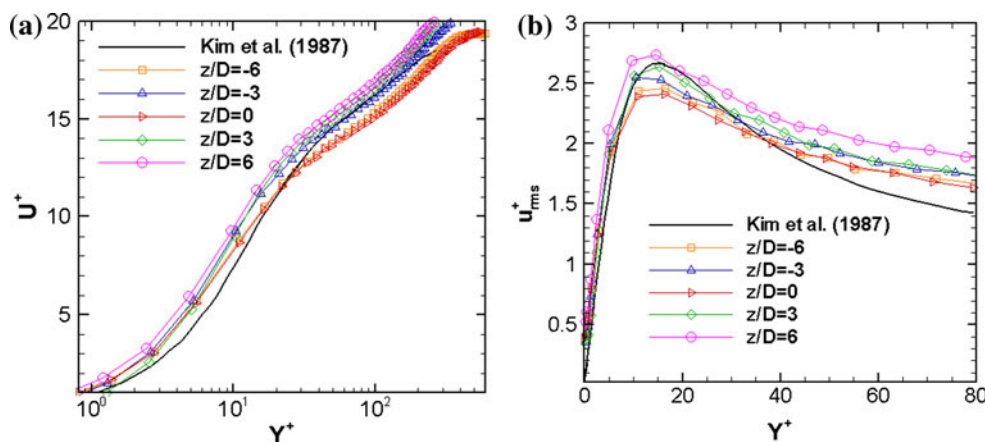
$$U\{\bar{U}\} = 1.96 \times \left[ \frac{\overline{u^2}}{N} \right]^{0.5} \tag{1}$$

$$U\{\sqrt{u^2}\} = 1.96 \times \left[ \frac{\left\{ \overline{u^4} - (\overline{u^2})^2 \right\}}{4N\overline{u^2}} \right]^{0.5} \tag{2}$$

A constant mass flow rate for the injecting air is ensured by using a calibrated orifice tube at sonic conditions. The absolute upstream pressure of orifice tube is measured by a Druck pressure transducer and sampled by an Agilent data acquisition system. A desktop computer containing the calibration data delivers the injection flow rate through a LabVIEW program. Calibration is performed by using a separate panel mounted rotameter. The injectant air is pulsed by a 130-mm diameter loudspeaker, which is operated by an ITT Instruments-GX240 signal generator in order to generate sinusoidal pulses at required frequencies,  $f_s$ , and a JB SYSTEMS-VX400 stereo amplifier to raise the output signals. Air is injected near the diaphragm of the loudspeaker by three symmetrically located ports of the loudspeaker enclosure. Figure 3 shows a schematic diagram of the injection system.

The experiments are performed with a time-resolved PIV system. The test section walls of the wind tunnel consist of a thin glass sheet of 5 mm thickness to obtain better illumination of the working region. The main stream flow is seeded by a Puffer-6 (Silver Series) smoke generator, while the injectant flow is seeded by grape-seed oil with a particle size of a few microns. The TR-PIV system is comprised of a LaVISION (High Speed Star) camera with a 10-bit C-MOS imaging sensor, maximum resolution of  $1,024 \times 1,024$  pixels<sup>2</sup> (up to 3,000 fps). The flow domain is illuminated by NewWave Pégasus, double-pulsed Nd:YAG Laser ( $\lambda = 527$  nm,  $E = 2 \times 10$  mJ at

**Fig. 2** Comparison of (a) mean and (b) RMS velocities normalized with friction velocity, 'lines with symbol' present study (LDV), 'straight line' Kim et al. (1987)



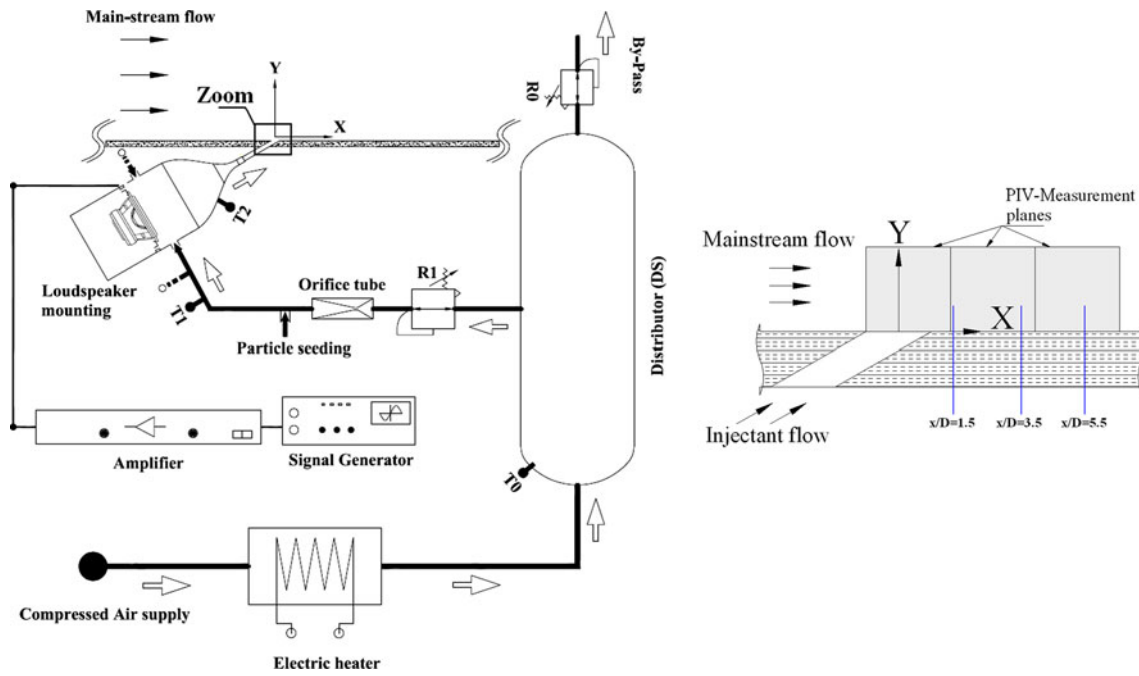


**Fig. 3** Schematic diagram of the flow injection system and the zones of TR-PIV measurement

1 kHz,  $f = 1\text{--}10,000$  Hz). A LaVISION high-speed controller mediates the system for initial data recording in the camera memory and subsequent transfer to a desktop computer. The results are presented for a study domain consisting of three  $1,024 \times 1,024$  pixels<sup>2</sup> consecutive planes with an on-field dimension of  $33.7 \times 33.7$  mm<sup>2</sup> for each plane. The vector calculation for the instantaneous velocity field was performed by a LaVISION software package, using the cross-correlation scheme with an ultimate size of interrogation window of  $12 \times 12$  pixels<sup>2</sup> along with 50% overlapping, which gives a  $171 \times 171$  vector domain for each measurement plane.

The PIV data acquisition frequencies,  $f_{acq}$ , for the particle image were set in a way that it is always equal to an exact integral multiple of flow excitation frequency  $f_s$  (i.e.,  $f_{acq} = n \times f_s$ , where  $n \geq 1$ ). The maximum data acquisition frequency  $f_{acq}$  of the system is restrained by the specified level of PIV spatial resolution. Under this constraint, a maximum possible acquisition frequency being the exact integral multiple of excitation frequency was chosen and used to determine the number of time instants in a period of excitation. For the range of forcing frequency considered, the number of time instants,  $n$ , locked in a period varies from 4 to 10 instants/period. The measured velocity field can be decomposed in the following way (Ligrani et al. 1996b);

$$U(t) = \bar{U} + \tilde{U}(t) + u(t) \quad (3)$$

where  $U(t)$  is the evolution of instantaneous velocity in time,  $\bar{U}$  is the time average component of velocity, and  $\tilde{U}$  is the periodic component of velocity;  $\tilde{U}(t) = U_a \cdot \cos(\omega t +$

$\phi)$  and  $u(t)$  is the fluctuating component of velocity. The results for flow field parameters are shown with time  $t_j$ , for which the equivalent phase value can be written as  $\theta_j = 2\pi \cdot (t_j)/T$ . In order to make the velocity field in (3) independent of the periodic term, the data classification in time was performed with a time interval equivalent to the period of data acquisition frequency. This reduces the result into mean and fluctuating components of velocity locked at  $n$  time or phase instants in the period of excitation,

$$U(t_{i,j}) = \bar{U} + u(t_{i,j}); \quad 1 \leq j \leq n \quad \text{and} \quad (4)$$

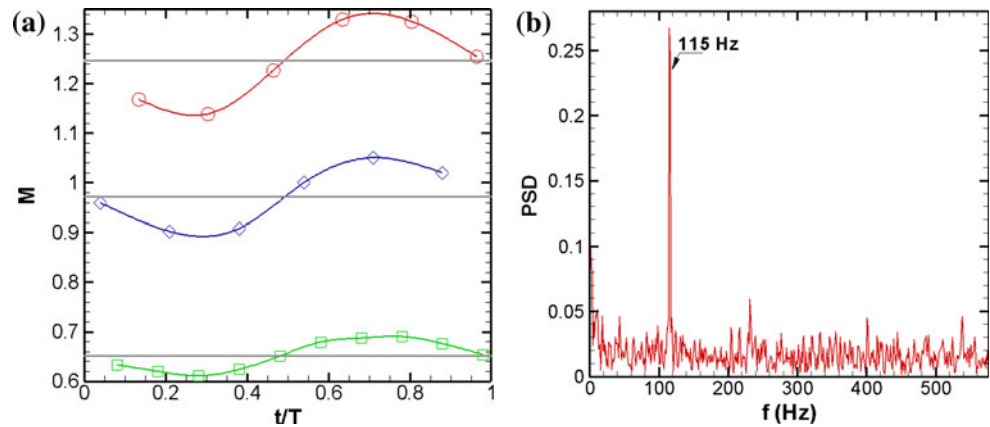
$$i = j + (k \cdot f_{acq})/f_s; \quad k \in \mathbb{N}_0$$

The application of ensemble averaging over index  $i$  of  $U(t_{i,j})$  provides the averaged phase or time instant quantities at each index of  $j$ . The grouping of phase averaged results along a single index reduces to

$$\bar{U}(t_j) = \bar{U} + \tilde{U}(t_j) \quad (5)$$

The study of film cooling behavior with injectant flow pulsation was performed by setting different forcing frequencies  $f_s$  and amplitudes  $U_a$  from preestablished pulse conditions, which were obtained from a hot-wire survey using a TSI IFA-300 constant temperature hot-wire anemometer containing a platinum sensor of  $5 \mu\text{m}$  diameter and  $1.2$  mm length. The measurements at the hole exit plane allow determining the optimum working range of the loudspeaker for a given range of excitation frequency, considering the limitations of maximum

**Fig. 4** **(a)** Periodic variation of average blowing ratio,  $\bar{M} = 0.65, 1$  and  $1.25$  at  $St = 0.3$ , **(b)** frequency response determined at the hole exit from TR-PIV measurement for a case with  $\bar{M} = 0.65$  and  $St = 0.3$  (115 Hz)



excursion capacity of loudspeaker diaphragm at high frequencies and the comfortably reproducible pulses at low frequencies as per the manufacturer’s specifications. The statistical error associated with high resolution temporal measurement using a hot-wire is 0.1 and 0.4% for  $\bar{U}$  and  $\sqrt{u^2}$ . A large number of samples ( $N \approx 131,000$ ) were taken to ensure the statistical convergence, and a high data rate ( $\approx 40,000$  Hz) for achieving highly time-resolved phase-averaged velocity results after the posttreatment.

The average blowing ratios,  $\bar{M}$ , for the pulsation case at  $St = 0.3$  are shown in Fig. 4a for  $\bar{M} = 0.65, 1$ , and  $1.25$ . The temporal variations are estimated by performing the integral-averaging of the velocity profile extracted from phase-locked results at the hole exit. The velocity amplitude,  $U_a$ , of periodic signal  $\tilde{U} = U_a \cdot \cos(\omega t + \phi)$  can be expressed under a nondimensionalized form  $U_a/U_h$ . This ratio is approximately constant at 8%. Here,  $U_h$  is the nominal velocity of hole flow. It is determined by performing velocity measurement by PIV on various lateral planes at the hole exit and then performing the velocity integration on the exit plane, which appears as an elliptical surface for inclined injection. These measurements enable us to fine tune the pressure regulator lying on the upstream side of the injection flow delivery system for required nominal velocity of the jet at the hole exit.

An example of applied excitation through a 1-D spectrum calculated from the results of TR-PIV for  $\bar{M} = 0.65$  at  $St = 0.3$  (115 Hz) is shown in Fig. 4b. It was observed that the presence of intermediate components in the delivery line, such as a honeycomb structure, a convergent section, and the tube, do not modify the excitation frequency at the hole exit.

For the measurements of TR-PIV, the level of statistical variation in the rms value of streamwise and normal components of velocity fluctuations  $\sqrt{u^2}$ ,  $\sqrt{v^2}$  and their correlation giving a component of Reynolds stress  $\overline{uv}$  are estimated by using (2) and (6). The uncertainty calculations

are based on the set of formulae proposed for a general distribution of measured flow variables, which basically suggests that the author’s method is capable of taking into account any deviation from the normal distribution (Benedict and Gould 1996).

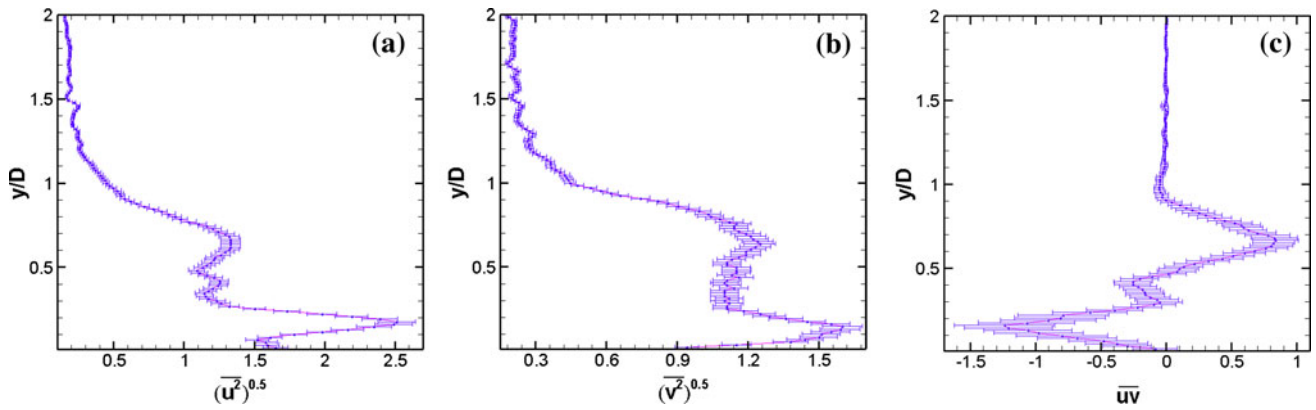
$$\cup\{\overline{uv}\} = 1.96 \times \left[ \left\{ \overline{u^2v^2} - (\overline{uv})^2 \right\} / N \right]^{0.5} \quad (6)$$

Figure 5 shows the level of uncertainties for an average blowing ratio of 1.25 by a profile locating at  $x/D = 1.5$ . The maximum deviations from the respective value of the profile ( $\sqrt{u^2}$ ,  $\sqrt{v^2}$ , and  $\overline{uv}$ ) with a confidence interval of 95% are  $\pm 5$ ,  $\pm 5$ , and  $\pm 23\%$ , respectively.

### 3 Results

#### 3.1 Velocity profile at the hole exit

The profiles of the resultant of mean velocity components  $\sqrt{(\bar{U}^2 + \bar{V}^2)}$  measured nearest the hole exit plane under steady blowing are presented in Fig. 6 after normalization by the nominal hole velocity,  $U_h$ . Measurement conditions include the flow from the injection hole only and the flow from both mainstream and injection hole at velocities, which correspond to the blowing ratio of  $\bar{M} = 0.65$  and  $1$ . A comparison with Seo et al. (1998) is presented to show the change in the form of velocity profiles at the hole exit. The reference case used a hole length to diameter ratio of 10 and an injection angle of  $35^\circ$  comparing to  $7.7$  and  $30^\circ$  in the present case. The velocity profiles measured along the central plane and near the hole exit ( $y \approx 0.8$  mm) show an increase in jet velocity, which is larger than the velocity at respective blowing ratio maintained at the hole exit. This is also reported by Pietrzyk et al. (1989) in film cooling measurement. The increase in velocity is because of the diversion of jet fluid toward the downstream by the



**Fig. 5** Uncertainty estimates of rms value of velocity fluctuations and their correlation,  $\bar{M} = 1.25$  and  $x/D = 1.5$ , (a)  $\sqrt{u'^2}$ , (b)  $\sqrt{v'^2}$  and (c)  $\overline{uv}$

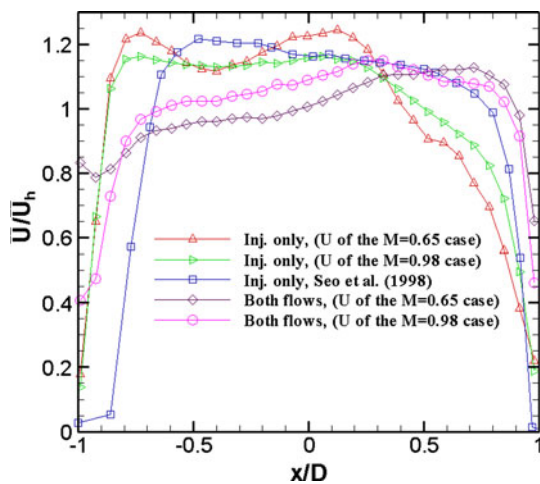


**Fig. 6** The profiles of resultant of mean velocity components  $\sqrt{\overline{U^2 + V^2}}$  at hole exit normalized with hole nominal velocity for cases with both flows and the cases without free-stream flow (injection only), where the jet velocity corresponds to the cases of  $\bar{M} = 0.65$  and 1

mainstream flow. The resulting rate of strain and bending cause some acceleration of jet fluid. In the absence of mainstream flow, the maximum in velocity profile appears on the upstream side, which is skewed to the downstream side for the two flow cases. The profile skewness is relatively high for  $M = 0.65$ , which is pushed slightly back upstream as the blowing ratio rises to 1 (Pietrzyk et al. 1989; Walters and Leylek 2000; Yuen and Martinez-Botas 2003). One of the reasons for such variation as mentioned in many references is the use of sharp entrance at the tube inlet, which results in flow separation inside the tube. Separation effects become more severe at higher tube velocities. Walters and Leylek (2000) explained the role of streamwise vorticity appearing on the lateral edges of the hole and vertical momentum of the jet in specifying the orientation of counter-rotating vortex pair along with

the shape of velocity profile at the hole exit. In present case, the injection tube has a length of  $7.7D$  and is connected with standard fitting on the upstream side, which possess some variation in the flow cross-sectional area and lacks cleanness at the joint interface. This may result in an increase of vorticity ejecting from the hole at higher injection flow rate. High vertical momentum and strong streamwise vortices originating from the hole shifts the maximum in jet velocity at the hole exit plane to the upstream side. At low blowing ratio, the resulting pressure distribution is attributed by the formation of a high pressure region on the leading side and low pressure region on the trailing side of the jet, which causes profile skewness toward the downstream side.

### 3.2 No pulsation

Figure 7a–c shows the variation in mean streamwise velocity fields at different blowing ratios in a steady/continuous blowing condition ( $St = 0$ ). The distribution of injectant in the near wall region is superior in the case of  $\bar{M} = 0.65$  as injectant penetrates less into the free-stream than for  $\bar{M} = 1$  and 1.25. The act of higher jet penetration due to large momentum ratio was referred to “Jetting” in many studies (Burd et al. 1996; Walters and Leylek 2000). The flow between the bottom side of the jet and the wall is linked with a number of complex activities, including the presence of a low pressure region as a result of the initial blockage offered by the leading surface of the jet and the subsequent ingestion of mainstream flow interacting with the wake and wall vortices. The mean flow field provided here can be considered as benchmark results to compare against the ones with pulsation.

A comparison with hot-wire results presented by Ligrani et al. (1996b) for streamwise velocity profile  $\overline{U}/\overline{U_\infty}$  and the profile of Reynolds shear stress component  $-2 \cdot \overline{uv}/\overline{U_\infty^2}$  are

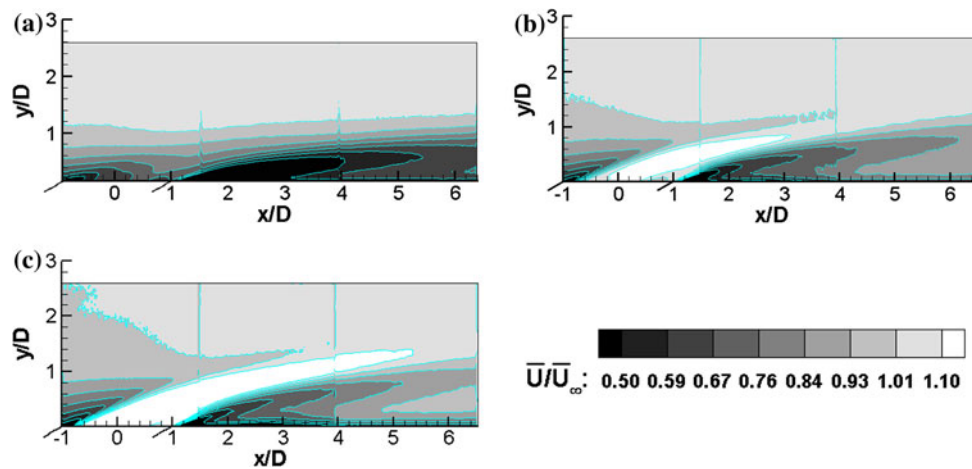


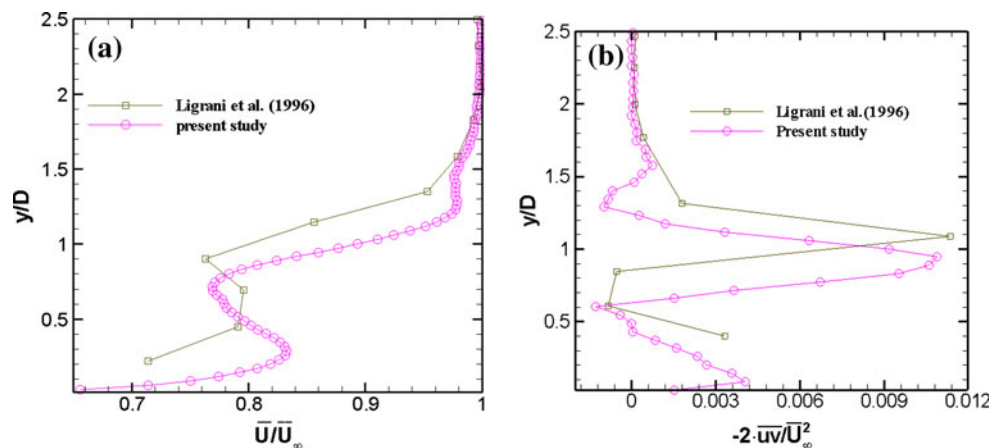
**Fig. 7** Velocity field  $\bar{U}/\bar{U}_\infty$  without pulsation, (a)  $\bar{M} = 0.65$ , (b)  $\bar{M} = 1$ , (c)  $\bar{M} = 1.25$

shown in Fig. 8a and b. The comparison is made for steady blowing with  $\bar{M} = 1$  and at a downstream location of  $x/D = 5.5$ . The slight shift in these profiles is because of higher injection angle and injection Reynolds number,  $35^\circ$  and 15,000, in the reference case and  $30^\circ$  and 8,437 in the present study.

The flow characteristics as a function of average blowing ratio  $\bar{M}$  with steady blowing are shown for streamwise velocity and Reynolds shear stresses profiles at different streamwise positions  $x/D = 1.5, 3.5$ , and  $5.5$  in Fig. 9. At  $\bar{M} = 0.65$ , Fig. 9a shows that the injectant flow at  $x/D = 1.5$  remains completely attached to the wall and the velocity profile appears similar to one of a turbulent boundary layer. At the downstream positions, the jet lifts off slightly from the wall and the shear layer due to the interaction of the high-speed free-stream and relatively low-speed injectant flow becomes evident. For the case with  $\bar{M} = 1$ , Fig. 9b shows higher penetration of the jet in the mainstream flow. The near downstream profile shows an increment of injectant flow velocity slightly above the wall in the core region of the jet. In the downstream, jet trajectory follows a continuous lift-off with  $x/D$ , and at

$x/D = 5.5$ , the higher velocity zone of the profile vanishes completely. In Fig. 9c, eminent lifting-off of the jet body is quite obvious due to the higher vertical momentum of the jet,  $\bar{M} = 1.25$ . Higher penetration of the jet causes greater ingestion of mainstream flow into the low pressure field. Figure 9d shows that for  $\bar{M} = 0.65$ , the shear stress correlation is relatively high in the vicinity of the wall for a near downstream profile at  $x/D = 1.5$ , compared with  $x/D = 3.5$  and  $5.5$  where the jet tends to curved away from the wall. On the downstream, the jet attains the position of maximum shearing stress at a vertical distance, which is slightly higher compared with the respective  $\bar{U}/\bar{U}_\infty$  profiles. This is consistent with the other two cases,  $\bar{M} = 1$  and  $1.25$ , and indicating the interface between jet and free-stream flows. The maximum positive shear stress values for  $x/D = 3.5$  and  $5.5$  are 0.012 and 0.013 at  $y/D = 0.63$  and 0.85, respectively. The effects of shear stresses are negligible after  $y/D = 1.35$ . At  $\bar{M} = 1$ , Fig. 9e shows that the higher jet momentum causes the low velocity region between the jet and the wall to become large for  $x/D = 1.5$  and have the highest positive shear stress 0.032, at

**Fig. 8** Profile comparison for steady blowing at  $\bar{M} = 1$ ,  $x/D = 5.5$ , (a) Streamwise velocity, (b) Reynolds shear stress



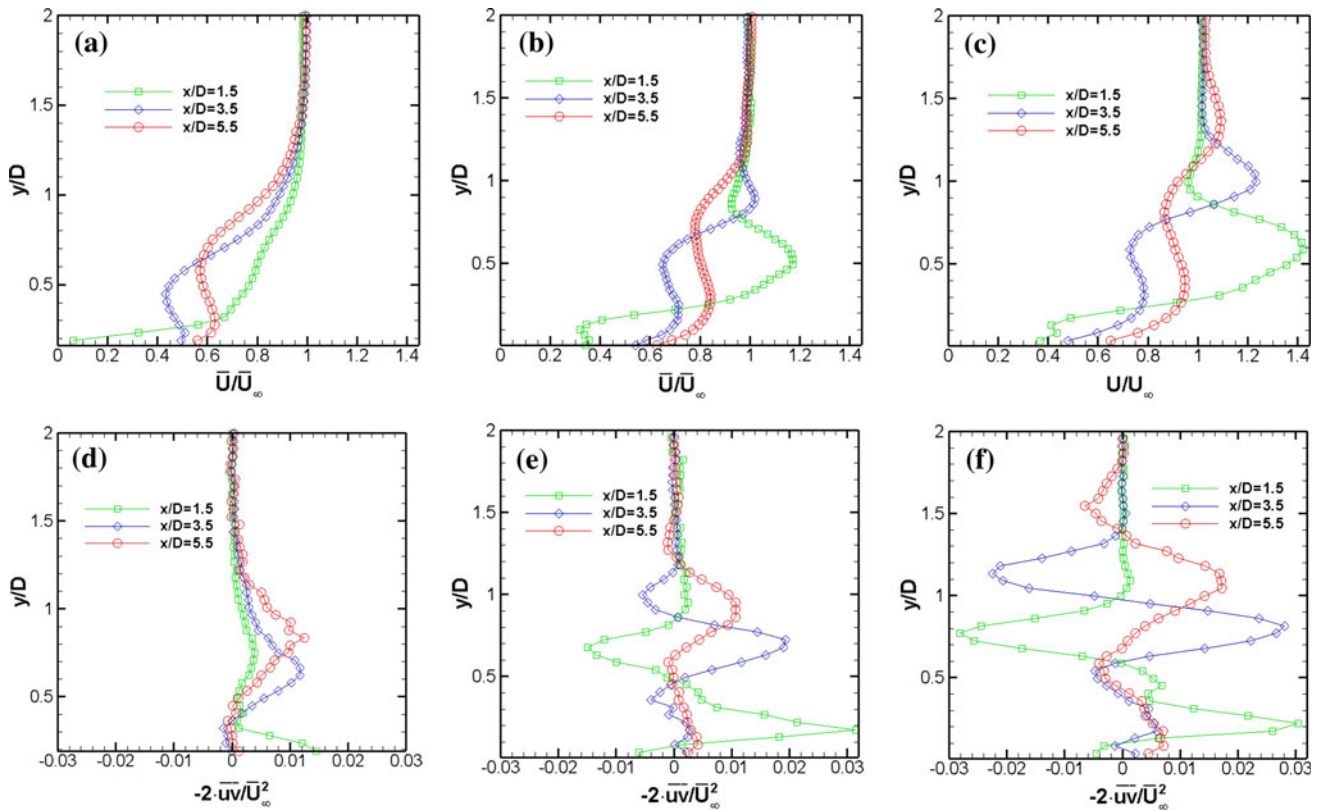


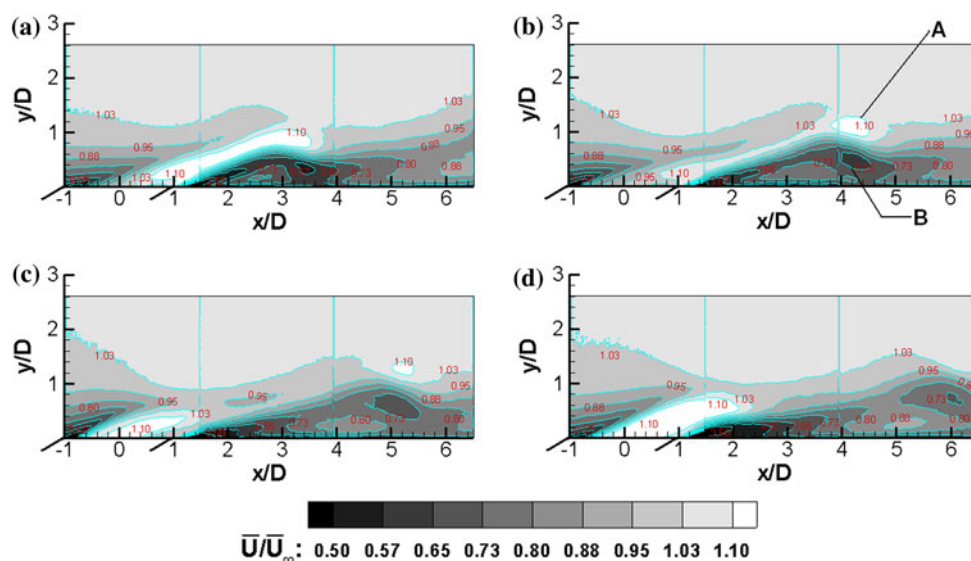
**Fig. 9** Velocity and shear stress profiles with steady blowing at  $x/D = 1.5, 3.5,$  and  $5.5,$  (a)  $\bar{M} = 0.65, \bar{U}/\bar{U}_\infty,$  (b)  $\bar{M} = 1, \bar{U}/\bar{U}_\infty,$  (c)  $\bar{M} = 1.25, \bar{U}/\bar{U}_\infty,$  (d)  $\bar{M} = 0.65, -2\bar{u}\bar{v}/\bar{U}_\infty^2,$  (e)  $\bar{M} = 1, -2\bar{u}\bar{v}/\bar{U}_\infty^2,$  (f)  $\bar{M} = 1.25, -2\bar{u}\bar{v}/\bar{U}_\infty^2$

$y/D = 0.18$ . The shear stress becomes zero in the core and again obtains a maximum negative value of  $-0.015$  in the upper jet boundary ( $y/D = 0.68$ ). For other downstream profiles, at  $\bar{M} = 1$ , the shear stress is lower owing to the loss of momentum of the jet fluid. The location of maximum shear stress on bottom side is shifted to  $y/D = 0.71$  and  $0.91$ , respectively. The flow field sees almost negligible shearing effect beyond  $y/D = 1.5$  on the upper boundary. At  $\bar{M} = 1.25$ , Fig. 9f shows that the higher vertical momentum of the jet further widens the low velocity zone underneath the jet due to increasing lift-off. At this situation, the velocity profile at the hole exit, which is normally skewed toward the downstream edge due to the flow pressure distribution effects at low blowing ratio is pushed toward the upstream edge due to increased influence of injection tube vortices (Walters and Leylek 2000), see Fig. 6. This causes an increment in maximum negative value of shear stress at the upper side to  $-0.029$  at  $y/D = 0.76$  for near downstream profile at  $x/D = 1.5$  and subsequently for other profiles at  $x/D = 3.5$  and  $5.5$  to  $-0.023$  and  $-0.0064$  at  $y/D = 1.15$  and  $1.55$ , respectively. The effects of shear stress are insignificant after  $y/D = 1.9$ . At a higher blowing ratio, the upper side of the jet is expected to be a zone where the upstream boundary layer

vortices of the mainstream flow interact with vorticity ejecting from the hole and later form some coherent counter-rotating entity due to the rolling up of the shear layer and the tilting of the jet in streamwise direction. On the lower side of the jet, the uplifting of the jet, entrainment of mainstream flow and wake activity cause an increase in the mixing of two flows locally (Kelso et al. 1996; Walters and Leylek 2000).

### 3.3 With pulsation

The application of injectant flow pulsation in a film cooled turbulent boundary layer seems to bear some important consequences, compared with the normal behavior with continuous blowing. Figure 10a–d shows a general mechanism of flow modification through the distribution of streamwise velocity  $\bar{U}/\bar{U}_\infty$  for  $\bar{M} = 1$  and  $St = 0.2$  over different times of a pulsating cycle. It is evident from the first image at time  $t/T = 0.19$  that the jet flow tends to lift significantly from the wall due to initial acceleration and bears a flow field underneath of relatively low speed; the region is referred to as the wake region. The periodic pulsation at  $t/T = 0.41$  causes splitting of the jet body at a streamwise distance of  $x/D = 3.85$  (zone labeled as ‘A’ in



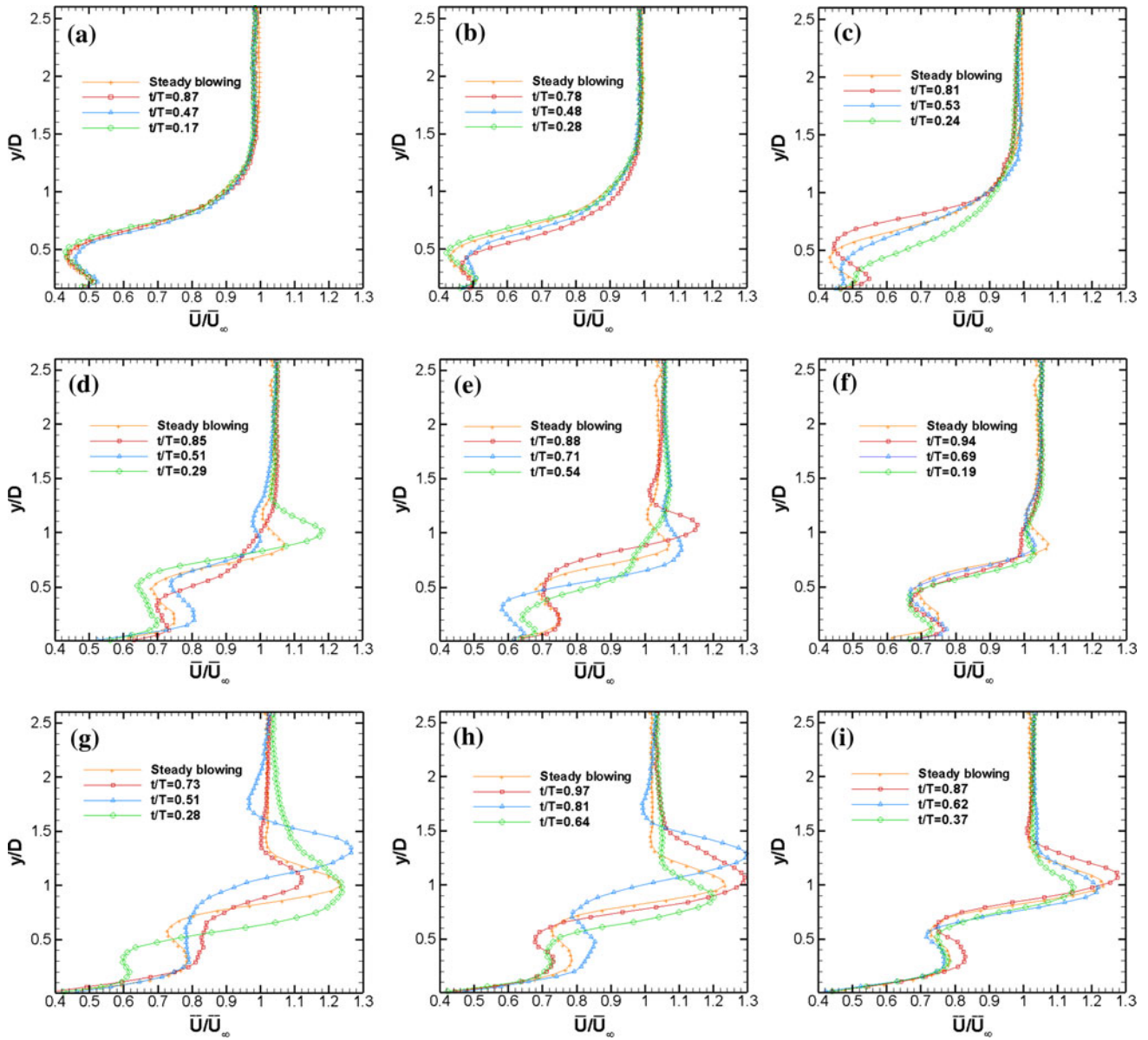
**Fig. 10** Velocity distribution  $\overline{U}/\overline{U}_\infty$ ,  $\overline{M} = 1$ ,  $St = 0.2$ ; (a)  $t/T = 0.19$ , (b)  $t/T = 0.41$ , (c)  $t/T = 0.63$ , and (d)  $t/T = 0.86$

Fig. 10b), which is followed by widening of the wake region under jet inertia (zone labeled as ‘B’ in Fig. 10b). At this instant, the main stream flow also appears to ingest a bit inside the hole. At  $t/T = 0.63$ , the injectant flow re-originate from the hole but remains covered by the mainstream flow. The near wall flow in the downstream region exhibits the shedding of vortices in wake region. The downstream movement of these structures is coupled with subsequent growth and velocity changes. At  $t/T = 0.86$ , the acceleration of injectant flow approaches to a point of maximum blowing, along with the consistent development of the flow in the wake region. The injectant flow trajectory under these effects moves toward and away from the wall under pulsating effects, which promises to improve the relative concentration of injectant compared with that of steady blowing.

The flow field variations due to imposed injectant flow pulsation for the whole range of experimental conditions are shown through the profiles of streamwise component of velocity locating at  $x/D = 3.5$ , Fig. 11a–i. The times shown in figures were determined from the phase orientation observed 2 mm above the hole exit. The phase orientation of the number of point locked in a period changes with the spatial location. However, the pattern of temporal variation of the flow remains periodic all over. It is also reminded that the number of average time instants is not constant for all  $\overline{M}$  and  $St$  studied. For  $\overline{M} = 0.65$ , the profiles of  $\overline{U}/\overline{U}_\infty$  are shown in Fig. 11a–c for  $St = 0.2, 0.3$  and  $0.5$ , respectively. It can be observed that the pulsation causes periodic variations in jet trajectory, and profiles of phase-averaged velocity seem to lie above and below the steady blowing case. Also, the zone of cross-wise variation extends considerably with the increment of  $St$  for  $\overline{M} = 0.65$ . It should

be noticed that some instants of jet flow belonging to the upper part of pulse cycle may cause the instantaneous uplifting of the jet, which would lead to the increased entrainment of near wall flow or a poorer wall coverage against cross-stream flow compared with the steady blowing situation. At  $\overline{M} = 1$ , the jet lifted-off further from the wall, and significant variation in velocity profiles across the steady flow situation is observed in Fig. 11d, e. At higher excitation of  $St = 0.5$ , the modification imposed on the flow do not have sufficient time to acquire the overall effects produced in one pulsation cycle, meanwhile the next period starts. Therefore, modifications produced in a particular period could not diffuse around a great deal within a given time span and so the effects are not fully established, see Fig. 11f. The resulting flow field exhibits a rippling jet trajectory with short pulsating span and a trend of frequent splitting (a case of high frequency excitation is described in the last part of manuscript). At  $\overline{M} = 1.25$ , as shown in Fig. 11g–i, the zone of variation across the highly uplifted steady flow profile is the one that is greater than all other cases for both  $St = 0.2$  and  $0.3$ . Also, the significant jet acceleration on the downstream side with higher injectant flow rate appears to be more detrimental at the instant, which lies on the upper part of the pulsation period. However, the combination of activities such as higher lift-off and the collapsing of jet at low frequency pulsation exhibits some interesting consequences on the far-end.

Figure 12a–d shows the distribution of flow Reynolds shear stress  $-2 \cdot \overline{uv}/\overline{U_\infty^2}$  at different times for  $\overline{M} = 1$  and  $St = 0.2$ . The contours seem to contain three different types of shear flow zones. The first one is due to the upper boundary of the jet and is negative; the second one is due to



**Fig. 11** Velocity profiles  $\bar{U}/\bar{U}_\infty$  with pulsation at  $x/D = 3.5$ . **a**  $\bar{M} = 0.65, St = 0.2$ , **(b)**  $\bar{M} = 0.65, St = 0.3$ , **(c)**  $\bar{M} = 0.65, St = 0.5$ , **(d)**  $\bar{M} = 1, St = 0.2$ , **(e)**  $\bar{M} = 1, St = 0.3$ , **(f)**  $\bar{M} = 1, St = 0.5$ , **(g)**  $\bar{M} = 1.25, St = 0.2$ , **(h)**  $\bar{M} = 1.25, St = 0.3$ , and **(i)**  $\bar{M} = 1.25, St = 0.5$

the lower boundary of the jet and is positive; and the last one, which originates from the near downstream location of the hole and also has negative shear stresses. The former is the wake flow region, which appears to shed downstream with a certain periodic variation of injectant flow rate. For the first instant at  $t/T = 0.19$ , the injection velocity is high and the overall jet body moves away from the wall and allows the development of a wake region under it. At  $t/T = 0.41$ , the jet trajectory bends down a bit due to initiation of the lower half of the pulsation period causing a reduction in injectant flow. Such bending toward the wall then triggers splitting of wake vortices. At  $t/T = 0.63$ , the wake structure moves further downstream and part of the

fluid with negative shear splits up followed by the splitting of the zone with positive shear. At the same time, flow at the hole exit begins to rise. At  $t/T = 0.86$ , the parts of fluid with positive and negative shears seem to move in succession down in the shedding zone.

In Fig. 13a–i, the variations in the flow field due to injectant flow pulsation are presented by the shear stress profiles at  $x/D = 3.5$  for the range of blowing ratio and Strouhal number considered. Figure 13a–c shows the variation in shear stresses at  $\bar{M} = 0.65$  for  $St = 0.2, 0.3$  and  $0.5$ . It can be observed that the variation along the vertical direction amplifies with an increase in  $St$ , especially for  $St = 0.5$ . The portion with negative stresses is considerably

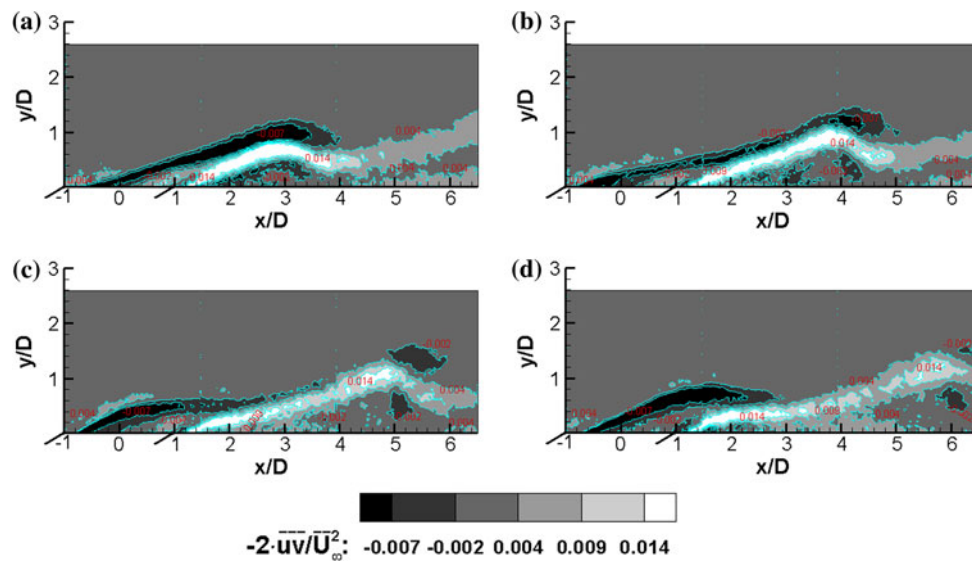


**Fig. 12** Reynolds shear stress distribution  $-2\overline{uv}/U_\infty^2$ ,  $\overline{M} = 1$ ,  $St = 0.2$ ; (a)  $t/T = 0.19$ , (b)  $t/T = 0.41$ , (c)  $t/T = 0.63$ , and (d)  $t/T = 0.86$

low for both  $St = 0.2$  and  $0.3$  and merely exists for  $St = 0.5$ . At  $\overline{M} = 1$ , Fig. 13d–f shows that the periodic variations with higher lift-off carry large influences in the shear affected zone compared with the previous case. At higher frequencies, the effect of pulsation is not fully established under short time duration of successive pulses and the resulting variation in shear stresses is comparatively low across the steady flow profile. The part of negative shearing stresses is particularly high for  $\overline{M} = 1.25$ , as shown in Fig. 13g–i. This is due to the slight shift in velocity profile at hole exit toward the upstream. Also, the ambit of spatial variation for shear stress is even larger for the range of  $St$  considered. These effects make the jet highly unstable due to high lift-off and jet movement in larger span under low pulsing condition could easily lead to an early break down. However, broken jet with higher momentum of fluctuating velocity component established at jet boundary is able to bring some part of injectant flow in the near-wall region in following the periodic variation of jet trajectory and increases the presence of injectant flow on average basis compared with the steady blowing. As one can expect that the shear stresses can play a dominant role in the mean momentum transfer by turbulent motion from the jet boundary.

Figure 14a–d shows the relative importance of normal stresses in different sections of the flow field formed at  $\overline{M} = 1$  and  $St = 0.2$  by presenting a ratio of the RMS quantities of velocity fluctuation  $R' = \sqrt{\overline{u^2}}/\sqrt{\overline{v^2}}$ . This term generally gives an idea of global isotropy/anisotropy in a given flow. The contour plot seems to indicate three different zones of increased importance in the flow field. The first one is the zone containing a part of upstream flow

and the upper and lower jet boundary with a magnitude greater than one,  $\sqrt{\overline{u^2}} > \sqrt{\overline{v^2}}$ ; second one constitutes the inner part of jet where values are less than one,  $\sqrt{\overline{u^2}} < \sqrt{\overline{v^2}}$ ; and the third zone lies below the jet in the wake region again with values less than one. At the first instant,  $t/T = 0.19$ , the zone of the jet core dominated by the normal component  $\sqrt{\overline{v^2}}$  appears to extend in the downstream direction with accelerating jet. The part of flow lying below the jet also with  $\sqrt{\overline{u^2}} < \sqrt{\overline{v^2}}$  seems to emerge just after the emergence of the jet and lasts until its splitting in following the induced periodic variation of injectant flow. At  $t/T = 0.41$ , the jet starts to bend toward the wall and the development of the flow in the downstream side brings the zones of low stress ratio close to each other in the near wall region. As the development of the wake slightly lags the growing of the jet in the downstream flow, so there is a part of jet with low streamwise stresses, which moves a bit ahead of the point where the flow from two different regions with low streamwise stresses meet. Such movement is also visible in later instants  $t/T = 0.63$  and  $0.86$ . The sequence of images shows that splitting of the wake occurs due to a reversing of the lift-off event, while for jet, at reinitiation after the falling of injectant flow rate. The stresses in the wall region lying on the downstream side of the hole seem to be dominated by streamwise stresses and also appear to move in accordance with the variation in the jet due to induced pulsation. It can be noticed that the pulsing of injectant with a mean blowing ratio leading to separation is able to reorient the injectant close to the wall during the lower part of pulsing cycle.

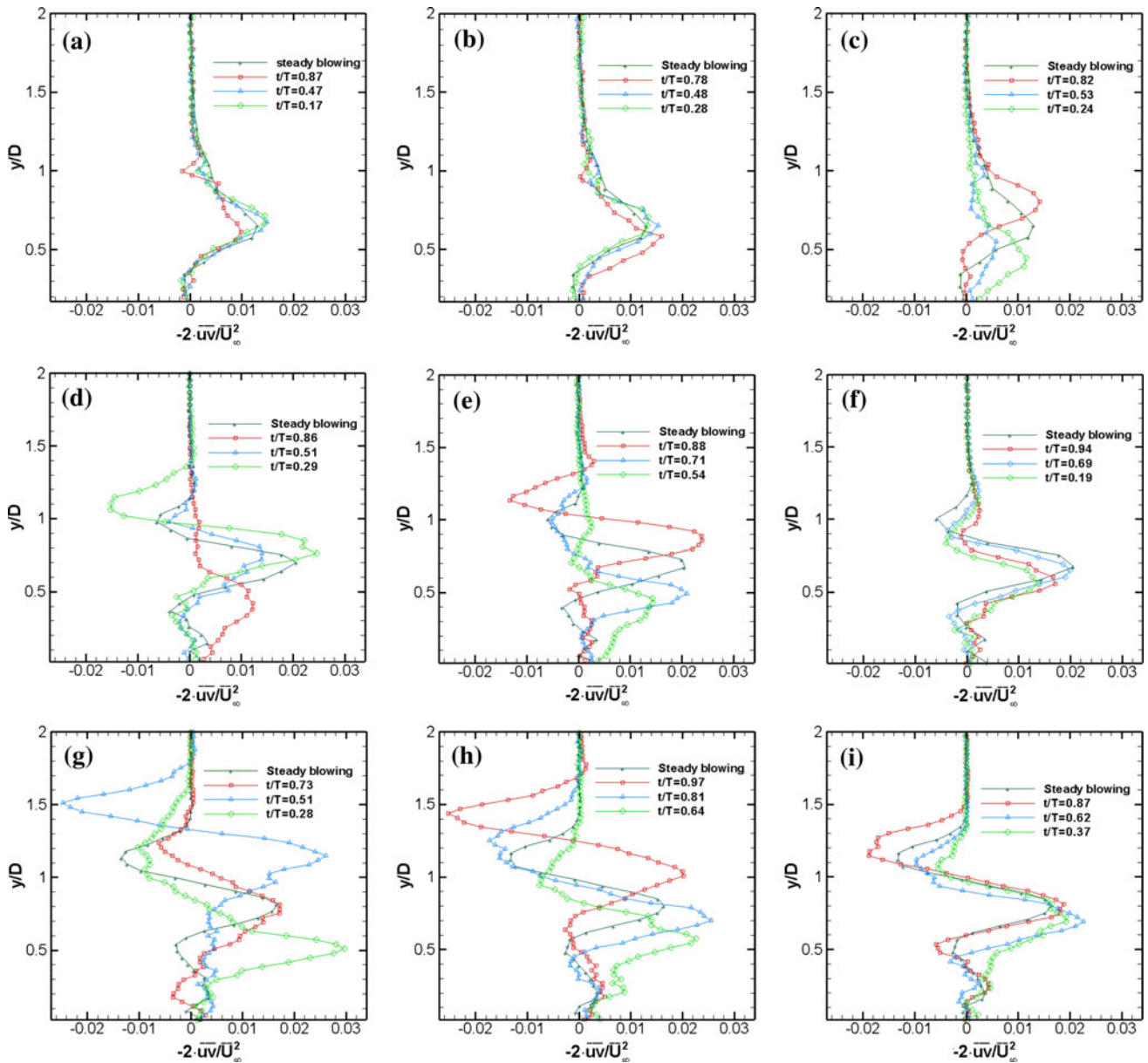


**Fig. 13** Reynolds shear stress profiles  $-2\bar{uv}/U_\infty^2$  with pulsation at  $x/D = 3.5$ , (a)  $\bar{M} = 0.65$ ,  $St = 0.2$ , (b)  $\bar{M} = 0.65$ ,  $St = 0.3$ , (c)  $\bar{M} = 0.65$ ,  $St = 0.5$ , (d)  $\bar{M} = 1$ ,  $St = 0.2$ , (e)  $\bar{M} = 1$ ,  $St = 0.3$ , (f)  $\bar{M} = 1$ ,  $St = 0.5$ , (g)  $\bar{M} = 1.25$ ,  $St = 0.2$ , (h)  $\bar{M} = 1.25$ ,  $St = 0.3$ , and (i)  $\bar{M} = 1.25$ ,  $St = 0.5$

The contours of vorticity distribution along the width of injection plate are shown for  $\bar{M} = 1.25$  and  $St = 0.5$  in Fig. 15a–d. These results are included to show the detrimental aspect of pulsation under higher Strouhal number conditions for a separated jet. It can be observed that the different zones with pertinent vorticity are consistent with the previous discussion as the variation in upper and lower jet boundary and the zone of wake evolve in a similar way, except for the variations leading to collapsing of the jet, which appear to take place much more rapidly. The trajectory of injectant in the downstream direction shows

small rippling effects as the adjacent pulsation cycles do not allow the flow to establish fully on the periodic effects. The zone of dominant vorticity lies on the lower jet boundary and appears to sustain longer under jet pulsation. These effects promote the mixing rate locally and drive them out to influence the flow in the near wall region. The distribution of injectant on the downstream side in such cases is less effective in terms of wall coverage as the coolant trajectory with frequent feeding of broken jet contents in downstream flow always seem to orient away from the wall.

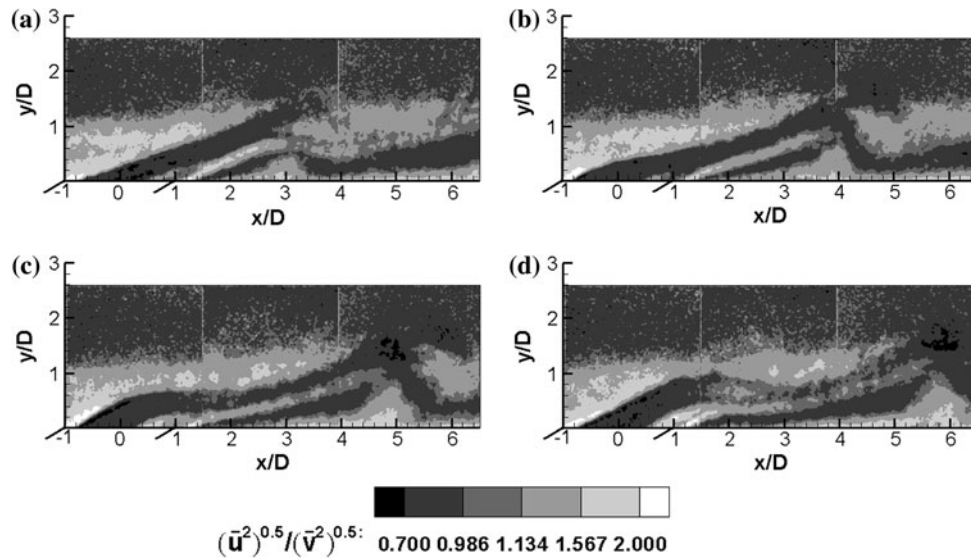


**Fig. 14** Distribution of Reynolds normal stress ratio  $\sqrt{\bar{u}^2}/\sqrt{\bar{v}^2}$ ,  $\bar{M} = 1$ ,  $St = 0.2$ ; (a)  $t/T = 0.19$ , (b)  $t/T = 0.41$ , (c)  $t/T = 0.63$ , and (d)  $t/T = 0.86$

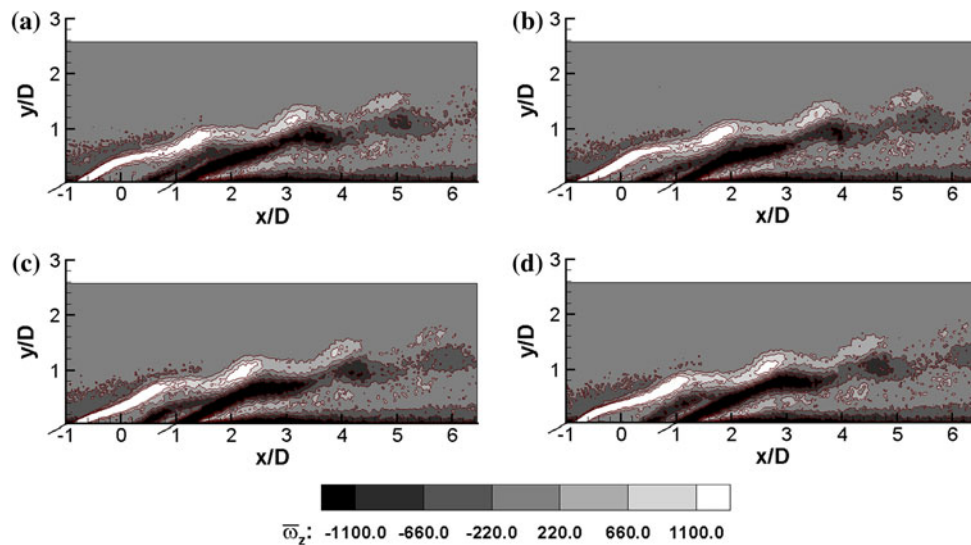


**Fig. 15** Vorticity distribution  $\bar{\omega}_z$ ,  $\bar{M} = 1.25$ ,  $St = 0.5$ ; (a)  $t/T = 0.25$ , (b)  $t/T = 0.5$ , (c)  $t/T = 0.75$ , and (d)  $t/T = 1.0$

### 4 Conclusion

The current investigation has shown that jet pulsation results in a complex distribution of both averaged phase-instant velocity and Reynolds stress components in the flow field. The flow field exhibits that periodic forcing and lift-off attributed to large spatial variations in jet trajectory, which leads to events like: jet splitting and shedding of the wake. It was observed that jet splitting under induce pulsation causes the flow in the wake region to shed in succession. The study has shown that pulsation brings some improvement in wall coverage only at higher blowing

ratios and low frequency of excitation, where the injectant propagating with periodically varying trajectory could bring part of injectant flow in close proximity to the wall and improved injectant coverage compared with steady blowing. At  $\bar{M} = 0.65$ , pulsation at  $St = 0.5$  was found particularly detrimental for wall coverage compared with steady blowing conditions, because in this situation, flow of the injectant over the wall is no longer continuous, and the smooth distribution of coolant is significantly compromised. At  $\bar{M} = 1$  and  $1.25$ , the low frequency shedding has ample time to readjust jet position in the near wall region following the downstream variation of jet trajectory.

However, at higher pulsation rates, jet variations due to back-by-back cycles of excitation and continuous induction of early jet splitting direct the jet flow away from the wall.

The physics of the flow can be further unveiled after the future investigation of thermal aspects of the flow field by using the technique of infra-red thermography for determining the parameters of wall coverage and a cold-wire survey for analyzing mixing of two flows interacting with a slight temperature difference.

## References

- Andreopoulos J (1983) Heat transfer measurement in a heated jet-pipe flow issuing into a cold cross stream. *Phys Fluids* 26:3201–3210
- Andreopoulos J (1985) On the structure of jets in a crossflow. *J Fluid Mech* 157:163–197
- Benedict LH, Gould RD (1996) Towards better uncertainty estimates for turbulence statistics. *Exp Fluids* 22:129–136
- Bons JP, Rivir JB, Mac Arthur CD, Pestian DJ (1996) The effect of unsteadiness on film cooling effectiveness. Wright Laboratory, WL-TR-96–2096
- Brundage AL, Plesniak MW, Ramadhyani S (1999) Influence of coolant feed direction and hole length on film cooling jet velocity profiles. International gas turbine and aeroengine congress and exhibition, June 1999, Indianapolis, Indiana
- Burd SW, Kaszeta RW, Simon TW (1996) Measurement in film cooling flows: hole L/D and turbulence intensity effects. Gas turbine heat transfer session, 1996 IMECE conference, Atlanta, GA
- Dorignac E, Vullierme JJ, Deniboire P, Foucault E, Bousgarbies JL (1992) Thermographie Infrarouge et tomographie laser appliqués à l'étude des films de refroidissement. 5ème colloque national de visualisation et de traitement d'images en mécanique des fluides, pp 2–5 Juin 1992, Poitiers
- Dorignac E, Vullierme JJ, Delouche E, Garem JH, Leblanc R (1993) Blowing rate effects on the heat transfer coefficient on a film heated surface at transonic speed. In: Proceedings of the international symposium on experimental and computational aerodynamics of internal flow, July 12–15 1993, Prague
- Eckert ERG (1970) Gas-to-gas film cooling. Published in *Inzhenerno-Rizicheskii Zhurnal*, SpringerLink, 19:426–440
- Eriksen VL, Goldstein RJ (1974) Heat transfer and film cooling following injection through inclined circular tubes. *ASME J Heat Transf* 96:239–245
- Foucault E, Deniboire P, Bousgarbies JL, Vullierme JJ, Dorignac E, (1992) Etude expérimentale du transfert de chaleur près d'une paroi plane chauffée en présence d'injection multiples (Ecoulement subsonique). Heat transfer and cooling in gas turbine, AGARD-CP-527, p 4
- Goldstein RJ, Eckert ERG (1974) Effects of hole geometry and density on three-dimensional film cooling. *Int J Heat Mass Transf* 17:595–607
- Kartuzova O, Danila D, Ibrahim MB (2009) Computational simulation of cylindrical film hole with jet pulsation on flat plates. *AIAA J Propul* 6(25):1249–1258
- Kelso RM, Lim TT, Perry AE (1996) An experimental study of round jets in cross-flow. *J Fluid Mech* 306:111–144
- Kim J, Moin P, Moser R (1987) Turbulence statistics in fully developed channel flow at low Reynolds number. *J Fluid Mech* 177:133–166
- Lee SW, Lee JS, Ro ST (1994) Experimental study on the flow characteristics of streamwise inclined jets in crossflow on flat plate. *ASME J Turbomach* 116:97–105
- Ligrani PM, Ciriello S, Bishop DT (1992) Heat transfer, adiabatic effectiveness, and injectant distribution downstream of a single row and two staggered rows of compound angle film cooling holes. *ASME J Turbomach* 114:687–700
- Ligrani PM, Gong R, Cuthrell JM (1996a) Bulk flow pulsations and film cooling-I: injectant behavior. *Int J Heat Mass Transf* 39:2271–2282
- Ligrani PM, Gong R, Cuthrell JM (1996b) Bulk flow pulsations and film cooling-II: flow structure and film effectiveness. *Int J Heat Mass Transf* 39:2283–2292
- Ligrani PM, Gong R, Cuthrell JM, Lee JS (1997) Effects of bulk flow pulsations on film-cooled boundary layer structure. *ASME J Fluids Eng* 119:56–66
- Marek CJ, Tacina RR (1975) Effect of free-stream turbulence on film cooling. NASA technical note, NASA TN D-7958
- Moussa ZM, Trischka JW, Eskinazi S (1977) The near field in the mixing of a round jet with a cross-stream. *J Fluid Mech* 80:49–80
- Muldoon F, Acharya S (2009) DNS study of pulsed film cooling for enhanced cooling effectiveness. *Int J Heat Mass Transf* 52: 3118–3127
- Pietrzyk JR, Bogard DG, Crawford ME (1989) Hydrodynamic measurement of jets in crossflow for gas turbine film cooling application. *ASME J Turbomach* 111:139–145
- Rutledge JL, King PI, Rivir R (2009) CFD prediction of the frequency dependence of pulsed film cooling heat flux on a turbine blade leading edge. In: Proceedings of the 47th AIAA aerospace sciences meeting, Jan 2009, Orlando. AIAA paper 2009–0680
- Sargison JE, Guo SM, Oldfield MLG, Lock GD, Rawlinson AJ (2002) A converging slot-hole film-cooling geometry. Part I: low-speed flat plate heat transfer and loss. *ASME J Turbomach* 124: 453–460
- Seo HJ, Lee JS, Ligrani PM (1998) The effect of injection hole length on film cooling with bulk flow pulsation. *Int J Heat Mass Transf* 41:3515–3528
- Sinha AK, Bogard DG, Crawford ME (1991) Gas turbine film cooling: Flowfield due to a second row of holes. *ASME J Turbomach* 113:450–456
- Walters DK, Leylek JH (2000) A detailed analysis of film cooling physics. Part I: streamwise injection with cylindrical holes. *ASME J Turbomach* 122:102–111
- Yuen CHN, Martinez-Botas RF (2003) Film cooling characteristics of a single round hole at various streamwise angles in a crossflow. Part I: effectiveness. *Int J Heat Mass Transf* 46:221–235



---

---

---

## **Résumé**

Le refroidissement par film froid consiste à refroidir une paroi en injectant un écoulement froid pour protéger celle-ci. Un banc d'essai simplifié d'une configuration d'étude de « film cooling » a été réalisé pour caractériser l'influence d'un écoulement chauffé et pulsé provenant d'un trou cylindrique incliné à 30° dans un écoulement principal thermiquement uniforme. Les taux de soufflage ( $\overline{M}$ ) étudiés sont égaux à 0,65, 1 et 1,25. Les pulsations ont été générées par un haut-parleur à des fréquences de pulsation adimensionnalisées ( $St$ ) de 0, 0,2, 0,3 et 0,5. Les aspects aérodynamiques et thermiques de l'écoulement ont été étudiés, en utilisant des techniques de mesure avancées incluant la P.I.V. résolue en temps, la thermographie infrarouge, la vélocimétrie fil-chaud et la thermométrie fil-froid. Pour  $\overline{M} = 0,65$ , sans pulsation, l'écoulement injecté couvre une partie importante de la paroi. Dans le cas pulsé, cette distribution optimale est considérablement dégradée quelque soit la fréquence de pulsation. Pour  $\overline{M} = 1$  et 1,25, sans pulsation, on observe un décollement de l'écoulement qui dégrade la protection film de la paroi. Dans ces cas, la pulsation induit de grandes variations spatiales à la fois de la trajectoire, de l'éclatement du jet et du passage des structures turbulentes dans le sillage de jet à cause de la variation périodique du débit de jet. On a constaté que la pulsation améliore la protection de la paroi pour des excitations de basse fréquence pour des taux de soufflage important ( $\overline{M} = 1$  et 1,25).

## **Abstract**

A test rig incorporating injection from a single cylindrical hole inclined at 30° to a thermally uniform mainstream flow was used to study the effects of injectant pulsation in film cooling configuration. The average blowing ratio ( $\overline{M}$ ) were 0.65, 1 and 1.25. The periodic variations in injectant flow were rendered by a loudspeaker based pulsation system to non-dimensionalized excitation frequency ( $St$ ) of 0, 0.2, 0.3 and 0.5. Both aerodynamic and thermal aspects of the flow were studied, using the advanced measuring techniques incorporating the system of Time-resolved PIV, Infrared thermography, Hot wire and cold wire. Pulsation cases resulting in a close-wall orientation of injectant fluid compared to steady blowing bearing outward orientation were only observed in few cases. At  $\overline{M} = 0.65$ , jet fluid remains aligned and covers a significant part of the wall under steady blowing. However, under the cases of pulsation that optimum distribution of coolant is significantly compromised. At higher blowing ratios, the injectant lift-off degrades the film protection of the wall. Pulsation under these cases induces large spatial variations in the jet trajectory, collapsing of the jet body and the shedding of wake structures due to the periodic variation of injection flow rate. It was found that the pulsation improves wall coverage of the injectant fluid under low frequency excitation as the separation of the jet from the wall becomes evident ( $\overline{M} = 1$  and 1.25).

## **Mots clés**

- Convection forcé
  - Refroidissement / chauffage
  - Turbulence
  - Efficacité de film
  - TR-PIV
  - Thermographie IR
  - Fil chaud
  - Fil froid
-